The Numerical Modelling Of Scenarios For The Herbig-Haro Object HH30

A thesis submitted for the degree of
Doctor of Philosophy

by

Chris Lynch

School of Physical Sciences

University of Kent
Canterbury
U.K

November 2017
Word Count: 52,624

Declaration

This thesis has not been submitted as an exercise for a degree at any other university.

Except where stated, the work described therein was carried out by me alone.

I give permission for the Library to lend or copy this thesis upon request.

SIGNED:

Dedicated to
Anna and Alice

Acknowledgements

Firstly, I wish to thank my primary supervisor, Prof. Michael Smith, for all of his guidance, support and insight during my PhD. He has always had time to give advice and assistance whenever it has been needed and his help has been invaluable.

I also wish to thank my secondary supervisor Dr. Jinqqui Miao for her support over the course of my doctoral studies.

I would also like to acknowledge the general help and assistance of Dr. Dirk Froebrich whose advice and insights never fail to enlighten.

I am very grateful to the Science and Technologies Facilities Council (STFC) for awarding me a scholarship without which I would not have been able to pursue my research. I must also give a mention to Prof. Martin Hendry of the University of Glasgow, who hosted the STFC Introductory Summer School in 2010, which was a wonderful kick-start to my PhD studies.

I would also like to acknowledge the support of the South East Physics Network (SEPnet) who provided many useful resources, especially access to the SCIAMA HPC facility at the Institute of Cosmology and Gravitation in Portsmouth. On that note, a personal thanks to Gary Burton who manages that facility and who has provided frequent assistance.

Use of ZEUS-3D, developed by D. Clarke at the ICA (http://www.ica.smu.ca) with support from NSERC, is acknowledged; and thanks go to Gerhard Suttner for the use of his enhanced chemistry and cooling routines.

Additional thanks go to everyone at the University of Kent Centre for Astrophysics and Planetary Science who supported and encouraged me in my studies and research. There are too many to mention but specially noted and in no particular order are Tim Kinnear, Michael Knight, Jonathan Talbot, Dave Pickup, Joe Mist, Michael Woods, Andy Morris, Agata Makiela, Mark Price, Jodie Smith, Paul Butler, Anne Buckner, Ryan Laird, and George Ionnadis. Others too, who I am sure I have forgotten to mention, but who assisted me in small but significant ways. It is not an easy thing to embark on a doctorate when well advanced into one's fourth decade, after a lengthy absence from academia; but you all helped to make the journey a little less daunting.

In the tradition of saving the best until last, I must mention the friends and family members without whose support and belief in me this accomplishment, such as it is, would have been quite impossible. My father, Robert Lynch, who has always been a ready listener and whose own eagerness for lifelong learning provided me with a role model; my mother and stepfather, Janet and Andy Todd, both taken from us much too soon, and whose sudden loss led to much thinking about the importance of a life lived well; also, a certain group of long-serving and supportive friends who meet on certain nights to perform arcane rituals in a cellar involving regular polyhedrons, the less said about that the better perhaps; and Mick Laing of the Milites de Bec, one day you said to me 'You've got to go for your dreams' so this is all your fault!

And finally, the most heartfelt and profound thanks of all go to my long-suffering wife and daughter, Anna and Alice, whose love, patience, tolerance and words of encouragement have sustained me; and especially, their tolerance for my lengthy conversational diversions on the subject of Astrophysical Jets, which were perhaps not the ideal subject matter for a family discussion over breakfast.

Summary

Protostellar Jets offer an observational window into the births of stars. The characteristics of these jets may tell us something of the nature of the originating objects and the processes that govern their evolution.

The classical T-Tauri star HH30 in Taurus-Auriga exhibits a well-collimated plume of hot, optically-emitting atomic and partially ionised Hydrogen, and also a colder, dense, wide-angle molecular Hydrogen ouflow. Observations suggest HH30 is a binary system system, surrounded by a circumbinary accretion disc. We investigated the propagation and interaction of dual atomic and molecular outflows from HH30, using a series of numerical simulations with parameters informed by observational campaigns. These 3-dimensional models were computed using the established Eulerian astrophysics code ZEUS-MP, with in-house modifications and an enhanced chemistry and cooling module. These simulations assumed off-domain launch and tracked the evolution of the jets over spatial scale of $\sim$ 100 AU, and with a timescale $\sim$ 100 - 200 years. The propagation in this region is of special interest, as this is where the greatest difference between the two scenarios is likely to emerge. Our work here differs from 'classical' simulations of jet propagation by virtue of one or both outflow sources moving in an orbit.

Two competing scenarios were investigated, in which the morphology of the light-year scale outflow from HH30 is explained by different kinds of motion of the atomic outflow source, and in which the launch site of the molecular outflow differs. In both cases a velocity-pulsed atomic jet emerges from the more massive binary object. In the Orbital scenario, the orbital motion of the primary explains the morphology seen at large scale, while the molecular flow is launched from the secondary partner; in the Precessional scenario, precession of the primary dominates the morphology, while launch of the molecular flow is from the inner edge of the circumbinary disc. The binary orbit and inner depletion zone of the circumbinary disc differs between the scenarios, with the Precessional scenario having a much smaller orbit and correspondingly reduced inner depletion zone.

Control simulations were also carried out in which only the atomic jet was present.

Clear structural differences emerge between the models that include molecular wind, versus their atomic-only counterparts. The Orbital dual-outflow case is characterised by the formation and destruction of low-density voids and lateral flaring of ionised material, producing dramatic H-α lobes that spread outwards from the main jet column. In the Precessional case, whether single or dual-outflow, it is evident that strong ionisation is occurring in the jet periphery originating close to the jet inlet. The smaller-orbit jet of the Precessional model results in a continual ionisation shock on the jet periphery, stronger than internal shocks arising from the velocity signal, which then propagates downstream, resembling a screw-thread of ionisation wrapped around the jet; suggesting that this may be a feature of jets launched from close or contact binary protostars.

We compare the effects of the two different kinds of perturbing molecular outflow on the faster atomic jet; position, velocity, line mass per unit length, temperature and other variables, as a function of distance x (AU) from the binary source. Linear and quadratic fit functions are determined to facilitate comparison with observation. These quantify the expected behaviours of the atomic jet in the presence of the two different kinds of molecular flow. Where the fit function domains overlap direct comparisons may be drawn; where $26 < x < 42$ AU, the average velocity as a function of distance is $V_x(x) = (1.39 \times 10^{-1} \pm 2.15 \times 10^{-3})x + (246.82 \pm 1.29)$ km s^{-1} in the Precessional model, while in the Orbital model we find $V_x(x) = (-3.26 \pm 0.26)x + (269.57 \pm 6.75)$ km s^{-1}. In the region $10 < x < 60$ AU, the Precessional model has temperature dependence $T(x) = (64.53 \pm 12.54)x + (3535 \pm 330)$ K. Whilst in the same region of the Orbital model, $T(x) = (401.99 \pm 333.19)x + (4258.4 \pm 1340.3)$ K.

Using code written in-house to calculate emission using rate coefficients for photon production, we generated synthetic observations; spatially resolved images, velocity channel maps and position-velocity diagrams. We find the morphology of the synthetic emissions from the two scenarios when compared to HST R-band imaging of HH30 suggests that the Orbital case is unlikely, whilst the Precessional case is supported.

Finally we present mass-velocity spectra, to investigate ways in which the presence of one or other type of molecular outflow alters the spectra, creating a distinct signature. The shallow-angle spectra matching the aspect angle of HH30 itself are examined and the link between outflow scenario and time variability discussed. Spectra from the same dual outflow systems observed at different aspect angles to the sky plane are given, to provide a means to confirm these senarios in other HH30-like T-Tauri stars.

Contents

List of Tables

List of Figures

Publications

A list of publications resulting from work presented in this thesis is given below.

In Preparation

Lynch, C. and Smith, M. D. Numerical simulations of the development and propagation of co-orbital and circumbinary jets and winds from young stars. I Evolution of physical properties

Lynch, C. and Smith, M. D. Numerical simulations of the development and propagation of co-orbital and circumbinary jets and winds from young stars. II Analysis of observable signatures

Lynch, C. and Smith, M. D. Numerical simulations of the development and propagation of co-orbital and circumbinary jets and wiunds from young stars. III Atomic and molecular imaging

Chapter 1

An Overview of Star Formation

1.1 The Seven Stages of Low-Mass Star Formation

We will begin by examining the star formation process, and thereby identify when, in this process, we expect to observe protostellar jets, and how we expect jet characteristics to vary as the Young Stellar Object evolves into a Zero Age Main Sequence star. It should first be emphasised that the seven stage model is not delineated by any sharply defined boundaries in the natural behaviour of the objects in question, which evolve as a graduated continuum; rather, it is a human convenience, a means of classifying observations and describing the process in a stepwise fashion.

The seven stage process outlined here is only accepted as a description of how the majority of low-mass ($M_\star < 8M_\odot$) stars form (Smith, 2004)(100). The mechanism by which higher mass stars form is still the subject of debate as it seems likely that they form in a different manner to low-mass stars.

1.2 Stage 1: Molecular Clouds

Star formation occurs within massive clouds of cool, dense molecular Hydrogen gas. These cloud complexes were first discovered in the 1970s by sky surveys of CO molecular transitions such as the 2.6 mm rotational line of $^{12}C^{16}O$, in the vicinity of HII regions and infrared sources. It is estimated that around 80% or more of the molecular hydrogen

in the Milky Way galaxy is contained in such clouds, which are also permeated by dust grains which act as catalysing sites for the formation of H_2. (Smith, 2004)(100)

The factories of star assembly are the Giant Molecular Clouds (see Fig.1.1). These massive cloud complexes may contain upwards of 10^6 $M_\odot$ of material. Their mass aside, they differ from other, more diffuse types of galactic cloud by virtue of being held together by their own internal gravity rather than the external pressure of a hotter, lighter surrounding medium. (Stahler & Palla, 2011)(109)

Based on surveys of the ages of the young stellar populations within, GMCs might typically survive for $\sim 3 \times 10^7$ years before being dispersed by winds and ionising radiation from hot O and B type stars. Other methods based on measurements of molecular abundances suggest a lifetime of only 10^6 years (Larsen, 2003). The general picture that emerges is that these clouds are not much longer-lived than the stars they form.

Table 1.1 lists some of the distinguishing features of GMCs, compared to other types of interstellar cloud. Molecular cloud densities average around 10^{-21} g cm^{-3}, around 1000 times greater than the average ISM density, and with an average temperature lower than that of the Cold Neutral ISM by a factor of 5.

In order for a molecular cloud to form, it is first necessary for an accumulation of mainly atomic Hydrogen to gather, possibly as the result of a density wave that sweeps up material in the galactic disk. A sufficiently large, dense accumulation of material provides a self-shielding effect against ionising UV radiation from massive O and B stars in the neighbourhood. A Photo-Dissociation Region forms in the outer layers of the cloud, which absorbs incident Extreme UV photons. Molecules and even atoms cannot survive

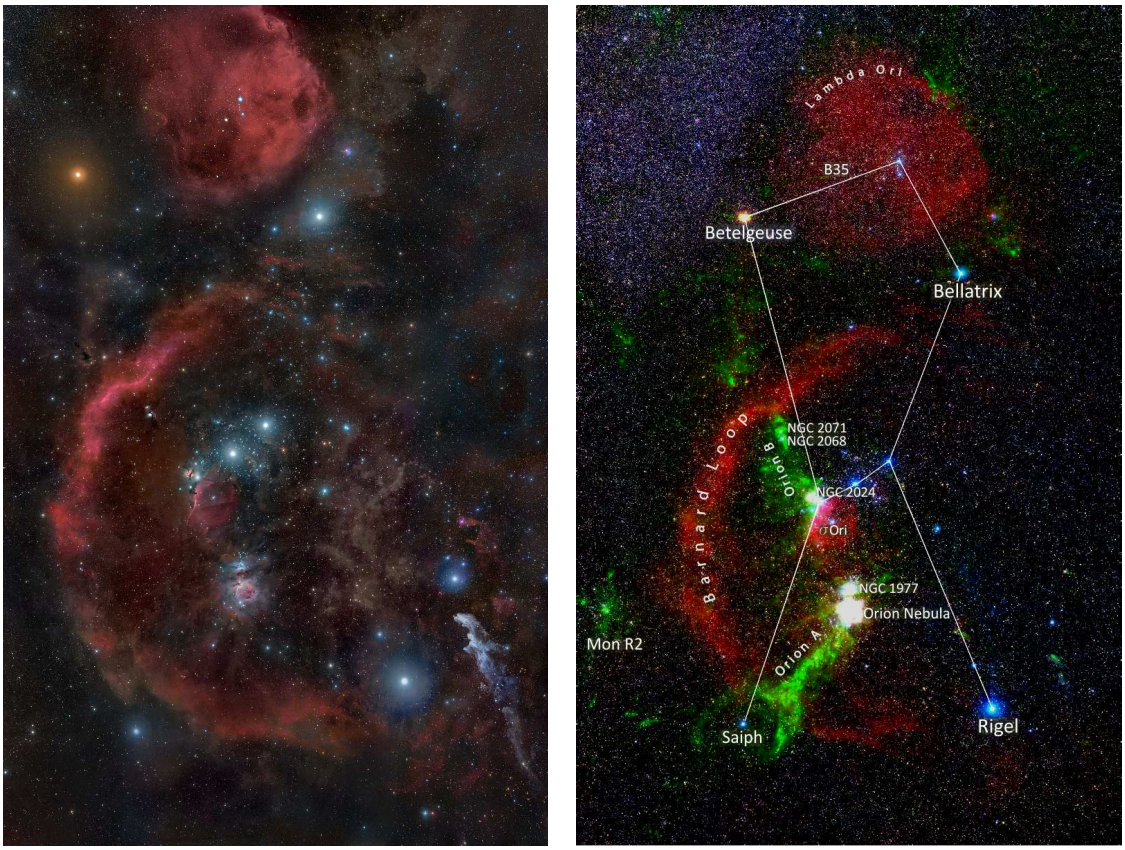

(a) Optical with enhanced H-α (b) Optical with K-Band Extinction (green)

Figure 1.1: Two composite images of the Orion constellation showing the surrounding nebulas of the Orion Molecular Cloud complex. (a) image made by Rogelio Bernal Andreo in October 2010, a mosaic of broadband optical images with additional R-band filter imaging providing enhancement of 656nm H-α emission (red, true colour) produced by HII regions. (b) image with annotation produced by Marco Lombardi, using base optical image by Wei-Hao Wang, IfA, University of Hawaii; with superimposed false colour K-band extinction map compiled from 2MASS data, showing clouds of molecular Hydrogen in green. Additional contrast enhancement has been applied.

Image credit: Image (a) featured at http://apod.nasa.gov/apod/ap101023.html used under a Creative Commons Attribution-ShareAlike 3.0 Unported license, details at https://creativecommons.org/licenses/by-sa/3.0/deed.en Image (b) reproduced from Lombardi M., Alves J., & Lada C. J., A&A 535, A16, 2011 DOI: 10.1051/0004-6361/201116915

in this boundary layer. Further into the cloud, longer wavelength Far UV photons with energies of below 13.6eV can penetrate and dissociate molecules and ionise some heavier atoms such as Carbon. Deeper still beyond this atomic envelope is an interior region where molecular Hydrogen may form and survive.

Dust grains, composed mainly of silicon and carbon compounds, serve as important coolants; collisions with gas atoms and molecules produce lattice vibrations which decay by emission of IR photons (Stahler & Palla, 2011)(109). It has also long been thought that dust grain surface catalysis plays a significant role in the formation of H_2 molecules (Hollenbach, Salpeter, 1971). Formation of H_2 also cools the cloud as the dust grains absorb the liberated binding energy and re-radiate as infra-red. These longer wavelength photons are able to pass through the cloud and carry energy away.

Table 1.1: Physical Properties of Molecular Clouds

Cloud Type	A_V (mag)	n_{tot} (cm^{-3})	L (pc)	T (K)	M ($M_\odot$)	Examples
Diffuse	1	500	3	50	50	ρ Ophiuchi
Giant Molecular Clouds	2	100	50	15	10^5	Orion
Dark Clouds						
Complexes	5	500	10	10	10^4	Taurus-Auriga
Individual	10	10^3	2	10	30	B1
Dense Cores / Bok Globules	10	10^4	0.1	10	10	TMC-1/B335

(Table reproduced from Stahler & Palla, 2011)(109))

1.3 Stage 2: Turbulent Fragmentation

Simple classical theories of gravitational collapse suggest that a large homogenous cloud above a certain mass M_J, the *Jeans Mass*, contained within a diameter λ_J, the *Jeans Length*, will undergo gravitational collapse from an initial state of hydrostatic equilibrium when subject to perturbation (Jeans, 1928).

$$M_J = \frac{\pi}{6}\rho_0\lambda_J^3 \tag{1.1}$$

$$\lambda_J = \left(\frac{\pi a^2}{G\rho_0}\right)^{1/2} \tag{1.2}$$

p_0, ρ_0 are initial pressure, density and $a = \sqrt{p_0/\rho_0}$ is the isothermal sound speed.

But since we do not see stars with millions of solar masses, it cannot be the case that an entire Giant Molecular Cloud can collapse to form a single star. Hoyle (1953) suggested a solution; both the Jeans Mass and Jeans Length are dependent on the inverse square root of density, so if the cloud collapses isothermally, as the density increases the Jeans Mass and Length decrease, thus leading to sub-regions of the collapsing cloud undergoing their own independent collapse; leading to a hierarchical fragmentation of the original large cloud and the formation of many stars (see Fig.1.2).

Modern observations have revealed Molecular Clouds to be far from tranquil environments, but rather, regions that are significantly disturbed by supersonic turbulence (e.g. Heyer & Brunt, 2007). Turbulent flow is characterized by a hierarchy of scales that transports kinetic energy down from a large scale, anisotropic flow, to smaller scale flows characterised by chaotic changes in velocity and direction. The most abundant source of this turbulence is likely to be supernova explosions, dissipating 3 x 10^{-26} erg cm^{-3} s^{-1} in our galaxy based on an estimate of 1 supernova explosion per 50 years. Jets and outflows from young stars formed within the clouds themselves are also likely to be suppliers of turbulent energy, but their rate of energy dissipation is estimated to be weaker than supernovae by around 2 orders of magnitude (Mac Low & Klessen, 2004).

Far-infrared and submillimetre observations by the SPIRE (Griffin et al., 2010)(38) and PACS (Poglitsch et al., 2010)(82) instruments of the Herschel space observatory have

contributed to the advancement of a filament-based theory of star formation. Filaments harbouring dense pre-stellar cores and candidate Class 0 protostars have been revealed in molecular clouds in the Serpens-Aquila Rift, and the Core Mass Function (CMF) has been found to closely resemble the stellar Initial Mass Function (IMF) (André et al., 2010)(6). A majority of bound prestellar cores in Aquila are found in supercritical filaments, where the mass per unit length of the filament M_{line} is greater than the unmagnetised critical line mass for gravitational collapse $M_{line,crit}^{unmag} = 2{c_s}^2/G$, where c_s is the isothermal sound speed (Inutsuka & Miyama, 1997)(51). Filaments are also seen in more diffuse, non star-forming clouds such as the Polaris Flare region in Ursa Minor, demonstrating a star-formation path beginning in the diffuse ISM. (André et al., 2010)(6)

Recent simulations of molecular cloud evolution using various combinations of physics found that MHD turbulence was an essential ingredient to explain the widths of filaments, finding a near-universal width of 0.10 ± 0.02 pc which closely agrees with the Aquila and Polaris observations; the column density of the star-forming Aquila filaments being greater than those in the non star-forming Polaris but the width being approximately similar. A theory of the scaling of supersonic MHD turbulence suggests that this universal filament width corresponds to the transitional scale at which turbulence becomes subsonic in molecular clouds. (Federath, 2016)(29)

1.4 Stage 3: Prestellar Core

We must now consider the physics of a clump of prestellar material undergoing gravitational contraction to become a protostar. The simplest model excludes the effects of clump rotation, internal turbulent motion, magnetic fields, and ambipolar diffusion (see Fig.1.2). We will also assume no outward pressure holding up the collapse and no interactions between particles other than gravitational forces.

Let us take a spherical homogeneous cloud of radius R exactly satisfying the Jeans criteria given in equations 1.1 and 1.2, and then allow it to be perturbed from its equilibrium state so that it begins to fall inwards. Given a cloud of mass M, an expression for the free-fall time t_{ff} for a small element of fluid of mass $m << M$ to fall under gravity to the centre of the cloud from a distance R may be derived as follows:

Consider the trajectory of m as an elliptical orbit about the centre of mass of the cloud, and let the orbital eccentricity $e = 1$ - i.e. a degenerate ellipse with a semi-minor axis length of zero and semi-major axis $R/2$; it is really just a straight line connecting two points separated by a distance R. As our fluid element m moves through the apsides of this degenerate orbit it theoretically executes a 'hairpin turn' and returns back along its approach path (if it were somehow permitted to complete an orbit - which will not be the case).

Now M is very much larger than m, hence the centre of mass of M remains approximately stationary at one focus of this ellipse. But because of its extreme eccentricity, the foci of the ellipse are actually coincident with the ends of the line, and so the centroid of M is situated at one of these. At this point we note that, as m falls towards the centre of M, at the same time the whole of M is also collapsing in upon itself, and if we think of M as being constructed of concentric spherical shells of matter, the outer shells of material will not overtake the inner shells as they fall; thus the total material contributing to the gravitational force on the element m does not alter during the collapse, and so M may be represented throughout m's motion by a point mass at the end of the line opposite to the starting point of m.

We now apply Kepler's Third Law to this degenerate elliptical orbit, since the free-fall time of m from apapsis $\rightarrow$ periapsis is simply given by one-half of the full orbital period. And so, given that $M >> m$, we find:

$$t_{ff} \sim \frac{R^{3/2}}{\sqrt{GM}} \tag{1.3}$$

and thus it follows that the average free-fall velocity will be:

$$V_{ff} \sim \sqrt{\frac{GM}{R}} \tag{1.4}$$

In practise, inter-particle collisions convert gravitational potential energy into thermal energy as the clump contracts. While the material remains optically thin this energy is radiated into space and the process remains nearly isothermal in nature. Our simple model of a homogenous cloud is an inaccurate picture, however; the compressive forces

that gave rise to the clump will most likely have produced a cloud that is denser towards the centre and more rarefied in its outer layers. Thus, the centre collapses more rapidly. When the core reaches a density of $\sim 10^{11}$ cm^{-3}, it is no longer transparent to thermal radiation and the collapse process behaves adiabatically. The temperature and pressure in the inner core start to rise.

A temporary state of hydrostatic equilibrium occurs when the number density in the core reaches $\sim 10^{13}$ cm^{-3}; at this point, thermal pressure supports the core against further gravitational collapse. This is referred to as the 'first hydrostatic core'. But material continues to infall from the surrounding halo of material as it contracts, and the temperature continues to rise. At $\sim$ 2000K, molecular hydrogen dissociates, and dissociative cooling of the material permits further collapse. The temperature and density continue to rise as the collapsing core material breaks into atoms, and starts to ionise. Full ionisation occurs at around 10^4 K, and 10^{23} cm^{-3}. A 'second hydrostatic core' forms with $\sim$ 0.001 M. and radius R.. This is the protostar, which will continue to accrete mass from the surrounding envelope which will provide $\sim$ 99% of the star's final mass.

Increasingly beyond this stage, the angular momentum and magnetic field of the cloud material, drawn in and concentrated by the process of collapse, play an important role in the further evolution of the system.

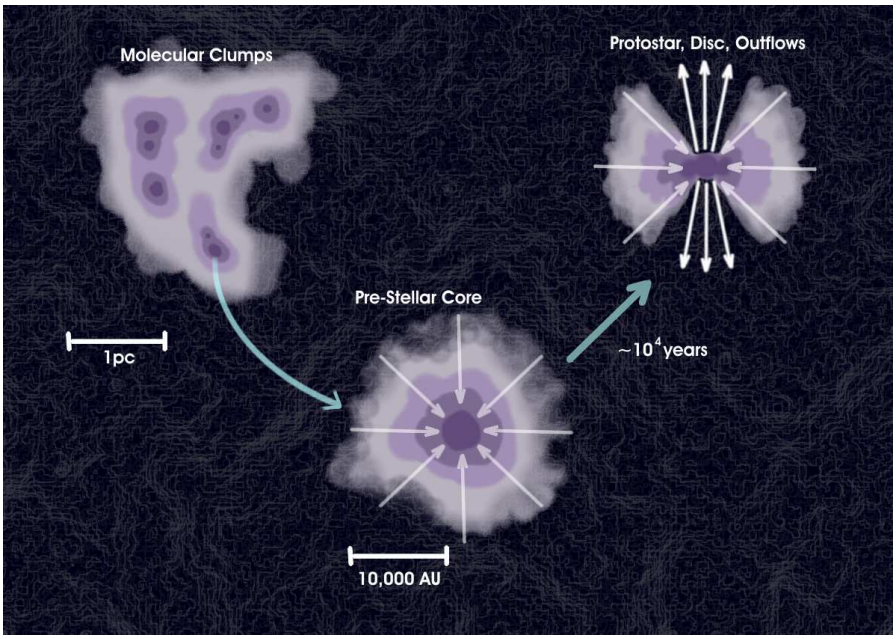

Figure 1.2: Low Mass Star Formation Paradigm

1.5 Stage 4: Class 0 - Submillimetre Protostar

The exact moment at which a starless core passes the transition into a core containing a protostar - the moment of star birth, or Age Zero - is a matter for some debate. One milestone that may be used conceptually, though the moment may be difficult to observe, is the point at which a *thermally enclosed* sphere of material exists within the core. Thermal enclosure is the state in which photons originating within the sphere cannot escape directly but instead feed a reservoir of energy within a surrounding photosphere. This forms a bottleneck preventing the efficient evacuation of photons.

While stars are in the protostellar phase, nuclear fusion burning has not yet commenced, and the energy they radiate arises wholly from the release of gravitational potential energy due to accretion and collapse. In the earliest stages of protostellar development, this radiated energy does not reach us directly, but must pass through the surrounding envelope of gas and dust that absorbs and re-radiates at longer wavelengths, producing a spectrum poorly resembling a blackbody emitter such as a main sequence star.

Spectral Energy Distribution - the distribution of radiated power with wavelength - offers us a way of classifying protostars. The slope of the SED in the infrared region of the spectrum is used to track the evolution of young stars because it tells us to what extent the protostar remains cloaked in a dusty gaseous envelope. In the earlier stages we expect a large amount of luminosity in the far-infrared region of the spectrum as the protostellar envelope absorbs and re-emits radiation from the central object; in later stages, we expect the material in the envelope to have been accreted or dispersed, and the central object to reveal itself in near-infrared and optical wavelengths.

Spectral Index α_λ is defined as follows:

$$\alpha_\lambda = \frac{d(log\lambda S_\lambda)}{d(log\lambda)} \tag{1.5}$$

Where S_λ is the distribution function describing the observed luminosity per unit wavelength.

Where a Young Stellar Object has $\alpha_\lambda > 0$ in the infrared (2 - 20 μm), thus indicating a

Spectral Energy Distribution that is rising with increasing wavelength, it is designated a Protostar, that is to say a Class 0 or I object (see Fig.1.3).

Further dividing lines exist that help us separate the Class 0 protostars from Class I objects. The *bolometric luminosity*, L_{bol}, is the total power radiated by an object as measured across all wavelengths (Chen et al, 1995)(15); while L_{smm} is the total radiated power measured at wavelengths greater than 350 μm. Class 0 sources, then, are those for which $L_{smm}/L_{bol} > 0.005$, which corresponds to more than half the total mass of the system remaining in the envelope rather than the central protostar. The emission of Class 0 objects is dominated by submillimetre radiation. The L_{smm}/L_{bol} ratio is expected to decrease as the protostar evolves and its envelope disappears.

Another means of identification of protostellar class, is *bolometric temperature*. This quantity, is the temperature of a blackbody whose spectrum has the same mean frequency $<\nu>$ as that of the spectrum of the observed object. The bolometric temperature is related to the mean frequency as follows (Myers & Ladd, 1993)(75):

$$T_{bol} = 1.25\frac{<\nu>}{100GHz}K \tag{1.6}$$

Class 0 protostars are classed in this system as objects for which $T_{bol} < 70$K; and in fact this agrees closely with the classification based on bolometric luminosity.

Molecular outflows are associated with Class 0 protostars. These are well-collimated, highly powerful and bipolar in nature. They are a useful signature for detection of protostars that are otherwise hidden from observation.

1.6 Accretion Disk Formation: Jets Appear

As the Class 0 object is forming, material from the envelope is beginning to concentrate into an equatorial region defined by the plane normal to the overall angular momentum vector of the protostellar core. This bulk angular momentum, preserved by the self-gravity of the star-forming clump, is inherited from the turbulence within its parent molecular cloud. Hence as this collapses to form a protostar, the principle of conservation

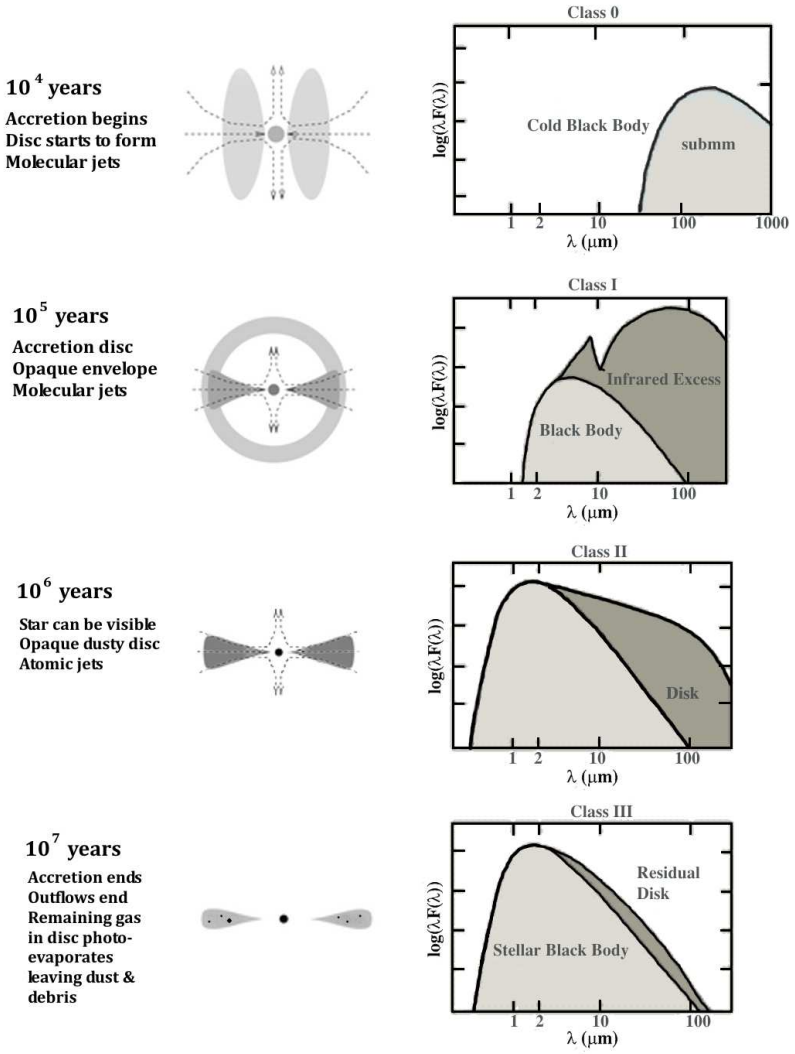

Figure 1.3: Protostellar evolution, showing typical time spent in each phase and key features. [Annotated composite of figures found in the public domain; schematic protostar images based on (5); spectral energy distributions adapted from `http://newt.phys.unsw.edu.au/jacara/pilotscience.php`]

of angular momentum suggests the collapse will not occur isotropically, but will instead favour a somewhat oblate geometry. Eventually, this takes the form of an accretion disk surrounding the protostar.(Alecian, 2013)(2). Though a variety of possible evolutionary paths exist (Williams, Cieza, 2011)(121) the existence of accretion disks is virtually beyond dispute being supported by many direct observations, for example the externally illuminated discs of young stars in the Orion Nebula (McCaughrean, 1997; Bally et al, 1998)(67)(10) and the edge-on disc seen surrounding our particular object of interest in this thesis, the T-Tauri star HH30 in Taurus-Auriga (Guilloteau et al, 2008)(39).

As the dimensions of the collapsing core diminish, the moment of inertia decreases and

thus we expect the angular velocity of the material to increase to conserve angular momentum (Alecian, 2013)(2). Here we are met with a problem, since if we consider a material element of the clump to be orbiting about the clump's centre of mass, reducing the radius of its orbit by a factor of two, for example, results in a fourfold reduction of its moment of inertia; requiring a corresponding fourfold increase in its angular velocity. But from simple mechanics this implies an eightfold increase in the central force required to maintain the material element in its orbit; and yet, we have only halved the radius, and so by Newton's law of gravitation the force on the material element has only increased by a factor of four. A mechanism is required that can explain how material in the accretion disk can gradually move into closer orbits and eventually be absorbed by the central protostar.

A simplified description of disk formation follows, based on Stahler & Palla (2011)(109). Let us imagine our collapsing clump of material to begin as a spherical cloud surrounding a denser, central protostellar core. Further let us simply assume that this configuration begins in a state of uniform rotation about an axis (which we align with the z-coordinate axis) at angular speed Ω_0, inherited from the parent cloud from which it formed. Realistically, this is not a dynamically stable or self-consistent model, but serves as a simplified theoretical starting point. A given material element begins at a distance R_0 from the centre of the clump, and its position vector with respect to the centre makes an angle θ_0 with the z-axis (see Fig.1.4). Thus, its specific angular momentum vector, normal to the equatorial plane, has magnitude:

$$h = \Omega_0 {R_0}^2 sin\ \theta_0 \tag{1.7}$$

Now allow the material to fall inwards towards the central protostar, which has mass M_*. In general, an infalling material element will trace an eccentric parabolic orbit as it swings around the centre and returns outwards. At periastron, its distance of approach will be R_{min}, and at this point its maximum velocity V_{max} is attained. From Newton's Law of Gravitation, we have the limit for the material to remain gravitationally bound:

$$V_{max} = \sqrt{\frac{2GM_*}{R_{min}}} \tag{1.8}$$

Let ϕ be defined as the angle the current position vector of the material element makes with the position vector at periastron, while R is the distance from the central object. The equation describing the parabolic trajectory of the material element in the plane at angle θ_0 to the z-axis is then:

$$R = \frac{R_{eq}}{1 + cos\ \phi} \tag{1.9}$$

R_{eq} is the *semilatus rectum* of the parabola, i.e. the distance from the focus of the parabola (which is the centre of the protostar) to the line of the parabola along an axis perpendicular to the axis of symmetry. This axis happens to lie in the equatorial plane of the rotating cloud - hence R_{rq}.

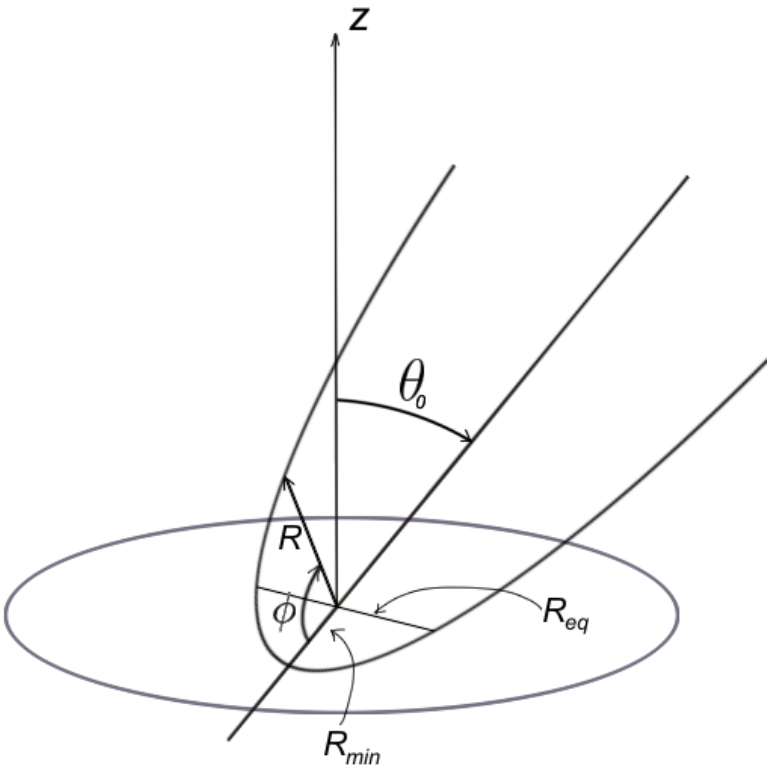

Figure 1.4: Diagram showing parabolic path taken by a material element of a rotating collapsing cloud [Based on a figure from Stahler & Palla, 2011](109)

When $\phi = 0$, the material element would theoretically be at its point of closest approach a distance R_{min} from the centre, and it is evident from 1.9 that

$$R_{min} = \frac{R_{eq}}{2} \tag{1.10}$$

Returning to the specific angular momentum, the general vector expression is:

$$\vec{h} = \vec{r} \times \vec{v} \tag{1.11}$$

This remains constant as the material infalls though $\vec{v}$ and $\vec{r}$ vary along the trajectory. At the point of closest approach of the material element to the centre we may say the following:

$$h^2 = {V_{max}}^2 {R_{min}}^2 \tag{1.12}$$

Combining this with 1.8 and 1.10 and rearranging we find:

$$R_{eq} = \frac{h^2}{GM_*} \tag{1.13}$$

From conservation of angular momentum, h will be equal in magnitude to the initial specific angular momentum and so substituting 1.7 into 1.14 we find that

$$R_{eq} = \frac{{\Omega_0}^2 {R_0}^4 sin^2\ \theta_0}{GM_*} \tag{1.14}$$

Material that begins at an inclination angle $\theta = 90°$ has the highest angular momentum and largest centrifugal radius for a given starting distance from the origin R_0.

$$R_c = \frac{{\Omega_0}^2 {R_0}^4}{GM_*} \tag{1.15}$$

This material, then, tends to remain in the equatorial plane, forming a mid-plane disk. Meanwhile, a material element at smaller inclination angle to the z-axis has lower angular momentum, and will pass closer to the centre thus more readily accreting onto the protostar. As the material element falls, it will collide with the material orbiting in the mid-plane disk and lose its vertical component of motion, though keeping its components of motion in the plane of the equator; thus adding to the accretion disk.

The simplest description of an accretion disk, is that of a thin disk of fluid annuli undergoing Keplerian differential rotation (Thompson, 2006)(119) though in practise, the outer regions of accretion discs tend to be flared (Alecian, 2011)(2). Evidence has been

found for Keplerian rotation in accretion disks from observations of the velocity fields in these disks, e.g. Williams, Cieza (2011)(121) (See Fig.1.5).

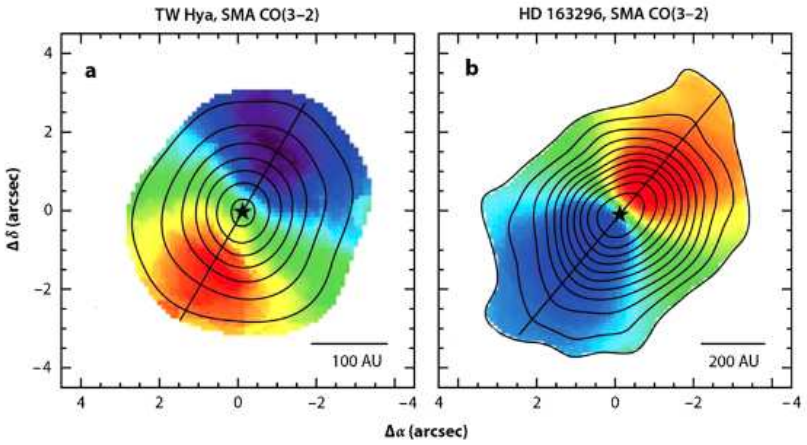

Figure 1.5: Luminous Mass vs. Velocity for a bipolar outflow in OMC 2/3. [Figure reproduced with adjustment from Williams & Cieza, 2011 (121)]

The Keplerian angular velocity as a function of radius is given by:

$$\omega = \sqrt{\frac{GM_*}{r^3}} \tag{1.16}$$

Due to viscous interaction there is friction between adjacent annuli, which redistributes angular momentum and converts gravitational potential energy of the material into heat which is lost radiatively. This loss of potential energy implies that the material falls closer in towards the central protostar, which according to Kepler's Law requires that it increase its angular velocity $\omega \propto r^{-3/2}$ and thus also its orbital kinetic energy $E \propto r^{-1}$. This increase in kinetic energy must also come from the loss of gravitational potential energy. Half of the gravitational potential loss from infall goes into Keplerian speed-up and half is radiated away as heat (Thompson, 2006)(119).

The material in adjacent annuli is actually gaseous and intermingles; material in the inner annulus closer to the centre has higher angular momentum and through friction imparts some of its angular momentum to the material in the outer annulus. Thus, an outwards transport of angular momentum is established in the disc, while mass, and energy that is not radiated off, is transported inwards (Lynden-Bell, Pringle, 2008)(64). This suggests an accretion disc that feeds material onto the central object while the remains of the surrounding core feed additional material into the disc (Alecian, 2011)(2).

In modern accretion disc theory, this picture is considered over-simplistic. Magnetic fields, advected inwards from the parent cloud, thread the weakly ionised material of the accretion disk (see Fig.2.4.5) and provide braking and efficient extraction of angular momentum through launching of winds and jets (Pudritz et al, 2006)(85).

Numerical magnetohydrodynamic simulations of accretion discs have helped us to develop a rich picture of accretion disc behaviour around many kinds of objects. There are many other features in the modern picture of accretion discs such as spiral density waves (Stahler & Palla, 2011)(109), accretion streams (Colombo et al, 2016)(18) and flaring interactions between the disc and central object (Orlanda et al, 2011)(79) that are outside the scope of this thesis.

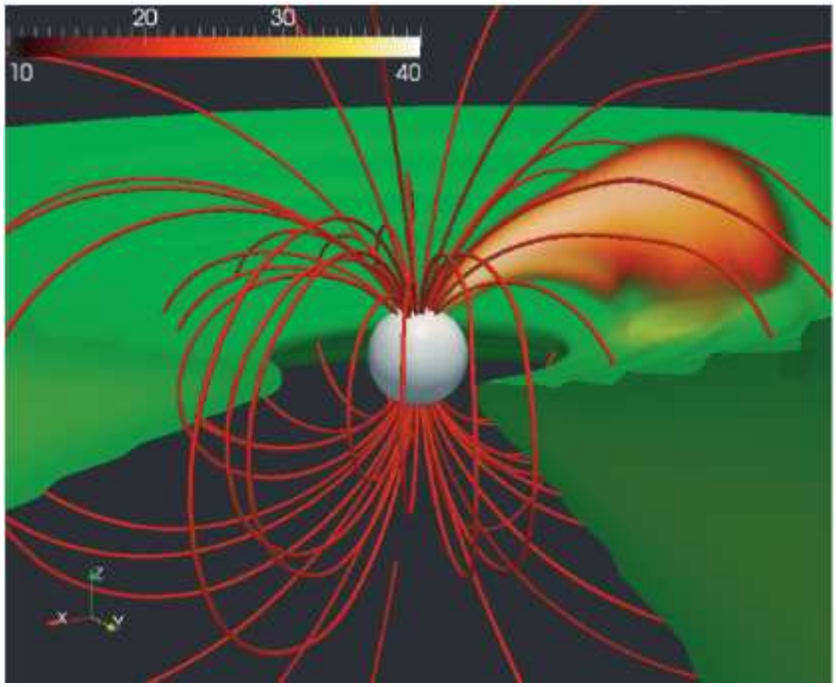

Figure 1.6: MHD simulation of accretion disc evolution. Green solid contours show the mass density of the disc. Magnetic field is indicated by the red lines. A bright flare has been triggered funnelling ionised material along magnetic field lines from the inner disc onto the stellar surface (upper left colour scale indicates temperature). [Figure reproduced with adjustment from Orlando et al, 2011](79)

1.7 Stage 5: Class I - Infrared Protostar

After a timescale approaching $\approx 10^5$ years, the protostar has accreted over half of the mass of its surrounding envelope; its own SED begins to emerge as the peak shifts out of the submillimetre and far-IR end of the spectrum. A far-infrared excess persists due to the lingering amounts of material in the envelope that scatter radiation from the central object.

The bolometric temperature of Class I objects is found to be 70K $< T_{bol} <$ 650K. The Spectral Energy Distribution of such objects is broader than expected for a simple black-body because of the large FIR excess. There is a frequently occurring absorption dip in the SED at 10 μm indicating the presence of silicate dust (Smith, 2004)(100).

Like their Class 0 forbears, Class I sources often produce bipolar molecular outflows. An example observation can be seen in Fig.1.7. These are not as energetic as those produced by the Class 0's, but because the Class I phase lasts 5-10 times as long as Class 0, the majority of observed molecular outflows originate from Class I sources. Accretion-driven launch models predict that outflow power is tied to the accretion rate; thus, we see weaker outflows in the later stage protostars, when accretion occurs at slower rates.

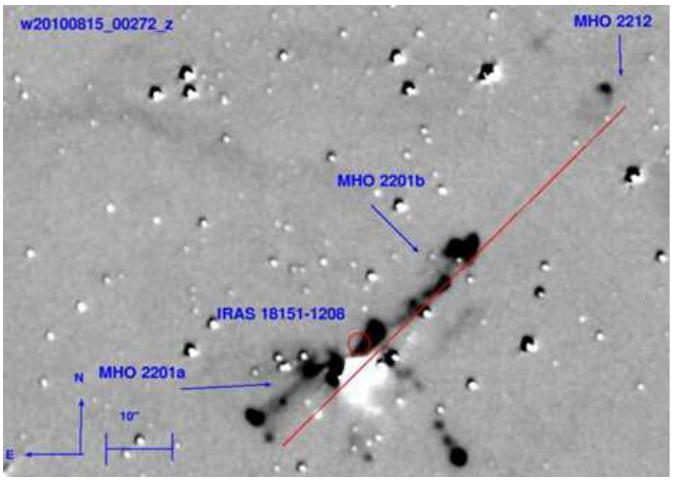

Figure 1.7: Example of a molecular jet from a massive protostar: a very bright bipolar jet emanates from IRAS 18151-1208, imaged in the UWISH2 survey, showing knots of 2.12 μm molecular hydrogen emission. (Ioannidis, Froebrich, 2012)(52)

1.8 Stage 6: Class II - Classical T-Tauri Star

It is after roughly 10^6 years that the Young Stellar Object has fully dispersed or accreted its envelope and has become visible at optical wavelengths. Bolometric temperature of the central object is now in the range 650K $< T_{bol} <$ 2800K. It has become a Class II YSO; otherwise known as a Classical T-Tauri Star (CTTS). Table 1.2 compares the characteristics of Class II YSOs with other evolutionary stages.

This type of star was first classified in 1945 (Joy, 1945)(53). They took their name from the prototypical CTTS found in Taurus (see Fig.1.8). Class II stars have masses and surface temperatures similar to that of the Sun, but they are brighter and more active. They exhibit fast rotation, with periods of $\sim$ 1-8 days. Strong winds and atomic outflows are a feature of these systems; and these plus accretion columns of material streaming onto the central object, the possible cause of the many bright starspots that cover up to 20% of their surface, are now seen as giving rise to the observation of Hydrogen Balmer series lines, in particular the H-α line, and forbidden lines of singly ionised Sulfur and neutral Oxygen. Infrared and submillimetre excess on their SED's arise from the presence of an accretion disc that surrounds the object, rather than an envelope. The early stages of planet formation may already have started to occur within the disc (Fig.3.3).

Class II / III YSO's are usually referred to as Pre-Main Sequence Stars, rather than Protostars.

Table 1.2: Young Stellar Object Classification

Class	SED slope	Physical Properties	Observational Characteristics
0	-	$M_{env} > M_* > M_{disc}$ $T_{bol} <$ 70K	No optical or near-IR emission molecular jets
I	$\alpha_{IR} > 0$	$M_* > M_{env} \sim M_{disc}$ 70K $< T_{bol} <$ 650K	optically obscured, IR excess molecular jets
II	-1.6 $< \alpha_{IR} <$ 0	$M_{disc}/M_* \sim 1\%$, $M_{env} \sim 0$ 650K $< T_{bol} <$ 2800K	strong Hα and UV emission accreting disc, atomic jets
III	$\alpha_{IR} <$ -1.6	$M_{disc}/M_* \ll 1\%$, $M_{env} \sim 0$ 2800K $< T_{bol}$	passive disc, weak or no accretion fast rotation, $\sim$ 1 - 2 days

Table compiled from (Smith, 2004)(100) & (Williams & Cieza, 2011)(121). Sometimes, an intermediate stage is considered between Class I and II, designated as Flat Spectrum (FS), where -0.3 $< \alpha_{IR} <$ 0.3. This was proposed by Greene et al., 1994 (37)

1.9 Stage 7: Class III - Weak T-Tauri Star

A Sun-like star spends a few million years in the Class II stage of Pre-Main Sequence evolution, before becoming a Class III object. These are often described as Weak-line T-Tauri Stars, as they have Hydrogen lines in their emission spectrum but at much lower line strengths. By this stage, the gaseous material in the accretion disc has been fully consumed, leaving a dusty debris disk which may provide the material for planet formation; the star has reached its final mass and the SED for Class III objects resembles a blackbody spectrum with only a small infrared excess (see Fig. 1.3). With the disappearance of accretion, outflows have also ceased.

Class III YSOs often rotate even more rapidly than Class II objects, with typical periods $\approx$ 1-2 days (Marilli E., et al., 2005)(65). Without the accretion disc and columns providing a braking effect, the star's rotation rate is free to increase as its radius diminishes.

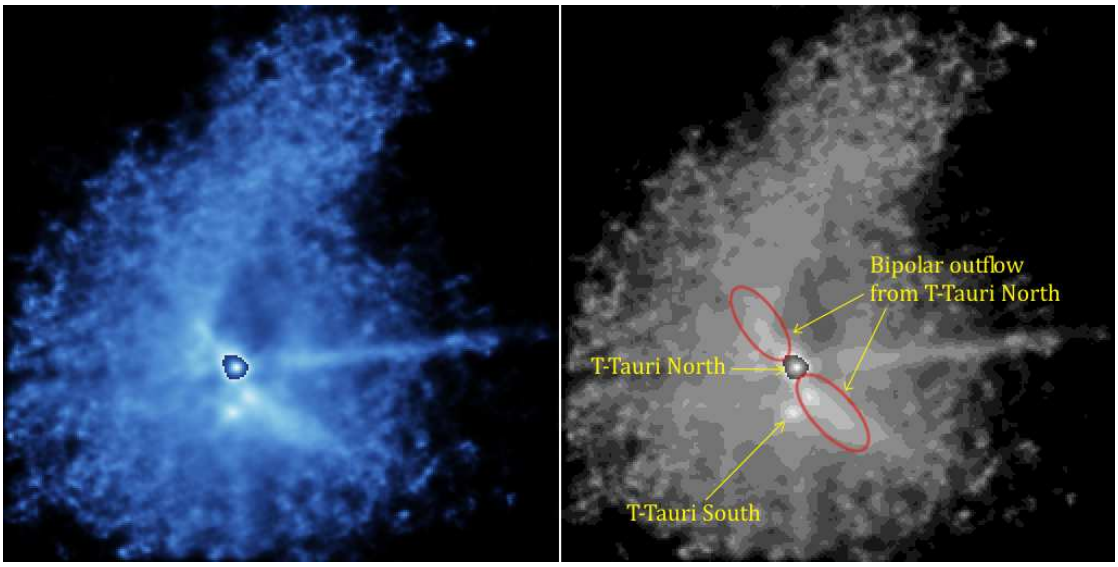

Figure 1.8: The first classical T-Tauri star: T-Tauri, imaged in the near-infrared J-band by the Canada-France-Hawaii Telescope with adaptive optics; revealing T-Tauri to be a binary system with associated outflows. [Image credit: left panel - Roddier, Roddier, Graves et al., 1998 (91); right panel is author's added schematic]

1.10 Pre-Main Sequence Stellar Evolution

The Hertzsprung-Russell diagram is a way of visualising the properties of stellar populations and their lifecycles. It is a plot of stellar luminosity or magnitude versus surface temperature or some proxy thereof (originally, spectral type or colour). The appearance of a particular H-R plot is dependent on the stellar population that it depicts; a plot based on all observed stars in the Milky Way appears different to a plot of a particular star cluster, for example. The majority of luminous stars in a galactic population will lie on a curve called the Main Sequence. These stars remain on this curve for most of their lifespan, due to the longevity of the Hydrogen-burning phase (typically $\sim 10^{10}$ yrs).

While a star's luminosity may be deduced observationally, its effective blackbody surface temperature T_{eff} may only be modelled theoretically and so when T_{eff} is used as a plot axis the diagram is referred to as a *Theoretical H-R Diagram*. Often a log-log plot of total theoretical energy emitted per unit time, L_*, versus T_{eff} is employed.

An H-R diagram can be a useful way of conceptualising the evolution of young stars. Having a lower effective surface temperature than main sequence stars of equivalent mass, they begin life on a curve which is to the right of the main sequence curve (see Fig.1.9). This birthline does not represent the true protostellar phase of Class 0 objects, because these protostars are so obscured by dense surrounding clouds of gas and dust that their emitted radiation is entirely at longer wavelengths than visible light, and is more characteristic of the dust cloud itself than of the surface of the protostar.

The birthline, then, represents the earliest stage at which the star becomes optically visible. But with no Hydrogen fusion yet occurring to provide a balancing radiation pressure, the young star continues to contract and the object's luminosity L_* and effective temperature T_{eff} change with time. The evolutionary paths taken by young stars on the H-R diagram as they move toward the main sequence are called Hayashi Tracks.

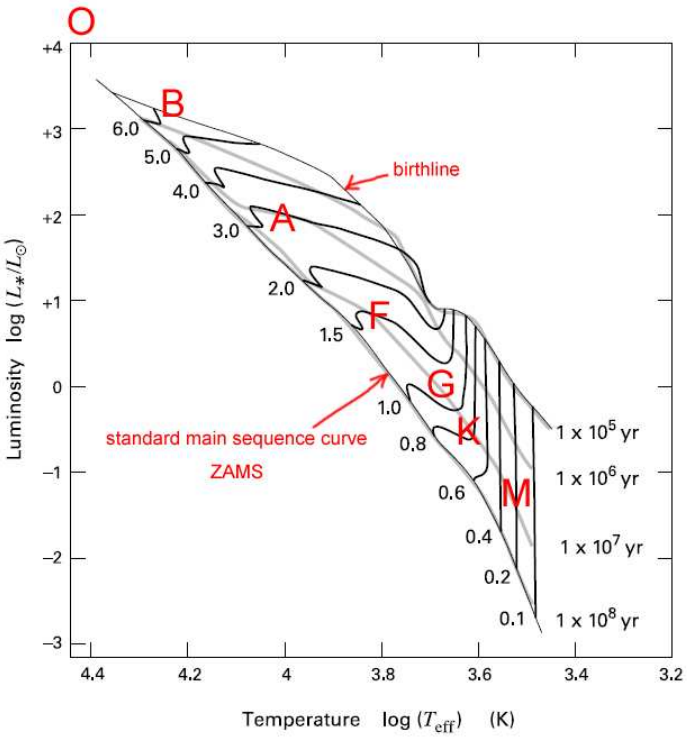

Figure 1.9: Theoretical Hertzsprung-Russell Diagram for Pre-Main Sequence Stars. Hayashi Tracks are shown for the evolution of model protostars, labelled by mass from $0.1M_{\odot}$ to $6M_{\odot}$. Grey curves are isochrones labelled according to age in years, and corresponding to the stages I to III of pre-main sequence evolution until reaching ZAMS at 1 x 10^8 yrs. [Annotated figure reproduced from Stahler & Palla, 2011]

1.11 Chapter Summary

1. We have seen how Giant Molecular Clouds are the factories of star assembly; the seven-stage paradigm for the formation of low mass stars has been examined and the four standard classes of Young Stellar Objects have been identified.

2. Accretion disc formation has been discussed and the launching of jets from systems with accretion discs has been introduced in context.

3. The youngest protostars, Class 0/I, launch powerful molecular jets traceable by infrared, and submillimetre/millimetre emission.

4. Class II - Classical T-Tauri Stars - launch light, fast optically visible atomic jets.

5. Class III - Weak T-Tauri Stars - by now accretion and outflows are largely absent.

Chapter 2

Protostellar Jets

2.1 Early Evidence for Jets

The earliest evidence for the existence of protostellar outflows arrived in the 1950's with the work of Herbig (1951)(45) and Haro (1952)(40) from which the optical emission nebulae known as Herbig-Haro objects receive their name (see Fig.2.1). These nebulae are often found in pairs associated with bipolar outflows from a central protostar, though their significance as indicators of outflow activity was not fully recognised until the mid-70's; when it was realised that they could be shock fronts in the surrounding medium driven by supersonic winds (Schwartz, 1975)(96).

As the outflow-driven origins of Herbig-Haro objects came to the fore, another strand of jet research was ongoing. The first discovery of radio galaxies was in 1944 by the amateur radio astronomer Grote Reber, whose radio map of the sky is widely regarded as a pioneering achievement in the field of radio astronomy (Reber, 1944; Kellerman, 2003)(88)(56). Reber's map drew attention to the high-intensity radio source Cygnus A, though its extragalactic nature was not confirmed until some 10 years later (Baade, Minkowski, 1954)(9). Its highly active nature was thought by some to be the result of an ongoing collision with another galaxy; but by the early 1960's a new theory was gaining ground, that the radio emissions were the synchrotron radiation produced by jets of relativistic particles (Shklovskii, 1960; Ginzburg, 1961)(95)(36). By the mid-70s the synchrotron nature of the radio emissions was confirmed and it had become evident that

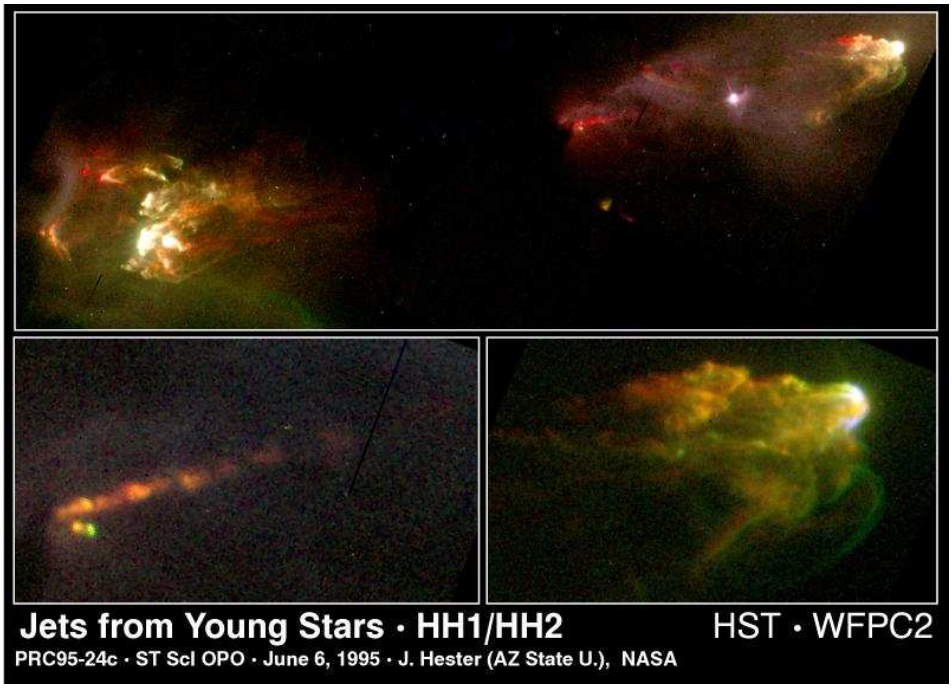

Figure 2.1: HH1/HH2, located near the Orion Nebula and discovered by George Herbig and Guillermo Haro were the prototypical Herbig-Haro objects. The HST/WFPC2 image shows emission nebulae arising from bipolar protostellar jets impacting on the surrounding medium. The whole structure spans one light-year. In between the two outflow lobes, obscured by dust, is the driving protostar (Image courtesy of NASA).

a large fraction of galactic clusters hosted a 'radio loud' Active Galactic Nucleus (Burns & Owen, 1977)(13).

The search was on to identify a launch mechanism for these extragalactic jets; and this led Blandford & Payne in 1982 (11) to develop a magneto-centrifugal launch model for radio jets that would eventually form the basis of launch models for protostellar jets.

2.2 Jet and Outflow Structure

Figure 2.2 is a simplified schematic showing the key elements of a typical jet from a YSO. The jet column is a collimated stream of excess accretion material of density ρ_j launched by some mechanism such as that identified by Blandford and Payne (11) at supersonic velocity V_j into a surrounding ambient medium of density ρ_a, velocity V_a. Generally, $V_a \ll V_j$, and in our jet models $V_a = 0$. Such an arrangement is expected to form a forward/reverse shock pair.

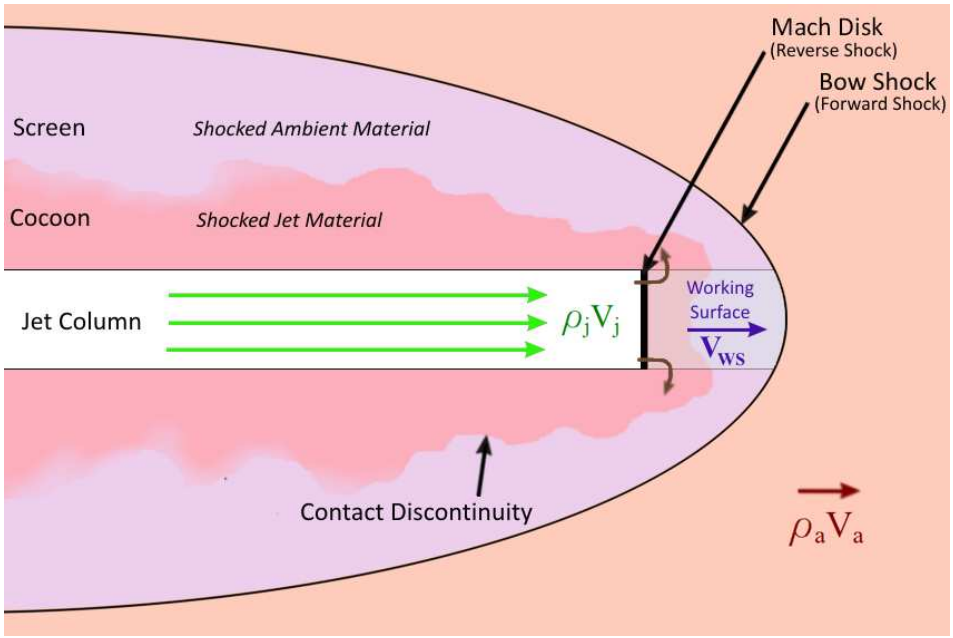

Figure 2.2: Simplified Schematic Diagram of Jet Structure.

Jet material is decelerated by a reverse shock in the form of a Mach Disk at the head of the jet; the material passing through this shock is decelerated and heated as it enters the high-pressure post-impact region of the jet/outflow structure which is referred to as the "beam cap" or "working surface". The pressure in this region is of the order M^2 higher than the pressure of the undisturbed ambient medium where M is the jet Mach number (Smith, M. D. et al 1985) (102). Shocked material escapes from the sides of the working surface and falls behind the advancing head of the jet column; this is an apparent backflow in the reference frame of the Mach Disk. The region of shocked jet material immediately surrounding the jet column is referred to as the "Cocoon". Meanwhile, the forward or Bow shock accelerates and heats the material of the ambient medium.

This leads to the formation of a layer of shocked ISM surrounding the jet cocoon layer, which is sometimes referred to as the "Screen" or "Sheath". These layers are separated by a contact discontinuity; the material on either side of this interface is in pressure balance though at differing temperatures and densities. Initially, the pressure equilibrium inhibits the intermixing of the materials, though they may eventually undergo turbulent intermixing.(Chakrabarti, 1988)(14)

A distinction must be drawn between the *jet*, and what is referred to as the *outflow*. The jet is, exclusively, the material launched from the source YSO, whilst the outflow is the totality of material set in motion by the jet propagation as it transfers its momentum and energy to the surrounding medium. Non-jet material that is set in motion by the jet is said to have been *entrained*. There are two kinds of entrainment that are usually considered; acceleration by the bow shock that entrains material into the screen layer, and subsequent intermixing of the shocked ambient medium with the shocked jet material in the cocoon.

Referring to Fig. 2.2, the ratio of jet to ambient density $\eta = \rho_j/\rho_a$ is a key parameter that determines the behaviour of the jet. Under conditions of zero ambient velocity in the reference frame of the jet source, by matching momentum fluxes the velocity of advance of the working surface is given by (14):

$$V_{ws} \approx \frac{\sqrt{\eta}\, V_j}{1 + \sqrt{\eta}} \tag{2.1}$$

In the case of light jets, where $\eta < 1$, the velocity of the working surface is slow compared with that of the jet itself and this leads to larger amounts of material being processed through the Mach disk and backflowing to form the cocoon. These lighter jets are characteristic of atomic flows from later-stage YSOs. Where $\eta > 1$, which is the case for molecular jets from Class 0 & 1 protostars, the velocity of the working surface is not much greater than that of the jet itself and there is less shock-processed material to feed the growth of the cocoon (Chakrabarti, 1988)(14).

This is a basic picture of jet and outflow structure. In fact, the shock dynamics evident in supersonic jets are often more complex, as we shall see when we examine the computational jet propagation models of Norman et al. (1982)(78). See also Fig. 2.3.

2.3 Computational Modelling: Launch and Propagation Mechanisms

Discrete numerical models of protostellar jets, solved computationally to simulate jet evolution over timescales that exceed our present window of observations by orders of magnitude, are the connecting tissue between theory and observation; these models can include all the significant physics required to simulate a propagating jet, and the chemical processes of its constituent material. Synthetic observations are another layer of simulation that can be derived from the outputs of a physical jet model. Thus, these simulations may assist us in constraining the range of possibilities by testing the behaviour of jets over a parameter space and comparing the results with observation.

Computational simulations generally focus on either models of launch, or models of propagation (in which the launch is assumed to occur "off-domain"). This is mainly due to the disparate length scales involved, with launch mechanisms dominating the behaviour of the jet only within $\sim$ 10AU of the jet source, and a launch-agnostic interaction with the environment being of greater significance at $>$ 20AU.

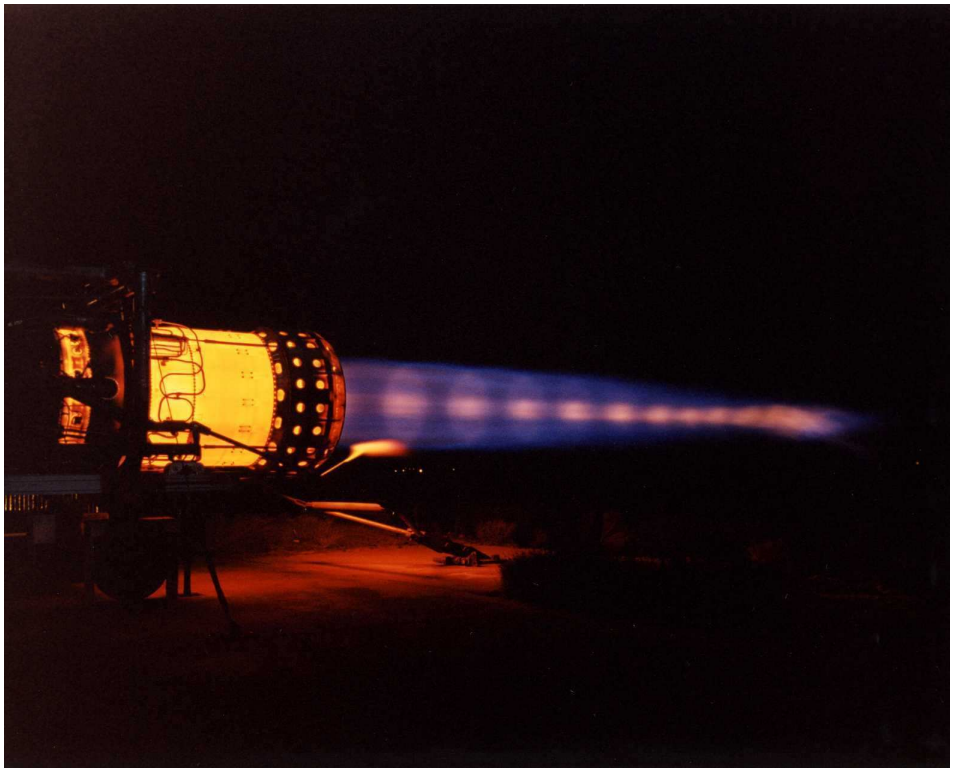

Figure 2.3: Complex shock structure within a jet flow: Pratt & Whitney J58 engine with full afterburner. The knots of bright emission seen in the exhaust are known as shock diamonds, a feature of over-expanded jets (Image courtesy of NASA).

2.4 Some launch theory: the Blandford/Payne model

Blandford and Payne's 1982 paper *Hydromagnetic flows from accretion discs and the production of radio jets*(11) paved the way for the magneto-centrifugal class of jet launch model, amongst which it could be argued that the most well established is the 'Disc Wind' model (Pudritz & Norman, 1983)(84). Other magnetic launch models include the 'X Wind' model, which differs from 'Disc Wind' mainly in the assumptions it makes about accretion disc field geometry, with the magnetic field being concentrated in a narrow zone within the accretion disc's co-rotation radius rather than being distributed broadly across the disc (Shu et al., 1994)(98); and also the 'Magnetic Towers' model in which the beam luminosity is dominated by the Poynting flux out to large distances from the launch site, in contrast to the magneto-centrifugal models (Huarte-Espinosa et al., 2012)(48).

2.4.1 Overview

In order for material in a Keplerian accretion disc to lose its gravitational binding energy and flow onto a central object, it must also lose its orbital angular momentum. Binding energy is generally converted to thermal energy during the course of in-fall by a variety of dissipative processes, whilst viscous or magnetic torques may transport angular momentum (and some energy) outwards in the disc; or else companion tidal interactions may be invoked in binary systems. These mechanisms may have difficulty explaining how objects are able to form within timescales that are consistent with observation, or else there may be no attendant sink for orbital angular momentum in the case of some objects.

The case considered by Blandford and Payne is that of a massive black hole at the centre of a radio galaxy. They examine a possible mechanism for extraction of the excess angular momentum by magnetohydrodynamic transport of material from the surface of an accretion disc that is threaded with 'open' field lines; this material then carries away the angular momentum in a jet which moves perpendicular to the disc along the axis of rotation. This is in contrast to earlier models that invoke purely electromagnetic torques. In these models, a force-free magnetosphere is assumed above and below the disc (i.e.

a negligible gas pressure in comparison with magnetic pressure, thereby simplifying the equations describing the magnetic field and momentum transport).

2.4.2 Development of the model

The analytical model is based on a generalised and simplified accretion disc surface upon which the magnetic field lines are anchored. The system is represented axisymmetrically, in cylindrical coordinates, the disc surface being treated as a boundary condition along the r-coordinate, and the z-coordinate alignment perpendicular to the plane of the disc. Ideal MHD is assumed, with no resistive term appearing in Ohm's law and displacement currents assumed to be negligible. However the force-free condition does not apply in this case, with gas pressure appearing in the momentum equation. The equations are for a stationary system with no transient terms included; the solutions describe the fully developed flow.

To specify the disc boundary conditions, it is assumed that the Alfvén speed of the flow ($V_A \propto B\rho^{-1/2}$) scales in the same way as the Keplerian linear velocity ($V_K \propto r^{-1/2}$). By assuming a profile for angular momentum loss from the disc at the Keplerian velocity that is independent of radius, it can be found that the density of material lost from the disc to the outflow obeys the scaling $\rho \propto r^{-3/2}$, and thus $B \propto r^{-5/4}$ in order that $V_A \propto r^{-1/2}$.

Field lines that emerge from the accretion disc may be considered as 'frozen' into the medium due to the high magnetic Reynolds number of the disc and the magnetosphere in the vicinity of the disc. Hence, these field lines co-rotate with the disc in accordance with Ferroro's (1937) law of isorotation and may provide an energetically favourable path by which material may flow from the surface of the disc, carrying away energy and angular momentum whilst providing a braking torque to the disc. The material may be considered to flow outward along these field lines while maintaining constant angular velocity, analogous to beads on wires that are flung outwards by centrifugal force (see Fig.2.4).

The equipotential surfaces for the gravitational and centrifugal potential of material starting at the disc surface ($z = 0$) and at a given radial distance r_0 are found to obey

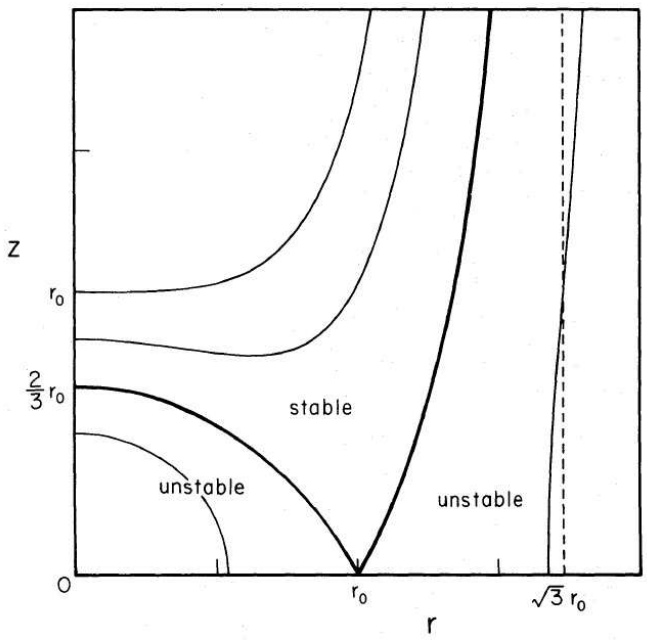

Figure 2.4: Equipotential surfaces for a bead on a wire co-rotating with the Keplerian angular velocity $(GM/r_0^3)^{1/2}$ at a radius r_0, released from rest at r_0. Figure reproduced from Blandford & Payne (1982)

the relation:

$$\phi(r,z) = -\frac{GM}{r_0}\left[\frac{1}{2}\left(\frac{r}{r_0}\right)^2 + \frac{r_0}{(r^2+z^2)^{1/2}}\right] \tag{2.2}$$

It is demonstrated that for cold material, if the poloidal component of the field makes an angle of 60° or less to the outward radius vector, then the gas will be flung outwards by centrifugal force as it overcomes the gravitational potential barrier. The thermal state of the disc material can further modify this result, making it easier for material to escape the disc and thereby increasing the angular range in which the poloidal field component can satisfy these conditions and act as a channel for magnetohydrodynamic flow.

A set of MHD equations is presented, based on the work of several prior authors (Chandrasekar 1956; Mestel 1961). Isothermal cold MHD flow is assumed. The equations are to be solved for the structure of the field lines, and hence the flow variables, as a function of height above the disc.

Techniques for solving the equations include expansions to second order around a point, numerical integration, and use of L'Hopital's rule to find the value of derivatives at critical points. It is argued that there is in fact only one critical point of practical importance,

which occurs at $m = 1$, where m is the square of the Alfvén Mach number. Parameters are identified that determine the character of the solutions; by making a suitable choice of values for these parameters, numerical integrations can be performed that will determine the field line structure for Super-Alfvénic flows that are expected to produce collimated jets.

Self-similar solutions are sought which are scale-invariant with spherical distance from the origin; hence a scaling is introduced for the position and velocity vectors so that quantities within the axisymmetric flow will scale as power laws of the spherical radius. However, self-similarity with respect to spherical radius is considered to become an increasingly artificial condition to impose on the flow variables at greater distances from the disc, where the flow is expected to exhibit self-similarity with respect to cylindrical radius instead, hence the numerical integrations are terminated at an arbitrary height above the disc. The aim of the analysis is simply to demonstrate the feasibility of collimated jets launched by magnetic fields rather than describe the full time-dependent evolution of such a jet, and so this is considered satisfactory for this purpose.

The imposition of self-similarity on the solutions ignores the boundary conditions at large and small disc radius. It is assumed that external pressure balances the magnetic and inertial stresses of the outflow exiting the problem domain at r_{0max} (see Fig. 2.4).

2.4.3 Solution close to the disc

The numerical integrations confirm the requirement that the field lines make an angle of 60° or less to the outwardly-directed radius of the disc. Close to disc, inertial stresses are overwhelmed by magnetic stresses and the field acts as if force-free and in isorotation with the accretion disc. The field lines are outwardly directed from the centre of rotation but not strictly so; the balance of magnetic pressure gradient and magnetic tension bend them somewhat inwards towards the rotation axis.

Initially, material is driven centrifugally out along these field lines, but the magnetic pressure gradient rapidly become more important than the centrifugal force as a mechanism for accelerating the material out to the point where bulk inertia becomes dominant (i.e. where the fast-mode magnetosonic wave speed is exceeded) and isorotation ends.

2.4.4 Solution far from the disc

Approximate solutions to the equations for the far-field flow indicate two kinds of Super-Alfvénic flow (identified by $n >= 1$, where the parameter n is the square of the fast-mode Mach number). The first kind of flow asymptotically increases towards $n = 1$ as the flow radius approaches infinity. The energy carried away by this flow comprises 1/3 bulk kinetic energy, whilst the remaining 2/3 is Poynting flux.

In the second type of flow, speed reaches $n > 1$ a finite height above the disc.

There exists a turning point in the radial velocity at $n = n_t$, a critical value of n (which is determined - non-trivially - from the solution parameters). Prior to attaining this value, the radial velocity is directed outwards and the flow expands to larger radii as it rises above the disc surface. Beyond n_t, the radial velocity is negative and the flow converges towards the z-axis, thereby collimating the jet.

At larger distances from the disc, the magnetic field becomes predominantly toroidal. Centrifugal force, whilst responsible for driving the initial flow from the disc, recedes in importance and the magnetic pressure is mainly responsible for balancing the inwardly-directed hoop stresses of the toroidal field.

The authors remark that the implication, from examining the energy equation for this type of flow, is that where $n > 1$ the kinetic energy flux becomes the dominant component in the outflow luminosity; although the Poynting flux will always make a significant contribution in a cold MHD flow because the magnetic field pressure is required to support the jet against the hoop stresses of the toroidal field in the transverse direction. However thermal effects will modify the solution such that gas pressure can support the jet in the transverse direction, and this allows for the magnetic contribution to outflow luminosity to become arbitrarily small.

The solutions indicate most of the jet power is concentrated towards the central axis, whilst angular momentum and magnetic flux are carried in the outer layers. Solutions also exist that imply low velocity, uncollimated flows, which are deemed not to be of immediate interest.

The choking-off of flow in solutions where $n > 1$ is discussed, but it is considered not

to be an issue given that gas pressure can ultimately support the jet against transverse collapse, and that as the radius of the jet diminishes, the centrifugal force becomes more effective at preventing choked flow.

2.4.5 Further Discussion and Conclusion

The authors present some discussion of the way in which their results are affected by assumption of a more complex disc and field geometry. A disk of non-infinitesimal thickness is considered, with a corona and a convoluted field geometry in which only a fraction of the field lines emerging from the disc are 'open' lines, the others turning back on themselves and reconnecting with the disc surface without emerging from the corona. It is found that the gas pressure gradient and gravitational forces have no substantial effect on the geometry of the field lines within the corona and that the magnetic field remains effectively force-free.

The model is then applied to the scenario of a massive black hole surrounded by an accretion disc. Some key results of this analysis are that it is only necessary for a fraction of the accreted gas to participate in the outflow to efficiently extract angular momentum and gravitational binding energy from the disc; and that the outflow has a different velocity at each radius, with outflow from the outer parts of the disc having a much lower velocity than that driven from the inner parts of the disc.

Closing remarks are made about how the more complex and unstable dynamics expected in real accretion discs may be expected to affect the outflow. Magnetic field will be continuously advected inwards by accreting gas; dynamo action within the disc will generate closed magnetic field loops; explosive reconnection events in the disc will generate flares (such as those seen in Fig.) that might carry magnetic field lines outwards beyond the Alfvén and magnetosonic critical points and thereby contribute to the flow. The far flow field may also exhibit instabilities due to velocity shear.

It is finally noted that the mechanism for magneto-centrifugally driven jet collimation and launching that has been investigated is not specific to the SMBH accretion disc scenario, but may also apply to objects of much smaller masses.

2.5 Simulating propagation: Norman et al on supersonic jets

In common with the 1982 Blandford & Payne paper (11), the Norman, Smarr, Winkler & Smith publication of the same year, *Structure and dynamics of supersonic jets*(78), has extragalactic 'radio' jets in mind; but approaches the problem from the propagation perspective. This paper is more strongly focussed on numerical modelling techniques and demonstrates the accuracy of the code by first comparing results with laboratory jet experiments performed in the 1940's. The structural features of propagating jets are then examined. The emphasis is on hot, light atomic jets in pressure balance with the surroundings; and so we might expect some differences in the behaviour of dense molecular jets such as those produced by early-stage protostars, and indeed this is borne out by other simulations (e.g. Moraghan, Smith & Rosen, 2006)(69). However, we may expect all supersonic jets to share some common features. The value in studying this paper, is in its attention to detail when examining the evolving jet structure.

2.5.1 Overview

The efficacy of the Blandford-Rees (1974, 1978) beam model is examined, as applied to extragalactic jets. Numerical experiments examine the structure of 3 basic jet components: beam, working surface and cocoon (see the schematic in Fig.2.2). Jets are injected continuously into a stationary uniform ambient medium - the launching mechanism is not examined, this is assumed to operate outside of the problem domain and only the propagation is of interest.

The main aim is to examine jets that are in pressure balance with the ambient medium (and thus at high temperature with respect to the medium). Such a jet in pressure balance with its surroundings is referred to as 'matched'. If the ratio K of jet pressure to ambient pressure is greater than unity, the jet is referred to as 'underexpanded'; if K is less than unity the jet is referred to as 'overexpanded'.

2.5.2 Underexpanded jets: numerical models vs. experiment

As an initial test of the numerical method to be employed, a simulation of an underexpanded jet with $K = 2.75$ is performed. This is because experimental data is available on such jets in a laboratory environment. The numerical treatment is found to conform well to the theory of underexpanded jet behaviour (Courant and Friedrichs, 1948) and the experimental results of Ladenburg et al. (1949). The simulation exhibits all the expected features - rarefaction zone, incident shock, reflected shock, Mach-disk shock and slipline discontinuity. (A slipline is a surface along which normal velocity components are continuous but tangential components are discontinuous).

2.5.3 Further simulations: pressure matched jets

Subsequently, attention is devoted to axisymmetric simulation of pressure-matched jets at Mach numbers 6, 3 and 1.5, in the case where the jet is light ($\rho_b/\rho_m = 0.1$), and also in the case where the jet density is equal to the surroundings. Ideal gas dynamics are assumed and both gases are of specific heat ratio $\gamma = 5/3$, i.e. that of the ISM in the atomic state. The radius of the beam is R_b and the problem domain encompasses $0 < R < 7.5R_b$; whilst the scaling choice is:

$$\rho'_m = C'_m = R'_b = 1 \tag{2.3}$$

Primed quantities are the re-scaled values; the unit of density is ρ_m and that of length is R_b, while that of time is

$$R_b/C_m = R_b(\rho_m/\gamma P_m)^{1/2} \tag{2.4}$$

- this is the time it takes sound waves to cross a distance R_b in the ambient medium. The reference kinetic luminosity is thus:

$$L'_m = \rho'_m {R'_b}^2 {C'_m}^3 = 1 \tag{2.5}$$

and dimensionless beam kinetic luminosity:

$$L'_b = \pi {R'_b}^2 {\rho'}_b {M'_b}^3 {C'_b}^3 \tag{2.6}$$

The pressure ratio constraint K requires that

$$\rho'_b {C'_b}^2 = K \rho'_m {C'_m}^2 \tag{2.7}$$

and since $K = \rho'_m = C'_m = 1$ then $\rho'_b {C'_b}^2 = 1$.

By employing a simulation resolution of 60 x 240 = 14,400 grid nodes over a typical evolution of 10,000-12,000 timesteps, features of the flow are resolved in great detail (see Fig.2.5). The results are summarised at Table 2.1.

2.5.4 Discussion of flow structure

Where the Mach number of the beam, $\mathbf{M_b}$, is sufficiently high ($\mathbf{M_b \geq 6}$), the jet beam propagates efficiently, with backflow from the working surface building a cocoon surrounding the beam. This cocoon's flow is supersonic where the temperature of the beam is an order of magnitude greater than the ambient medium. A Mach-disk shock front at the end of the beam decelerates beam material; the strength of this shock is generally much greater than the bow shock that runs ahead of the jet.

Particular attention is drawn to the structure at the head of the Mach 6 jet; the beam terminates with a Mach-disk in a similar manner to an underexpanded jet, with associated incident and reflected shocks behind and ahead, and a slipline discontinuity running ahead of the Mach-disk perimeter, defining a trapped region of high pressure jet material just beyond the Mach-disk that is referred to as the beam cap. Additional features that are present include a nozzle-like internal shock structure which persists several jet radii behind the leading Mach-disk shock; and a surrounding low-pressure torus which lies ahead of the leading Mach-disk and encircles the reflected shock.

Jet material in the outer sheath of the beam passes through the incident and reflected

shocks and emerges outside the beam cap. Caught between the central zone of high pressure in the beam cap and the surrounding low-pressure torus this material turns outwards as it flows onward and is diverted through an angle of 180° around the region of low pressure, thus feeding the cocoon surrounding the jet beam.

Where M_b is intermediate ($\approx$ 3), cocoon backflow becomes subsonic and hence unstable, tapering inwards towards the jet beam as the backflow mixes with the surrounding IGM through the Kelvin-Helmholtz instability. These jets also exhibit vortex shedding as in the $M_b = 6$ case.

Where M_b is low ($\leq$ 1.5), cocoons do not form, the jet instead giving rise to lobes in the vicinity of the working surface. These lobes are K-H unstable and possess ragged rearward boundaries where mixing with the IGM occurs. Whilst these lobes possess internal vortical motion in the case of hot, light jets in pressure balance with the IGM, where the jet is denser and cooler (density and temperature in balance with the IGM), the medium constituents participate in the vortical motion as $C_b = C_{IGM}$. Efficient entrainment at the working surface results.

Table 2.1: Underexpanded Jets: Survey parameters and summary

M_b	ρ_b/ρ_m	C_b	L_b	Comments
6.0	0.1	10	2145	Extensive cocoon, supersonic backflow, vortex shedding, stable beam, internal shocks
3.0	0.1	10	268	Unstable cocoon/lobe, vortex shedding, stable beam, internal shocks
1.5	0.1	10	33	No cocoon, unstable lobe, stable beam
6.0	1.0	1.0	679	Cocoon "roll-up", vortex shedding, stable beam, internal shocks
1.5	1.0	1.0	11	No cocoon, unstable lobe, unstable beam, entrainment

(Table reproduced from Norman, Smarr, Winkler & Smith (1982)(78))

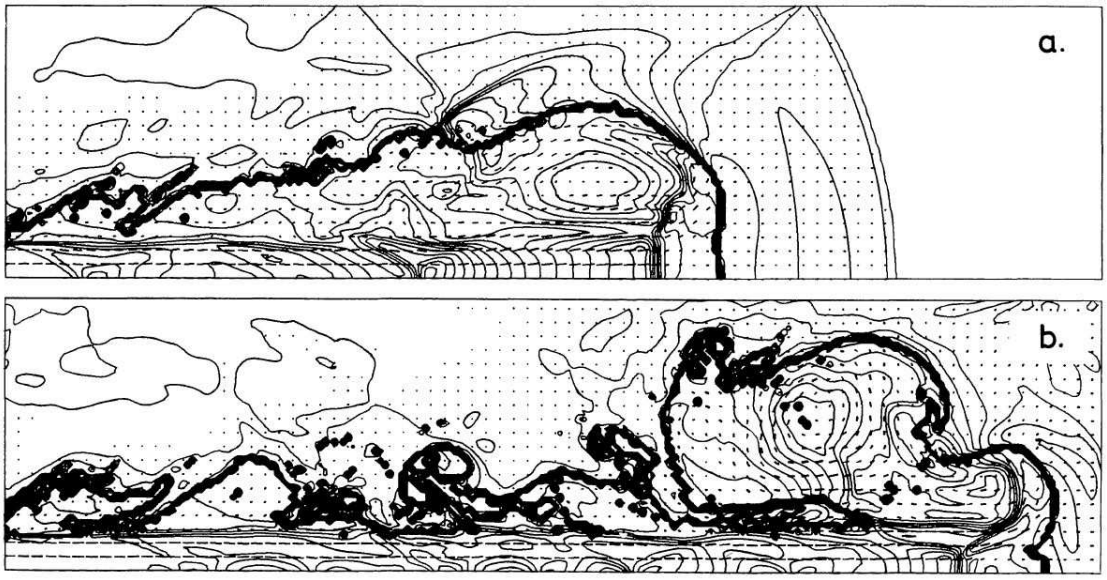

Figure 2.5: Structure and stability of a hot Mach 3 jet: (a) A well-developed low pressure 'eye' causes the characteristic underexpanded shock configuration at the working surface. (b) Vortex shedding and disruption of the cocoon. Note the incursions into the jet column which give rise to internal shocks. Figure reproduced from Norman, Smarr, Winkler & Smith (1982)(78)

2.5.5 Long Term Stability

In order to study the long-term stability of the working surface of the $\mathrm{M_b} = \mathbf{6}$ **jet**, a backwards velocity is added to the whole simulation equal to the bow shock velocity in the IGM rest frame, thereby transforming to the rest frame of the bow shock and allowing the simulation to develop over a long period of time without the head of the jet leaving the problem domain. A quasi-periodic instability in the jet head is exhibited, called 'vortex shedding', in which the low-pressure system surrounding the jet head would detach and roll back along the beam's length, disrupting the cocoon and creating internal shocks within the beam as seen in Fig.2.5. For the light, hot jet with $M_b = 6$, it is found that the period $t_{vs} \sim 2.8$ and the characteristic wavelength $\lambda_{vs} \sim 7.8$.

The vortex-shedding is found to be related to the beam's kinetic luminosity, $L_b = \pi R_b^2 M_b^3 / q_b^{1/2}$, and therefore much more sensitive to the beam Mach number M_b than the beam density q_b. At lower Mach numbers, the vortices inflate more slowly and grow to be larger. Also, if the density of the beam is similar to that of the surrounding medium, and therefore the sound speeds are similar, then the medium gas becomes efficiently entrained by the vortices.

2.5.6 Internal Shock Structure

Internal shock structure is a common feature of supersonic jet beams. Any pressure perturbation will cause an oblique shock to develop in the beam, moving inwards at the beam's sound speed C_b and sweeping along the beam axis at the supersonic flow rate $M_b C_b$. The models of Mach 6 and Mach 3 jets exhibit quasi-periodic pressure fluctuations caused by these shocks with a wavelength that seems related to the beam diameter, therefore suggesting a mechanism driven by Kelvin-Helmholtz instabilities at the cocoon / IGM boundary.

The shocks re-collimate the beam by turning gas inwards towards the jet axis. It is found that the shock structure is a more prominent feature close to the head of the jet; this is where the vortices are strongest. Further back along the jet beam, the vortices and shock structures tire.

2.5.7 Conclusion

In conclusion, the findings of the numerical models are discussed in the context of extra-galactic jets, and it is hypothesised that the knots of bright emission observed in these phenomena may be explained by the internal shock structures observed in the model outputs. The M87 jet in particular is discussed, visible in optical emission and 2cm radio maps; this exhibits a train of brightening knots outwards from the galactic nucleus until the designated Knot A is reached, with further knots downstream from this point diminishing in intensity. The first train of knots, it is suggested, are of diminishing intensity further upstream because the perturbations to the beam are weaker, having already tired; whilst downstream from Knot A, knots grow weaker because the flow momentum has been exhausted, producing weaker shocks until the subsonic regime is reached.

It is finally noted that MHD and mode coupling effects are not captured by the ideal fluid equations, and these may be important for flow stability and collimation; and (in the case of relativistic jets) whether energy loss through synchrotron radiation is important to the jet dynamics.

2.6 Chapter Summary

1. We have examined some early evidence for jets, and the basics of jet structure (see Fig.2.2).

2. Blandford & Payne's model of magnetocentrifugal jet launch and collimation from an accreting disc has been examined. Jets are seen to be efficient channels for the removal of angular momentum from the disc.

3. Where magnetic field lines make an angle of 60° or less to the outwards radius vector of the accretion disc, material is magnetorotationally unstable and may be flung out from the accretion disc (see Fig.2.4). Where gas is thermally excited, the potential barrier is lower and a larger angle ($\sim 70°$) will satisfy the condition.

4. While the magnetic potential exceeds the kinetic energy of the outflung material, it is accelerated upwards and outwards along the magnetic field lines, which co-rotate with the disc.

5. There exists a turning point in the solution $n > n_t$, where the parameter n describes the square of the magnetosonic fast-mode Mach number of the flow. Beyond this point the radial velocity becomes negative and the flow reconverges towards the central jet axis, thus achieving collimation.

6. The solutions indicate that most of the jet power is concentrated towards the central axis; angular momentum and magnetic flux are carried in the outer layers.

7. Behaviour of propagating supersonic jets has been examined via the simulation work of Norman, Smarr, Winkler & Smith (78). Rich structure in the form of variations in density, pressure, temperature and velocity may arise within the jet column due to variations in ejection velocity at source, or the growth of fluid dynamic instabilities, either of which may cause shocks to develop in the jet column.

8. Supersonic jet beams are terminated by a 'head' that possesses a complex triple-shock Mach disk structure. A region of trapped high-pressure gas just ahead of the Mach disk is referred to as the beam cap. A torus of low-pressure gas surrounding the head of the jet turns the flow back on itself (see Fig.2.5)

9. Hot, light jets with high Mach number ($M_b >= 6$) build stable cocoons of back-flowing gas which surround and stabilise the primary jet column. At lower Mach numbers, unstable lobes build instead of cocoons. These lobes entrain the ambient medium efficiently when the jet gas is in temperature and density balance with the surroundings. The results are summarised at Table 2.1.

10. Supersonic jet beams are susceptible to internal shocks, which may be caused by any pressure fluctuation at the surface of the jet column - such as the quasi-vortex shedding phenomenon. Internal shocks tend to recollimate the beam, as they focus gas inwards towards the jet axis.

Chapter 3

T-Tauri Jet Observations

3.1 HL Tau and the Herbig-Haro object HH151

HL Tau is a T-Tauri star in the Taurus-Auriga cloud complex, located $\sim$ 140 pc distant in the 50M$\odot$, L1551 molecular cloud. This is a region of multi-generational star formation (See Fig. 3.4, subfigure (a)) that spans classes 0-III (Moriarty-Schieven, 2006)(70).

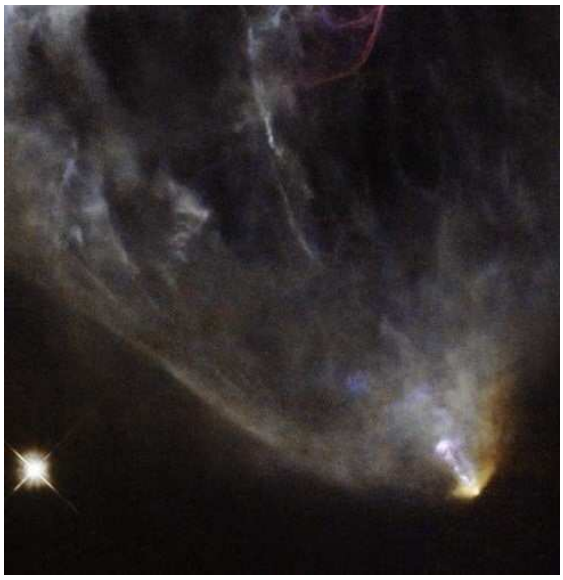

Figure 3.1: The HH151 jet from HL Tau; composite optical and near-IR image from the HST WFPC2. R-band image with enhanced narrowband Hα and [SII], with false colour IR at 814.0nm. Field of view is 1.7 $\times$ 1.8 arcminutes. HL Tau may be seen in the lower right corner of the image with the jet directed towards the upper left. The bright star in the lower left corner is XZ Tau. (Image courtesy of NASA / ESA)

One of the earliest discovered T-Tauri jets, HH151 (see Fig.3.1) was found by Mundt & Fried (1983)(72). Though it is now considered as a single outflow its curious features and changes in direction and morphology at first suggested the idea that it arose from the interaction of colliding jets from separate sources. The optical jet emerges from HL Tau at a 51° position angle and is initially well collimated and relatively faint; at 20" distance from the star however there is a change in direction of $\sim 14°$, whereupon the jet increases in relative brightness, and widens. Subsequent IR and submillimetre observations failed to confirm a hypothetical nearby source of a second jet that might have induced an abrupt change in direction and so this curious morphology is thought to arise from variations in the ambient medium; however, these variations may also be due to a wide-angle wind from XZ Tau (Movsessian et al., 2012)(71).

HH151 exhibits knots of brighter emission particularly after the bend in the jet. These knots exhibit detectable proper motions as demonstrated by Mundt et al. (1990)(74).

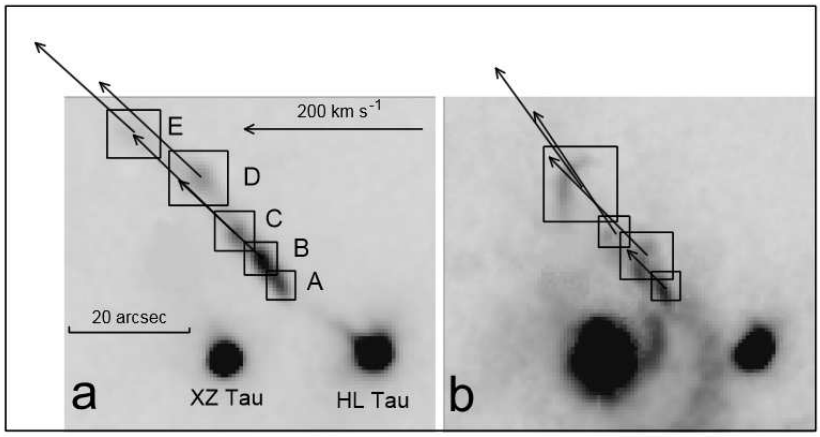

Figure 3.2: HL Tau & HH151 images in Hα taken with the 6m telescope at the SAO (Russia) with scanning & Fabry-Per ót interferometer. Two velocity channels are shown; (a) high velocity, $\sim$ 150 km/s; (b) low velocity, $\sim$ 50 km/s. (Image reproduced from Movsessian et al., 2012)(71)

Fabry-Perót interferometer observations in Hα have shown the structures in the jet to consist of fast-moving knots of optically emitting material with typical velocities of $\sim$ 150 km/s, and slower moving bows with a velocity in the region of $\sim$ 50 km/s (see Fig.3.2). The bow structures cross the jet and are ahead of the fast moving knots. It has been proposed that the fast-moving knotty structures are internal working surfaces in a variable velocity jet; this implies that they are 'shock sandwiches', i.e. Mach disc /

Bow shock pairs through which material is processed. The expectation then is that the fluid speed of material passing through these shock structures is greater than the proper motion of the structures themselves. Spectral imagery techniques confirm this and the average jet speed is found to be $\sim$ 250 km/s.(Movsessian et al., 2012)(71)

The slow-moving bows are suggested to arise from the interaction of the jet with a wide angle wind, demarcating a change of environment. The deflection and brightening of the HH151 jet as it enters this region lend credence to this hypothesis but the interpretation is less certain than that of the knots.

In recent years, HL Tau became the subject of additional interest, when the ALMA millimetre array produced the most detailed image so far taken of HL Tau (see Fig.3.3), revealing an accretion disc with well-defined rings surrounding the central T-Tauri star; suggesting that planet formation may be ongoing in the HL Tau system.

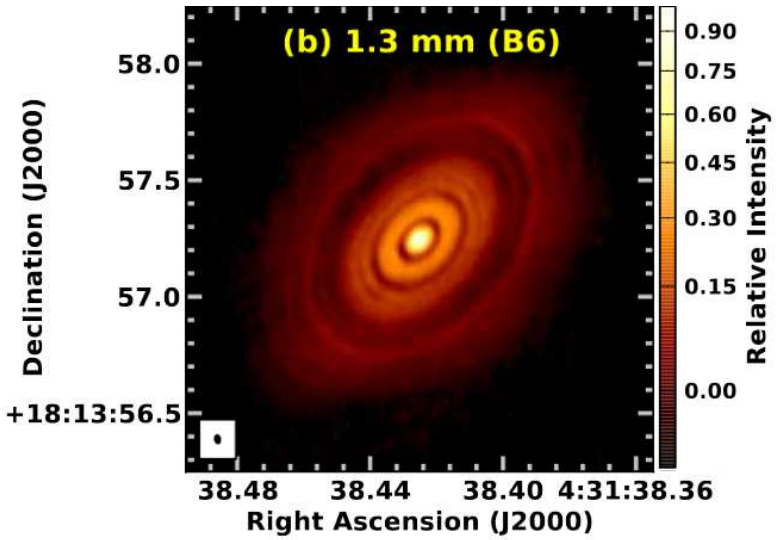

Figure 3.3: HL Tau 1.3mm image from ALMA, with angular resolution of 0.025" (3.5AU) revealing the presence of an accretion disc with well-defined rings, suggestive of planet formation. (Image from ALMA Partnership, 2015)(4)

3.2 Observational characteristics of the HH30 system

HH30 lies in the same region as HL Tau and was first identified as a protostar with associated jets at the same time (Mundt & Fried, 1983)(72). Much attention has been paid to the HH30* T-Tauri star and its outflows, because of its spectacular optical jet

(see Fig.3.5) and fortuitous inclination angle which places the jet almost in the sky plane (see Table 3.1). As HH30 is the focus of the research presented in this thesis, more detail is presented here on the observed characteristics.

3.2.1 The atomic outflow

A bipolar outflow system is seen to be radiating from the central object out to light-year scale, with the blue-shifted North-Eastern lobe appearing to be more continuously active (see Fig.3.4 subhigure (b)). HH30 refers to the Herbig-Haro objects at the terminus of the outflow (e.g. HH30-N for the cluster of knots at the northerly terminus); the source YSO is in fact designated HH30*, though the asterisk is frequently omitted in literature (Moriarty-Schieven, 2006)(70). HH30's proximate neighbours are also producing winds and jets, for example HL/XZ Tau (Anglada et al., 2007)(7).

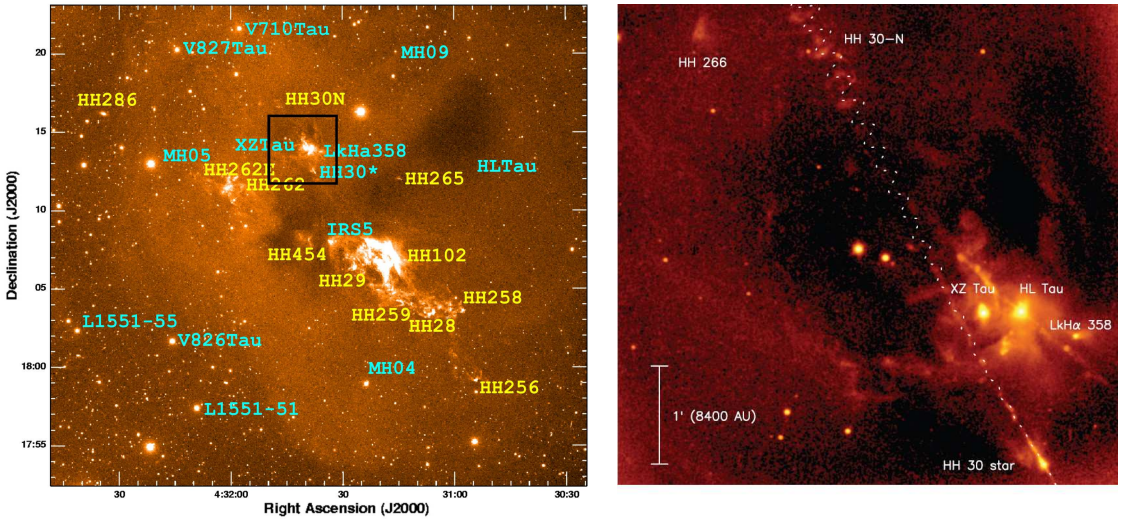

(a) the L1551 molecular cloud

(b) inset (a): the HH30 jet region

Figure 3.4: HH30 in L1551, in the Taurus-Auriga Cloud Complex. Images from the Nordic Optical Telescope in [SII] 671.6nm / 673.2nm show the large-scale outflow spanning $\sim$ 0.5 LY. Images from (a)(70) with some enhanced annotation, (b)(7)

The optically visible HH30 Jet / Counterjet structure has been studied with CCD imaging since the 1980's (Mundt et al., 1983, 1988)(72)(73). Knots of bright emission are moving away from the source object at speeds ranging from 100-300 km/s. There is a wiggling, possibly helical pattern in the outflow – but the motion of individual knots remains ballistic along a radial trajectory from the source (subject to side winds from other stars), rather than actually moving in a helical fashion. This implies that the helical

pattern is imposed on the outflow by the behaviour of the source object. Precession, or orbital motion, may be involved (Moriarty-Schieven, 2006; Anglada, 2007)(70)(7).

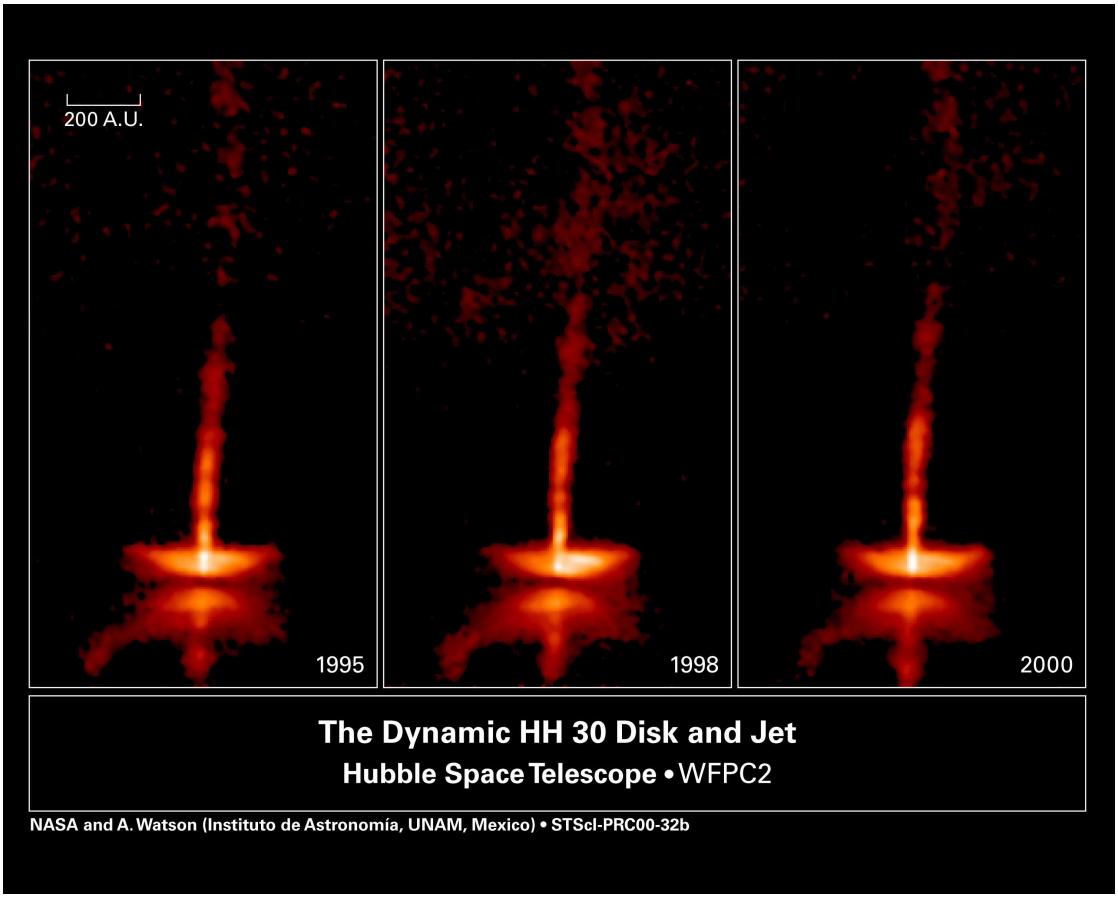

Figure 3.5: HST/WFPC2 images of HH30 with R-band filter, showing jet/counterjet and accretion disc structure (675nm, Δ89nm) (Image courtesy of NASA / ESA)

The HH30 jet has been imaged at various intervals since 1994 by the WFPC2 instrument (Wide Field Planetary Camera 2). Images taken with the R-band filter, (675nm, Δ 89nm), in which the dominant spectral line is the Hα line (656.28nm), show detail of the accretion disc and emerging jet / counterjet in a clearly resolved structure spanning $\sim$ 1000AU (see Fig.3.5). Hα luminosity in the jet column is mainly a superposition of recombination emission from shocked H gas, and some additional reflected light emitted by the hot central object. Proper motion studies suggest a train of pulses emerging from the source. It is clear that at present the (blueshifted) North-East directed jet is much more active than the (redshifted) South-West directed counterjet within 1000AU of the source; although at light-year scales there are larger knots of emission moving away to the South at greater speeds than their northern counterparts, suggesting bursts of activity in the counterjet at some time in the past (Hartigan, Morse 2007)(41).

Luminosity seen from the bowl-like upper and lower surfaces of the disc is most likely to be reflected light alone. The variability in disc luminosity may be due to:

- Orbital motion of voids in the inner accretion disc
- Transiting clumps of disc material
- Flaring or hot spots due to accretion events

(Stapelfeldt et al., 1999)(111)

HH30 is thought to be composed of 2 objects; estimates tend to put the total mass at ~ 0.45 M$\odot$, with typical primary and secondary masses of ~ 0.31 M$\odot$ and ~ 0.14 M$\odot$ though these numbers vary depending on which model is chosen to explain the wiggling behaviour of the knots of bright emission in the jet and the parameter space of each model allows a range of solutions (Anglada et al., 2007)(7). Based on these numbers however, the mean orbital separation is 18AU, and the orbital period, 114 years. The co-orbiting objects are surrounded by a circumbinary accretion disc whose optically illuminated region spans a 500AU diameter (see schematic in Fig.3.6) with observations in molecular lines suggesting an extended diameter of $\sim$ 850AU (Pety et al., 2006)(81).

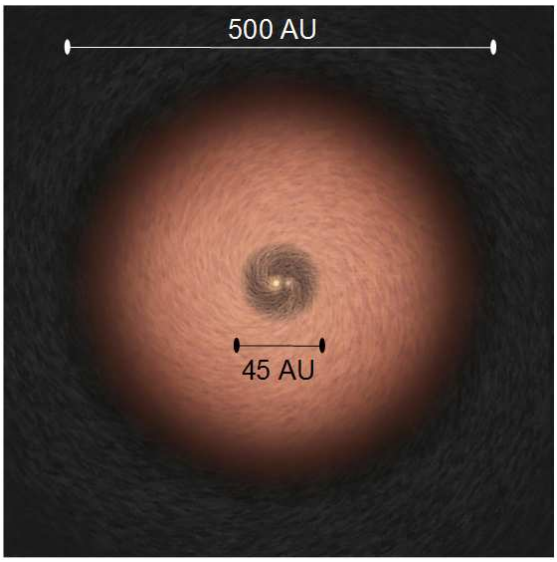

Figure 3.6: HH30 with circumbinary accretion disc, viewed perpendicular to the disc plane; schematic diagram only, central objects not to scale.

Estalella et al., (2012)(27) find that the binary components orbit within a depletion zone $\sim$ 40AU diameter, and that **the orbital motion is the primary driving influence causing the helical wiggling appearance of the jet at light-year scale, with precession acting as a secondary influence, if present at all**. This is a key point to which we shall return.

It has been suggested that, in addition to a longer-period variability in ejection velocity likely to give rise to the knots of bright emission found in the HH30 outflow at light-year scale (Raga et al, 1990)(86), there is a short-timescale variability (of the order of months) in the ejection velocity; possibly chaotic in nature, arising from variable accretion, which steepens into shock fronts that provide the main cause of heating and ionisation of the jet material (Hartigan, Morse 2007)(41)(Anglada, 2007)(7).

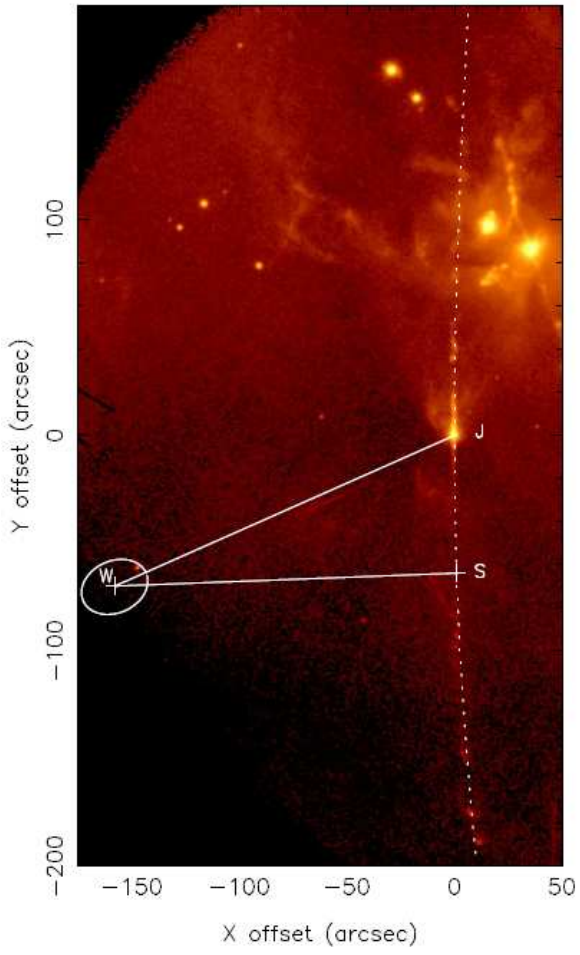

Figure 3.7: Sideways bend in the light-year scale HH30 jet and counterjet. An isotropic stellar wind is invoked to fit the dotted curve to the jet path. Positions of HH30 (J), wind source (W) and wind/jet stagnation point (S) are indicated. (Figure reproduced from Estalella et al., 2012)(27)

The light-year scale outflow appears to be driven sideways in the sky plane, exhibiting a West-facing 'C' shape curve (See Fig. 3.7) that may arise from systemic velocity, or impinging outflows or winds from nearby objects (Estalella et al., 2012)(27).

Estimates of the outflow inclination with respect to the sky plane vary, depending on author, and also choice of end-point; for example, if the HH-30N nebula is considered as the end-point, the inclination towards the observer of the blue-shifted lobe is 40° (Anglada, 2007)(7).

De Colle et al. (2010)(20) provide a more nuanced view in a 1000AU span about HH30, with a tomographic reconstruction of the three-dimensional structure of the HH30 jet (see Fig.3.8) based on data from Hartigan & Morse (2007)(41). This suggests, in the case of the blueshifted North-East jet, an inclination out of the sky plane of barely more than 1° over the first 400AU, deviating more strongly towards the observer beyond this limit; whilst the less active redshifted counterjet shows stronger directional variation but with a trend of $\sim 2.5°$ away from the observer immediately from its departure point.

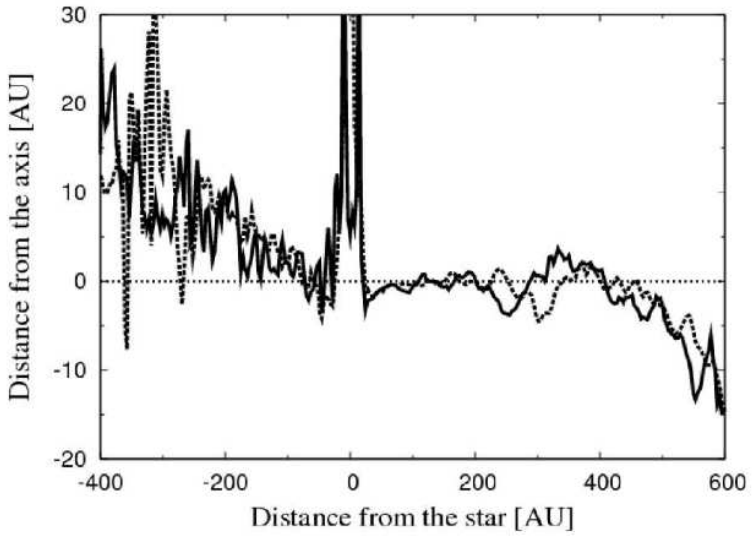

Figure 3.8: Tomographic Reconstruction of HH30 inclination in the range -400AU $<$ x $<$ 600AU, where the x-axis is in the sky plane perpendicular to the intersection of the accretion disc plane and the sky plane (this line forming the z-axis). The y-axis is perpendicular to the sky plane and directed away from the observer. The positive x-direction is $\approx$ North-East. (Figure reproduced from De Colle et al., 2010)(20)

3.2.2 The molecular outflow

A parallel strand of investigation into the HH30 system involved observation in molecular lines, such as the work of Pety et al (2006)(81) imaging HH30 in HCO^+ and several isotopologues of the CO molecule which emit in millimetre wavelengths. This revealed a great deal about HH30 including Keplerian rotation of the accretion disc in the ^{13}CO(2-1) 1.35mm line, but of particular interest for our work has been the observation of a slower-moving, cold, dense outflow imaged in the ^{13}CO(2-1) 1.3mm line (see Fig.3.9). This outflow is only observed emerging from the North-facing side of the accretion disc, where the atomic outflow is also active, and is quiescent on the South face, similar to the atomic counterjet.

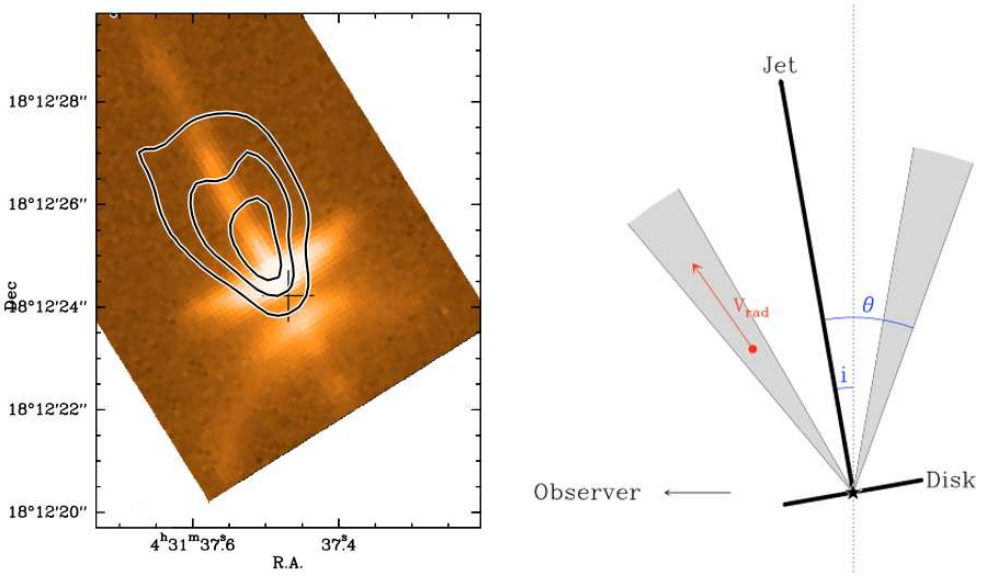

(a) ^{12}CO J=2-1 contour image of HH30 Outflow

(b) Ad Hoc Model of the Molecular Outflow

Figure 3.9: Left Panel: ^{12}CO J=2-1 contour image of HH30 Outflow overplotted on a 670nm and 787.7nm composite image from the HST (Burrows et al. 1996). Right Panel: ad hoc model of the molecular outflow, used for computing synthetic images. Emitting gas forms a hollow conical structure, tilted at a small angle i towards the observer (the dotted line denotes the sky plane). Images reproduced from Pety et al., 2006 (81)

Synthetic images generated from the conical ad hoc model are found to agree closely with the morphology of the observed HH30 molecular outflow (see Fig.3.10).

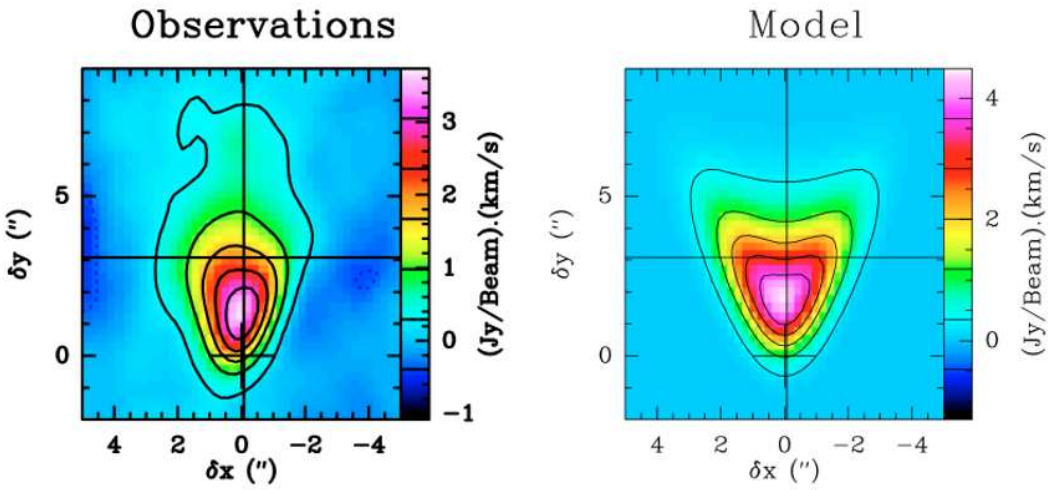

Figure 3.10: HH30 ^{12}CO outflow observation vs. synthetic image generated from ad hoc model with best fit parameters. Image reproduced from Pety et al., 2006 (81)

Later work by Tambovtseva & Grinin (2008)(118) goes a stage further in developing a working model of the HH30 molecular outflow, by performing simulations in which the outflow material is composed of particles that are ejected ballistically into the problem domain (See Tambovtseva & Grinin, 2002 (117) for a complete description of the method). Four scenarios are investigated, based on the work of Anglada et al (2007)(7); the first three scenarios assume orbital motion of the molecular outflow source, with varying parameterization. The fourth scenario assumes that the binary system is very close and that the wiggle in the atomic jet arises from tidally-induced precession. In this scenario, the molecular outflow originates from the circumbinary disc (see Fig.3.11), whose inner radius is much smaller (3AU) because of the tight binary orbit (0.75AU).

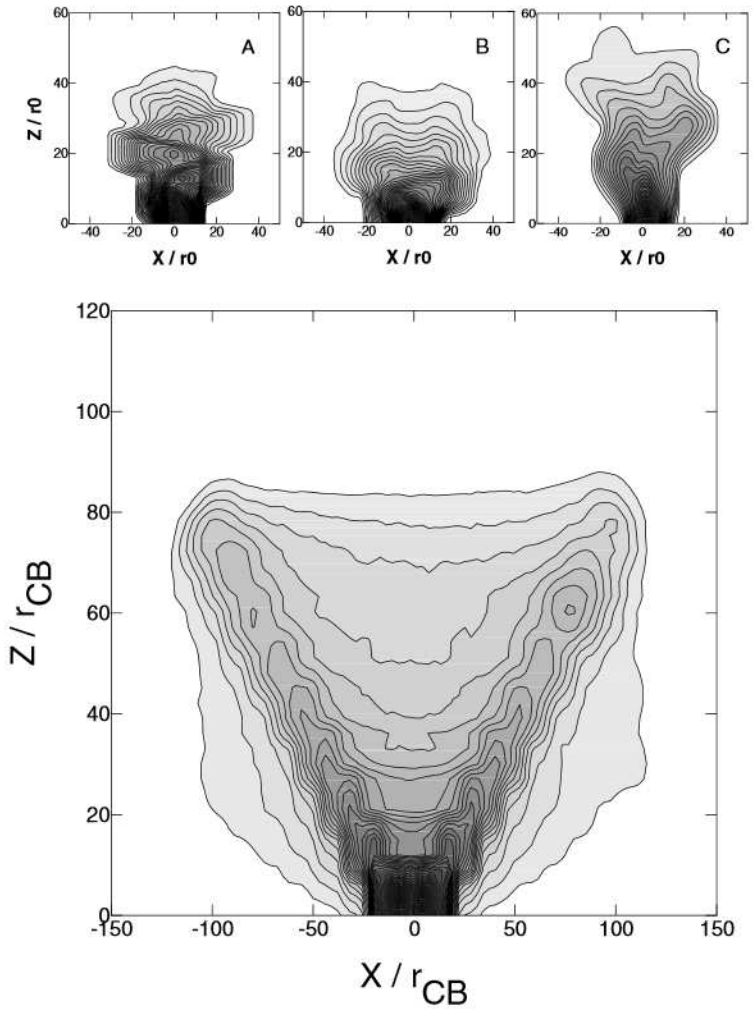

Figure 3.11: HH30 ^{12}CO outflow ballistic particle models, mapped in isodensity contours. The upper three scenarios A-C are orbital models with different radial velocities and half-opening angles. The bottom, larger image is scenario D which assumes precession is responsible for the HH30 atomic jet wiggle; hence the molecular outflow is driven by the circumbinary disc. Image reproduced from Tambovtseva & Grinin, 2008 (118)

Tambovtseva & Grinin find that the model which assumes a very close binary orbit and a circumbinary disc source (Fig.3.11, bottom panel) produces closer resemblance to the observed morphology of the molecular outflow. **This implies that precession of the atomic jet source is the primary origin of jet wiggling, with orbital motion a lesser influence**.

Table 3.1 summarises the key observational findings which informed our models of HH30.

Table 3.1: Observed Parameters of the HH30 system

	Pety 2006 (81)	Anglada 2007 (7)	Hartigan 2007 (41)	De Colle 2010 (20)	Estalella 2012 (27)	Unit
Velocity (Systemic)	7.25±0.04					km s^{-1}
CB Disc Outer Radius	420±25				~ 250	AU
CB Disc Inner Radius					~ 40	
CS Disc Outer Radius					$\lesssim 6.00$	
CS Disc Inner Radius					~ 0.07	
Disc Axis Position Angle	32±2	31.6				deg
Disc Inclination Angle	84±3					deg
Disc Rotation Vector	North-East					
Disc Temperature	12					K
Precession Angle (A) [2]		1.42±0.12				deg
Precession Period (A) [2]		53±15				yrs
Half Opening Angle (A)		1.43±0.12	2.6±0.4	2.4		deg
Half Opening Angle (M)	30±2					deg
Binary Separation [1]		9-18			18±0.6	AU
Binary Separation [2]		< 1				
Absolute Orbit (P) [1]					5.7±0.9	AU
Orbit Period [1]		53±			114±2	yrs
Orbit Period [2]		< 1±				yrs
Orbital Phase Angle (P)					95±11	deg
Orbital Velocity (P) [1]					1.5±0.2	km s^{-1}
Orbital Velocity (S) [1]		2-5				km s^{-1}
Flow Source (A) [1]		Secondary			Primary	
Flow Source (A) [2]		Primary				
Flow Velocity, Radial (A)	200±0.09	100-300				km s^{-1}
Flow Velocity, Radial (M)	12±2					km s^{-1}
Flow Velocity, Azim. (A)						km s^{-1}
Flow Velocity, Azim. (M)	< 1.00					km s^{-1}
Flow Velocity Variability						
Flow Inclination, North (A)				~ 1	5	deg
Flow Mass (A)	2×10^{-8}					$M_\odot$
Flow Mass (M)	2×10^{-5}					$M_\odot$
Flow Mass Flux (A)	1×10^{-9}			1×10^{-8}		$M_\odot$ yr^{-1}
Flow Mass Flux (M)	6.3×10^{-8}					$M_\odot$ yr^{-1}
Flow Momentum (A)	4×10^{-6}					$M_\odot$ km s^{-1}
Flow Momentum (M)	2.4×10^{-4}					$M_\odot$ km s^{-1}
Flow Momentum Flux (A)	2.6×10^{-7}					$M_\odot$ km s^{-1} / yr
Flow Momentum Flux (M)	7.5×10^{-7}					$M_\odot$ km s^{-1} / yr
Flow Ionisation (A)			0.05-0.40			
Flow Temperature (A)			7.26×10^3	$\sim 1 \times 10^4$		K
Flow No. Density (A)			1×10^6			
Flow Width (A) @ 20 AU			14±3	15		AU
Flow Width (A) @ 500 AU			36±4	30		AU
Stellar Mass (Total) [1]	0.45±0.04	0.25-2			0.45±0.04	$M_\odot$
Stellar Mass (P) [1]		0.25-1			0.31±0.04	$M_\odot$
Stellar Mass (S) [1]					0.14±0.03	$M_\odot$
Stellar Mass (P) [2]		0.1-1				$M_\odot$
Stellar Mass (S) [2]		0.01-0.04				$M_\odot$
Stellar Luminosity (Total)	0.2					$L_\odot$

Summarises the findings of a number of observations and investigations into the nature of HH30. This is not intended to be exhaustive, but provides the basis for our choice of model parameters. (A) designates a parameter relating to the atomic jet; (M), the molecular outflow. [1] and [2] are alternative scenarios - [1] is orbital, [2] is precession. Any parameter not identified as either is agnostic or else, by default, assumes the orbital scenario.

3.3 Chapter Summary

1. Observations of two jets from classical T-Tauri (Class II) stars have been discussed. Firstly, HL Tau, which hosts an accretion disc imaged by ALMA, that has been shown to possess a system of rings suggestive of planet formation (Fig.3.3); this star is the source of HH151, an optical jet that contains knots and bows of bright emission (Fig.3.2). Secondly, HH30, 'poster child' of the T-Tauri stars, possessing an edge-on accretion disc and a jet/counterjet outflow in the sky plane that has a well-defined helical 'wiggle' (Fig.3.4).

2. HH30 has a well-collimated, vigorous jet of optically emitting material emerging from one side in a semi-continuous plume out to $\sim$ 1000AU (Fig.3.5). Elongated knots of hot gas propagate from the source at speeds ranging from 100-300 km/s, radiating strongly in the Hα line. Table 3.1 summarises many of the observed dynamic characteristics of the outflow.

3. It is also found that HH30 possesses a slow-moving (12 km/s) molecular outflow emerging from the source in a wide angle (30° half-opening) on the same side as the plume of optical material (Fig.3.9). Ad hoc and ballistic particle modelling confirm that a 'hollow' conical structure produces synthetic images which correspond well to the observed ^{12}CO 1.3mm emission (Fig.3.11).

4. Two explanations of the 'wiggling' of the HH30 optical outflow have been offered; both consider the source to be a binary system (Fig.3.6). One hypothesis is that orbital motion is mainly responsible for the wiggling; in this case, the binary separation is $\sim$ 15AU. This suggests the CB disc has an inner radius of $\sim$ 45AU. In this scenario, the molecular outflow emerges from the individual accretion disc of one of the objects in the binary pair.

5. The alternative hypothesis is that the wiggling of the HH30 optical jet is mainly due to tidally-induced precession of its source. In this scenario, the binary pair are very close, $<$1AU separation, and the inner radius of the CB disc, is $\sim$ 3AU. In this case, the molecular outflow is considered to be launched from the inner regions of the CB disc.

6. Analytical modelling of the atomic jet wiggle has suggested that the first scenario is the more likely, with the molecular outflow therefore being produced by an orbiting binary partner also. However, computational modelling of the behaviour of the molecular outflow in the two cases favours the precession-driven scenario.

7. The aim of the research presented in this thesis is to work with fully three-dimensional numerical models of the propagation of both outflows in the region within $\sim$ 120AU of the outflow source(s), generated using the well-established Eulerian astrophysical code ZEUS-MP, to examine and compare their interaction in both the orbital-driven and precession-driven scenarios.

Chapter 4

Methods

4.1 The equations of Astrophysical Fluid Dynamics

4.1.1 Physical Equations

We begin this chapter by discussing the equations of astrophysical fluid dynamics. These equations are presented in various forms depending on the particular application and what physical quantities of interest are subject to a condition of dynamic evolution. The equation set that is presented here is that which is solved numerically by the standard implementation of the ZEUS-MP astrophysics code. Compressible, non-viscous, non-thermally-conducting flow is assumed; in addition, there are equations for the evolution of radiation energy density and magnetic flux density (the latter simply being the induction equation of the Ideal-MHD approximation). These couple to the transport equations for momentum and energy by the inclusion of suitable source terms on the right hand side of these equations.

The full ZEUS-MP equation set is as follows (Hayes et al., 2006)(44):

Continuity:

$$\frac{D\rho}{Dt} + \rho\nabla \cdot \mathbf{v} = 0 \tag{4.1}$$

Momentum:

$$\rho\frac{D\mathbf{v}}{Dt} = -\nabla p + \left(\frac{\chi}{c}\right) + \frac{1}{4\pi}(\nabla \times \mathbf{B})\times\mathbf{B} - \rho\nabla\Phi \tag{4.2}$$

Energy:

$$\rho\frac{D}{Dt}\left(\frac{e}{\rho}\right) + p\nabla \cdot \mathbf{v} = c\kappa_E E - 4\pi\kappa_P B_P \tag{4.3}$$

Radiation:

$$\rho\frac{D}{Dt}\left(\frac{E}{\rho}\right) + \nabla \cdot \mathbf{F} + \nabla\mathbf{v}\mathbf{P} = 4\pi\kappa_P B_P - c\kappa_E E \tag{4.4}$$

Magnetic Flux:

$$\frac{\partial\mathbf{B}}{\partial t} = \nabla \times (\mathbf{v} \times \mathbf{B}) \tag{4.5}$$

Some further definitions:

Planck Function:

$$B_P = \frac{\sigma}{\pi}T^4 \tag{4.6}$$

Flux-mean, Planck-mean, and Energy-mean opacities:

$$\chi = \frac{1}{\mathbf{F}}\int_0^\infty \chi(\nu)\mathbf{F}(\nu)d\nu \tag{4.7}$$

$$\kappa_P = \frac{1}{B_P}\int_0^\infty \chi(\nu)B_P(\nu)d\nu \tag{4.8}$$

$$\kappa_E = \frac{1}{E}\int_0^\infty \chi(\nu)E(\nu)d\nu \tag{4.9}$$

Radiation Flux:

$$\mathbf{F} = -\left(\frac{c\Lambda_E}{\chi}\right)\nabla E \tag{4.10}$$

(where Λ_E is a flux limiter to ensure that radiation propagation remains bounded by the speed of light)

Radiation Stress Tensor:

$$\mathbf{P} = \mathbf{f}E \tag{4.11}$$

where $\mathbf{f}$ is approximated by:

$$\mathbf{f} = \frac{1}{2}(1-f)\mathbf{I} + \frac{1}{2}(3f-1)\hat{\mathbf{n}}\hat{\mathbf{n}} \tag{4.12}$$

$$\hat{\mathbf{n}} = \frac{\nabla E}{|\nabla E|} \tag{4.13}$$

$$f = \Lambda_E + \left(\frac{\Lambda_E |\nabla E|}{\chi E}\right)^2 \tag{4.14}$$

($\mathbf{I}$ is the unit tensor)

Gravitational Potential:

$$\nabla^2 \Phi = 4\pi G\rho \tag{4.15}$$

It should be finally noted that a thermodynamic equation of state is required to close the equations:

$$p = (\gamma - 1)e \tag{4.16}$$

4.1.2 Simplified Equations

In our jet models, radiation is not considered as a driving force, as the stars are pre-main sequence and are well below the Eddington Limit of luminosity. A further simplification, is effects of gravitation are not considered; the specific kinetic energy of jet material entering our problem domain is ~ 2000 times that of its gravitational potential energy. This results in a reduced set of equations as follows:

Continuity:

$$\frac{D\rho}{Dt} + \rho\nabla \cdot \mathbf{v} = 0 \tag{4.17}$$

Momentum:

$$\rho\frac{D\mathbf{v}}{Dt} = -\nabla p + \frac{1}{4\pi}(\nabla \times \mathbf{B})\times\mathbf{B} \tag{4.18}$$

Energy:

$$\rho\frac{D}{Dt}\left(\frac{e}{\rho}\right) + p\nabla \cdot \mathbf{v} + \Lambda(T, n, f) = 0 \tag{4.19}$$

Magnetic Flux:

$$\frac{\partial\mathbf{B}}{\partial t} = \nabla \times (\mathbf{v} \times \mathbf{B}) \tag{4.20}$$

Equation of State:

This is required to close the equations above. It is simply the Ideal Gas Equation.

$$p = (\gamma - 1)e \tag{4.21}$$

In which γ is the Adiabatic Index, the ratio of the specific heat capacity at constant pressure C_P, to the specific heat capacity at constant volume, C_V.

Note that the energy equation 4.19 contains an additional term Λ, the cooling function, with arguments T = Temperature, n = number density of Hydrogen nuclei, and f = molecular Hydrogen abundance. This is explained in the section that follows.

4.1.3 The Role of Cooling

The gaseous ambient medium and injected jet material in our models begin at temperatures in the range 30K - 1000K, but during the dynamic evolution of the models temperatures of the order of 10^4K - 10^5K are reached in and around the central jet column as material is processed through supersonic shocks at velocities of 200 - 300 km/s; the rearward-facing shocks decelerate the material and convert bulk kinetic energy into thermal energy.

Energetic inter-particle collisions lead to dissociation and ionisation of molecules and atoms; these collisions may also excite bound electrons into higher, unstable energy states, or may excite vibrational and rotational energy states of molecules. Through recombination and spontaneous de-excitation, higher energy states decay through a cascade of transitions producing a spectrum of emission and, if the emitted photons are able to escape without being re-absorbed, this radiatively cools the material. Another cooling mechanism is dust grain cooling, whereby collisions with gas particles transfer thermal energy to dust grains, that radiate this energy away as infrared or millimetre wavelength photons and thereby cool the medium (Smith, 2004)(100). This is in contrast to adiabatic models, in which hot material may only thermally relax through contact or intermixing with other material at a lower temperature.

The standard implementation of ZEUS-MP contains basic chemistry for simple Hydrogen 3-species chemistry (H_2, H, H^+). Options are implemented for other 'zoos' of chemical species, but the 3-species chemistry was considered sufficient for our purposes, as the emission lines for our synthetic images could all be computed in postprocessing either directly from Hydrogen species populations or by proxy based on those populations, and more complex chemistry would increase run times and storage requirements. However, the version of the ZEUS-MP code used for the jet models herein does employ enhanced cooling functions which were developed by Suttner et al. (1997)(115). These compute the cooling and chemistry terms implicitly to ensure stability; this is carried out in a separate step to the compressional PdV heating calculation. The cooling temperature exponents are pre-tabulated to improve performance, and two separate temperature regimes are identified which are handled by different routines, T $<$ 3000K and T $>$ 3000k, since

cooling efficiency is dominated by different components in each regime.

We saw earlier that the energy equation 4.19 involves a term Λ describing cooling effects. The overall cooling function consists of 13 sub-functions which model various different processes that cool the heated medium.

$$\rho \frac{D}{Dt}\left(\frac{e}{\rho}\right) + p\nabla \cdot \mathbf{v} + \Lambda(T, n, f) = 0 \tag{4.22}$$

$$\Lambda(T, n, f) = \sum_{i=1}^{13} \Lambda_i \tag{4.23}$$

These sub-functions are given at Appendix D.

4.1.4 Derivation of the Equations

The equations in the form presented above are known as the Euler Equations, and are a simplified form of the more general Navier-Stokes equations which also include terms for viscosity. These equations describe the behaviour of the fluid at the macroscopic level and are derived by considering the behaviour of 'parcels' of fluid continua rather than examining the microscopic behaviour of its constituent particles. This is a valid assumption to make when the mean free path of the particles is much shorter than the length scale of the system under consideration.

Appendix A presents a derivation of these equations.

4.2 ZEUS-MP: A code to simulate radiating and magnetized flows

4.2.1 Solving the equations of Astrophysical MHD

The equations governing the behaviour of jets do not lend themselves to analytic solution in a realistic scenario and so approximate numerical methods are often used to model the physics. Eulerian codes (grid-based) are usually preferred as there are expectations of fluid dynamic instabilities which are not well-handled by Lagrangian (particle-based) methods such as SPH (Agertz et al, 2007)(1); Lagrangian codes have also suffered difficulties in modelling magnetic fields, although recent developments may lead to improved capabilities in this regard (Price et al., 2008)(83).

The code used to model jets in this thesis is ZEUS-MP, a massively parallel Eulerian code written in FORTRAN, and based on finite difference algorithms. The ZEUS family of codes has a long and respectable history in computational astrophysics; they have the advantage of being very flexible as well as a proven track record of reliability in handling many astrophysical problems, and jets in particular as the code was originally developed to model extragalactic jets.

Sections 4.2.2 through 4.2.3 that follow are largely based on content from *Simulating Radiating and Magnetized Flows in Multiple Dimensions with ZEUS-MP* (Hayes et al., 2006)(44). In the interests of brevity details of the methods of finite differencing, the Courant stability condition and staggered grids and operator splitting are omitted here, but the author's own exposition of these techniques is offered at Appendix B.

4.2.2 Overview of ZEUS-MP

The earliest version of the ZEUS Eulerian multiphysics code was released by David Clarke in 1988 for simulation of MHD radio jets; the code then evolved through two parallel development forks called ZEUS-2D and ZEUS-3D, each offering different features and solution methods; and then, drawing from developments in both of these codes, ZEUS-MP was released in 2006 by John Hayes and Michael Norman. This massively parallel version of the code allows the problem domain to be divided into a set of tiles each of which is solved independently in each timestep, with information exchange at the

boundaries being handled by MPI (Message Passing Interface) library calls.

The authors of ZEUS-MP noted at the time of its release that other codes had emerged based on Godunov methods which are intrinsically second-order accurate and conservative, with superior ability to resolve shock fronts at identical resolution. However they point to tests that demonstrate ZEUS-MP to be a reliable and numerically well-behaved code when applied to particular classes of problems, in comparison to codes based on different solution schemes. Also, ZEUS-MP has the advantage of being a very versatile code that is readily adaptable by users to incorporate new physics or alternative solution schemes.

It is noted that the ZEUS-MP solution scheme is non-conservative as it evolves the internal gas energy rather than a total internal energy equation; thus, conservation errors in energy are of particular interest. In three adiabatic test problems, namely the Sedov-Taylor Blast Wave, Riemann Problem, and Orszag-Tang Vortex, the conservation errors were found to be 1.4%, 0.8%, and 1.6% respectively.

It is also important to verify adherence to the $\nabla \cdot \mathbf{B} = 0$ constraint. The field evolution algorithm is constructed in a way that ensures a divergence-free field but machine rounding errors can still introduce a non-zero divergence. Amongst a suite of test problems, the only solution found by the authors to manifest a non-zero divergence was the 2D Orszag-Tang Vortex, which still satisfied the constraint to within $1 : 10^{12}$.

A number of shortcomings in the existing ZEUS-MP code are noted that must, if necessary, be dealt with by user customisation; although some of these may be addressed in a future release. Possible improvements to the solver algorithms, such as a better preconditioner for the Conjugate Gradient solver, are an active area of research.

Some of the equations that ZEUS-MP solves are time-marching in nature and may be solved explicitly - that is to say, the value at a given spatial grid points at time step (n+1) are wholly determined by values of the given and neighbouring grid points at the previous time step (n). However, not all operations can be performed in this way. Poisson Gravity and Radiation Flux equations give rise to a system of linear equations that must be solved implicitly. Iterative methods must be used, but those selected must lend themselves to domain decomposition methods to enable parallelisation. Gauss-Seidel is rejected for this

reason; whilst Jacobi, although not spatially recursive and therefore decomposable, has a high computational cost. Instead, three linear solvers are implemented in ZEUS-MP - Conjugate Gradient, Multigrid, and - for problems on 3D Cartesian meshes with triply periodic boundary conditions - a Fast Fourier Transform method. A full discussion of these methods is beyond the scope of this review, although the paper does go into some detail and provides full equations in an appendix.

Still other versions of the ZEUS code base are in usage. DZEUS is a double-precision version of the ZEUS-3D code; and AZEUS, based on the DZEUS code, implements adaptive mesh refinement which dynamically scales the spatial grid to the features of the solution. AMR is an attractive feature, but for this project it was decided to use ZEUS-MP for reasons of compatibility with pre-existing modules implementing enhanced molecular chemistry and cooling.

4.2.3 Some features of ZEUS-MP

Artificial Viscosity

This is incorporated to smooth shocks across a couple of zones so that they are correctly handled by the numerical algorithm and provides a means of viscous dissipation of the bulk kinetic energy of material passing through the shock. It is computed as part of the source step. Two kinds of artificial viscosity are available, von Neumann & Richtmeyer (quadratic, upwinded flow velocity differences), and linear (dependent on local sound speed and simple flow velocity differences).

Magnetohydrodynamics and Method of Characteristics

An important requirement of the magnetic flux density $\mathbf{B}$ is that it must satisfy $\nabla \cdot \mathbf{B} = 0$. Also, fluids that evolve according to the equations of MHD can exhibit three kinds of wave behaviour - fast and slow magnetosonic waves (longitudinal, compressive waves), and at an intermediate speed between these, Alfvén waves (transverse, noncompressive). The magnetosonic waves are handled satisfactorily by the same algorithms that work for hydrodynamic waves, but the Alfvén waves require tight coupling between components of

velocity and magnetic flux which are perpendicular to the propagation direction. ZEUS-MP uses a method which, to give it its full title, is the "Hawley Stone Method Of Characteristics and Constrained Transport", or HSMOCCT hereafter (Hawley & Stone, 1995)(43). Essentially, this method resolves the magnetic induction and the transport of momentum as part of the same operation rather than treating them in separate stages, which has previously led to difficulties.

Multispecies Advection

Only one set of equations is solved by ZEUS-MP for mass fluxes and so it is not possible to track separate momentum distributions for different species. But provided it is acceptable that the different species be mutually advected, then ZEUS-MP is able to track mass concentrations of different species across the mesh. A concentration array X_n is used, where ρX_n expresses the mass fraction of species n throughout the grid.

Radiation

Rather than solve a full time-dependent radiation momentum equation, a Flux Limited Diffusion approximation is employed (Levermore & Pomraning, 1981)(63). A cautionary note; flux limiters are designed to function well for fairly transparent media, where $\lambda/\delta t > c$. In media where the physical mean free path λ between photon interactions is much less than the zone size, the propagation speed is much less than c and so the flux limiter provides no constraint, which can give rise to unrealistically rapid heating. This tends to be more of a problem in terrestrial rather than astrophysical applications, but should be borne in mind. Another issue to note is that the FLD equation for flux depends on the local gradient in E, the radiation energy density. This means that radiation tends to flow in the direction of these gradients even if this is not physically expected.

Note: Radiation physics is not used in our jet models.

Gravity

There are three ways in which ZEUS-MP can treat gravity - point-mass potential, spherically symmetric gravity, and a full Poisson potential which will determine the self gravity of an arbitrary distribution of matter.

Note: Gravitational physics is not used in our jet models.

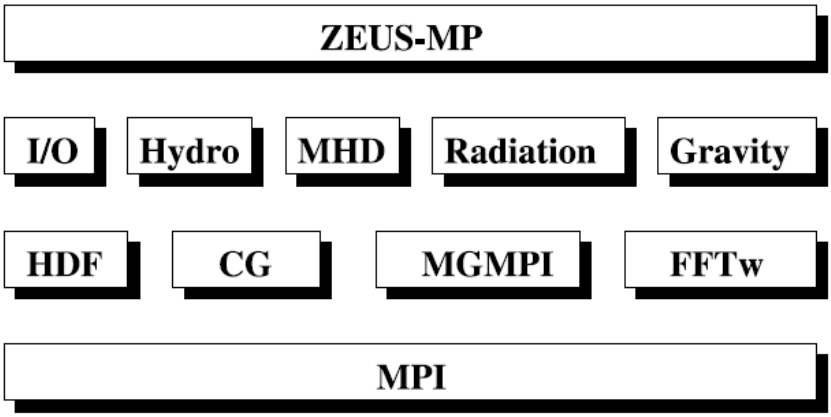

Figure 4.1: Software implementation within ZEUS-MP (Figure reproduced from Hayes et al., 2006 (44))

4.3 Utilising the ZEUS-MP Code

4.3.1 Use in Parallel Computing Environments

ZEUS-MP is a code that is designed for use on MIMD systems - Multiple Instruction, Multiple Data. The hardware architecture of MIMD systems varies. Some systems have a Shared Memory Architecture (SMA) where multiple CPUs access a globally shared, contiguous pool of memory. Each running process may be provided with its own protected working memory allocation within the pool of RAM. On such a platform with a shared address space, processors may interact with each other by reading and writing communication data to memory. Sometimes these are called Multiprocessor systems. Their advantage is that they make efficient use of memory and the tight coupling of the hardware reduces latency.

A Distributed System or Cluster is an alternative arrangement in which each CPU has its own separate, local RAM, each processor thus acting as an autonomous computer. A network provides the necessary means for processors to communicate with each other. Sometimes these are called Multicomputer systems. Their advantage is that they are readily scalable by adding more processing units, and can be implemented with cheap, non-specialised hardware.

It is not at all unusual for hybrid arrangements to occur, wherein a Distributed System is built from multiple SMA machines.

When Eulerian grid-based codes run on MIMD systems, it is often the case that the spatial problem domain is decomposed into many subdomains, each of which is solved by its own CPU that is dedicated to the task (Multiple Instruction), with its own separate memory space to store the arrays of variables that describe the physical state of the problem subdomain (Multiple Data).

CPUs in such a system are referred to as ‘cores’. A group of cores with a shared pool of memory between them is referred to as a ‘node’. The way that the problem domain is distributed onto the cores is called a ‘tiling’ of the domain. Processes must swap information with each advancing timestep in order to update the local boundary conditions of the subdomains that they are solving.

ZEUS-MP uses the Message Passing Interface protocol (MPI) for inter-process communication. MPI is mainly designed for Distributed Systems, though MPI 3.0 onwards supports Shared Memory systems also. There are various different implementations of the MPI protocol available, some of which are architecture-specific such as Intel MPI and which require a license; while others, such as OpenMPI, are free.

OpenMPI should not be confused with OpenMP. The latter is a different parallel computing protocol that is designed specifically for SMA systems.

ZEUS-MP is written in FORTRAN 77, having retained its historical usage of that language, and requires JPEG, SZIP and HDF4 libraries for compilation, and a suitable MPI library such as OpenMPI or Intel MPI. An MPI version of the Fortran compiler may also be required. Compiler and library options should be specified in the Makefile for ZEUS-MP.

Further discussion of HPC systems architecture and their classifications according to Flynn's classic scheme may be found in (Flynn, 1972)(33). An accessible summary of MPI vs. OpenMP code parallelisation architectures may be found at (Ghildiyal, 2014)(35).

4.3.2 Setting up a problem with ZEUS-MP

The ZEUSMP.DEF file

Some parameters and modules must be specified at compile-time in the ZEUSMP.DEF file which is usually found in the source code directory. This file is specified with an #include directive at the start of the main ZEUSMP.F program file. ZEUSMP.DEF contains macro definitions that specify what physics will be included in the ZEUS-MP models - in our work, Radiation and Gravitational physics options are disabled, while Chemistry, Cooling and Multispecies tracking are enabled. An additional option has been introduced to activate or deactivate Keplerian orbital motion of the jet source.

Within ZEUSMP.DEF, the user specifies the array dimensions of the problem grid in zones along the X, Y and Z axes. The initial setup file for the problem is also specified; this is a Fortran procedure that initialises the values of physical variables such as density, specific energy and velocity components, and the chemical fractions. This file is called JET.F in our work and is a modified form of the test problem file that came with the ZEUS-MP software distribution.

Two special procedures may be identified in the ZEUSMP.DEF file, labelled SPECIAL and SPECIALTRANS. The SPECIAL procedure runs on each main program loop pass, after the Source step. The SPECIALTRANS procedure runs on each main program loop pass, after the Transport step. Our jet models use procedures called H1WIGGLE and H2WIGGLE to evolve the dynamic behaviour of the inlets for our material flows into the problem domain, which are coded in the Fortran source file of the same name; this is identified as the SPECIALTRANS procedure in the definition file. H1WIGGLE handles the inflow of atomic material and H2WIGGLE handles inflow of molecular material. (In the models that are for atomic jets only, H2WIGGLE is deactivated).

The problem setup file and the special procedure(s) must be added as sources and object linkages in the appropriate sections of the ZEUS-MP Makefile before compilation.

The ZMP_INP file

This file usually resides in the working directory of the zeusmp.x compiled executable file. It contains input parameters that are read by the program at run-time. Some of these are parameters that might be varied frequently between model runs that have the same basic physics and same problem grid dimensions (in zones), and so it is useful to be able to change these by simply editing the zmp_inp file without recompiling the code.

These parameters include:

- MPI Tiling
- Runtime Limits: Timesteps, Absolute Time (s)
- Artificial Viscosity (Quadratic, Linear)
- Courant Stability Parameter
- Boundary Types: Inflow, Outflow
- Grid Control: Domain Size, No. of Zones, Inter-zone Ratio
- Adiabatic Ratio
- Jet Radius, Mach Number
- Ambient Density, Pressure, Internal Energy
- Jet : Ambient Density & Pressure Ratios
- Jet Rotation (Radians s^{-1})
- Poloidal / Toroidal Plasma Beta
- Toroidal Field Peak as a fraction of Jet radius
- Velocity & Density Pulse Characteristics (Time Period, Amplitude)
- Coradius of Binary System; Masses of Binary Partners (Solar Masses)
- Frequency of Data Dumps

The zmp_inp file is read when the zeusmp.x program is initially setting the problem up; however, with suitable coding of the HWIGGLE procedures, it becomes possible to have the zmp_inp file re-read on each pass of the main loop and thus for some parameters to be altered interactively during a model run.

System of Units used in ZEUS-MP

The physical constants used by ZEUS-MP are defined in the CONS.H file, and are set up to perform calculations in the CGS system of units; hence input parameters are assumed to follow this convention. It is possible by use of suitable scaling to set up models in dimensionless form; however, the enhanced Chemistry & Cooling module our project uses is tied to the CGS system so this is the convention adopted in our jet models.

Table 4.1: Useful Constants and Relationships For Jet Models

Quantity / Constant	Relationship / Value	CGS unit
Mass of Hydrogen Atom	$m_H = 1.6733 \times 10^{-24}$	g
Boltzmann Constant	$k_B = 1.380658 \times 10^{-16}$	Erg K^{-1}
Pressure Ratio, Jet : Ambient	$prat = \frac{P_J}{P_A}$	-
Density Ratio, Jet : Ambient	$drat = \frac{\rho_J}{\rho_A}$	-
Sound Speed, Ambient	$C_A = \sqrt{\frac{\gamma_A P_A}{\rho_A}}$	cm s^{-1}
Sound Speed, Jet	$C_J = C_A \sqrt{\frac{prat}{drat}}$	cm s^{-1}
H_2 Relative Abundance	$f = \frac{n(H_2)}{n(H)+n(H^+)+2n(H_2)}$	-
Adiabatic Exponent	$\gamma = \frac{5.5-3f}{3.3-f}$	-
Energy Density, Ambient	$e_A = \frac{\rho_A C_A^2}{\gamma_A(\gamma_A-1)}$	Erg cm^{-3}
Temperature, Ambient	$T_A = m_H \times \frac{1.4}{(1.1-f)} \times \frac{P_A}{\rho_A k_B}$	Kelvin (K)
Temperature, Jet	$T_J = T_A \times \frac{prat}{drat}$	Kelvin (K)

MPI Tiling

The tiling geometry of a ZEUS-MP model is determined by the MPITOP parameter namelist in the zmp_inp file. This might read as follows:

mpitop ntiles(1)=4,ntiles(2)=3,ntiles(3)=3,periodic=3*.false.

This means that the problem domain will be divided into 4 sections along the x-axis, and 3 sections along the y and z axes respectively; thus, the total number of subdomains that ZEUS will solve, is 4 x 3 x 3 = 36. (The periodic parameter is used to specify periodic boundary conditions, but is not used in our models and is always set to 3*.False.). An alternative tiling arrangement that would generate the same number of subdomains would be:

mpitop ntiles(1)=36,ntiles(2)=1,ntiles(3)=1,periodic=3*.false.

In this arrangement, the problem domain is divided into 36 slices, transverse to the x-axis. The number of grid zones in each subdomain is the same as for the 4 x 3 x 3 arrangement. In principle, there should be no difference in the two arrangements as far as solving the equations goes, but there are sometimes practical considerations involving system architecture or the nature of the problem being solved that favour one arrangement over the other.

There are certain limitations to tiling geometry. A tile must comprise a whole number of grid zones along each of its dimensions; and the minimum number of zones in each direction is 8.

4.3.3 ZEUS-MP Job Submission

University of Kent CAPS: Forge

A computing resource housed at the University of Kent Centre for Astrophysics and Planetary Science, FORGE is an SGI Altix ICE 8400 series rack-mounted blade server with 16 computing nodes, each of which has 8 cores for a total of 128 available processors. Each node has 12GB of available RAM. FORGE was used for the early prototype models during the project, but eventually as larger models with many more grid zones were

required this led to a move to SCIAMA as the main computing resource.

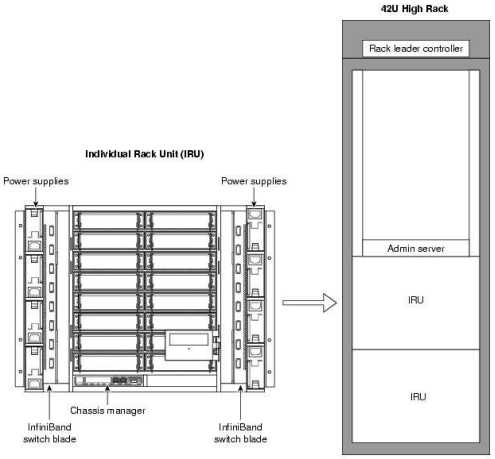

Figure 4.2: SGI ALTIX ICE 8400 Server, image from http://techpubs.sgi.com

SSH is used to log into one of the compute nodes to launch an MPI job. Job submission on FORGE is accomplished with a bash script, which loads the MPT module and then uses the MPIRUN command as in the following example:

```
#!/bin/bash
source /usr/share/modules/init/bash
module load mpt/1.23
echo 'hello'
mpirun r1i0n10, r1i0n9, r1i0n8, r1i0n7 8 zeusmp.x
```

The above script requests the use of the 4 listed compute nodes, and 8 cores on each node, for a total of 32 cores. This number must match the number of tiles specified in the zmp_inp file.

University of Portsmouth ICG: SCIAMA

SCIAMA is a High Performance Computing cluster housed at the Institute of Cosmology and Gravitation at the University of Portsmouth. At the time of writing SCIAMA has 2742 compute cores with 12 cores per node; each node has 24GB of RAM. A PBS queuing software system allows jobs to be submitted and queued as they await available computing resources. Access to SCIAMA is facilitated through the South East Physics Network (SEPnet).

Figure 4.3: SCIAMA Specification; screen grab of www.sciama.icg.port.ac.uk

The following example shows a 160 core job submission bash script for SCIAMA containing PBS queuing directives:

```
#!/bin/bash
#PBS -N zeusthing.64.2
#PBS -l nodes=40:ppn=4
#PBS -l walltime=240:00:00
#PBS -o out_zeusthing.64.2.$PBS_JOBID
#PBS -e err_zeusthing.64.2.$PBS_JOBID
#PBS -d /users/cl332ukc/ZMP1/test64.2/MP/exe
#PBS -M cl332@kent.ac.uk

cd /users/cl332ukc/ZMP1/test64.2/MP/exe
mpirun -np 160 zeusmp.x
```

4.3.4 Using HSPLICE to combine output files

Each problem tile is solved on a separate processor (core) and gives rise to a separate output file with the passage of each dump time interval. These output files may be inspected independently if desired using appropriate tools, but in order to produce a complete view of the problem domain they must be stitched together. HSPLICE is a

utility that takes output files from ZEUS-MP and combines them.

HSPLICE is written in Fortran 77 and must be compiled using a suitable compiler. Some editing of the source code is sometimes necessary as user tiling and grid arrangements may exceed the default parameters assumed within the source code. The compiled code is usually placed in the working directory and when it runs it reads the zmp_inp file for details of zone sizes.

HSPLICE is not, itself, a parallelised code, and runs on a single processor.

4.3.5 Scaling Tests on Forge

Early on in the project, some test problems were run on Forge using various tiling geometries, to see if there was any marked speed advantage in using a particular geometry. Speed-up is defined as the ratio of total CPU time spent by all processors on a computation, vs. 'Wall Time', that is to say the time taken on the clock from the start of the run to its finish. Each test problem was run twice in case of any spurious slow-down caused by other processes (access to computing resources on Forge was not exclusive) but no significant differences in results were observed between runs of the same problem. As the results show, alternative tiling geometries for the same number of cores show little difference over the range $1 \leq n \leq 8$, though in every case a transverse slicing of the domain with respect to the Jet axis (i direction) was the fastest by a small margin.

Table 4.2: Scaling Tests on Forge

Test Id	Cores	Tiling i	Tiling j	Tiling k	Average Wall Time (s)	Average CPU Time (s)	Speed-Up
1	1	1	1	1	1.86E+04	1.76E+04	0.95
2a	2	2	1	1	1.15E+04	2.10E+04	1.83
2b	2	1	2	1	8.38E+03	1.50E+04	1.79
3a	3	3	1	1	7.42E+03	1.99E+04	2.68
3b	3	1	3	1	6.53E+03	1.71E+04	2.62
4a	4	1	2	2	5.18E+03	1.76E+04	3.40
4b	4	2	1	2	5.70E+03	1.97E+04	3.45
4c	4	1	1	4	5.31E+03	1.83E+04	3.45
4d	4	4	1	1	6.40E+03	2.23E+04	3.49
5a	5	5	1	1	6.02E+03	2.61E+04	4.33
5b	5	1	5	1	5.12E+03	2.14E+04	4.18
7a	7	7	1	1	5.38E+03	3.30E+04	6.15
7b	7	1	7	1	4.35E+03	2.62E+04	6.01
8a	8	2	2	2	4.22E+03	2.87E+04	6.80
8b	8	8	1	1	5.12E+03	3.58E+04	7.00
8c	8	1	8	1	4.03E+03	2.67E+04	6.63
8d	8	4	2	1	5.06E+03	3.45E+04	6.83
8e	8	2	4	1	4.48E+03	3.04E+04	6.79
8f	8	1	4	2	4.35E+03	2.91E+04	6.69

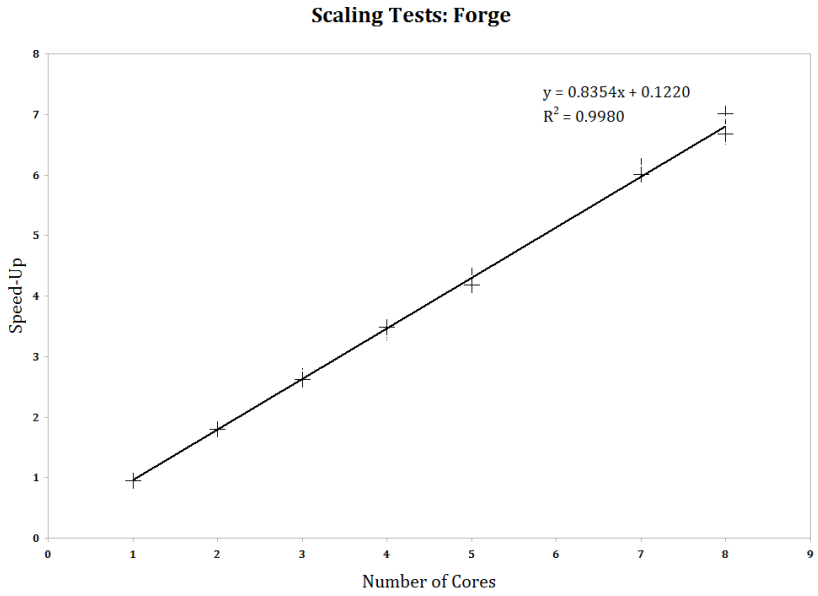

Figure 4.4: Scaling Tests on Forge

4.4 Orbital Motion of the Jet Source

4.4.1 The Case for Orbital Motion

In this thesis, results will be presented from computational models of protostellar jets that are launched from a source undergoing orbital motion as part of a binary system. Numerical models of protostellar jets often assume a frame of reference in which the jet / counterjet source is at rest with respect to the surrounding medium, or else in a state of rectilinear motion. However, from n-body simulations of star cluster formation, and from our physical observations of the end products of star formation, these sources are often expected to occur in binary systems and will therefore be subject to central acceleration rather than the inertial frame in which they are frequently modelled. Axisymmetric approximations are often used to reduce computational demands and to focus attention on a particular piece of jet physics, but in the case of jets from an orbiting source, this is not possible and a full 3-dimensional model must be computed.

4.4.2 The Kepler Equation

Johannes Kepler is mainly remembered for his work in establishing the mathematical basis of the heliocentric solar system. More mathematician than observational astronomer, he was a student of Tycho Brae and formulated the three Keplerian Laws of Planetary Motion, the first two of which he published in his Astronomia Nova ("New Astronomy") in 1609 and the third in his Harmonices Mundi ("Harmonies of the World") in 1619.

The Kepler Equation describes the motion of a planetary body moving in an elliptical orbit about the centre of mass of a system consisting of itself, and a second co-gravitating body which in Kepler's work was identified as the Sun. In the case of our Solar System the common centre of mass is not very distant from the centre of the second body itself; in the Sun-Jupiter system this common centre of orbit or "barycentre" is just outside the Sun's surface.

The Kepler Equation also describes the elliptical orbit of a member of a stable binary star system such as that shown in Fig.4.5. In such a system the binary partners co-orbit a common centre just as planets and the Sun do; this barycentre lies at one of the foci of

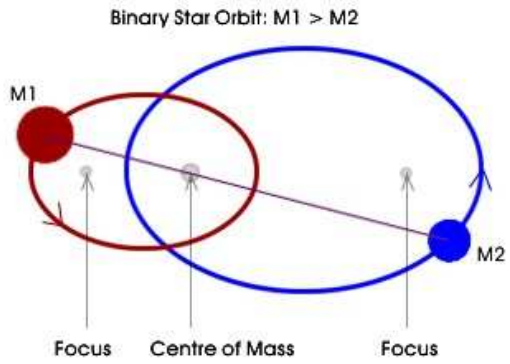

Figure 4.5: Co-orbiting Binary System

each elliptical orbit, which are co-incident. Depending on the mass ratio of the partners the barycentre may be well outside both objects, but might also be embedded within one of the objects if it is very much more massive than its partner.

Orbital Period, T:

$$T^2 = \frac{4\pi^2 a^3}{G(m_1 + m_2)} \tag{4.24}$$

Relationship between Eccentric Anomaly, E, and Mean Anomaly, M(t):

$$M(t) = \frac{2\pi t}{T} = E - \epsilon \cdot sin(E) \tag{4.25}$$

Relationship between True Anomaly, θ, and Eccentric Anomaly:

$$cos(\theta) = \frac{cos(E) - \epsilon}{1 - \epsilon \cdot cos(E)} \tag{4.26}$$

Radial distance from barycentre as function of True Anomaly:

$$r(\theta) = \frac{a(1 - \epsilon^2)}{1 + \epsilon cos(\theta)} \tag{4.27}$$

We assume in our models that we are dealing with a binary protostellar system that possesses sufficient orbital stability to be well-described by the Kepler Equation. In reality, the objects we are dealing with are still in the process of accretion from a surrounding circumbinary disc of infalling material, so their mass will be time-varying and hence orbital characteristics will not be constant. However, the time scales of the simulated jets are

small in comparison to the accretion timescale and so the assumption of constant mass is a reasonable one. It is also possible that the orbits might be perturbed by anisotropy in the gravitational attraction of the surrounding accretion disc if there are local variations in the amount of matter in the disc. We assume that any accretion disc clumpiness is not biased significantly in any direction and thus any such perturbations may be ignored for our purposes.

4.4.3 Implementing an Orbiting Source

In our implementation, the centre of the jet inlet on the $x = 0$ boundary is repositioned with each timestep, with the motion corresponding to that described by the Kepler Equation. The key to this is determining the eccentric anomaly, E. Rearranging equation 4.25 into a non time-dependent form:

$$f(E) = 0 = E - \epsilon \cdot sin(E) - \frac{2\pi t_0}{T} \tag{4.28}$$

where t_0 is a specified, and thus constant, interval of time. This is a transcendental equation the roots of which may not be determined analytically, so a numerical method is required. In our implementation the Newton-Raphson method is used, which converges to 8 d.p. of accuracy after 5 iterations:

$$E_{n+1} = E_n - \frac{E_n - \epsilon \cdot sin(E_n) - E_0}{1 - \epsilon \cdot cos(E_n)} \tag{4.29}$$

in which the initial guess E_0 is taken to be the mean anomaly $\frac{2\pi t_0}{T}$.

Then from 4.26 we may calculate the True Anomaly θ, and from 4.27 we find the radial distance from the barycentre. It is then simple trigonometry to calculate where the centre of the jet inlet must lie.

4.5 Synthetic Image Generation

4.5.1 Motivation for Synthetic Images

Outputs from ZEUS-MP models are limited to the physical variables of density, specific internal energy, 3 velocity components, and the relative proportions of the chemical species being tracked which in our models are limited to Hydrogen in its various states; H, H_2, H^+.

When observing a jet from a protostar, we are not able to measure these quantities directly, and must attempt to infer them from various emission line diagnostics and an understanding of the physics involved. Consideration must be given to alternative hypotheses and the success with which they are able to consistently explain the observed phenomena across multiple sources.

Generation of synthetic emission lines from computationally modelled jets forms an essential part of this process. In the simplest of analyses a synthetic image can provide us with guidance in selecting the parameters of a successful explanatory model - if our synthetic image looks nothing like the observation, it is fair to assume that our model needs to be corrected or discarded; or at least, a plausible explanation, such as interaction with the environment, should be supplied to justify our continued usage of that model.

In addition to 'raw' synthetic images, there are other kinds of synthetic observations that may be produced, such as position-velocity diagrams and velocity channel maps.

4.5.2 The MULTISYNTH synthetic image code

During the course of our research, a flexible synthetic emissions code was developed which we called MULTISYNTH. This is an interpreter script that runs in the IDL® environment. IDL® is a product of Exelis Visual Information Solutions, Inc., a subsidiary of Harris Corporation (Exelis VIS). IDL® stands for Interactive Data Language. The Exelis VIS website can be found at `http://www.exelisvis.com`.

MULTISYNTH is described in more depth in Appendix J.

4.6 Prototype Simulations

The initial requirement was to find a model that would produce a plume of optically-emitting material of approximately similar dimensions and morphology to the R-band images of HH30 taken with the WFPC2 instrument of the Hubble Space Telescope (see Fig.3.5). Simulations involved variations of jet velocity, density, pressure and temperature; variable velocity and density pulsation; rotation, precession, and orbital motion; and magnetic field. The combination of poloidal field and orbital motion was not handled well by the code. Toroidal field was made to work with orbiting jets, but the main effect was to modify the bow shock into a conical morphology, with little effect on the behaviour of the jet column at stable field strengths. A decision was made to continue the study without their inclusion. See Appendix C for more discussion on MHD jets in ZEUS-MP.

4.6.1 The Long Jet Simulations

Figures 4.6 through 4.10 show outputs from simulations that were carried out in order to establish suitable parameters for the atomic outflow component of the dual outflow scenarios. These prototyping exercises were informed by the observed parameters of the HH30 jet (see table 3.1). In the absence of a wide-angle molecular flow, a long problem domain was feasible; a $1280 \times 175 \times 175$ mesh was employed, running on 160 cores. The jet was $10\times$ overpressured with respect to ambient and its inlet radius was 7AU. [1]

The early stages of jet propagation exhibited classic features and by the time the jet had propagated to 200AU distance from the source inlet the symmetry of the bow shock had collapsed, resulting in a ragged appearance. The bow shock is susceptible to this disruption of symmetry due to thermal instabilities arising from radiative cooling; this behaviour has been studied in previous 3D simulation work e.g. Stone, Norman (1994)(112), and more recently has been demonstrated in laboratory experiments by Suzuki-Vidal et al., 2015 (116).

[1] Fully detailed parameters of these simulations are not provided here as their inclusion is to provide background understanding only.

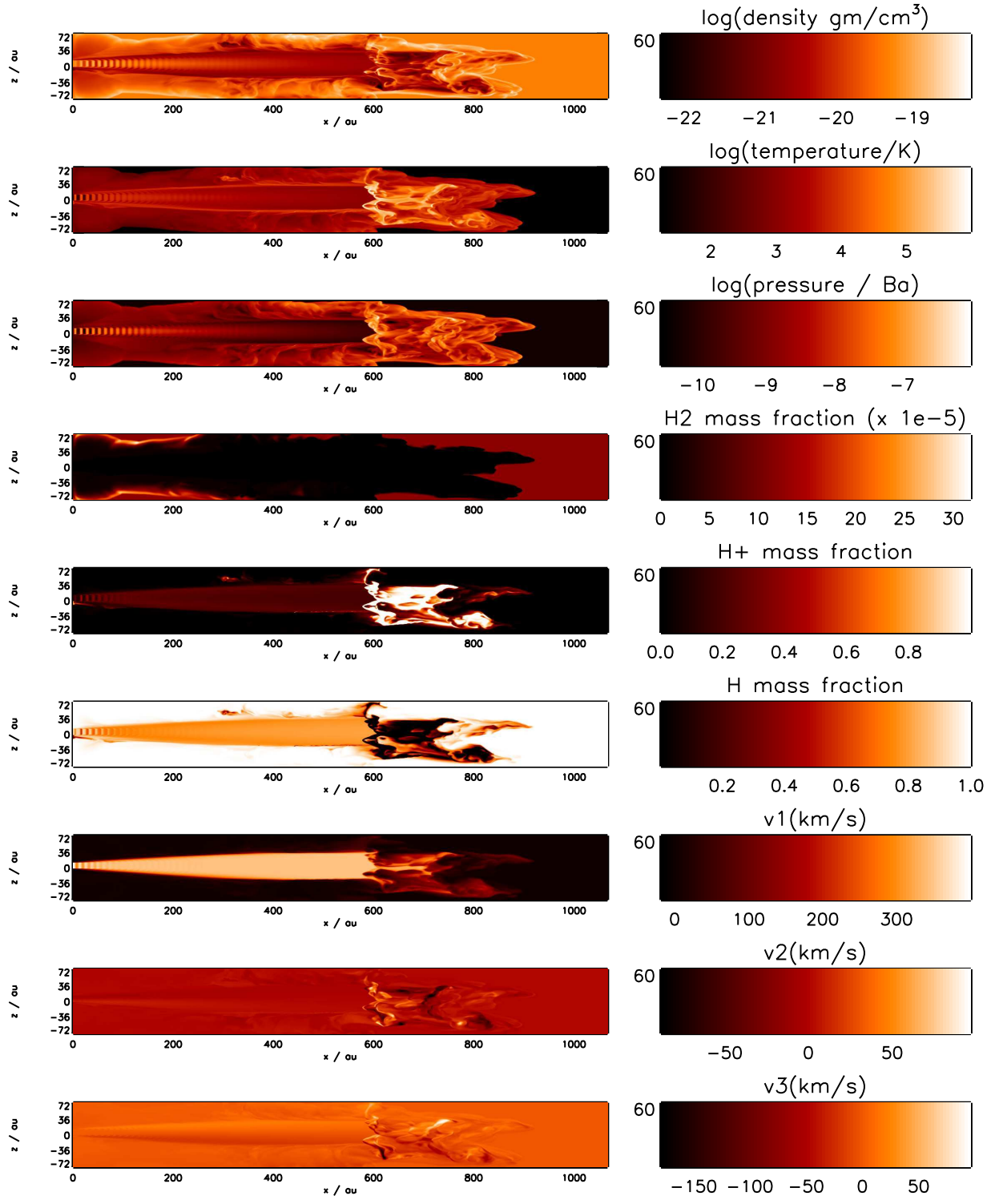

Figure 4.6: HH30 Atomic Jet Prototype: Physical Variables, T=63 years. This jet is from an orbiting inlet the motion of which resembles the Orbital series of models (ORB.x) that are the subject of later discussion.

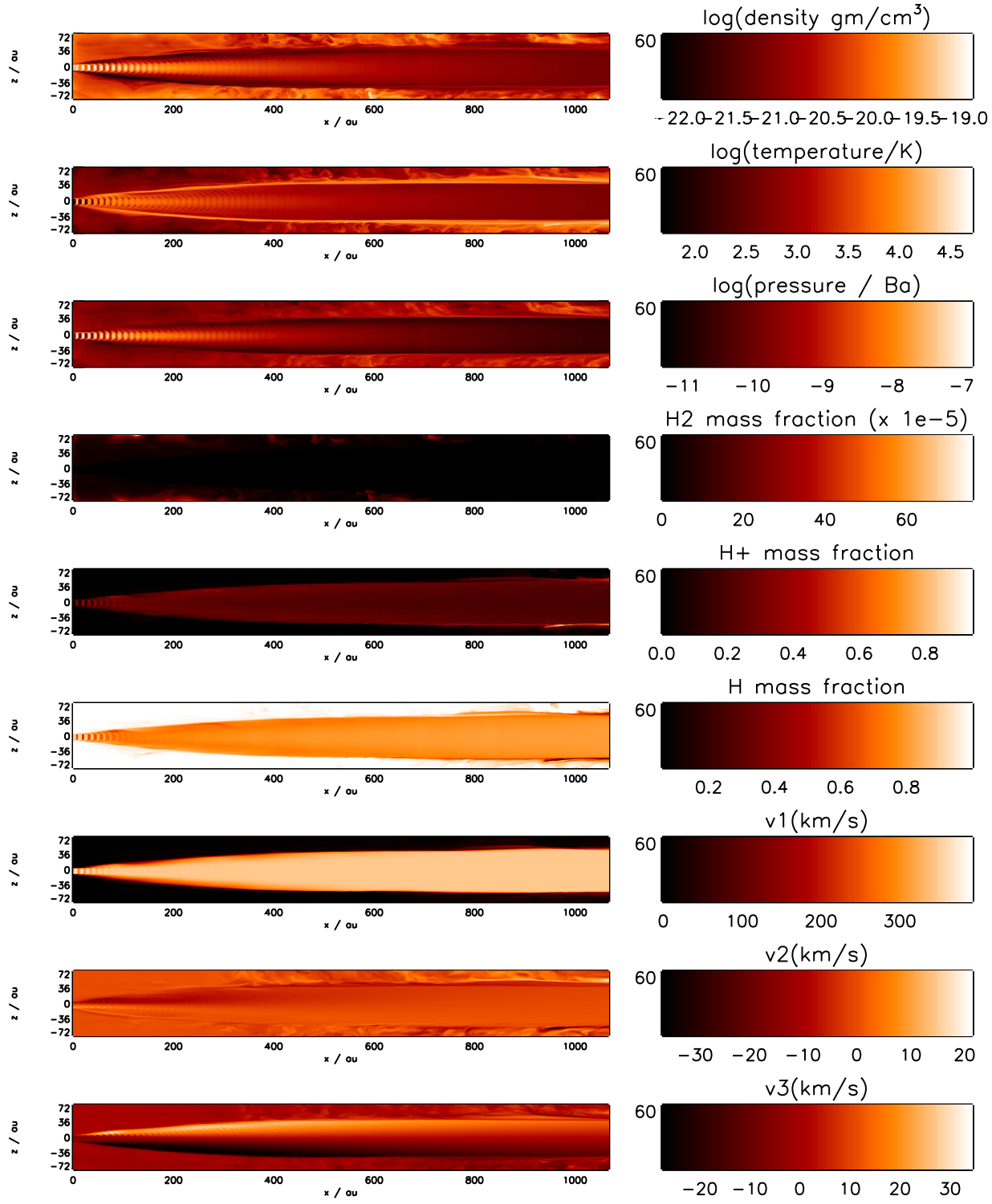

Figure 4.7: HH30 Atomic Jet Prototype: Physical Variables, T=189 years. This jet is from an orbiting inlet the motion of which resembles the Orbital series of models (ORB.x) that are the subject of later discussion.

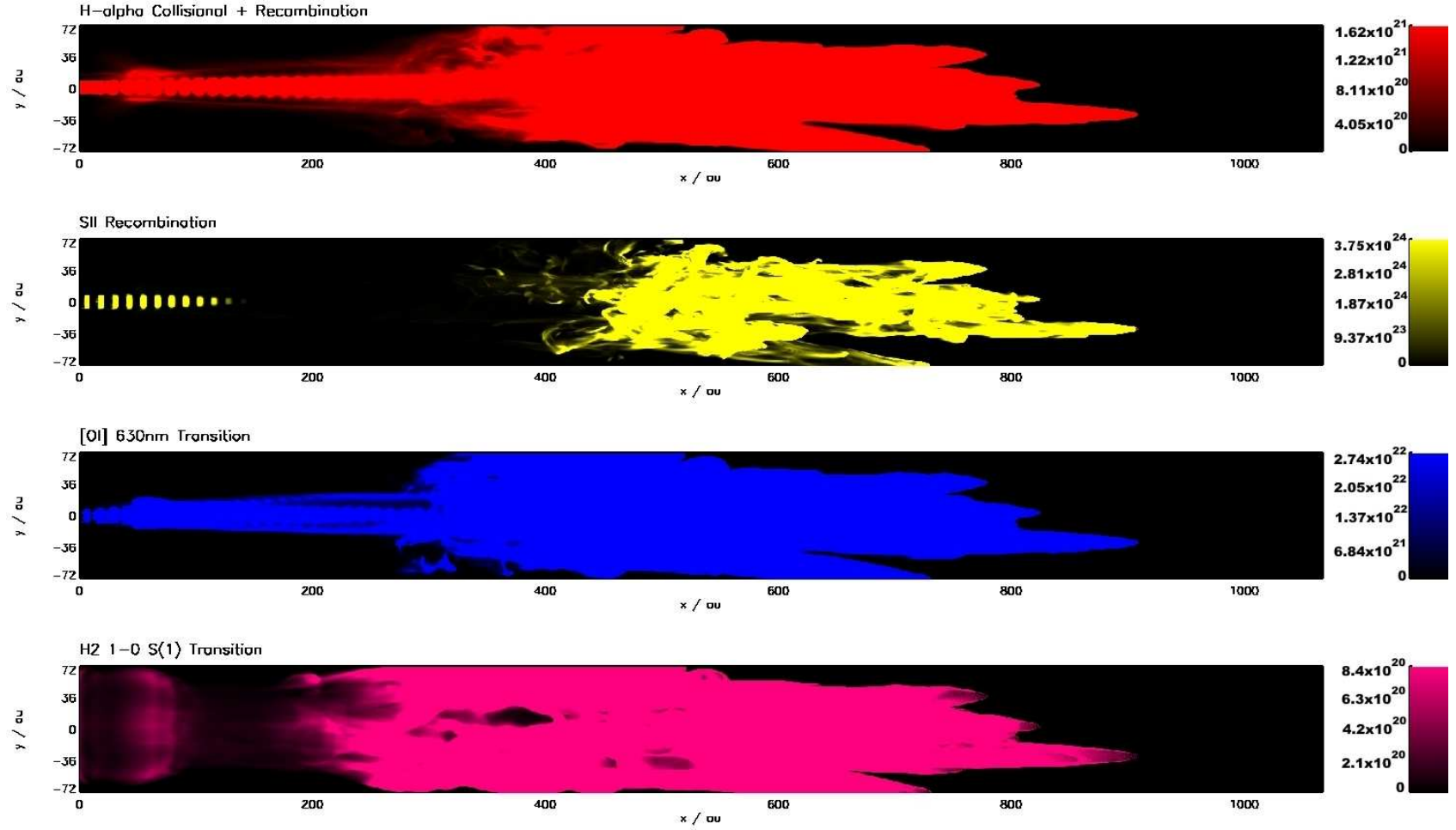

Figure 4.8: Prototyping the HH30 atomic jet: synthetic emissions from four spectral lines, T=49 years. This jet is from an orbiting inlet the motion of which resembles the Orbital series of models (ORB.x) that are the subject of later discussion. The relative colour scaling is linear and representative of line-of-sight integrated source emission though no filter is applied to account for instrument spatial resolution limits.

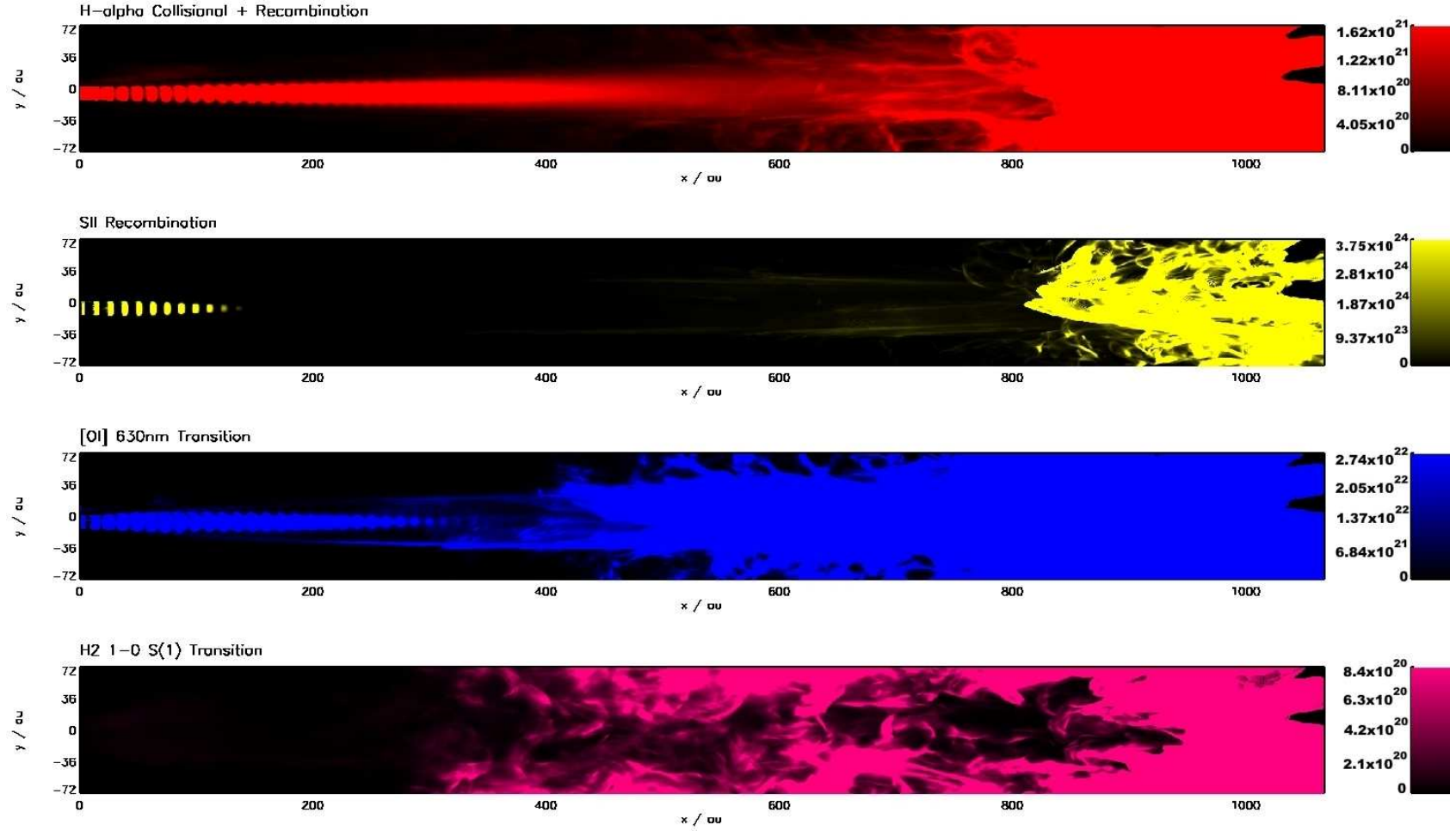

Figure 4.9: Prototyping the HH30 atomic jet: synthetic emissions from four spectral lines, T=98 years. This jet is from an orbiting inlet the motion of which resembles the Orbital series of models (ORB.x) that are the subject of later discussion. The relative colour scaling is linear and representative of line-of-sight integrated source emission though no filter is applied to account for instrument spatial resolution limits.

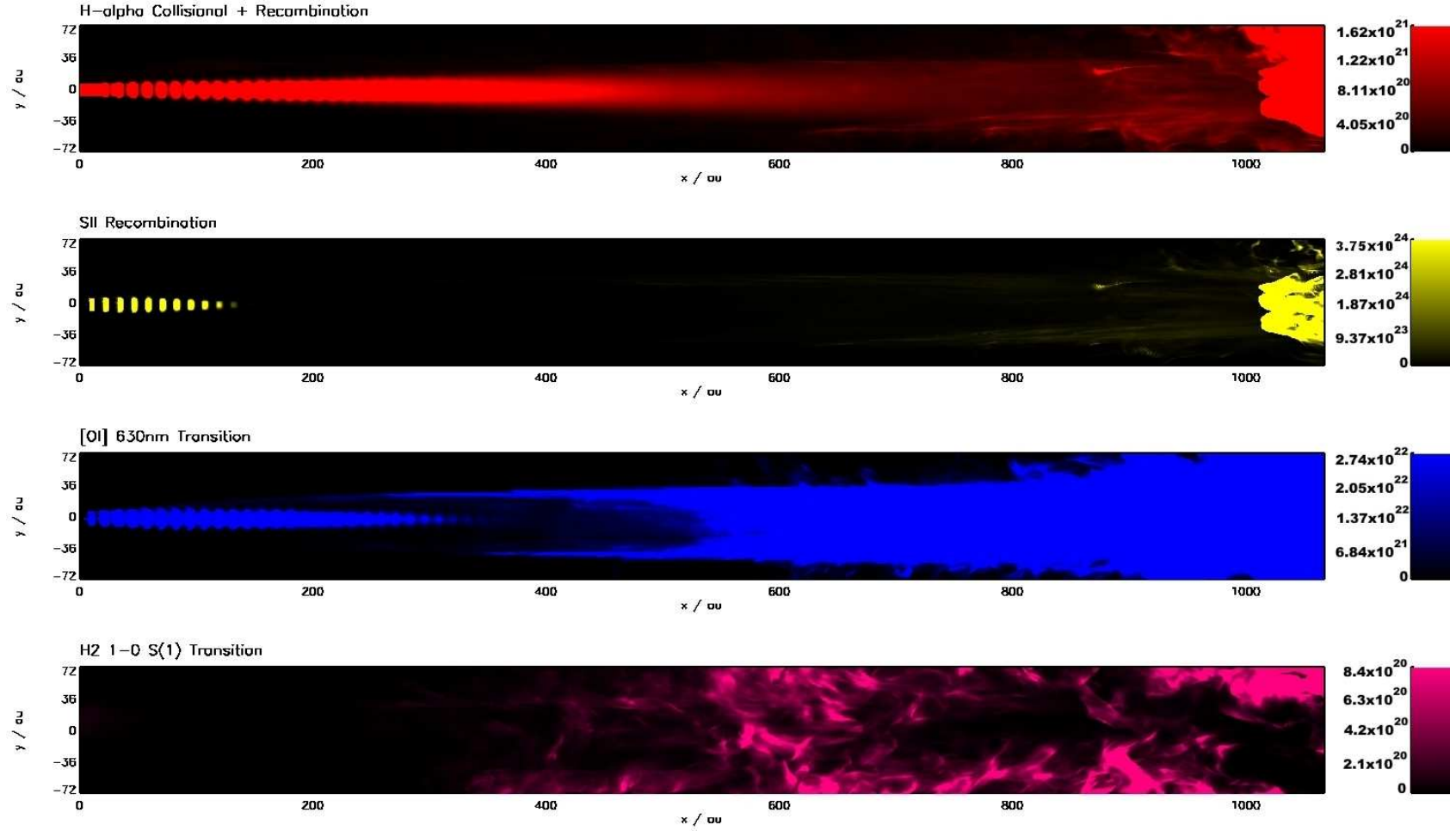

Figure 4.10: Prototyping the HH30 atomic jet: synthetic emissions from four spectral lines, T=148 years. This jet is from an orbiting inlet the motion of which resembles the Orbital series of models (ORB.x) that are the subject of later discussion. The relative colour scaling is linear and representative of line-of-sight integrated source emission though no filter is applied to account for instrument spatial resolution limits.

4.7 Chapter Summary

1. The equations of Astrophysical Fluid Dynamics have been discussed, and distinction drawn between the complete equation set, and the reduced equation set solved in our models, which do not consider radiative transfer and gravitation. The difference between the inviscid Euler equations, and the more general Navier-Stokes equations, has been explained.

2. The role of cooling by atomic and molecular transitions has been examined, as an additional term that modifies the Energy Equation.

3. We have reviewed the ZEUS-MP Astrophysics code and looked at its key features (see Fig.4.1). The role of Artificial Viscosity, and the HSMOCCT algorithm for consistent evolution of magnetic fields have been briefly discussed.

4. We have discussed the practical usage of ZEUS-MP. A brief discussion of parallel computing architectures and protocols has been given. We have looked at problem setup, tiling geometry and job submission. The use of the HSPLICE code, to stitch together the multiple HDF output files produced by ZEUS-MP, has been explained. The results of some scaling test runs have been presented demonstrating linear speed-up of ZEUS-MP computing jobs as a function of the number of cores used for the job (see Fig.4.4).

5. We have looked at orbital motion, and the implementation of a jet inlet that moves in a Keplerian orbit has been discussed.

6. Synthetic image generation has been discussed; the in-house MULTISYNTH post-processing code for IDL® has been introduced. This is discussed in greater detail in Appendix G.

7. Outputs from atomic jet prototyping simulations have been presented with brief discussion (see Figs 4.6 through 4.10).

Chapter 5

Simulating the Propagation of Dual Outflows from HH30

5.1 Background

5.1.1 Research Goals

To re-state the ambitions outlined at the end of Chapter One, the aim of the work presented here has been to investigate the principal differences between two dual-outflow scenarios for HH30, identified as the Precessional Model and Orbital Model. Achievable choices for this project were made based on alternative scenarios suggested by the work of Estalella et al. (2012)(27) and Tambovtseva & Grinin (2008)(118); see Fig.5.1.

Other configurations are possible and may form the basis of future work. One such alternative is the Concentric Model, wherein both outflows emerge from the same source. Prototype runs with this model suggested that the structure resulting from this setup would be very similar to the Precessional Model. It was decided to prioritise the latter for the purposes of this project, in order to test the hypothesis of Tambovtseva & Grinin (2008)(118), but future work may be undertaken with the Concentric and other alternative models, as discussed in our Conclusion.

It is hoped that the findings of this work may be helpful in determining the configuration of the outflow sources in HH30, or other T-Tauri binaries that may have a similar

combination of outflows.

It should be noted that protostellar jets are frequently bipolar in nature. HH30 has a second red-shifted outflow emerging from its southern face. This outflow is less active and lacks an apparent molecular component (see Fig.3.9). The work presented here focuses solely on the blue shifted outflows from the more active northern face of HH30.

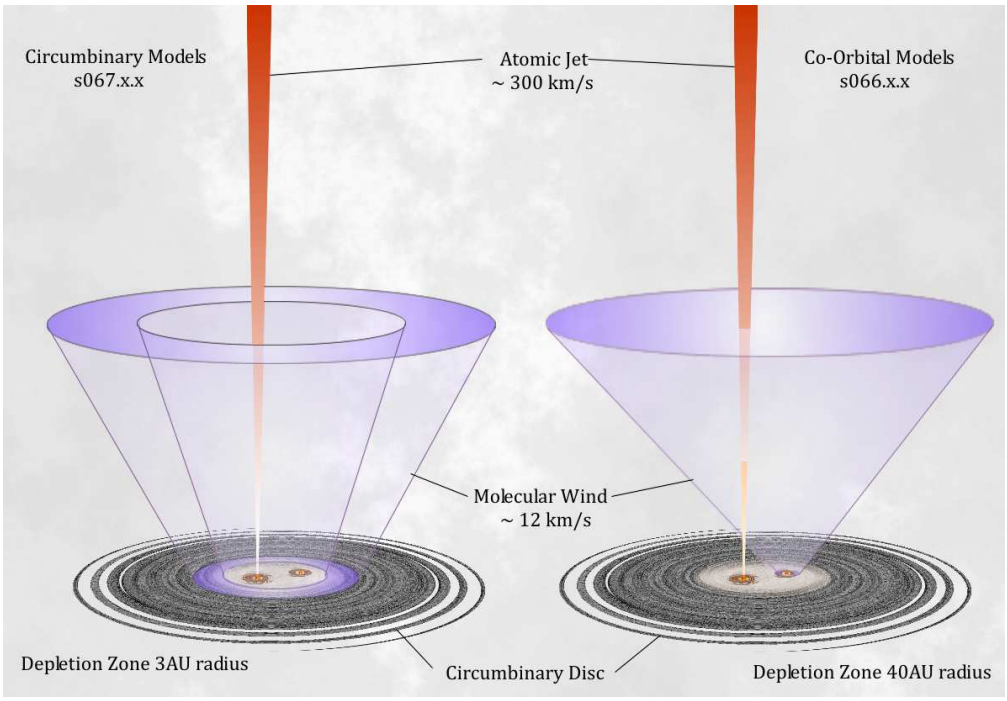

Figure 5.1: A schematic diagram of Precessional (PRE.x) vs. Orbital (ORB.x) models, not to scale. A 'control' simulation within each model series was performed with the atomic jet only.

In this chapter, the emphasis is on the underlying structure of the simulated outflows. Analysis remains broadly independent of observation methods; we look for characteristic signatures that differentiate the two model types but in terms of physical variables such as density, temperature and velocity fields. It is left to observational astronomy to find ways of determining the actual distribution of these physical variables in real outflows.

Later in chapter 6 we turn our attention to synthetic emissions; whereupon the emphasis shifts to production of 'realistic' images and analysis of the time-dependent synthetic outputs. However this sequence of presentation does not exactly reflect the order in which the work was carried out. The first phase involved development of the code to handle the orbital motion of the jet inlet, and also identifying launch parameters that would

produce an acceptable atomic jet which would resemble the plume of optically emitting material seen in HH30. But in order to make that judgement it was also necessary to generate synthetic emissions; so the MULTISYNTH code was developed fairly early on in the project and used to check the outputs.

5.2 Dual Outflow Simulation Parameters

A process of ad hoc experimentation with simulations and their resulting synthetic emission eventually led to choices of configuration with which to generate results suitable for further analysis. These choices are discussed in the section that follows.

5.2.1 Introducing the Molecular Outflow

The prototyping exercises discussed in section 4.6 mainly concentrated on creating a fast atomic jet which, when post-processed to produce synthetic images in Hα, would resemble to some degree the R-band images of HH30 captured by the HST (See Figs. 3.5 and 4.6 through 4.10). This was a time-consuming phase of the project involving many test runs and parameter variations.

Introducing a second, molecular outflow was a little tricky to code. Initial attempts to modify the HWIGGLE.F procedure used for the atomic jet, so that a single procedure would produce two jets of different material, were abandoned in favour of a more modular approach using two separate procedures, H1WIGGLE.F and H2WIGGLE.F. The potential pitfall of this approach is that each procedure has no awareness of the actions of the other. In our code implementation, values of boundary condition array elements are used as semaphores between the procedures.

There was no method that could be found to sensibly implement a boundary condition where the two outflows were already interacting prior to their incursion into the domain, so after some experimentation it was decided to avoid this type of scenario.

However, once these coding issues had been resolved and limitations of the approach had been determined, it was a relatively short cycle of parameter variation and testing compared to the atomic jet, before choices of 'ideal' parameters for the two types of molecular

outflow were settled on. Synthetic imaging in the ^{12}CO 1.3mm line for both types of outflow scenarios - Precessional vs. Orbital - soon demonstrated a high degree of similarity with the work of Pety et al. (2006)(81) and Tambovtseva & Grinin (2008)(118).

5.2.2 Model Geometry

Due to the wide angle of the molecular flow, simulations required a model geometry with a larger span in the y and z dimensions. With the singular atomic jet models, their narrow opening angle and high speed permitted a narrow problem domain with a large longitudinal span as previously discussed. However it was apparent that increasing the lateral dimensions of the problem domain to accommodate an additional 30° molecular outflow, without truncating the problem domain, would require greater computing resources than those available. It was also desirable to increase the spatial resolution to capture the features of the flow in more detail for final results.

Hence the results presented here are from simulations with a considerably shorter problem domain than that used in the prototyping exercises. Though the extent to which the results may be usefully compared with observation is restricted by the shorter longitudinal domain size, it is reasonable to assume that the most significant differences between the scenarios will appear within the first 110AU of the launch regions of the outflows.

Table 5.1 summarises the problem domain setup for ZEUS-MP used in the models that follow. The wide lateral span in y and z dimensions of the models, compared with the longitudinal x direction that aligns with the jet axes, is atypical of jet models. Because the prototyping exercises with the atomic jet models had already succeeded in simulating a lengthy 'optical' jet demonstrating expected features, we could have confidence in their behaviour within a truncated problem domain where the focus would be the early stages of interaction between atomic and molecular outflows.

Table 5.1: Standard Model Geometry

Coordinate	Min (cm)	Max (cm)	Span (cm)	Grid Zones	Zone Size (cm)	MPI Tiling	Zones /Tile
x	0	1.600E+15	1.600E+15	160	1.0E+13	20	8
y	-1.725E+15	1.725E+15	3.450E+15	345	1.0E+13	3	115
z	-1.725E+15	1.725E+15	3.450E+15	345	1.0E+13	3	115

The MPI tiling geometry may be thought of as a stack in the x-dimension of 20 thin slabs 8 zones in width, each slab consisting of a 3 x 3 arrangement of square 115 x 115 zone tiles in the y-z plane. This has the advantage of fully containing the flow inlets and their orbits within the central tile. During tests of magnetohydrodynamic models it was found that difficulties arose when orbiting jet inlets crossed tile boundaries; these would cause the code to halt when $\nabla \vec{B} = 0$ tolerance was exceeded. This called into question whether undesirable numerical artefacts might also arise from a pure hydrodynamic jet inlet crossing a tile boundary; insufficient to halt the code but affecting the validity of results obtained.

Although the simulations presented here are for the pure hydrodynamic case (Plasma-β $= \infty$), future work may revisit the simulations for finite Plasma-β values. For this reason, and as a cautionary measure, a configuration that avoided material inlets crossing tile boundaries was adhered to.

The division of the problem domain into thin slabs in the longitudinal (x) direction served two purposes. The first was simply to facilitate a large number of CPU 'workers' to operate on the problem domain (a multiple of 9 due to y-z tiling). This was subject to a trade-off in terms of queuing time on SCIAMA. Detailed statistics on queuing times were not maintained during the project but they were generally quite unpredictable, especially for larger job requests. A job involving upwards of 200 cores might typically wait for more than a week before running (although during less busy times such a job might run immediately). The 180 core configuration that was eventually settled on, arising from a choice of 20 longitudinal slabs worked well and queuing times were generally satisfactory.

The need for adequate spatial resolution drove the choice of zone size, and thus determined the constraint on the problem domain span in the x-dimension. The ZEUS-MP solvers are generally second order, and in particular the artificial viscosity algorithm, thus a minimum of 4 zones is a requirement to adequately resolve discontinuous flow features. With the shortest time period velocity pulse that we experimented with, a total of 11 small-scale 'knots' of shocked material spanned the problem domain of 1.6×10^{15} cm (see Figure 5.6 (a)). Each knot is sandwiched between a pair of velocity shocks; thus at least $2 \times 11 \times 4 = 88$ grid zones should be the minimum requirement for adequate resolution.

At our chosen zone size of 10^{13} cm in the x-direction, this provides > 7 zones per shock discontinuity. (Test runs at half this spatial resolution, and so < 4 zones, did indeed fail to provide adequate resolution of the velocity shocks).

It is also the case that 8 zones is the minimum tile span for ZEUS-MP's domain-decomposed solver algorithms to operate; the code will simply halt if fewer zones are specified.

The need to accurately depict the circular flow inlets on the x = 0 boundary was a driver of spatial resolution in the y-z plane; both commonsense and prior experiment suggested that a radius of at least 4 zones should be implemented to produce a footprint that could reasonably be called 'circular'. To avoid numerical anisotropies in the solution of the fluid dynamical equations, it was desirable to use the same zone size of 10^{13} cm that applied to the x-direction. Our chosen diameter of 1.1×10^{14} cm for the atomic jet inlet depicts inflow at a distance of $\sim$ 10 AU from the source object, which is justified by the range of flow widths observed at 20 AU distance by Hartigan & Morse (2007)(41) and a simplified assumption of linear flow expansion under pressure beyond the magnetically dominated region of the flow near the source; with this diameter, the zone size of 10^{13} cm results in a zonal radius of 5.5 for the atomic jet. This implies that the centre of the jet is coincident with a zone centre rather than a grid node in a static-inlet jet model where the jet inlet is simply placed at the centre of a 345 x 345 plane boundary. Though somewhat atypical of ZEUS-MP jet models, in any case with a jet inlet that moves in an orbital fashion, any coincidence of the centre of the jet inlet with respect to nodes of the grid is arbitrary. Fractional inlet zones are catered for in the HWIGGLE.F routines by volumetric pro-rata weighting of the chemical fractions, and by mass-weighted averaging of the velocity components of material in the zone.

5.2.3 Outflow and Medium Parameters

Table 5.2 summarises the choices of parameters for the outflows introduced into the problem domain, plus those of the ambient medium itself which was chosen to be entirely atomic with a temperature of $\sim$ 100K. This choice was based partly on the experience of the prototyping exercises, in which an atomic jet into an atomic medium was found to

be 'well-behaved' in terms of code stability. It was also reasoned that the environment in the vicinity of a T-Tauri star (< 100AU) would already have been swept of cold, dense molecular material by winds and jets and be populated with a warmer, diffuse atomic medium. There was also the undeniable advantage of making the molecular outflow easier to isolate in the model outputs against a mainly atomic background.

In fact, the simulations themselves were allowed to run for a sufficient length of time to 'nature' their own problem domains; particularly in the simulation runs where a molecular outflow component was present, by the end of the simulation the outflows themselves were the dominant influence within the problem domain, not the initial environment. The dense, conical molecular flow would sweep away most of the ambient material in the region where it, and its atomic partner, were extant. Meanwhile, molecular cooling during the run would naturally result in a proportion of H_2 molecules appearing in what remained of the ambient medium on the fringes.

The parameters labelled 'Configurable' in table 5.2 are all settings that could be input to ZEUS via the ZMP_INP or ZEUSMP.DEF files, or else simple hard-coded constants. The 'Dependent' parameters are all quantities of interest that are directly calculated or otherwise determined as a result of the choices of the 'Configurable' parameters; see table 4.1 for formulae relevant to these calculations. Often, the need to satisfy particular values of dependent parameters, based on HH30 observations summarised in table 3.1, drove the choice of configurable parameters.

Table 5.2: Outflow and Medium Parameters

	Parameter	Atomic Outflow		Molecular Outflow		Atomic	Units
		Type I	Type II	Type I	Type II	Medium	
Configurable	Source Object	Primary	Primary	Secondary	CB Disc		
	Inner Radius				1.33E+14		cm
	Outer Radius	5.50E+13	5.50E+13	1.20E+14	3.20E+14		cm
	Density					1.2525E-18	g/cm^3
	Energy Density					1.3284E-08	erg/cm^3
	Density Ratio	1	1	50	10		
	Pressure Ratio	10	10	7.5	1.5		
	Mach No.	95	95	30	30		
	Rotation (Solid)	1.31E-08	1.31E-08	6.53E-09			rad/s
	Rotation (Kepler)				3.50E-09		rad/s
	Radius (Kepler)				2.20E+14		cm
	Orbital Separation	18	0.75				AU
	Mass (Primary)	0.31	0.44				$M_\odot$
	Mass (Secondary)	0.14	0.10				$M_\odot$
	Precession Rate		3.76E-09				rad/s
	Precession Angle		0.025				radians
Dependent	Inner R (zones)				13.265		
	Outer R (zones)	5.5	5.5	12	32		
	Orbit Period	3.59E+09	3.06E+07				s
	Precession Period		1.67E+09				s
	Adiabatic Exponent	1.66667	1.66667	1.42857	1.42857	1.66667	
	No. Density	7.00E+05	7.00E+05	3.50E+07	7.00E+06	7.00E+05	
	Density	1.25E-18	1.25E-18	6.26E-17	1.25E-17	1.25E-18	g/cm^3
	Temperature	1090	1090	16.4	30	109	K
	Sound Speed	3.43E+05	3.43E+05	3.89E+04	4.20E+04	1.09E+05	cm/s
	Inlet Flow Speed	3.26E+07	3.26E+07	1.26E+06	1.17E+06		cm/s
	Inlet Area	9.50E+27	9.50E+27	4.52E+28	2.66E+29		cm^2
	Mass Throughput	5.10E-09	5.10E-09	5.64E-08	6.15E-08		$M_\odot$ / yr

5.2.4 Simulation Runs

Four principal, longer timescale (175 yrs) runs were performed to establish fully developed flow for both atomic and molecular outflows and to examine their behaviour over full periods of orbital or precessional motion after the flow had become dynamically stable in terms of its activity and structure over large spatial scales. There were two simulations performed, for each of the Orbital and Precessional scenarios respectively; the first with both outflows, and the second with the atomic jet alone for comparison, to demonstrate the difference that the presence of the molecular outflow makes to the structure and observed emission of the atomic jet.

Six additional, shorter duration simulations were then carried out for each scenario; three with different velocity pulse time periods for the atomic jet; three with different values of orbital eccentricity. The data retained for these starts from 65 years into the outflow

evolution (by which time the outflows have crossed the problem domain and exhibit fully developed flow) and tracks the evolution over a further 22 years.

Table 5.3 summarises the characteristics of the simulation runs. The simulations are coded according to a simple scheme; **ORB.x** being the designation for 18AU binary separation models with co-orbital sources, in which the **orbital** motion dominates the morphology of the large-scale outflow; and **PRE.x** designating 0.75AU binary models with a circumbinary disc being the source for molecular flow where present, in which the **precession** of the atomic jet source is the dominant large-scale influence (see Fig.5.1 for additional clarity).

The velocity pulse period T_{vpulse} determines the period of the time-varying sinusoidal signal imposed on the velocity of injected material. For all the presented simulations, the Relative Amplitude parameter A_R used by HWIGGLE.F is set at 0.2. This generates a velocity signal:

$$V_J(t) = M \times C_J \times \frac{1 + A_R \, cos\omega_v t}{1 + A_R} \tag{5.1}$$

Where M is the Mach number of the jet, C_J is the jet sound speed, and $\omega_v = 2\pi/T_{vpulse}$. The maximum of this signal is MC_J and the minimum is 66% of this value.

The orbital eccentricity parameter, ϵ, is used in equation 4.29 to compute the Keplerian orbit of the jet inlet by the Newton-Raphson method.

The HDF data dumps are produced at simulation time intervals of 2.125 $\times 10^6$ seconds. This is chosen to be less than half of T_{vpulse}; It is a standard result in signal processing that in order to capture a sinusoidal signal the sampling frequency must be at least twice the highest frequency component of the signal. With our choice of $T_S \approx 2.5 T_{vpulse}$, 'strobe' effects are avoided in animations and the possibility exists to determine proper motions of structures within the flow.

Though only material phases of H are dynamically traced in the simulations, the model assumes a composition including He and other elements at a concentration typical of the ISM for chemistry and cooling purposes. This assumed composition permitted calculation by proxy of these concentrations when determining synthetic emissions. These

calculations are detailed in chapter four.

Full data retention was pursued as much as was practicable, to allow generation of synthetic emission animations and permit flexibility in time-domain analysis after the simulation runs were complete. Storage requirements were considerable. Each data dump in the listed simulations occupied 799 MB of memory space. Thus, the four 'primary' simulations required over 2 TB of storage each; whilst the twelve shorter simulations required 260.5 GB each. In addition, the post-processed outputs generated by MULTISYNTH added to the data requirements not inconsiderably.

Table 5.3: Simulation Runs

	Simulations	Outflows		Vpulse	Orbital	Retained Dumps			
		Atomic	Molecular	Period	ϵ	First	Last	T_1 (Y)	T_2 (Y)
Orbital	ORB.1	I	-	5.256E+06	0.00	1	2599	0	175
	ORB.2	I	I	5.256E+06	0.00	1	2599	0	175
	ORB.3.1	I	I	7.884E+06	0.00	975	1300	65	87
	ORB.3.2	I	I	1.051E+07	0.00	975	1300	65	87
	ORB.3.3	I	I	1.314E+07	0.00	975	1300	65	87
	ORB.4.1	I	I	5.256E+06	0.25	975	1300	65	87
	ORB.4.2	I	I	5.256E+06	0.50	975	1300	65	87
	ORB.4.3	I	I	5.256E+06	0.75	975	1300	65	87
Precessional	PRE.0	-	II	-	-	1	1199	0	80
	PRE.1	II	-	5.256E+06	0.00	1	2599	0	175
	PRE.2	II	II	5.256E+06	0.00	1	2599	0	175
	PRE.3.1	II	II	7.884E+06	0.00	975	1300	65	87
	PRE.3.2	II	II	1.051E+07	0.00	975	1300	65	87
	PRE.3.3	II	II	1.314E+07	0.00	975	1300	65	87
	PRE.4.1	II	II	5.256E+06	0.25	975	1300	65	87
	PRE.4.2	II	II	5.256E+06	0.50	975	1300	65	87
	PRE.4.3	II	II	5.256E+06	0.75	975	1300	65	87

Visualisations of the simulation outputs were generated using VisIt, an Open Source, interactive, scalable, visualization, animation and analysis tool provided by the Lawrence Livermore National Laboratory (2012)(16). Significant post-processing and additional graphical outputs were generated using IDL®.

5.3 The Orbital Scenario Simulations

These were the ORB.x series of simulation runs as specified in Table 5.3, and modelled a scenario in which the fast-moving, atomic, optically emitting outflow of HH30 or similar T-Tauri star is launched by the more massive binary partner in a two-star system, and the slow-moving, wide-angle molecular flow is launched from its lower-mass co-orbiting partner. In this scenario the co-radius is 18AU and the masses of the two objects are 0.31 $M_\odot$ and 0.14 $M_\odot$. There is no orbital eccentricity apart from the final three simulations in this set in which values of ϵ range from 0.25 to 0.75.

We examine here in detail the ORB.1 and ORB.2 models. ORB.1 simulates one outflow only, an atomic jet; while ORB.2 introduces a second, wide-angle molecular flow.

5.3.1 Single Atomic Outflow Case (ORB.1)

Figure 5.2 that follows shows a set of cross-sectional VisIt plots of the case where the molecular outflow is absent; simulation time is 87.5 years. Note that this figure is presented as a guide to the structure of the outflow; as part of a set of similar plots of the four principal simulation runs, it shares with those a common colour scaling of variables and as a result the features are somewhat faint in appearance. In spite of this, close examination suggests a spiral density wave radiating outwards from the jet column, induced in the surrounding medium by the orbital motion of the jet. Subfigure (a) shows the jet inlet at x=0cm, and figures (b) and (c) show the cross-sections at further intervals in the x-direction. In subfigure (d), the jet is seen entering the domain from the left. An expanding cocoon of lower density material surrounds the denser jet column. We also see from subfigure (d) that the pulsed velocity signal has given rise to small-scale density knots within the jet column, sandwiched between regions of lower density. The knots appear to be expanding in the direction of travel as they cross the domain and exit across the far x-boundary but remain well-collimated in the y-z plane.

The density knots are a feature of all the models though they become somewhat disrupted in the Orbital models where the atomic jet is in collision with the molecular outflow. Their proper motion is examined later on in the discussion of simulation run PRE.1.

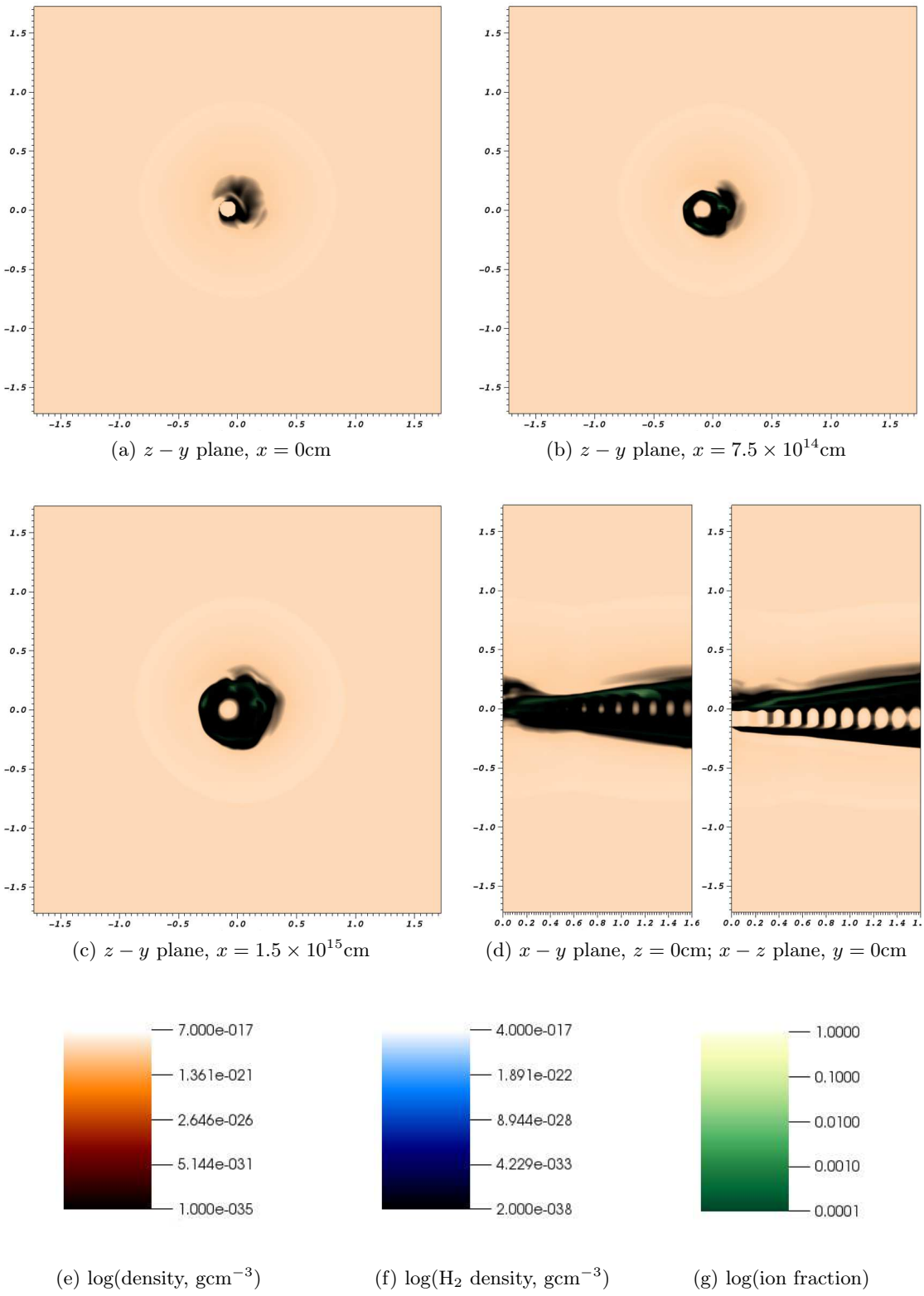

(a) $z-y$ plane, $x = 0$cm

(b) $z-y$ plane, $x = 7.5 \times 10^{14}$cm

(c) $z-y$ plane, $x = 1.5 \times 10^{15}$cm

(d) $x-y$ plane, $z = 0$cm; $x-z$ plane, $y = 0$cm

(e) log(density, gcm^{-3})

(f) log(H_2 density, gcm^{-3})

(g) log(ion fraction)

Figure 5.2: **Orbital Model ORB.1: 18AU binary, atomic-only outflow cross-sections at simulation time T=87.5 Years.** Axis scales are in units of 10^{15}cm. Ambient medium is atomic hydrogen with trace molecular hydrogen formed from cooling during the simulation. Underlying density plot is fully opaque. For clarity, H_2 and ionisation fraction overplots are at ramped opacity; 100% opacity at max value, transparent at minimum value.

Figures 5.3 through 5.6 that follow show the 18AU orbit, single atomic outflow of model ORB.1 at simulation time 175 yrs, and provide more detail on the dynamics of each cross-section plot. Note that a scale for the partial density of H_2 appears on the VisIt plots of model ORB.1 but since this model is an atomic jet into an atomic medium only trace H_2 appears, arising from the molecular cooling routine which models dust grain catalytic formation of molecules. The (b) subfigures in these plots show the 2d projection velocity field and thermal characteristics. From these plots it is evident that the low-density cocoon surrounding the jet column, and also the low-density regions within the jet, are populated by hot, partially ionised material. See in particular Fig. 5.6.

It is evident from these figures that the region surrounding the outer density shock is turbulent. Examination of early-stage outputs in the simulation reveals that material driven outwards by the expanding outflows passes through this shock and then becomes disorganised. This can be seen occurring in the time-stepped Fig.5.12 further on, in the section on simulation run ORB.2 which is the dual atomic-molecular outflow version of this model.

A common feature to all the models is flow expansion. This is expected as all of the outflows (atomic and molecular) are overpressured with respect to the ambient medium (see Table 5.2). Based on an estimated circular radius computed from the jet cross-sectional area (see Fig. 5.17) an approximate half-opening angle for the jet of the ORB.1 simulation is 8.5° degrees.

In Fig. 5.5, it appears that the expanding jet is transferring some of its x-direction momentum to the material in the boundary layer around the jet column and creating an entrained 'updraft'. This is evident in all the simulations from the region of lower pressure surrounding the jet columns, and the surrounding velocity fields.

Ionisation seems to be barely there in these plots. It is true that of the four models we examine in detail in this chapter, ORB.1 shows the weakest ionisation; in fact when we examine ionisation in model PRE.2 later in this chapter, we will revisit to ORB.1, and demonstrate that there is ionisation present in the internal working surfaces within the jet column.

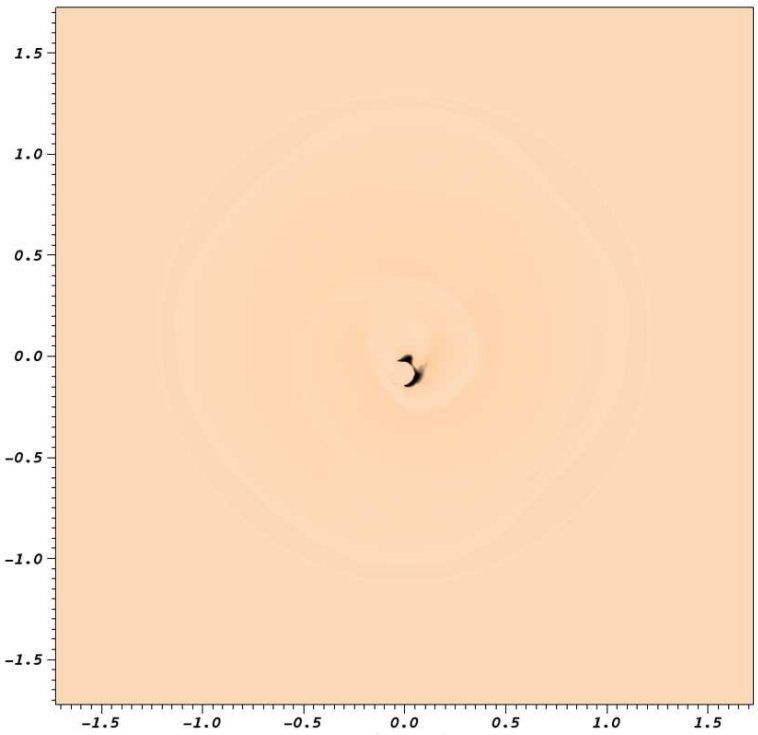

(a) density and composition; default material is HI

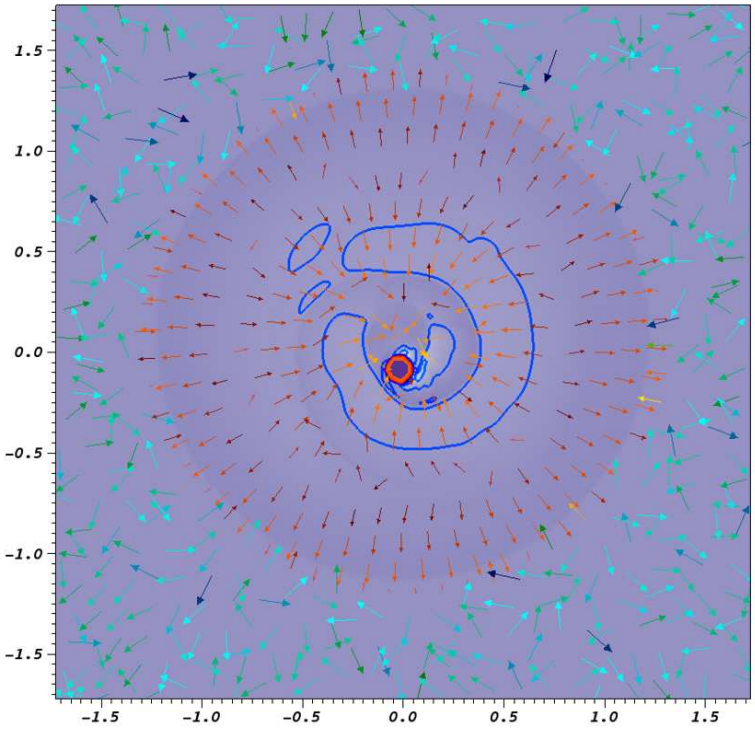

(b) pressure, temperature and velocity

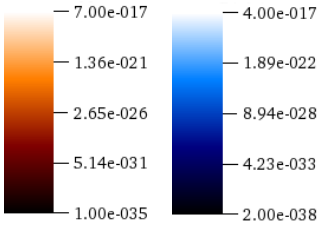

(c) (d)

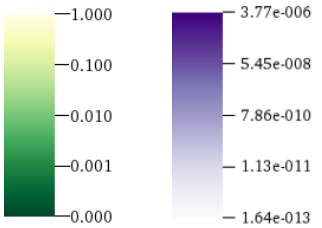

(e) (f)

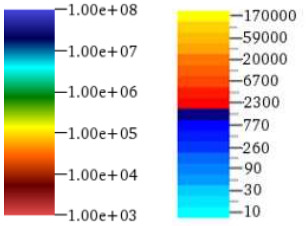

(g) (h)

Colour scaling:
(c) density, g/cm^3
(d) H_2 density, g/cm^3
(e) ion mass fraction
(f) pressure, Ba
(g) velocity, cm/s (vector)
(h) temperature, K (contour)

(c), (d), (e) apply to subfigure (a); (f), (g), (h) apply to subfigure (b). All scales are to $\log_{10}$ including vector magnitude. Vector glyphs are 2D projections; the tail indicates the vector origin.

Figure 5.3: **Orbital Model ORB.1: 18AU Binary, Atomic-Only outflow into an atomic ambient medium; z-y plane cross-section shown at x=0cm and simulation time T=175 Years.** Axis scales are in units of 10^{15}cm. For clarity, the underlying density plot in subfigure (a) is fully opaque, whilst H_2 and ionisation overplots are at ramped opacity; 100% opacity at max value, transparent at minimum.

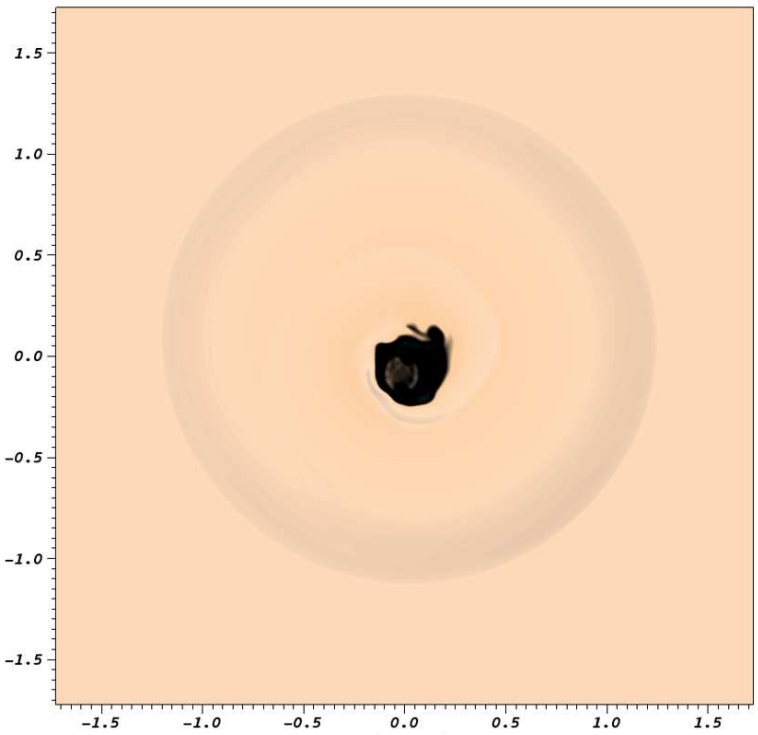

(a) density and composition; default material is HI

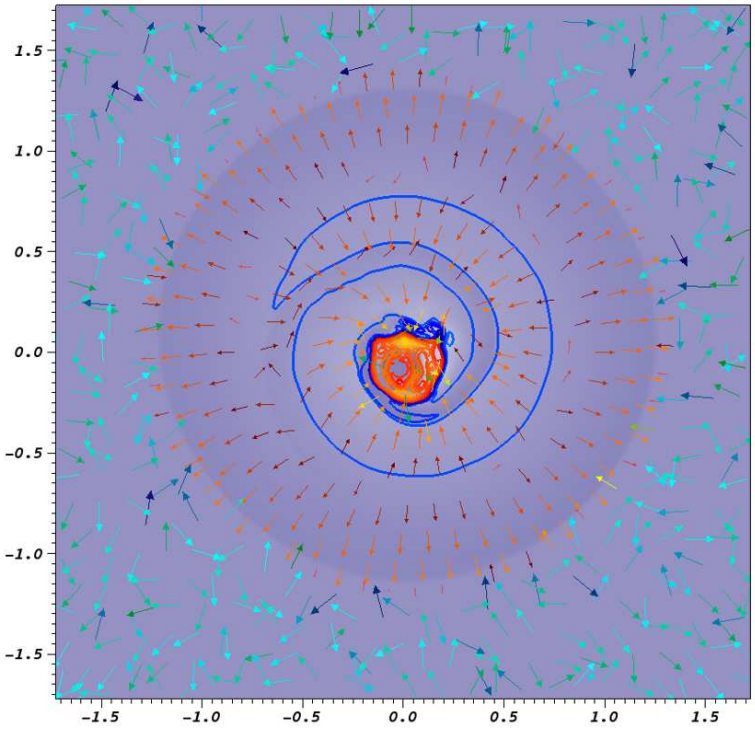

(b) pressure, temperature and velocity

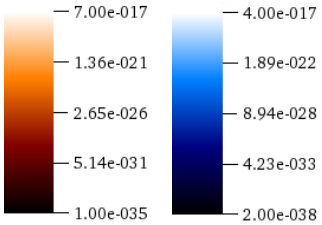

(c) (d)

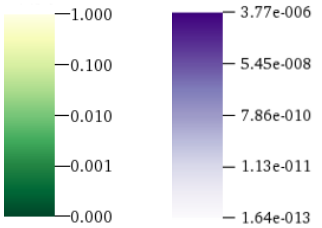

(e) (f)

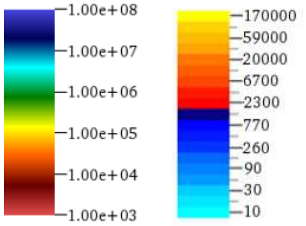

(g) (h)

Colour scaling:
(c) density, g/cm^3
(d) H_2 density, g/cm^3
(e) ion mass fraction
(f) pressure, Ba
(g) velocity, cm/s (vector)
(h) temperature, K (contour)

(c), (d), (e) apply to subfigure (a); (f), (g), (h) apply to subfigure (b). All scales are to $\log_{10}$ including vector magnitude. Vector glyphs are 2D projections; the tail indicates the vector origin.

Figure 5.4: **Orbital Model ORB.1: 18AU Binary, Atomic-Only outflow into an atomic ambient medium; z-y plane cross-section shown at x=7.5×10^{14}cm and simulation time T=175 Years.** Axis scales are in units of 10^{15}cm. For clarity, the underlying density plot in subfigure (a) is fully opaque, whilst H_2 and ionisation overplots are at ramped opacity; 100% opacity at max value, transparent at minimum.

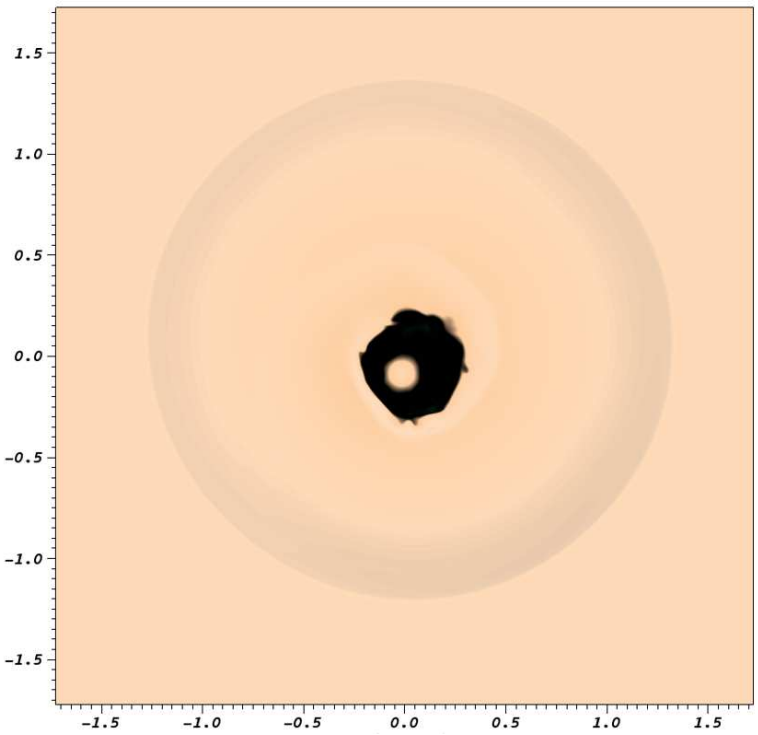

(a) density and composition; default material is HI

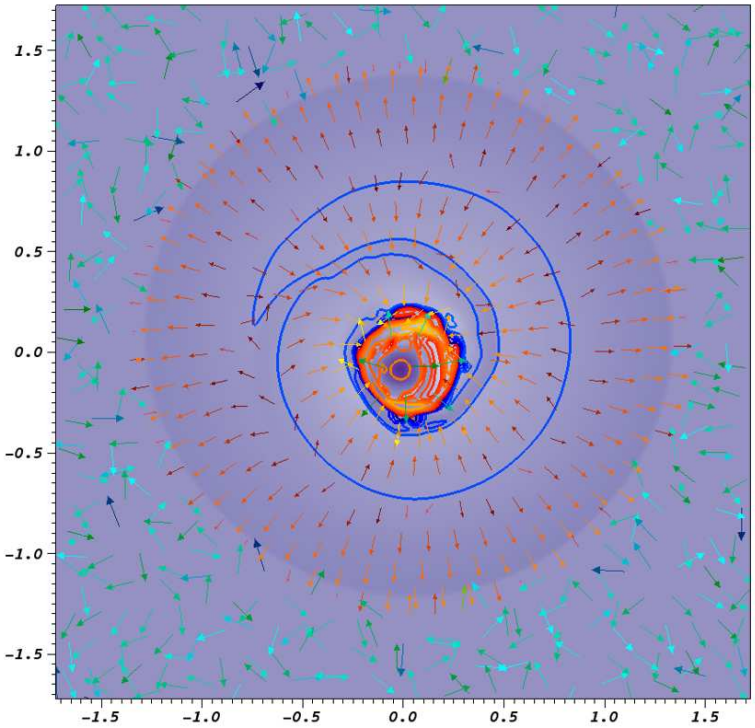

(b) pressure, temperature and velocity

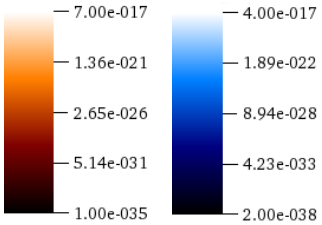

(c) (d)

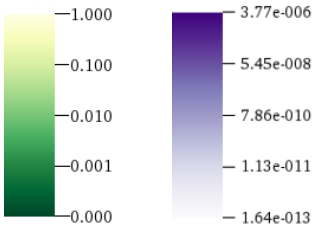

(e) (f)

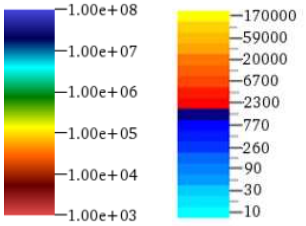

(g) (h)

Colour scaling:
(c) density, g/cm^3
(d) H_2 density, g/cm^3
(e) ion mass fraction
(f) pressure, Ba
(g) velocity, cm/s (vector)
(h) temperature, K (contour)

(c), (d), (e) apply to subfigure (a); (f), (g), (h) apply to subfigure (b). All scales are to $\log_{10}$ including vector magnitude. Vector glyphs are 2D projections; the tail indicates the vector origin.

Figure 5.5: **Orbital Model ORB.1: 18AU Binary, Atomic-Only outflow into an atomic ambient medium; z-y plane cross-section shown at x=1.5×10^{15}cm and simulation time T=175 Years.** Axis scales are in units of 10^{15}cm. For clarity, the underlying density plot in subfigure (a) is fully opaque, whilst H_2 and ionisation overplots are at ramped opacity; 100% opacity at max value, transparent at minimum.

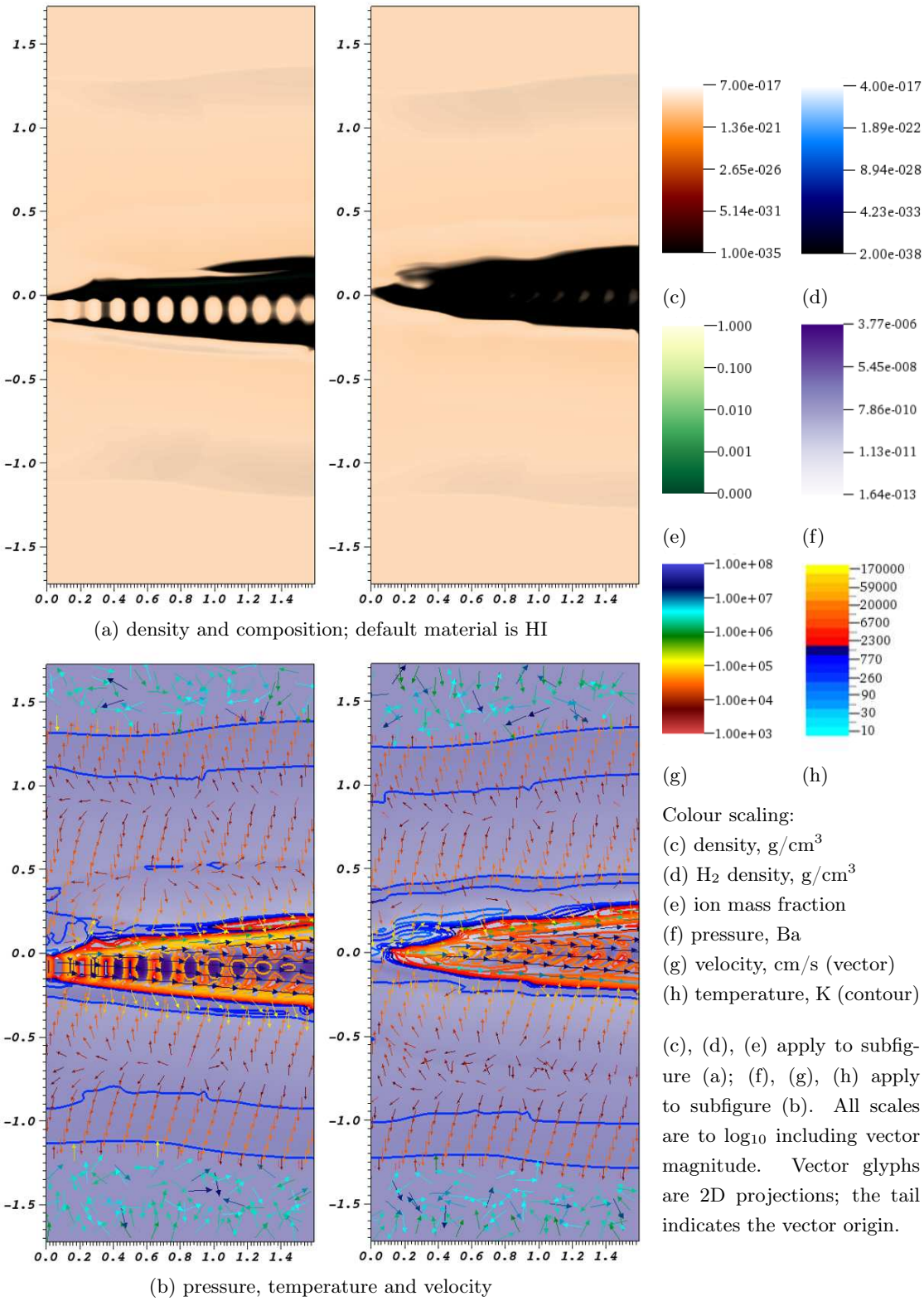

(a) density and composition; default material is HI

(b) pressure, temperature and velocity

Colour scaling:
(c) density, g/cm^3
(d) H_2 density, g/cm^3
(e) ion mass fraction
(f) pressure, Ba
(g) velocity, cm/s (vector)
(h) temperature, K (contour)

(c), (d), (e) apply to subfigure (a); (f), (g), (h) apply to subfigure (b). All scales are to $\log_{10}$ including vector magnitude. Vector glyphs are 2D projections; the tail indicates the vector origin.

Figure 5.6: **Orbital Model ORB.1: 18AU Binary, Atomic-Only outflow into an atomic ambient medium; x-y (L) and x-z plane (R) cross-sections shown at z, y=0cm and simulation time T=175 Years.** Axis scales are in units of 10^{15}cm. For clarity, the underlying density plot in subfigure (a) is fully opaque, whilst H_2 and ionisation overplots are at ramped opacity; 100% opacity at max value, transparent at minimum.

5.3.2 Dual Atomic-Molecular Outflow Case (simulation ORB.2)

We now introduce the molecular outflow, emerging from the secondary binary partner, and examine the significant differences that arise from the case where the atomic jet propagates in isolation. Figure 5.7 shows a set of cross-sectional VisIt plots of the case where both the atomic and molecular outflows are present; simulation time is 87.5 years. As before, this figure gives an overview of the structure of the outflow, and shares a common colour scaling of variables with the other VisIt plots of this nature presented in this chapter.

As with the co-orbital simulation we examined previously (ORB.1, see fig.5.5) in which only an atomic jet is present, a spiral density wave radiates outwards from the jet column, induced in the surrounding medium by the orbital motion of the jet. However, when we examine the dual outflow system at 100AU along the x-axis (see Subfigure (c) of Figure 5.7) we find that the expanding molecular flow is overtaking the density wave. An approximate calculation finds that the molecular flow expands at ~ 6 km/s radially from the x-axis as it propagates across the domain; whilst the sound speed in the ambient medium is 1.09 km/s (see Table 5.2).

In the early stages of propagation the molecular outflow is feeding material into the spiral density wave, which carries this material outwards just behind its advancing shock. This can be seen much more vividly in Figures 5.8 through 5.11, which show the flow at a more fully developed stage at 175 years of simulation time. By this stage, the slower moving density shock has caught up with and overtaken the molecular outflow at x = 100AU, since the opening angle of the molecular flow remains unchanged between this and the 87.5 year stage in Fig. 5.7.

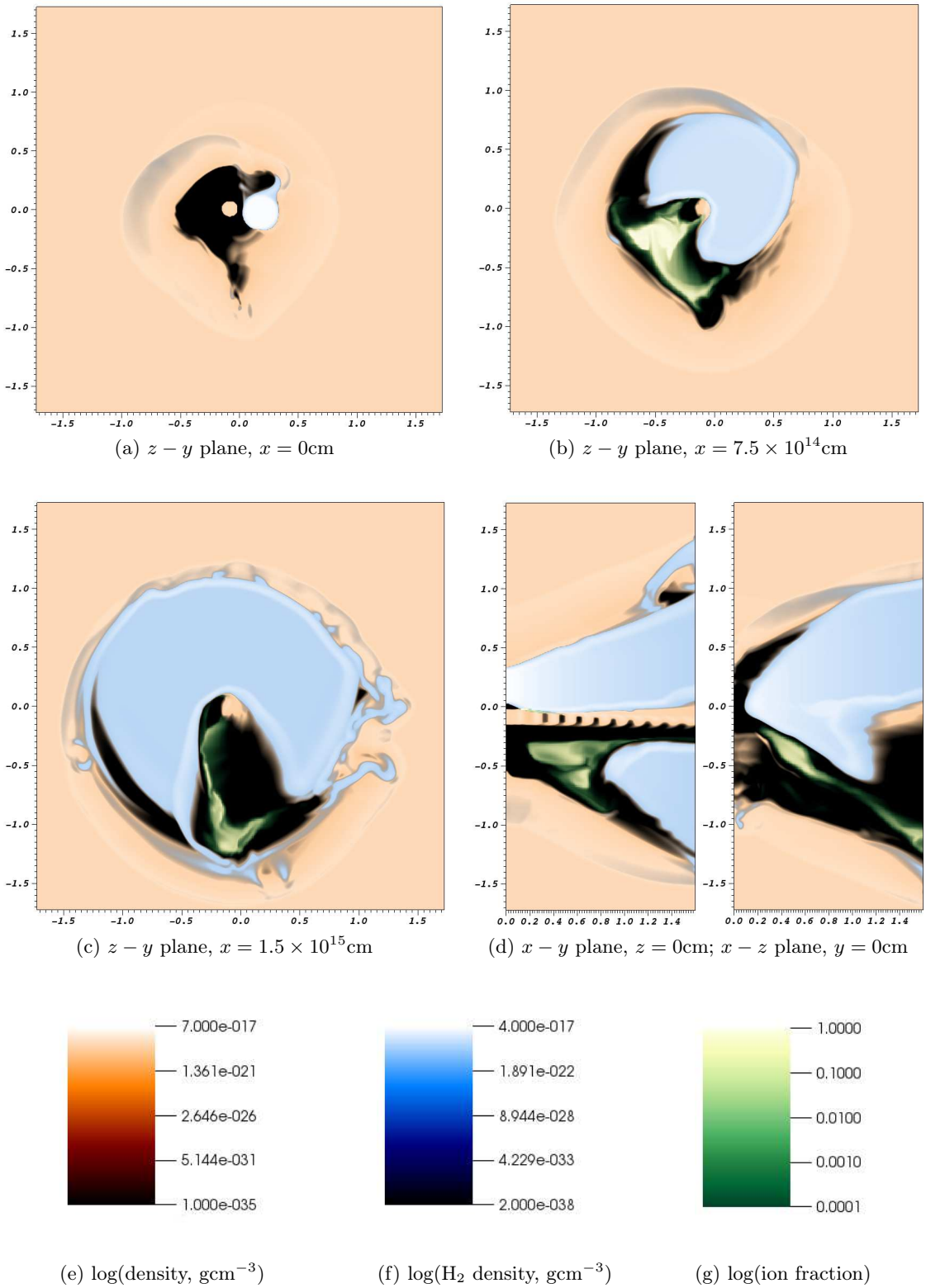

(a) $z-y$ plane, $x = 0$cm

(b) $z-y$ plane, $x = 7.5 \times 10^{14}$cm

(c) $z-y$ plane, $x = 1.5 \times 10^{15}$cm

(d) $x-y$ plane, $z = 0$cm; $x-z$ plane, $y = 0$cm

(e) log(density, gcm^{-3})

(f) log(H_2 density, gcm^{-3})

(g) log(ion fraction)

Figure 5.7: **Orbital Model ORB.2: 18AU Binary, atomic-molecular outflow cross-sections at simulation time T=87.5 Years.** Axis scales are in units of 10^{15}cm. Ambient medium is atomic hydrogen with trace molecular hydrogen formed from cooling during the simulation. Underlying density plot is fully opaque. For clarity, H_2 and ionisation fraction overplots are at ramped opacity; 100% opacity at max value, transparent at minimum value.

We may also observe that in addition to a well-mixed partial density of H_2 molecules in the expanding spiral density wave, there are 'gobbets' of wholly molecular material. In subfigure (c) of 5.7, we see evidence of shearing instability pulling molecular material out from the main outflow where it interacts with the density shock. In figures 5.8 through 5.10, it appears that lumps of H_2 are being flung outwards, possibly by the action of the atomic and molecular outflow columns from co-orbiting sources, as they stir the surrounding medium like a giant cosmic egg-whisk. Further on in this chapter, when we turn our attention to the Precessional model, we will see that although there is diffuse H_2 in the expanding shock surrounding the outflow system, these 'gobbets' of dense molecular material seen here in the Orbital model do not manifest.

We see in figure 5.11(d) that the pulsed velocity signal has given rise to small-scale density knots within the jet column, sandwiched between regions of lower density, just as we saw in the atomic-only case. However from around x = 20AU onwards, the atomic jet is in direct contact with the molecular outflow along an advancing face, and the integrity of the knots is severely compromised, as a large crossing shock from the impact point sweeps through the jet while the flow carries it forwards.

There is substantial ionisation occurring in this model, indicated by a green-white colour scale in the plots. The ionised material can be seen mainly in regions of very low density. However a more detailed examination will show that these are not the regions where ionisation is occurring.

Figure 5.10 demonstrates that the atomic outflow does not pass peacefully through its wide-angle molecular companion. A large cavity has been blasted out of the side of the conical molecular flow. This figure also gives a clue as to the origin of the ionised material; it is pouring out of the region where the leading face of the atomic jet is in contact with, and ploughing through, the molecular outflow.

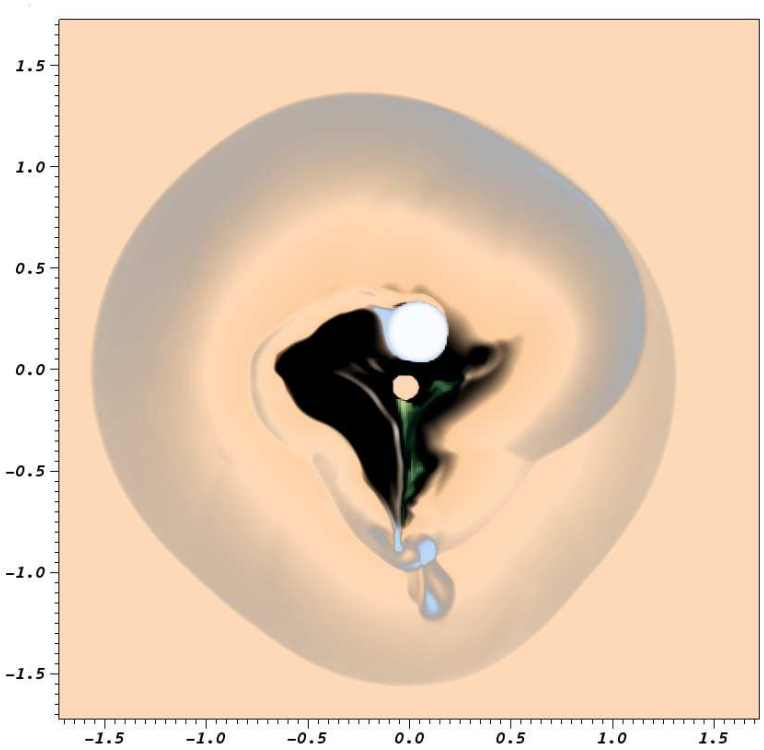

(a) density and composition; default material is HI

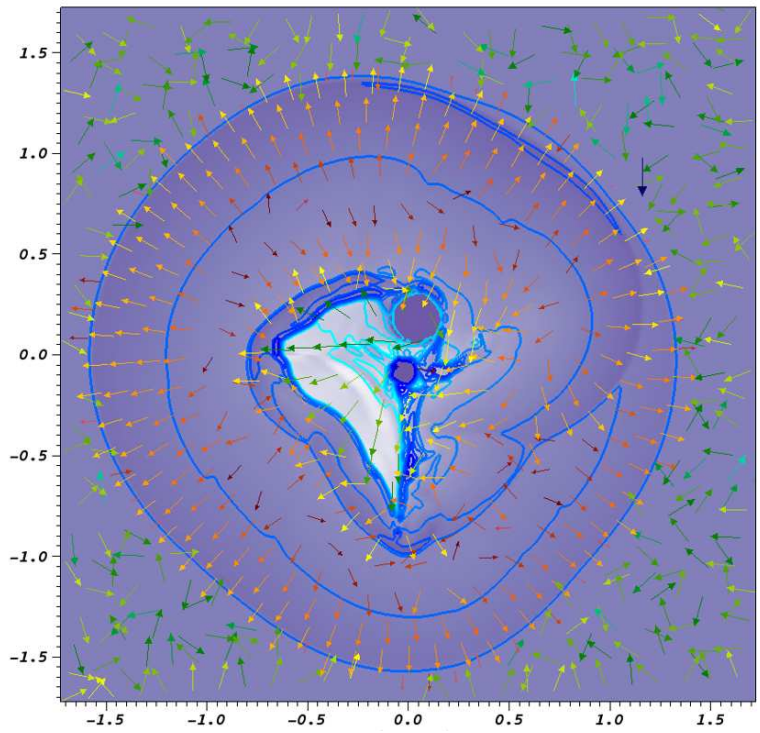

(b) pressure, temperature and velocity

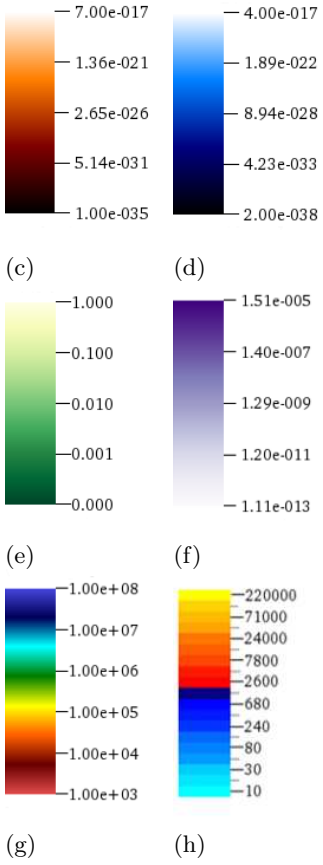

Colour scaling:
(c) density, g/cm^3
(d) H_2 density, g/cm^3
(e) ion mass fraction
(f) pressure, Ba
(g) velocity, cm/s (vector)
(h) temperature, K (contour)

(c), (d), (e) apply to subfigure (a); (f), (g), (h) apply to subfigure (b). All scales are to $\log_{10}$ including vector magnitude. Vector glyphs are 2D projections; the tail indicates the vector origin.

Figure 5.8: **Orbital Model ORB.2: 18AU Binary, atomic-molecular outflows into an atomic ambient medium; z-y plane cross-section shown at x=0cm and simulation time T=175 Years.** Axis scales are in units of 10^{15}cm. For clarity, the underlying density plot in subfigure (a) is fully opaque, whilst H_2 and ionisation overplots are at ramped opacity; 100% opacity at max value, transparent at minimum.

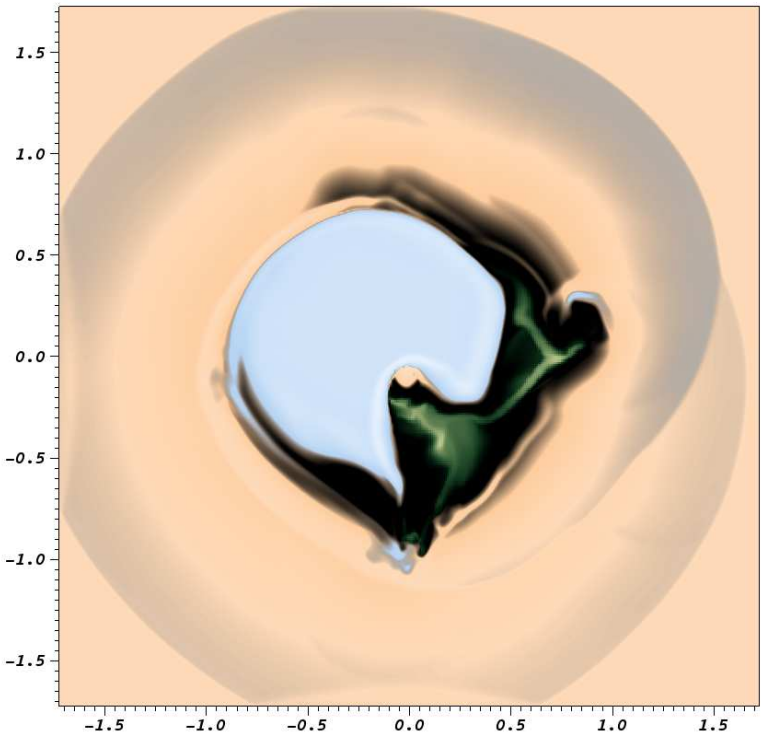

(a) density and composition; default material is HI

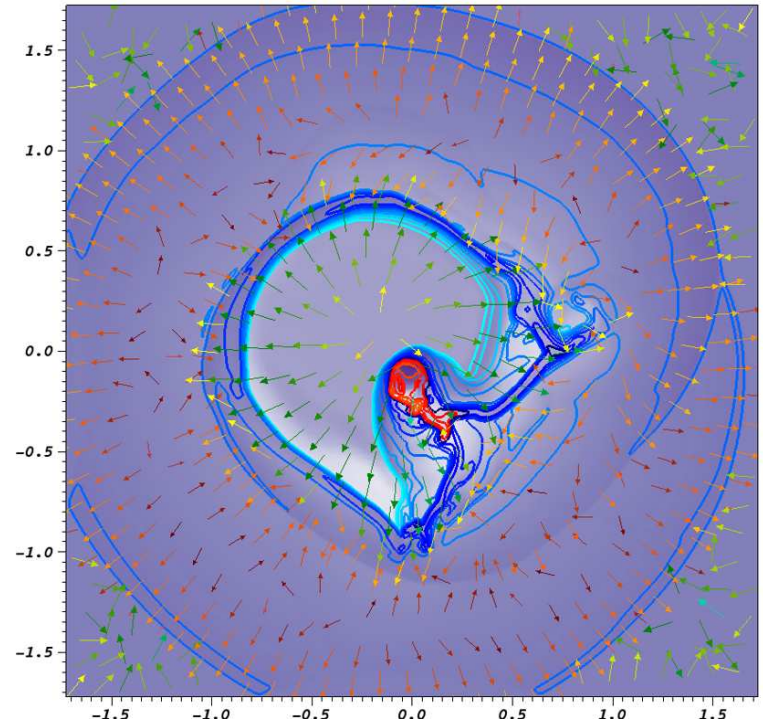

(b) pressure, temperature and velocity

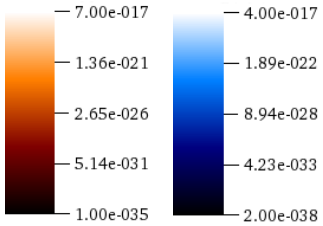

(c)

(d)

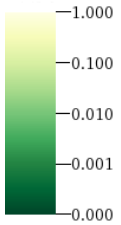

(e)

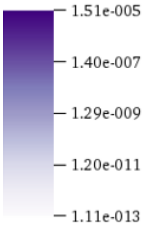

(f)

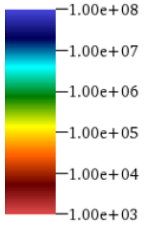

(g)

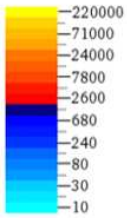

(h)

Colour scaling:
(c) density, g/cm^3
(d) H_2 density, g/cm^3
(e) ion mass fraction
(f) pressure, Ba
(g) velocity, cm/s (vector)
(h) temperature, K (contour)

(c), (d), (e) apply to subfigure (a); (f), (g), (h) apply to subfigure (b). All scales are to $\log_{10}$ including vector magnitude. Vector glyphs are 2D projections; the tail indicates the vector origin.

Figure 5.9: **Orbital Model ORB.2: 18AU Binary, atomic-molecular outflows into an atomic ambient medium; z-y plane cross-section shown at x=7.5×10^{14}cm and simulation time T=175 Years.** Axis scales are in units of 10^{15}cm. For clarity, the underlying density plot in subfigure (a) is fully opaque, whilst H_2 and ionisation overplots are at ramped opacity; 100% opacity at max value, transparent at minimum.

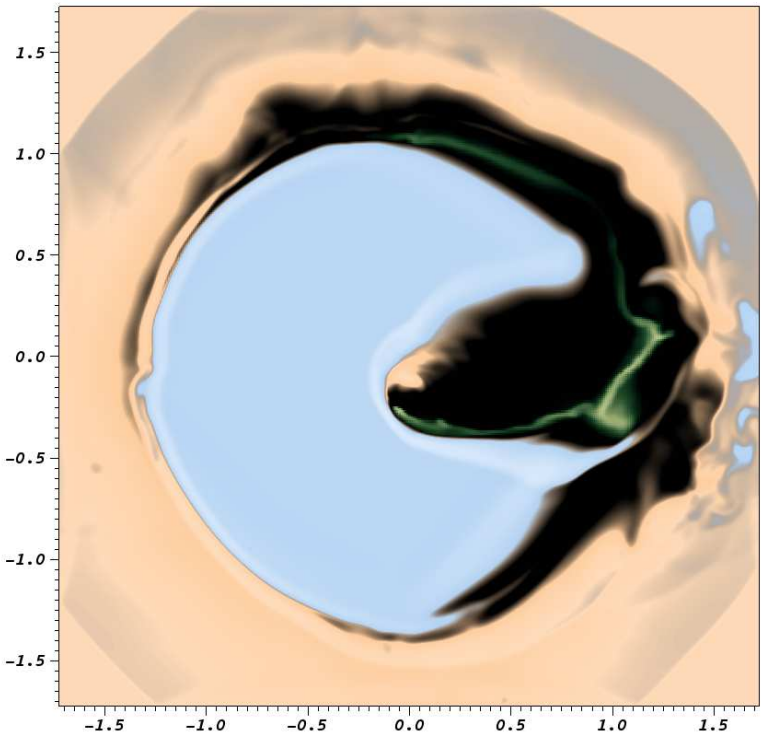

(a) density and composition; default material is HI

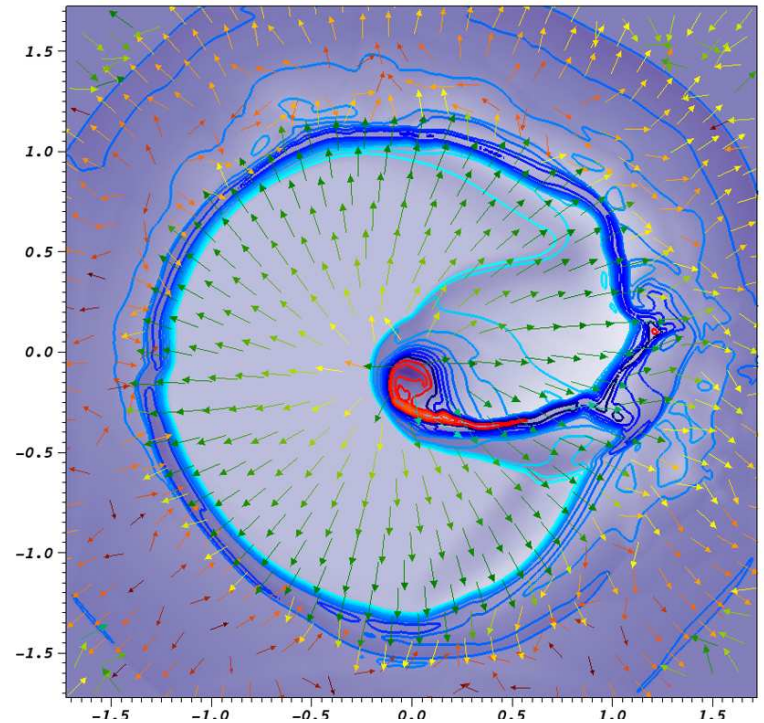

(b) pressure, temperature and velocity

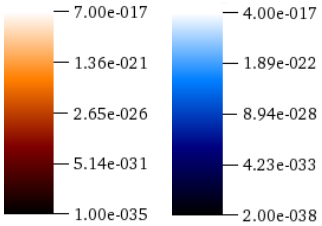

(c) (d)

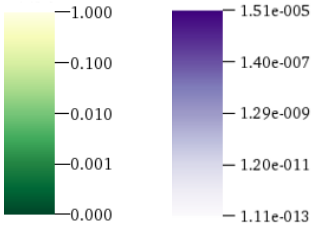

(e) (f)

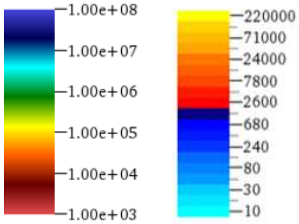

(g) (h)

Colour scaling:
(c) density, g/cm^3
(d) H_2 density, g/cm^3
(e) ion mass fraction
(f) pressure, Ba
(g) velocity, cm/s (vector)
(h) temperature, K (contour)

(c), (d), (e) apply to subfigure (a); (f), (g), (h) apply to subfigure (b). All scales are to $\log_{10}$ including vector magnitude. Vector glyphs are 2D projections; the tail indicates the vector origin.

Figure 5.10: **Orbital Model ORB.2: 18AU Binary, atomic-molecular outflows into an atomic ambient medium; z-y plane cross-section shown at x=1.5×10^{15}cm and simulation time T=175 Years.** Axis scales are in units of 10^{15}cm. For clarity, the underlying density plot in subfigure (a) is fully opaque, whilst H_2 and ionisation overplots are at ramped opacity; 100% opacity at max value, transparent at minimum.

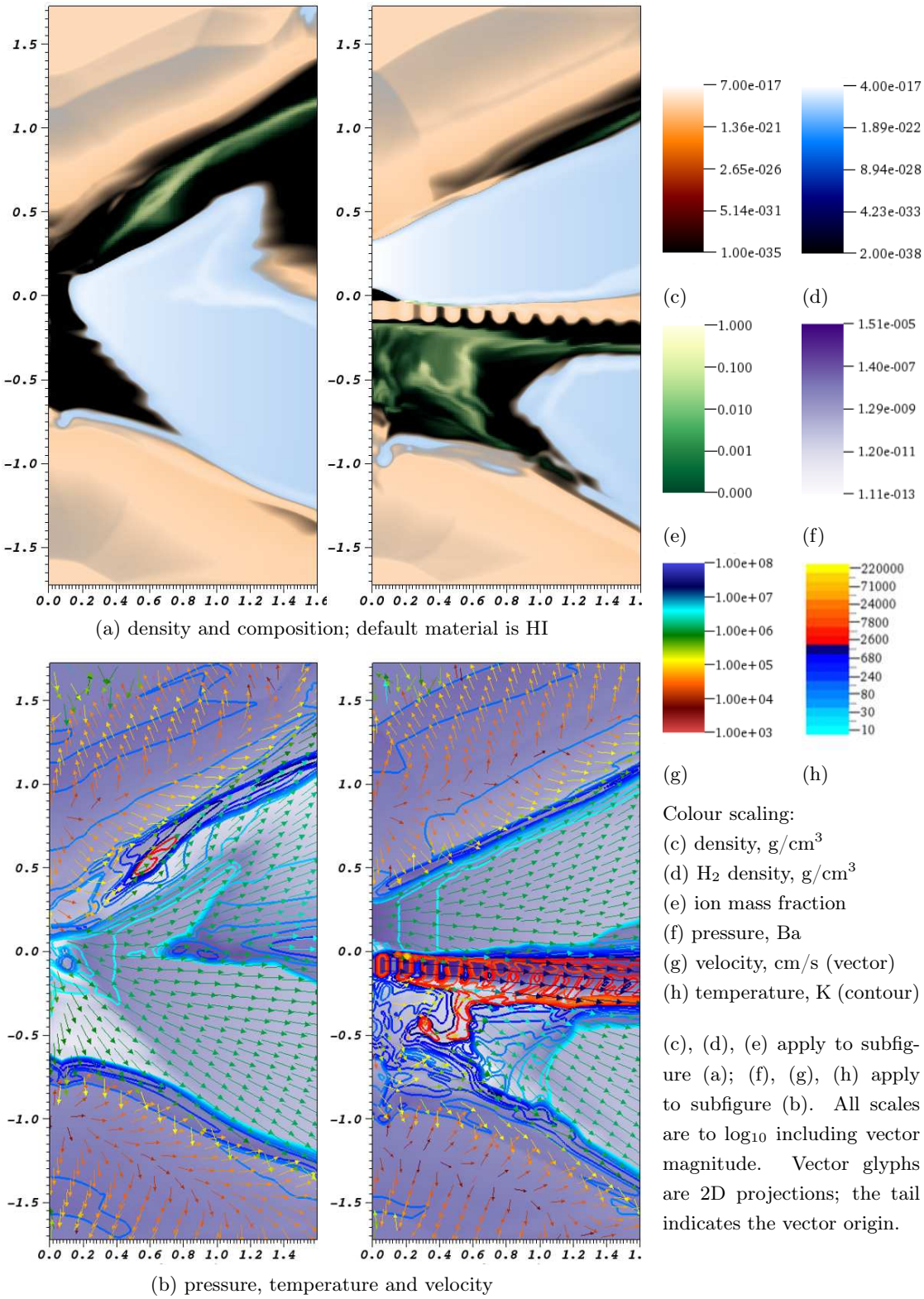

Colour scaling:
(c) density, g/cm^3
(d) H_2 density, g/cm^3
(e) ion mass fraction
(f) pressure, Ba
(g) velocity, cm/s (vector)
(h) temperature, K (contour)

(c), (d), (e) apply to subfigure (a); (f), (g), (h) apply to subfigure (b). All scales are to $\log_{10}$ including vector magnitude. Vector glyphs are 2D projections; the tail indicates the vector origin.

Figure 5.11: **Orbital Model ORB.2: 18AU Binary, atomic-molecular outflows into an atomic ambient medium; x-y (L) and x-z plane (R) cross-sections shown at z, y=0cm and simulation time T=175 Years.** Axis scales are in units of 10^{15}cm. For clarity, the underlying density plot in subfigure (a) is fully opaque, whilst H_2 and ionisation overplots are at ramped opacity; 100% opacity at max value, transparent at minimum.

5.3.3 Orbital Model ORB.2: Time Evolution

A careful examination of figure 5.8 (b) reveals an interesting feature; to the 'South' and 'West' of the barycentre of the two-jet system, a region of very low pressure ($\sim 10^{-13}$ Ba) and temperature ($\sim$ 10 K) has formed. The velocity field suggests that the inflation of this cavity and drop in pressure and temperature is due to a rapid expansion of material, most of which appears to be sloughing from the molecular outflow column.

Figure 5.12 that follows depicts the time-evolution of the two jet columns close to the inlets where these cavities form, and clarifies what is occurring. The cavity begins as the trailing wake of the molecular outflow, and as this outflow moves off, material is drawn from the outflow by the pressure differential. The material rushes across this low-density region and meets the far 'wall' where the pressure it exerts supports the cavity against collapse. It gradually inflates radially outwards even as the continuing progress of the molecular outflow pushes open more wake in the ambient medium.

This situation does not persist indefinitely. As the atomic jet swings around in its orbit it penetrates into the cavity. The first effect of this is to disturb the flow and prevent further inflation of the cavity, though the flow separates in a portion of the cavity that calves off to form the starting point for a new cavity (see the 81 years frame of Figure 5.12). Then, by the 94 years frame, a dramatic flaring event has occurred; an eruption of ionised material at 10^4 - 10^5 K from the vicinity of the atomic jet column floods out into the low density cavity. The process then begins again.

In addition to helping to understand the formation of cavities, Figure 5.12 also demonstrates the flow being driven outwards into the ambient medium faster than the spiral density wave; on passing through the forward shock the flow becomes disorganised as previously remarked on.

Figure 5.13 shows one time frame in the evolution of the ORB.2 model in greater detail, and also includes the colour scales for Fig. 5.12.

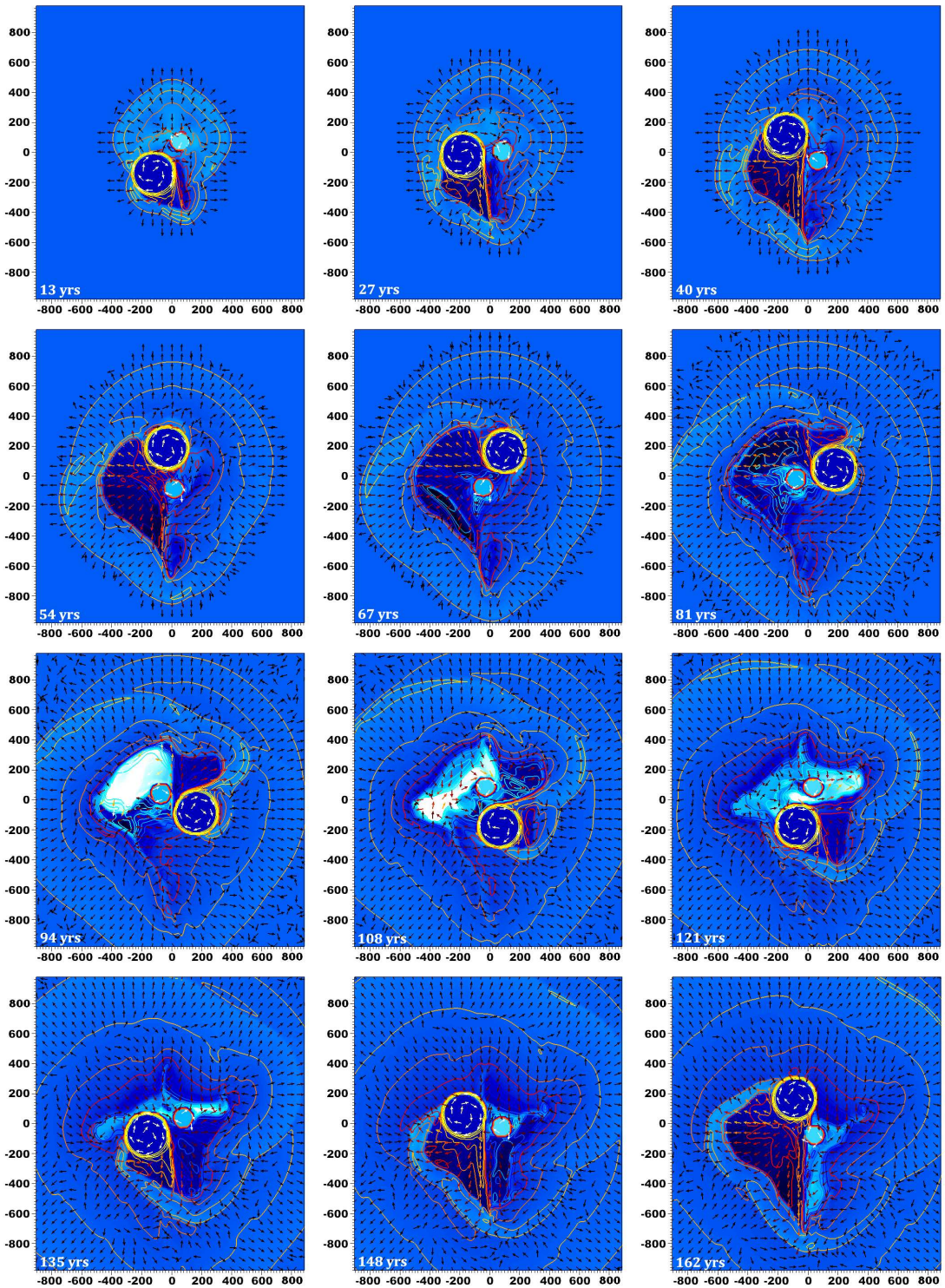

Figure 5.12: 18AU Atomic Primary, Molecular Secondary, orbitally driven interaction; cross sections at x=3.2×10^{13} cm. Background (blue) shows temperature. Velocity vectors are constant length, colour-scaled. Contours show density. Colour scales for this diagram are given in figure 5.13. Model number: ORB.2

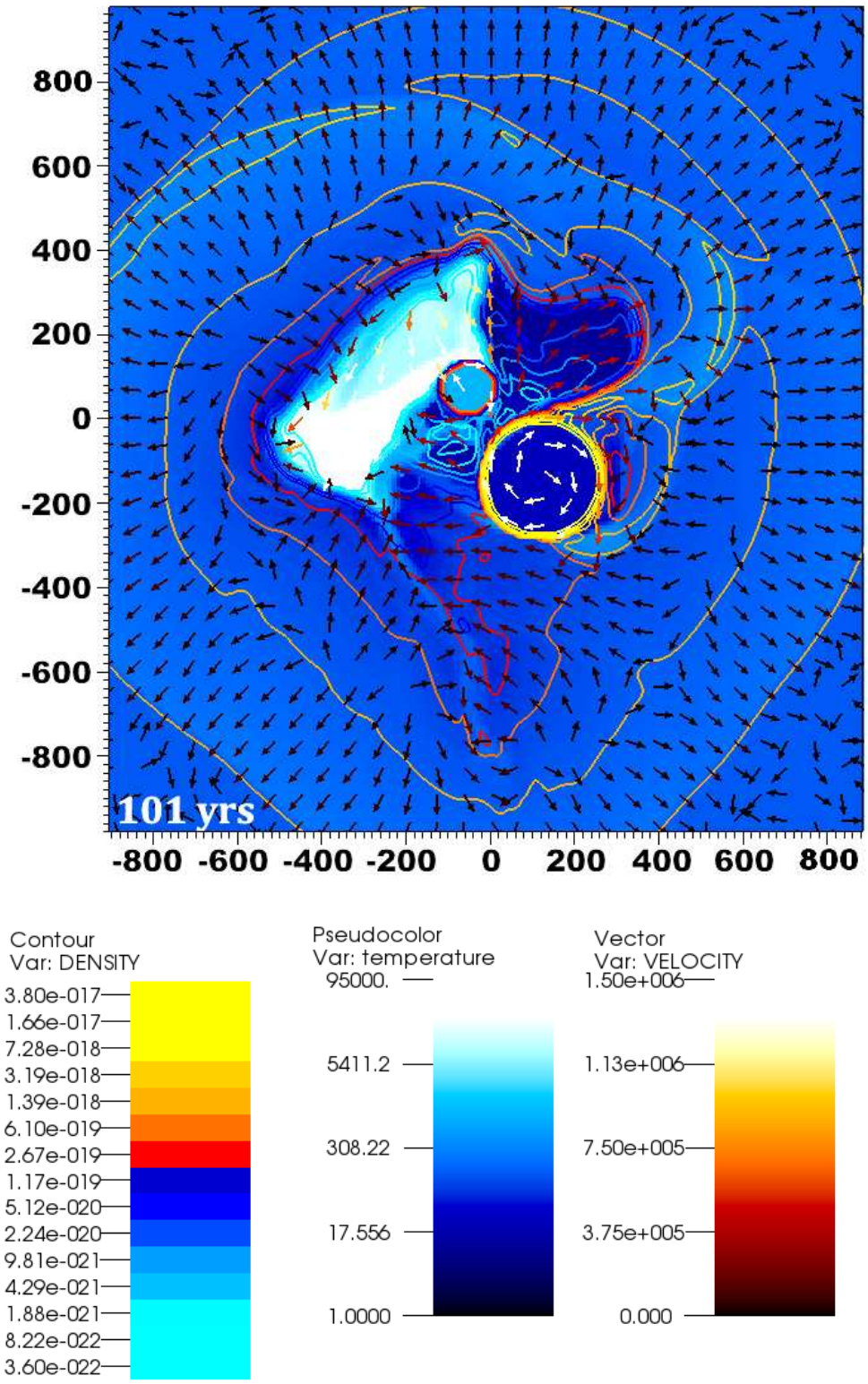

Figure 5.13: 18AU Atomic Primary, Molecular Secondary, orbitally driven interaction; cross sections at x=3.2×10^{13} cm. Background (blue) shows temperature. Velocity vectors are constant length, colour-scaled. Contours show density. Model number: ORB.2

5.3.4 Longitudinal Analysis of Orbital Models

Quantities of interest pertaining to the mainly atomic jet (including its non-atomic components such as ionised or entrained molecular Hydrogen) were analysed as a function of distance along the (barycentric) x-axis of the problem domain, using IDL® post-processing scripts developed for the purpose. The fast-moving material whose properties we were interested in could be isolated with a filter that selected for zones where V_x was greater than 50 km/s. The exception was the analysis of ionised material which simply selected material of that nature irrespective of velocity.

Generally, quantities examined were averaged over a slice of monozonal thickness for each of the 160 values of the x-coordinate, weighted by density or volume as appropriate; or in some cases the total quantity was determined. The graphs presented here include plots of the atomic-molecular co-orbital model (ORB.2) represented by solid lines, and of the atomic-only co-orbital model (ORB.1) by dashed lines. Given the density of data points, the single-valued nature of the functions and lack of meaningful error that may be attached, simple connected lines have been used rather than showing separate data points.

Given the fact that quantities are being averaged over the cross-sectional area of the jet, it is reasonable to extend this principle in the x-direction also, so that each data point represents the average over a three-dimensional region of the jet. Therefore trend graphs smoothed in the x-direction are shown to the right of each plot. Near-Gaussian smoothing is employed over a smoothing window equal to two jet inlet diameters. This averages the variations related to the velocity pulsations of the atomic jet.

Nearly every graph shows a dramatic change in the behaviour of the atomic jet that encounters the molecular outflow, the point of contact being $x \approx 15$AU from the inlet boundary. In the smoothed graphs the effect shifts downstream, to around 20-25AU.

In figure 5.14, we see, perhaps surprisingly, an inward deflection towards the x-axis, before the jet is deflected outwards, as we might naturally expect. The likely explanation for this is that the atomic jet entrains molecular material at the point where it first encounters the dense molecular wind; thus sufficient x-momentum is imparted to some molecular material to push it into the $>$ 50 km/s velocity range we are selecting, thereby suddenly

weighting the average position of the centre of mass closer to the radial origin. After this initial inward deflection, we see an outwards deflection increasing monotonically in an apparent exponential rise, the radial limit of which may not be much greater than that of the undeflected atomic-only jet although a more elongated problem domain would be required to investigate this further.

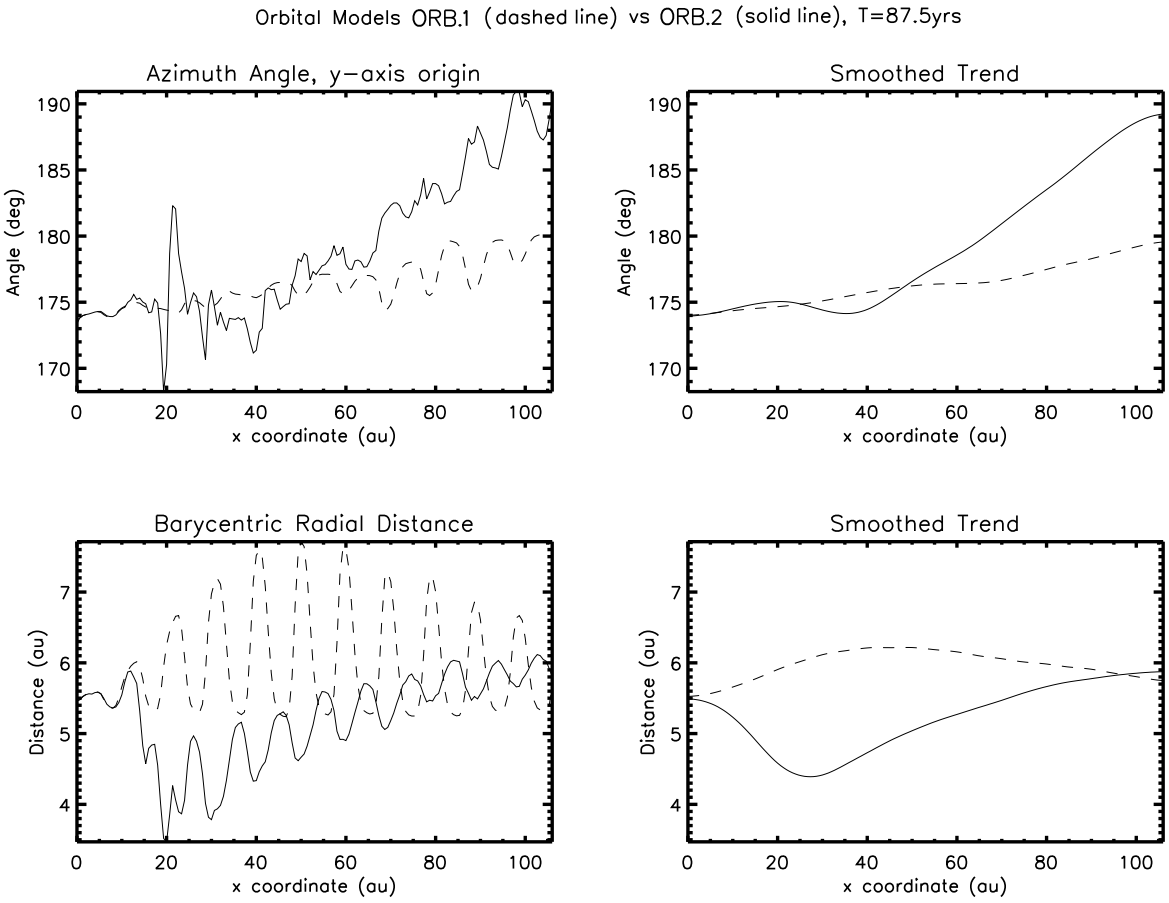

Figure 5.14: Orbital Models: atomic jet azimuth angle and radial distance, along propagation axis, T=87.5 years. Radial distance is in the y-z plane and directed outward with respect to the domain x-axis, which passes through the barycentre of the binary system. Azimuth angle is in the y-z plane and directed in an anticlockwise sense about the domain x-axis. Model numbers: ORB.2 (with molecular outflow) and ORB.1 (without).

However, figure 5.14 shows that the azimuth angle deflection attained by the end of the problem domain differs more conclusively from the unperturbed atomic jet (the azimuthal deflection of which is simply related to the jet's orbital motion): a difference of $9.5° \pm 0.1°$. This has implications for the winding ratio or pitch, of the large-scale helical outflow beyond the short domain examined here.

Figure 5.15 adds to the picture of the atomic jet deflection, showing the differences arising in radial and tangential velocities; suggesting that deflection will continue to increase beyond the problem domain.

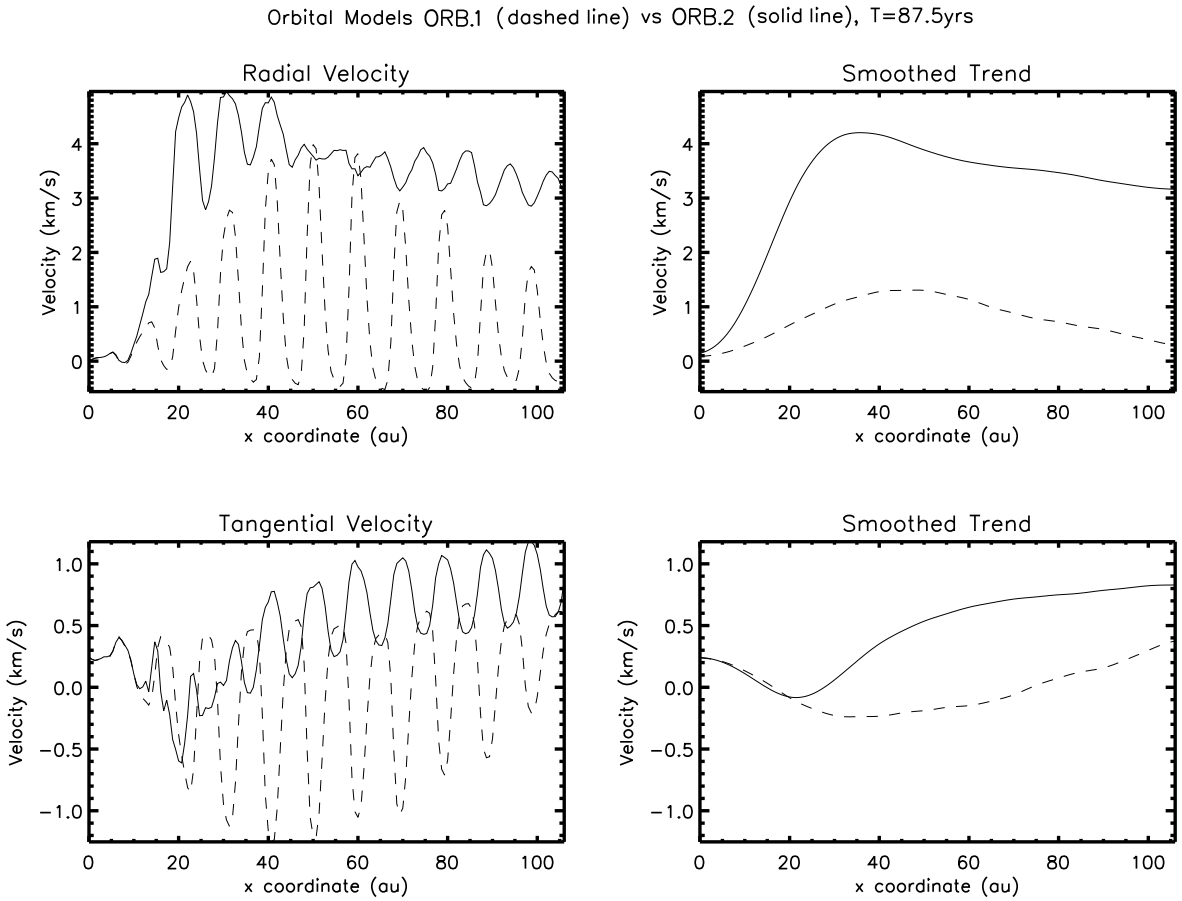

Figure 5.15: Orbital Models: atomic jet net radial and tangential velocities along propagation axis, T=87.5 years. Radial velocity component is in the y-z plane and directed outward with respect to the domain x-axis which passes through the barycentre of the binary system. Tangential velocity is in the y-z plane and directed in a right-handed sense perpendicular to a normal line radiating from the x-axis and passing through the jet's plane centroid. Model numbers: ORB.2 (with molecular outflow) and ORB.1 (without).

Figure 5.16 deals with V_x the forward-directed velocity of the atomic jet, which in the case of HH30 lies almost in the sky plane for the first 400AU of propagation. We see that there is a dramatic fall in the average velocity of the jet material from the point at which it encounters the molecular outflow; around 100 km/s negative differential against a velocity of 250 - 270 km/s, remaining near-constant in the velocity smoothed trend until the jet exits the domain. However - the peak velocity of material in the jet is

virtually unchanged from the scenario where no molecular component is present.

Figure 5.17 shows that the width of the velocity distribution in the perturbed jet has narrowed, and also the width of the jet itself has reduced, its cross-sectional area being only 65% of the unperturbed jet.

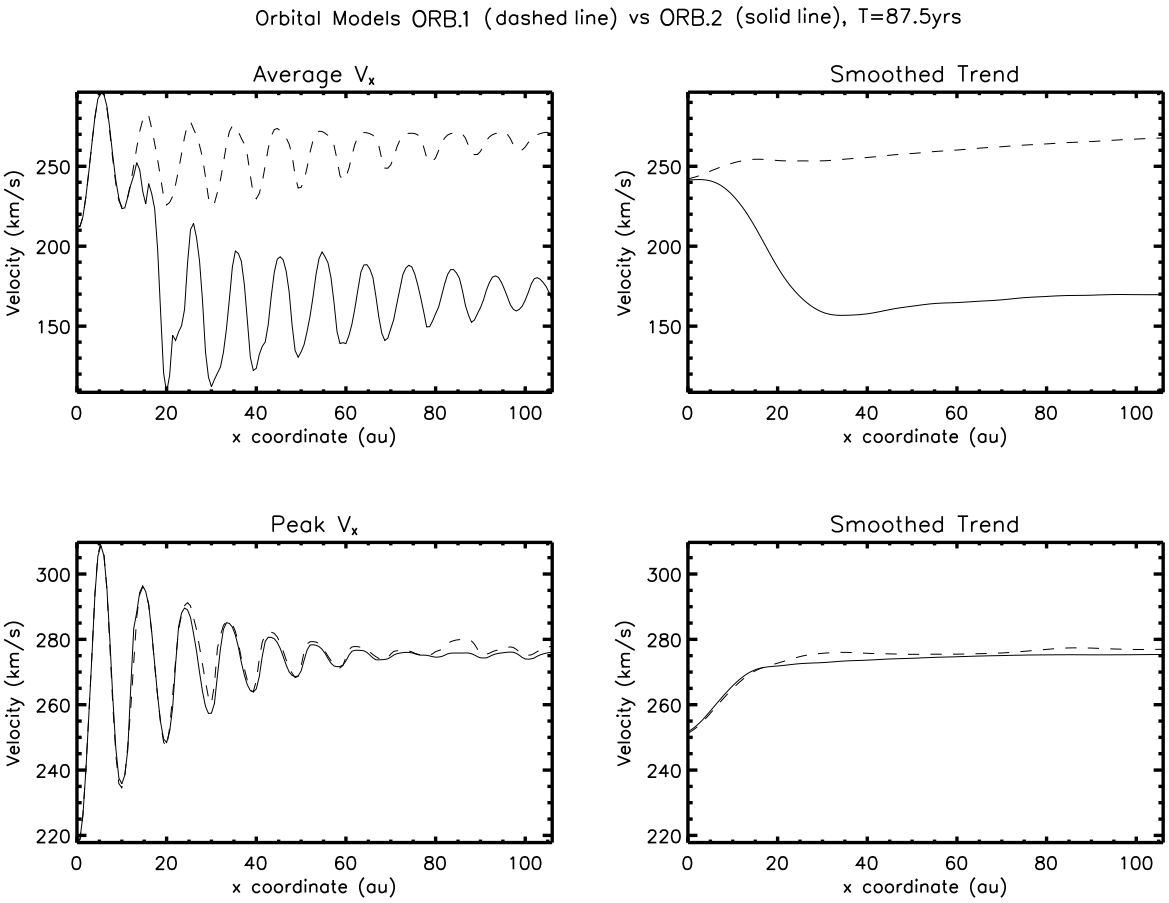

Figure 5.16: Orbital Models: atomic jet average and peak velocity along propagation axis, T=87.5 years. Model numbers: ORB.2 (with molecular outflow) and ORB.1 (without).

Figures 5.18 and 5.19 show various other quantities of interest, with self-evident differences between the perturbed and unperturbed jet.

The mass per unit jet length shows a significant rise after the point of contact with the molecular wind, being approximately double its unperturbed value. Since the momentum (in the same figure) has increased by $\sim 18\%$, we expect the velocity to reduce to $\sim 59\%$ of its value. Referring to figure 5.16, an approximate calculation finds the velocity to have reduced to $\sim 58\%$. These calculations are approximate because the jet is not a closed

system due to entrainment and mixing, and we do not expect exact conservation of momentum; nonetheless, we find it is still an almost-conserved quantity over the 100AU of our problem domain.

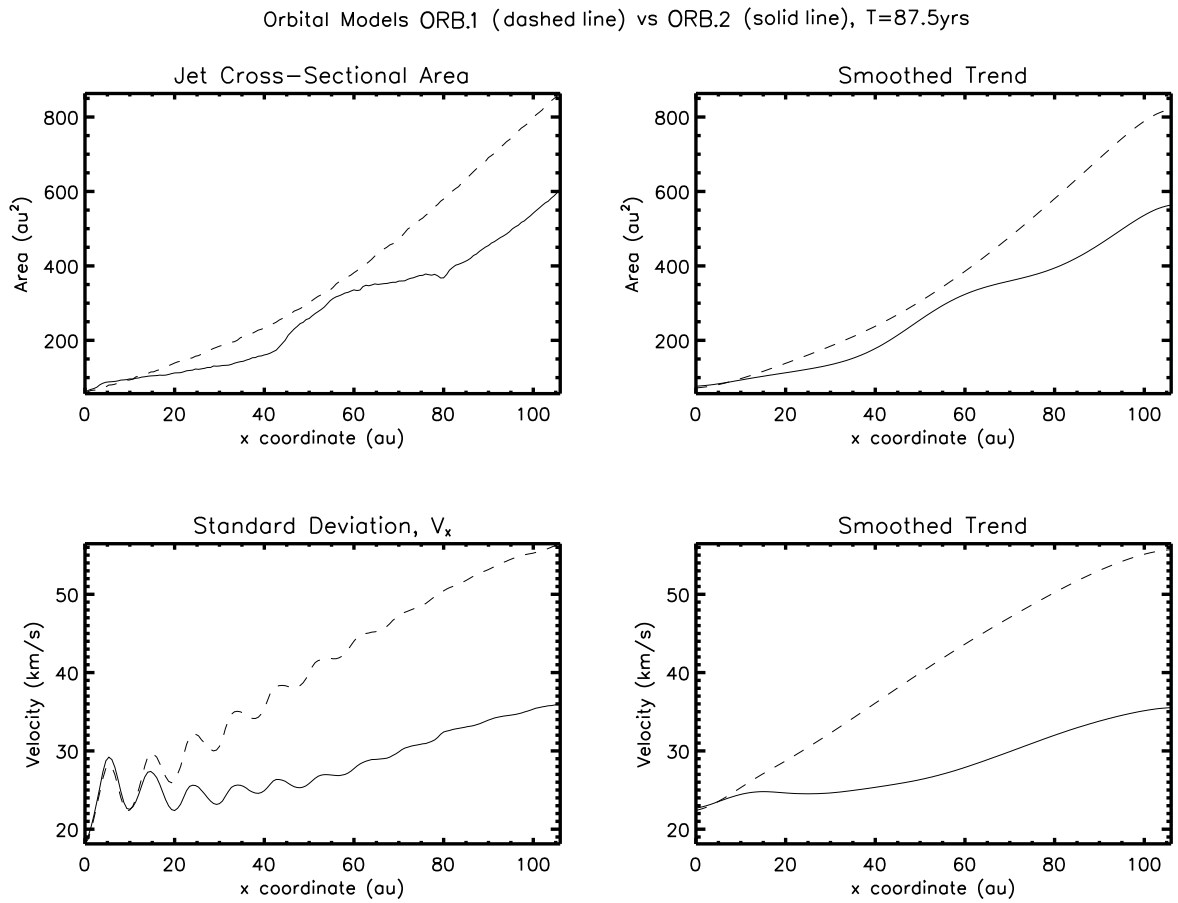

Figure 5.17: Orbital Models: atomic jet x-sectional area and velocity standard deviation along propagation axis, T=87.5 years. Model numbers: ORB.2 (with molecular outflow) and ORB.1 (without).

The other noteworthy difference is ionisation - see fig. 5.19. Within the first 20AU of propagation the perturbed jet produces an ionised mass 3-4 orders of magnitude greater than the unperturbed jet. In the dual outflow co-orbital model it is the interaction between the outflows that produces the overwhelming majority of ionisation. This increased ionisation persists out until the exit boundary by which time the difference has fallen to one order of magnitude.

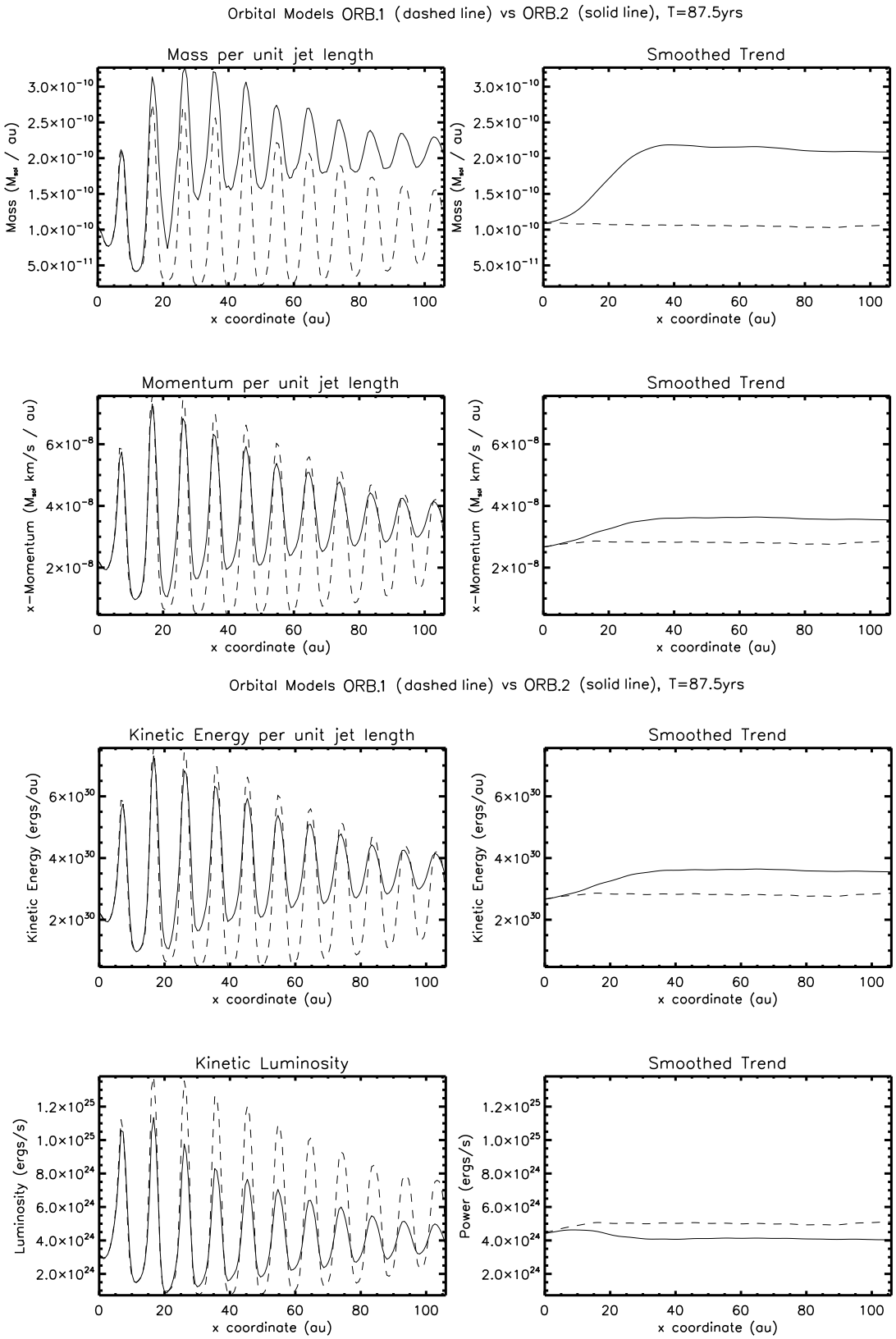

Figure 5.18: Orbital Models: atomic jet mass, momentum, kinetic energy and kinetic luminosity along propagation axis, T=87.5 years. Model numbers: ORB.2 (with molecular outflow) and ORB.1 (without).

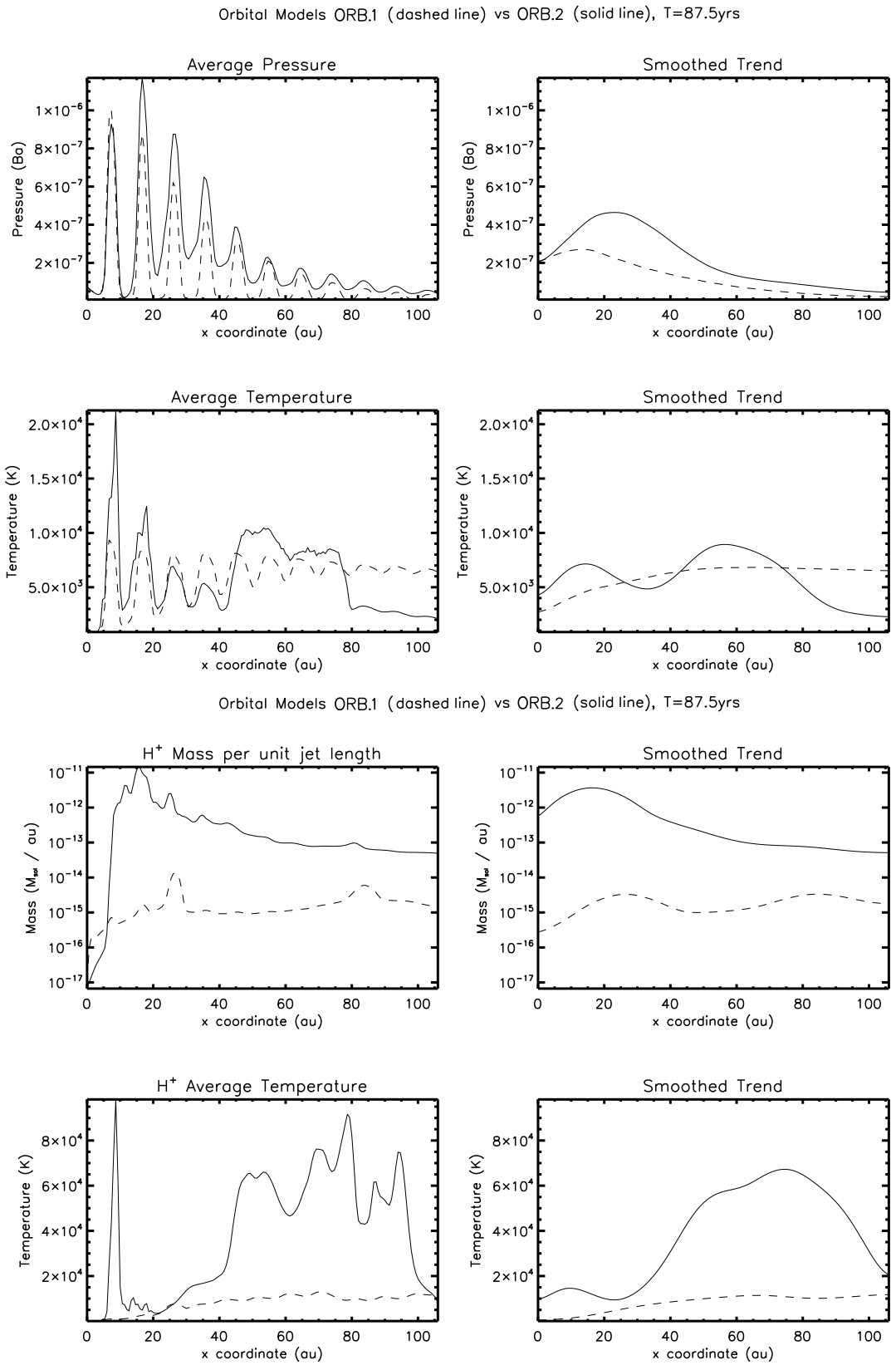

Figure 5.19: Orbital Models: atomic jet pressure, temperature, ionisation and ion temperature along propagation axis, T=87.5 years. Model numbers: ORB.2 (with molecular outflow) and ORB.1 (without).

5.4 The Precessional Scenario Simulations

5.4.1 Single Atomic Outflow Case (simulation PRE.1)

The immediately striking feature of this simulation evident in figure 5.20 is the plume of ionised material that envelops the central jet column. In other respects, there appears to be little difference between this and ORB.1, the atomic-only Orbital simulation. There is a series of small density knots that rapidly develop from a signal that begins purely as a velocity perturbation. As with ORB.1, there are 11 distinct knots spanning the problem domain. An expanding density shock, the trailing remnant of the initial bow shock that has since left the domain, surrounds the jet and its hot, low-density cocoon; unlike ORB.1 there is no spiral geometry to the shock.

So, what gives rise to the strong ionisation we see in this model? The difference between this and the earlier atomic-only model we examined lies in the orbital parameters. This model has a binary orbit separation of 0.75AU, while the other had an 18AU separation. Essentially, this jet remains in place and 'wiggles' furiously about the barycentre with a Keplerian orbit velocity of 26 km/s, while the other jet moves gradually through the ambient medium at 5 km/s.

We shall examine in more detail why this produces greater ionisation when we turn our attention to simulation PRE.2, the dual-outflow version of the Precessional scenario.

Figures 5.21 to 5.24 reveal more details about the flow. Despite the differences in ionisation we see many similar features with simulation ORB.1 (see figs. 5.3 to 5.6). As with the single outflow model there is an entrained updraft evident from the velocity and pressure fields.

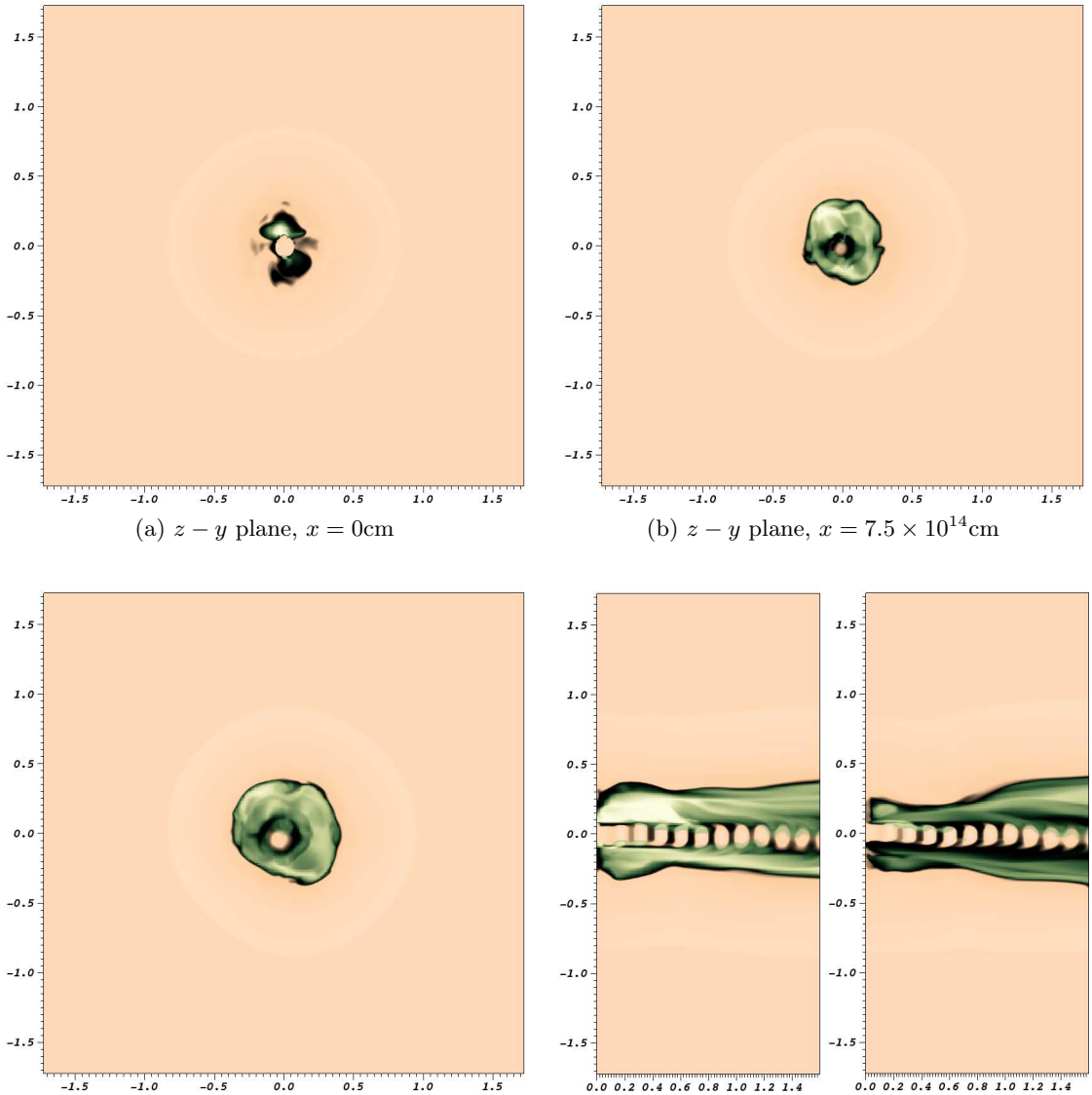

(a) $z-y$ plane, $x = 0$cm

(b) $z-y$ plane, $x = 7.5 \times 10^{14}$cm

(c) $z-y$ plane, $x = 1.5 \times 10^{15}$cm

(d) $x-y$ plane, $z = 0$cm; $x-z$ plane, $y = 0$cm

(e) log(density, gcm^{-3})

(f) log(H_2 density, gcm^{-3})

(g) log(ion fraction)

Figure 5.20: **Precessional Model PRE.1: 0.75AU binary, atomic-only outflow cross-sections at simulation time T=87.5 Years.** Axis scales are in units of 10^{15}cm. Ambient medium is atomic hydrogen with trace molecular hydrogen formed from cooling during the simulation. Underlying density plot is fully opaque. For clarity, H_2 and ionisation fraction overplots are at ramped opacity; 100% opacity at max value, transparent at minimum value.

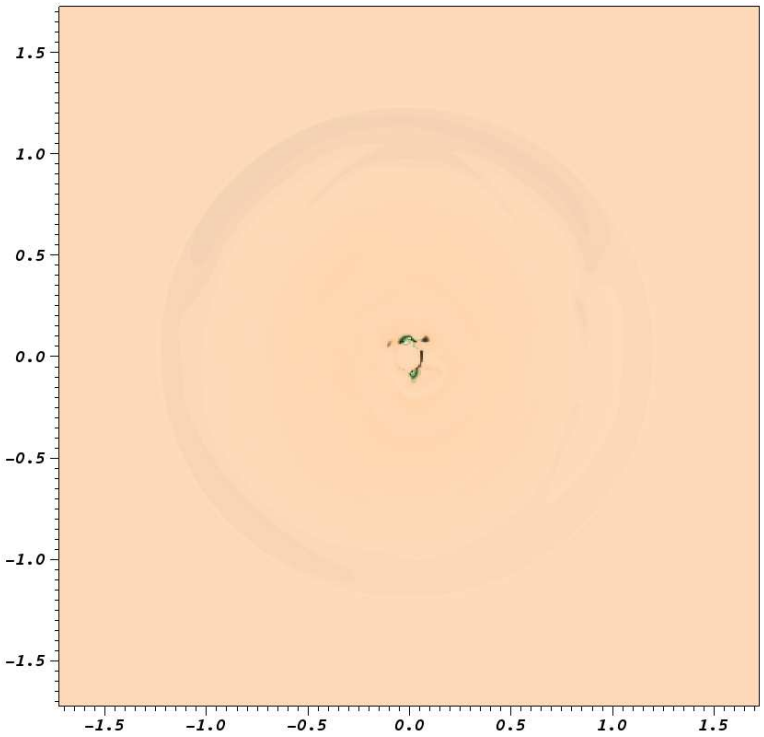

(a) density and composition; default material is HI

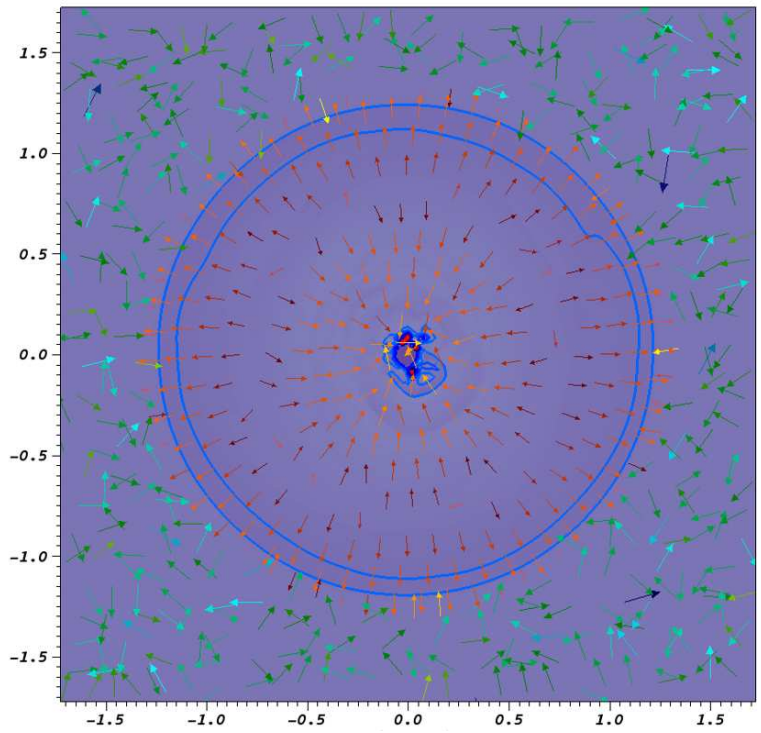

(b) pressure, temperature and velocity

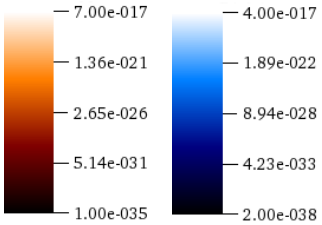

(c) (d)

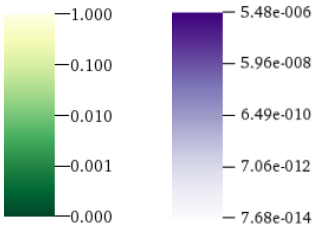

(e) (f)

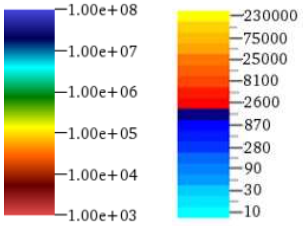

(g) (h)

Colour scaling:
(c) density, g/cm^3
(d) H_2 density, g/cm^3
(e) ion mass fraction
(f) pressure, Ba
(g) velocity, cm/s (vector)
(h) temperature, K (contour)

(c), (d), (e) apply to subfigure (a); (f), (g), (h) apply to subfigure (b). All scales are to $\log_{10}$ including vector magnitude. Vector glyphs are 2D projections; the tail indicates the vector origin.

Figure 5.21: **Precessional Model PRE.1: 0.75AU Binary, atomic-only outflow into an atomic ambient medium; z-y plane cross-section shown at x=0cm and simulation time T=175 Years.** Axis scales are in units of 10^{15}cm. For clarity, the underlying density plot in subfigure (a) is fully opaque, whilst H_2 and ionisation overplots are at ramped opacity; 100% opacity at max value, transparent at minimum.

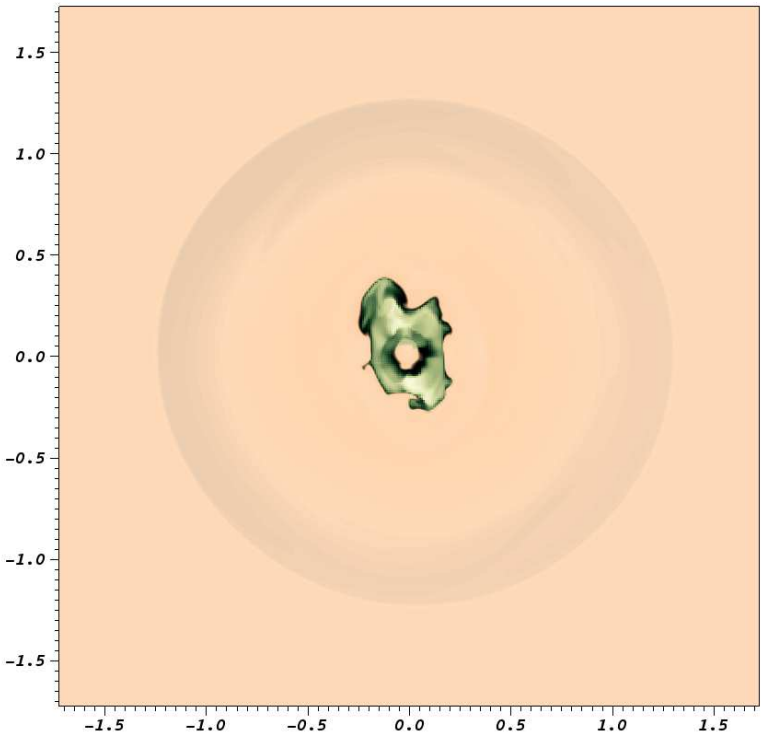

(a) density and composition; default material is HI

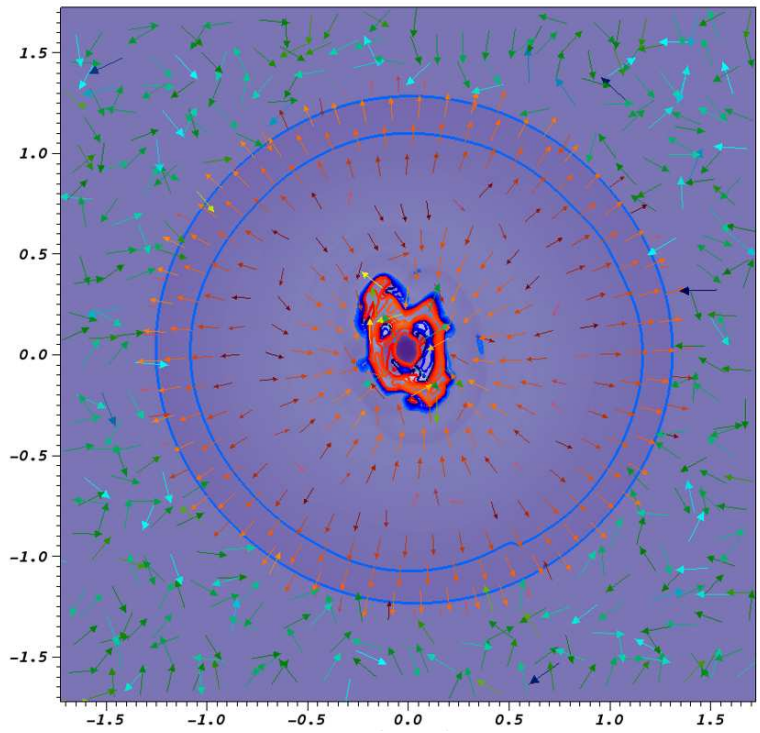

(b) pressure, temperature and velocity

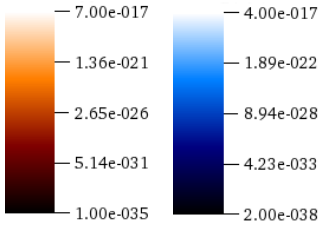

(c) (d)

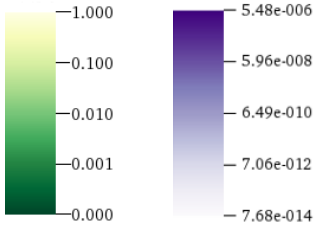

(e) (f)

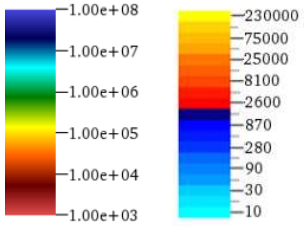

(g) (h)

Colour scaling:
(c) density, g/cm^3
(d) H_2 density, g/cm^3
(e) ion mass fraction
(f) pressure, Ba
(g) velocity, cm/s (vector)
(h) temperature, K (contour)

(c), (d), (e) apply to subfigure (a); (f), (g), (h) apply to subfigure (b). All scales are to $\log_{10}$ including vector magnitude. Vector glyphs are 2D projections; the tail indicates the vector origin.

Figure 5.22: **Precessional Model PRE.1: 0.75AU Binary, atomic-only outflow into an atomic ambient medium; z-y plane cross-section shown at x=7.5×10^{14}cm and simulation time T=175 Years.** Axis scales are in units of 10^{15}cm. For clarity, the underlying density plot in subfigure (a) is fully opaque, whilst H_2 and ionisation overplots are at ramped opacity; 100% opacity at max value, transparent at minimum.

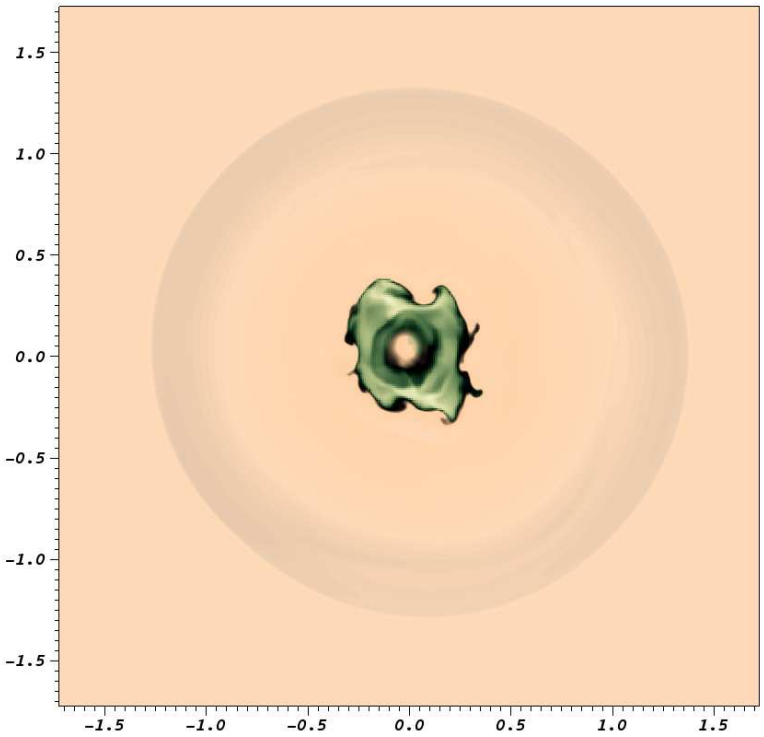

(a) density and composition; default material is HI

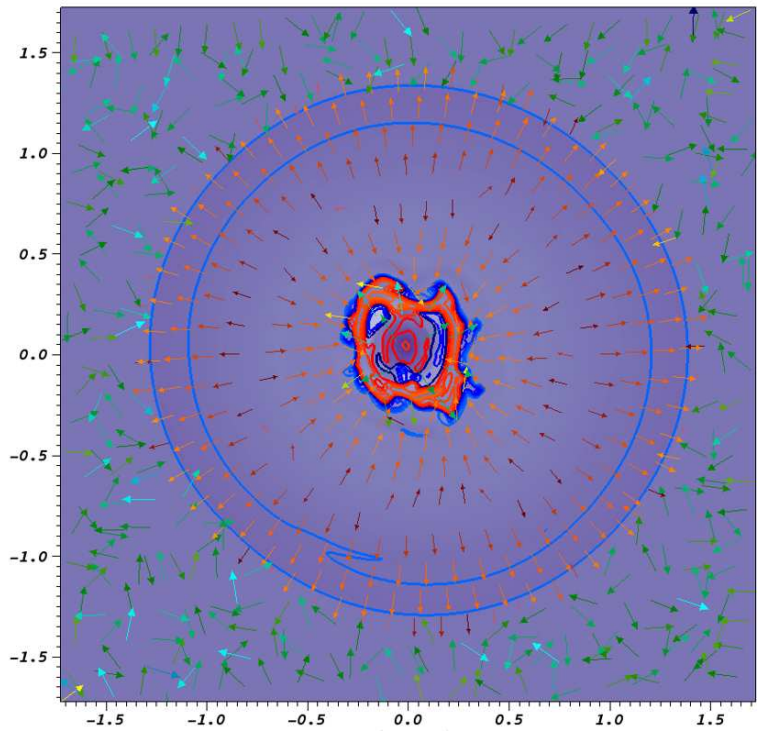

(b) pressure, temperature and velocity

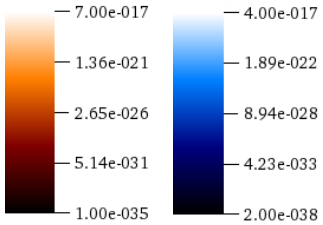

(c) (d)

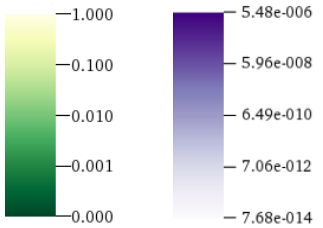

(e) (f)

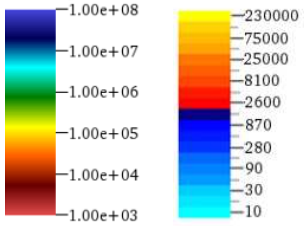

(g) (h)

Colour scaling:
(c) density, g/cm^3
(d) H_2 density, g/cm^3
(e) ion mass fraction
(f) pressure, Ba
(g) velocity, cm/s (vector)
(h) temperature, K (contour)

(c), (d), (e) apply to subfigure (a); (f), (g), (h) apply to subfigure (b). All scales are to $\log_{10}$ including vector magnitude. Vector glyphs are 2D projections; the tail indicates the vector origin.

Figure 5.23: **Precessional Model PRE.1: 0.75AU Binary, atomic-only outflow into an atomic ambient medium; z-y plane cross-section shown at x=1.5×10^{15}cm and simulation time T=175 Years.** Axis scales are in units of 10^{15}cm. For clarity, the underlying density plot in subfigure (a) is fully opaque, whilst H_2 and ionisation overplots are at ramped opacity; 100% opacity at max value, transparent at minimum.

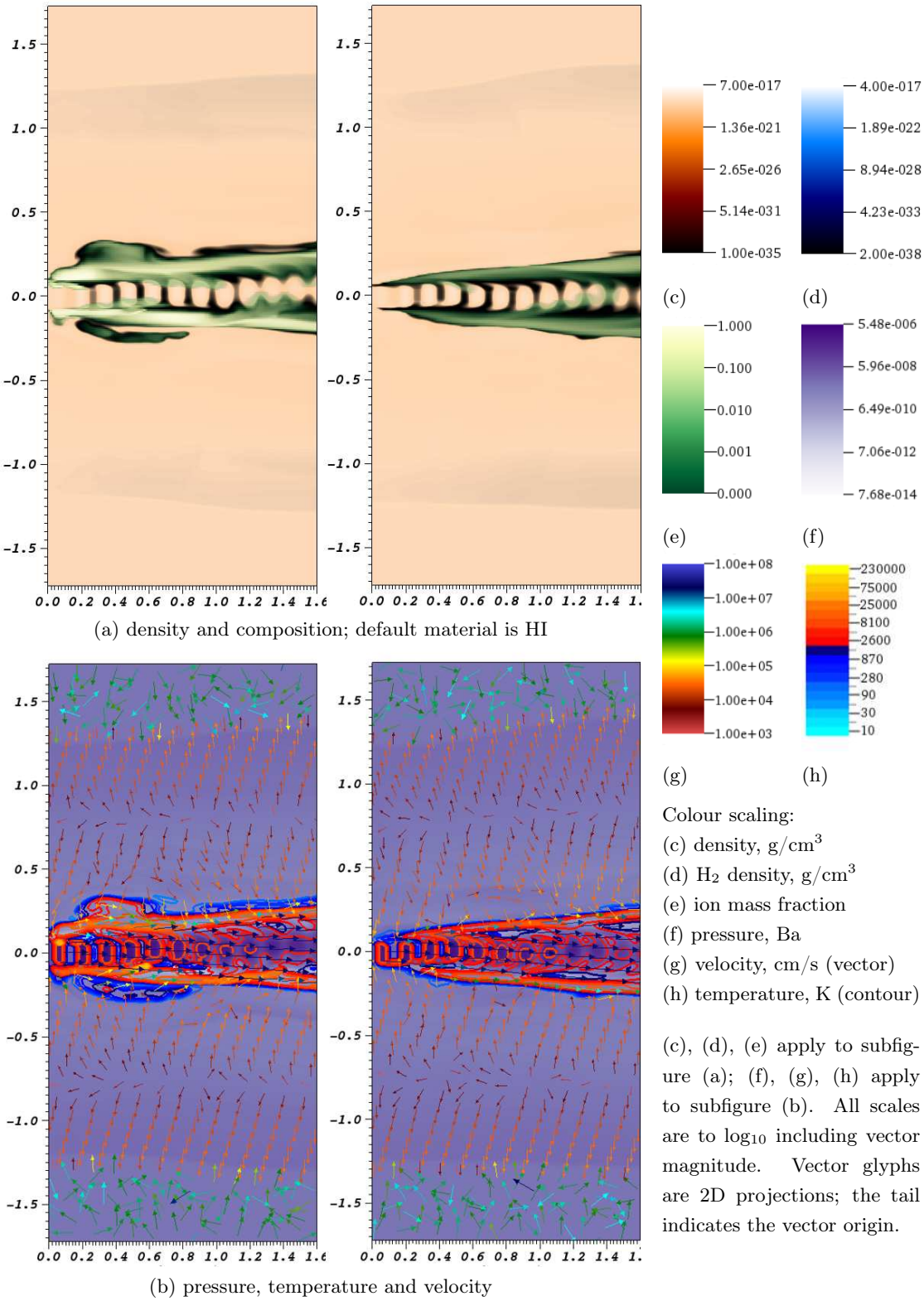

(a) density and composition; default material is HI

(b) pressure, temperature and velocity

Colour scaling:
(c) density, g/cm^3
(d) H_2 density, g/cm^3
(e) ion mass fraction
(f) pressure, Ba
(g) velocity, cm/s (vector)
(h) temperature, K (contour)

(c), (d), (e) apply to subfigure (a); (f), (g), (h) apply to subfigure (b). All scales are to $\log_{10}$ including vector magnitude. Vector glyphs are 2D projections; the tail indicates the vector origin.

Figure 5.24: **Precessional Model PRE.1: 0.75AU Binary, atomic-only outflow into an atomic ambient medium; x-y (L) and x-z plane (R) cross-sections shown at z, y=0cm and simulation time T=175 Years.** Axis scales are in units of 10^{15}cm. For clarity, the underlying density plot in subfigure (a) is fully opaque, whilst H_2 and ionisation overplots are at ramped opacity; 100% opacity at max value, transparent at minimum.

5.4.2 Dual Atomic-Molecular Outflow Case (simulation PRE.2)

Figure 5.25 shows the structure of the dual outflow version of the Precessional scenario. The molecular outflow can be seen propagating from the inner part of the circumbinary accretion disc. Unlike the Orbital dual-outflow model ORB.2, the lateral expansion is here driven mainly by the Keplerian rotational velocity profile rather than the pressure differential, although the outflow is 1.5 $\times$ overpressured with respect to the ambient medium. We see the expanding remnant of the bow shock in the ambient medium as before but this is dominated by the bow shock of the molecular outflow.

The morphology of the molecular outflow agrees very well with the ad hoc and ballistic particle models used by Pety et al., 2006 (81) and Tambovtseva & Grinin, 2008 (118); see figures 3.9 and 3.11.

The features of the central pulsed atomic jet column are virtually identical to those we have already seen in the atomic-only case for this scenario. This includes the enveloping cocoon of ionised material. To the eye, there appears to be less ionisation than in the case where the molecular outflow is absent. In fact there are differences in the pattern of ionisation and ion temperature as will be shown later.

In figure 5.25(b) we see a low density cavity has been carved out from the ambient medium enclosed by the conical molecular flow. This kind of evacuated region does not have an equivalent in the atomic-only Precessional simulation. The ambient medium is prevented from flowing back into the cavity by waves of hot, light, partially ionised material expanding out from the atomic jet periphery and impacting against the boundary of the denser material. As the simulation progresses the cavity is slowly inflated as the ambient material is eroded (Compare figs. 5.25(b) at T=87.5 years and 5.27 at T=175 years).

Figures 5.26 to 5.29 reveal more details about the flow dynamics.

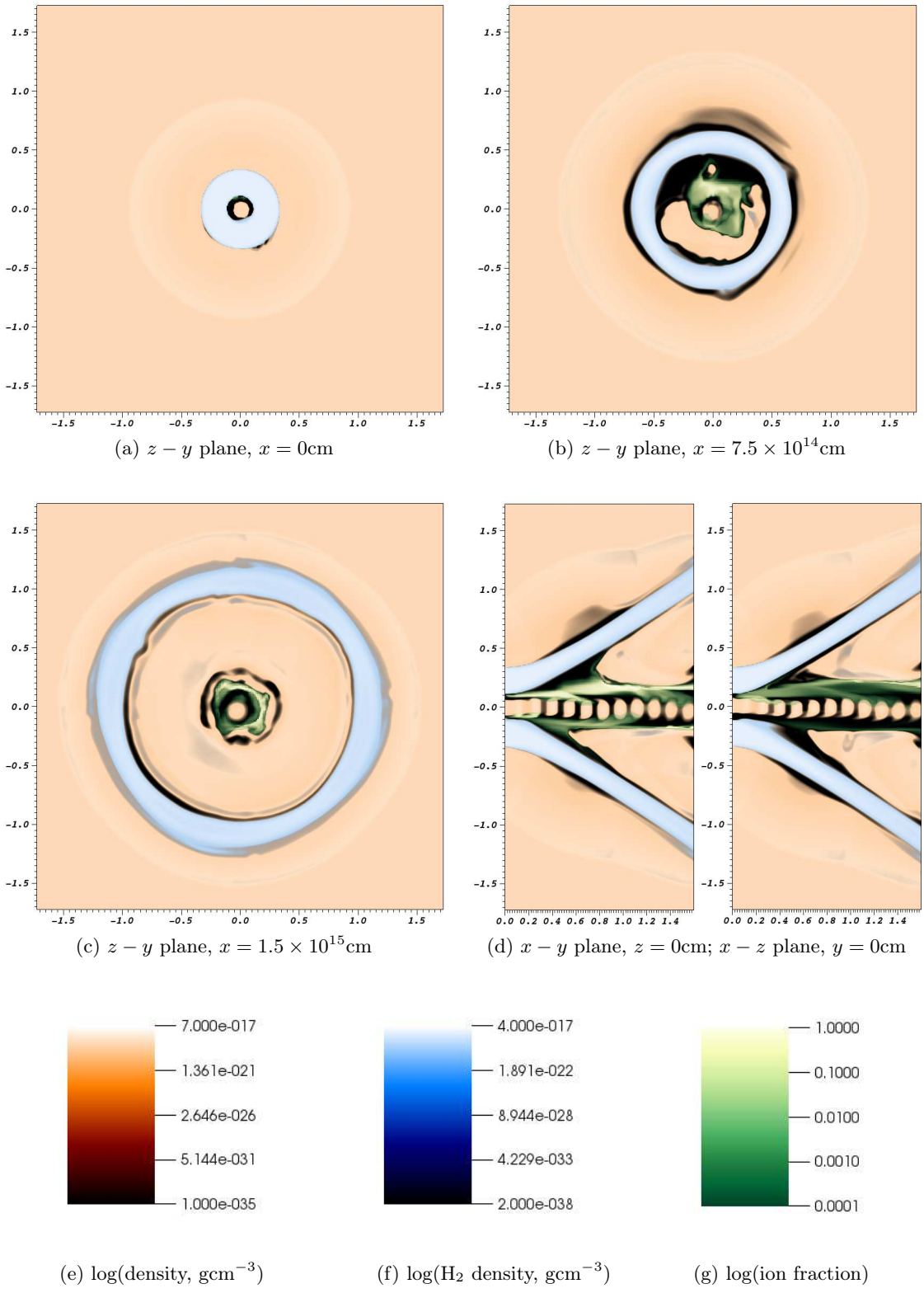

(a) $z-y$ plane, $x = 0$cm

(b) $z-y$ plane, $x = 7.5 \times 10^{14}$cm

(c) $z-y$ plane, $x = 1.5 \times 10^{15}$cm

(d) $x-y$ plane, $z = 0$cm; $x-z$ plane, $y = 0$cm

(e) log(density, gcm^{-3})

(f) log(H_2 density, gcm^{-3})

(g) log(ion fraction)

Figure 5.25: **Precessional Model PRE.2: 0.75AU binary, atomic-molecular outflow cross-sections at simulation time T=87.5 Years.** Axis scales are in units of 10^{15}cm. Ambient medium is atomic hydrogen with trace molecular hydrogen formed from cooling during the simulation. Underlying density plot is fully opaque. For clarity, H_2 and ionisation fraction overplots are at ramped opacity; 100% opacity at max value, transparent at minimum value.

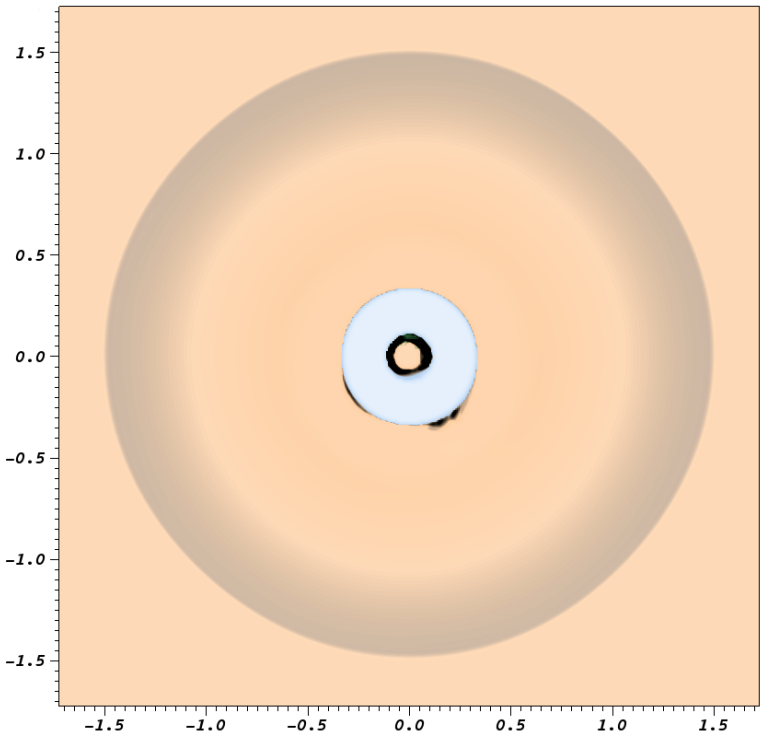

(a) density and composition; default material is HI

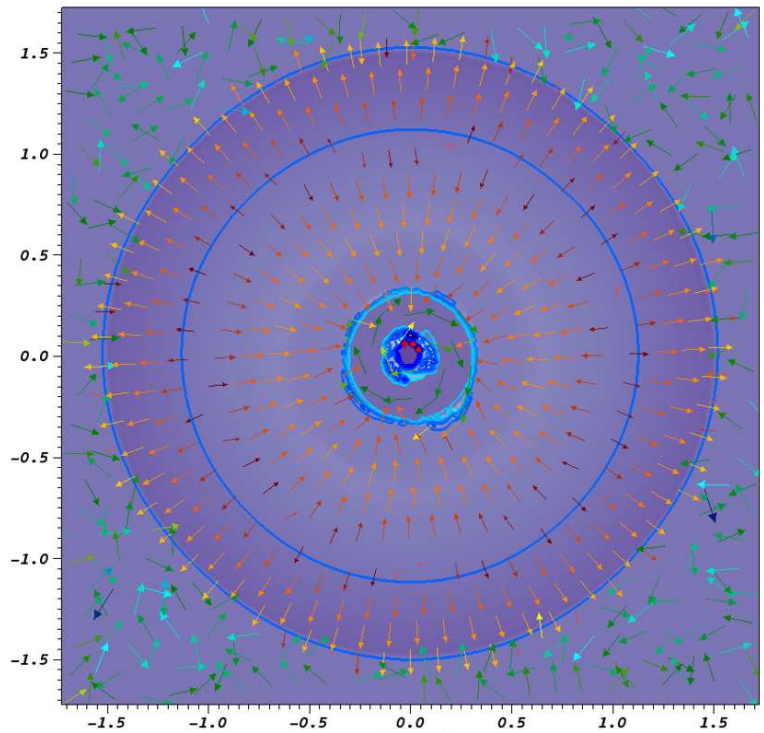

(b) pressure, temperature and velocity

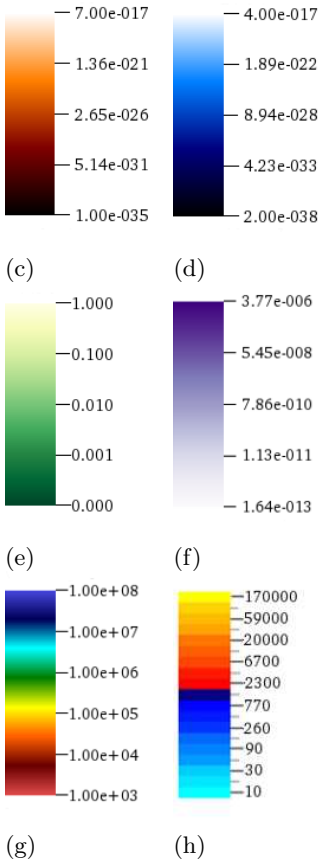

Colour scaling:
(c) density, g/cm^3
(d) H_2 density, g/cm^3
(e) ion mass fraction
(f) pressure, Ba
(g) velocity, cm/s (vector)
(h) temperature, K (contour)

(c), (d), (e) apply to subfigure (a); (f), (g), (h) apply to subfigure (b). All scales are to $\log_{10}$ including vector magnitude. Vector glyphs are 2D projections; the tail indicates the vector origin.

Figure 5.26: **Precessional Model PRE.2: 0.75AU Binary, atomic-molecular outflows into an atomic ambient medium; z-y plane cross-section shown at x=0cm and simulation time T=175 Years.** Axis scales are in units of 10^{15}cm. For clarity, the underlying density plot in subfigure (a) is fully opaque, whilst H_2 and ionisation overplots are at ramped opacity; 100% opacity at max value, transparent at minimum.

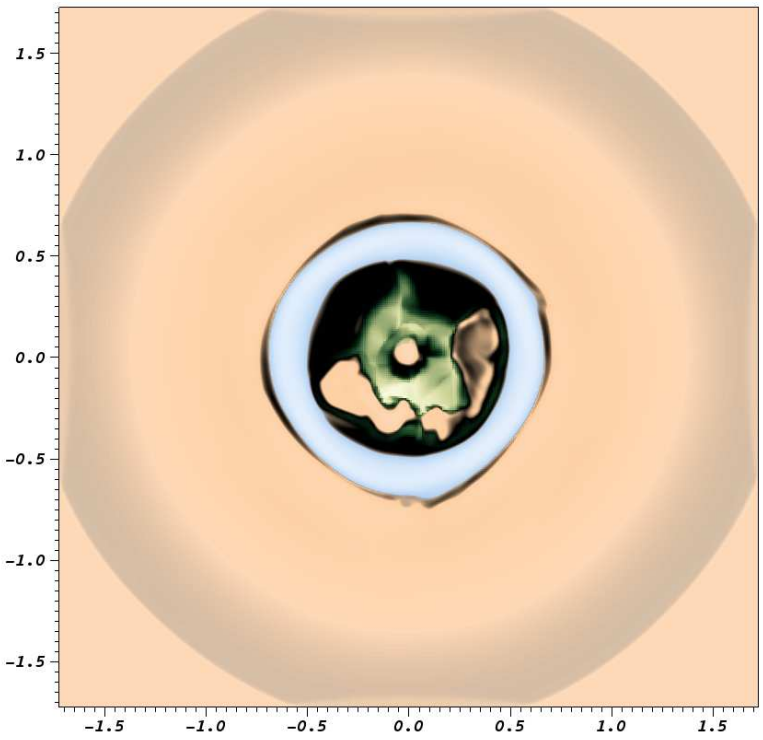

(a) density and composition; default material is HI

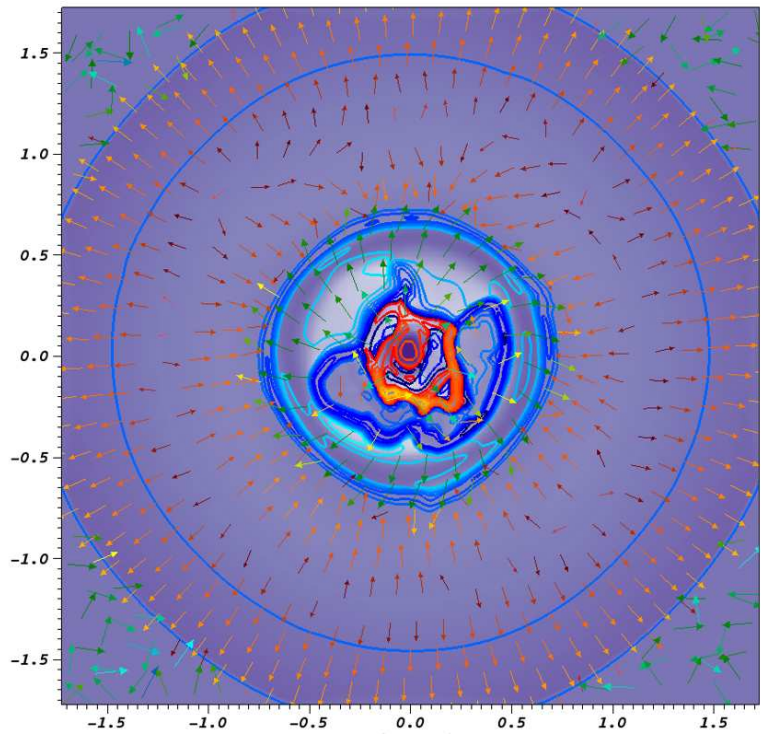

(b) pressure, temperature and velocity

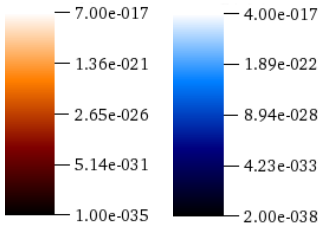

(c) (d)

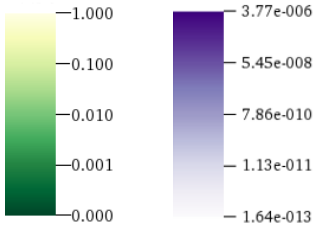

(e) (f)

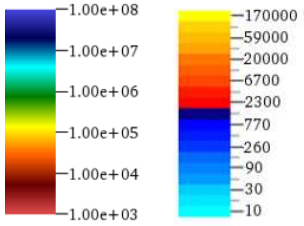

(g) (h)

Colour scaling:
(c) density, g/cm^3
(d) H_2 density, g/cm^3
(e) ion mass fraction
(f) pressure, Ba
(g) velocity, cm/s (vector)
(h) temperature, K (contour)

(c), (d), (e) apply to subfigure (a); (f), (g), (h) apply to subfigure (b). All scales are to $\log_{10}$ including vector magnitude. Vector glyphs are 2D projections; the tail indicates the vector origin.

Figure 5.27: **Precessional Model PRE.2: 0.75AU Binary, atomic-molecular outflows into an atomic ambient medium; z-y plane cross-section shown at x=7.5×10^{14}cm and simulation time T=175 Years.** Axis scales are in units of 10^{15}cm. For clarity, the underlying density plot in subfigure (a) is fully opaque, whilst H_2 and ionisation overplots are at ramped opacity; 100% opacity at max value, transparent at minimum.

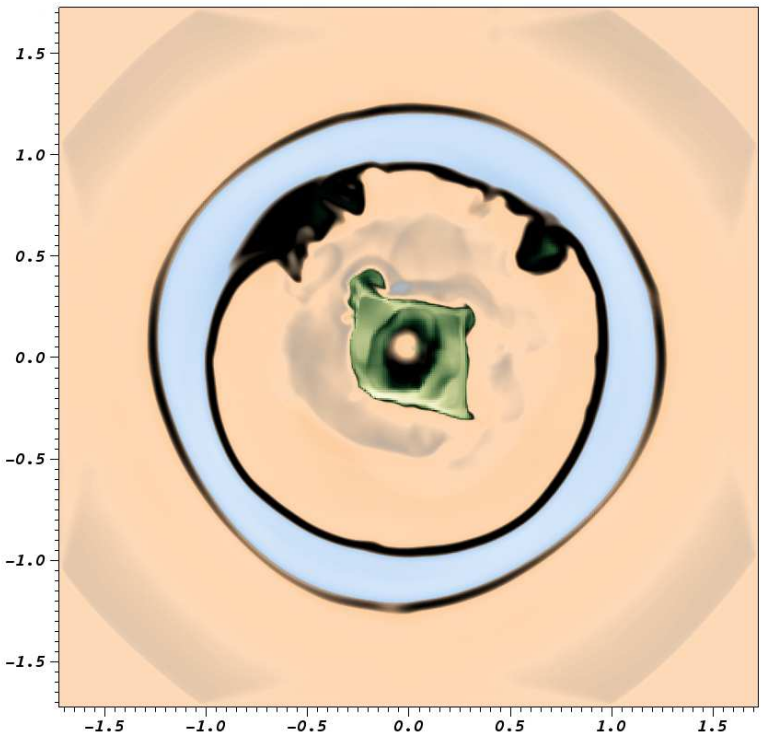

(a) density and composition; default material is HI

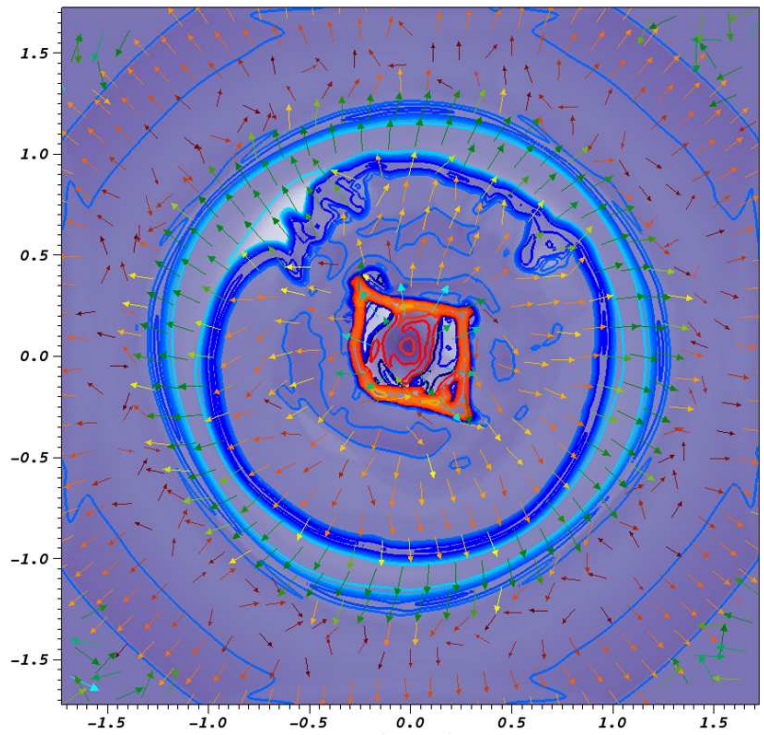

(b) pressure, temperature and velocity

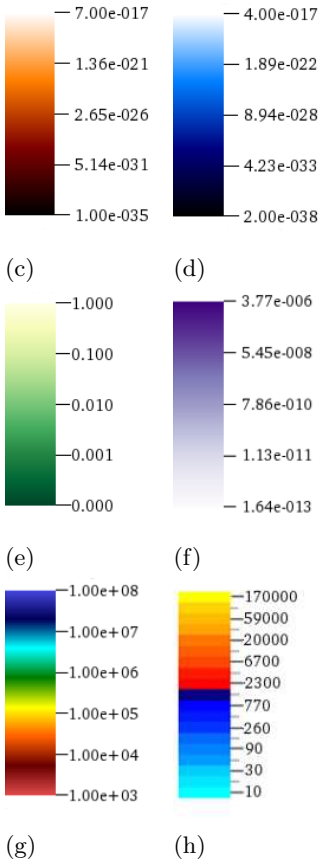

Colour scaling:
(c) density, g/cm^3
(d) H_2 density, g/cm^3
(e) ion mass fraction
(f) pressure, Ba
(g) velocity, cm/s (vector)
(h) temperature, K (contour)

(c), (d), (e) apply to subfigure (a); (f), (g), (h) apply to subfigure (b). All scales are to $\log_{10}$ including vector magnitude. Vector glyphs are 2D projections; the tail indicates the vector origin.

Figure 5.28: **Precessional Model PRE.2: 0.75AU Binary, atomic-molecular outflows into an atomic ambient medium; z-y plane cross-section shown at x=1.5×10^{15}cm and simulation time T=175 Years.** Axis scales are in units of 10^{15}cm. For clarity, the underlying density plot in subfigure (a) is fully opaque, whilst H_2 and ionisation overplots are at ramped opacity; 100% opacity at max value, transparent at minimum.

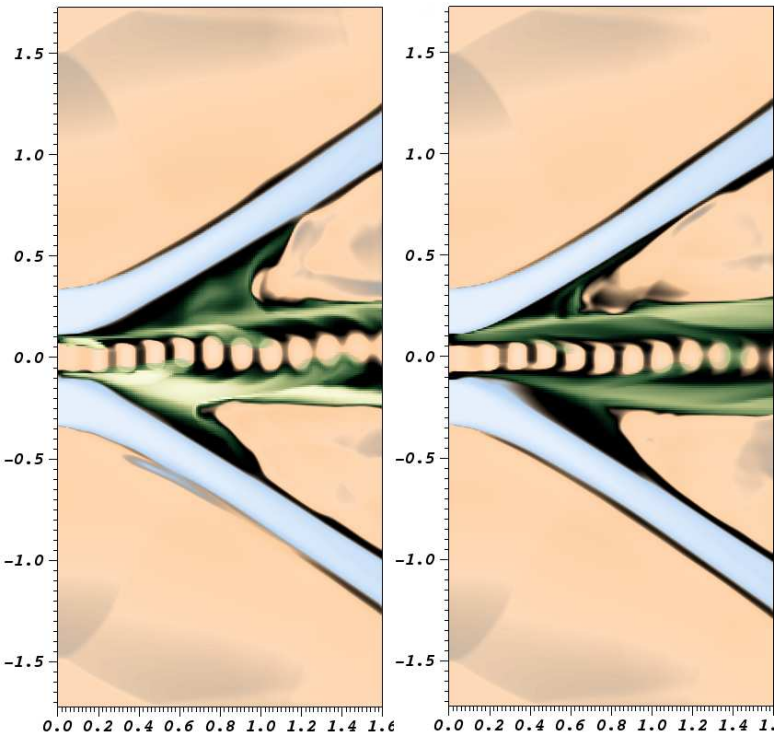

(a) density and composition; default material is HI

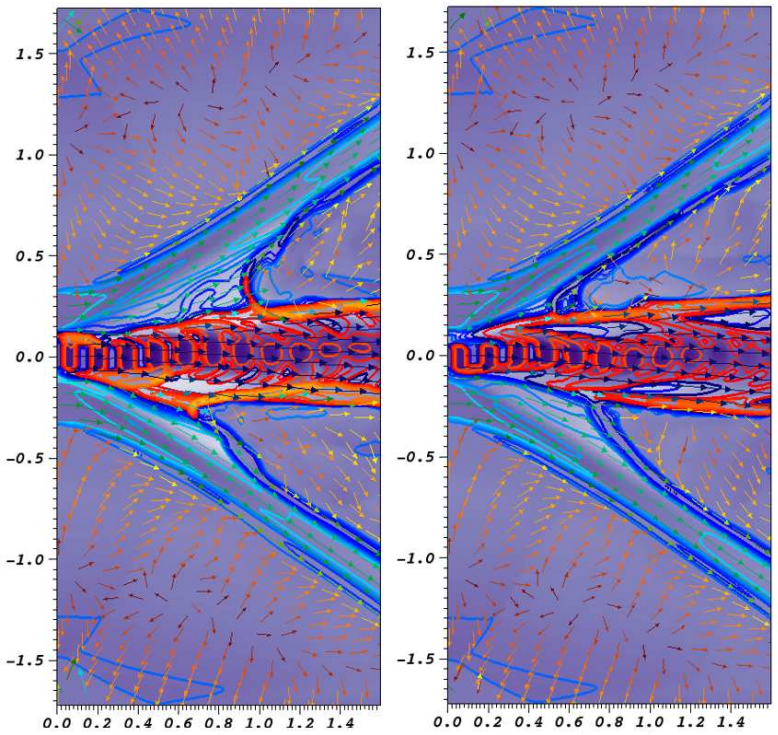

(b) pressure, temperature and velocity

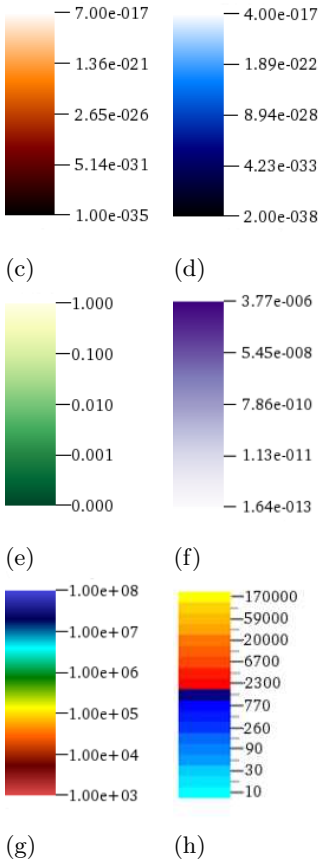

Colour scaling:
(c) density, g/cm^3
(d) H_2 density, g/cm^3
(e) ion mass fraction
(f) pressure, Ba
(g) velocity, cm/s (vector)
(h) temperature, K (contour)

(c), (d), (e) apply to subfigure (a); (f), (g), (h) apply to subfigure (b). All scales are to $\log_{10}$ including vector magnitude. Vector glyphs are 2D projections; the tail indicates the vector origin.

Figure 5.29: **Precessional Model PRE.2: 0.75AU Binary, atomic-molecular outflows into an atomic ambient medium; x-y (L) and x-z plane (R) cross-sections shown at z, y=0cm and simulation time T=175 Years.** Axis scales are in units of 10^{15}cm. For clarity, the underlying density plot in subfigure (a) is fully opaque, whilst H_2 and ionisation overplots are at ramped opacity; 100% opacity at max value, transparent at minimum.

5.4.3 Precessional Model PRE.2: Temperature and Ionisation

Figure 5.30 shows temperature profiles across the lateral span of the domain in the PRE.2 model at several distances along the barycentric (x) axis. Note the logarithmic temperature scale. The small outer 'shoulders' are the bow shock from the molecular outflow, propagating outwards at the medium sound speed. Deep 'Troughs' indicate the cold molecular material from the circumbinary disc. The central hot region shows the presence of the jet. Note that the region immediately surrounding the jet is hotter than the jet itself. The very high temperatures developed in the periphery of the jet increase with distance from the jet inlet boundary (see legend), while the temperature in the jet column is seen to be decreasing.

In order to understand the mode of ionisation that occurs in this model, it is instructive to examine the velocity behaviour of material in the jet as it orbits tightly about the barycentre. Figure 5.31 compares the centre-line velocity signal down the middle of the jet with the velocity variation on the jet periphery.

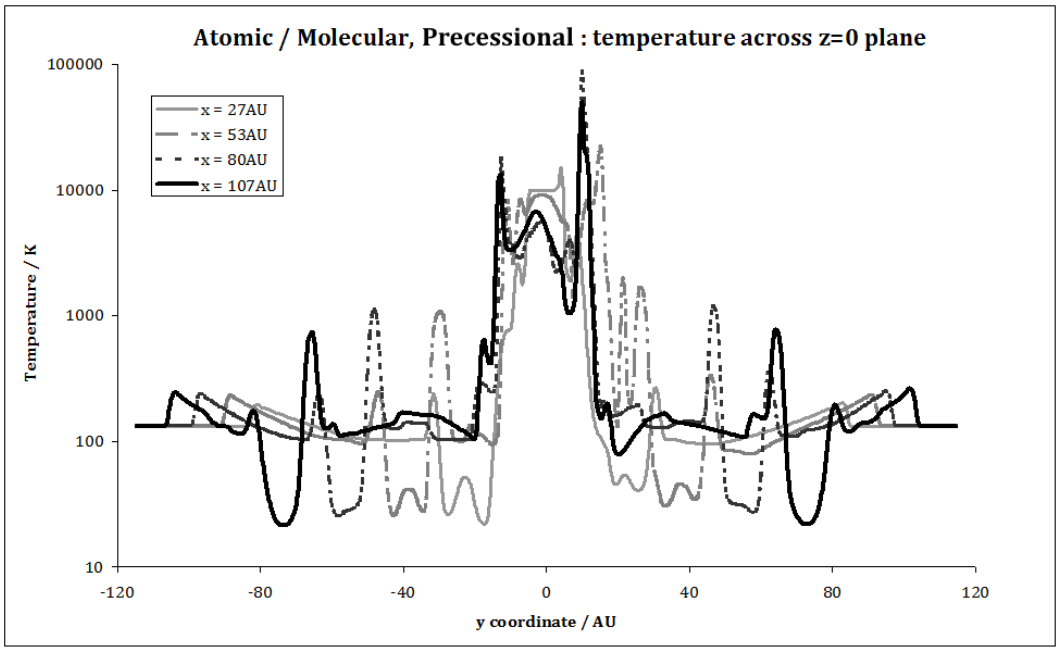

Figure 5.30: Temperature profiles for model PRE.2 across the z=0 central plane at selected distances from the inlet (x-axis values)

The velocity signal at the jet inlet is $2.717 \pm 0.543 \times 10^7$ cm/s varying sinusoidally. The centre-line velocity eventually settles at a mean value of $2.746 \pm 0.014 \times 10^7$ cm/s at the outgoing boundary; though there is some suggestion in the signal that the velocity amplitude might be re-intensifying in line with the findings of Smith et al. (1996)(105). It is evident that the velocity difference at the jet periphery is greater than within the jet column itself with an initial steep fall of 54% from the value at the inlet boundary over the first 6AU followed by a small recovery before another sharp fall to 73% below inlet value by 11AU.

This, then, explains how the cocoon of hot ionised material comes to envelop the jet columns of the Precessional Models (including PRE.1 which has no molecular component). As the centre of the 3.67AU radius jet inlet describes a 0.75AU orbit about the barycentre, the periphery of the jet is subject to a continual strong oblique shock, almost as abrupt as the main jet bow shock, in contact with the ambient medium that refocuses the jet inwards. The expansion of the hot gas drives a crossing shock inwards towards the jet centre. Furthermore this shock is a feature that winds around the jet column like a screw thread as the motion of the jet carries the disturbance downstream at the Mach speed of the flow (see Figs. 5.4.3 & 5.33).

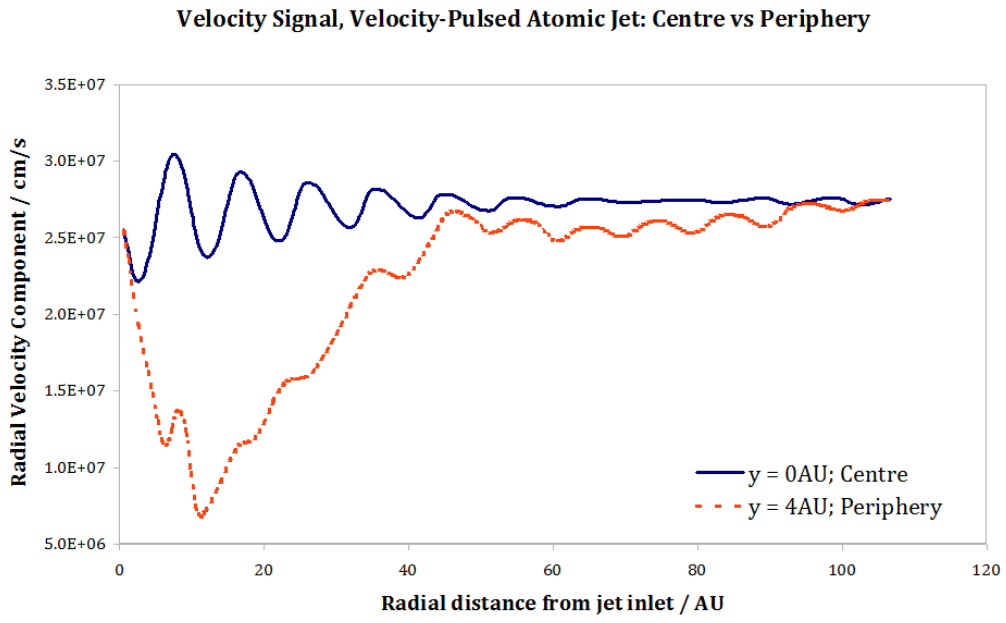

Figure 5.31: Centre-line vs. Peripheral velocity signal along the axis of the pulsed atomic jet in the dual atomic-molecular, Precessional model PRE.2. These can be seen to correspond to the emerging ionisation region in the bottom left corner of Fig.5.4.3

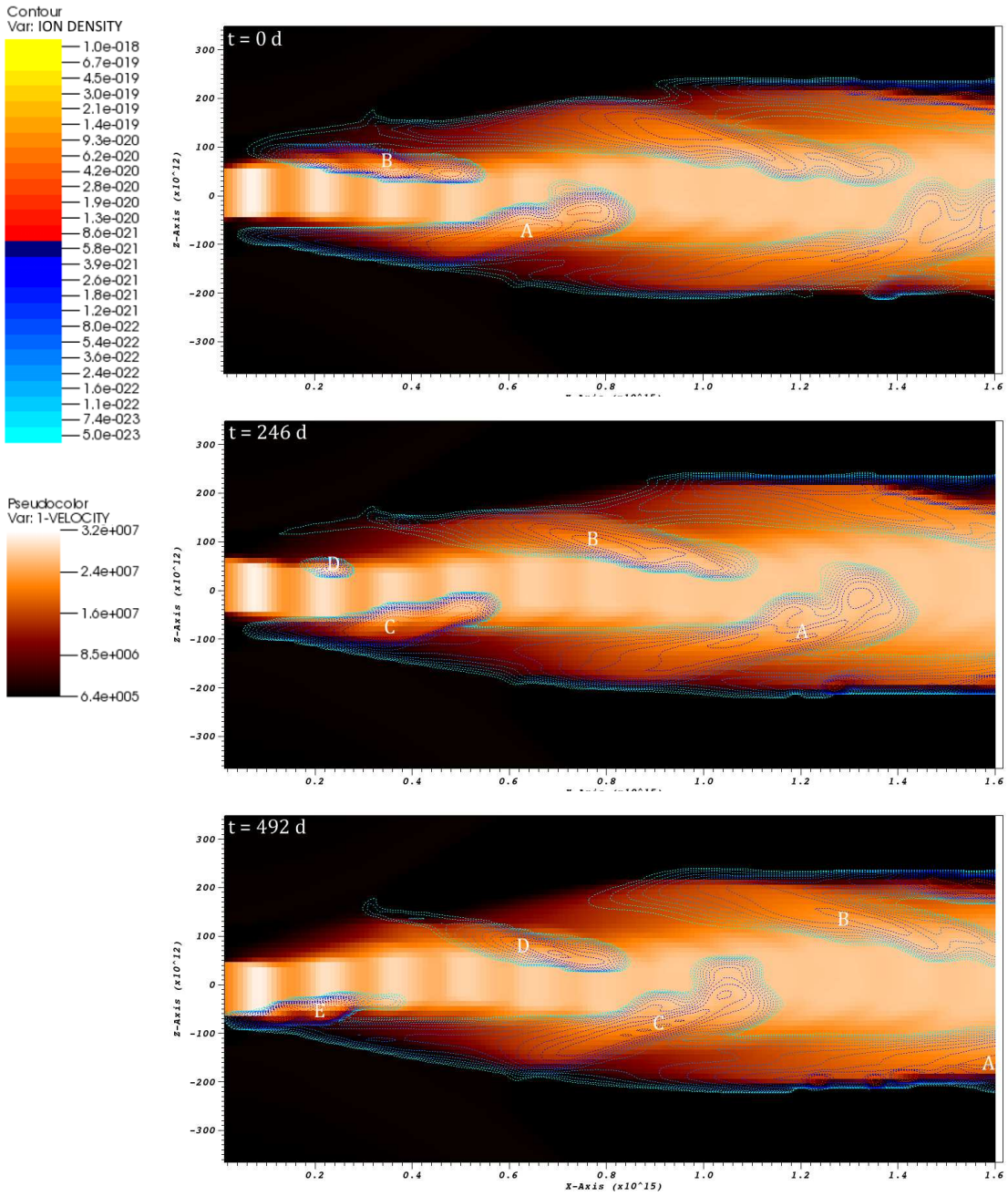

Figure 5.32: Formation and propagation of ionised regions on the periphery of the atomic jet in model PRE.2. Cross-sections at z = 0. Underlying colour plot is the V_x component (cm s^{-1}). Overlaid contours (g cm^{-3}) are partial density of ionised Hydrogen. Axes are cm scale. A, B, C, D are regions of strong ionisation; in fact cross-sections through a continuous shock that winds around the jet column.

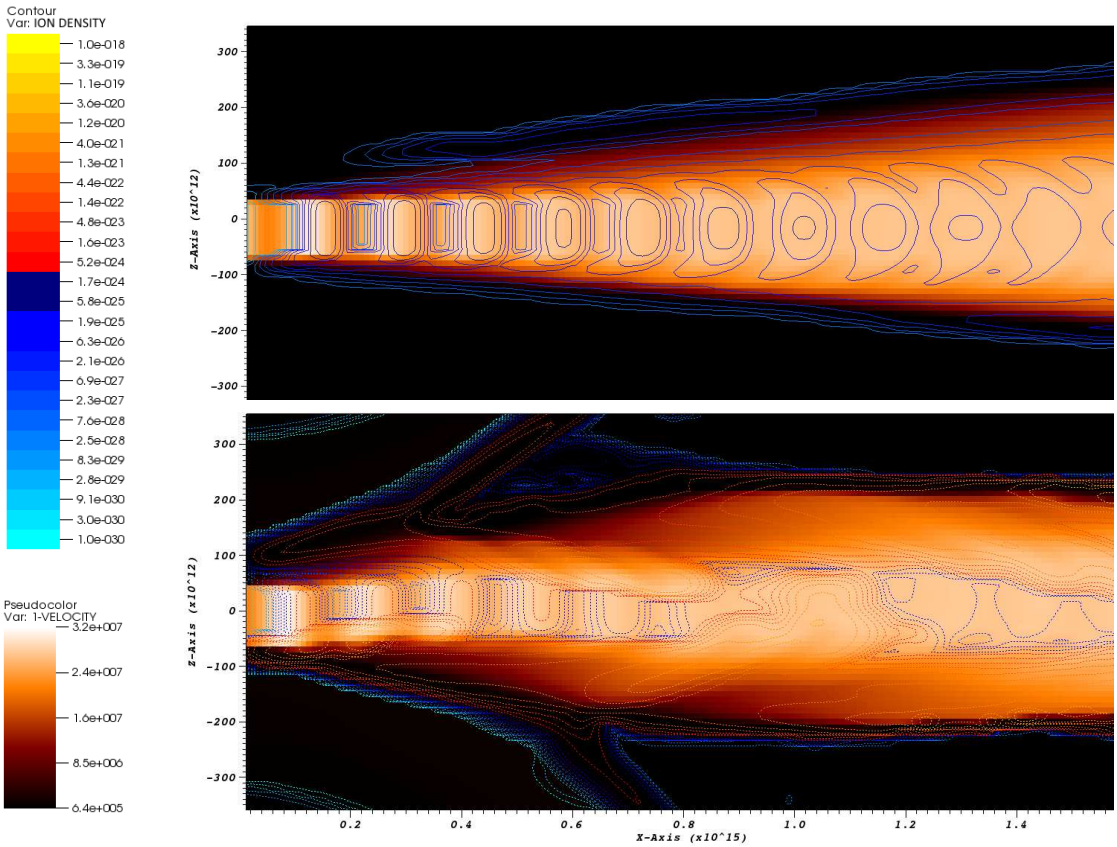

Figure 5.33: Comparison of ionisation modes in Orbital model ORB.1 (upper panel) vs. Precessional model PRE.2 (lower panel). Colour plot is the V_x component (cm s^{-1}); contours (g cm^{-3}) are partial density of ionised Hydrogen; axes are cm scale. In Fig.5.4.3, the contour scale excludes regions of low ionisation to highlight the peripheral screw-thread ionisation shock; here the range is expanded to include lower ion densities. The weakly ionised 'arms' branching off above and below the jet column in model PRE.2 are material entrained into the boundary layer of the slow-moving molecular flow.

5.4.4 Precessional Model PRE.2: Proper Motion

Because the data dump rate is less than half the crossing time for one whole wavelength at the maximum jet speed, it is possible to track proper motions of the knots of higher density material in the jet column. The propagation of the knots remains at a group velocity of $2.745 \pm 0.211 \times 10^7$ cm/s throughout the jet column out to 100AU. This is very close to the mean material centre-line phase velocity of 2.746×10^7 cm/s; however this phase velocity varies dramatically during the first 60AU of the jet column, with a differential amplitude of 9.95×10^6 cm/s across the first density knot despite the near-constant motion of the knots, suggesting that material is being processed through shocks within the jet column.

This feature was examined specifically for model PRE.2. However the density knots and their spacing exhibit no differences between all the models with the same velocity pulse characteristics.

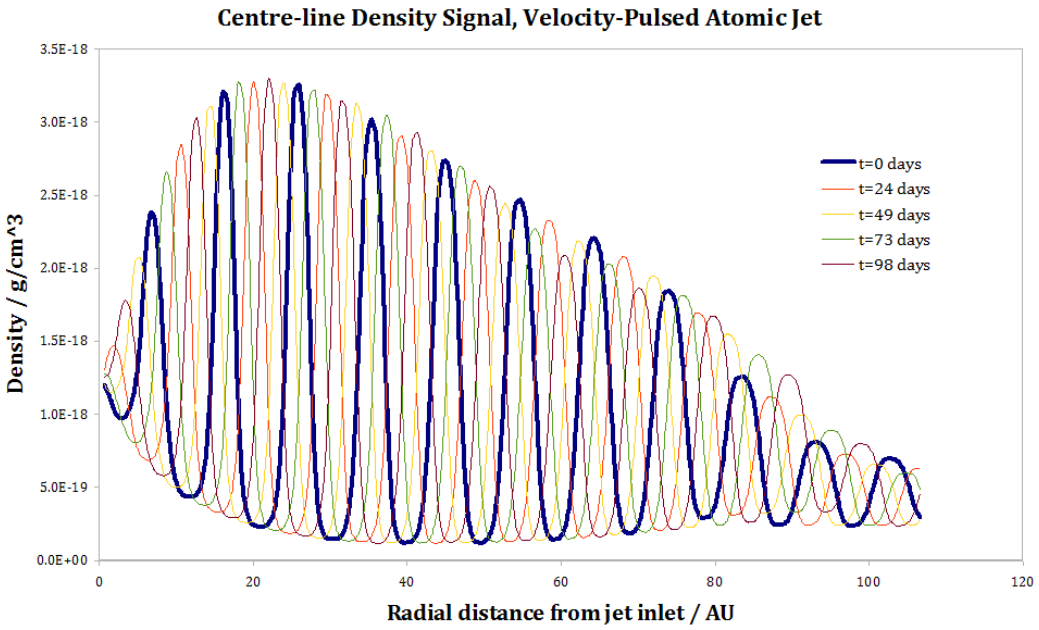

Figure 5.34: Centre-line density signal along the axis of the pulsed atomic jet in model PRE.2. An additional four time frames are included to show signal propagation.

5.4.5 Longitudinal Analysis of Precessional Models

The first thing to note is the similarity between the longitudinal profiles in most of the plots; this is in contrast to the Orbital models where the presence of the molecular wind altered the behaviour of the atomic jet in most plots.

In Figure 5.35 we see what is perhaps the most significant difference between the dual atomic/molecular outflow model and the atomic outflow in isolation; at x $\approx$ 55AU, in the presence of the surrounding molecular outflow, the jet column and hot cocoon recollimates, with the cross sectional area falling off and then stabilising.

At distance x $\lesssim$ 55AU, we see from figure 5.36 that the ionisation and temperature are lower in the dual outflow circumbinary model than in the single outflow model, but from 55AU onwards this trend reverses as the ionisation in PRE.2 dramatically rises.

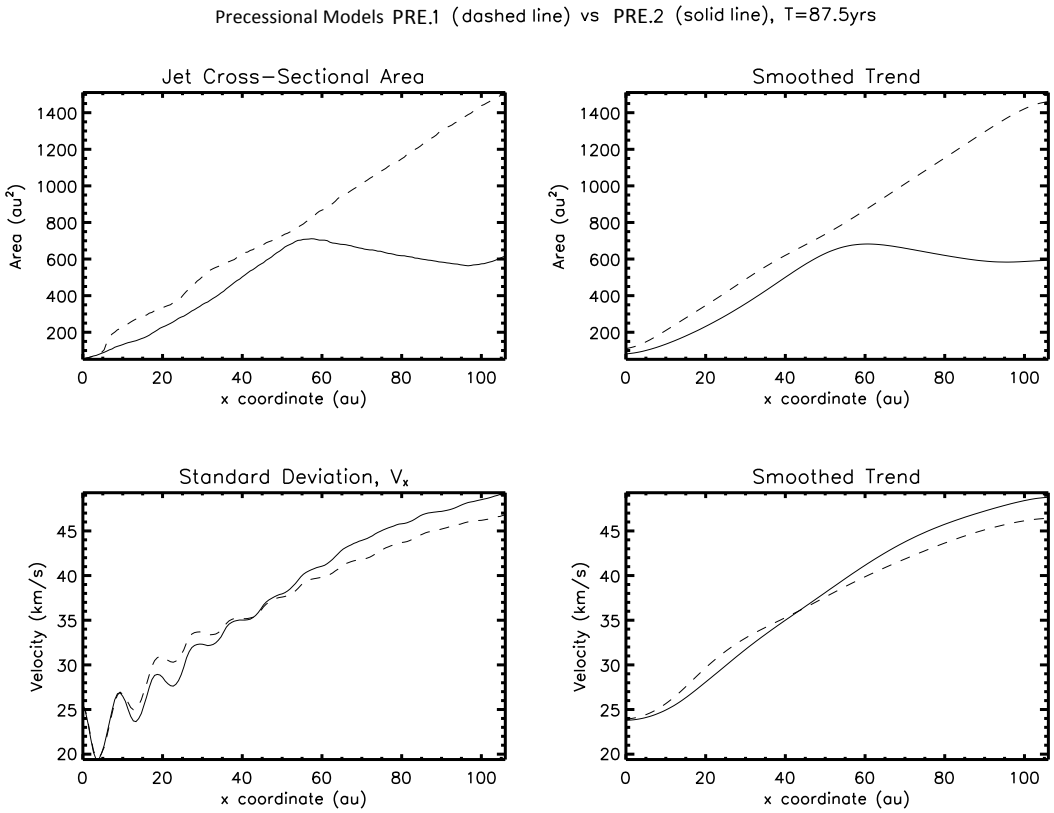

Figure 5.35: Precessional Models: atomic jet x-sectional area, velocity standard deviation, azimuth angle and radial distance along propagation axis, T=87.5 years. Model numbers: PRE.2 (with molecular outflow) and PRE.1 (without).

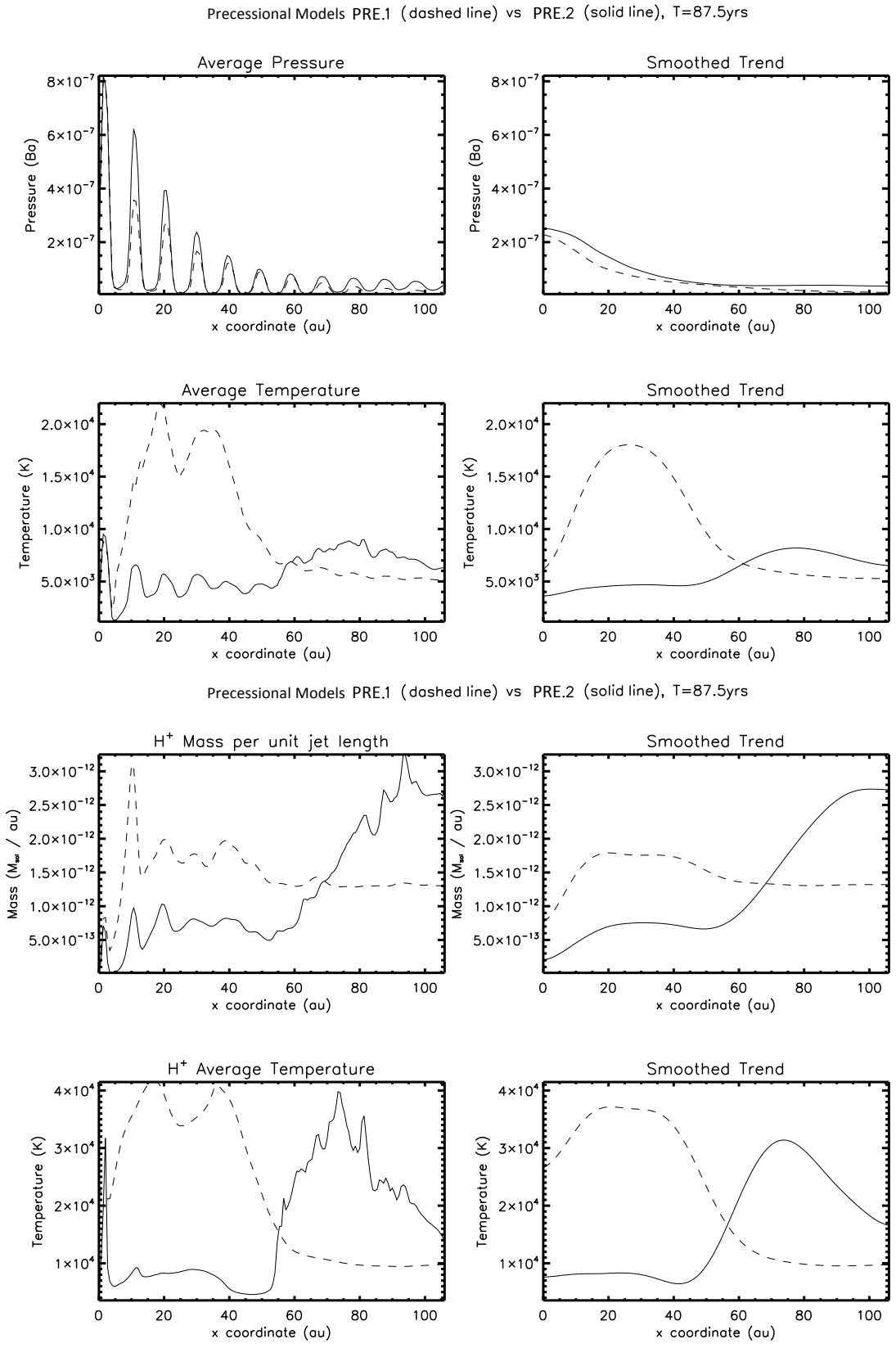

Figure 5.36: Precessional Models: atomic jet pressure, temperature, ionisation and ion temperature along propagation axis, T=87.5 years. Model numbers: PRE.2 (with molecular outflow) and PRE.1 (without).

Examining Figure 5.29, we note that at ≈ 55AU distance along the x-axis (8.25×10^{14} cm), the hot, partly ionised cocoon surrounding the jet column encounters a denser region of ambient medium that is enclosed by the conical molecular outflow. It is forced into a narrow channel which further heats and ionises the material, most probably by a combination of compressive heating and shock heating of jet matter that impacts against the 'funnel walls' of the region of denser material. Compare this with the atomic-only circumbinary model PRE.1 (see Fig.5.24), wherein the path for the forward flow of hot cocoon material has already been cleared.

We have shown here the longitudinal Precessional plots where the dual outflow model differs significantly from the atomic-only control. Full plots are at Appendix F.

5.5 Comparisons: Orbital vs. Precessional

5.5.1 Three-dimensional plots in two variables

Figures 5.37 and 5.38 that follow depict the four main models we have been discussing in 3 dimensions as wireframe plots. There are two variables plotted, density of molecular Hydrogen, and density fraction of ionised Hydrogen.

5.5.2 Single Variable Section plots

At Appendix E, Figures E.1 through E.2 are additional section plots provided for reference, showing all four models together on the same page. Each plot is a single scalar variable or vector component. This can sometimes be more useful for clarification of outflow behaviour than plots which try to depict multiple variable fields.

5.5.3 Longitudinal Comparisons

At Appendix F, Figures F.9 through F.12 show the longitudinal characteristics of the Precessional model vs. the Orbital model plotted on the same axes for comparison.

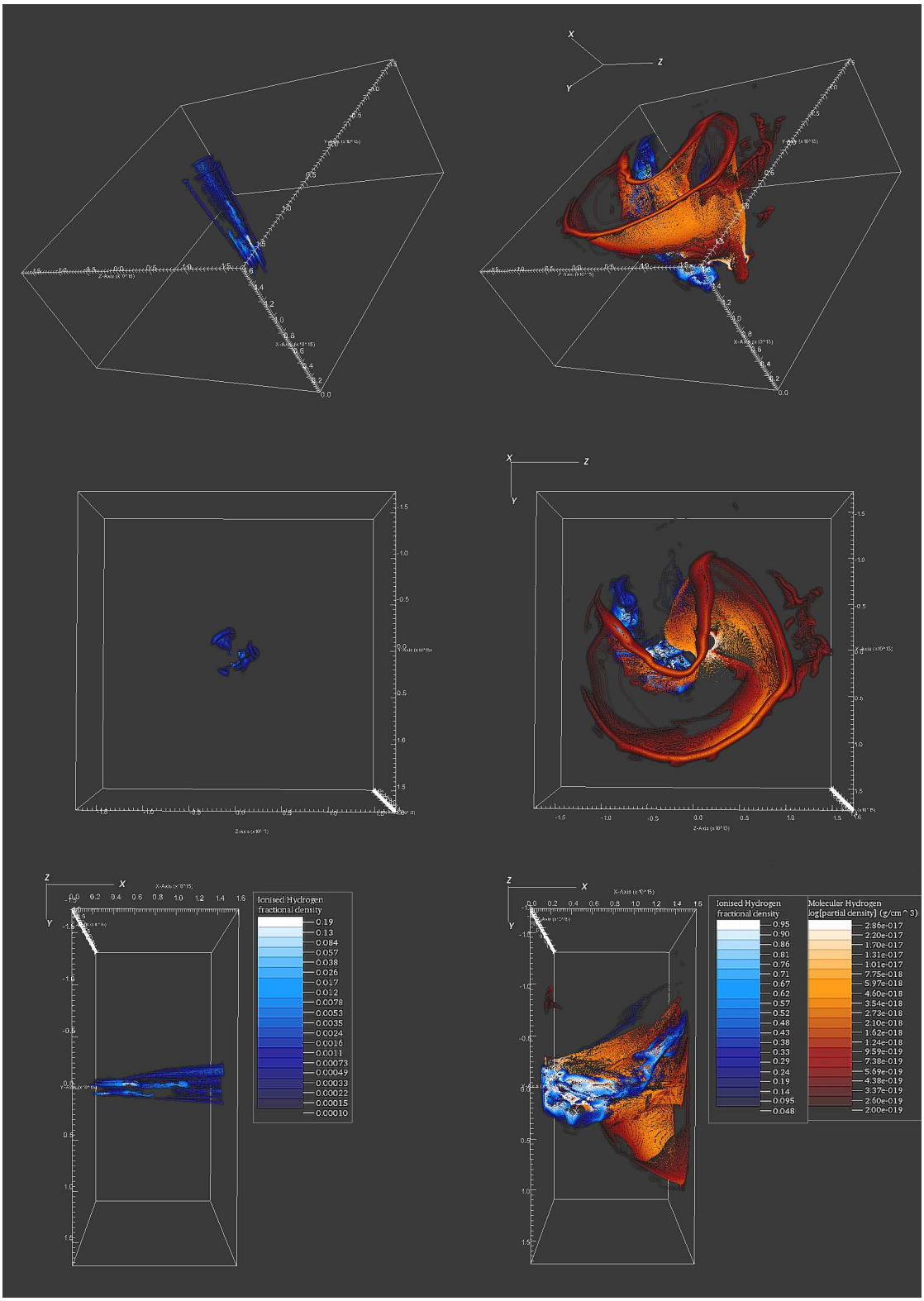

Figure 5.37: Orbital Models in 3 dimensions: 18AU Binary, Atomic-Only (left column) vs. Atomic-Molecular (right column) 3D projection wireframe plots seen from different aspect angles at simulation time T=87.5 Years. Blue represents ionised material, orange represents molecular material. Axis scales are in units of 10^{15}cm. Simulation Numbers ORB.1 (L), ORB.2 (R).

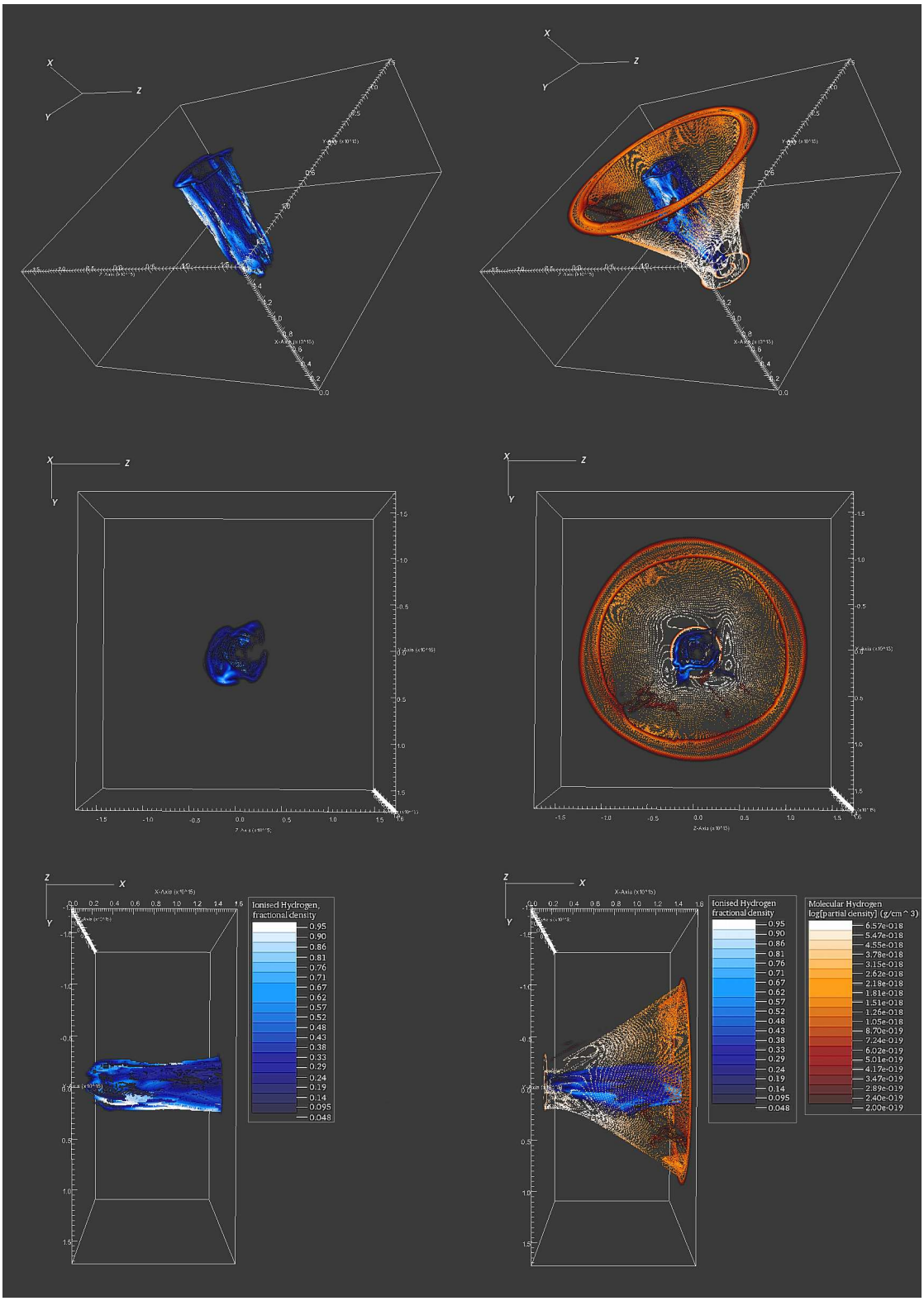

Figure 5.38: Precessional Models in 3 dimensions: 0.75AU Binary, Atomic-Only (left column) vs. Atomic-Molecular (right column), wireframe plots seen from different aspect angles at simulation time T=87.5 Years. Blue represents ionised material, orange represents molecular material. Axis scales are in units of 10^{15}cm. Simulation Numbers PRE.1 (L), PRE.2 (R).

5.5.4 Longitudinal Comparison: 20-Year Average

Four physical jet characteristics were chosen from the set to examine their stability over a period of time, with the aim of identifying reliable means by which the source of the molecular flow might be determined in an HH30-like system:

- Cross-Sectional Area
- Average Velocity
- Mass per Unit Length
- Average Temperature

NB only the models with the molecular wind were used in this analysis (PRE.2 & ORB.2). Averages were taken over a slice of monozonal thickness for each x-coordinate value, and the x-dependence was then smoothed over 2 jet radii as described in 5.3.4[1]. Fourteen equally spaced sample frames were selected over a simulation time period of 20 years. These were averaged and their standard deviations determined. Fitting of polynomial trendlines was employed to 6th order; some graphs could satisfy $R^2 > 0.95$ with lower order functions but 6th order was used throughout for consistency.

Figures 5.39 through 5.42 show the outcome of this analysis. The Precessional model shows the greatest stability in area, mass per unit length and average temperature; the Orbital model is slightly more stable in terms of average velocity. The Orbital model exhibits a large range of variability in cross-sectional area between 30-70AU distance from the jet source (our domain begins 10AU from source so this appears as 20-60AU on our graph). There is also a large variability in temperature between 30-90AU from source in the Orbital model with some extremely high temperatures appearing (but with 'quiescent' temperatures lower than the typical temperature of the Precessional model). We associate these ranges of highly variable behaviour with the 'flaring zone' of the Orbital model.

[1] this corresponds to a spatial resolution of $\sim$ 14AU which is the resolution limit of WFPC2 on the HST.

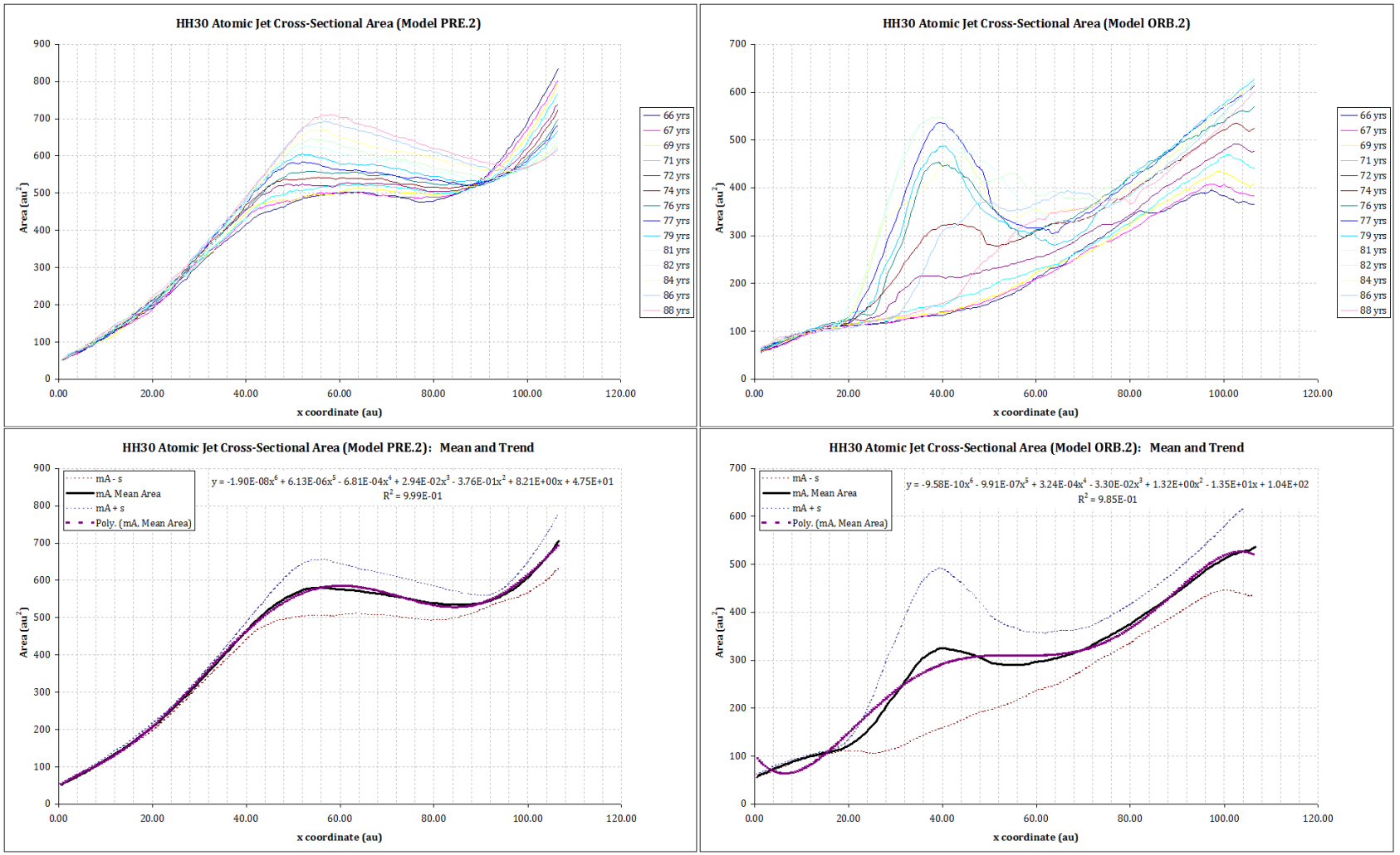

Figure 5.39: Precessional vs. Orbital: atomic jet x-sectional area, simulation time 66<T<88 years. Model numbers: PRE.2 (Precessional); ORB.2 (Orbital)

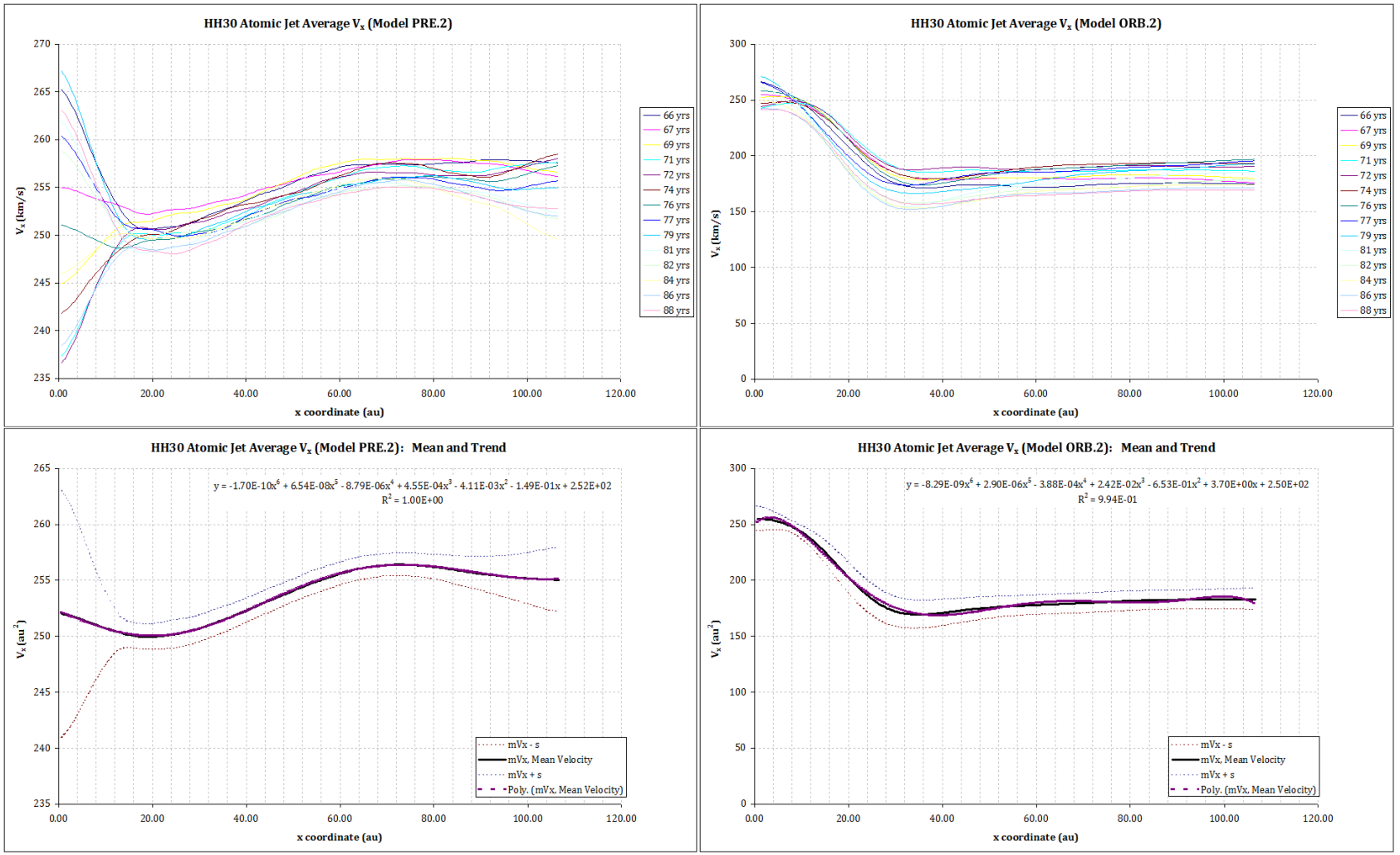

Figure 5.40: Precessional vs. Orbital: atomic jet average material velocity, simulation time 66<T<88 years. Model numbers: PRE.2 (Precessional); ORB.2 (Orbital)

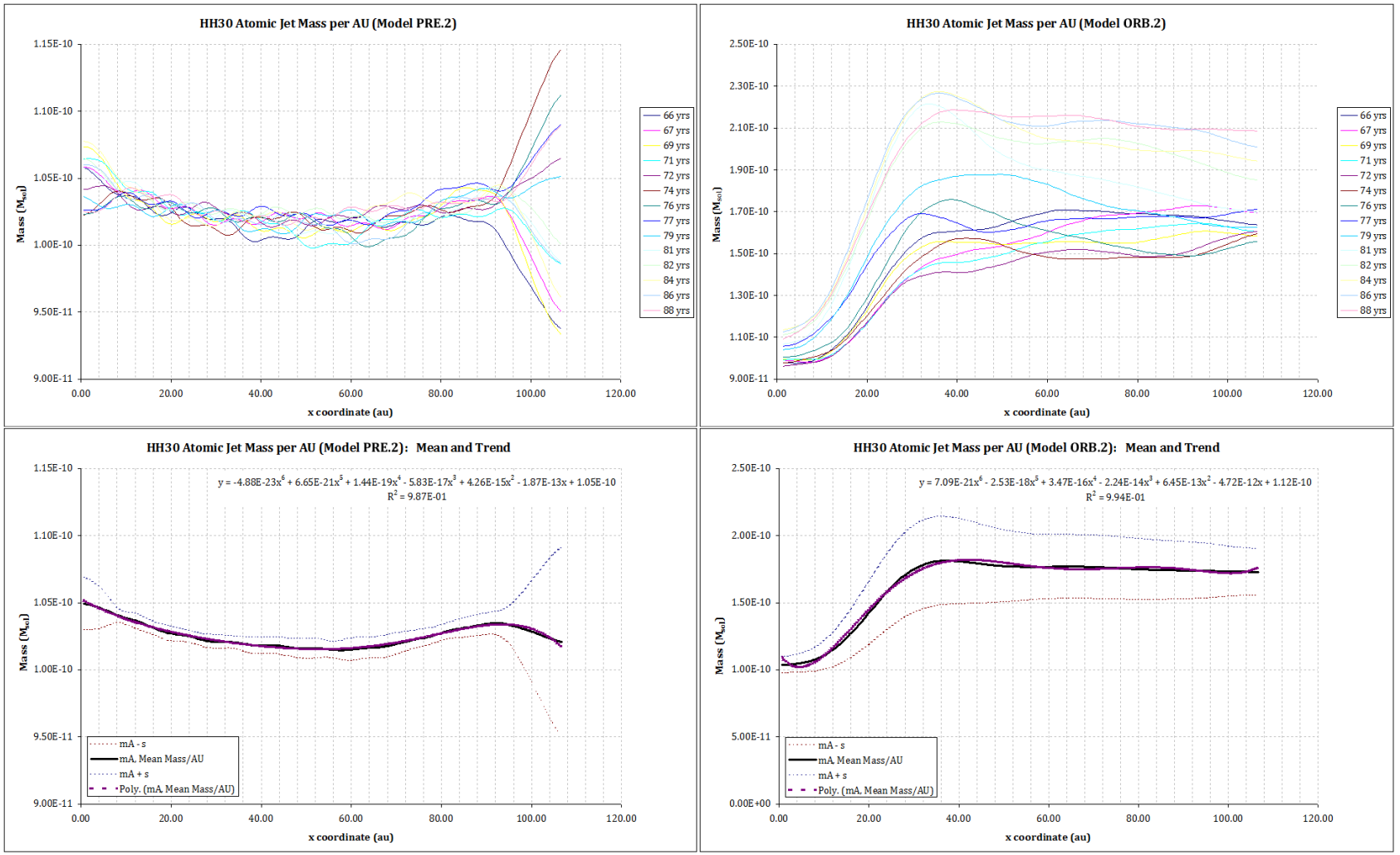

Figure 5.41: Precessional vs. Orbital: atomic jet mass per AU, simulation time 66<T<88 years. Model numbers: PRE.2 (Precessional); ORB.2 (Orbital)

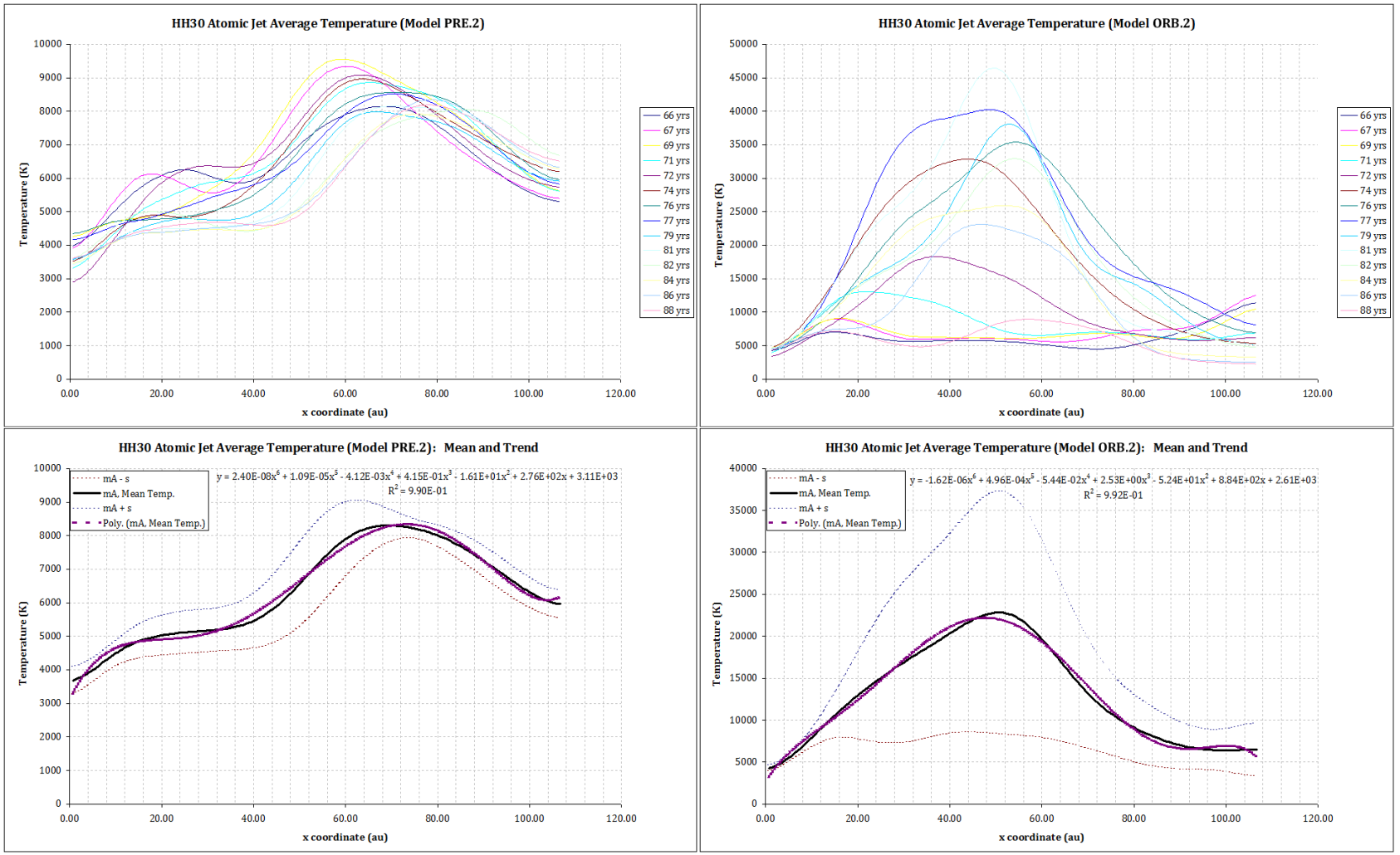

Figure 5.42: Precessional vs. Orbital: average temperature, simulation time 66<T<88 years. Model numbers: PRE.2 (Precessional); ORB.2 (Orbital)

5.5.5 Longitudinal Comparison: Regression Coefficients

The 6th order polynomial fits to our time-averaged longitudinal results are of interest from a theoretical perspective, but observational comparisons to these functions may prove difficult. Simpler 'broken' linear or quadratic functions may prove more useful comparators. By inspection, our graphs were divided into up to three regions of differing behaviour, and linear or quadratic regression performed for each region. Linearisation was preferred except in cases that yielded a very poor fit. Uncertainties are 1-σ and arise from time variability based on the assumption that the observer is unable to constrain the jet's evolutionary stage to within 20 years, and also assume our sampling represents a period of typical jet behaviour. Table 5.4 summarises these results for the Precessional (PRE.2) and Orbital (ORB.2) models.

Table 5.4: Simulated Atomic Jet Physical Quantities, Regression Coefficients

		Physical Quantity	Start (AU)	End (AU)	Coefficients x^2	Coefficients x	Coefficients x^0	Units
Precessional	Region 1	Area	10	50		10.51±0.43	14.81±0.69	AU^2
		Velocity						km s^{-1}
		Mass						$M_\odot$ / AU
		Temperature	10	78		64.53±12.54	3535±330.4	K
	Region 2	Area	50	102			550.39±56.24	AU^2
		Velocity	26	82		1.39E-01±2.15E-03	246.82±1.29	km s^{-1}
		Mass	18	102	1.31E-15±4.20E-17	-1.34E-13±7.96E-15	1.05E-10±3.70E-13	$M_\odot$ / AU
		Temperature	78	117		-71.39±2.81	13572.5±161.5	K
	Region 3	Area	102	117		11.22±4.59	-506.24±416.45	AU^2
		Velocity	82	117		-4.68E-02±5.65E-02	259.88±3.4	km s^{-1}
		Mass						$M_\odot$ / AU
		Temperature						K
Orbital	Region 1	Area	10	26	2.30E-02±6.20E-03	2.08±0.03	66.91±3.5	AU^2
		Velocity	10	42		-3.26±0.26	269.57±6.75	km s^{-1}
		Mass	10	46		2.70E-12±9.59E-13	8.96E-11±3.00E-12	$M_\odot$ / AU
		Temperature	10	60		401.99±333.19	4258.4±1340.3	K
	Region 2	Area	26	74		4.03±0.69	94.43±65.93	AU^2
		Velocity	42	117		1.93E-01±4.05E-02	165.11±12.25	km s^{-1}
		Mass	46	117		-1.05E-13±1.80E-13	1.84E-10±3.67E-11	$M_\odot$ / AU
		Temperature	60	117	7.54±6.66	-1517.45±1277.35	82596±63679	K
	Region 3	Area	74	117	2.30E-02±6.20E-03	2.08±0.03	66.91±3.5	AU^2
		Velocity						km s^{-1}
		Mass						$M_\odot$ / AU
		Temperature						K

5.6 Chapter Summary

1. The parameters of our actual working simulations have been presented (see Table 5.2). Parameters were informed by observations (see Table 3.1) although did not always follow exactly depending on consistency requirements imposed by the construction of the model and the physics involved. Four principal simulations were performed; two with a cold ($\leq$ 30K), dense ($\geq$ 10 $\times$ ambient) , slower-moving (12 km/s) molecular wind accompanying the atomic outflow in different configurations (Precessional vs. Orbital); two 'control' simulations with the atomic outflow only.

2. The hot ($>$ 1000K) atomic jet was 10 $\times$ overpressured with respect to ambient and modulated with a sinusoidal velocity pulse signal; the period was 5.26 $\times$ 10^6 s. The jet's minimum pulsed inlet velocity was 66% of its maximum velocity of 326 km/s. An atomic ambient medium was assumed for the T-Tauri close environment; medium gradients and other inhomogeneities were eschewed as the modelled outflows would be run for enough simulation time to 'nature' their own domains.

3. Our main working simulations necessarily covered a shorter span of jet propagation (107AU) than the early prototyping simulations discussed at the end of Chapter 4 due to the need to accommodate the wide-angle molecular flow within the limits of available computing resources, and the desire for better resolution. The main atomic jet bow shock departed the problem domain well before the simulation time window in which results were calculated as we wished to examine the jet's steady-state behaviour.

4. The Orbital simulations have been discussed, with section plots of physical variables to illustrate the dynamics. In the absence of the molecular flow, the primary mode of ionisation is atomic jet material processed through internal working surfaces within the pulsed jet column. When the co-orbital molecular flow is introduced the main source of ionisation is the shock boundary between the atomic and molecular outflows. The orbital dynamics of the two outflows produce some interesting structure in the surrounding medium, with low-density voids forming in the wake of the dense molecular outflow, which are then invaded and destroyed by the atomic outflow; this produces dramatic lateral flares of ionised material. Analysis of the jet's

longitudinal characteristics was performed. Various differences emerged between the perturbed and unperturbed atomic jet.

5. The Precessional simulations have been discussed. It was found that the general pattern of ionisation was broadly similar in both cases, with or without the attendant circumbinary molecular flow. Ionised material was predominant in the jet periphery, a feature that was missing in the larger orbit atomic jet model used as a control for the Orbital model. It was deduced that the small, fast orbiting jet of the Precessional model produced a continual large velocity shock.

6. Within the space interior to the conical circumbinary wind, a low-density region was found to have been evacuated near the cone apex. This shielded the atomic jet from interaction with the ambient medium; the ionisation and temperature were accordingly lower in the dual-outflow model in this region, than in the atomic-only control simulation.

7. The proper motion of the knots of higher density material in the atomic jet column was investigated. It was found that the group velocity of the knots, of $2.745 \pm 0.211 \times 10^7$ cm/s was close to the mean centre-line velocity: 2.746×10^7 cm/s.

8. Time-averaged discrete functions of the (barycentric, jet-parallel) x-coordinate were determined for jet cross-sectional area, average velocity, mass per unit length and temperature, averaging 14 curves over a 20 year period for each physical quantity. Lines of best fit were determined by 6th order polynomial fitting.

9. A simpler schema was devised for observational matching by breaking each curve into 2-3 regions of differing behaviour and linear or quadratic regression performed. Example: in the region $10 < \mathrm{x} < 60$ AU from the source object, the Precessional model has temperature dependence $T = (64.53 \pm 12.54)x + (3535 \pm 330)$ K. Whilst in the same region of the Orbital model, $T = (401.99 \pm 333.19)x + (4258.4 \pm 1340.3)$ K. Larger uncertainties in the Orbital model arise from the high degree of variability.

Chapter 6

Synthetic Observations of HH30

6.1 Background

6.1.1 Research Goals

In Chapter 5 we explored two alternative models for a dual-outflow system in HH30, the Orbital and Precessional models (as outlined in Fig. 5.1). Simulation outputs were examined in detail and the differences in the dynamics of the two models were discussed. In this chapter we will examine other ways in which we may discriminate between Orbital and Precessional dual atomic/molecular outflow systems using various kinds of synthetic observation.

We begin with a brief discussion of our MULTISYNTH synthetic observation code. We will then examine Mass-Velocity spectra of an HH30-like system viewed at different aspect angles. The M-V spectra of the four principal models viewed at shallow angle (1°) will then be examined; the shallow viewing angle being more realistic for comparison to HH30. Next we present synthetic position-velocity maps and accompanying line profiles in several emission lines, and discuss the connection between these and the m-v spectra. Following on from this, we will look at velocity channel maps for the H-α & ^{12}CO J=2-1 lines which reveal the predicted proper motions of emitting material by velocity regime. Finally we will look at spatially resolved synthetic observations of the Precessional and Orbital models.

6.2 MULTISYNTH - An IDL® Synthetic Image Code

6.2.1 MULTISYNTH Description

The MULTISYNTH program was written in IDL® 7.0 with the specific purpose of generating synthetic observations from our protostellar jet models. The code structure was made flexible such that it might be adapted for other astrophysical applications. The original basis of MULTISYNTH was an IDL® code (Moraghan A., Smith M.D.S.) for generating MPG movies from ZEUS output files, though much capability has been added since.

MULTISYNTH generates synthetic image flux files and accompanying position-velocity distribution files in HDF 4 format, which are used as input to further IDL® scripts producing particular outputs. One flux file and one p-v distribution file is generated for each of four emission lines, plus column density and p-v distribution files for the column densities binned by radial velocity with respect to the observer. A set of files can be generated for up to six aspect angles θ, where θ is the angle the model's principal (x) axis makes to the sky plane.

In addition, two modified versions of MULTISYNTH were developed, MSYNMVPOS & MSYNMVNEG, which bin mass per species by the logarithm of the velocity component in the observer's direction (red-shifted and blue-shifted material being binned into separate file outputs). The outputs from these are used to generate Mass-Velocity spectra. These and other functions of MULTISYNTH were performed as post-processing operations, since integrating them into the ZEUS-MP code was difficult because of the parallel architecture. Though this was disadvantageous in terms of speed, there was an advantage of modularity in being able to re-generate synthetic image data with different parameters or coefficients from the ZEUS-MP HDF output without having to re-run ZEUS-MP.

6.2.2 Further IDL® codes in the MULTISYNTH suite

Several other programs were written to post-process the outputs from MULTISYNTH.

- MSYNVCHAN, which generates 4-channel velocity maps of 3 emission lines for a selected time frame. Postscript output.
- MSYNMVPLOT, which generates a 4 by 2 set of Mass-Velocity spectrum plots from the HDF outputs of the MSYNMVXXX scripts. Postscript output.
- MSYNPOSVEL, which outputs position-velocity plots and line profiles for 4 emission lines, for a selected time frame. Postscript output.
- MSYNMOV, written to process up to 8 flux file sets of 4 emission lines into a single MPEG movie, also producing one JPEG snapshot per file set.
- MSYNSTATS, which calculates statistics from up to 8 flux file sets of 4 emission lines, e.g. total emission of each line within a selected region per time frame, and outputs these figures to a text file.

MULTISYNTH is described in more detail at Appendix G.

Table 6.1: Emission lines synthesised

Species	λ	Temperature (K)	Shock Velocity
H	656.28 nm		
[SII]	671.7 nm	~ 10000	> 50 km/s
[OI]	630.0 nm		
[FeII]	1.64 μm	$\sim 6000 - 8000$	30-50 km/s
^{12}CO	1.3 mm	~ 10	N/A

6.3 Mass-Velocity Spectra

6.3.1 Mass-Velocity Spectrum Concepts

Intensity-Velocity and inferred underlying Mass-Velocity spectra have often been used to characterise outflow behaviour in observational studies of molecular emission lines (Rodriguez et al. (1982)(92); Lada & Fich (1996)(59)). The mass-velocity relationship of a material flow field driven by a protostellar jet offers a means of characterising an otherwise complex hydrodynamic system. The m-v spectrum for all material in the region of interest may help to determine the transfer of momentum from the jet to the ambient medium and thereby constrain the parameters of an observed system that is poorly spatially resolved.

Stahler (1993)(108) notes that in m-v relations for a number of molecular outflows, the bulk of the mass is moving at relatively low speeds, and that at faster speeds the detected mass falls off according to a power law which is similar regardless of the total outflow mass. A first-order power law approximation to the m-v spectrum may be stated as:

$$\frac{dm(v_r)}{dv_r} \propto {v_r}^{-\gamma} \tag{6.1}$$

A global relation of this nature that is similar for observations of whole outflows spanning a variety of ages, lengths and degrees of collimation, also implies a similar local relation that holds true over every section of the outflow along the jet axis (Stahler, 1993)(108). The observed mass-velocity relations often exhibit broken power laws with a shallow gradient $\gamma = 1.0 - 2.0$ at velocities below some break-point ~ 10.0 km/s, and steeper gradients ~ 5.0 at higher velocities (Yu et al., 2000 (125) (126); Su et al., 2004 (113)); though this is not always the case (Yu, Billawa & Bally, 1999)(124).

Observations of high-mass YSO outflows have indicated that their m-v spectra possess a larger range of power law exponents than their low-mass counterparts, with $\gamma \sim 10.0$ in some cases. If corrected for optical depth, the true γ values would be larger (Ridge, Moore, 2001)(90).

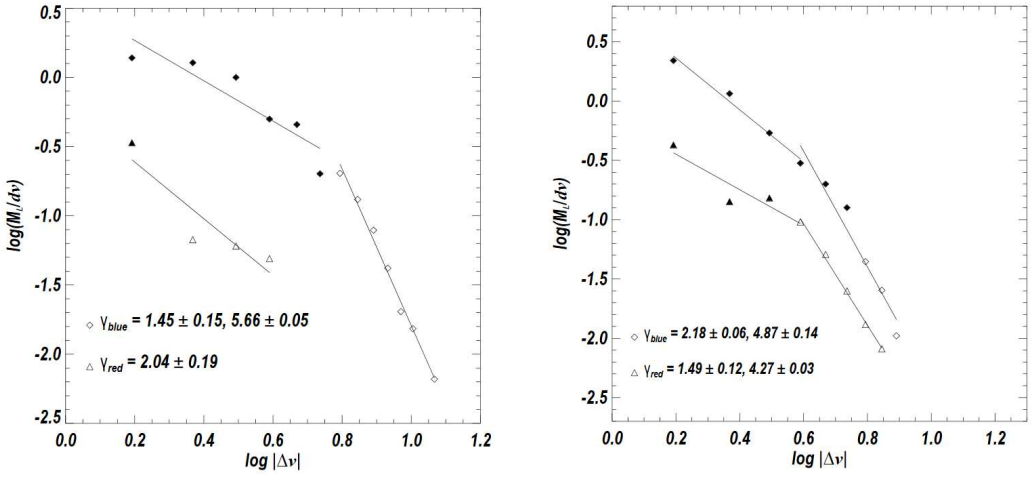

Figure 6.1: Luminous Mass vs Velocity for bipolar outflows YBD-4/5 in OMC-2/3, after subtraction of ambient cloud emission. The left panel shows the spectrum for the west lobe, right panel is the east lobe. Diamonds are points for blueshifted material, triangles are points for the redshifted material. Axis units are $M_\odot$ km^{-1} s (vertical) and km s^{-1} (horizontal). Solid points represent mass calculated directly from ^{13}CO emission ; hollow points represent mass M calculated from ^{12}CO emission with optical depth correction.[Figure reproduced from Yu, et al. 2000 (125)]

Analytical models have attempted to explain broken power laws in molecular mass-velocity relations. The thin-shell bow-shock model of Zhang & Zheng, (1997)(127) makes the common assumption of optically thin CO line emission and no velocity dependent emissivity factors, thus integrated column density and the observed integrated intensity are in direct proportion across the velocity range. In this model, at an inclination angle of 40° a 300 km/s jet exhibits a broken power law with γ=1.8 at velocities below 12 km/s, and γ=5.6 in the velocity range 12-50 km/s.

Numerical simulations of jet-driven outflows with shock dissociation and heating have been successful in reproducing power law mass-velocity relations with γ values broadly corresponding to molecular outflow observations (Smith et al, 1997)(104), lending support to the "prompt entrainment" model whereby momentum transfer to the ambient medium occurs in bow shocks near the jet head, and in the associated shock "wings". In the case of (104) the intensity-velocity relations for a 100 km/s jet outflow are found to possess $\gamma \approx 1.2 - 1.6$ up to $\sim$ 10 km/s after which the slope steepens. Gradients become shallower with an increased break velocity at steeper viewing angle in the expected fashion. Jet precession and pulsation are found to have little effect on the shape of the m-v spectra, a result confirmed by Downes & Ray (1999)(24) who also found that effi-

ciency of momentum transfer from the jet to the ambient medium decreases with higher jet/ambient density ratios due to a more streamlined bow shock that entrains less material. It is commonly found in numerical models that increasing simulated outflow age produces steeper γ values; as time elapses a larger proportion of material set in motion lies in the slower-moving bow shock wings, than in the shock head.

The nature and origin of the "break-point" in the intensity-velocity and mass-velocity relations has been questioned. As previously noted the break appears in many outflow observations, and both analytical and numerical models have predicted the steepening of the mass-velocity spectrum after a break-point due to dissociation of molecules near the head of the bow shock. But Downes, Cabrit (2003)(23) find that a no post-shock mixing numerical model produces an m-v relation with an unbroken $\gamma \approx 1.5$. The authors find instead that a break arises in the CO intensity-velocity spectra at $\approx$ 20-30 km/s, using a T^{-1} dependence in the CO line strength above the line excitation temperature due to partition between higher excited states. Their work also confirms steepening of γ with outflow age, converging on a value of 1.5 for the mass-velocity (using a 215 km/s jet and a 30° inclination angle) and a non-dependence on short-period outflow variability. Early on in the evolution of the numerical model, it is noted that simulated m-v spectra are flatter than observation, at low velocities. Long-duration simulations (2300 yr.) have demonstrated a gradually increasing power-law exponent, reaching a value $\gamma \approx 1.6$ after 1500 yrs and remaining constant thereafter (Keegan, Downes, 2005)(55).

Comparisons of mass spectra for simulated outflows driven by atomic and molecular jets at various velocities indicate little difference between the spectra at high velocities, but at low ($<$ 100 km/s) velocities, atomic mass spectra produce larger γ values. Because atomic emission lines are only excited within narrow physical parameters it is difficult to observe atomic mass spectra directly; but mass-velocity plots for the molecular material set in motion by atomic jets penetrating into a molecular medium may be fruitfully compared to observation (Moraghan et al, 2006)(69).

6.3.2 Dual-Jet Mass-Velocity Spectra

The mass spectra we present here differ in a number of respects from earlier work. The principal difference is the two disparate outflows; fast atomic vs. slow molecular. These penetrated into an atomic medium. The main purpose in studying these spectra was to differentiate between two very different scenarios for HH30, or an HH30-like outflow system.

There are some important caveats to the use of mass-velocity spectra in the context of our models. The region we are modelling is quite close to the base of the outflow and our model presents a two-dimensional span of only 106.7AU x 230AU. At 140pc distance this is only 0.76" $\times$ 1.64" in the sky plane. Compare this with the overall size of the molecular outflow in HH30 imaged by Pety J., et al., (2006)(81), which is approximately 2" $\times$ 1.5".

Mass-Velocity relations have generally been used to characterise larger-scale outflows. The self-similarity over larger scales of the m-v spectra we determined from our models is by no means assured; in fact, it seems possible that distinguishing features of the spectra for the Precessional and Orbital models may be eliminated if subsumed into a substantially larger outflow. This could hamper their use as a diagnostic for the nature of more distant objects, as the spatial resolution could be larger than the entire model span and thus include material beyond the model's spatial limits. However as previously noted, observations of outflows of varying dimensions, velocity and total outflow mass show a good deal of similarity in their mass-velocity relations, and it may be the case that some local behaviours found in these small-domain simulations may also be applicable to the larger-scale outflow provided that the leading bow shock is excluded from the analysis.

HH30 is a somewhat special case, its optical jet being aligned nearly parallel with the sky plane. However, we should not assume that HH30 is the only T-Tauri star that has both an optically visible, atomic jet with a molecular companion outflow. For increased utility, therefore, synthetic M-V spectra were generated for several angles pointing outwards from the sky plane: 15°, 30°, 45° & 60°. The decision was made to limit the inclination angle to 60° as greater inclinations imply a more constrained region of sky along the x-axis,

making comparisons between observation and our short-span models increasingly difficult due to spatial resolution limits; also, in order to make comparisons at angles where the outflow is directed towards the observer, the leading bow shock and working surface should be included; but this feature was absent in our models.

We adopted a convention similar to that of Moraghan et al., (2006)(69), but specified different velocity ranges for the determination of our power laws. This is because all of our simulation runs used a fast atomic jet with a mean velocity of ≈ 275 km/s and peak velocity of 326 km/s, requiring a broader velocity range; the pulsed nature of the fast jet also meant we had an interest in capturing more detail in the upper velocity region of the graph. The chosen velocity ranges were:

- 1-2 km/s
- 2-10 km/s
- 10-50 km/s
- 50-250km/s

The mass m here is the total mass as a function of velocity, and may be determined numerically from a model output frame by integrating the mass elements over the space dimensions and binning them according to velocity v_r. This radial velocity is the component of velocity in the direction away from the observer. The exponent γ is the negative gradient of the spectrum when a log-log plot of $dm(v_r)/dv_r$ is plotted against v_r.

M-V spectra were produced for Total Mass, Molecular Mass, and Atomic Mass, and γ values calculated for the four velocity ranges by fitting a straight line to the data in each range and determining the gradient. M-V spectra for the ionised Hydrogen component were also produced; γ values were not computed for these plots as this type of analysis did not appear to be meaningful, although the spectra themselves held some interest. Spectra were generated for blueshifted and redshifted material and plotted on the same axes with the redshifted component depicted by a dotted line. Values of γ are only calculated for the blueshifted component.

6.3.3 Four-Angle Mass-Velocity Spectrum Plots

Figures are 8 × M-V spectra per page, Precessional vs. Orbital at 4 angles:

- All Species Spectrum: Atomic Jet 6.2, Atomic & Molecular 6.3
- H Spectrum: Atomic Jet 6.5, Atomic & Molecular 6.6
- H_2 Spectrum: Atomic & Molecular 6.9
- H^+ Spectrum: Atomic & Molecular J

Due to the combined atomic-molecular flow at disparate velocities, a negative γ sometimes occurs; particularly near the upper end of the velocity scale when the plot swings upwards to a hook-like feature. This resembles the m-v spectra in Moraghan et al., (2006)(69) where a spike often appears at the upper end of the velocity range denoting the jet velocity; because our jet is pulsed, the upswing to a peak is a more graceful affair. Data points beyond the final velocity peak were not included in γ determinations.

Mass-Velocity γ values are by convention classed as:

- shallow ($\gamma < 2$)
- intermediate ($2 < \gamma < 4$)
- steep ($4 < \gamma$)

For our purposes we add a fourth classification:

- inverted ($\gamma < 0$)

Fig. 6.2 is nearly identical to Fig. 6.5; both being, essentially, atomic jets into an atomic medium, with the former only differing from the latter by virtue of small traces of H_2 and H^+. In all the spectra for simulations that included a molecular outflow, there is a 'break point' at around 10 km/s or soon after on the log(velocity) scale, at which the gradient changes, usually becoming steeper in the 3rd velocity range particularly in the All-Species and H_2 spectra, but also evident in the atomic Hydrogen plots. This break point increases with increasing angle, but only very gradually. Here we associate this point with the velocity of the material in the molecular flow. It appears in both Precessional and Orbital scenarios for the atomic H m-v spectrum, thereby suggesting a possible means of detecting a companion molecular flow when direct detection by emission lines is poor, or the proximity of a molecular flow to an atomic jet is uncertain.

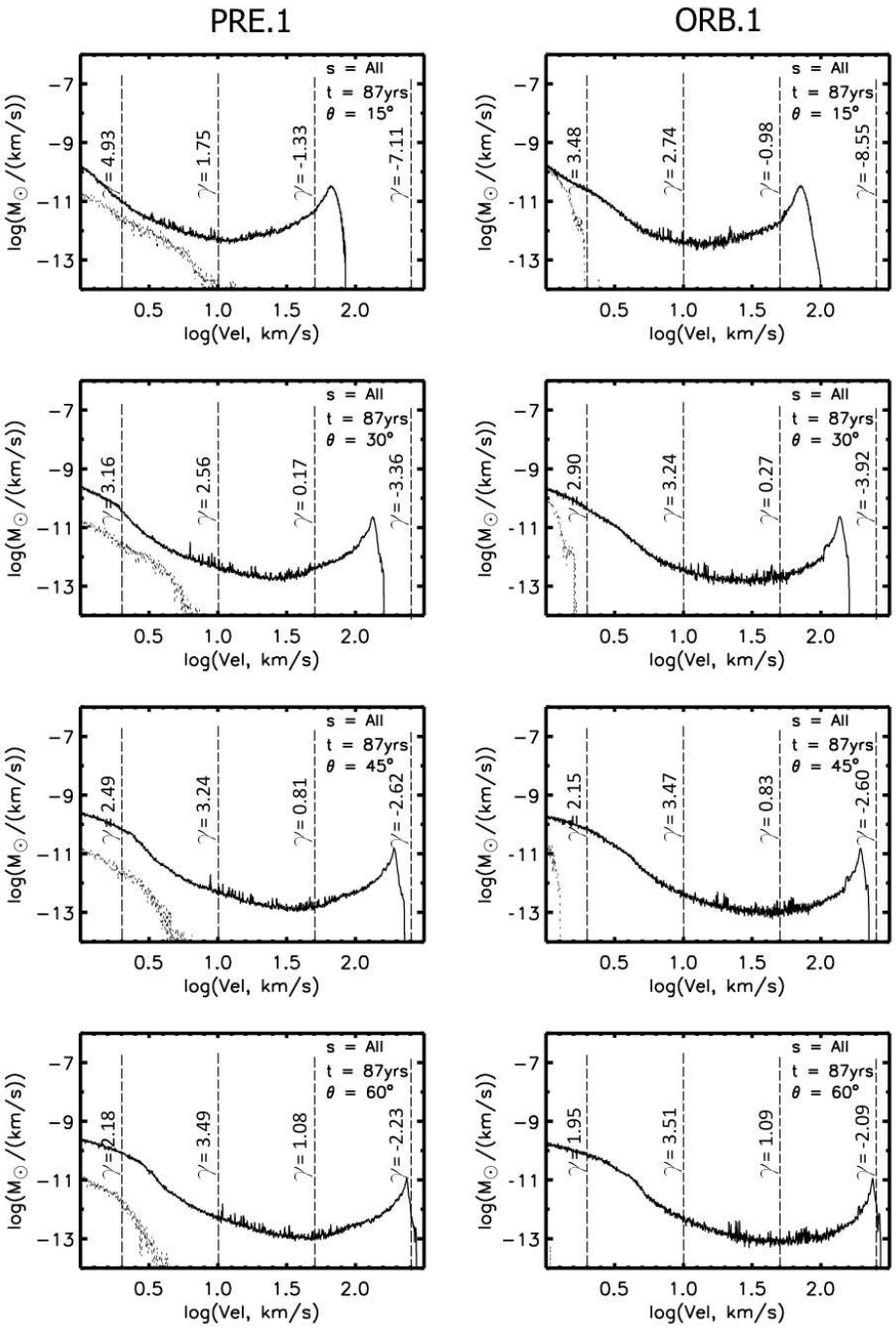

Figure 6.2: All-Species Mass-Velocity Spectra: atomic-only outflow scenarios, 4 aspect angles, simulation time T=87.5 years. Model numbers: Precessional, PRE.1; Orbital, ORB.1

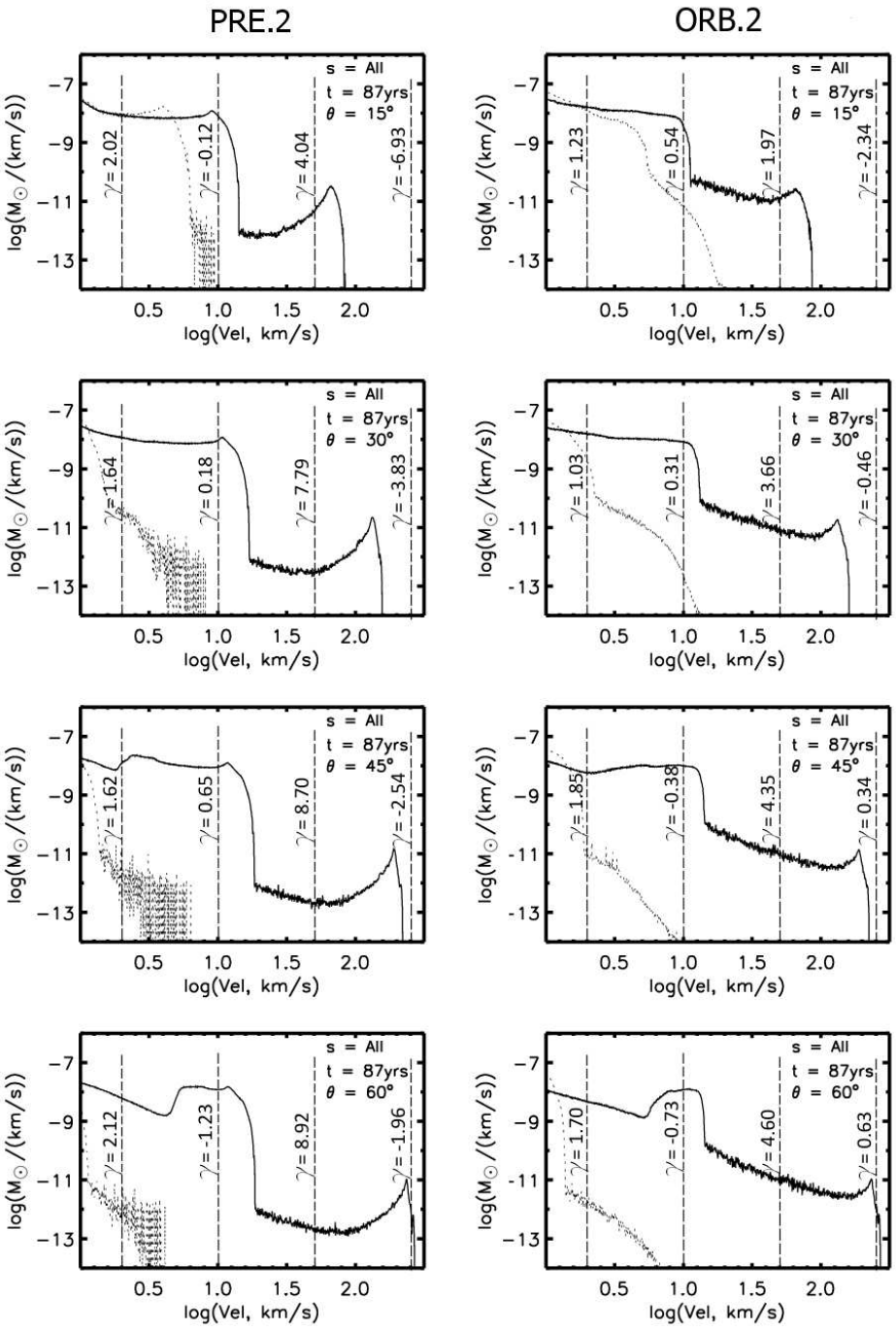

Figure 6.3: All-Species Mass-Velocity Spectra: dual atomic-molecular outflow scenarios, 4 aspect angles, simulation time T=87.5 years. Model numbers: Precessional, PRE.2; Orbital, ORB.2

Table 6.2: **All-Species Mass-Velocity γ values** for four velocity regimes of blue-shifted material viewed at four aspect angles. Dual atomic/molecular outflow runs and pure atomic outflow runs are cross-tabulated against the Precessional and Orbital models.

γ_{All}		1-2 (km/s)		2-10 (km/s)		10-50 (km/s)		50-250 (km/s)	
		PRE	ORB	PRE	ORB	PRE	ORB	PRE	ORB
15º	1. Atomic	4.93	3.48	1.75	2.74	-1.33	-0.98	-7.11	-8.55
	2. Dual A/M	2.02	1.23	-0.12	0.54	4.04	1.97	-6.93	-2.34
30º	1. Atomic	3.16	2.90	2.56	3.24	0.17	0.27	-3.36	-3.92
	2. Dual A/M	1.64	1.03	0.18	0.31	7.79	3.66	-3.83	-0.46
45º	1. Atomic	2.49	2.15	3.24	3.47	0.81	0.83	-2.62	-2.60
	2. Dual A/M	1.62	1.85	0.65	-0.38	8.70	4.35	-2.54	0.34
60º	1. Atomic	2.18	1.95	3.49	3.51	1.08	1.09	-2.23	-2.09
	2. Dual A/M	2.12	1.70	-1.23	-0.73	8.92	4.60	-1.96	0.63

The preceding Figs. 6.2 & 6.3 show the M-V spectra for all species i.e. the total mass. Table 6.1 above summarises the γ values; Fig.6.4 that follows provides a visual summary. For a given viewing angle and type of model, the peak of the 'hook' remains unaltered by the presence of the molecular outflow. This is in agreement with our earlier finding that the peak jet velocity remains the same in all four models. In the dual atomic/molecular flow models of Fig. 6.3, the low velocity regime is clearly dominated by a 'molecular plateau' giving shallow or inverted γ, followed by a steep 'cliff' in the 10-50 km/s velocity range [1]. There are subtle differences between the molecular plateau shapes of the Precessional and Orbital models; there is a characteristic dip to a shallow minimum, followed by a rise to a 'mini-hook', in the Precessional model at all four angles. Meanwhile, the Orbital model has a shorter 'cliff drop' due to more material in the third velocity range.

[1]The shape of the plot calls into question the use of linear regression, making γ values a blunt tool in this situation; though the suitability depends on the frequency of observational data points along the velocity range

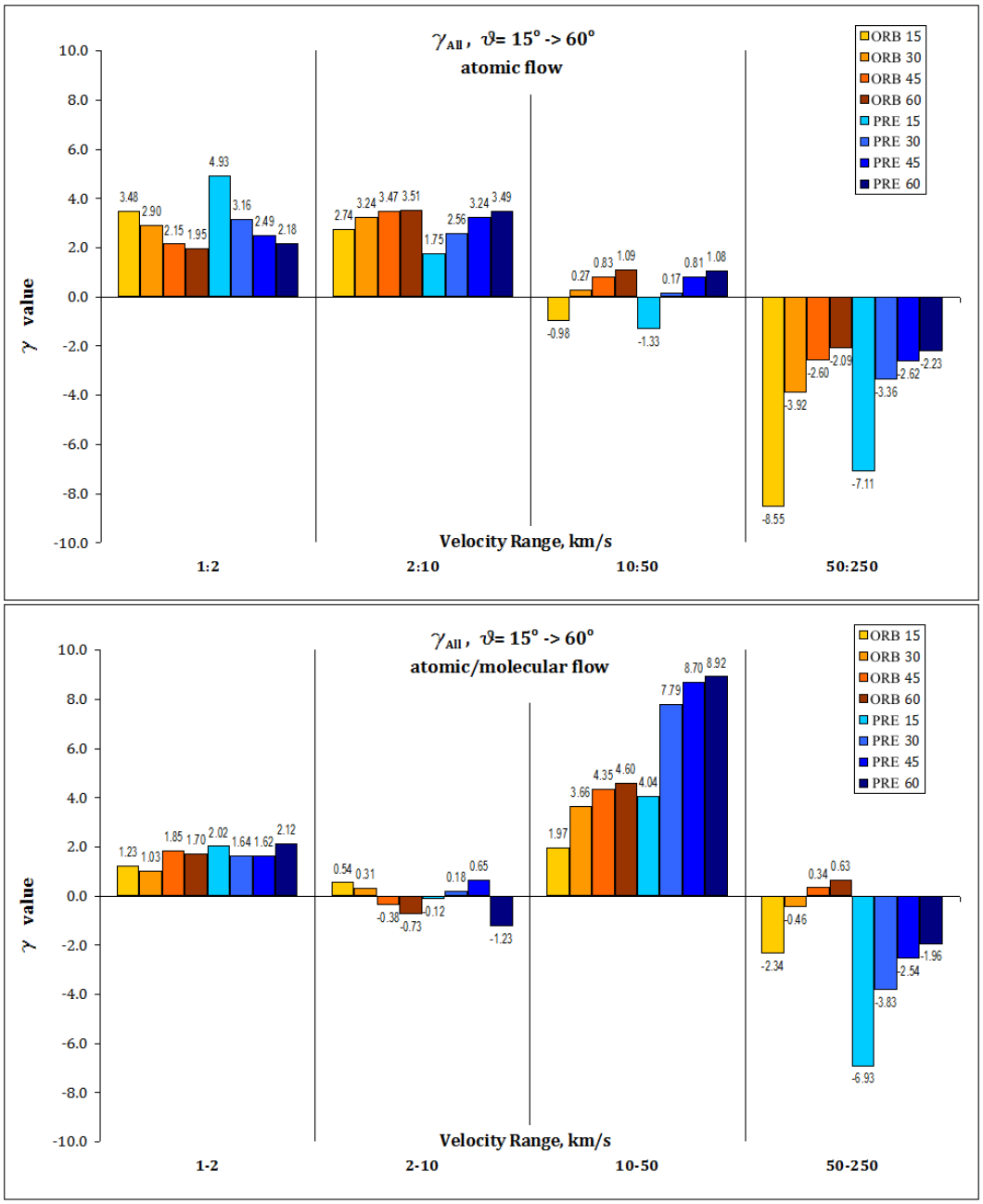

Figure 6.4: Graphical comparison of Mass-Velocity spectrum values for blue-shifted material viewed at aspect angles of 15°, 30°, 45°, 60°, using total mass for all species. Bar heights represent γ values at T=87 years . Blue bars are Precessional model values, orange bars are Orbital. Upper plot shows atomic-only flows, Precessional model PRE.1 vs. Orbital model ORB.1; lower plot shows dual atomic-molecular flows, Precessional model PRE.2 vs. Orbital model ORB.2.

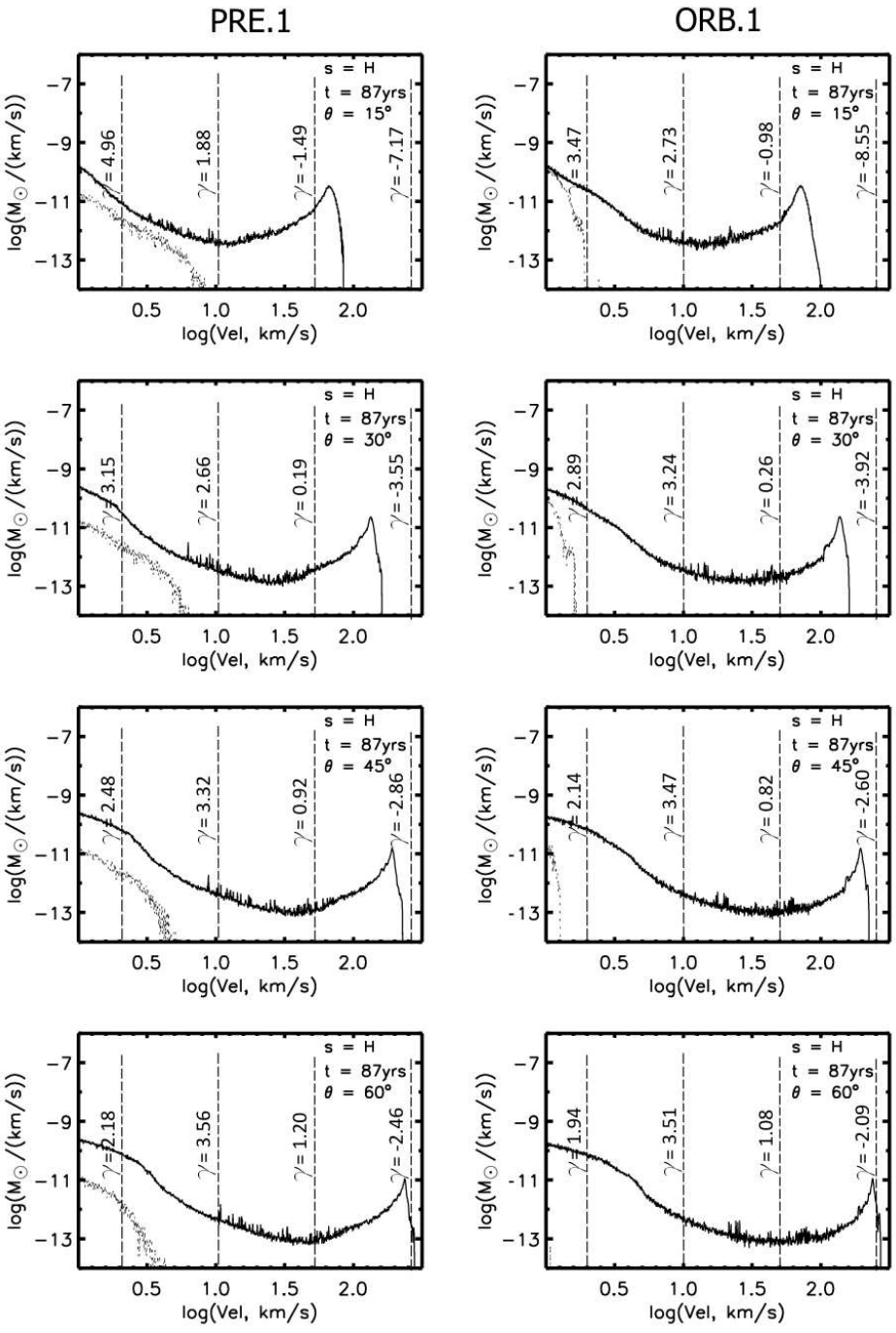

Figure 6.5: Atomic Hydrogen Mass-Velocity Spectra: atomic-only outflow scenarios, 4 aspect angles, simulation time T=87.5 years. Model numbers: Precessional, PRE.1; Orbital, ORB.1

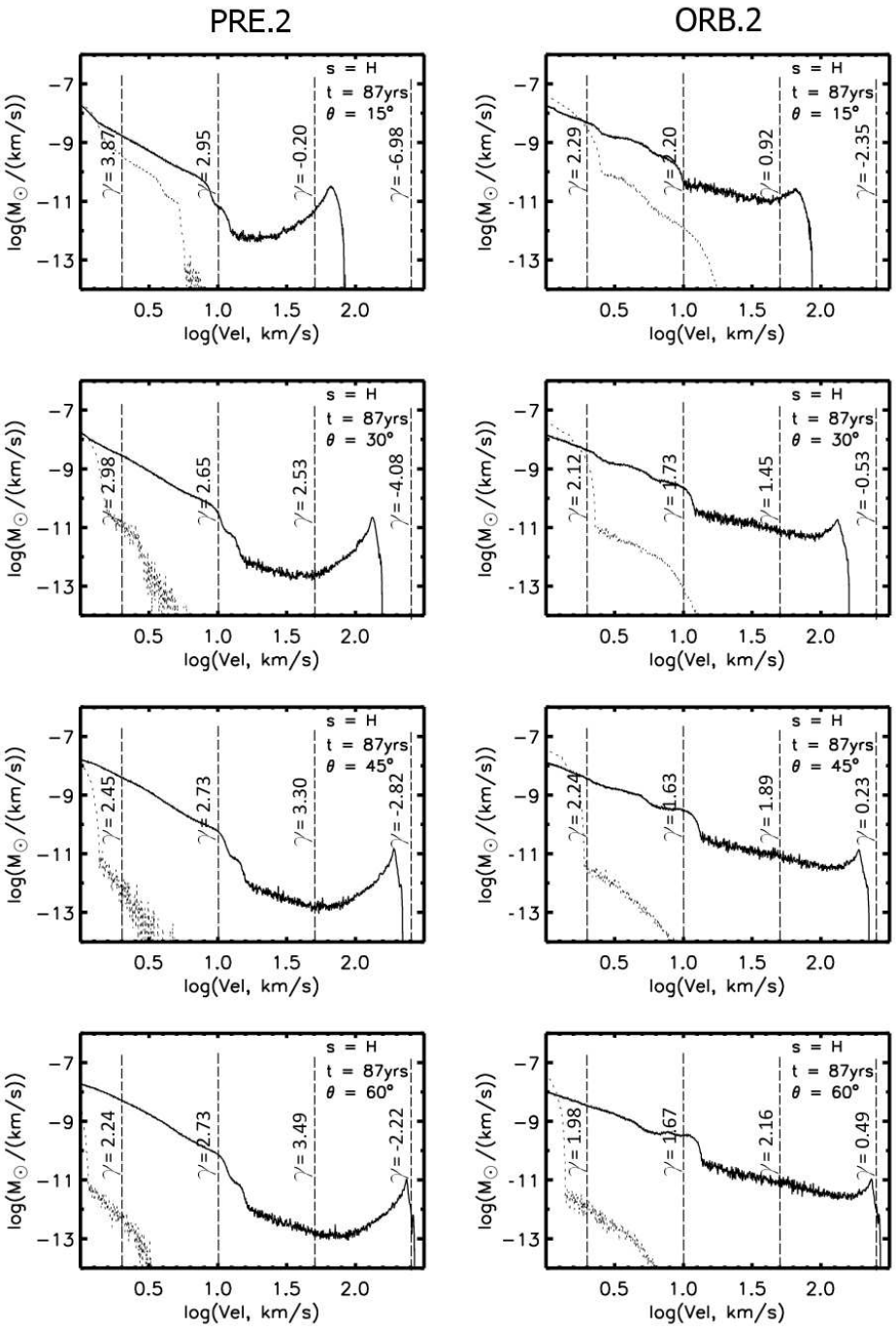

Figure 6.6: Atomic Hydrogen Mass-Velocity Spectra: dual atomic-molecular outflow scenarios, all species, 4 aspect angles, simulation time T=87.5 years. Model numbers: Precessional, PRE.2; Orbital, ORB.2

Table 6.3: **Atomic Hydrogen Mass-Velocity γ values** for four velocity regimes of blue-shifted material viewed at four aspect angles. Dual atomic/molecular outflow runs and pure atomic outflow runs are cross-tabulated against the Precessional and Orbital models.

γ_H		1-2 (km/s)		2-10 (km/s)		10-50 (km/s)		50-250 (km/s)	
		PRE	ORB	PRE	ORB	PRE	ORB	PRE	ORB
15º	1. Atomic	4.96	3.47	1.88	2.73	-1.49	-0.98	-7.17	-8.55
	2. Dual A/M	3.87	2.29	2.95	2.20	-0.20	0.92	-6.98	-2.35
30º	1. Atomic	3.15	2.89	2.66	3.24	0.19	0.26	-3.55	-3.92
	2. Dual A/M	2.98	2.12	2.65	1.73	2.53	1.45	-4.08	-0.53
45º	1. Atomic	2.48	2.14	3.32	3.47	0.92	0.82	-2.86	-2.60
	2. Dual A/M	2.45	2.24	2.73	1.63	3.30	1.89	-2.82	0.23
60º	1. Atomic	2.18	1.94	3.56	3.51	1.20	1.08	-2.46	-2.09
	2. Dual A/M	2.24	1.98	2.73	1.67	3.49	2.16	-2.22	0.49

The preceding Figs. 6.5 & 6.6 show the M-V spectra for atomic Hydrogen. Table 6.2 above summarises the γ values; Fig. 6.7 that follows provides a visual summary. As already noted, the significant detail here is that the Atomic Hydrogen M-V spectrum plots show a 'break point' in the third velocity range when there is a molecular outflow present. In the absence of a molecular outflow the spectra exhibit a continuous descent into a minimum in the 10-50 km/s range followed by a rise to the atomic jet velocity 'hook' at the end. There is a hint of a break point in the 2-10 km/s range of the atomic-only plots, which becomes more evident with increasing velocity. This early break point is not evident when the molecular outflow is involved.

As with the All-Species M-V plots (Fig. 6.3), there is more material in the 10-50 km/s range for the Orbital model, than the Precessional model. This is likely to be related to the lowering of the average velocity when the atomic jet interacts with the molecular wind, accompanied by an increase in unit mass per jet length (see Figs. 5.18 & 5.16).

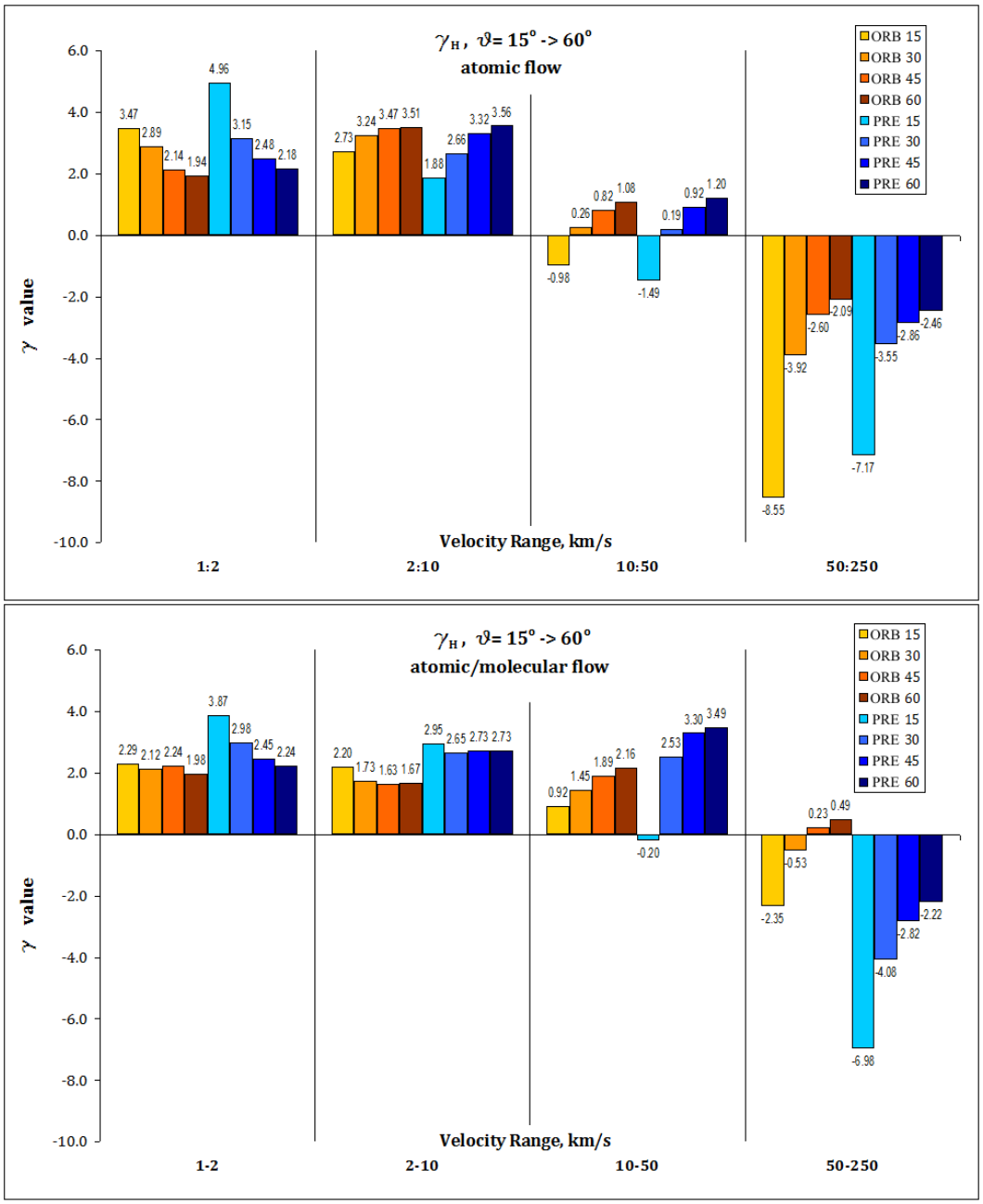

Figure 6.7: Graphical comparison of Mass-Velocity spectrum values for blue-shifted atomic Hydrogen viewed at aspect angles of 15°, 30°, 45°, 60°, using total mass for all species. Bar heights represent γ values at T=87 years . Blue bars are Precessional model values, orange bars are Orbital. Upper plot shows atomic-only flows, Precessional model PRE.1 vs. Orbital model ORB.1; lower plot shows dual atomic-molecular flows, Precessional model PRE.2 vs. Orbital model ORB.2.

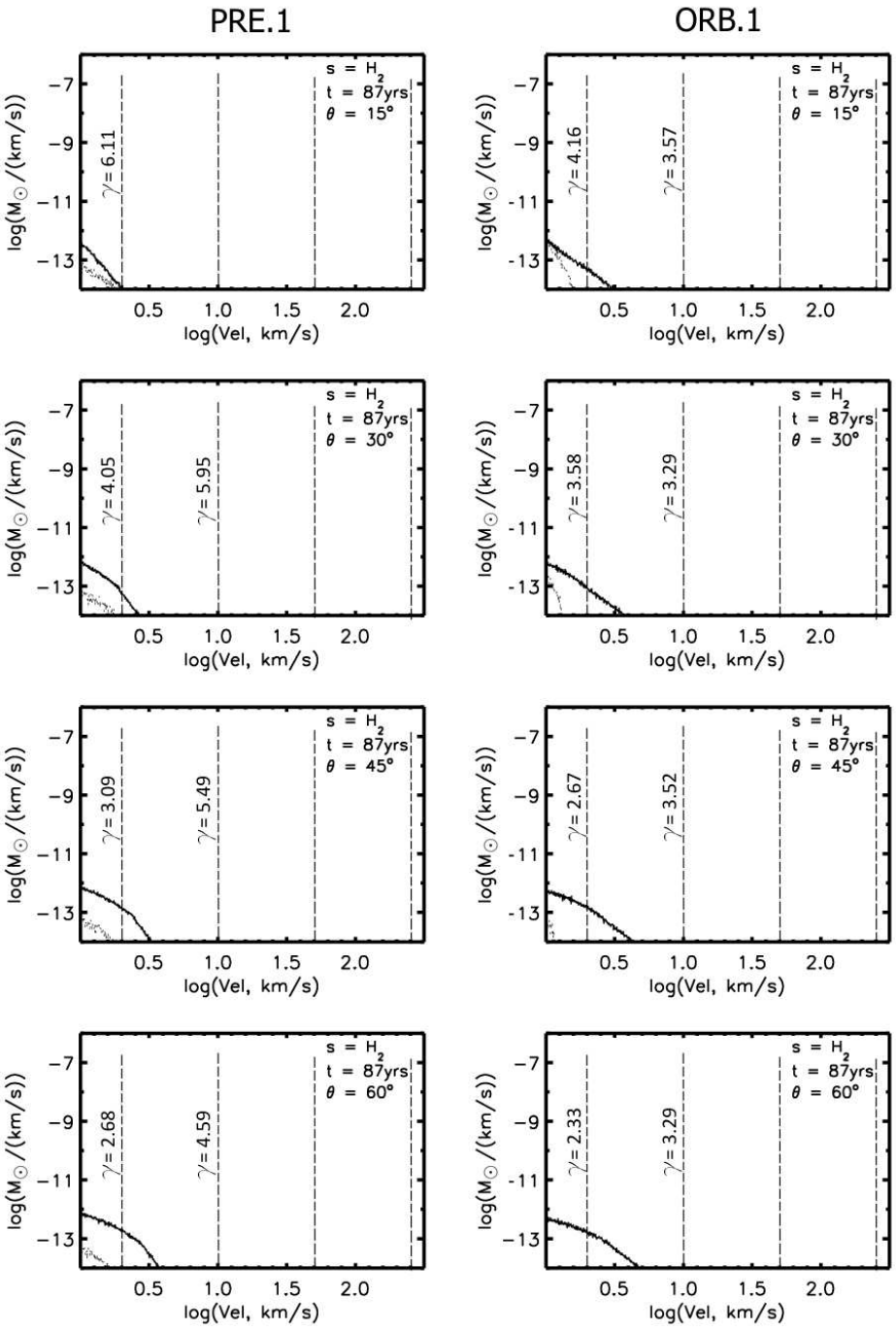

Figure 6.8: Molecular Hydrogen Mass-Velocity Spectra: atomic-only outflow scenarios, 4 aspect angles, simulation time T=87.5 years. Model numbers: Precessional, PRE.1; Orbital, ORB.1

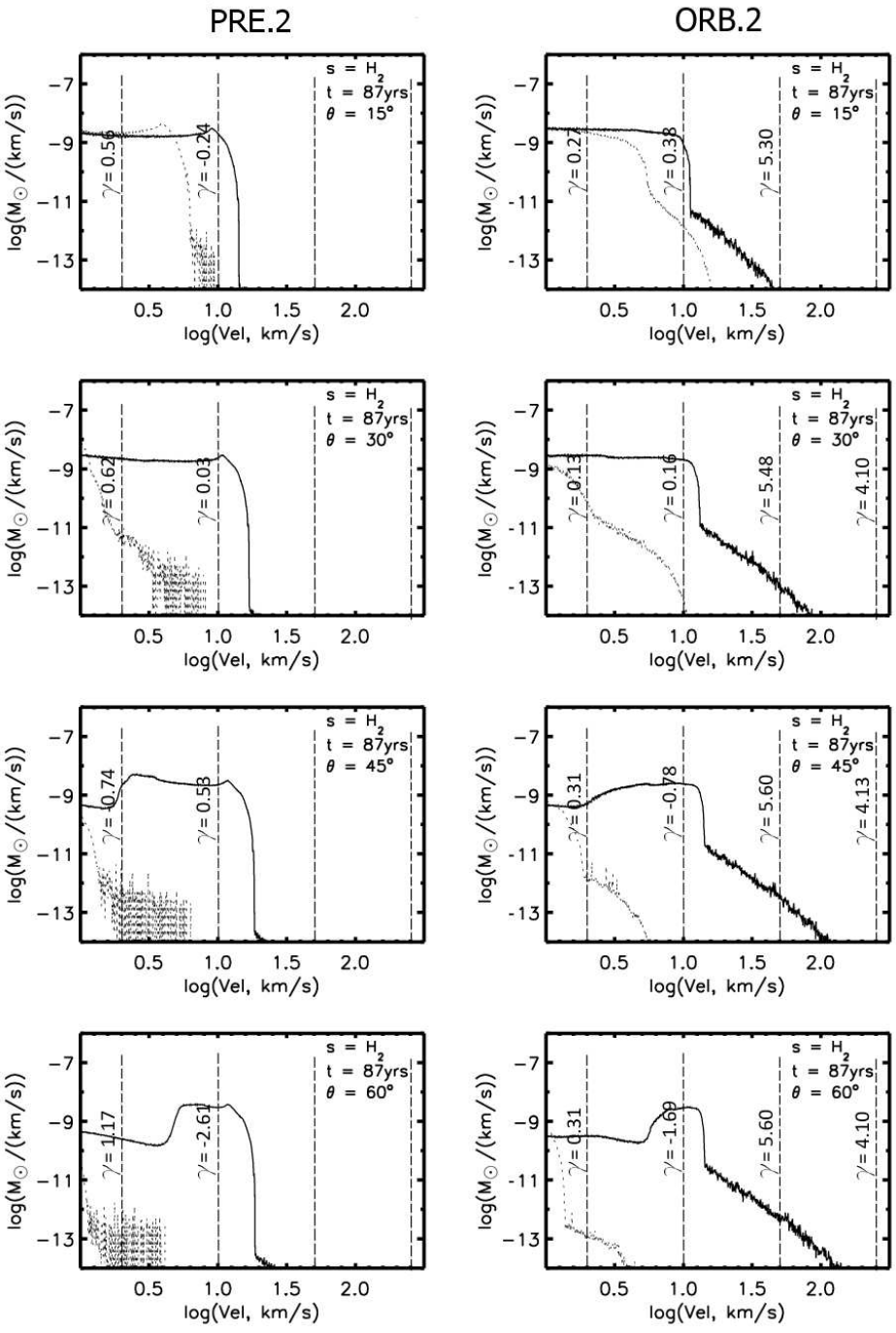

Figure 6.9: Molecular Hydrogen Mass-Velocity Spectra: dual atomic-molecular outflow scenarios, all species, 4 aspect angles, simulation time T=87.5 years. Model numbers: Precessional, PRE.2; Orbital, ORB.2

Table 6.4: **Molecular Hydrogen Mass-Velocity γ values** for four velocity regimes of blue-shifted material viewed at four aspect angles. Dual atomic/molecular outflow runs and pure atomic outflow runs are cross-tabulated against the Precessional and Orbital models.

γ_{H_2}		1-2 (km/s)		2-10 (km/s)		10-50 (km/s)		50-250 (km/s)	
		PRE	ORB	PRE	ORB	PRE	ORB	PRE	ORB
15º	1. Atomic	6.11	4.16	0.00	3.57				
	2. Dual A/M	0.56	0.27	-0.24	0.38		5.30		
30º	1. Atomic	4.05	3.58	5.95	3.29				
	2. Dual A/M	0.62	0.13	0.03	0.16		5.48		4.10
45º	1. Atomic	3.09	2.67	5.49	3.52				
	2. Dual A/M	-0.74	0.31	0.53	-0.78		5.60		4.13
60º	1. Atomic	2.68	2.33	4.59	3.29				
	2. Dual A/M	1.17	0.31	-2.61	-1.69		5.60		4.10

The preceding Figs. 6.8 & 6.9 show the M-V spectra for molecular Hydrogen. Table 6.3 above summarises the γ values; Fig.6.10 that follows provides a visual summary. Figure 6.8 is provided for completeness; it shows the low-velocity M-V spectra for the trace H_2 that is present in the atomic-only models. Meanwhile Fig. 6.9 reveals the 'molecular plateaus' uncomplicated by the addition of the atomic jet 'hook'. The characteristic molecular features we noted previously for the all-species plot are all repeated here confirming the dominance of the low-velocity regime by the molecular outflows. There is however an interesting difference between the Orbital and Precessional spectra; the presence of molecular material beyond the 'cliff' in the 10-50 km/s range for the 15° plot and extending into the 50-250 km/s range for larger viewing angles.

This is clear evidence that H_2 is entrained by the fast atomic jet in the Orbital models, but not entrained in the Precessional models.

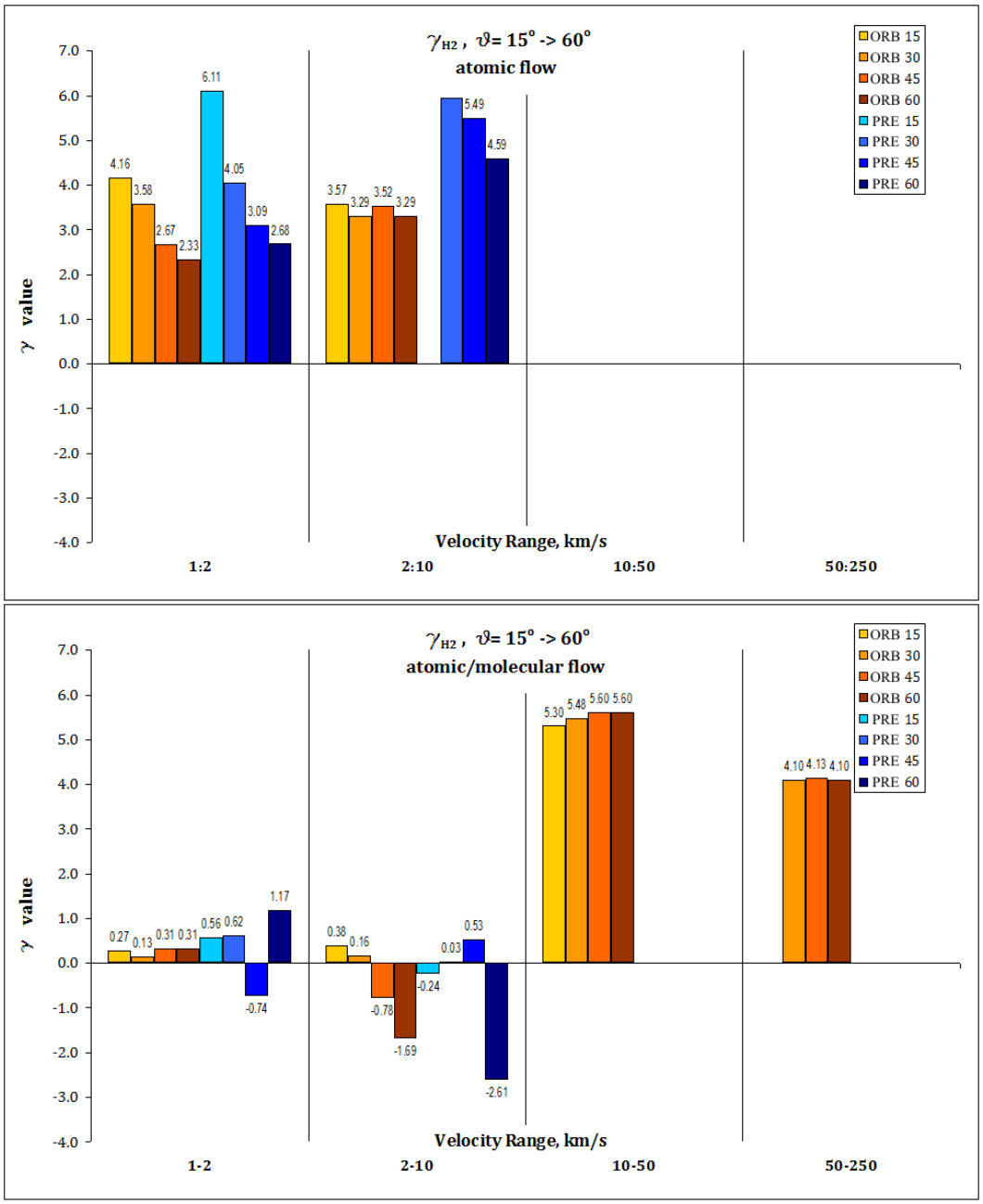

Figure 6.10: Graphical comparison of Mass-Velocity spectrum values for blue-shifted molecular Hydrogen viewed at aspect angles of 15°, 30°, 45°, 60°, using total mass for all species. Bar heights represent γ values at T=87 years . Blue bars are Precessional model values, orange bars are Orbital. Upper plot shows atomic-only flows, Precessional model PRE.1 vs. Orbital model ORB.1; lower plot shows dual atomic-molecular flows, Precessional model PRE.2 vs. Orbital model ORB.2.

6.3.4 Shallow-Angle Mass-Velocity Spectra for HH30

In addition to the Mass-Velocity spectra at viewing angles in multiples of 15°, m-v data was also generated and plotted for an angle of 1° to more closely resemble HH30 itself. Taking a slightly different approach we generated m-v spectra at four time intervals (67, 74, 80 & 87 years) for all species at $\theta = 1°$. We then computed the average γ values over this 20-year timespan.

Because of the shallow viewing angle, it became sensible to calculate the γ values for both blueshifted and redshifted material. Also, as jet velocity components are less dominant at this angle, there were no atomic 'hooks' in the higher velocity regions of the plots.

Due to the lower velocity regime, it was decided to use a scheme similar to that of Moraghan et al., (2006)(69):

- 2-4 km/s
- 4-8 km/s
- 8-16 km/s
- 16-32 km/s

In the interests of brevity, example plots only are presented here. Figures 6.11 & 6.12 show m-v spectra for all species at viewing angle 1°, for one timeframe. Figure 6.13 shows m-v spectra for atomic Hydrogen only, but for the four timeframes.

Tables 6.4 & 6.5 summarise the γ values for blueshifted and redshifted material, respectively.

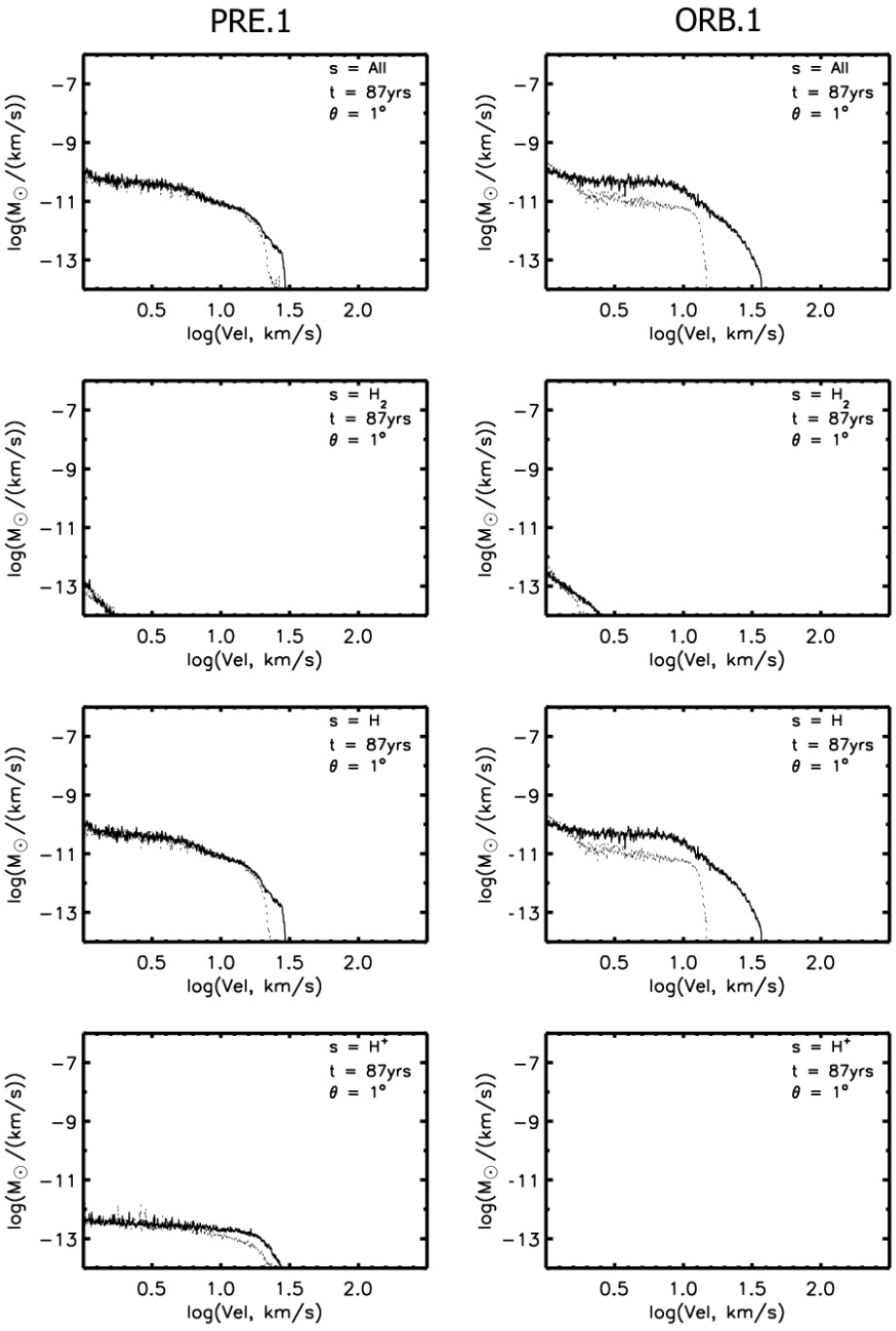

Figure 6.11: Multispecies Mass-Velocity Spectra: atomic-only outflow scenarios, all Hydrogen species, aspect angle θ=1°, simulation time T=87.5 years. Model numbers: Precessional, PRE.1; Orbital, ORB.1

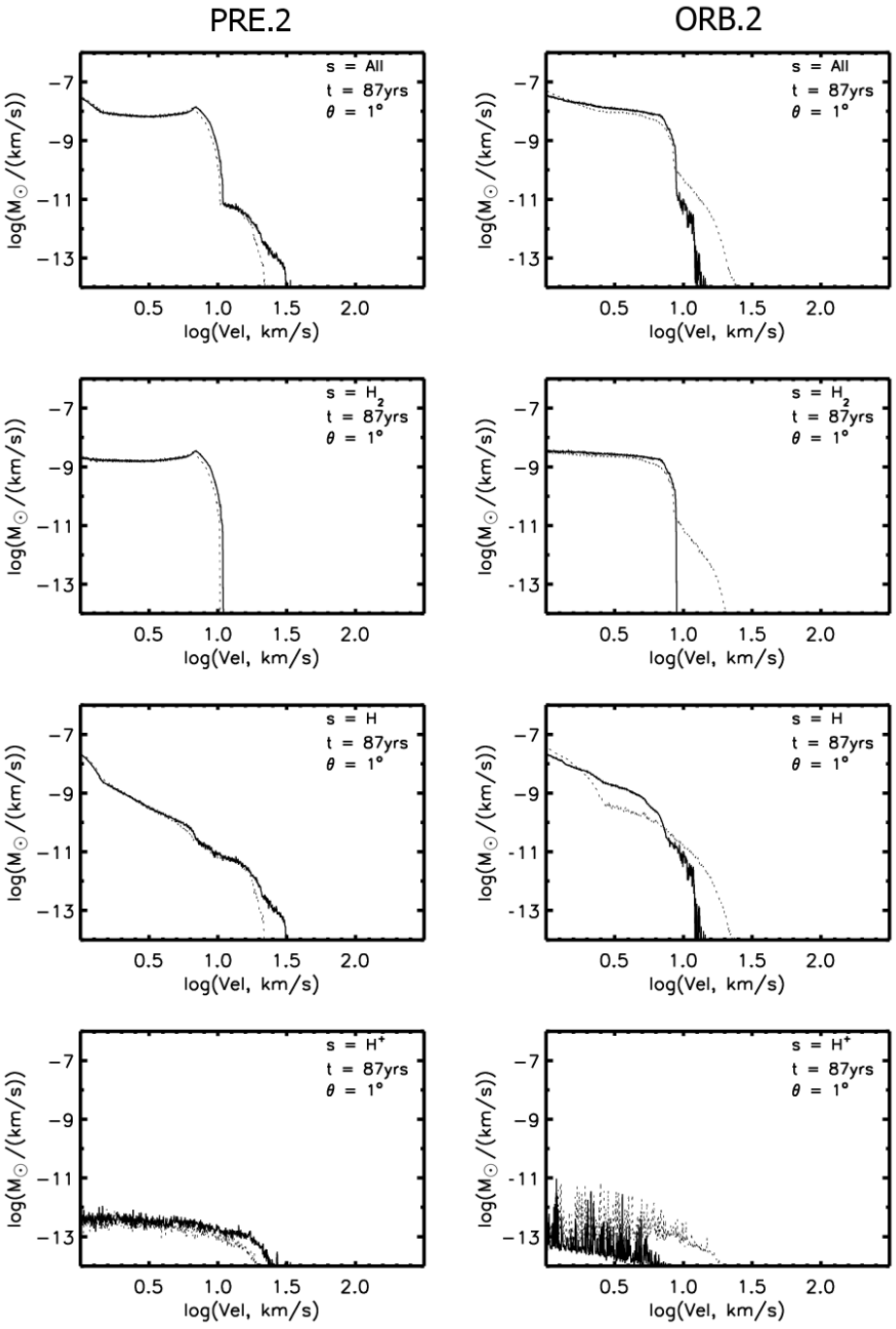

Figure 6.12: Multispecies Mass-Velocity Spectra: atomic-molecular outflow scenarios, all Hydrogen species, aspect angle θ=1°, simulation time T=87.5 years. Model numbers: Precessional, PRE.2; Orbital, ORB.2

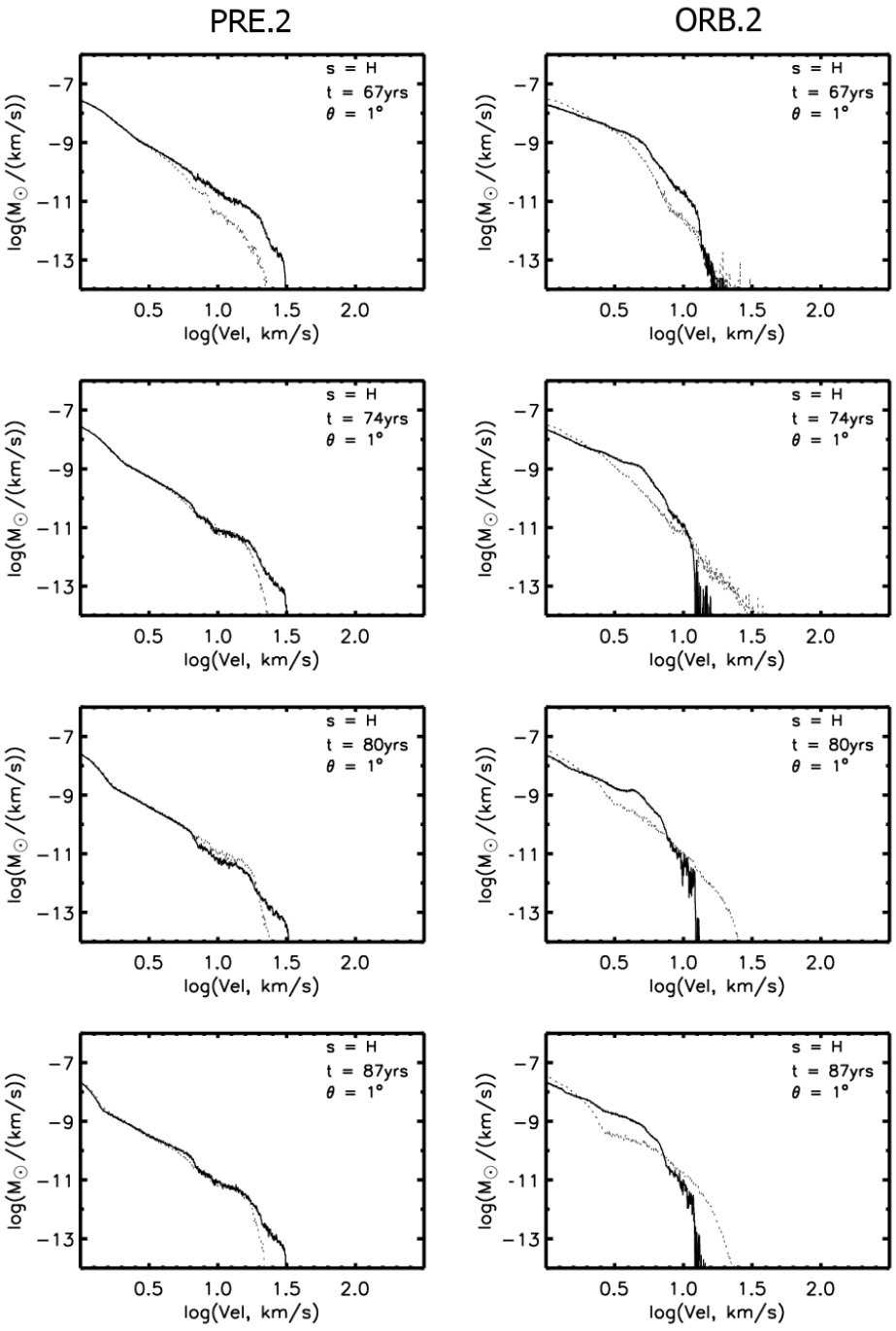

Figure 6.13: Time-varying Mass-Velocity Spectra: atomic-molecular outflow scenarios, Atomic Hydrogen spectrum, aspect angle θ=1°, simulation times from 67 to 87 years. Model numbers: Precessional, PRE.2; Orbital, ORB.2

Table 6.5: **Blue-shifted Mass-Velocity 20-year average γ values** for four velocity regimes viewed at a 1° aspect angle, for all Hydrogen species. Dual atomic/molecular outflow runs and pure atomic outflow runs are cross-tabulated against the Precessional and Orbital models.

Blue Shifted		2-4 (km/s)		4-8 (km/s)		8-16 (km/s)		16-32 (km/s)	
		PRE	ORB	PRE	ORB	PRE	ORB	PRE	ORB
γ_{All}	1. Atomic	0.51		1.17	0.39	1.70	3.18	7.01	5.94
	2. Dual A/M	0.25	0.59	-0.65	1.69	13.09	17.38	6.94	
γ_H	1. Atomic	0.50		1.19	0.39	1.74	3.18	7.09	5.94
	2. Dual A/M	2.69	1.98	3.81	5.62	2.32	11.69	7.08	
γ_{H_2}	1. Atomic		2.60						
	2. Dual A/M	-0.02	0.23	-0.70	1.47	18.24	25.74		

Table 6.6: **Red-shifted Mass-Velocity 20-year average γ values** for four velocity regimes viewed at a 1° aspect angle, for all Hydrogen species. Dual atomic/molecular outflow runs and pure atomic outflow runs are cross-tabulated against the Precessional and Orbital models.

Red Shifted		2-4 (km/s)		4-8 (km/s)		8-16 (km/s)		16-32 (km/s)	
		PRE	ORB	PRE	ORB	PRE	ORB	PRE	ORB
γ_{All}	1. Atomic	10.56		2.18	5.90	1.25	0.78	0.49	0.74
	2. Dual A/M	13.82	8.07	12.09	7.44	0.08	2.50	0.22	0.75
γ_H	1. Atomic	10.08		2.20	5.90	1.25	0.78	0.50	0.74
	2. Dual A/M	14.07	7.11	2.90	5.84	3.85	4.74	2.96	3.58
γ_{H_2}	1. Atomic								
	2. Dual A/M		7.55	17.84	7.79	0.04	2.45	-0.06	0.32

Figure 6.14 provides a visual summary of data from tables 6.4 & 6.5, for the All Species mass spectra. This displays both blueshifted (R) and redshifted (L) values in one graph. The number of time values used in the average is too small for standard error limits to be meaningful; instead error bars indicate max/min values. Figure 6.15 is as per Fig. 6.14 but for atomic Hydrogen mass only.

Figure 6.16 summarises the γ values for molecular Hydrogen, for the dual outflow atomic/molecular models. There is no graph for H_2 in the atomic-only models; at shallow viewing angle, there is nothing to graph above 2 km/s for the trace amounts of H_2.

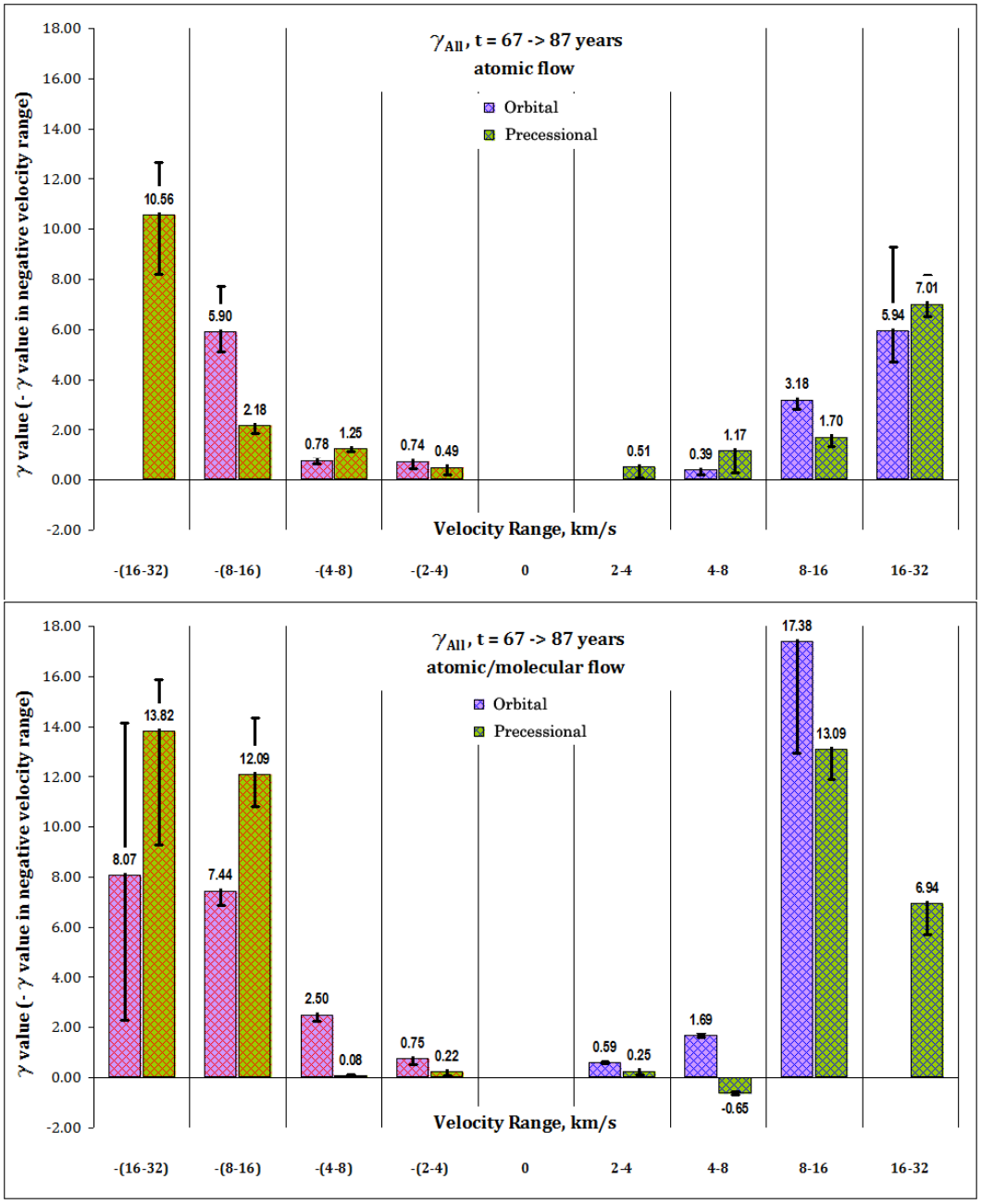

Figure 6.14: Graphical comparison of Mass-Velocity spectrum γ values using total mass for all species. Bar heights represent average γ over a 20-year period. Error bars show max and min values. Upper plot shows atomic-only flows, Precessional model PRE.1 vs. Orbital model ORB.1; lower plot shows dual atomic-molecular flows, Precessional model PRE.2 vs. Orbital model ORB.2.

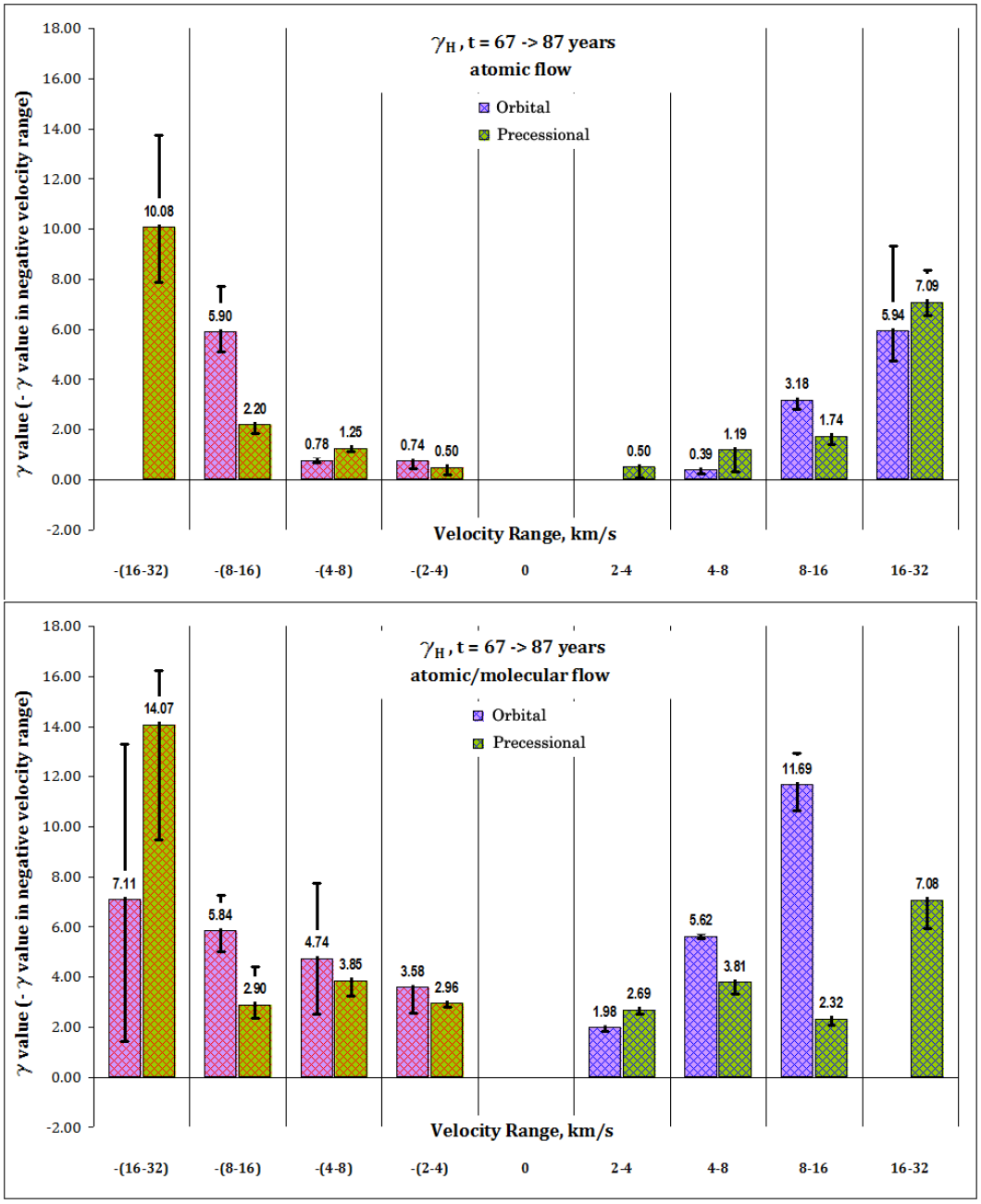

Figure 6.15: Graphical comparison of Mass-Velocity spectrum γ values using atomic Hydrogen mass. Bar heights represent average γ over a 20-year period. Error bars show max and min values. Upper plot shows atomic-only flows, Precessional model PRE.1 vs. Orbital model ORB.1; lower plot shows dual atomic-molecular flows, Precessional model PRE.2 vs. Orbital model ORB.2.

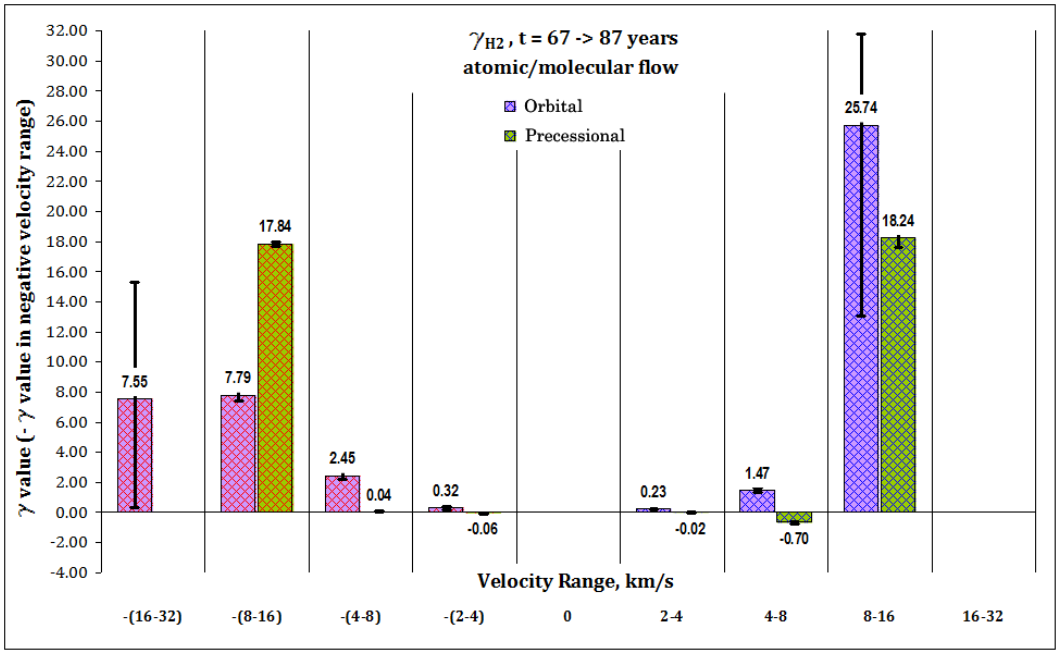

Figure 6.16: Graphical comparison of Mass-Velocity spectrum values using molecular Hydrogen mass. Bar heights represent average γ over a 20-year period. Error bars show max and min values. Single plot shows dual atomic-molecular flows, Precessional model PRE.2 vs. Orbital model ORB.2. Molecular Hydrogen, although present in trace amounts, is too sparse in the atomic-only flow models to produce meaningful M-V spectrum plots.

6.3.5 Discussion of the Shallow-Angle M-V Spectra

The first point to note is that the presence of the molecular outflow leads to larger γ values in most velocity ranges, for both Precessional and Orbital scenarios (there are two marginal exceptions, Orbital red-shifted 8-16 & Precessional blue-shifted 16-32).

The second point to note, is the approximate symmetry in the red/blue-shift spectra for the Precessional models, when examining γ values for the lower velocity ranges (2-4, 4-8, 8-16). This symmetry is evident for both the atomic-only model and the dual outflow atomic/molecular model. This is in contrast with the Orbital models, which show distinctly asymmetric γ values.

The third point to note, is that the Orbital model γ values are clearly more variable than the Precessional values across the 20-year period. This is to be expected given the large-scale dynamic variability that the outflow arrangement in this model produces.

6.4 Synthetic Position-Velocity Diagrams and Emission Line Profiles

Our IDL® code MSYNPOSVEL was written to produce synthetic position-velocity diagrams. These 2D plots are spatially resolved in the x-dimension and resolved by velocity of material elements, radially with respect to an observer at aspect angle $\theta = 1°$, in the y-dimension. P-V diagrams are more usually associated with bipolar outflows, with a spatially resolved dimension that is perpendicular rather than parallel to the jet axis. In our case we are investigating a single-sided outflow system and our p-v diagrams depict the velocity ranges in the jet(s) with spatial resolution along the jet.

Velocity distribution data is stored in the MULTISYNTH output 'dist' (distribution) files. Total emission along the line of sight is binned in 1000 velocity channels. MSYNPOSVEL produces the p-v diagrams from this data along with emission line profiles at three positions along the x-axis, and a total emission profile. Presented in figures 6.17 through 6.20 are p-v diagrams and line profiles for the Orbital and Precessional models including molecular wind (ORB.2 and PRE.2), for emission lines H-α, [SII], [OI],^{12}CO J=2-1. The line profiles are determined for two simulation epochs; $0 < T < 87.5$ years and $87.5 < T < 175$ years. In the first epoch, the flows are not fully developed, with atomic and molecular components still traversing the domain. In the second epoch the outflow(s) have settled into a persistent configuration. There is nonetheless a high degree of variability particularly with regard to atomic emission and so the emission plots show the median profiles together with the upper and lower quartile limits of the intensity range.

Appendix I presents additional diagrams, including those for [SII], [OI] and [FeII] emission.

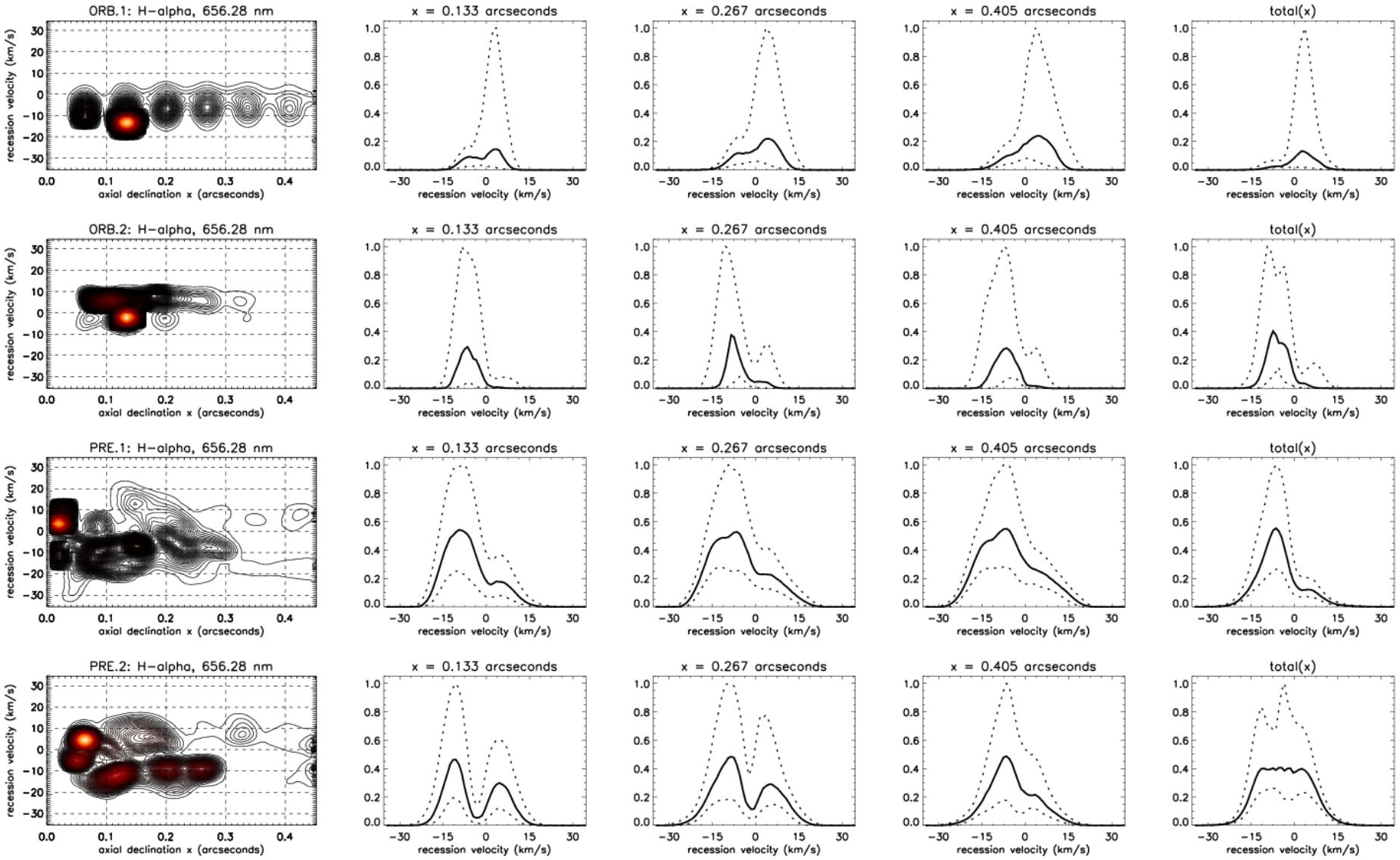

Figure 6.17: Position-Velocity diagrams and line profiles for the H-α line, T=87.5 years, for the four simulated HH30 outflow scenarios in the early stage while the flows are still developing. Angular declination from the source object is in the direction of the outflow, along an axis parallel to the sky plane. λ dispersion arises from the recession velocity of emitting material in km/sec. The P-V plots are instantaneous examples at 87.5 yrs; contour scale is notional but linear. The line profiles indicate median emission over $0 < T < 87.5$ yrs; dashed lines are the upper and lower quartile boundaries for time variation. Total line profile is for whole-field emission; profiles with specified declination are given for comparison with a spatially resolved jet. Intensity is stated in dimensionless units of the upper quartile peak for each emission line.

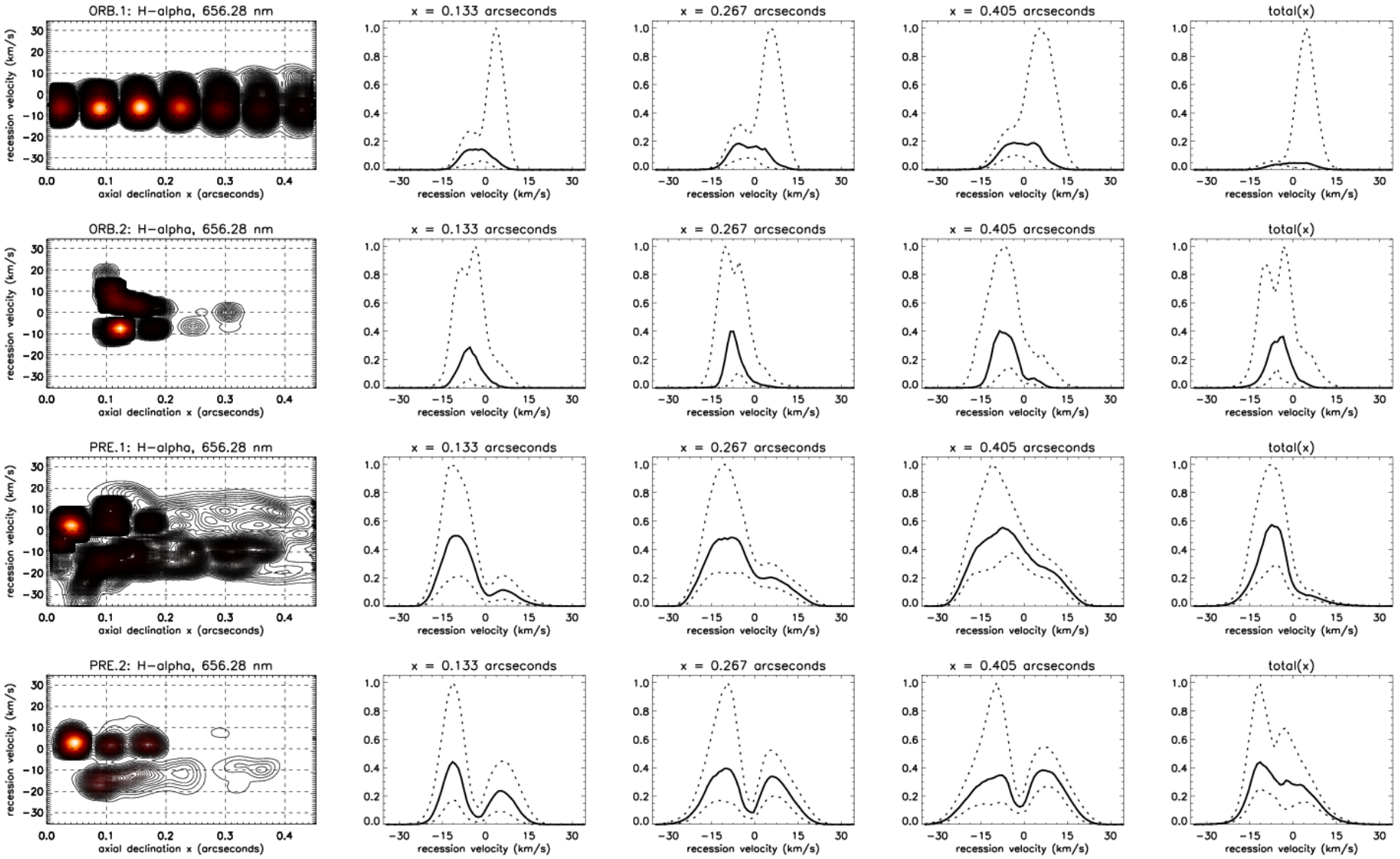

Figure 6.18: Position-Velocity diagrams and line profiles for the H-α line, T=175 years, for the four simulated HH30 outflow scenarios when flows are well-developed. Angular declination from the source object is in the direction of the outflow, along an axis parallel to the sky plane. λ dispersion arises from the recession velocity of emitting material in km/sec. The P-V plots are instantaneous examples at 175 yrs; contour scale is notional but linear. The line profiles indicate median emission over $87.5 < T < 175$ yrs; dashed lines are the upper and lower quartile boundaries for time variation. Total line profile is for whole-field emission; profiles with specified declination are given for comparison with a spatially resolved jet. Intensity is stated in dimensionless units of the upper quartile peak for each emission line.

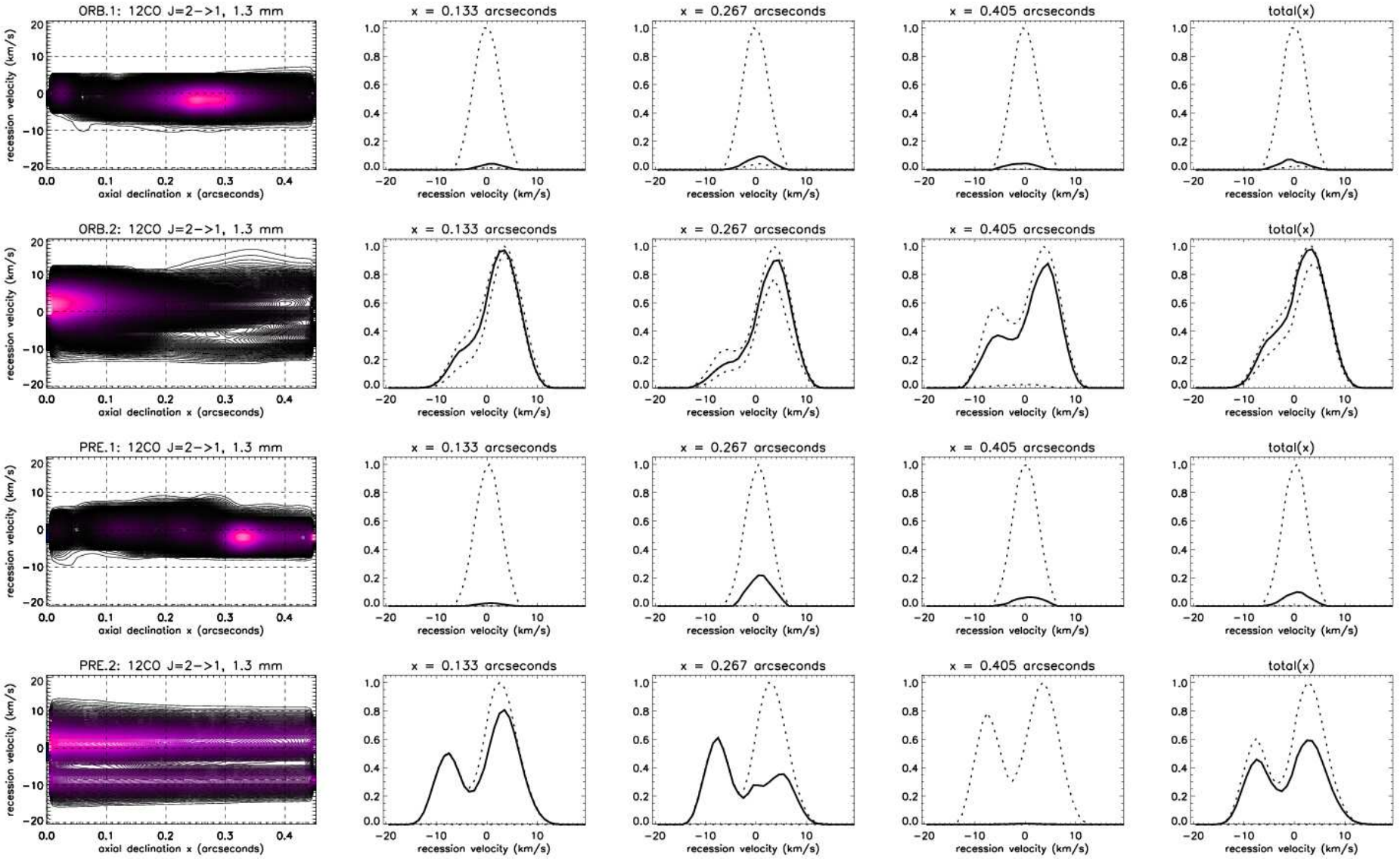

Figure 6.19: Position-Velocity diagrams and line profiles for the ^{12}CO J=2-1 line, T=87.5 years, for the four simulated HH30 outflow scenarios in the early stage while the flows are still developing. Angular declination from the source object is in the direction of the outflow, along an axis parallel to the sky plane. λ dispersion arises from the recession velocity of emitting material in km/sec. The P-V plots are instantaneous examples at 87.5 yrs; contour scale is notional but linear. The line profiles indicate median emission over $0 < T < 87.5$ yrs; dashed lines are the upper and lower quartile boundaries for time variation. Total line profile is for whole-field emission; profiles with specified declination are given for comparison with a spatially resolved jet. Intensity is stated in dimensionless units of the upper quartile peak for each emission line.

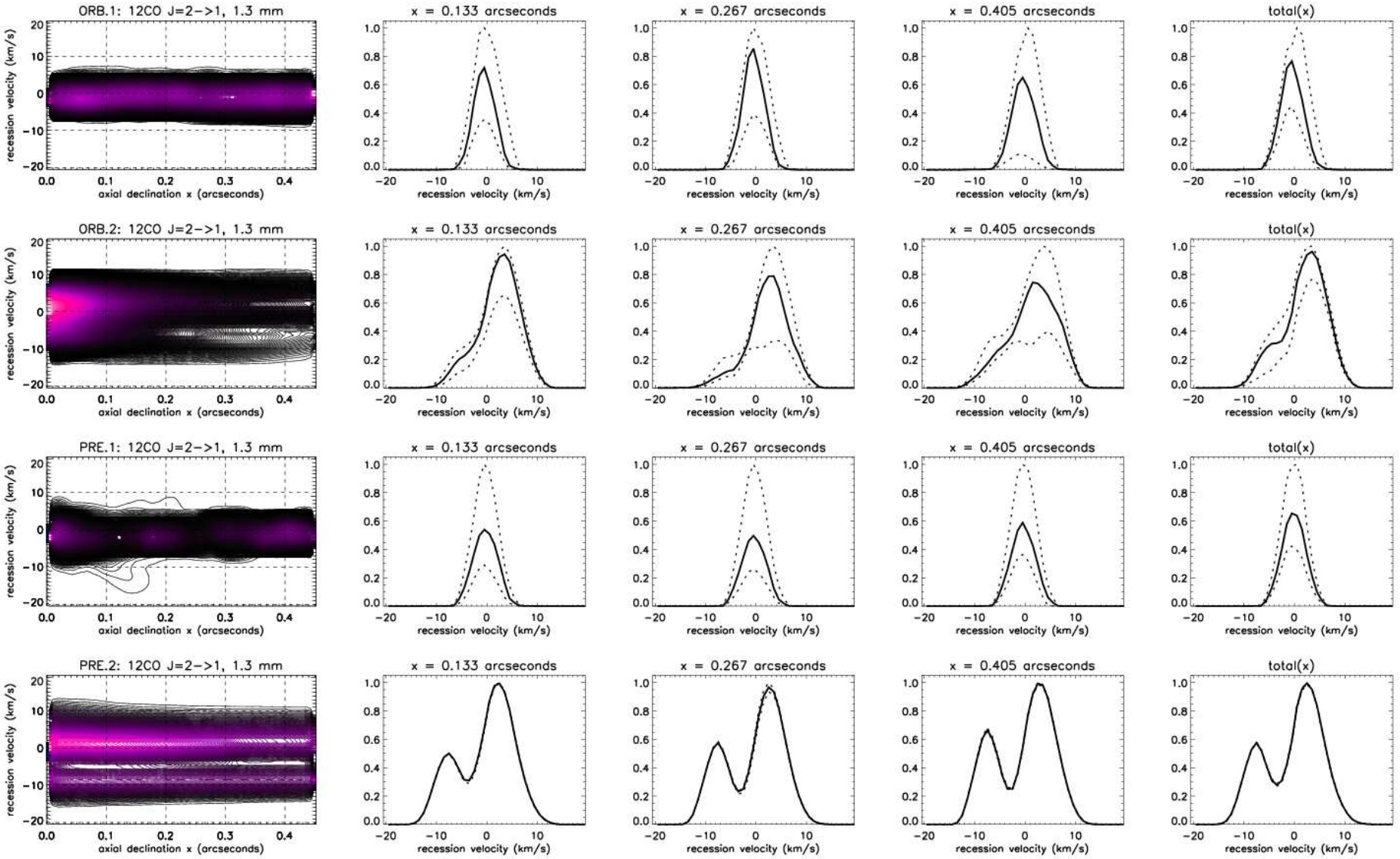

Figure 6.20: Position-Velocity diagrams and line profiles for the ^{12}CO J=2-1 line, T=175 years, for the four simulated HH30 outflow scenarios when flows are well-developed. Angular declination from the source object is in the direction of the outflow, along an axis parallel to the sky plane. λ dispersion arises from the recession velocity of emitting material in km/sec. The P-V plots are instantaneous examples at 175 yrs; contour scale is notional but linear. The line profiles indicate median emission over $87.5 < T < 175$ yrs; dashed lines are the upper and lower quartile boundaries for time variation. Total line profile is for whole-field emission; profiles with specified declination are given for comparison with a spatially resolved jet. Intensity is stated in dimensionless units of the upper quartile peak for each emission line.

6.4.1 M-V Spectra and Emission Line Profiles

The mass-velocity relationship connects to emission line profiles through Doppler broadening of the spectral line. However, the temperature-dependent rate coefficient for the transition is also a factor in determining the emission line characteristics, and the velocity of the material has implications for its probable temperature; slow-moving material is likely to be cold and dense, while faster-moving material is shock-processed and at higher temperature.

The excitation temperature for the ^{12}CO J=2-1 1.3mm line is $\sim$ 11K making it a useful tracer for cold slow-moving material. Above 4000K, the CO molecule dissociates; as this is higher than the thermal decomposition point for H2 it makes CO an effective tracer for H2 across a broad temperature range.

Emission lines from level transitions in atoms or ions are excited by higher temperatures (10^4K) and stronger shocks (50+ km/s), with efficient photon production determined by the range of temperatures in which a population of the species in question can exist without further thermal decomposition, though in the case of the H-α line photon production by recombination is choked off at very high temperatures by diminishing electron capture cross section at higher thermal velocities. The population of heavier metals such as Iron is also affected by release from dust grains that are destroyed in shocks, a process known as 'sputtering'.

Both the M-V spectra and the P-V diagrams and line profiles are generated by line-of-sight integration of the material species tracked by the simulation, but the emission line intensity calculation includes the photon production rate coefficient and determination of the population of collision partners (if not directly tracked in the model), both as a function of temperature.

In protostellar outflows, the M-V spectrum is dominated by slower-moving material in both simulations and observation. The low end of the velocity scale is characterised by stochastic velocity fluctuations arising from entrainment in the mixing layer between the cocoon of processed jet material and the surrounding sheath of entrained ambient gas, and other processes such as vortex shedding from the working surface. A wiggling jet due to precession or orbital motion is also likely to generate turbulent vortices in the

surrounding material (for example see Fig. 5.12).

These randomly distributed velocities projected along the line of sight may reasonably be expected to produce a Gaussian broadening of emission lines (Lazarian, Pogosyan, 2006)(60).

Grid-based simulations are resolution-limited in their ability to model turbulent motion, and higher resolution models may produce broader line profiles by capturing small-scale velocity fluctuations superposed on the larger-scale material velocity field. A significant question in the case of double-peaked line profiles is whether this additional broadening will fill in the space between the line peaks, making it harder to distinguish these as double-peaked emission lines.

Rotating structures tend to produce double-peaked velocity dispersion when viewed along line-of-sight. This is a signature feature of accretion discs (Horne, Marsh, 1986)(47) but in our models we see this effect most clearly when the synthetic ^{12}CO emission is examined for the dual-outflow scenario PRE.2 in which the molecular outflow is a rotating hollow cone. Each elliptical annular section through this cone as viewed by the observer will have a similar pattern of line of sight velocity projection to a rotating accretion disc with a large central depletion zone.

The largest emission peaks for the dual-outflow scenarios are red-shifted and this is unexpected given that the outflow is angled slightly towards the observer. There is an asymmetry in the computation of the line profile that might give rise to this. When the conical molecular flow is tilted towards the observer, the conical sections along lines of sight pass through a faster, denser flow on the far side of the elliptical annulus than on the near side because of greater proximity to the outflow source. At small inclination angle the projected velocity component along the line-of-sight is biased linearly in favour of blue-shifted material; but this is counteracted by a second-order bias in favour of red-shifted material, arising from combined velocity and density asymmetry. Intuitively, this seems only likely to hold true while the inclination angle remains small; it also assumes that the 2D integration grid truncates the conical outflow asymmetrically. Whether these effects at small inclination angle would be sufficient to produce the asymmetric distribution of emission evident in Fig. 6.20 requires further investigation.

The H-α line profiles all show blue-shifted primary peaks apart from in the anomalous ORB.1 model. A blue-shifted peak is expected because the H-α production mainly arises in the fast-moving material of the jet column, and unlike the wide-angled conical molecular flows any asymmetry arising from observer inclination angle will be minimal as all the material is concentrated into a small region of space. The line of sight projected jet velocity component dominates the velocity spectrum for this component.

There is no ready explanation for the anomalous red-shift of the ORB.1 H-α peak. The principal difference that separates this from the other models is that H-α production mainly occurs in the internal working surfaces within the atomic jet column, rather than in peripheral shocks or direct collision with dense molecular material. The red-shifted H-α peak is also apparent in the early-stage development of the ORB.1 jet. This suggests that for some reason material that is moving away from the observer is producing H-α photons in greater numbers than material moving towards, or there is more material moving away than towards, neither of which seem intuitively correct.

Whilst this warrants further investigation, it should be pointed out that ORB.1 produces substantially less H-α emission than any of the other 3 principal models. This is confirmed by Fig. 6.11 which shows that the presence of ionised Hydrogen is comparatively negligible for this model. It is conceivable that the production of H-α in the ORB.1 model is weak enough that a small numerical bias in the model or synthetic image code can dominate the physics in a way that is not evident in the models that generate strong H-α emission.

6.5 Synthetic Velocity Channel Maps

Our IDL® code MSYNVCHAN was written to produce synthetic velocity channel maps. Velocity channel data is stored in the MULTISYNTH output flux files. Total emission along the line of sight is integrated and binned in four velocity channels according to the proper motion of material parallel to the x-axis, i.e. the jet injection axis in HH30. Our choice of velocity channel bounds arose from ad hoc experimentation to see which gave the most well-defined separation across the board in the four principal models. Our channels were:

- 0-5 km/s
- 5-20 km/s
- 20-280 km/s
- 280+ km/s

Presented in figures 6.21 through 6.24 are channel maps for the Precessional and Orbital model column densities and the previously discussed H-α, [SII], [OI], ^{12}CO and [FeII] emission lines; at t = 175 years, the end of our large principal simulation runs. Only the maps for the dual atomic/molecular models are shown here (ORB.2 and PRE.2). These channel maps are all integrated in the z-dimension and at aspect angle $\theta = 1°$.

The velocity channel maps are a useful tool to explore and compare the velocity structure of the different models. However their utility in comparison to observation is limited by the need to pick out discrete structures in motion that are within the capabilities of instruments to resolve spatially with an observing campaign of adequate frequency. Proper motions of large-scale (100AU) knots of emission from longer period variability have already been the subject of investigation (Hartigan, Morse 2007)(41) but the moving structures identified in our channel maps are below the 10AU length scale and their dynamic timescale is of the order of months.

The prior observations of HH30 in the H-α line with the highest spatial resolution have been with the HST/WFPC2 instrument which resolves down to 14 AU at 140 pc, while the Plateau De Bure interferometer resolves the ^{12}CO 1.3 mm line to 140 AU (Pety et al,

2006)(81). These resolutions are not sufficient to confirm the existence of the structures in our models or track their proper motion. However, the ALMA array operating in Band 6 is able to resolve the 1.3 mm line in HH30 to 14 AU (ALMA Partnership, 2017)(3); furthermore, the James Webb Space Telescope's NIRCam instrument, which has a lower wavelength limit of 600 nm, promises the capability to resolve details of H-α emission down to 4.5 AU at this distance (STScI, 2017)(76).

The structures in the 280+ km/s range are the most discrete and separable. These small fast moving knots lie close to the source and the variable velocity signal that creates them by shocking the jet column material relaxes to the mean jet velocity within 40 AU. In our models the velocity signal is sinusoidal but in practise may be stochastic in nature, though with an average period of the order of 2 months (Estalella et al., 2012)(27). Though our channel maps indicate some entrained molecular material the detail will be below the resolution limit of ALMA; so atomic lines must suffice. The JWST seems to offer the best prospect for their detection. In the ORB.1 model only, the moving train of knots persists in the 20-280 km/s range (see Fig.6.21); in other models the knots are observationally overwhelmed by emission from other material in the same velocity range, or physically destroyed by contact with the dense molecular secondary outflow.

The other candidates for optical detection are the slow-moving irregular lobes of H-α that appear in the 0-5 km/s channel of the ORB.2 model (Fig.6.23). However no observations of HH30 have so far revealed anything like these structures.

Moving inhomogenous structures do appear in the ^{12}CO 1.3 mm line in our channel maps, but their length scales are a few AU and below even ALMA's spatial resolution capability; though the overall larger-scale morphology of the molecular flow should be determinable even if proper motions remain unseen. However the emission line profile seems the most reliable way of differentiating between models using 1.3 mm observations (see Fig.6.20).

Following on from the velocity channel maps, Table 6.7 lists discussion comments on the physical interpretation of figures 6.21 through 6.24. Additional channel maps are given in Appendix H; these include a set of maps for another time frame (t=87.5 years); and emission lines [SII], [OI], and [FeII], for further interest.

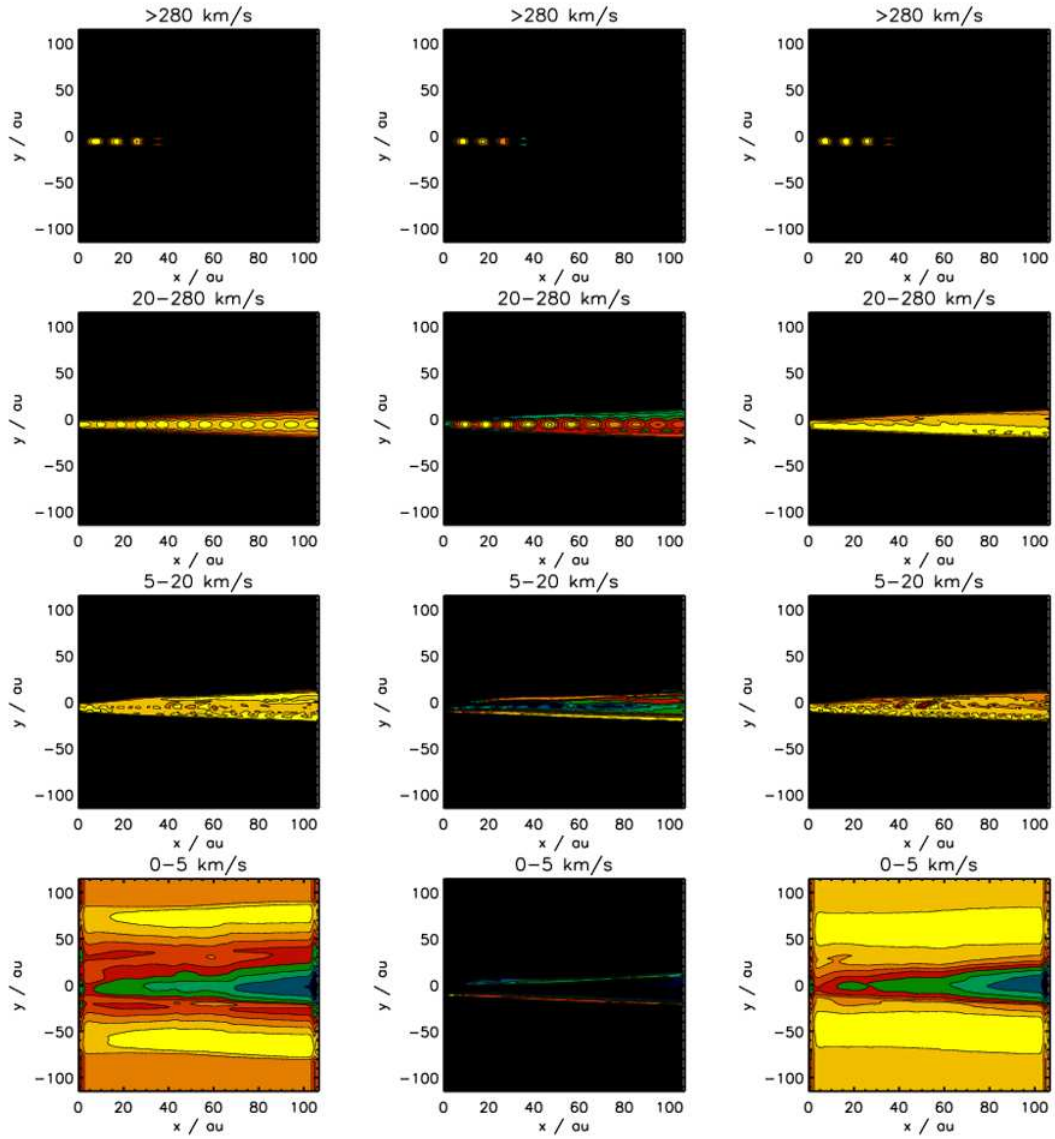

(a) column density (b) H-α, 656.28 nm (c) ^{12}CO, 1.3mm

Figure 6.21: **Model: ORB.1, V_x Channel Maps for ρ_c, H-α, ^{12}CO J=2-1**. Simulation time T=175 Years. Dual atomic-molecular outflows from co-orbiting sources. Axis scales are in Astronomical Units. Note x axis is 2 times y axis scale. Notional 30-contour colour scaling (yellow = highest, blue = lowest, black = zero) indicates column density of, or depth-integrated radiant flux produced by, material in motion within the indicated velocity bounds. Plots are scaled independently

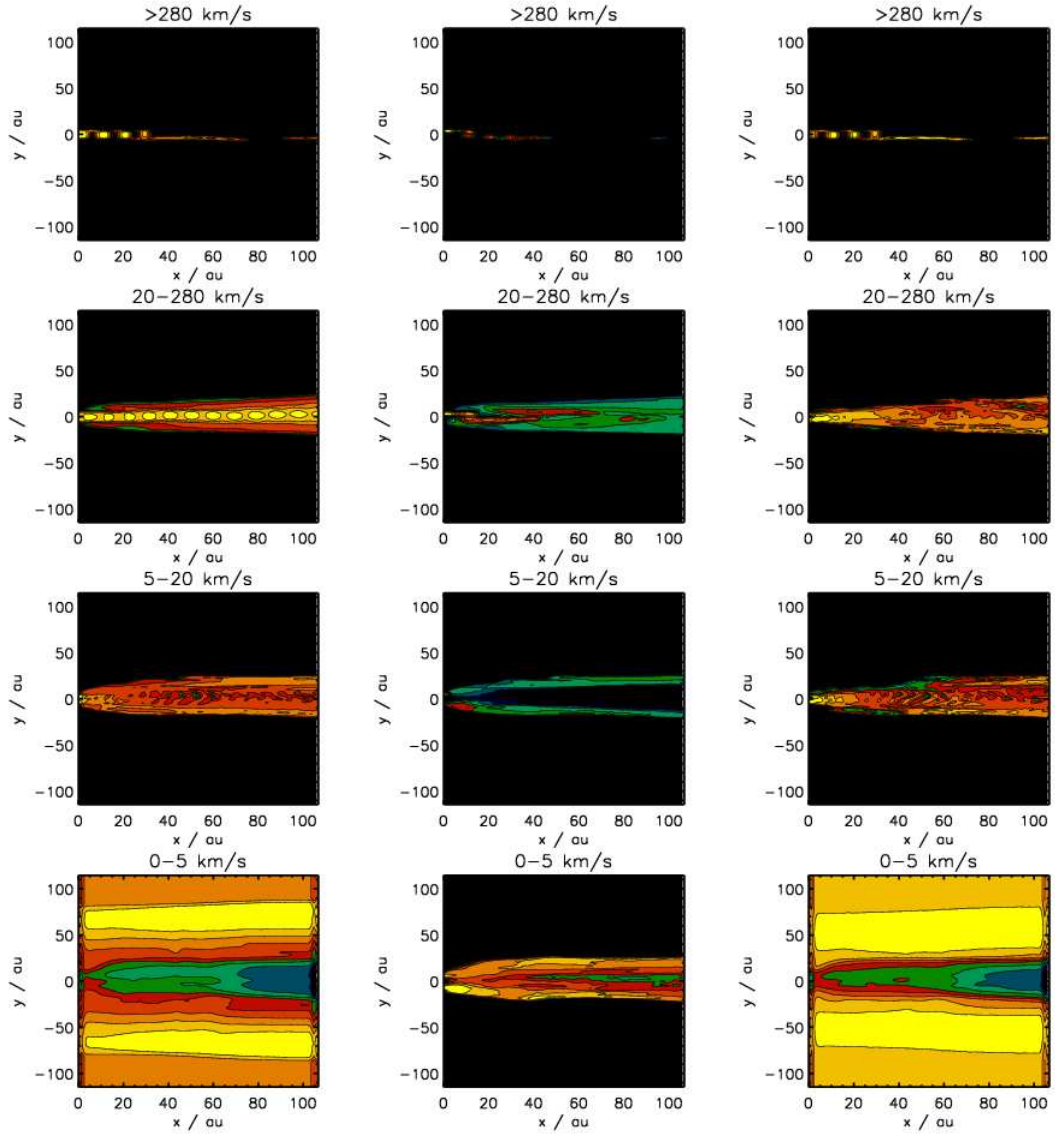

(a) column density (b) H-α, 656.28 nm (c) ^{12}CO, 1.3mm

Figure 6.22: **Model: PRE.1, V$_x$ Channel Maps for ρ_c, H-α, ^{12}CO J=2-1**. Simulation time T=175 Years. Small-orbit atomic outflow, circumbinary molecular flow. Axis scales are in Astronomical Units. Note x axis is 2 times y axis scale. Notional 30-contour colour scaling (yellow = highest, blue = lowest, black = zero) indicates column density of, or depth-integrated radiant flux produced by, material in motion within the indicated velocity bounds. Plots are scaled independently.

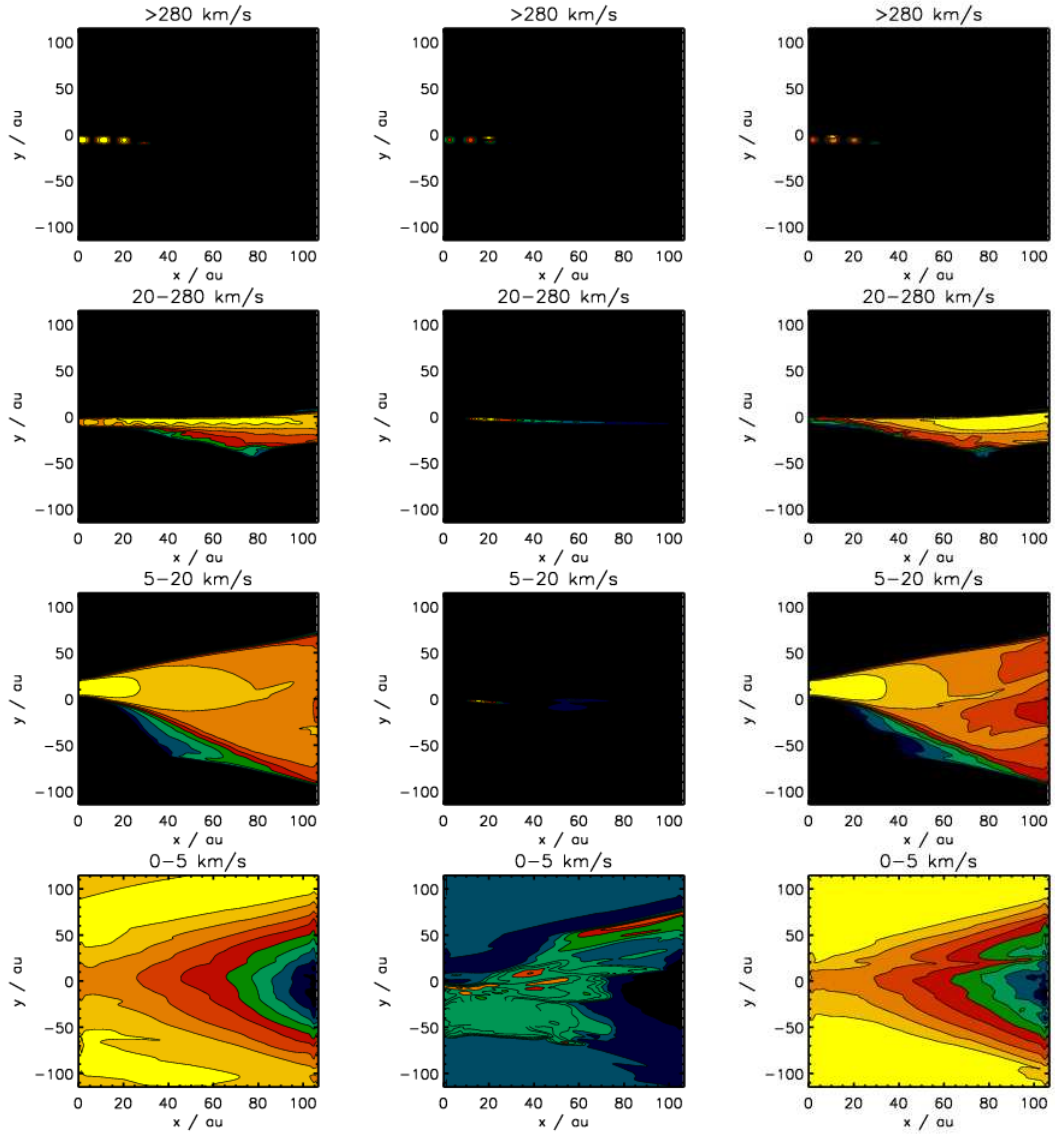

(a) column density (b) H-α, 656.28 nm (c) ^{12}CO, 1.3mm

Figure 6.23: **Model: ORB.2, V_x Channel Maps for ρ_c, H-α, ^{12}CO J=2-1**. Simulation time T=175 Years. Dual atomic-molecular outflows from co-orbiting sources. Axis scales are in Astronomical Units. Note x axis is 2 times y axis scale. Notional 30-contour colour scaling (yellow = highest, blue = lowest, black = zero) indicates column density of, or depth-integrated radiant flux produced by, material in motion within the indicated velocity bounds. Plots are scaled independently

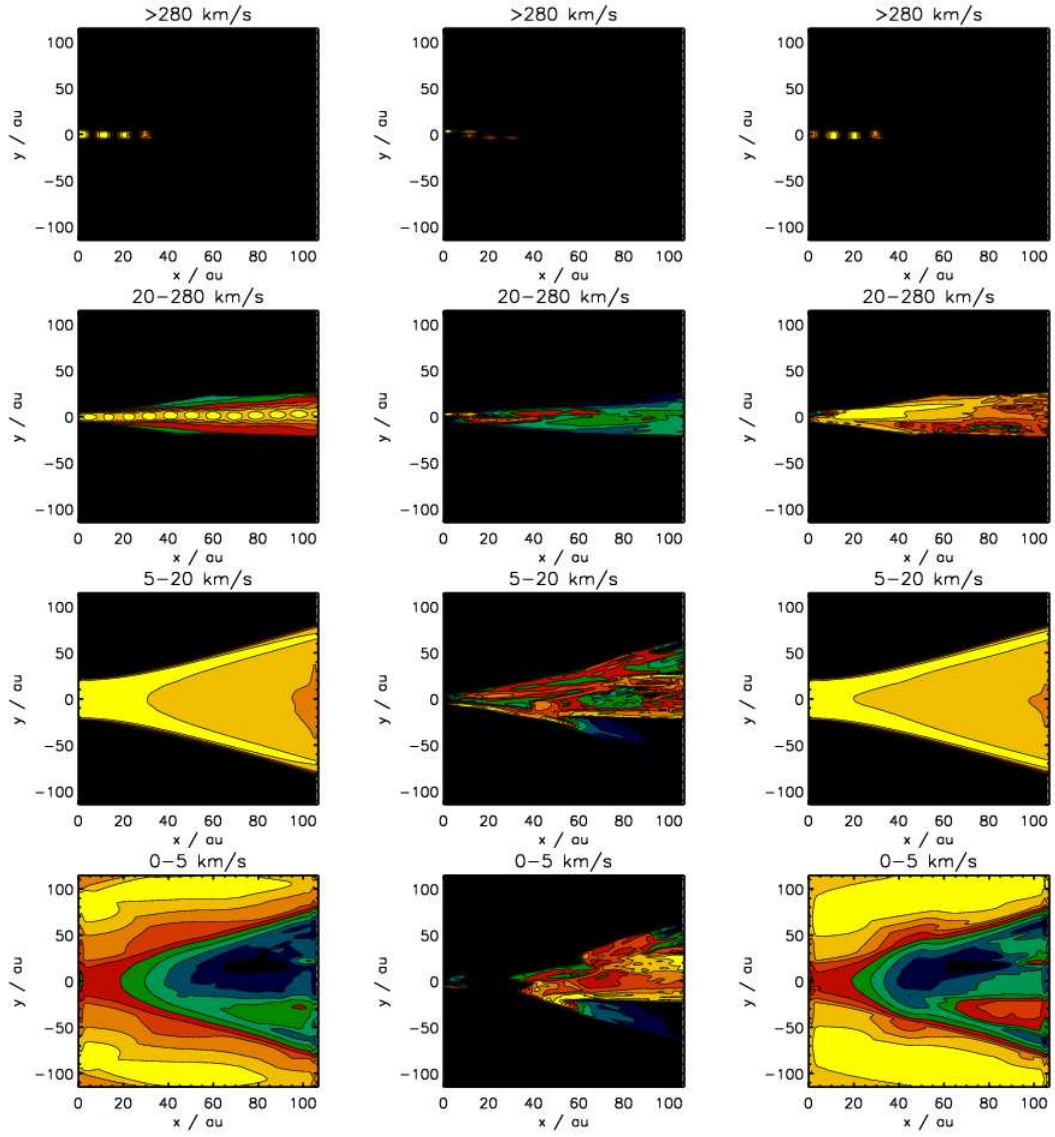

(a) column density (b) H-α, 656.28 nm (c) ^{12}CO, 1.3mm

Figure 6.24: **Model: PRE.2, V$_x$ Channel Maps for ρ_c, H-α, ^{12}CO J=2-1**. Simulation time T=175 Years. Small-orbit atomic outflow, circumbinary molecular flow. Axis scales are in Astronomical Units. Note x axis is 2 times y axis scale. Notional 30-contour colour scaling (yellow = highest, blue = lowest, black = zero) indicates column density of, or depth-integrated radiant flux produced by, material in motion within the indicated velocity bounds. Plots are scaled independently.

Table 6.7: Physical interpretation of the Velocity Channel Maps for H-α & ^{12}CO J=2-1

Model	Emission	km/s	Discussion
ORB.1	^{12}CO 1.3mm	0-5	Background cold ambient molecular material surrounds warmer molecular material entrained by the expanding bow shock around the jet column
		5-20	Ambient molecular material undergoes secondary entrainment by the jet cocoon's outer layers
		20-280	Ambient molecular material entrained by jet cocoon, inner layer; most occupies the lower end of velocity range
		280+	Ambient molecular material locally entrained by jet column; trace amount, short-lived
	H-α 653nm	0-5	Small amounts of emitting material decelerated into the lower velocity range in the cocoon's outer layer
		5-20	As above, but more emitting material found in this velocity range
		20-280	Highest degree of ionisation occurs in the working surfaces of the pulsed jet; ionised material escapes laterally to the jet cocoon
		280+	Ionised material in internal working surfaces in the highest velocity range, close to the jet source; the velocity signal flattens out to the mean velocity after 40AU
ORB.2	^{12}CO 1.3mm	0-5	Background ambient molecular material surrounds central region increasingly devoid of slow-moving molecular material due to expanding conical molecular outflow
		5-20	The expanding secondary molecular outflow is evident from the conical morphology of material in this velocity range
		20-280	Molecular material, mainly from the secondary outflow (from 20AU+) has been entrained by the atomic jet passing through the cone
		280+	Ambient molecular material locally entrained by the jet column before impact with the secondary outflow; trace amount, short-lived
	H-α 653nm	0-5	Most of the H-alpha emitting material is in this velocity range; generated at the shearing shock interface between the fast atomic jet and slow-moving molecular outflow and then pouring out into the low-density cavity left in the orbiting jet's wake.
		5-20	Minimal amounts of emitting material in this velocity range
		20-280	Some emitting material generated at the shear shock interface is entrained by the fast-moving atomic jet
		280+	Ionised material in internal working surfaces in the highest velocity range, close to the jet source; these structures do not persist beyond contact with the secondary molecular flow
PRE.1	^{12}CO 1.3mm	0-5	Background cold ambient molecular material surrounds warmer molecular material entrained by the expanding bow shock around the jet column
		5-20	Ambient molecular material undergoes secondary entrainment by the jet cocoon's outer layers
		20-280	Ambient molecular material entrained by jet cocoon, inner layer; most occupies the lower end of velocity range
		280+	Ambient molecular material locally entrained by jet column, but entrainment occurs across a longer span of the jet column than for ORB.1; suggesting that either the smaller orbit, or the precession angle, is increasing the efficiency of entrainment
	H-α 653nm	0-5	H-alpha emitting material surrounds the tightly orbiting jet column, produced by the screw-thread ionisation shock and escaping to form the cocoon
		5-20	Further traces of ionised cocoon material appear in this velocity range
		20-280	Ionised material in this range, also generated by the peripheral screw-thread shock, is internal to the jet column and swept downstream at the jet velocity
		280+	Traces of ionised material within the jet in the highest velocity range; the velocity signal flattens out to the mean velocity after 40AU
PRE.2	^{12}CO 1.3mm	0-5	Background ambient molecular material surrounds central region increasingly devoid of slow-moving molecular material due to expanding conical molecular outflow
		5-20	The expanding secondary molecular outflow is evident from the conical morphology of material in this velocity range; the hollow cavity inside the cone is also evident
		20-280	Molecular material, mainly from the secondary outflow, is entrained by the outer layers of the atomic jet cocoon. The temperatures in the cocoon rise along its length and the molecules do not survive; most of this material is gone by 60AU distance from source
		280+	Ambient molecular material locally entrained by jet column; trace amount, short-lived
	H-α 653nm	0-5	The cocoon of slow-moving H-alpha emitting material produced by the peripheral screw-thread ionisation shock fills the cavity within the conical molecular flow
		5-20	Further traces of ionised cocoon material appear in this velocity range
		20-280	Ionised material in this range, also generated by the peripheral screw-thread shock, is internal to the jet column and swept downstream at the jet velocity
		280+	Traces of ionised material within the jet in the highest velocity range; the velocity signal flattens out to the mean velocity after 40AU

6.6 Four-Scenario Synthetic Image Comparison

We end this chapter with a look at synthetic images resolved in two dimensions. Figures 6.25 through 6.27 that follow were generated by MULTISYNTH, and show optical or near-IR emission as 24-bit RGB false colour maps accompanied by contours indicating the presence of molecular material. They depict the four principal simulations ORB.1, ORB.2, PRE.1 and PRE.2 (See tables 5.2 & 5.3 for ZEUS-MP setup parameters of these models).

Three image sets are presented here:

- H-α 656.28 nm
- [SII] 671.7 nm
- [FeII] 1.64 μm

In the models that include a secondary molecular outflow, ^{12}CO 1.3 mm emission is also depicted. The optical and near-IR emission is smoothed over a radius of 11 grid zones in order to emulate the spatial resolution limit of the HST WFPC2, 0.1" or 14 AU at a distance of 140pc. The molecular ^{12}CO emission is unsmoothed, the contours indicating the positioning of the molecular outflow so that its influence on the optically-emitting material is made clear.

The synthetic emission of either of the Precessional models can be seen as morphologically similar to the HH30 jet as imaged so far by the HST (compare Fig. 6.25 with Fig. 3.5, in particular the region where the optical jet is seen emerging from the 'bowl') .

There appears to be a 'protrusion' on the upper side of the jet in the Precessional model PRE.2 visible in the H-α line which actually marks the boundary of some denser, atomic gas which is being impacted by gusts of hotter, lighter material in the jet periphery. This is a feature that is gradually being eroded in the underlying physical model.

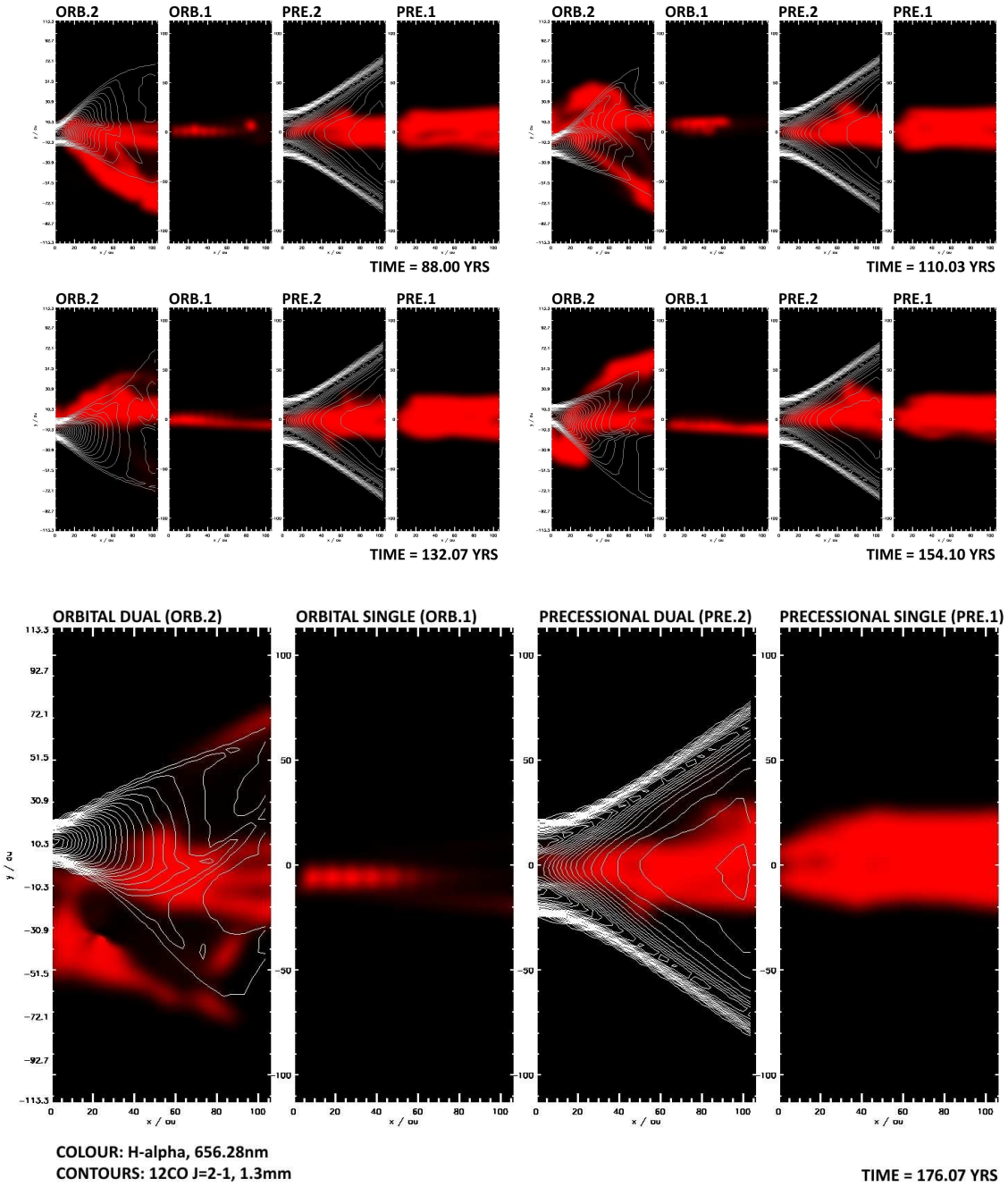

Figure 6.25: Synthetic H-α Four Model Plot at 88, 110, 132, 154 and 176 years (from top left, L->R and downwards). False colour optical emission, smoothed with 14AU radius to match HST/WFPC2 pixel resolution of 0.1" at 140pc. Contours indicate molecular material (unsmoothed).

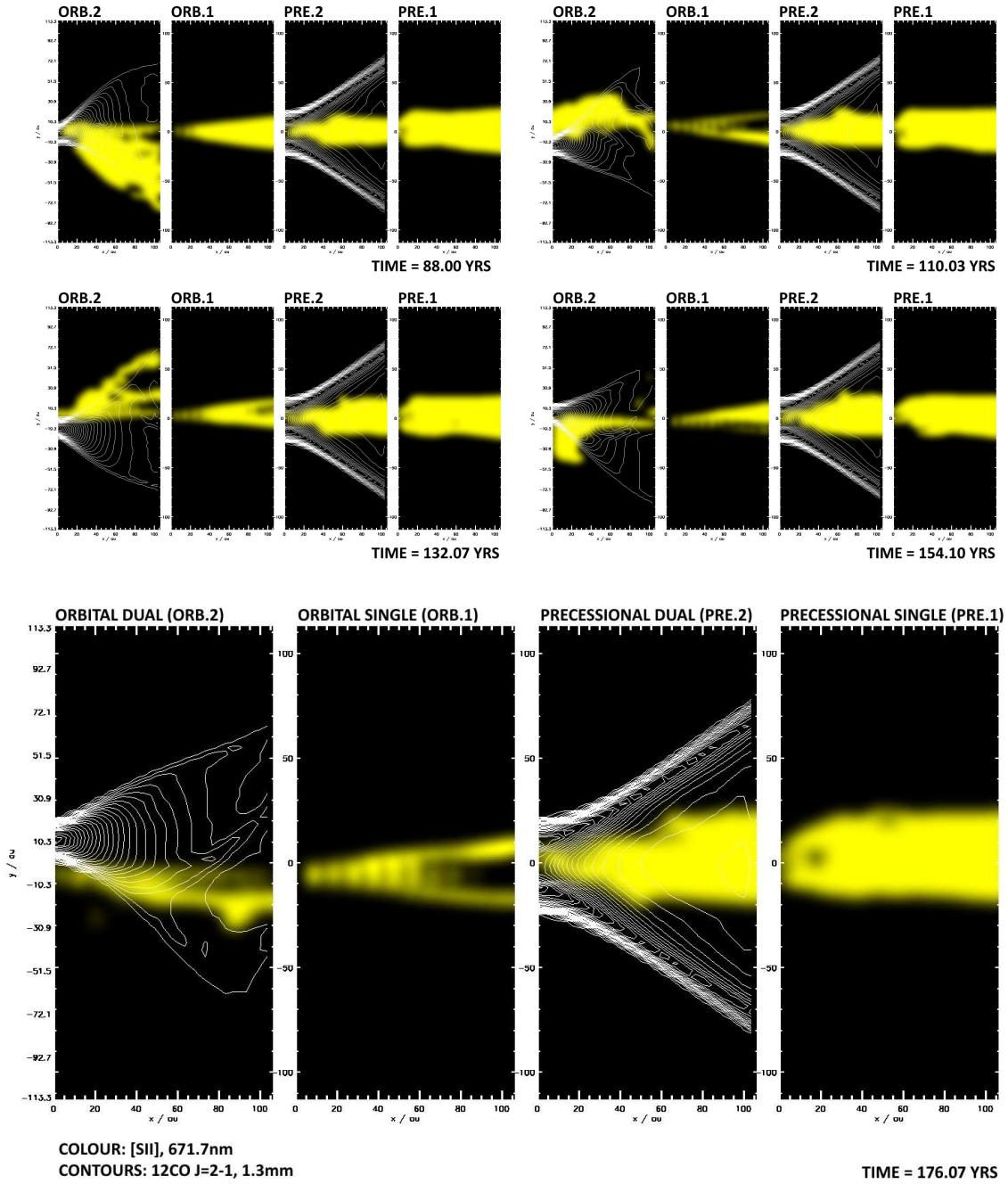

Figure 6.26: Synthetic [SII] 671.7nm Four Model Plot at 88, 110, 132, 154 and 176 years (from top left, L->R and downwards). False colour optical emission, smoothed with 14AU radius to match HST/WFPC2 pixel resolution of 0.1" at 140pc. Contours indicate molecular material (unsmoothed).

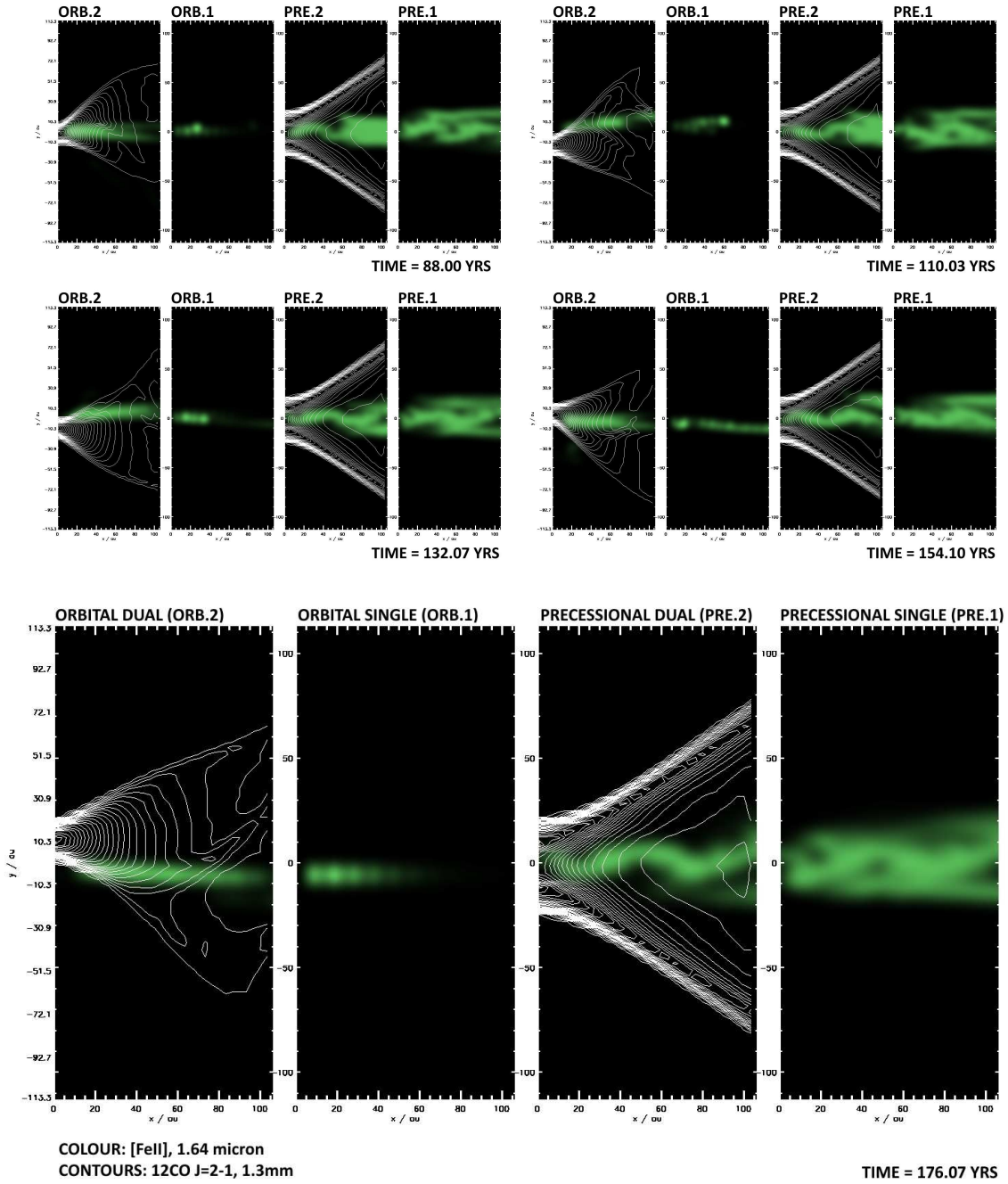

Figure 6.27: Synthetic [FeII] 1.64 μm Four Model Plot at 88, 110, 132, 154 and 176 years (from top left, L->R and downwards). False colour NIR emission, smoothed with 14AU radius to match HST/WFPC2 pixel resolution of 0.1" at 140pc. Contours indicate molecular material (unsmoothed).

6.7 Chapter Summary

1. Synthetic image generation has been discussed; the in-house MULTISYNTH post-processing code for IDL® has been introduced and the program structure explained. Emission lines currently implemented in MULTISYNTH have been examined.

2. Mass-Velocity spectra for the three Hydrogen species and total mass were determined for the four principal models, viewed at angles of 15°, 30°, 45°, & 60° for comparison with the m-v spectra of other T-Tauri stars that may have a dual-outflow system similar to HH30 seen from different viewing angles. Values of γ for blue-shifted material were calculated for a velocity scheme of 1-2, 2-10, 10-50 and 50-250 km/s.

3. For the dual-outflow models, the total mass m-v spectrum and molecular Hydrogen m-v spectrum both exhibit a shallow/inverted γ 'plateau' in the low velocity range up to 10 km/s; the width of the plateau diminishes as viewing angle increases (see Fig. 6.3). The Precessional model has a distinctive 'dip' rising to a 'mini-hook' in this low-velocity region that is absent from the Orbital model plots.

4. Both models exhibit a 'break point' and a 'cliff drop' in the m-v spectrum soon after 10 km/s at all viewing angles. The drop is less steep in the Orbital model, due to additional mass in the third (10-50 km/s) velocity range. This is atomic material that has been slowed by the jet's passage through the molecular wind, and molecular material that has been entrained. The molecular Hydrogen plots confirm the entrainment of molecular material into the 10-50 km/s range in the Orbital model. This is not present in the Precessional model.

5. The molecular wind 'break point' even appears in the atomic Hydrogen m-v spectra for the dual-outflow models (see Fig. 6.6). There is no analogous break-point in the spectra for the atomic-only control models. This suggests a means of inferring the presence of a molecular outflow when direct detection is poor or the proximity of a molecular flow to an atomic jet is uncertain.

6. Mass-Velocity spectra for the three Hydrogen species and total mass were determined for the four models, at a shallow angle (1°), for four time frames. Average values of γ were determined for a velocity scheme of 2-4, 4-8, 8-16, 16-32 km/s, for both blue-shifted and red-shifted material. These shallow-angle spectra are suitable for comparison to HH30.

7. All but two γ values are greater in the dual atomic/molecular outflow models than in the atomic-only control models. There is an approximate symmetry to the γ values for the red/blue-shifted material in the Precessional model, in the three lower velocity ranges; this symmetry is absent in the Orbital γ values (see Fig. 6.15). Orbital γ values are also more variable than those for the Precessional model.

8. Synthetic position-velocity diagrams have been presented (Figs. 6.17 through 6.20 and Appendix I). The ^{12}CO 1.3 mm emission line appears to offer the most reliable differentiator of molecular outflow from an orbital partner (ORB-like) or circumbinary disc (PRE-like), the latter possessing a double-peaked emission line compared to the single peak of the former.

9. Optical emission lines are quite time-variable and appear to be less reliable predictors than the molecular line. Lines for the PRE.2 model do exhibit a double peak but only when sampled quite close to the jet source ($\sim$ 0.133"). The main peaks are blue-shifted in optical emission lines for all models except ORB.1 which has a peculiarly red-shifted peak with a very high degree of variability (see Fig. 6.18). However this result is suspect, for reasons discussed.

10. Synthetic velocity channel maps have been presented (Figs. 6.23 & 6.24 and Appendix H). The velocity channel maps suggest that the principal differentiator between Orbital and Precessional models in terms of proper motion of emitting material, is that in the Orbital model most of the material producing H-α emissions may be found in the lower velocity range: 0-5 km/s. While in the Precessional model more H-α material is found in the middle ranges, 5-20 km/s and 20-280 km/s.

11. Observational comparison to the synthetic velocity channel maps will prove difficult due to the high angular resolution required to identify structures smaller than 10 AU exhibiting proper motion. ALMA and, eventually, JWST offer prospects for resolving these structures in molecular and optical emission respectively, with the latter's NIRCam instrument required to resolve knots from stochastic short-period pulses in the jet within 20-40 AU of the jet source.

12. Resolved synthetic image comparisons have been presented of the four principal models (see Figs. 6.25 through 6.27). The ionisation flares identified in Chapter 5 as being a feature of the Orbital model (see Fig. 5.12) are placed in an observational context here as they produce spectacular outbursts of H-α emission close to the base of the jet. By contrast the Precessional model results in a more collimated morphology of optical emission; and this is evidently a narrower collimation in the presence of the circumbinary molecular wind.

Chapter 7

Coda

7.1 Observational Comparisons

7.1.1 Synthetic vs Observed Image in H-α

The jets and outflows of HH30 are, in one sense, in a particularly fortuitous arrangement for observation due to the edge-on view of the system with respect to the accretion disc which places the jets almost in the sky plane. However, this comes at a price in terms of modelling the system if, as we have shown in this thesis, the wide-angled molecular wind is to be included in the model. This necessitates a larger computational problem domain in the horizontal, if the jet axis is vertical. In our simulations, constraints on computing resource resulted in a relatively short span of jet being modelled. This was justified by considering that in a dual-outflow arrangement the differences between scenarios would be most evident in the region not far from the launch site(s).

Our synthetic images do certainly show some clear differences in morphology between some of the scenarios. The large-orbit models ORB.1 and ORB.2, the first a standalone atomic jet, the second including a wide-angle molecular flow from a secondary object, have very clear differences in morphology. Furthermore, it is difficult to justify either of these models when viewed in context together with the HST images of HH30 (see Fig. 7.1; the reader may also wish to re-examine Fig. 5.1, and Tables 5.2 and 5.3 to be reminded of the geometry and launch parameters of these jets).

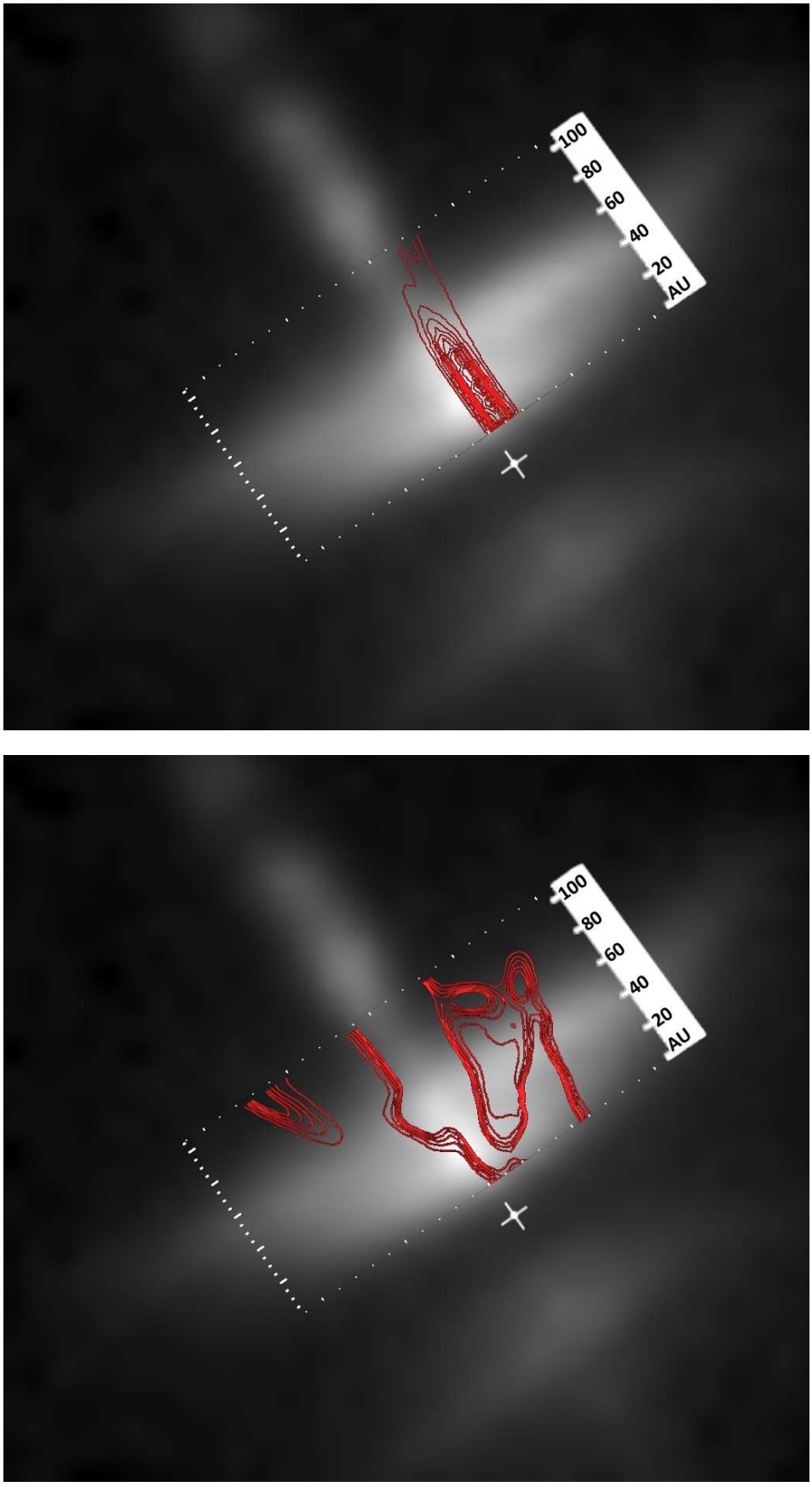

Figure 7.1: Synthetic H-α vs HST/WFPC2 Observation; Orbital Models ORB.1 (upper panel) and ORB.2 (lower panel). Contours are linear and notional, for morphological comparison. FITS data courtesy of the NASA HST Archive.

These figures illustrate the main drawback with our short-domain models when compared with an edge-on system like HH30; the presence of the illuminated 'bowl' of the accretion disc itself makes direct comparison with the section of the jet close to the source object difficult.

There is one sense in which the ORB.2 model is attractive, with its lateral flaring of ionised material, in that it might afford a new explanation for the variable luminosity seen in the disc of HH30, which has previously been explained by accretion flaring events or transiting material clumps orbiting in the disc itself. However in our ORB.2 simulation these luminous outbursts from the side of the jet appear to extend well beyond the luminous region of the accretion disc. As seen in the lower panel of Fig. 7.1, knots of strongly emitting material actually exit the far boundary of the problem domain in a wide angle. This occurs with such frequency during the simulation that it seems unlikely this behaviour would have escaped attention during the Hubble observations of HH30. Nevertheless, some smaller-scale version of this arrangement that dissipates less jet power into the lateral flaring events remains an intriguing possibility.

However, from this point forward we set aside the ORB.x models as self-evidently failing to produce an optical jet that matches observation, and turn our attention to the small-orbit, "precessional" models PRE.1 and PRE.2 models. These are seen in context with observation in Fig. 7.2.

It is less straightforward to intuitively decide which of these scenarios more closely resembles the optical jet in HH30. Here the disc luminosity is a hindrance to visual comparison. From the work of Tambovtseva & Grinin (2008)(118) and Pety et. al. (2006)(81), a molecular flow is expected to be present and emerging from the inner parts of the circumbinary disc, as has been implemented in PRE.2 so we may be more inclined to prefer this model. However a more careful examination is called for.

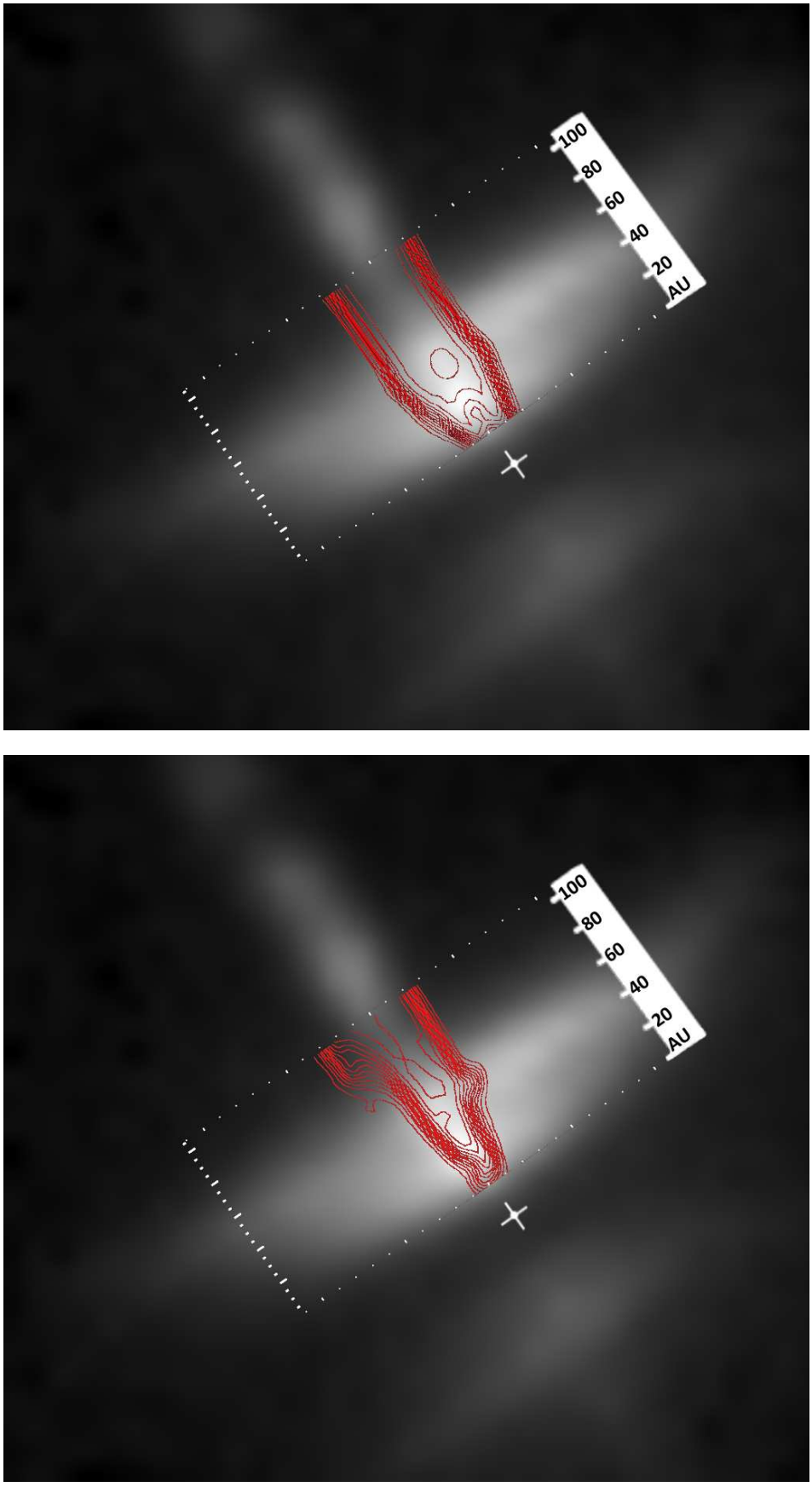

Figure 7.2: Synthetic H-α vs HST/WFPC2 Observation; Precessional Models PRE.1 (upper panel) and PRE.2 (lower panel). Contours are linear and notional, for morphological comparison. FITS data courtesy of the NASA HST Archive.

Efforts were made to produce an image from an HST archive observation in which the jet was isolated from the accretion disc. For each candidate image a mask was produced that might provide an approximate subtraction of the disc luminosity from the foreground. Eschewing a mathematically rigorous approach in favour of a simpler heuristic proof of concept at this stage of investigation, the mask was constructed using the luminous 'wings' to either side of the jet and the central gap was in-filled using stretched strips of the image cut from either side of the gap and blended in the centre with a freeform blurring tool in Corel PHOTOPAINT®. Figure 7.3 shows the most successful outcome from this process. An 8-bit grey-scale TIFF image was generated from HST FITS data file hst_08771_04_wfpc2_f675w_wf_drz with linear scaling and a suitable choice of reference pixels for maximum (white) and minimum (black) that excluded low-intensity background noise from the range. The mask was then constructed and subtracted from the image, isolating the jet component. The mask is non-ideal, as we have no way of rigorously discriminating between the foreground H-α luminosity in the disc and the luminosity of the jet itself; other portions of the disc demonstrate that its luminosity is not smoothly distributed. However for our purposes all the synthetic images to be compared to the observational image would be operating at similar disadvantage. Whilst we cannot consider the masked image to be a 'true' image of the HH30 jet it does an acceptable job of isolating the general morphology.

Synthetic images in H-α were selected from four time frames in the PRE.1 and PRE.2 models and rotated to align with the observational image. A mirrored version of each was also produced so that both 'handedness' of synthetic observation could be tested against. These were generated as 8-bit grey-scaled images with the intensity sharing a common scaling with the observational image. Figure 7.4 shows thumbnails of these images. Using VisIt, these synthetic images were compared to the observational image in their common spatial region and the R.M.S. difference in intensity catalogued for each one. Table 7.1 summarises these quantities scaled to the peak intensity.

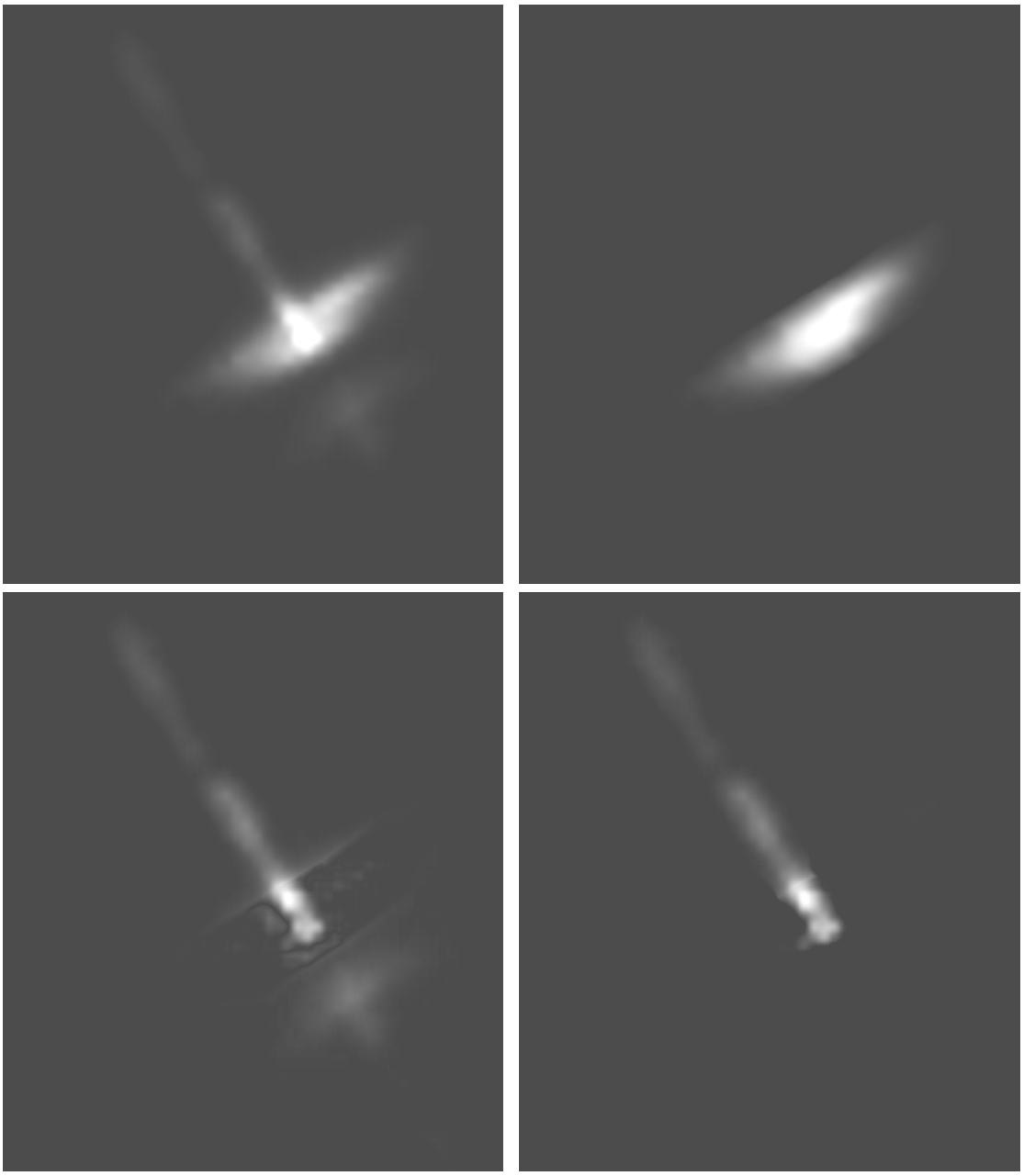

Figure 7.3: Isolating the HH30 Jet for synthetic image comparison. Top left: base image from the NASA HST Archive, taken with the WFPC2 with R-band filter in which the strongest emission line is H-α. Top right: disc mask prepared using portions of disc flanking the jet, with heuristic centre infill. Bottom left: Image with disc subtracted using mask, revealing the jet base. Bottom right: Further clean-up of non-jet material and artefacts produces final image used for comparison. (NB contrast altered from actual images for presentation purposes.)

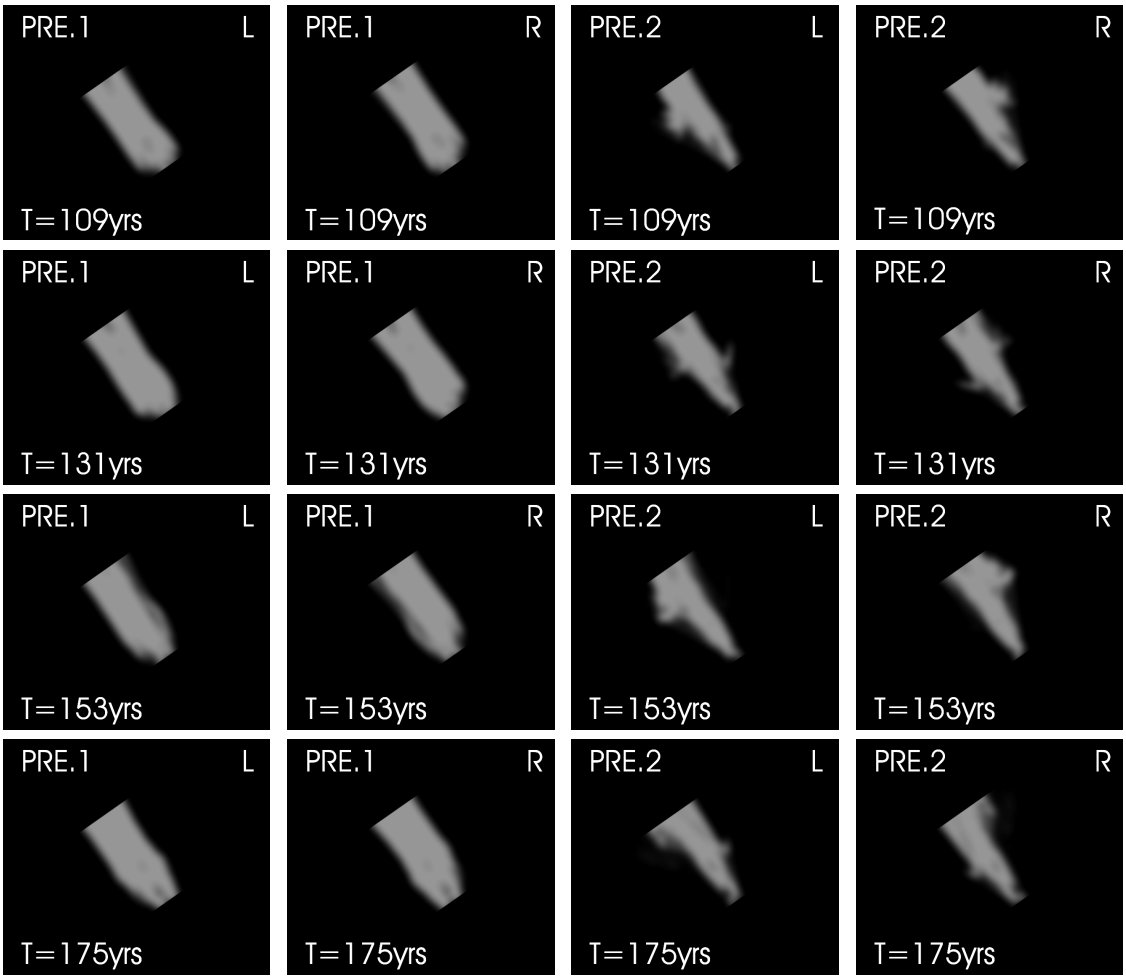

Figure 7.4: HH30 Jet Synthetic Images in H-α, selected for comparison with observational image. Linear 8-bit greyscale representation of intensity. The images show the first 100 AUs approximately of the jet propagation. Left and Right hand representations are mirrored through the plane of the jet axis perpendicular to the page.

The findings in Table 7.1 appears to validate the PRE.2 model as the most likely of our scenarios. PRE.2 has the lowest mean R.M.S. intensity variance across the four time frames in both left-handed and right-handed versions, the lowest overall mean R.M.S. intensity, and lowest minimum value. The right-handed version appears to be preferred against the left. The physical interpretation of this in the context of our model suggests that the jet precesses in a clockwise fashion with respect to its own axis, to an observer at the jet source looking in the direction of propagation. The long-term behaviour of the PRE.2 model is determined by precession; conversely, the orbital period is ~ 1 year and there is little that can be inferred about the direction of orbit from the preferred handedness of this synthetic image comparison.

Table 7.1: R.M.S. intensity difference / peak intensity: Synthetic vs Observed Jet

Time	Atomic Only		Dual Outflow		L/R Averages	
(yrs)	PRE.1 (L)	PRE.1 (R)	PRE.2 (L)	PRE.2 (R)	PRE.1	PRE.2
109	0.110	0.140	0.140	0.100	0.125	0.120
131	0.150	0.150	0.140	0.100	0.150	0.120
153	0.140	0.130	0.140	0.120	0.135	0.130
175	0.150	0.150	0.100	0.100	0.150	0.100
MEAN	0.138	0.140	0.128	0.103	0.139	0.116
STDEV	0.020	0.007	0.021	0.009	0.012	0.013
MIN	0.110	0.130	0.100	0.100	0.125	0.100

7.1.2 Further Comparisons

Hartigan & Morse (2007) found a rise in temperature for the HH30 jet over the first 100 AU of propagation, reaching 7260 K assuming a number density of 10^6. Our findings for the Precessional model accord well with this (see Fig. 5.36) and we also see a rise in ionisation over the same range, only in the dual-outflow Precessional model; in contrast, the single-outflow Precessional control model sees higher temperatures exceeding 15000 K near the launch site but declining thereafter, and the dual-outflow Orbital model also exhibits its highest temperatures in the upstream side of the domain, falling to $\sim$ 1000 K by the time the domain is traversed, possibly due to the entrainment of colder molecular material. The atomic-only Orbital control model does show a gradual rise to $\sim$ 6500 K by 100 AU, which is slightly at odds with other evidence as previously discussed, that strongly suggests that there is a molecular outflow present.

There are areas where our findings differ from Hartigan & Morse. Most notable is half-opening angle, which is found to be $2.6° \pm 0.4°$ in their study; other observers have deduced similar values. Our Precessional model including the molecular wind recollimates but at 107 AU the approximate half-opening angle from source is $\sim 5.7°$ based on cross-sectional area from Fig. 5.35. A Precessional simulation over a longer domain might find better agreement with observation.

7.2 Research Conclusions

Based on observations made by Tambovtseva & Grinin (2008)(118) and Estalella et al., (2012)(27), we have investigated two possible scenarios for the atomic jet and molecular wind outflows emerging from the North-East facing side of the binary T-Tauri star HH30 and its associated accretion disc. These are referred to as the 'Orbital' and 'Precessional' scenarios (respectively identifying the wiggle-inducing motion of the atomic source that dominates the light year scale outflow morphology in corresponding analytical models; see Fig. 5.1). Using ZEUS-MP, full 3D hydrodynamic models were implemented in Cartesian co-ordinates using 3-species Hydrogen chemistry and enhanced chemistry and cooling routines. We included two control models in our analysis, which launched identical atomic jets to the competing dual-outflow scenarios, but which lacked the molecular component.

In Chapter 5 we examined and discussed the dynamics of the four models. We found differences between the models including molecular wind, and their atomic-only control model counterparts; these differences were more significant in the Orbital case, with the orbital dynamics of the two outflows producing low-density voids in the surrounding medium, subsequently invaded and destroyed by the atomic outflow; soon after which lateral flares of ionised material, originating at the leading face of the atomic jet as it sheared through the molecular outflow, would flood into the void regions. Meanwhile in both the Precessional simulations it was evident that large amounts of ionisation were occurring in the hot periphery of the jet. It was deduced that the small-orbit jet of the Precessional model produced a continual large ionisation shock on the jet periphery due to a 73% drop in velocity; which then propagated downstream, resembling a screw-thread of ionisation wrapped around the jet. This may be a feature of jets from small-orbit sources such as close or contact binary protostars.

In the large-orbit (18 AU) Orbital control model, the primary mode of ionisation was found to be atomic jet material processed through internal working surfaces within the pulsed jet column; however this was the least active model in terms of ionisation.

Various other differences became apparent between the perturbed and unperturbed atomic jets when we studied their characteristics as a function of distance along the barycentric

axis, the x-axis of our simulation domain. The Orbital molecular flow deflected the atomic jet in an azimuthal fashion, the change in angle being $9.5° \pm 0.1°$ greater than that of the unperturbed jet over a distance of 107AU. Overall radial deflection out from the x-axis turned out to be the same in both models over 107AU, although the trend suggests that the Orbital model will eventually produce greater outward deflection leading to an expanding helical outflow structure at large distances. Examination of velocity differences between the dual-outflow and control Orbital model lends weight to this idea.

It was also found that in the presence of the co-orbital molecular outflow, the average velocity of the atomic jet material was reduced to 58% of its original value after its encounter with the molecular material, although the peak velocity did not change. A corresponding increase in mass per unit length of the outflow occurred, leading to near-conservation of the jet momentum to within 1%, while the jet cross-sectional area reduced by $\sim 35\%$ compared to control. The ionised mass in the perturbed jet was found to be 3-4 orders of magnitude greater than the control simulation in the first quarter of the domain; falling to 1 order of magnitude over the full span of the domain.

The differences between the Precessional dual-outflow simulation and its atomic-only control were less stark in most physical variables. However of particular note, is the finding that in the dual-outflow Precessional model, the jet column and its hot cocoon recollimated at $\approx$ 55AU, while the cross-section of the jet in the atomic-only control simulation continued a linear increase. This recollimation appears to be associated with a persistent region of higher-density ambient medium that 'plugs' the hollow molecular cone and was resistant to being swept aside by the peripheral jet flow over the timescale of the simulation (175 years).

We investigated the proper motion of high-density knots within the atomic jet column, and found that the knots' rate of transport was extremely close to the mean centre-line velocity of 2.746×10^7 cm/s - the knots themselves exhibiting a velocity of $2.745 \pm 0.211 \times 10^7$ cm/s, a result well within the limits of uncertainty. However, the material velocity varied dramatically about the mean during the first $\sim$ 60 AU of the propagation path, with a difference of 9.95×10^6 cm/s across the first density knot. After 60 AU the velocity variations wash out but show signs of reviving near the far edge of the domain, suggesting re-brightening.

Fourteen curves selected over a 20 year period of simulation time were averaged to determined longitudinal jet characteristics for cross-sectional area, average velocity, mass per unit length and temperature, with associated uncertainty due to the observer's lack of knowledge regarding what point in the jet evolution the observation was taking place. Lines of best fit were determined by 6th order polynomial fitting; but by breaking each curve into 2-3 regions of differing behaviour and performing linear or quadratic regression, a simpler schema for observational matching was devised. Table 5.4 summarises the coefficients found for the linear or quadratic functions, and is a key result of this research.

To assist in identification of other T-Tauri stars that may have a dual-outflow system similar to HH30, the mass-velocity spectra of our models viewed at angles of 15°, 30°, 45°, & 60° were determined. Values of γ for blue-shifted material were calculated for velocity ranges of 1-2, 2-10, 10-50 and 50-250 km/s.

It was found that the total mass m-v spectrum and molecular Hydrogen m-v spectrum both exhibit a shallow/inverted γ 'plateau' in the low velocity range up to 10 km/s for the dual-outflow models. The width of the plateau diminished as viewing angle increased. The Precessional model had a distinctive 'dip' rising to a 'mini-hook' in this low-velocity region. We did not see this feature in the Orbital spectra.

We also determined the mass-velocity spectra at a shallow angle (1°), for four time frames, suitable for comparison to HH30. We calculated average values of γ for a velocity scheme of 2-4, 4-8, 8-16, 16-32 km/s, for both blue-shifted and red-shifted material. We found that all but two γ values were greater in the dual atomic/molecular outflow models than in the controls. An approximate symmetry was noted in the γ values for the red/blue-shifted material in the Precessional model, in the three lower velocity ranges, while this symmetry was absent in the Orbital γ values. Orbital γ values were also found to be more variable than those for the Precessional model.

In the simulations that included a molecular wind, a 'break point' and a 'cliff drop' in the m-v spectrum appeared soon after 10 km/s at all viewing angles, for both scenarios (CO and CB). This 'break point' was even present in the atomic Hydrogen m-v spectra for the dual-outflow models. It did not appear at all in the spectra for the atomic-only control

models, suggesting a means of inferring the presence or absence of a molecular outflow when direct detection is poor or the proximity of a molecular flow to an atomic jet is uncertain. Meanwhile, the 'cliff drop' was less severe in the Orbital model than the Precessional. The reason for this was identified as additional mass in the third (10-50 km/s) velocity range of the co-orbital model. The molecular Hydrogen spectra confirmed the entrainment of molecular material into the 10-50 km/s range. This entrainment did not occur in the Precessional model, and this offers another key observational differentiator between the two models.

We looked at synthetic velocity channel maps, and noted that most of the optically-emitting material in the Orbital model is slow-moving (< 5 km/s) whereas in the Precessional model there is plenty of optical material above 20 km/s. And when we examined synthetic position-velocity diagrams, we found that the most reliable means of differentiating between the scenarios was the ^{12}CO J=2-1 1.3 mm emission line, which was double-peaked in the Precessional model, single-peaked in the Orbital model. Comparison with the proper motions evident in the synthetic velocity channel maps will require next-generation observations with ALMA or, eventually, the JWST to obtain sufficient spatial resolution.

We examined synthetic images in the H-α, [SII] and [FeII] emission lines. Though these images cover a short region of jet propagation, the morphology of optically emitting material that is closest to the actual HH30 jet, by visual inspection, is that of the Precessional model. We simply do not see the extended lateral lobes of optically emitting material in the HST/WFPC2 images of HH30.

Our investigations drew to a close with a more detailed comparison of the synthetic images in H-α to observation, by heuristically constructing a mask to subtract disc luminosity from the HST image and determining R.M.S. variance between synthetic and observed emission. This analysis confirms our model PRE.2, the small-orbit model of HH30 in which precession is the main driver of the large-scale 'wiggle' of the atomic jet, with an accompanying molecular outflow from the inner part of the circumbinary disc, as the most likely scenario for HH30.

7.3 Future Prospects

The work presented in this thesis may be regarded as a starting point in the investigation of dual-outflow propagation and interaction, and many future stands of research suggest themselves to build on the work presented here.

The exposition of the structure of the Orbital and Precessional scenarios in Chapter 3 has thrown into relief the dynamic differences between these arrangements. However the results presented here reflect only one choice of parameters for each of the models and their control models. Thus our practical results such as the coefficients presented in Table 5.4 have a narrow range of applicability; for example, zero or low orbital eccentricity.

There is ongoing work to investigate the effects of varying the parameters of a dual-outflow system, using the toolkit of codes and techniques we have discussed. Table 5.3 listed a number of 'short' simulation runs with different values of time period for the velocity pulses and different values of orbital eccentricity. The analysis of the results of these simulations is ongoing and is intended for future publication. So far, it appears that the variation of the pulse time period has very little, if any, effect on the overall dynamics of the dual-outflow system though the effect on synthetic emissions may be more tangible; however, initial investigation suggests that the orbital eccentricity does affect the longitudinal characteristics of the atomic jet, which will have implications for the general applicability of the results in Figures 5.39 through 5.42 and the Table 5.3 coefficients. If an empirical law can be determined that connects eccentricity to the values of coefficients in the fit functions, this will provide a useful means of constraining the eccentricity in a system where the orbital behaviour of the partners cannot be directly observed. Work on this continues.

Another ongoing strand of research is a time-domain analysis of synthetic emissions. In this, the time variation of the production of emission is examined, principally for differences between the Precessional and Orbital models. But the possibility of constraining parameters of the system also exists, in particular the time periods of various oscillations - such as jet pulsation and orbital period. A dual-outflow system produces much unpredictable and turbulent behaviour in its detailed structure and this makes extraction of these signals non-trivial and not a foregone conclusion amidst the turbulent noise.

However the work that has already been carried out on this suggests that some signals indicating the dynamic parameters of the system do remain prominent and would affect the observed photometric variability of the system. The short period pulses we have used in our atomic jet are there to mimic the stochastic fluctuations of variable accretion and their effect on the temperature and ionisation, but the possibility exists that orbital dynamics of a binary system may impose harmonic oscillations on the accretion rate and thereby, the behaviour of the jet. Early results suggest that a dedicated observing campaign, possibly by an automated space observatory such as GAIA, may be able to find these signals, after deconvolution of other sources of photometric variability. Inclusion of the research that has been carried out on this so far would have extended the length of this thesis noticeably so this has been retained for future publication.

There are many ways in which the work here may be built on by including more physics in the models. The inclusion of magnetic field advected with the jet and present in the ambient medium is likely to be a fruitful means to a better understanding of the behaviour of the dual jet system. Some observers (e.g. Hartigan & Morse, 2007 (41)) have calculated field values in the mG range present in the jet. Knowledge of the field strength in the molecular outflow remains poor. The most likely effect of magnetic fields will be stronger collimation of the ionised material in the working surfaces within the jet by magnetic hoop stresses (De Colle, Raga, Esquivel, 2008)(21). Given the vigorous nature of the lateral ionisation flares in the Orbital model and the fact that the ionised material that participates in this comes from the contact surface between the outflows, it seems unlikely this will have much effect on the morphology of emissions in co-orbital simulations. The possible effect on the characteristics of the Precessional flow seem less certain and worth investigating.

The gravity of the T-Tauri star is unlikely to change the behaviour of the 275 km/s atomic jet, but may influence the shape of the slow moving molecular outflow. More significantly, it may affect the morphology of observed emissions in the Orbital model; since the velocity channel analysis indicated that most of the H-α-emitting material in that model is moving quite slowly in the x-direction, with $V_x < 5$km/s. Close to the inlet end of the problem domain where gravity from the star is strongest there could be a significant effect on the trajectory of such slow moving material.

The relative size of the problem domain in our models limits the spatial range of observational comparison. It is an unfortunate truth that 3-dimensional models strive to compete with 2.5D simulations for size of domain and resolution. The orbital nature of our models makes axisymmetric simplification unviable. Larger models may be specified but on a practical level the computing resources they require imply lengthy queuing times on the facilities we are presently using. Nevertheless, running a larger version of the models and applying the same analysis is a simple way to expand on this research and compare with observational studies of HH30, many of which examine the jet over a spatial domain of 500-1000 AU length.

There are more configurations of dual outflows. The Concentric Model, in which both outflows emerge from the same source, was considered similar to the Precessional model and a choice was made to explore the latter for the purposes of this thesis. But there are some differences that make it worth investigating in future work. It may be that a graduated launch profile for a large radius jet in which the injected material is molecular at its outer perimeter with a graduated increase in temperature and molecular dissociation until the jet becomes hot and atomic at its centre is a more realistic model.

An intriguing configuration that warrants further investigation is one involving *three* outflows - a circumbinary molecular wind, an atomic jet from the primary and another molecular outflow from the secondary. Such a second molecular outflow has not been evident in molecular emission imaging so far, but may be below the level of detectability relative to the much more prominent circumbinary flow. If this secondary outflow interacts with the atomic jet very soon after launch, either due to being very wide in ejection angle or precessing at a steep angle, it might offer another possible explanation for the variable luminosity observed in the disc of HH30.

Bibliography

[1] Agertz O., et al., 2007. *Fundamental differences between SPH and grid methods*, Monthly Notices of the Royal Astronomical Society, 380, 3, 963-978 http://dx.doi.org/10.1111/j.1365-2966.2007.12183.x

[2] Alecian, E., 2013. *An Introduction to Accretion Disks*, The Environments of the Sun and the Stars, Lecture Notes in Physics, Volume 857, p. 183 http://dx.doi.org/10.1007/978-3-642-30648-8_7

[3] ALMA Partnership, 2017. *ALMA Basics*, website last accessed 01/11/2017 https://almascience.nrao.edu/about-alma/alma-basics

[4] ALMA Partnership, 2015. *The 2014 ALMA Long Baseline Campaign: First Results from High Angular Resolution Observations toward the HL Tau Region*, The Astrophysical Journal Letters, 808, 1, L3, 10. http://dx.doi.org/10.1088/2041-8205/808/1/L3

[5] André P., 1994. *Observations of protostars and protostellar stages in the cold Universe*, eds. Montmerle T., Lada C.J., Mirabel I.F., & Thanh Van J.T., Editions Frontières, p.179

[6] André P., et al., 2010. *From filamentary clouds to prestellar cores to the stellar IMF: Initial highlights from the Herschel Gould Belt Survey*, Astronomy and Astrophysics, 518, L102, 7

[7] Anglada G., López R., Estalella R., Masegosa J., Riera A., Raga A.C., 2007. *Proper Motions of the Jets in the Region of HH 30 and HL/XZ Tau: Evidence for a Binary Exciting Source of the HH 30 Jet*, The Astronomical Journal, 133, 6, 2799

[8] Arnaud, M., Rothenflug, R., 1985. *An updated evaluation of recombination and ionization rates*, Astronomy and Astrophysics Supplement Series, 60, 425-457. http://adsabs.harvard.edu/abs/1985A&AS...60..425A

[9] Baade, W., Minkowski, R., 1954. *Identification of the Radio Sources in Cassiopeia, Cygnus A, and Puppis A.*, Astrophysical Journal, 119, 206. http://dx.doi.org/10.1086/145812

[10] Bally, J., Sutherland, R.S., Devine, D., Johnstone, D., 1998. *Externally Illuminated Young Stellar Environments in the Orion Nebula: Hubble Space Telescope Planetary Camera and Ultraviolet Observations*, The Astronomical Journal, 116, 1, pp. 293-321. http://dx.doi.org/10.1086/300399

[11] Blandford R.D., Payne D.G., 1982. *Hydromagnetic flows from accretion discs and the production of radio jets*, MNRAS, 199, pp. 883

[12] Begelman, M.C., Blandford, R.D., Rees, M.J., 1984. *Theory of extragalactic radio sources*, Reviews of Modern Physics, 56, 2, 255-351 http://dx.doi.org/10.1103/RevModPhys.56.255

[13] Burns, J.O., Owen, F.N., 1977. *A statistical investigation of radio sources in the directions of Zwicky clusters of galaxies*, Astrophysical Journal, 1, 217, 34-44. http://dx.doi.org/10.1086/155549

[14] Chakrabarti, S. K., 1988. *On the dynamics of fluid in the working surface of a supersonic jet*, MNRAS 235, pp. 33 http://adsabs.harvard.edu/abs/1988MNRAS.235...33C

[15] Chen H., Myers P.C., Ladd E.F., Wood D.O.S., 1995. *Bolometric temperature and young stars in the Taurus and Ophiuchus complexes*, The Astrophysical Journal, 445, 1, 377

[16] Childs, H., Brugger, E., Whitlock, B., Meredith, J., Ahern, S., Pugmire, D., Biagas, K., Miller, M., Harrison, C., Weber, G.H., Krishnan, H., Fogal, T., Sanderson, A., Garth, C., Bethel, E.W., Camp, D., Rübel, O., Durant, M., Favre, J.M., Navrátil, P., 2012. *VisIt: An End-User Tool For Visualizing and Analyzing Very Large Data*,

High Performance Visualization–Enabling Extreme-Scale Scientific Insight, Oct, 357-372

[17] Clarke D.A., 1996. *A Consistent Method of Characteristics for Multidimensional Magnetohydrodynamics*, The Astrophysical Journal, 457, 291

[18] Colombo, S., Orlando, S., Peres, G., Argiroffi, C., Reale, F., 2011. *Impacts of fragmented accretion streams onto Classical T Tauri Stars: UV and X-ray emission lines*, Astronomy & Astrophysics, eprint arXiv:1607.03009. http://adsabs.harvard.edu/abs/2016arXiv160703009C

[19] Clarke D.A., 2010. *On the reliability of ZEUS-3D*, The Astrophysical Journal Supplement Series, 187, 119

[20] De Colle F., Del Burgo C., Raga A.C., 2010. *Tomographic Reconstruction of the Three-dimensional Structure of the HH30 Jet*, The Astronomical Journal, 721, 2, 929. http://dx.doi.org/10.1088/0004-637X/721/2/929

[21] De Colle F. , Raga A. C., Esquivel A. , 2008. *The Dynamics of Internal Working Surfaces in Magnetohydrodynamic Jets*, The Astrophysical Journal, 689, 302

[22] Dong, R., Draine, B.T., 2011. *H and Free-free Emission from the Warm Ionized Medium*, The Astronomical Journal, 727, 1, 35, 11. http://dx.doi.org/10.1088/0004-637X/727/1/35

[23] Downes, T. P., Cabrit, S., 2003 *The mass-velocity and intensity-velocity relations in jet-driven molecular outflows*, A&A, 403, p.135-140. http://dx.doi.org/10.1051/0004-6361:20030363

[24] Downes, T. P., Ray, T. P., 1999 *On the transfer of momentum from stellar jets to molecular outflows*, A&A, 345, p.977-985 http://adsabs.harvard.edu/abs/1999A&A...345..977D

[25] Draine B.T., 2011. *Physics of the Interstellar and Intergalactic Medium*, Princeton University Press, ISBN: 978-0-691-12214-4

[26] Esquivel A., Raga A.C., De Colle F. , 2007, Astronomy & Astrophysics, 468, 613

[27] Estalella R., López R., Anglada G., Gómez G., Riera A., Carrasco-González C., 2012. *The Counterjet of HH30: New Light on Its Driving Binary Source*,The Astronomical Journal, 144, 2, 61, 15; arXiv:1206.3391

[28] Fairbairn, A.R., 1969. *The Dissociation of Carbon Monoxide*, Proceedings of the Royal Society of London. Series A, Mathematical and Physical Sciences, 312, 1509, 207-227 http://dx.doi.org/10.1098/rspa.1969.0149

[29] Federrath, C., 2016. *On the universality of interstellar filaments: theory meets simulations and observations*, Monthly Notices of the Royal Astronomical Society, 457, 1, 375-388 http://dx.doi.org/10.1093/mnras/stv2880

[30] Fendt C., 2009. *Magnetohydrodynamic jets from different launch configurations*, Astrophysics and Space Science Proceedings, 3, 131

[31] Fiege J.D., Pudritz R.E., 2000. *Polarized Sub-Millimetre Emission from Filamentary Molecular Clouds*, The Astrophysical Journal, 544, 2, 830

[32] Field, G.B., Steigman, G., 1971. *Charge Transfer and Ionization Equilibrium in the Interstellar Medium*, Astrophysical Journal, 166, 59 http://dx.doi.org/10.1086/150941

[33] Flynn M.J., 1972. *Some Computer Organizations and Their Effectiveness*, IEEE Transactions on Computers, 21, 9 http://dx.doi.org/10.1109/TC.1972.5009071

[34] Frank A., Ray T.P., Cabrit S., Hartigan P., Arce H.G., Bacciotti F., Bally J., Benisty M., Eislöffel J., Güdel M., Lebedev S., Nisini B., Raga A., 2014. Jets and Outflows from Star to Cloud: Observations Confront Theory, Protostars and Planets VI, University of Arizona Press, 914, 451

[35] Ghildiyal, P., 2014. *MPI vs OpenMP: A Short Introduction Plus Comparison (Parallel Computing)* , Accessed online June 2016 at: http://pawangh.blogspot.co.uk/2014/05/mpi-vs-openmp.html

[36] Ginzburg, V.L., 1961. *On the Nature of the Radio Galaxies*, Soviet Astronomy, 5, 282. http://adsabs.harvard.edu/abs/1961SvA.....5..282G

[37] Greene, T.P., Wilking, B.A., Andre, P., Young, E.T., Lada, C.J., 1994. *Further mid-infrared study of the rho Ophiuchi cloud young stellar population: Luminosities and masses of pre-main-sequence stars*, The Astrophysical Journal, Part 1, 434, 2, 614-626, http://dx.doi.org/10.1086/174763

[38] Griffin, M.J., et al., 2010. *The Herschel-SPIRE instrument and its in-flight performance*, Astronomy and Astrophysics, 518, L3, 7 http://dx.doi.org/10.1051/0004-6361/201014519

[39] Guilloteau, S., Dutrey, A., Pety, J., Gueth, F., 2008. *Resolving the circumbinary dust disk surrounding HH 30*, Astronomy and Astrophysics, 478, 2, pp.L31-L34, http://dx.doi.org/10.1051/0004-6361:20079053

[40] Haro G., 1952, ApJ, 115, 572

[41] Hartigan P., Morse J., 2007. *Collimation, Proper Motions, and Physical Conditions in the HH30 Jet from HST Slitless Spectroscopy*, The Astrophysical Journal, 660, 1, 426

[42] Hartmann L., 1999. *Comparisons between the accretion flows of low- and intermediate-mass stars*, New Astronomy Reviews, 43, 1, 1

[43] Hawley, J.F., Stone, J.M., 1995. *MOCCT: A numerical technique for astrophysical MHD*, Computer Physics Communications, 89, 1-3, 127-148. http://dx.doi.org/10.1016/0010-4655(95)00190-Q

[44] Hayes J.C., Norman M.L., Fiedler R.A., Bordner J.O., Pak S.L., Clark S.E., ud-Doula A., Mac Low M-M. , 2006. *Simulating radiating and magnetized flows in multiple dimensions with ZEUS-MP*, The Astrophysical Journal Supplement Series, 165, 188. http://dx.doi.org/10.1086/504594

[45] Herbig G. H., 1951, ApJ, 113, 697

[46] Hollenbach, D., McKee, C.F., 1989. *Molecule formation and infrared emission in fast interstellar shocks. III - Results for J shocks in molecular clouds*, Astrophysical Journal, 1, 342, 306-336. http://dx.doi.org/10.1086/167595

[47] Horne, K., Marsh, T. R., 1986. *Emission line formation in accretion discs*, Monthly Notices of the Royal Astronomical Society, 218, pp. 761-773. http://dx.doi.org/10.1093/mnras/218.4.761

[48] Huarte-Espinosa M., Frank A., Blackman E.G., Ciardi A., Hartigan P., Lebedev S.V., Chittenden J.P., 2012. *Comparing Poynting-flux dominated magnetic towers with kinetic-energy dominated jets*, ApJ, 757, 66

[49] Hughes, A.M., Wilner, D.J., Andrews, S.M., Qi, C., Hogerheijde, M.R., 2011. *Empirical Constraints on Turbulence in Protoplanetary Accretion Disks*, The Astrophysical Journal, 727, 2, 85, 17, http://dx.doi.org/10.1088/0004-637X/727/2/85

[50] Hurley J. R., Aarseth S.J., Shara M.M., 2007, Astrophysical Journal, 665, 707

[51] Inutsuka, S., Miyama, S.M., 1997. *A Production Mechanism for Clusters of Dense Cores*, The Astrophysical Journal, 480, 2, 681-693 http://adsabs.harvard.edu/abs/1997ApJ...480..681I

[52] Ioannidis G., Froebrich D., 2012 *YSO jets in the Galactic Plane from UWISH2: I - MHO catalogue for Serpens and Aquila*, Monthly Notices of the Royal Astronomical Society, 421, 4, 3257

[53] Joy A., 1945 *T Tauri variable stars*, Contributions from the Mount Wilson Observatory / Carnegie Institution of Washington, vol. 709, pp.1-28

[54] Kaufman, M.J., Neufeld, D.A., 1993 *Hot Water In The ISM: Masing and Non-Masing Emission From Non-Dissociative Shocks*, Bulletin of the American Astronomical Society, 25, 1432. http://adsabs.harvard.edu/abs/1993AAS...183.9201K

[55] Keegan, R., Downes, T. P., 2005 *Long-duration simulations of the evolution of jet-driven molecular outflows*, Astronomy and Astrophysics, 437, 2, pp.517-524. http://dx.doi.org/10.1051/0004-6361:20042253

[56] Kellermann, K.I., 2003. *Obituary: Grote Reber, 1911-2002*, Bulletin of the American Astronomical Society, 35, 5, 1472-1473. http://adsabs.harvard.edu/abs/2003BAAS...35.1472K

[57] Kim J-H., Krumholtz M.R., Wise J.H., Turk M.J., Goldbaum N.J., Abel T., 2013. *Dwarf Galaxies with Ionizing Radiation Feedback II: Spatially-Resolved Star Formation Relation*, The Astrophysical Journal, 779, 1, 8, 17

[58] Krumholtz M.R., 2014. *Diffuse Matter in Space*, Astronomy 230 Lecture Series. Last accessed online at `https://sites.google.com/a/ucsc.edu/krumholz/teaching-and-courses/ast-230-s-14`

[59] Lada, C. J., Fich, M., 1996. *The Structure and Energetics of a Highly Collimated Bipolar Outflow: NGC 2264G*, Astrophysical Journal, 459, pp. 578. `http://dx.doi.org/10.1086/176929`

[60] Lazarian, A., Pogosyan, D.M., 2006. *Studying Turbulence Using Doppler-broadened Lines: Velocity Coordinate Spectrum*, The Astrophysical Journal, 652, pp. 1348-1365. `http://dx.doi.org/10.1086/508012`

[61] Lepp, S., Shull, J.M., 1983. *The kinetic theory of H2 dissociation*, Astrophysical Journal, 1, 270, 578-582. `http://dx.doi.org/10.1086/161149`

[62] Li, L-X., 2002. *Jet Collimation by Small-Scale Magnetic Fields*, Astrophysical Journal, 564, 108. `https://arxiv.org/abs/astro-ph/0108469v1`

[63] Levermore, C.D., Pomraning, G.C., 1981 *A flux-limited diffusion theory*, Astrophysical Journal, 1, 248, 321-334. `http://dx.doi.org/10.1086/159157`

[64] Lynden-Bell, D., Pringle, J.E., 2008. *The evolution of viscous discs and the origin of the nebular variables*, Monthly Notices of the Royal Astronomical Society, 168, p.603 - 637, `http://dx.doi.org/10.1093/mnras/168.3.603`

[65] Marilli E., Frasca A., Covino E., Alcalá J.M., Catalano S., Fernández M., Arellano Ferro A., Rubio-Herrera E., Spezzi L., 2007. *Rotational periods of solar-mass young stars in Orion*Astronomy & Astrophysics, 463, 3, 1081

[66] Matthews, B. C., Wilson, C. D., Fiege, J. D., 2001. *Magnetic Fields in Star-Forming Clouds: How Can FIRST Contribute?*, The Promise of the Herschel Space Observatory, ESA-SP 460, 463

[67] McCaughrean, M. J., 1997. *Direct Imaging of Circumstellar Disks in the Orion Nebula*, Accretion Phenomena and Related Outflows; IAU Colloquium 163. ASP

Conference Series, 121, 546. http://adsabs.harvard.edu/abs/1997ASPC..121..546M

[68] McKee, C.F., Storey, J.W.V., Watson, D.M., Green, S., 1982. *Far-infrared rotational emission by carbon monoxide*, Astrophysical Journal, 1, 259, 647-656. http://dx.doi.org/10.1086/160200

[69] Moraghan A., Smith M.D., Rosen A., 2006. *Velocity study of axisymmetric protostellar jets with molecular cooling*, Monthly Notices of the Royal Astronomical Society, 371, pp. 1448-1458. http://adsabs.harvard.edu/abs/2006MNRAS.371.1448M

[70] Moriarty-Schieven G.H., Johnstone D., Bally J., Jenness T., 2006. *Multigenerational Star Formation in L1551*, The Astrophysical Journal, 645, 1, 357

[71] Movsessian T.A., Magakian T.Yu., Moiseev A.V., 2012. *Kinematics and the origin of the internal structures in HL Tauri jet (HH 151)*, Astronomy & Astrophysics, 541, A16, 6

[72] Mundt, R., Fried, J.W., 1983. *Jets from young stars*, Astrophysical Journal, 2, 274, L83-L86. http://dx.doi.org/10.1086/184155

[73] Mundt, R., Buehrke, T., 1988. *A close association of five jet and outflow sources in the HL Tauri region*, Astrophysical Journal, 2, 333, L69-L72. http://dx.doi.org/10.1086/185283

[74] Mundt, R., Buehrke, T., Solf, J., Ray, T. P., Raga, A. C. 1990. *Optical jets and outflows in the HL Tauri region*, Astronomy and Astrophysics, 232, 1, 37-61. http://adsabs.harvard.edu/abs/1990A&A...232...37M

[75] Myers, P.C., Ladd, E.F., 1994. *Bolometric Temperatures of Young Stellar Objects*, The Astrophysical Journal, 413, 47-50, http://dx.doi.org/10.1086/186956

[76] Space Telescope Science Institute, 2017. *Instrumentation: NIRCam*, website last accessed 01/11/2017 https://jwst.stsci.edu/instrumentation/nircam

[77] Norman M.L., 2000. *Introducing ZEUS-MP: A 3D, Parallel, Multiphysics Code for Astrophysical Fluid Dynamics*, Astrophysical Plasmas: Theory, Codes & Models, pub. Astronomy & Astrophysics, Last accessed at http://arxiv.org/pdf/astro-ph/0005109v1.pdf (23 Jan 2016)

[78] Norman M.L., Smarr L., Winkler K.-H.A., Smith M.D., 1982. *Structure and Dynamics of Supersonic Jets*, Astronomy & Astrophysics, 113:285-302. http://adsabs.harvard.edu/abs/1982A&A...113..285N

[79] Orlando S., Reale F., Peres G., & Mignone A., 2011. *Mass accretion to young stars triggered by flaring activity in circumstellar discs*, Monthly Notices of the Royal Astronomical Society, 415, 3380–3392. http://dx.doi.org/10.1111/j.1365-2966.2011.18954.x

[80] O'Sullivan S., Ray T.P., 2000. *Numerical simulations of steady and pulsed non-adiabatic magnetised jets from young stars*, Astronomy & Astrophysics, 363, 355

[81] Pety J., Gueth F., Guilloteau S., Dutrey, A., 2006. *Plateau de Bure interferometer observations of the disk and outflow of HH 30*, Astronomy & Astrophysics, 458, 3, 841

[82] Poglitsch, A., et al., 2010. *The Photodetector Array Camera and Spectrometer (PACS) on the Herschel Space Observatory*, Astronomy and Astrophysics, 518, L2, 12 http://dx.doi.org/10.1051/0004-6361/201014535

[83] Price D.J., Bate M.J., Dobbs C.L., 2008. *Magnetic fields in star formation: from galaxies to stars*, Accessed online at https://arxiv.org/abs/0804.4647v1

[84] Pudritz R., Norman C., 1983. The Astrophysical Journal, 274:677

[85] Pudritz R., Ouyed R., Fendt C., Brandenburg A., 2006 *Disk Winds, Jets, and Outflows: Theoretical and Computational Foundations*, Protostars and Planets V, University of Arizona Press

[86] Raga, A.C., Binette, L., Canto, J., Calvet, N., 1990 *Stellar jets with intrinsically variable sources*, Astrophysical Journal, 1, 364, 601-610. http://dx.doi.org/10.1086/169443

[87] Ramsey J.P., Clarke D.A., 2010. *Simulating protostellar jets simoultaneously at launching and observational scales*, Accepted for publication in The Astrophysical Journal 16 December 2010, Last accessed at http://arxiv.org/pdf/1012.3723v1.pdf (11 May 2012)

[88] Reber, G., 1944. *Cosmic Static*, Astrophysical Journal, 100, 279. http://dx.doi.org/10.1086/144668

[89] Reynolds, R.J., 1989. *Lower limits on the temperature and hydrogen ionization fraction in the diffuse, ionized interstellar gas*, Astrophysical Journal, 1, 345, 811-814. http://dx.doi.org/10.1086/167952

[90] Ridge, N. A., Moore, T. J. T., 2001. *A single distance sample of molecular outflows from high-mass young stellar objects*, Astronomy and Astrophysics, 378, pp. 495-508. http://dx.doi.org/10.1051/0004-6361:20011180

[91] Roddier C., Roddier F., Graves J.E., et al. 1998, *Proceedings of the ESO/OSA Topical Meeting on Astronomy with Adaptive Optics* (ed., D. Bonaccini, ESO), pp. 389-399.

[92] Rodriguez, L. F., Carral, P., Ho, P. T. P., Moran, J. M., 1982, *Anisotropic mass outflow in regions of star formation*, The Astrophysical Journal, 260, pp. 635-646. http://dx.doi.org/10.1086/160285

[93] Shapiro, P.R., Kang, H., 1987. *Hydrogen molecules and the radiative cooling of pregalactic shocks*, Astrophysical Journal, 1, 318, 32-65. http://dx.doi.org/10.1086/165350

[94] Sheikhnezami, S., Fendt, C., Porth, O.; Vaidya, B., Ghanbari, J., 2012. *Bipolar Jets Launched from Magnetically Diffusive Accretion Disks. I. Ejection Efficiency versus Field Strength and Diffusivity*, The Astrophysical Journal, 757, 1, 65, 23. http://dx.doi.org/10.1088/0004-637X/757/1/65

[95] Shklovskii, I.S., 1960. *Secular Variation of the Flux and Intensity of Radio Emission from Discrete Sources*, Soviet Astronomy, 4, 243. http://adsabs.harvard.edu/abs/1960SvA.....4..243S

[96] Schwartz R.D., 1975. *T Tauri Nebulae and Herbig-Haro Nebulae - Evidence for excitation by a strong stellar wind*, Astrophysical Journal, 195, 1, 631-642. http://dx.doi.org/10.1086/153364

[97] Sheikhnezami S., Fendt C., Porth O., Vaidya B., Ghanbari J., 2012. *Bipolar jets*

launched accretion disks. I. Ejection efficiency vs field strength and diffusivity, The Astrophysical Journal, 757, 1, 65, 23

[98] Shu F., Najita J., Ostriker E., Wilkin F., Ruden S., Lizano S. , 1994a, The Astrophysical Journal, 429:781

[99] Smith, M.D., 1994. *Strong evidence for a molecular jump shock in the HH 90/91 outflow*, Astronomy and Astrophysics, 289, 1, 256-260. http://adsabs.harvard.edu/abs/1994A&A...289..256S

[100] Smith M.D., 2004. *The Origin of Stars*, Imperial College Press, ISBN-10: 1860944892

[101] Smith M.D., 2012. *Astrophysical Jets and Beams*, Cambridge University Press, ISBN-10: 0521834767

[102] Smith, M. D., Norman, M. L., Winkler, K.-H. A., Smarr, L., 1985. *Hotspots in radio galaxies - A comparison with hydrodynamic simulations*, MNRAS 214, pp. 67-85. http://adsabs.harvard.edu/abs/1985MNRAS.214...67S

[103] Smith, M.D. & Rosen, A., 2003. *The instability of fast shocks in molecular clouds*, Monthly Notice of the Royal Astronomical Society, 339, 1, 133-147. http://dx.doi.org/10.1046/j.1365-8711.2003.06155.x

[104] Smith, M.D., Suttner, G., Yorke, H.W., 1997. *Numerical hydrodynamic simulations of jet-driven bipolar outflows*, A&A, 323, pp. 223-230 http://adsabs.harvard.edu/abs/1997A&A...323..223S

[105] Smith M.D., Suttner G., Zinnecker H., 1996. *Intermediate teeth in pulsed jets: a motivation for high resolution observations*, Astronomy & Astrophysics, 320, 325-332. http://adsabs.harvard.edu/abs/1997A&A...320..325S

[106] Smith, M.D., Volker, R., Suttner, G., Yorke, H.W., 1997. *The Class 0 Outflow Hammered Out?*, Herbig-Haro Flows and the Birth of Stars; IAU Symposium 182, 303-312. http://adsabs.harvard.edu/abs/1997IAUS..182..303S

[107] Staff J.E., Koning N., Ouyed R., A., Pudritz, R.E., 2015. *Hubble Space Telescope scale 3D simulations of MHD disc winds: a rotating two-component jet structure*

[108] Stahler S. W., 1993. *The kinematics of molecular outflows*, Astrophysical Journal, 1, 422, 2, pp. 616-620. http://dx.doi.org/10.1086/173754

[109] Stahler S. W., Palla F., 2011. *The Formation of Stars*, Wiley-VCH, ISBN: 978-3-527-40559-6

[110] Stanke T., 2000. *An unbiased infrared H2 search for embedded flows from young stars in Orion A*, Accessed online at http://arxiv.org/abs/1204.0800 (27 June 2015)

[111] Stapelfeldt, K.R., Watson, A.M., et al, 1999. *A Variable Asymmetry in the Circumstellar Disk of HH 30*, The Astrophysical Journal, 516, 2, L95-L98.

[112] Stone J.M., Norman M.L., 1994. *Numerical Simulations of Protostellar Jets with Nonequilibrium Cooling. III. Three-Dimensional Results*, The Astrophysical Journal, 420, 237

[113] Su, Y-N., Zhang, Q., Lim, J., 2004 *Bipolar Molecular Outflows from High-Mass Protostars*, The Astrophysical Journal, 604, 1, pp. 258-271. http://dx.doi.org/10.1086/381880

[114] Sutherland, R.S., Dopita, M.A., 1993 *Cooling functions for low-density astrophysical plasmas*, Astrophysical Journal Supplement Series 88, 1, 253-327. http://dx.doi.org/10.1086/191823

[115] Suttner, G., Smith, M.D., Yorke, H.W., Zinnecker, H., 1997 *Multi-dimensional numerical simulations of molecular jets.*, Astronomy and Astrophysics, 318, 595-607. http://adsabs.harvard.edu/abs/1997A&A...318..595S

[116] Suzuki-Vidal, F., et al., 2015 *Bow shock fragmentation driven by a thermal instability in laboratory-astrophysics experiments*, The Astrophysical Journal, 815, 2, 96, 9 http://dx.doi.org/10.1088/0004-637X/815/2/96

[117] Tambovtseva, L. V., Grinin, V. P., 2002. *Disk Wind in Young Binaries with Low-Mass Secondary Components: Optical Observational Manifestations*, Astronomy Letters, 28, 601-616. http://dx.doi.org/10.1134/1.1505504

[118] Tambovtseva, L. V., Grinin, V. P., 2008. *Disc wind in the HH 30 binary models*, Monthly Notices of the Royal Astronomical Society, 387, 3, 1313-1317. http://dx.doi.org/10.1111/j.1365-2966.2008.13329.x

[119] Thompson M.J., 2006. *An Introduction to Astrophysical Fluid Dynamics*, Imperial College Press, ISBN: 1-86094-633-X

[120] Downes T. P., Cabrit S. 2003. *The mass-velocity and intensity-velocity relations in jet-driven molecular outflows*, A&A. 403 (2003) 135 https://arxiv.org/abs/astro-ph/0303329v1

[121] Williams P., Cieza L.A., 2011. *Protoplanetary Disks and Their Evolution*, Annual Review of Astronomy & Astrophysics, 49, 67 http://arxiv.org/abs/1103.0556

[122] Winkler, K.-H.A., Norman, M.L., Mihalas,D., 1984. *Adaptive-mesh radiation hydrodynamics. I - The radiation transport equation in a completely adaptive coordinate system. II - The radiation and fluid equations in relativistic flows*, Journal of Quantitative Spectroscopy and Radiative Transfer, 31, 473-489. http://dx.doi.org/10.1016/0022-4073(84)90054-2

[123] Wolfire M.G., Konigl A., 1991. *Molecular line emission models of Herbig-Haro objects. I - H2 emission*, The Astrophysical Journal, Part I, Vol 383, p. 205-225, Accessed online at http://dx.doi.org/10.1086/170777 (28 June 2015)

[124] Yu, K.C., Billawala, Y., Bally, J., 1999. *Parsec-Scale CO Outflow and H2 Jets in Barnard 5*, The Astronomical Journal, 118, 6, pp. 2940-2961. http://dx.doi.org/10.1086/301123

[125] Yu, K.C., Billawala, Y., Smith, M.D., Bally, J., Butner, H.M., 2000. *A Multi-wavelength Study of Outflows in OMC-2/3*, The Astronomical Journal, 120, 4, 1974-2006. http://dx.doi.org/10.1086/301565

[126] Yu, K.C., Billawala, Y., Smith, M.D., Bally, J., Butner, H.M., 2001. *Erratum: "A Multiwavelength Study of Outflows in OMC-2/3" [Astron. J. 120, 1974 (2000)]*, The Astronomical Journal, 121, 2, 1214. http://stacks.iop.org/1538-3881/121/i=2/a=1214

[127] Zhang, Q., Zheng, X., 1997. *The Role of Bow Shocks in Bipolar Molecular Outflows*, The Astrophysical Journal, 474, 2, pp. 719-723. http://dx.doi.org/10.1086/303497

Appendices

Appendix A

Derivation of the Equations of Astrophysical Fluid Dynamics

We will examine the derivation of the Euler equations for astrophysical environments in detail; this is an expanded form of the derivation that may be found in Thompson (2006)(119).

The Continuity Equation

This equation expresses the principle of conservation of mass in a situation where matter is neither being created or destroyed to any significant degree by binding energy interactions such as nuclear fusion. Within a particular control volume of space we expect the following to hold true:

rate of mass accumulation = rate of mass influx - rate of mass eflux

We consider the net rate of mass eflux from a control volume V bounded by a surface S in the derivation that follows. Thus, if there happens to be an influx of mass into the control volume in question, this would be expressed as a negative eflux.

The control volume V exists within a time-evolving compressible fluid field of density $\rho(x, y, z)$ which advects according to a velocity field $\vec{u}(x, y, z)$. A differential element of the surface S is a vector $d\vec{S}$ given by the unit vector multiplied by the scalar area of the element dS.

The rate at which material flows out through dS will be determined by the density ρ, times the component of velocity $\vec{u}$ which is normal to the surface at that point given by $\vec{u} \cdot \underline{\hat{n}}$ or $u \cdot cos(\theta)$, times the area dS - in other words, $\rho\vec{u} \cdot d\vec{S}$ which gives the total mass eflux per second through $d\vec{S}$.

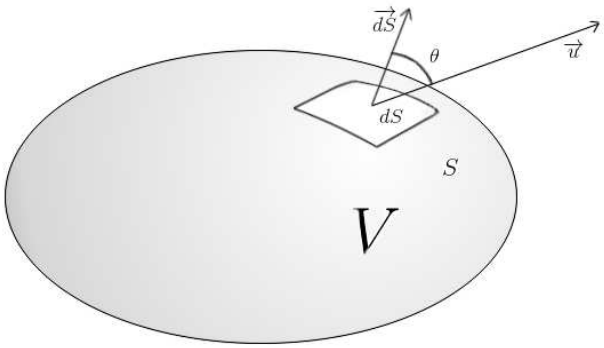

Figure A.1: Fluid Volume V showing differential surface element dS through which a fluid of density ρ flows at velocity $\vec{u}$

It follows that the overall net eflux of mass from the volume V can be found by integrating this expression over the whole surface S:

$$\oint_S \rho\vec{u} \cdot d\vec{S} \tag{A.1}$$

this by the Divergence Theorem yields:

$$\oint_S \rho\vec{u} \cdot d\vec{S} = \int_V \nabla \cdot (\rho\vec{u}) dV \tag{A.2}$$

Using the vector identity

$$\nabla \cdot (\vec{A} \cdot \vec{B}) = (\nabla \cdot \vec{A})\vec{B} + \vec{A}(\nabla \cdot \vec{B}) \tag{A.3}$$

we can expand the contents of the right-hand integral of equation $A.2$ as follows:

$$\nabla \cdot (\rho\vec{u}) = (\nabla \cdot \rho)\vec{u} + \rho(\nabla \cdot \vec{u}) \tag{A.4}$$

$$\nabla \cdot (\rho\vec{u}) = \left(\frac{\partial\rho}{\partial x}\hat{i} + \frac{\partial\rho}{\partial y}\hat{j} + \frac{\partial\rho}{\partial z}\hat{k}\right)\vec{u} + \rho(\nabla \cdot \vec{u}) \tag{A.5}$$

$$\nabla \cdot (\rho\vec{u}) = \left(\frac{\partial\rho}{\partial x}\hat{i} + \frac{\partial\rho}{\partial y}\hat{j} + \frac{\partial\rho}{\partial z}\hat{k}\right)\vec{u} + \rho(\nabla \cdot \vec{u}) \tag{A.6}$$

$$\nabla \cdot (\rho\vec{u}) = \left(\frac{\partial \rho}{\partial x}\hat{i} + \frac{\partial \rho}{\partial y}\hat{j} + \frac{\partial \rho}{\partial z}\hat{k}\right) \cdot \left(\frac{\partial x}{\partial t}\hat{i} + \frac{\partial y}{\partial t}\hat{j} + \frac{\partial z}{\partial t}\hat{k}\right) + \rho(\nabla \cdot \vec{u}) \tag{A.7}$$

$$\nabla \cdot (\rho\vec{u}) = \left(\frac{\partial \rho}{\partial x} \cdot \frac{\partial x}{\partial t} + \frac{\partial \rho}{\partial y} \cdot \frac{\partial y}{\partial t} + \frac{\partial \rho}{\partial z} \cdot \frac{\partial z}{\partial t}\right) + \rho(\nabla \cdot \vec{u}) \tag{A.8}$$

It is important to note that the velocity terms are not the velocity of a point entity undergoing translational motion in the coordinate frame, but the velocity of fluid advecting through a fixed point in space. Consider now the change in density $\delta\rho_1$ that arises at a point in space when an inhomogeneous fluid medium advects by small increments $\delta x, \delta y, \delta z$ past that point:

$$\delta\rho_1 = \frac{\partial \rho}{\partial x} \cdot -\delta x + \frac{\partial \rho}{\partial y} \cdot -\delta y + \frac{\partial \rho}{\partial z} \cdot -\delta z \tag{A.9}$$

The negative spatial increments reflect the fact that we are considering the motion of the fluid gradients with respect to our point of interest. A positive density gradient with respect to the x coordinate will only give rise to an increase in density where the motion of the fluid is in the negative sense with respect to the x coordinate.

There is another mechanism by which the density at a point in space may change, and this is by velocity divergence which will produce an influx or eflux of material at the point in proportion to the local density and the time increment δt:

$$\delta\rho_2 = -\rho \cdot \frac{\partial u_x}{\partial x}\delta t - \rho \cdot \frac{\partial u_y}{\partial y}\delta t - \rho \cdot \frac{\partial u_z}{\partial z}\delta t = -\rho(\nabla \cdot \vec{u})\delta t \tag{A.10}$$

Again, the minus signs are to ensure that positive divergence leads to a removal of material from the point of interest. Combining these two mechanisms for density change we have:

$$\delta\rho = \delta\rho_1 + \delta\rho_2 = -\frac{\partial \rho}{\partial x}\delta x - \frac{\partial \rho}{\partial y}\delta y - \frac{\partial \rho}{\partial z}\delta z - \rho(\nabla \cdot \vec{u})\delta t \tag{A.11}$$

Now express this as a rate of change by dividing by δt and allowing $\delta t \to \partial t$:

$$-\frac{\partial \rho}{\partial t} = \frac{\partial \rho}{\partial x} \cdot \frac{\partial x}{\partial t} + \frac{\partial \rho}{\partial y} \cdot \frac{\partial y}{\partial t} + \frac{\partial \rho}{\partial z} \cdot \frac{\partial z}{\partial t} + \rho(\nabla \cdot \vec{u}) \tag{A.12}$$

Thus we see that equation $A.8$ simplifies to:

$$\nabla \cdot (\rho \vec{u}) = -\frac{\partial \rho}{\partial t} \tag{A.13}$$

Substituting the R.H.S. back into equation $A.2$ yields:

$$\oint_S \rho \vec{u} \cdot d\vec{S} = -\int_V \frac{\partial \rho}{\partial t} dV \tag{A.14}$$

Applying the Liebniz Integral Rule to the R.H.S. yields the Bulk Continuity Equation for compressible flow:

$$\oint_S \rho \vec{u} \cdot d\vec{S} = -\frac{d}{dt} \int_V \rho dV \tag{A.15}$$

which can also be combined with equation $A.2$ and expressed as:

$$\int_V \nabla \cdot (\rho \vec{u}) dV = -\frac{dM}{dt} \tag{A.16}$$

the R.H.S. of which is the rate of change of total mass M within the control volume as a result of compressible flow. Collecting terms of equation $A.13$ onto the L.H.S. gives the standard conservation form of the Differential Continuity Equation:

$$\frac{\partial \rho}{\partial t} + \nabla \cdot (\rho \vec{u}) = 0 \tag{A.17}$$

Using the vector operator identity shown at $A.3$ again, we can derive the Lagrangian form of the Continuity Equation:

$$\begin{aligned} \frac{\partial \rho}{\partial t} + \vec{u} \cdot \nabla \rho + \rho \nabla \cdot \vec{u} = 0 \\ \frac{D\rho}{Dt} + \rho \nabla \cdot \vec{u} = 0 \end{aligned} \tag{A.18}$$

where the operator $\frac{D}{Dt}$ is the Material or Convective Derivative, defined as:

$$\frac{D}{Dt} = \frac{\partial}{\partial t} + \vec{u} \cdot \nabla \tag{A.19}$$

The Material Derivative expresses, at a fixed point in space, the rate of change of some intensive property expressed as a volumetric density, say p, which is being advected through that point in space by a flow field $\vec{u}(\vec{r}, t)$. If p is a conservative property, then in the absence of sources of p the relation

$$\frac{Dp}{Dt} = 0 \tag{A.20}$$

tells us that $\frac{\partial p}{\partial t}$, the rate of change of p w.r.t. time is given solely by the advection of the spatial gradients in p by the velocity field u.

$$\frac{\partial p}{\partial t} = -\vec{u} \cdot \nabla p \tag{A.21}$$

Alternatively, where property p exists as a field that the material is flowing through, then $\frac{Dp}{Dt}$ express the rate of change of p which is experienced in a local sense by an infinitesimal fluid parcel which is being advected through the field of p at velocity $\vec{u}(\vec{r}, t)$.

The Momentum Equation

We will use a slightly different method in our derivation of the Momentum equation, to illustrate an alternative approach. In our Continuity Equation derivation, we used a macroscopic control volume and constructed an integral equation from which we extracted the differential form(s) of the equation. Here we will consider a small cuboid differential volume and construct the differential form of the equation directly.

There are two mechanisms by which momentum transport occurs within a fluid; by advection, which is where the momentum is carried from place to place by bulk fluid flow, and the transport occurs in the same direction as the momentum vector itself; and by diffusion, which is viscous transport of momentum between layers moving at differing velocities. In astrophysical jets, the material is of too low a density for viscosity to play a significant role and so it is omitted from the equations; with the exception of shocks, where a form of artificial viscosity is applied by ZEUS-MP. So here we will derive the inviscid or Euler form of the Momentum Equation.

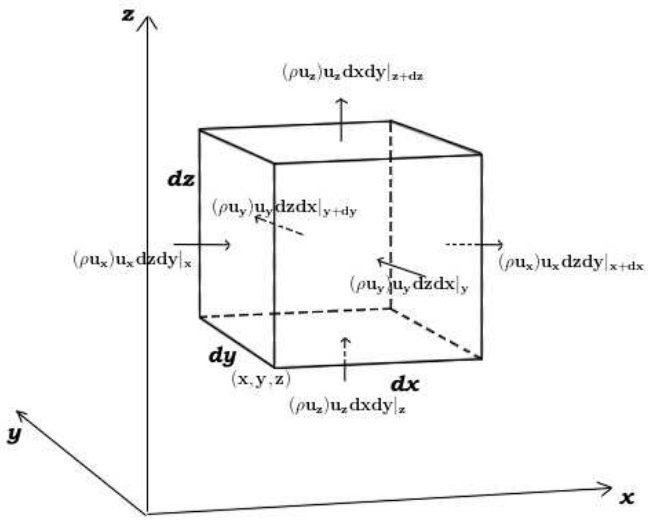

Figure A.2: Momentum transport across the faces of a cuboid differential fluid volume by advection of a fluid of density ρ flowing at velocity $\vec{u}$

Consider the advection of x-momentum Ax in the x-direction by the component of velocity u_x:

$$Ax_x\hat{i} = (\rho u_x\hat{i})u_x dzdy|_x - (\rho u_x\hat{i})u_x dzdy|_{x+dx}$$

The second term in the R.H.S. can be approximated by Taylor expansion to first order as:

$$(\rho u_x\hat{i})u_x dzdy|_{x+dx} = (\rho u_x\hat{i})u_x dzdy|_x + \frac{\partial(\rho u_x\hat{i})u_x}{\partial x}dxdydz$$

and so Ax_x simplifies to:

$$Ax_x\hat{i} = -\frac{\partial(\rho u_x\hat{i})u_x}{\partial x}dxdydz$$

There will also be advection of y-momentum Ay, and z-momentum Az in the x-direction by the component of velocity u_x:

$$Ay_x\hat{j} = -\frac{\partial(\rho u_y\hat{j})u_x}{\partial x}dxdydz\,; \qquad Az_x\hat{k} = -\frac{\partial(\rho u_z\hat{k})u_x}{\partial x}dxdydz$$

Combining these gives the total momentum change due to advection by u_x within the differential volume per interval of time:

$$Ax_x\hat{i} + Ay_x\hat{j} + Az_x\hat{k} = \vec{A_x}$$

and so

$$\vec{A_x} = -\left(\frac{\partial(\rho u_x \hat{i})u_x}{\partial x} + \frac{\partial(\rho u_y \hat{j})u_x}{\partial x} + \frac{\partial(\rho u_z \hat{k})u_x}{\partial x}\right) dxdydz$$

Product rule expansion:

$$\vec{A_x} = -\left[\left((\rho u_x \hat{i})\frac{\partial u_x}{\partial x} + (\rho u_y \hat{j})\frac{\partial u_x}{\partial x} + (\rho u_z \hat{k})\frac{\partial u_x}{\partial x}\right) + u_x\left(\frac{\partial(\rho u_x \hat{i})}{\partial x} + \frac{\partial(\rho u_y \hat{j})}{\partial x} + \frac{\partial(\rho u_z \hat{k})}{\partial x}\right)\right] dxdydz$$

Gathering terms we see that the momentum advected across the differential volume by u_x is given by:

$$\vec{A_x} = -\left((\rho\vec{u})\frac{\partial u_x}{\partial x} + u_x\frac{\partial(\rho\vec{u})}{\partial x}\right) dxdydz$$

The advective momentum change brought about by the other velocity components u_y, u_z may be derived in a similar fashion and all three components added:

$$\vec{A_x} + \vec{A_y} + \vec{A_z} = \vec{A}$$

Thus giving the overall total advective momentum change per unit time interval:

$$\vec{A} = -\left[\left((\rho\vec{u})\frac{\partial u_x}{\partial x} + (\rho\vec{u})\frac{\partial u_y}{\partial y} + (\rho\vec{u})\frac{\partial u_z}{\partial z}\right) + \left(u_x\frac{\partial(\rho\vec{u})}{\partial x} + u_y\frac{\partial(\rho\vec{u})}{\partial y} + u_z\frac{\partial(\rho\vec{u})}{\partial z}\right)\right] dxdydz$$

This may be expressed more succinctly as:

$$\vec{A} = -\left((\rho\vec{u})\nabla\cdot\vec{u} + \vec{u}\cdot\nabla(\rho\vec{u})\right) dxdydz \tag{A.22}$$

Force is defined as the rate of momentum change per unit time interval. If we now define $\vec{f}$ as the per unit volume total of all body forces (gravitational, magnetic etc) acting on the material within the differential volume element $dxdydz$, and we add this to our advective rate of momentum change expressed by equation A.22, this directly equates to the partial derivative of momentum with respect to time:

$$\frac{\partial(\rho\vec{u})}{\partial t}\cancel{dxdydz} = -\left((\rho\vec{u})\nabla\cdot\vec{u} + \vec{u}\cdot\nabla(\rho\vec{u})\right)\cancel{dxdydz} + \vec{f}\cancel{dxdydz}$$

With some rearrangement:

$$\frac{\partial(\rho\vec{u})}{\partial t} + \vec{u}\cdot\nabla(\rho\vec{u}) = -(\rho\vec{u})\nabla\cdot\vec{u} + \vec{f}$$

$$\frac{D(\rho\vec{u})}{Dt} = -(\rho\vec{u})\nabla\cdot\vec{u} + \vec{f} \tag{A.23}$$

At this point recall our Continuity Equation A.18:

$$\frac{D\rho}{Dt} + \rho\nabla\cdot\vec{u} = 0$$

Multiply by $\vec{u}$ and rearrange:

$$\vec{u}\frac{D\rho}{Dt} = -(\rho\vec{u})\nabla\cdot\vec{u}$$

Substitute into equation A.23 and rearrange:

$$\frac{D(\rho\vec{u})}{Dt} - \vec{u}\frac{D\rho}{Dt} = \vec{f}$$

$$\left(\rho\frac{D\vec{u}}{Dt} + \vec{u}\frac{D\rho}{Dt}\right) - \vec{u}\frac{D\rho}{Dt} = \vec{f}$$

$$\rho\frac{D\vec{u}}{Dt} = \vec{f} \tag{A.24}$$

We must now consider what body forces will be acting on a differential element of volume of material in a protostellar jet. Kinetic energy of launched material significantly exceeds its gravitational potential due to the source object and so we neglect gravitational force. Radiative pressure forces from photon flux are similarly negligible in the pre-stellar phase. The only forces that are considered significant are hydrodynamic forces from pressure differences, and the Lorentz force due to magnetic fields.

From an argument similar to that employed when we derived the expression for momentum transport, the hydrodynamic force F_{Hx} arising from pressure difference between

opposite faces of our cuboid lying perpendicular to the x-direction can be stated as:

$$F_{Hx} = \left[p - \left(p + \frac{\partial p}{\partial x} dx \right) \right] dydz$$

$$F_{Hx} = -\frac{\partial p}{\partial x} dxdydz$$

Assembling the F_{Hx}, F_{Hy}, F_{Hz} components of force we find:

$$\vec{F_H} = -\left(\frac{\partial p}{\partial x}\hat{i} + \frac{\partial p}{\partial y}\hat{j} + \frac{\partial p}{\partial z}\hat{k} \right) dxdydz$$

And thus the hydrostatic force per unit volume is simply:

$$\vec{F_H} = -\nabla p \tag{A.25}$$

It only remains now to state the Lorentz force for an ideal plasma, the derivation of which is to follow later and is given by:

$$\vec{J} \times \vec{B} = \frac{1}{4\pi} (\nabla \times \vec{B}) \times \vec{B} \tag{A.26}$$

Substituting A.25 and A.26 for the general force term $\vec{f}$ in equation A.24, we finally arrive at the form of the Momentum Equation used by ZEUS-MP in our jet models:

$$\rho \frac{D\vec{u}}{Dt} = -\nabla p + \frac{1}{4\pi} (\nabla \times \vec{B}) \times \vec{B} \tag{A.27}$$

The Energy Equation

We will again take a slightly different approach to deriving the energy equation, though we will make use of our previous Continuity and Momentum equation results in the derivation. We begin by considering a control volume of fluid $V(t)$ which is subject to advection by velocity field $\vec{u}(\vec{r}, t)$ and which thus may evolve in shape and size over time.

The rate of change of Total Energy (Kinetic plus Thermal) carried by the material is given by:

$$\frac{d}{dt}\int_{V(t)}\left(\frac{1}{2}\vec{u}^2+U\right)\rho dV \tag{A.28}$$

The specific thermal energy U (thermal energy per unit mass) is due to the random internal motions of the constituents of the material, whilst the kinetic energy per unit mass $\frac{1}{2}\vec{u}^2$ is due to the bulk motion of the fluid. We do not consider the rest mass-energy equivalence as there are no significant processes of dynamic mass-energy exchange here.

Applying Leibniz' Integral Rule and substituting the Continuity Equation A.18 to eliminate terms that sum to zero, we may express this as:

$$\int_{V(t)}\rho\frac{D}{Dt}\left(\frac{1}{2}\vec{u}^2+U\right)dV \tag{A.29}$$

This is a standard result when applying Leibniz' rule to material volumes. We now equate this to the totality of the rate of energy change produced by various mechanisms. This can be expressed in two parts; the rate of work done by body forces $\vec{f}$ acting upon the material within the control volume; and the rate of work done by pressure forces p acting on the boundary of the control volume. Simply stated, rate of work done on some material by a force is found by multiplying the force by the distance the material travels, then dividing by the time interval - so, the product of velocity and force.

$$\int_{V(t)}\rho\frac{D}{Dt}\left(\frac{1}{2}\vec{u}^2+U\right)dV=\oint_S -p\vec{u}\cdot d\vec{S}+\int_{V(t)}\vec{u}\cdot\vec{f}\rho dV \tag{A.30}$$

The work done by pressure is a negative term, because when the pressure acts outwards, so that the dot product of the velocity and the outwardly-directed surface vector is positive, then the control volume is doing work against its surroundings and thus losing energy. The product $\vec{f}\rho$ expresses force per unit volume. As we neglect gravity in our models, the only body force acting on the material is the Lorentz force, given by A.26, which from examination of the momentum equation A.27 can be seen to be a per unit volume force. Substituting the Lorentz force into the second term on the RHS of A.30,

and applying the Divergence Theorem to the first term on the R.H.S, we find:

$$\int \rho \frac{D}{Dt}\left(\frac{1}{2}\vec{u}^2 + U\right) dV = \int -\nabla \cdot (p\vec{u}) dV + \int \vec{u} \cdot \left(\frac{1}{4\pi}(\nabla \times \vec{B}) \times \vec{B}\right) dV \qquad \text{(A.31)}$$

Losing the integral signs we now consider this as a pointwise P.D.E.; expansion of the first term on the R.H.S. gives the following form of the Total Energy Equation:

$$\rho \frac{D}{Dt}\left(\frac{1}{2}\vec{u}^2 + U\right) = -\left[p\nabla \cdot \vec{u} + \vec{u} \cdot \nabla p\right] + \vec{u} \cdot \left(\frac{1}{4\pi}(\nabla \times \vec{B}) \times \vec{B}\right) \qquad \text{(A.32)}$$

We shall leave the equation in this form and now consider an equation that expresses only bulk Kinetic Energy. We can find this quite simply by taking the dot product of velocity $\vec{u}$ with the Momentum Equation A.27:

$$\rho \vec{u} \cdot \frac{D\vec{u}}{Dt} = -\vec{u} \cdot \nabla p + \vec{u} \cdot \left(\frac{1}{4\pi}(\nabla \times \vec{B}) \times \vec{B}\right) \qquad \text{(A.33)}$$

$$\rho \frac{D}{Dt}\left(\frac{1}{2}\vec{u}^2\right) = -\vec{u} \cdot \nabla p + \vec{u} \cdot \left(\frac{1}{4\pi}(\nabla \times \vec{B}) \times \vec{B}\right) \qquad \text{(A.34)}$$

Now subtract the Kinetic Energy Equation A.34 from the Total Energy Equation A.32 and we find:

$$\rho \frac{D}{Dt}(U) + p\nabla \cdot \mathbf{v} = 0 \qquad \text{(A.35)}$$

This is the Thermal Energy Equation. Re-expressing our per unit mass specific energy U as volumetric energy density e divided by mass density ρ we arrive at the form of the equation used by ZEUS-MP:

$$\rho \frac{D}{Dt}\left(\frac{e}{\rho}\right) + p\nabla \cdot \mathbf{v} = 0 \qquad \text{(A.36)}$$

There is one further modification to be included, however. Our jet models use cooling functions (Suttner et al., 1997)(115) which extract and radiate away thermal energy due to ionic recombination and collisional excitation / de-excitation of vibrational and

rotational modes in molecules. The correct Thermal Energy Equation is thus:

$$\rho \frac{D}{Dt}\left(\frac{e}{\rho}\right) + p\nabla \cdot \mathbf{v} + \Lambda(T, n, f) = 0 \tag{A.37}$$

Where Λ is the cooling function, T = Temperature, n = number density of Hydrogen nuclei, and f = molecular Hydrogen abundance.

The Ideal MHD Equations

ZEUS-MP assumes that the Ideal MHD condition holds, that is to say:

- High Magnetic Reynolds Number, $R_m = \mu\sigma u L$ (u = velocity, L = length scale)
- Low Plasma Beta, $\beta = 8\pi P/B^2$
- No free electric charges, $\rho_e = 0$

We take as our starting point Maxwell's Equations:

$$\nabla \cdot \vec{E} = \frac{\rho_e}{\epsilon_0} \tag{A.38}$$

$$\nabla \cdot \vec{B} = 0 \tag{A.39}$$

$$\nabla \times \vec{E} = -\frac{\partial \vec{B}}{\partial t} \tag{A.40}$$

$$\nabla \times \vec{B} = \mu_0 \vec{J} + \frac{1}{c^2}\frac{\partial \vec{E}}{\partial t} \tag{A.41}$$

Also, Ohm's Law for a conducting fluid:

$$\vec{J} = \sigma(\vec{E} + \vec{u} \times \vec{B}) \tag{A.42}$$

And, related to Ohm's Law, the *volumetric* Lorentz Force:

$$\vec{F} = \rho_e \vec{E} + J \times \vec{B} \tag{A.43}$$

First, we note that in the absence of free charges, Gauss' electric field law becomes:

$$\nabla \cdot \vec{E} = 0 \tag{A.44}$$

Next we demonstrate that the rightmost term in the Ampère-Maxwell relation (A.41), identified as the *displacement current*, is insignificant for Ideal MHD purposes. Ions / electrons in a plasma will move in a characteristic 'corkscrew' fashion about magnetic field lines, and we take it that their radius of gyration is very much smaller than the length scales of our problem; and we also note that the bulk velocities involved in our problem are very much smaller than the speed of light. Considering Faraday's law (A.40), it is apparent that the scale relationship between electric field $\vec{E}$ and a time-varying magnetic field $\vec{B'}$ may be expressed as:

$$E \sim \frac{L\,B'}{T} \tag{A.45}$$

Now let us consider, in the light of this, the scale of the contribution that the rightmost term in A.41 makes to the magnetic field, that is the self-inductance of B field due to a changing field $\vec{B'}$:

$$B \sim \frac{L^2\,B'}{c^2\,T^2} \tag{A.46}$$

Thus we see that, where the ratio of dynamic length scale to time scale is small w.r.t. the speed of light in the medium of interest, the contribution of this term to the magnetic field is correspondingly small. In the low velocity limit of astrophysical MHD, where the speed of light is close to that in vaccuo, this is indeed the case and so A.41 reduces to Ampère's Law, which neglects displacement current:

$$\nabla \times \vec{B} = \mu_0 \vec{J} \tag{A.47}$$

This is known as the *MHD Approximation*.

Moving onwards, rearranging Ohm's Law A.42 we find:

$$\vec{E} = \frac{\vec{J}}{\sigma} - \vec{u} \times \vec{B} \tag{A.48}$$

Taking the curl, we have:

$$\nabla \times \vec{E} = \nabla \times \frac{\vec{J}}{\sigma} - \nabla \times (\vec{u} \times \vec{B}) \tag{A.49}$$

And so from Faraday's Law (A.40) we see that:

$$\frac{\partial \vec{B}}{\partial t} = \nabla \times (\vec{u} \times \vec{B}) - \frac{1}{\sigma} \nabla \times \vec{J} \tag{A.50}$$

Using Ampère's Law (A.47) to substitute for $\vec{J}$:

$$\frac{\partial \vec{B}}{\partial t} = \nabla \times (\vec{u} \times \vec{B}) - \frac{1}{\mu_0 \sigma} \nabla \times (\nabla \times \vec{B}) \tag{A.51}$$

Using a vector identity:

$$\frac{\partial \vec{B}}{\partial t} = \nabla \times (\vec{u} \times \vec{B}) - \frac{1}{\mu_0 \sigma} \left[\cancel{\nabla (\nabla \cdot \vec{B})} - \nabla^2 \vec{B} \right] \tag{A.52}$$

We can eliminate the middle term on the R.H.S. using Gauss' magnetic field law (A.39) which states that $\nabla \vec{B} = 0$.

$$\frac{\partial \vec{B}}{\partial t} = \nabla \times (\vec{u} \times \vec{B}) + \lambda \nabla^2 \vec{B} \qquad \lambda = (\mu \sigma)^{-1} \tag{A.53}$$

This is the Magnetic Induction Equation. It is a transport equation for the B field. The quantity λ is called the magnetic diffusivity.

It is instructive to compare the scales of the two terms on the R.H.S. The first term is the convective term, whilst the second is the diffusive term.

$$\nabla \times (\vec{u} \times \vec{B}) \sim \frac{u\, B}{L} \tag{A.54}$$

$$\lambda \nabla^2 \vec{B} \sim \frac{\lambda\, B}{L^2} \tag{A.55}$$

The ratio of convection to diffusion is:

$$\frac{u\, B}{L} \frac{L^2}{\lambda\, B} = \mu \sigma u L \tag{A.56}$$

Which of course is R_m, the magnetic Reynolds number. We began this discussion by stating that $R_m >> 1$ in the Ideal MHD case which generally applies to astrophysical

plasmas. Hence, we may take it that convection dominates over magnetic diffusion, and the diffusive term may be taken to be negligible. So we arrive at the simplified form of the Induction Equation used by ZEUS-MP:

$$\frac{\partial \vec{B}}{\partial t} = \nabla \times (\vec{u} \times \vec{B}) \tag{A.57}$$

(It should be noted in passing that ZEUS-MP does however have some Non-Ideal MHD options that allow a certain amount of magnetic diffusion to be introduced, but these are not used in our jet models).

Finally, we must establish the magnetic contribution to the body force term of the momentum transport equation. Under the assumption of no free charge, and with the MHD approximation eliminating displacement current, the volumetric Lorentz Force equation (A.43) simplifies to:

$$\vec{F} = \frac{1}{\mu_0}(\nabla \times \vec{B}) \times \vec{B} \tag{A.58}$$

where we have used Ampère's Law to substitute for $\vec{J}$. In the C.G.S. unit system employed by ZEUS-MP, $\mu_0 = 4\pi$, and so we see that this volumetric force expression makes the necessary contribution in the momentum transport equation (A.27).

The Equation of State

As our starting point, we take the Ideal Gas Equation in its well-recognised form, in which n is the number of moles of gas and R is the molar gas constant:

$$pV = nRT \tag{A.59}$$

The molar heat capacity c is the thermal energy required per mole to raise the temperature of a gas by one degree. It is usually considered under conditions either of constant volume (c_v), in which the pressure increases as the temperature does, or constant pressure (c_p), whereby the gas is allowed to expand to do work against its surroundings as it heats up. For an ideal gas, $c_p - c_v = R$.

$$p = \frac{n}{V}(c_p - c_v)T \tag{A.60}$$

$$p = \left(\frac{c_p}{c_v} - 1\right)\frac{c_v n T}{V} \tag{A.61}$$

Recalling that c_v is the energy required to raise one mole of gas by one degree Kelvin, we can see that $c_v nT$ is simply the total thermal energy, E:

$$p = \left(\frac{c_p}{c_v} - 1\right)\frac{E}{V} \tag{A.62}$$

Replacing E/V with energy density, e, and c_p/c_v with the adiabatic ratio γ:

$$p = (\gamma - 1)e \tag{A.63}$$

This is the form of the equation used by ZEUS-MP.

However, the composition of the medium in our jet models varies due to chemistry, shock disassociation and recombination, and this means our adiabatic ratio γ will vary. So next we shall examine how this is calculated.

Each degree of freedom possessed by an atom or molecule contributes k_B Joules per Kelvin to the heat capacity of a quantity of the gas. Thus given a gas whose constituent

particles each possess d degrees of freedom the molar heat capacity of the gas at constant volume is given by:

$$c_v = \frac{d}{2} N_A k_B = \frac{d}{2} R \tag{A.64}$$

Considering one mole of gas, comprised of several chemical species, each will make a contribution according to its particular fraction, thus:

$$c_v = \frac{R}{2} \left(\frac{d_1 N_1 + d_2 N_2 + d_3 N_3 + ...}{N_A} \right) \tag{A.65}$$

In our jet models, there are three species that dominate contributions to the molar heat capacity; Atomic Hydrogen, Molecular Hydrogen, and Helium. Other trace elements such as Carbon and Oxygen certainly occur and are considered in effect in the molecular chemistry and cooling routines, but they make no significant contribution to the heat capacity.

Let n be the number of Hydrogen nuclei per unit volume. Let f be the ratio of the number of Hydrogen molecules per unit volume, to the number of Hydrogen nuclei per unit volume:

$$n(H_2) = fn \tag{A.66}$$

It stands to reason that if we know f, which will be in the range 0 to 0.5 (where 0 is a fully atomic medium, 0.5 a fully molecular medium) then we can calculate the number density of H atoms (or ions) thus:

$$n(H) = (1 - 2f)n \tag{A.67}$$

The number density of He atoms is simply given by the fact that Helium is known to constitute around 10% of the Interstellar Medium, and so:

$$n(He) = 0.1n \tag{A.68}$$

The total number density of particles is given by summing these quantities:

$$n_tot = (1-2f)n + fn + 0.1n = (1.1-f)n \tag{A.69}$$

The ratio of the number density of each species to the total number density, is the same as the molar fractions $\frac{N(H)}{N_A}$, $\frac{N(H_2)}{N_A}$, $\frac{N(He)}{N_A}$. The atomic constituents possess 3 degrees of freedom each, for translational motions; whilst molecular Hydrogen has two additional rotational degrees of freedom. Vibrational modes in the Hydrogen molecule are not excited at temperatures below 6000K; and above this limit, we expect near-total dissociation of the molecules. Putting it all together we have the following expression for the molar heat capacity at constant volume:

$$c_v = \frac{R}{2}\left(\frac{3(1-2f)n + 5fn + 3\times 0.1n}{(1.1-f)n}\right) = R\left(\frac{3.3-f}{2.2-2f}\right) \tag{A.70}$$

Since we know that $c_p - c_v = R$, it now becomes straightforward to calculate the adiabatic ratio $\gamma = \frac{c_p}{c_v}$:

$$\gamma = \frac{c_v + R}{c_v} = \frac{\left(\frac{3.3-f}{2.2-2f}\right) + 1}{\left(\frac{3.3-f}{2.2-2f}\right)} \tag{A.71}$$

$$\gamma = \frac{5.5-3f}{3.3-f} \tag{A.72}$$

This expresses the adiabatic ratio γ as a function of the fractional abundance of molecular Hydrogen, f. It can readily be seen that where $f = 0$, i.e. a fully atomic medium, $\gamma = \frac{5}{3}$; whilst a fully molecular medium with $f = 0.5$, we find $\gamma = \frac{10}{7}$.

Appendix B

ZEUS-MP Solution Methods

B.1 How the Euler equations are solved by ZEUS-MP

In Hayes' and Norman's 2006 paper (44), the methods by which ZEUS-MP solves the Astrophysical MHD equations for particular problem definitions are discussed in considerable detail. In the interests of brevity, we discuss only solution methods pertinent to our jet models. Basic but not exhaustive insight is provided.

B.1.1 Problem Reduction

It should be noted that many problems may be simplified, due to particular entities such as radiation flux or gravitational potential having a negligible effect over the dynamic timescale of the problem. This is the case with our jet models, and so ZEUS-MP solves a suitably reduced set of equations and field variables as given in section 4.1.2

B.1.2 Finite Differencing

A physical system whose behaviour within a problem domain is described by a set of partial differential equations and their boundary conditions, may not lend itself to being solved analytically, indeed it is the usual case that numerical methods must be employed. Finite Differencing offers a means to calculate an approximate solution at every point on a mesh of grid points, using simple first-order linear equations that compute the new

values of physical quantities after a small interval (timestep) of time using the prior (explicit), and possibly present (implicit), values of those quantities at the grid point of interest and its neighbours.

The method of Finite Differences relies on Taylor Series expansions of a function about a point. We will use a 2D case to illustrate but extension to 3D is straightforward enough.

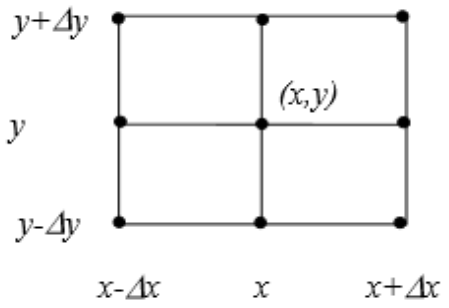

Figure B.1: Taylor Series expansion about a point x, y

Consider the function u expanded about the point (x, y):

$$u(x \pm \Delta x, y) = u(x, y) \pm \Delta x \frac{\partial u}{\partial x} + \frac{1}{2!}(\Delta x)^2 \frac{\partial^2 u}{\partial x^2} + O((\Delta x)^3) \tag{B.1}$$

$$u(x, y \pm \Delta y) = u(x, y) \pm \Delta y \frac{\partial u}{\partial y} + \frac{1}{2!}(\Delta y)^2 \frac{\partial^2 u}{\partial y^2} + O((\Delta y)^3) \tag{B.2}$$

If we make $\Delta x, \Delta y$ sufficiently small then the continuation of these expansions in higher order terms $O((\Delta x)^3), O((\Delta y)^3)$ may be neglected. This is *truncation* and gives rise to a small error known as *truncation error*.

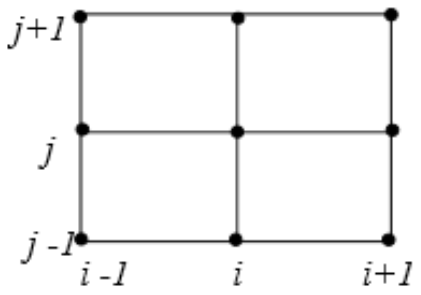

Figure B.2: Taylor Series discrete expansion about a point i, j

Now consider the case of a grid of discrete points. We replace $u(x, y)$ with $u_{i,j}$ where i, j are integer coordinates indicating how many spatial increments the point is from the origin.

- $u(x, y) = u_{i,j}$
- $u(x + \Delta x, y) = u_{i+1,j}$
- $u(x, y + \Delta y) = u_{i,j+1}$

Our Taylor's Series Expansions become:

$$u_{i\pm1,j} = u_{i,j} \pm \Delta x \left.\frac{\partial u}{\partial x}\right|_{i,j} + \frac{1}{2}(\Delta x)^2 \left.\frac{\partial^2 u}{\partial x^2}\right|_{i,j} + O((\Delta x)^3) \tag{B.3}$$

$$u_{i,j\pm1} = u_{i,j} \pm \Delta y \left.\frac{\partial u}{\partial y}\right|_{i,j} + \frac{1}{2}\Delta y^2 \left.\frac{\partial^2 u}{\partial y^2}\right|_{i,j} + O(\Delta y^3) \tag{B.4}$$

First-Order Accurate expressions for the partial derivatives of our function u may be obtained by rearranging these expansions and truncating residual terms in $\Delta x, \Delta y$ or higher powers thereof.

Forward Difference:

$$\left.\frac{\partial u}{\partial x}\right|_{i,j} = \frac{u_{i+1,j} - u_{i,j}}{\Delta x} + O(\Delta x) \tag{B.5}$$

Backward Difference:

$$\left.\frac{\partial u}{\partial x}\right|_{i,j} = \frac{u_{i,j} - u_{i-1,j}}{\Delta x} + O(\Delta x) \tag{B.6}$$

Second-Order Accurate expressions may be obtained by adding and subtracting Taylor's Series' for neighbouring points to either side of the point of interest. These are known as *Central Differences*.

$$\mathbf{B.3 - B.4:} \qquad \left.\frac{\partial u}{\partial x}\right|_{i,j} = \frac{u_{i+1,j} - u_{i-1,j}}{2\Delta x} + O(\Delta x^2) \tag{B.7}$$

$$\mathbf{B.3 + B.4:} \qquad \left.\frac{\partial^2 u}{\partial x^2}\right|_{i,j} = \frac{u_{i+1,j} - 2u_{i,j} + u_{i-1,j}}{\Delta x^2} + O(\Delta x^2) \tag{B.8}$$

Construction of forward, backward and central differences in two dimensions to first and second order accuracy yields six expressions when we take each dimension singly, though we could add others to our list using the 2D Taylor's series and taking combinations of small differences in both directions, and many more if we add a third dimension.

Approximating derivatives of a continuous function by use of this method of finite differences is an example of a *discretisation scheme*. Others exist and are widely used, such as finite volume and finite element analysis.

As an example of how finite differencing is employed in the solution of partial differential equations, let us consider the 1-D advection equation, which is the equation governing the transport of a scalar quantity $u(x)$ by a fluid disturbance travelling at speed v:

$$\frac{\partial u}{\partial t} + a\frac{\partial u}{\partial x} = 0 \tag{B.9}$$

This is a *hyperbolic* partial differential equation. We wish to find the solution $u(x)$ to the equation over all points in space x at successive intervals of time; this is referred to as a *time marching solution*. On our discrete grid we will assign the i direction to the spatial direction x and the j direction to the progress of time t. So $u_{i,j}$ describes the value of our scalar field at a given point in space $i\Delta x$ and time $j\Delta t$ where Δx is our grid spacing and Δt is our time increment.

Our choice of finite difference expressions must be a careful one. We begin with an initial state at time $t = 0$, described by $u_{i,0}$ and wish to evolve this forwards in time according to the equation; thus, our partial derivative with respect to time will be best described by a forward difference:

$$\frac{\partial u}{\partial t} = \frac{u_{i,j+1} - u_{i,j}}{\Delta t} + O(\Delta t) \tag{B.10}$$

The choice of finite difference expression for the spatial derivative is slightly less straightforward. Where the velocity of the disturbance v is a positive one, i.e. the disturbance flows forwards in the x direction, a backwards difference in space suggests itself as shown in equation B.6 as we expect the scalar field at coordinate i to be advected towards coordinate $i + 1$, so it makes sense to use the known preceding values along the propagation direction. This is referred to as *upwinding*.

However, there is then a choice of two alternatives; to calculate the value of the spatial derivative as it was at the preceding time step, referred to as an *Explicit* scheme, or to calculate the derivative as it is at the new timestep, which is an *Implicit* scheme.

Upwind Explicit Scheme:

$$\frac{\partial u}{\partial x} = \frac{u_{i,j} - u_{i-1,j}}{\Delta x} + O(\Delta x) \tag{B.11}$$

which combined with B.10 yields:

$$u_{i,j+1} = (1 - s)u_{i,j} + su_{i-1,j} \tag{B.12}$$

Upwind Implicit Scheme:

$$\frac{\partial u}{\partial x} = \frac{u_{i,j+1} - u_{i-1,j+1}}{\Delta x} + O(\Delta x) \tag{B.13}$$

which combined with B.10 yields:

$$u_{i,j+1} = \frac{u_{i,j} + s u_{i-1,j+1}}{(1+s)} \tag{B.14}$$

where in both Explicit and Implicit cases $s = a\frac{\Delta t}{\Delta x}$

A key difference is that when we calculate the spatial derivative from the preceding timestep j, all the values of the solution $u_{i,j}$ are already explicitly known, which reduces the calculation of the values of $u_{i,j+1}$ to a fairly simple piece of arithmetic. But in the implicit scheme, when we calculate the spatial derivative using the values at the new timestep, $u_{i,j+1}$, these values are not immediately known; this formulation leads to a system of equations that must be solved simultaneously, as a matrix.

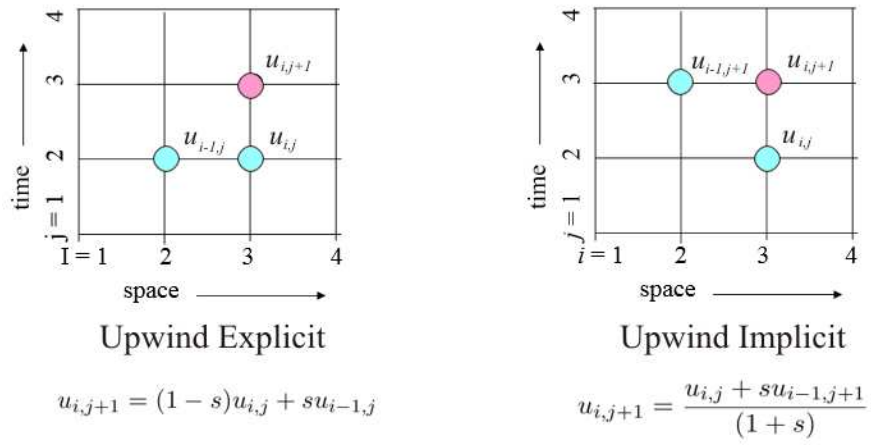

Figure B.3: Computational Molecules for Upwind Explicit vs. Implicit schemes. The pink dots represent the point in space and time for which the new value of the function is being calculated using the first-order Taylor series approximations of the derivatives that appear in the Advection Equation.

In fig.B.3, it can be seen clearly that in the Implicit scheme, the value of $u_{i,j+1}$ is dependent on the value of $u_{i-1,j+1}$, but this value itself may only be found by solving a similar equation, and this gives rise to the system of simultaneous equations. At each timestep, then, an Implicit scheme requires an operation such as matrix inversion to

determine the new function values. Direct matrix inversion tends to require extremely large amounts of computer memory for most problems of interest, and in practise iterative solvers such as Jacobi, Gauss-Seidel or Conjugate Gradient are employed to generate the new solution at each timestep. To compute the solution in both Explicit and Implicit cases requires boundary conditions for the equation to be provided.

B.1.3 Stability and the Courant Condition

Clearly, the Implicit approach to solving the equation in our example, and thus partial differential equations in general is considerably more computationally intensive than the Explicit approach, timestep-for-timestep. However there are important differences in the stability of the two approaches. By stability, we mean the tendency for the errors arising from discretisation of the problem, such as truncation errors, to remain bounded or to grow as the simulation progresses. Where there is a growth factor in the error of greater than unity then the solution will rapidly diverge from a physically realistic one.

Von-Neumann stability analysis may be applied to the case of our 1D hyperbolic Advection Equation to demonstrate the difference in stability. Suppose we have a function that represents the distribution of errors in our solution, across the problem domain x as time progresses. Let $E(x)$ be the first Fourier harmonic in a Fourier series for the error function. In discrete form we state the value of this harmonic at a point in space and time as $E_{i,j}$.

$$E_{i,j} = A_j e^{iI\theta} \qquad \theta = \frac{2\pi\Delta x}{L} \tag{B.15}$$

Where in this instance $I = \sqrt{-1}$ since i represents the discrete spatial coordinate for x. The coefficient A_j will have a value that is varying with time j. The inter-timestep growth factor G will be:

$$G = \frac{E_{i,j+1}}{E_{i,j}} = \frac{A_{j+1}}{A_j} \tag{B.16}$$

and in order for the solution to remain stable as time progresses, it must be the general case that for all timesteps j, $|G| \leq 1$.

Looking at the Explicit method first, as we proceed from one timestep j to the following

timestep $j+1$, the accumulated error $E_{i,j+1}$ will be given by:

$$E_{i,j+1} = (1-s)E_{i,j} + sE_{i-1,j} \tag{B.17}$$

Substituting B.15 gives

$$A_{j+1}e^{iI\theta} = (1-s)A_j e^{iI\theta} + sA_j e^{(i-1)I\theta} \tag{B.18}$$

And so:

$$G = \frac{A_{j+1}}{A_j} = 1 - s + se^{-I\theta} \tag{B.19}$$

If we think about all the possible values that G may take in the complex plane, it is apparent that they must lie on a circle of radius s centred on a point on the Real axis $(1-s, 0)$. Where $s > 1$ there exists the possibility that $|G| > 1$, since where $\theta = (2n+1)\pi, \;\; n \geq 0$, it is the case that $G = 1-2s$ and thus $G < -1$. The error growth factor may also exceed 1 where $s < 0$, since for the same value of θ, $G = 1-2s$ then implies $G > 1$. In fact, for all values of s within the interval bounded by these limits, the circle of values that G may take on the complex plane lies entirely within a unit radius of the origin and thus the stability condition is satisfied. So we reach the stability condition for the 1D Advection Equation discretised according to the Upwind Explicit scheme:

$$0 \leq s \leq 1 \quad , \quad s = a\frac{\Delta t}{\Delta x} \tag{B.20}$$

Now we subject the Implicit scheme to a similar analysis. Substituting B.15 into B.14 and rearranging, we find that:

$$G = \frac{A_{j+1}}{A_j} = \frac{1}{1 + s - se^{-I\theta}} \tag{B.21}$$

Use trig identities as follows:

$$e^{-I\theta} = cos(\theta) - Isin(\theta) \quad , \quad 2sin^2\left(\frac{\theta}{2}\right) = (1 - cos(\theta)) \tag{B.22}$$

This gives us

$$G = \frac{1}{1 + 2sin^2\left(\frac{\theta}{2}\right) + sIsin(\theta)} \tag{B.23}$$

From which it is evident that

$$|G|^2 = \frac{1}{\left[1 + 2sin^2\left(\frac{\theta}{2}\right)\right]^2 + \left[s\ sin(\theta)\right]^2} \tag{B.24}$$

It is clear that the denominator in this expression is always greater than 1, and thus it is always the case that the stability condition $|G| < 1$ is satisfied. The Upwind Implicit scheme for the 1D Advection Equation is unconditionally stable. This demonstrates the advantages of the Implicit formulation despite its greater computational demands.

The condition shown at B.20 is the Courant-Friedrichs-Lewy condition for the 1D Advection Equation, which is a first-order *hyperbolic* PDE. This equation deals with the advection of a passive scalar field by a constant flow field. But the equations of Astrophysical MHD are flow evolution equations, and deal with fluxes of Mass, Momentum, Energy and Magnetic Field that vary with time. These are examples of second-order *parabolic* PDEs.

It is only a little more complex to demonstrate that the stability condition for a discretised, Explicitly formulated parabolic PDE of the type:

$$\frac{\partial u}{\partial t} = \alpha \frac{\partial^2 u}{\partial x^2} + f \tag{B.25}$$

is given by:

$$0 \leq C \leq 0.5 \quad , \quad C = \alpha \frac{\Delta t}{\Delta x^2} \tag{B.26}$$

where C is the Courant parameter and α is identified as the *sound speed* in the flow medium; while Δt and Δx are the timestep and grid spacing, respectively. This can be rearranged to give the maximum size of timestep required for numerical stability for a given value of the Courant parameter:

$$\Delta t = C \frac{\Delta x^2}{\alpha} \quad , \quad 0 \leq C \leq 0.5 \tag{B.27}$$

B.1.4 Staggered Grid

In common with many other grid-based codes, ZEUS-MP maintains two meshes, one for scalar quantities such as density and internal energy, the other for vectors such as velocity and magnetic field. The scalar grid is spatially interspersed with the vector grid such that each scalar mesh point lies at the centre of six vector mesh points. These six points may be taken as the centres of six faces of a notional cubic cell containing the scalar mesh point. Three of the cube faces 'belong' to the scalar mesh point and their central data points carry the three components of vector field associated with the contents of that cell.

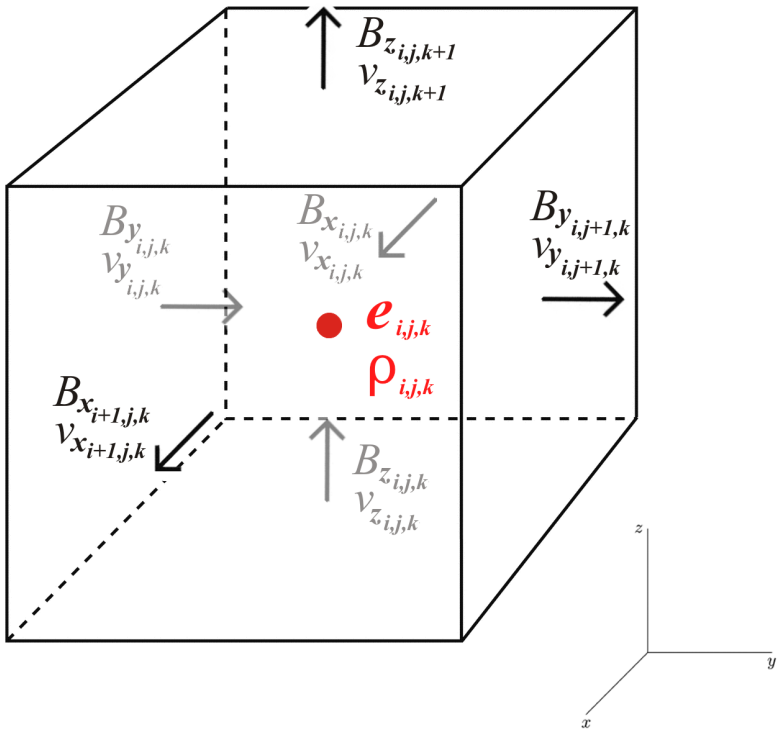

Figure B.4: ZEUS-MP Staggered Grid

B.1.5 Operator Splitting methods:

Operator Splitting is a technique for breaking down the solution of a partial differential equation into sub-parts that may be solved independently by the discretisation scheme that is best suited to each case, which may have advantages both in terms of stability and in terms of demand for computing resources. The principle may be illustrated in an abstract way as follows. Let us suppose we want to solve the following differential equation to find $U(\vec{r},t)$, given the initial state $U(\vec{r},0) = U_0$:

$$\frac{dU}{dt} + \mathcal{A}(U) = 0 \tag{B.28}$$

Where $\mathcal{A}$ is an operator, which may be as simple as a constant multiplier, or something more complex. Multiply by the integrating factor $e^{t\mathcal{A}}$ (itself an operator, albeit perhaps an awkward one) and integrating we obtain:

$$e^{t\mathcal{A}}U(\vec{r},t) = U_0 \tag{B.29}$$

$$U(\vec{r},t) = e^{-t\mathcal{A}}U_0 \tag{B.30}$$

Now suppose that the operator $\mathcal{A}$ can be split into parts:

$$\mathcal{A} = \mathcal{A}_1 + \mathcal{A}_2 \tag{B.31}$$

And that we may solve these subproblems in a similar way to the overall problem:

$$\frac{dU}{dt} + \mathcal{A}_j(U) = 0, \qquad j = 1,2 \tag{B.32}$$

$$U(\vec{r},t)_j = e^{-t\mathcal{A}_j}U_0, \qquad j = 1,2 \tag{B.33}$$

Now we may express the principle of operator splitting. We define $t_n = n\Delta t$, where Δt is a small, positive time increment. Given that U_0 could in fact be any arbitrary initial state of the system after n timesteps $U(t_n)$, we may reasonably hope that the following

holds true:

$$U(\vec{r}, t_{n+1}) \approx e^{-\Delta t \mathcal{A}_2} e^{-\Delta t \mathcal{A}_1} U(\vec{r}, t_n) \tag{B.34}$$

And that:

$$U(\vec{r}, t) = e^{-t\mathcal{A}} U_0 = \lim_{\Delta t \to 0} \left(e^{-\Delta t \mathcal{A}_2} e^{-\Delta t \mathcal{A}_1} \right)^n U_0 \tag{B.35}$$

If the operators $\mathcal{A}_1$, $\mathcal{A}_2$ commute then the method is exact since

$$e^{-\Delta t \mathcal{A}_2} e^{-\Delta t \mathcal{A}_1} = e^{-\Delta t \mathcal{A}} \tag{B.36}$$

A numerical solution method may be obtained by replacing the exact operators $e^{-\Delta t \mathcal{A}_j}$ with discrete approximations. These are then applied separately and consecutively to $U(\vec{r}, t_n)$ to find $U(\vec{r}, t_{n+1})$. This is simply another way to approach the finite differencing method used to solve equations like the 1D Advection Equation, if we replace $\mathcal{A}$ with a suitable differential operator. Generalised to 3D, it suggests that we may split advection in a 3D coordinate space into three separate advection operations, one for each dimension, and this indeed is what ZEUS-MP does.

Where equation B.36 does not exactly hold true, we may expect some small *splitting error* associated with the approximation.

B.1.6 Implementation of Operator Splitting in ZEUS-MP:

The formalism of Winkler et al (1984)(122) employs operator splitting to solve the transport equations in several stages.

- Source Step: Solve finite difference equations for the time-derivatives of Momentum and Energy to compute the net transient terms arising due to source terms such as hydrodynamic and magnetic pressure
- Method of Characteristics Step: Modify the transient terms for Momentum and Energy to account for the effects of magnetic tension, and solve the Magnetic Induction Equation to recalculate the B field, in a single operation

- Transport Step: Solve the integral form of the source-free advection equations for Mass, Momentum and Energy

The equations solved in the Source Step, including Artificial Viscosity **Q** are:

$$\rho\frac{\partial\vec{v}}{\partial t} = -\nabla p - \nabla(B^2/8\pi) - \nabla\cdot\mathbf{Q} \tag{B.37}$$

$$\frac{\partial e}{\partial t} = -p\nabla\cdot\vec{v} - \nabla\vec{v} : \mathbf{Q} \tag{B.38}$$

The Method of Characteristics + Constrained Transport step then modifies the Momentum transient, whilst also evolving the **B** field, as follows:

$$\rho\left.\frac{\partial\vec{v}}{\partial t}\right|_{final} = \rho\left.\frac{\partial\vec{v}}{\partial t}\right|_{source\ step} + \frac{1}{4\pi}(\mathbf{B}\cdot\nabla)\mathbf{B} \tag{B.39}$$

$$\frac{d}{dt}\int_S \mathbf{B}\cdot d\mathbf{S} = \oint_C \epsilon\cdot d\mathbf{l} \tag{B.40}$$

where the e.m.f. ϵ is given by:

$$\epsilon = (\vec{v} - \vec{v_g})\times\mathbf{B} \tag{B.41}$$

and in which $\vec{v_g}$ is the velocity of the grid itself, if non-stationary.

Note that all of our jet models use a stationary grid.

Finally, the Transport Step solves the following integral equations to compute the advection of material through the grid.

$$\frac{d}{dt}\int_V \rho dV = -\oint_S \rho(\vec{v} - \vec{v_g})\cdot d\mathbf{S} \tag{B.42}$$

$$\frac{d}{dt}\int_V \rho\vec{v} dV = -\oint_S \rho\vec{v}(\vec{v} - \vec{v_g})\cdot d\mathbf{S} \tag{B.43}$$

$$\frac{d}{dt}\int_V e dV = -\oint_S e(\vec{v} - \vec{v_g})\cdot d\mathbf{S} \tag{B.44}$$

Advection in each spatial direction is performed independently, but the three advection operations are cyclically permuted with each new timestep to avoid the appearance of numerical anisotropies as the system evolves. The advection is performed by computing

the 2nd-order upwind fluxes of the variables at the zone faces and then advecting them through the mesh in each of the three space dimensions in turn. A 'Consistent Transport' method is used, whereby quantities consistent with the mass density are advected: the mass density itself, the specific internal energy, and the specific momenta.

B.1.7 Timestep Calculation

The main advantage of the Implicit approach is that it allows large timesteps to be chosen whilst remaining stable; its disadvantage is that iterative solvers are required to compute each new timestep. Large timesteps are not an advantage in modelling flows where the dynamical timescale is short in comparison to the simulation run time and where the system state is being frequently dumped to output.

In general, ZEUS-MP adopts an Explicit approach to modelling dynamical flows although Implicit solution schemes and solvers are employed for some of the physics. For example, the Gravitational Potential equation is an instance of Poisson's Equation which is an *elliptic* PDE. The solution for the non-relativistic gravitational field depends only on the instantaneous distribution of matter; it is not a time-marching solution as it has no dependence on the values of the previous timestep, and thus by its nature requires an Implicit formulation and an iterative matrix solver. ZEUS-MP employs a choice of three solvers - Conjugate Gradient, Multigrid, and Fast Fourier Transform. These will not be detailed here as Gravity does not play a significant role in our jet models and hence is disabled in our runs.

The Explicitly formulated equations in ZEUS-MP require a timestep that satisfies the Courant-Friedrichs-Lewy stability condition (B.20). The grid spacing does not vary over time, hence in order to satisfy the condition, the timestep must change as the sound speed varies in the medium due to changing density and temperature. The parameter C is set manually by the user at the start of the run and does not change. A value of 0.5 is usually selected as smaller values imply shorter timesteps than are necessary for stability purposes, and this increases the length of time required for simulation runs.

In fact ZEUS-MP solves a large set of coupled PDEs and the calculation for each new timestep is more complex, though it follows the same basic principles:

$$\Delta t_{new} = \frac{C}{\sqrt{\Delta t_{cs}^{-2} + \Delta t_{v1}^{-2} + \Delta t_{v2}^{-2} + \Delta t_{v3}^{-2} + \Delta t_{al}^{-2} + \Delta t_{av}^{-2} + \Delta t_{rd}^{-2}}} \tag{B.45}$$

These Δt values in the denominator represent, respectively, the local sound crossing time, the local fluid crossing time along each coordinate, the local Alfvén wave crossing time, the local viscous timescale, and a radiation timescale factor (although the latter is not used in our jet models, which are non-radiative in nature).

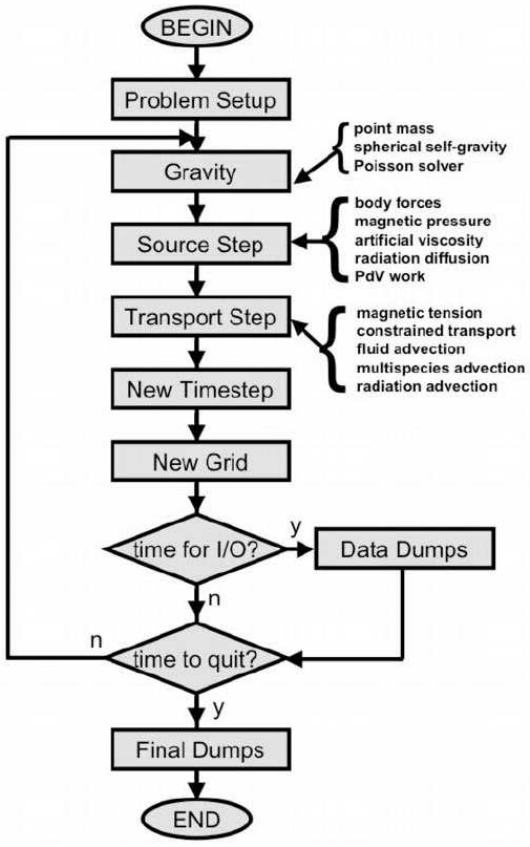

Figure B.5: ZEUS-MP Program Control Loop (Figure from Hayes et al., 2006 (44))

Appendix C

MHD Jets in ZEUS-MP

C.1 MHD Jets in ZEUS-MP

C.1.1 Magnetic Fields in Jets

Most of the accepted jet launch models imply the presence of a magnetic field that launches and collimates the jet (Smith, 2004)(100). A magnetic field threading the protostar and its accretion disc begins in a poloidal configuration, and accretion disc material is launched outwards along (notional) magnetic field lines by magnetocentrifugal action when field lines make a critical angle to the disc (Blandford, Payne, 1982)(11), extracting gravitational potential energy and angular momentum. At larger radii, as the magnetic field weakens the inertia of the material comes to dominate its motion and the poloidal field lines twist into an increasingly toroidal configuration (Fendt, 2009)(30). The toroidal field within a jet may be thought of as a field component which is azimuthal with respect to the jet axis; while the Poloidal field emerges up the centre of the jet then loops back on itself via the outer layers.

At larger distances, it is argued from flux conservation that the toroidal magnetic field becomes dominant (Begelman, Blandford, Rees, 1984)(12). It should be noted that, although the classical magnetocentrifugal jet launch model implies a large-scale, connected magnetic field threading the source object and extending out distantly along the jet, it has been argued that smaller-scale, tangled magnetic fields that close their flux loops

locally within the accretion disc, central object and propagating jet may be a more realistic picture. Nevertheless by similar arguments to the picture involving a large-scale field, toroidal field components are expected to become dominant at large distances from the jet source (Li, 2002)(62).

Equation A.58 expresses the volumetric Lorentz force:

$$\vec{F} = \frac{1}{\mu_0}(\nabla \times \vec{B}) \times \vec{B} \tag{A.58}$$

This may be expanded thus:

$$\vec{F} = -\frac{1}{2\mu_0}\nabla B^2 + \frac{1}{\mu_0}(\vec{B}\dot{\nabla})\vec{B} \tag{C.1}$$

Considering the implications of this as the Lorentz force term in the momentum equation A.27, the first, negatively signed term of the R.H.S. of C.1 is an outwards-directed, pressure-like force arising from a magnetic field gradient. The second, positively signed term, is an inwards-directed, tension-like force. It has been shown that in toroidal fields, it is this tension-like, 'hoop stress' that dominates, and thus contributes to the collimation of the jet (Li, 2002)(62). Conversely, in poloidal fields, magnetic pressure adds to thermal pressure and forces the jet to splay outwards, as is demonstrated in figure C.3 further on.

C.1.2 Helmholtz Decomposition

A Helmholtz-Analogous decomposition of the magnetic field expresses $\vec{B}$ in terms of 2 scalar potentials, ϕ and ψ:

$$\vec{B_{tor}} = \nabla \times \psi\vec{r} \tag{C.2}$$

$$\vec{B_{pol}} = \nabla \times (\nabla \times \phi\vec{r}) \tag{C.3}$$

$$\vec{B} = \nabla \times \psi\vec{r} + \nabla \times (\nabla\phi\vec{r}) \tag{C.4}$$

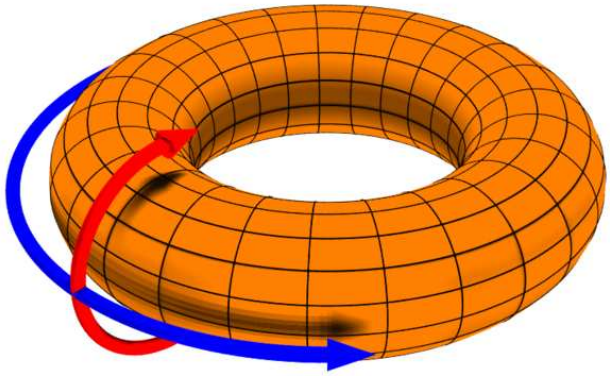

Figure C.1: Depiction of the Toroidal and Poloidal B-field decomposition. Toroidal field shown in blue, poloidal field shown in red. (Image by Dave Burke, 2010, Wikimedia Commons)

C.1.3 Implementation in ZEUS

Although ZEUS-MP has a sophisticated solver algorithm for magnetic fields, HSMOCCT (Hawley & Stone, 1995)(43), the base implementation only has very limited native support for magnetic fields to be defined within the problem domain and at the boundaries. It is only possible to define a curl-free ambient magnetic field with constant field strength and direction by a choice of input parameters in the ZMP_INP file. Such a field is assumed to close its flux loops outside the problem domain at considerable distance. There is no facility for magnetic field to be advected into the problem domain in a jet.

In order to facilitate MHD jet models, code was ported from ZEUS-3D, a different fork of the ZEUS code family. This B field code dynamically evolves the magnetic boundary conditions in such a way that toroidal and poloidal field components, corresponding to a Helmholtz Decomposition of the field, may be advected by the jets into the problem domain.

For both toroidal and poloidal field components in the ported magnetic field code, the field strength is determined by the Plasma-β parameter. This is defined as the ratio of thermal pressure to magnetic pressure.

$$\beta = \frac{P_{th}}{P_B} \tag{C.5}$$

Where magnetic pressure is given by:

$$P_B = \frac{B^2}{8\pi} \tag{C.6}$$

It can be seen that a low Plasma-β value (P-$\beta < 1$) implies that the pressure of the magnetic field dominates.

In the ported ZEUS code, the toroidal magnetic field strength profile across a jet of radius r_{jet} is defined by the following:

$$B_{tor}(r) = \begin{cases} B_{tor}(r_2)(sin(\pi f(r')))^2 & ; r' < 1 \\ 0; & r > 1 \end{cases} \tag{C.7}$$

where $r' = r/r_{jet}$, and $f(r')$ is defined as follows:

$$f(r') = \begin{cases} \frac{1}{2}\left(\frac{r'}{r_2}\right)^a & ; 0 < r' < r_2 \\ 1 - \frac{1}{2}\left(\frac{1-r'}{1-r_2}\right)^b & ; r_2 < r' < 1 \end{cases} \tag{C.8}$$

and where

$$\begin{aligned} a &= \frac{log(1/2)}{log(r_1/r_2)} \\ b &= \frac{log(1/2)}{log(1-r_3/1-r_2)} \end{aligned} \tag{C.9}$$

with the constraints that

$$\left(\frac{1-r_3}{1-r_2}\right)^{(1-r_2)} - \left(\frac{r_1}{r_2}\right)^{r_2} = 0; r_3 - r_1 = \sigma \tag{C.10}$$

r_2 and σ are the radial coordinate of the peak of the function, and the FWHM respectively; they are specified in the ZMP_INP file as *rpeak* and *sigma* respectively. r_3 is then determined by the MHD code using Newton-Raphson, from which r_1 is then found as $r_1 = r_3 - \sigma$. The value $B_{tor}(r_2)$ in equation C.7 is determined by the local thermal pressure and the Plasma$-\beta$ value which is specified in the ZMP_INP file as *btator*.

The poloidal field input parameters for the ZMP_INP file resemble those of the toroidal

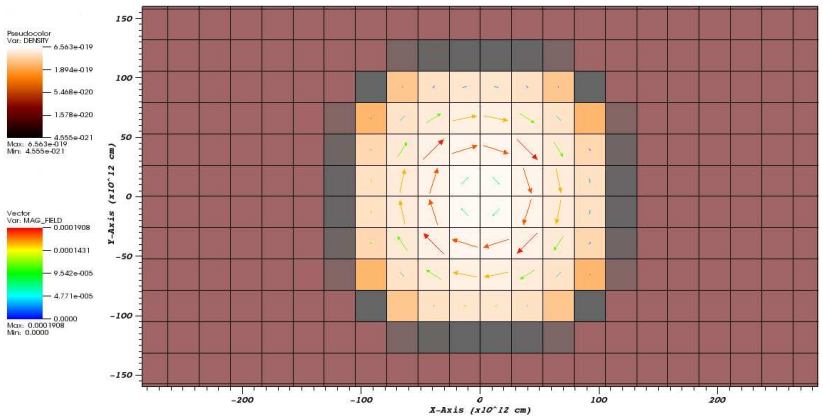

Figure C.2: Introduction of a toroidal field into a jet in ZEUS-MP; y-z plane cross-section at x=0 shows B field vectors in colour-scale on a log(density) background. Spatial dimensions are in cm. Density is in g cm^{-3} and B field magnitude is in Gauss.

field in some respects; *btapol* determines the Plasma$-\beta$ value of the poloidal field, while *zsigma* sets the axial HWHM (Half-Width, Half-Maximum) of the poloidal field's leading edge. ZEUS-3D constructs the poloidal field on the boundary from the magnetic vector potential, $\vec{A}$, and the poloidal flux loops are then advected into the problem domain as the jet material carries them in. Porting the code into ZEUS-MP required altering the depth of the magnetic boundary 'ghost zones' from two, to four.

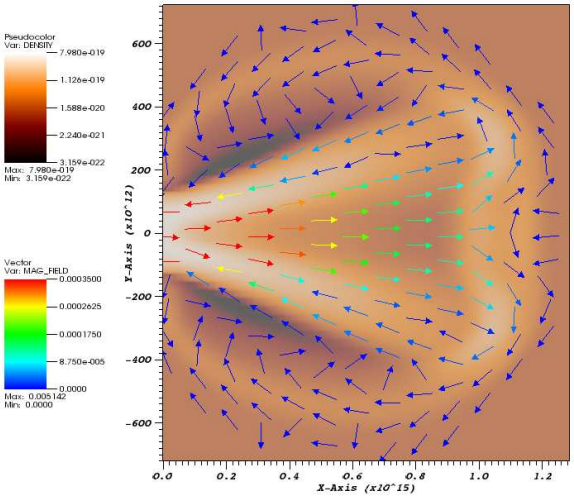

Figure C.3: Introduction of a pure poloidal field into a jet modelled in ZEUS-MP; field vectors shown in colour-scale presented on a log(density) background. Spatial dimensions of the model are in units of cm. Density is in g cm^{-3} and B field magnitude is in Gauss.

An additional switch, which was not used, is *ibpol*. This is a switch that determines whether to advect a single flux loop into the domain, or multiple loops. Another switch, *znode*, sets the relative positions of the footprints of the multiple flux loops.

C.1.4 MHD Stability Issues

The implementation of the dynamic magnetic field boundary conditions in ZEUS-MP achieved limited success. Jets from non-orbital sources could be simulated provided the Plasma-β was not too low; difficulties would arise with P-$\beta < 0.01$, with models becoming prone to developing localised magneto-thermal instabilities that produced extreme velocities in material due to the associated pressure gradients. Increasing the resolution of the model would exacerbate rather than remedy these issues. It was also the case that, whilst the dynamic magnetic boundaries would cope satisfactorily with advecting magnetised material into the problem domain carrying a well-ordered field, the code was not able to consistently handle the tangled fields that reached the far boundaries; localised build-up of residual field would occur at the boundary and this would lead to unstable behaviour that halted the code.

Jets from orbiting sources could carry magnetic field into the problem domain, provided the field was toroidal-only in nature. The code was not able to evolve the poloidal field at the same time as moving the jet inlet, in a self-consistent manner; tolerance limits on B-field divergence would be exceeded. Another problem with orbiting sources of MHD jets, particular to the parallelised nature of the ZEUS-MP code, is that crossing tile boundaries would disrupt the magnetic field profile. This could probably be resolved with further coding work to improve the parallelisation of the dynamic magnetic boundary condition evolution. However, to save time, workarounds were used; either the problem domain was tiled transverse to the jet axis dimension so that there were no tile boundaries for the jet inlet to cross, or else the problem domain was enlarged such that the jet inlet's orbit was fully contained within 1 tile.

It was found during prototyping runs, that by far the greatest effect of the introduction of magnetic field within the jet was to determine the shape of the bow shock at the front of the jet, with concentrations of toroidal field producing hoop stress that constrain the bow shock into a more narrow, conical profile and preventing the break-up of the shock due to Rayleigh-Taylor instability. Though this is an interesting effect, in our dual-jet models we are concerned with the jet column rather than the bow shock which exits the problem domain long before our time frame of interest.

It is possible that more pronounced effects on the morphology of the jet column may be observable with smaller values of P-β; but this did not seem feasible with the code in its present form, and so the binary jet simulations were carried out as hydrodynamic rather than MHD models. It is hoped that the stability problems with the code can be resolved and that MHD binary jet simulations may form the basis of future work.

Appendix D

The Cooling Functions

In Chapter 4, we saw that the energy equation A.37 involves a term Λ describing cooling effects. The overall cooling function consists of 13 sub-functions which model various different processes that cool the heated medium.

$$\rho \frac{D}{Dt}\left(\frac{e}{\rho}\right) + p\nabla \cdot \mathbf{v} + \Lambda(T, n, f) = 0 \tag{D.1}$$

$$\Lambda(T, n, f) = \sum_{i=1}^{13} \Lambda_i \tag{D.2}$$

These sub-functions are discussed below.

1. Λ_1: Dust / gas-grain cooling (Hollenbach, McKee 1989)(46)

   The following assumes a typical ISM composition. This is an approximation, as actual jet composition may vary.

   $$\Lambda_1 = n^2 \times L_g \tag{D.3}$$

   where L_g is:

   $$L_g = (3.8 \times 10^{-33})\sqrt{T}(T - T_g)(1.0 - 0.8\exp(-75/T))ergs^{-1}cm^3 \tag{D.4}$$

   T_g is the dust grain temperature, and is fixed at 20 K.

2. Λ_2: H_2 vibrational and rotational cooling (Lepp, Shull, 1983)(61)

   Vibrational coefficients are subscripted with v, rotational with r. Superscript H signifies high density, while L signifies low density.

$$\Lambda_2 = n_{H_2}\left(\frac{L_v^H}{1+(L_v^H/L_v^L)} + \frac{L_r^H}{1+(L_r^H/L_r^L)}\right) \tag{D.5}$$

   Where the L coefficients are as follows:

$$L_v^H = (1.10\times10^{-13} ergs^{-1}) exp(-6744K/T) \tag{D.6}$$

$$L_v^L = \left[n(H^0)\times k_H(0,1) + n(H_2)\times k_{H_2}(0,1)\right]\times(8.18\times10^{-13} ergs) \tag{D.7}$$

   where the $k(0,1)$ terms are collisional excitation rates for the $v=0\rightarrow1$ transition.

$$L_r^H = \begin{cases} (3.90\times10^{-19} ergs^{-1}) exp(-6118K/T); T > 1087K \\ dex\left[-19.24 + 0.474x - 1.247x^2\right]; T < 1087K \end{cases} \tag{D.8}$$

$$\frac{L_r^L}{Q(n)} = \begin{cases} (1.38\times10^{-22} ergs^{-1}) exp(-9243K/T); T > 4031K \\ dex\left[-22.90 - 0.553x - 1.148x^2\right]; T < 4031K \end{cases} \tag{D.9}$$

$$Q(n) = \left[n(H_2)^{0.77} + 1.2n(H^0)^{0.77}\right] \tag{D.10}$$

3. Λ_3: Atomic collisional cooling (Sutherland, Dopita 1993)(114)

$$\Lambda_3 = n_H^2 L_3 + 1.42\times10^{-27}(\times\sqrt{T} for T > 10,000K) \tag{D.11}$$

   The conditional temperature term is to account for thermal Bremsstrahlung.

4. Λ_4: H_2O rotational cooling (Neufeld, Kaufman 1993)(54)

$$\Lambda_4 = (n_{H_2} + 1.39n_H)\times n_{H_2O}\times1.32\times10^{-23}\left(\frac{T}{10^3}\right)^{\alpha} \tag{D.12}$$

$$\alpha = 1.35 - 0.3\times log\left(\frac{T}{10^3}\right) \tag{D.13}$$

5. Λ_5: H_2O vibrational cooling excited by H_2 collision (Hollenbach, McKee 1989)(46)

$$\Lambda_5 = 1.03 \times 10^{-26} n_{H_2} n_{H_2O} \times T exp\left(\frac{-2325}{T}\right) exp\left(\frac{-47.5}{T^{1/3}}\right) \tag{D.14}$$

6. Λ_6: H_2O vibrational cooling by atomic H collision (Hollenbach, McKee 1989)(46)

$$\Lambda_6 = 7.4 \times 10^{-27} n_H n_{H_2O} \times T exp\left(\frac{-2325}{T}\right) exp\left(\frac{-34.5}{T^{1/3}}\right) \tag{D.15}$$

7. Λ_7: H_2 collisional dissociation cooling (Shapiro, Kang 1987)(93)

$$\Lambda_7 = 7.18 \times 10^{-12}((n_{H_2}^2)(k_{D,H_2}) + (n_H)(n_{H_2})(k_{D,H})) \tag{D.16}$$

Where:

$$k_{D,H} = 1.2 \times 10^{-9} exp(-52400/T)(0.0933 exp(-17950/T))^{\beta} cm^{-3} s^{-1} \tag{D.17}$$

$$k_{D,H_2} = 1.2 \times 10^{-9} exp(-53300/T)(0.0908 exp(-16200/T))^{\beta} cm^{-3} s^{-1} \tag{D.18}$$

Cooling cross sections for H_2 are not well known for every case, leading to possible errors of up to 20% with an assumed para-to-ortho ratio of 1/3. Given the already large variation in magnitude of physical quantities in our models the impact of these errors in our results should not be too significant.

8. Λ_8: H_2 reformation heating (Smith, Rosen, 2003)(103)

$$\Lambda_8 = -L_7(n)(n_H)(1-\beta) \times 7.18 \times 10^{-12} \tag{D.19}$$

β is the fraction of energy released thermally rather than radiated away, and L_7 is defined as:

$$L_7 = (3 \times 10^{-18} cm^3 s^{-1}) \times \frac{\sqrt{T} f_a}{1 + 0.04\sqrt{T + T_g} + 210^{-3} T + 810^{-6} T^2} \tag{D.20}$$

and f_a is given by:

$$f_a = [1 + 10000 exp(-600/T_g)]^{-1} \tag{D.21}$$

9. Λ_9: CO vs. H, H_2 collisional cooling, rotational CO (McKee et al., 1982)(68)

$$\Lambda_9 = (n)(n_{CO})\frac{kT\sigma v_T}{1+\frac{n_a}{n_{cr}}+1.5\sqrt{\frac{n_a}{n_{cr}}}} \tag{D.22}$$

Where $v_T = \sqrt{\frac{8kT}{\pi m_{H_2}}}$, $n_a = 0.5(n_H + \sqrt{n_{H_2}})$, $n_{cr} = 3.3 \times 10^6 T_3^{0.75} cm^{-3}$ and $\sigma = 3.3 \times 10^{-16} T_3^{-0.25} cm^{-2}$, with $T_3 = T/1000K$.

10. Λ_{10} (& Λ_{11}): CO vs. H, H_2 collisional, vibrational CO (Neufeld, Kaufman 1993)(54)

$$\Lambda_{10} = 1.83 \times 10^{-26}(n_{H_2})(n_{CO})\sqrt{T}exp(3080/T)exp(-68/T^{\frac{1}{3}}) \tag{D.23}$$

11. Λ_{11}:

$$\Lambda_{11} = 1.28 \times 10^{-24}(n_{H_2})(n_{CO})\sqrt{T}exp(-3080/T)exp(-(2000/T)^{3.43}) \tag{D.24}$$

12. Λ_{12}: Fine structure 63μm Oxygen cooling (Smith, Rosen, 2003)(103)

$$\Lambda_{12} = 2.82 \times 10^{-18} n_O \frac{1}{\frac{1}{f_H}+\frac{A_{10}}{r_L}} \tag{D.25}$$

Where $r_L = r_H + r_{H_2}$ the combined collisional rate of H and H_2:

$$r_H = (n_H + 0.48 n_H)(4.37\times10^{-12}T^{0.66}0.6exp(-228/T)+1.06\times10^{-12}T^{0.8}0.2exp(-326/T)) \tag{D.26}$$

$$r_{H_2} = (n_{H_2})(2.88\times10^{-11}T^{0.35}0.6exp(-228/T)+6.68\times10^{-11}T^{0.31}0.2exp(-326/T)) \tag{D.27}$$

The spontaneous transition rate $A_{10} = 8.95 \times 10^{-5} s^{-1}$; and the fractional occupation rate of the $^3P_1$ level is given by:

$$f_H = \frac{0.6exp(-228/T)}{1+0.6exp(-228/T)+0.2exp(-326/T)} \tag{D.28}$$

13. Λ_{13}: OH cooling (Hollenbach, McKee 1989)(46)

$$\Lambda_{13} = 2.84 \times 10^{-28} n^2 T^{\frac{3}{2}} \tag{D.29}$$

Further detail on these cooling functions may be found in Smith & Rosen, 2003 (103).

Appendix E

Additional Section Plots

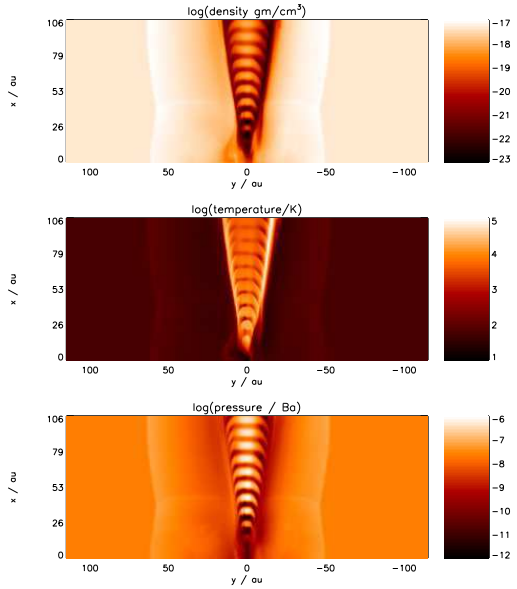

(a) ORB.1

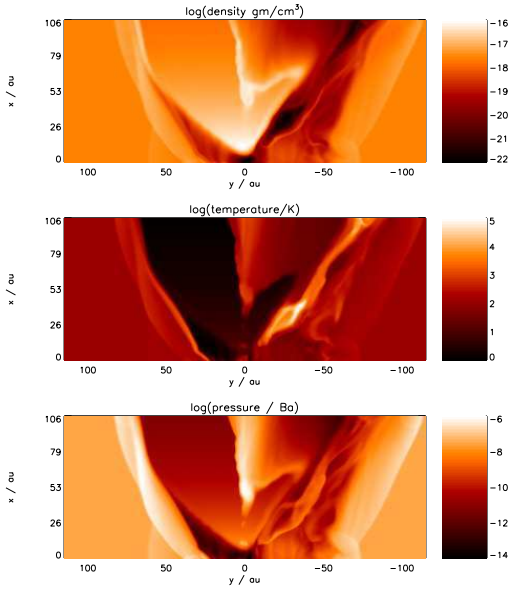

(b) ORB.2

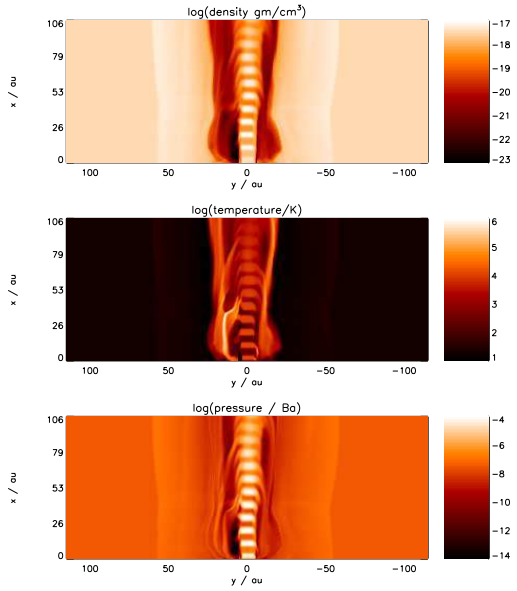

(c) PRE.1

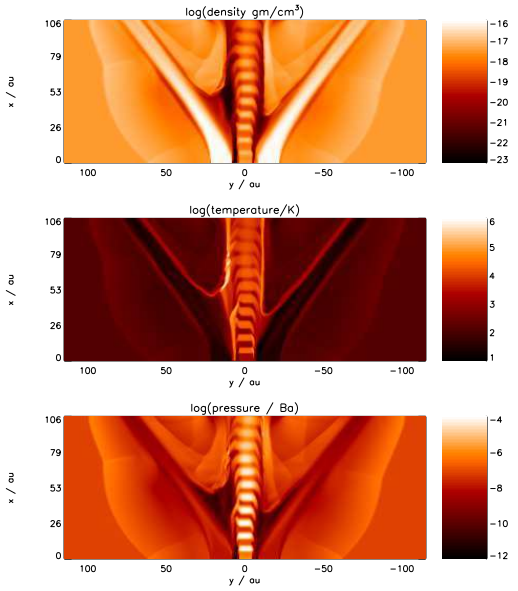

(d) PRE.2

Figure E.1: Density, Temperature and Pressure, 4-model comparison, x-y plane cross sections at z=0cm at simulation time T=87.5 years. Plots are scaled individually.

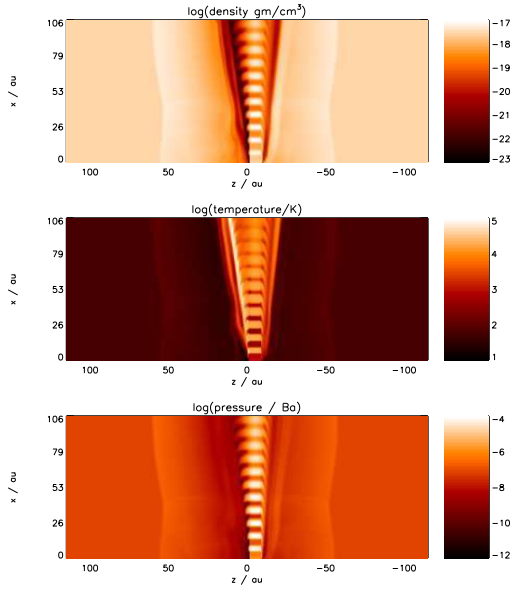

(a) ORB.1

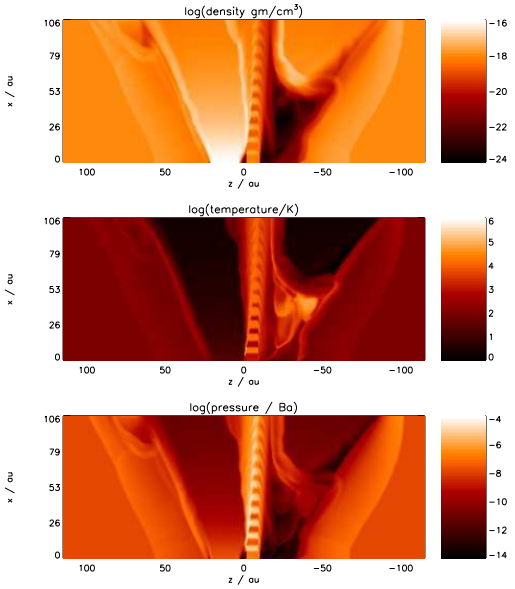

(b) ORB.2

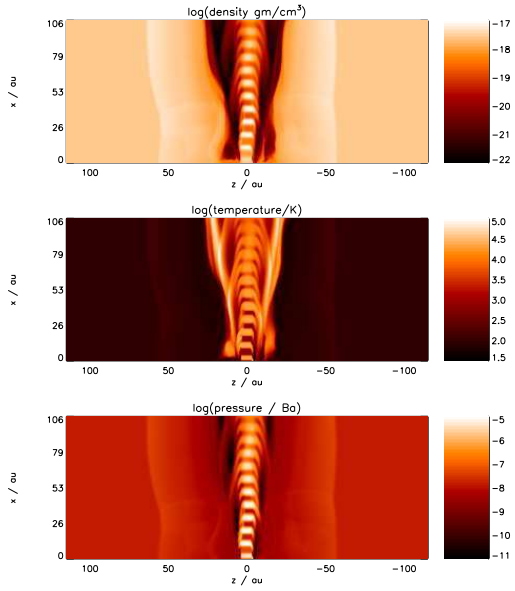

(c) PRE.1

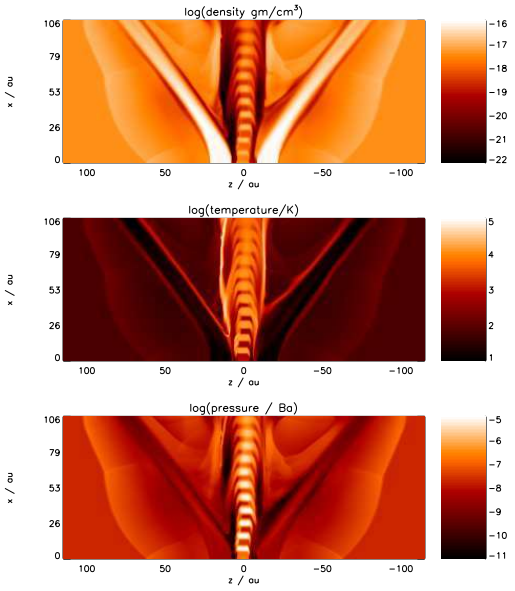

(d) PRE.2

Figure E.2: Density, Temperature and Pressure, 4-model comparison, x-z plane cross sections at y=0cm at simulation time T=87.5 years. Plots are scaled individually.

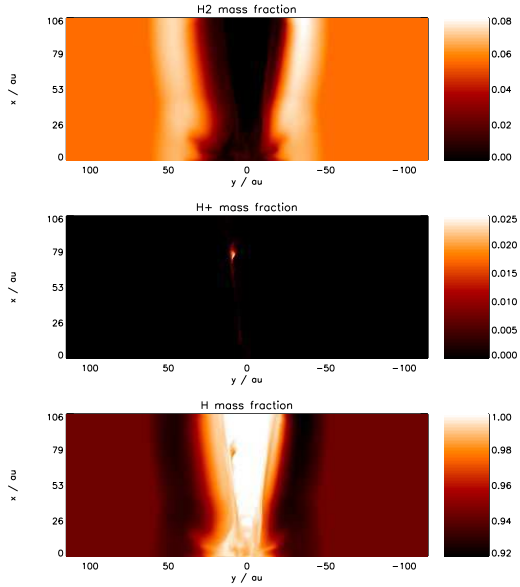

(a) ORB.1

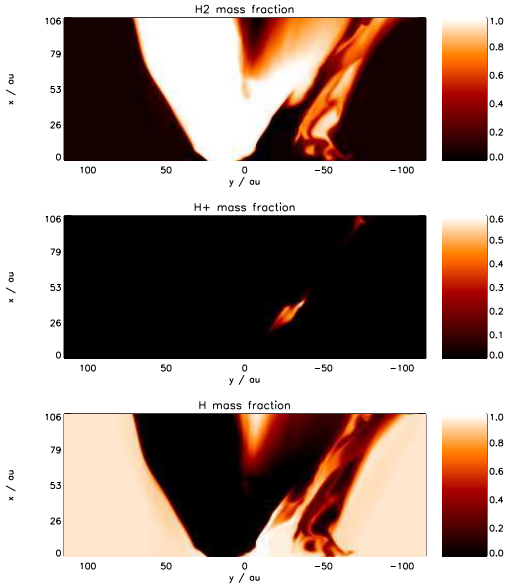

(b) ORB.2

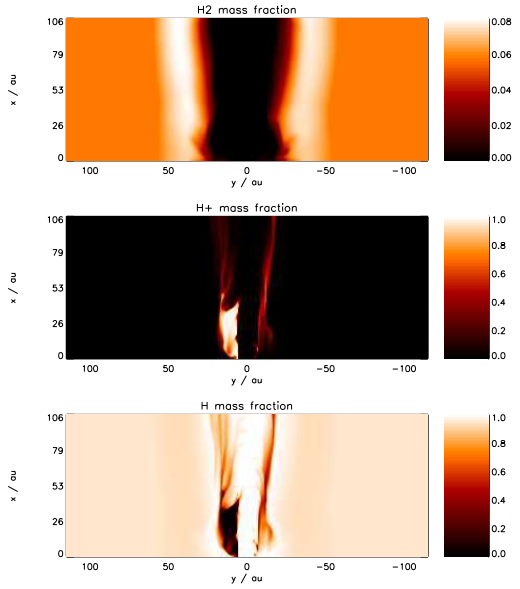

(c) PRE.1

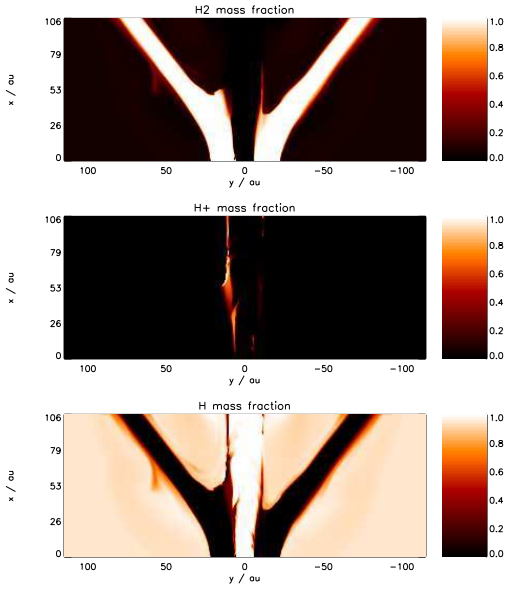

(d) PRE.2

Figure E.3: Chemical Density Fraction, 4-model comparison, x-y plane cross sections at z=0cm, at simulation time T=87.5 years. Plots are scaled individually.

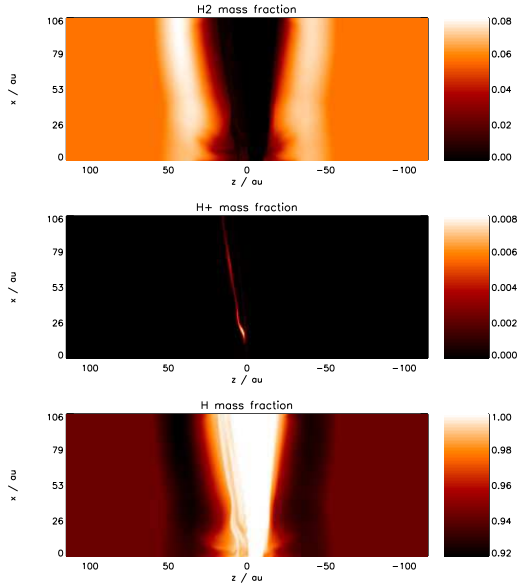

(a) ORB.1

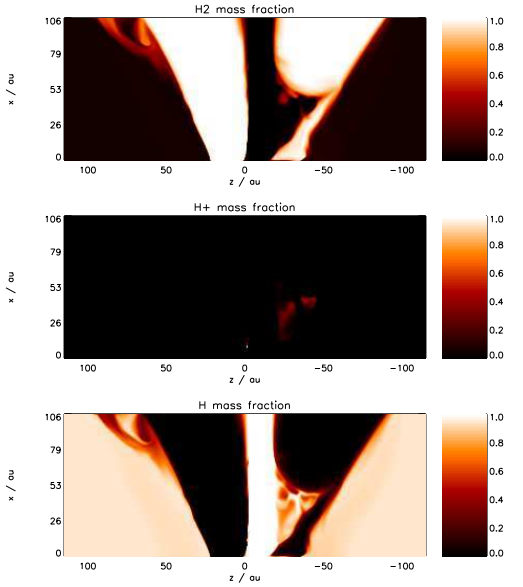

(b) ORB.2

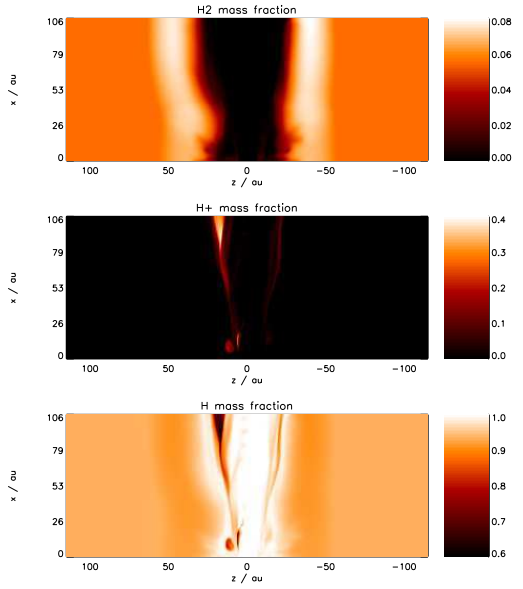

(c) PRE.1

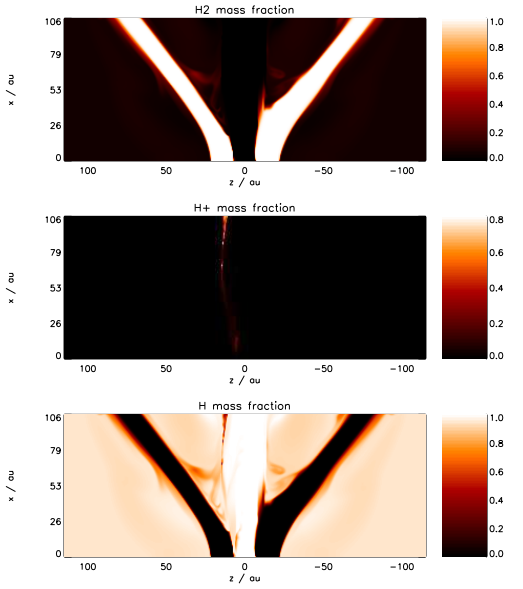

(d) PRE.2

Figure E.4: Chemical Density Fraction, 4-model comparison, x-z plane cross sections at y=0cm, at simulation time T=87.5 years. Plots are scaled individually.

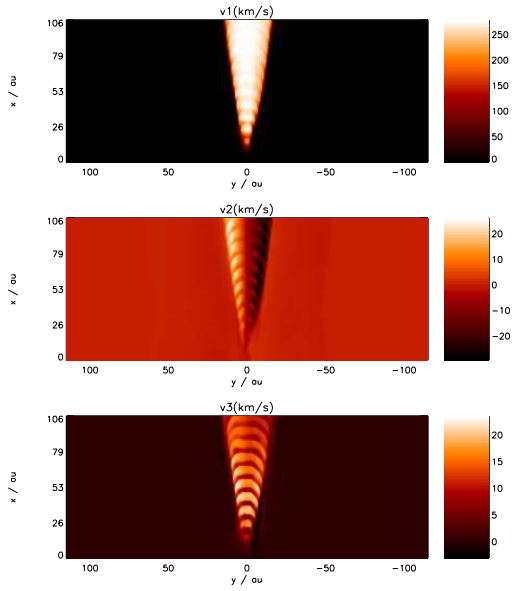

(a) ORB.1

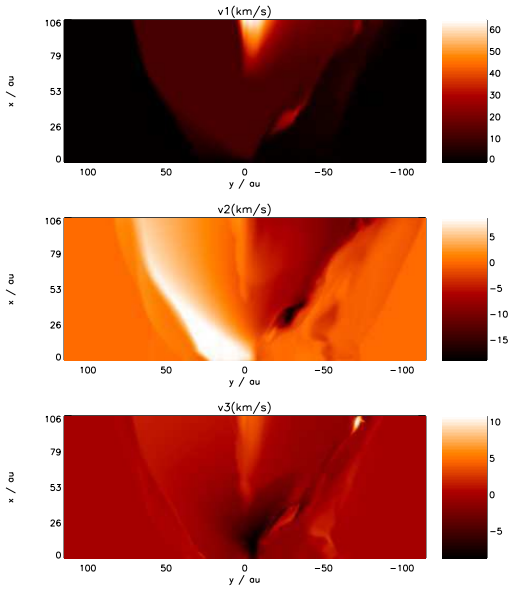

(b) ORB.2

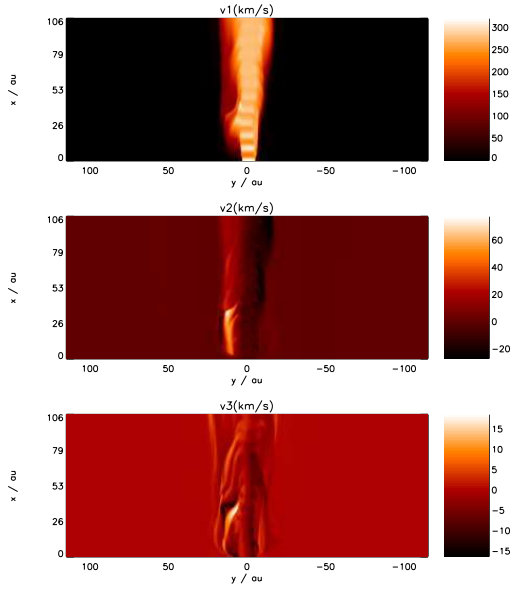

(c) PRE.1

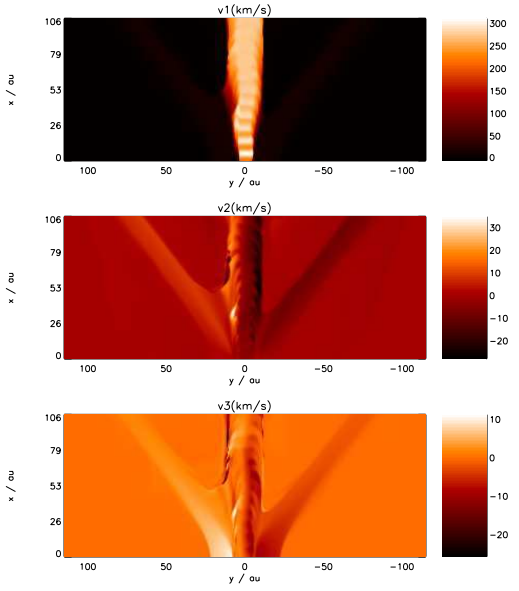

(d) PRE.2

Figure E.5: Cartesian velocity components represented as scalar fields, 4-model comparison, x-y plane cross sections at z=0cm, at simulation time T=87.5 years. Plots are scaled individually.

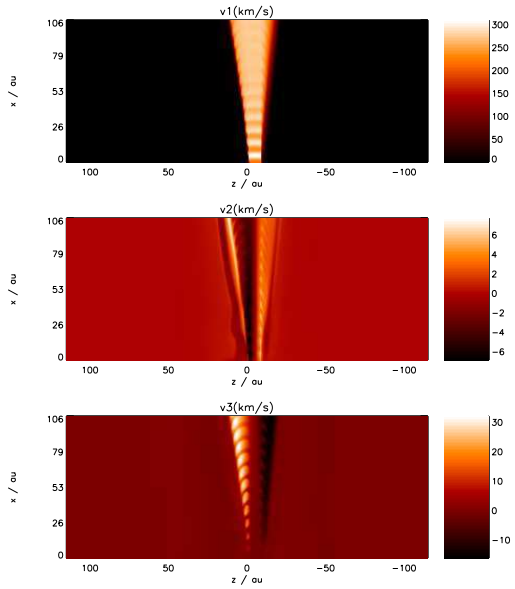

(a) ORB.1

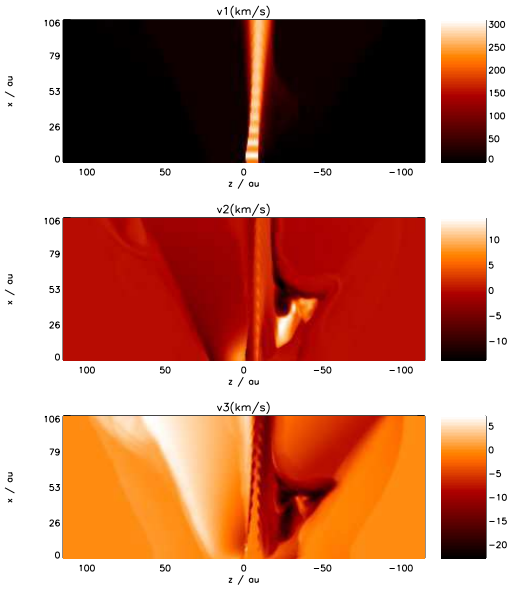

(b) ORB.2

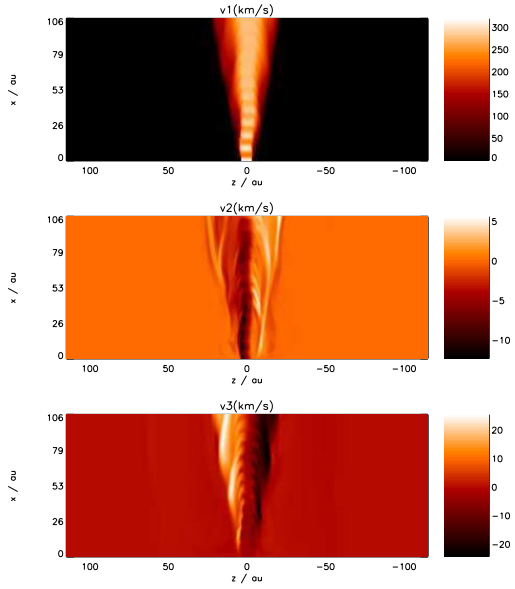

(c) PRE.1

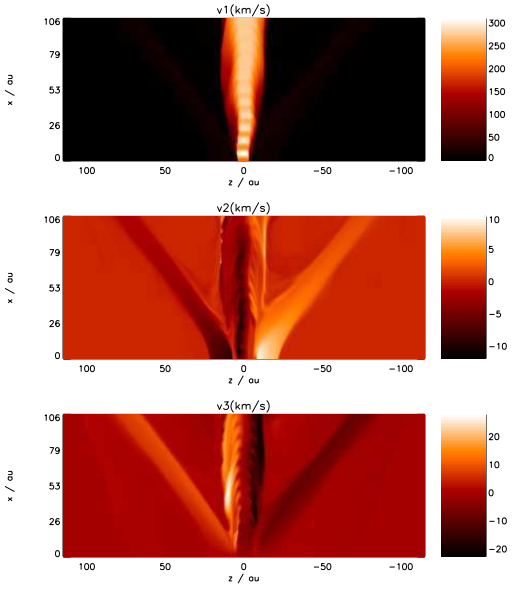

(d) PRE.2

Figure E.6: Cartesian velocity components represented as scalar fields, 4-model comparison, x-z plane cross sections at y=0cm, at simulation time T=87.5 years. Plots are scaled individually.

Appendix F

Longitudinal Comparisons

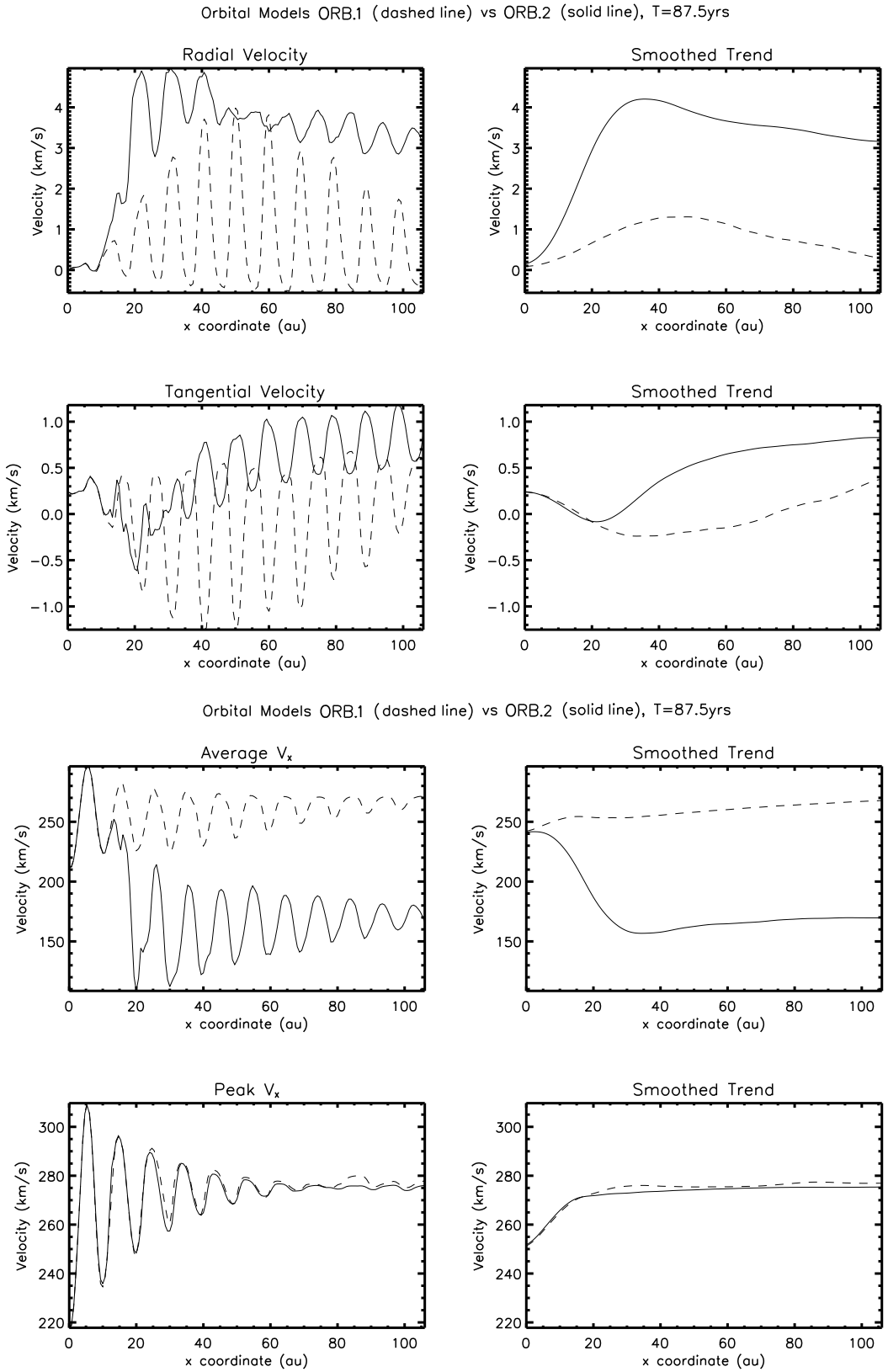

Figure F.1: Orbital models: atomic jet net radial, tangential, average and peak velocities along propagation axis, T=87.5 years. Radial velocity is directed outward with respect to the domain x-axis. Tangential velocity is directed in a right-handed sense perpendicular to a normal line radiating from the x-axis & passing through the jet's plane centroid. Models: ORB.2 (with molecular outflow) and ORB.1 (without).

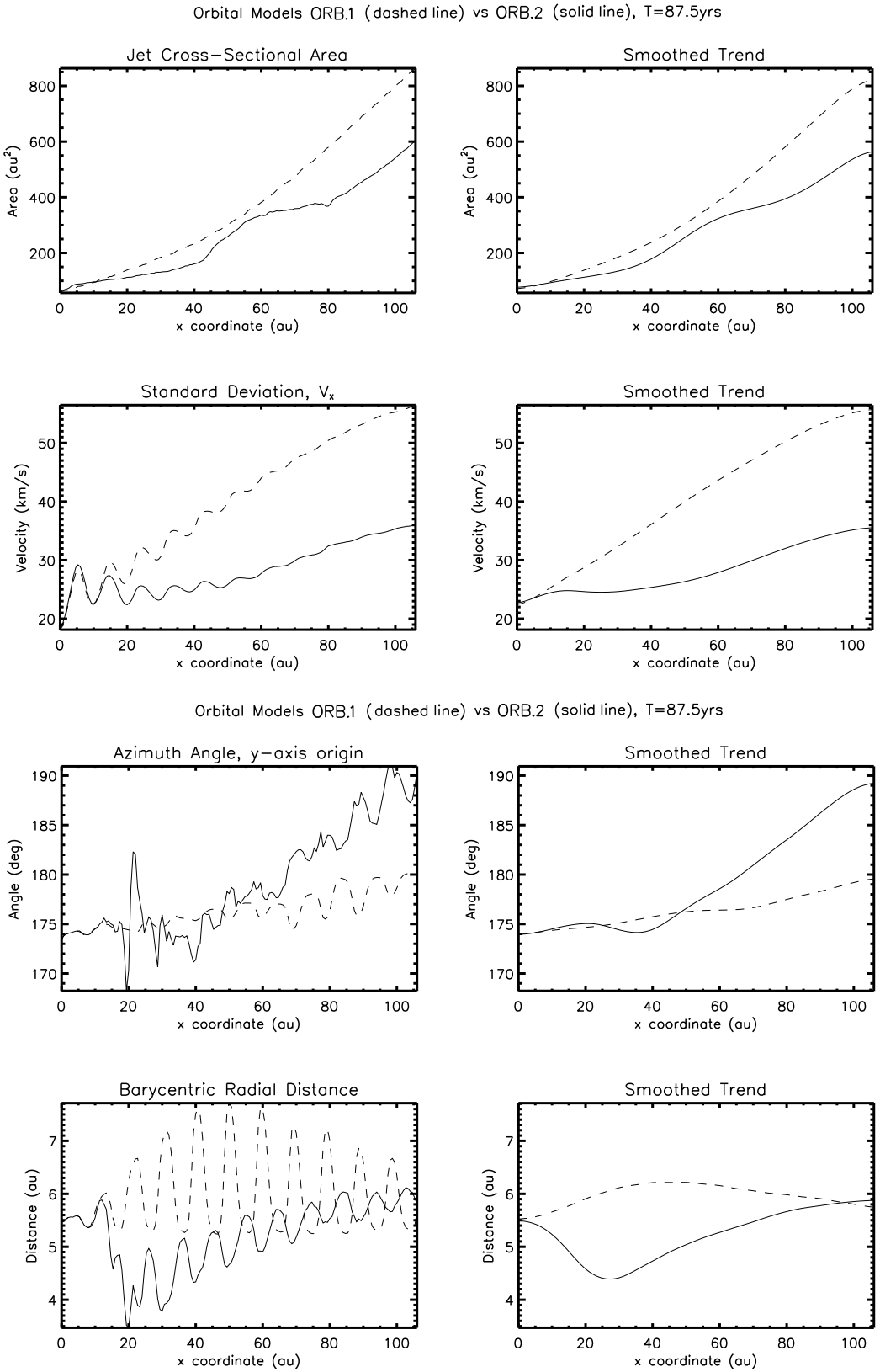

Figure F.2: Orbital models: atomic jet x-sectional area, velocity standard deviation, azimuth angle and radial distance along propagation axis, T=87.5 years. Radial distance is directed outward with respect to the domain x-axis. Azimuth angle is directed in an anticlockwise sense about the domain x-axis. Models: ORB.2 (with molecular outflow) and ORB.1 (without).

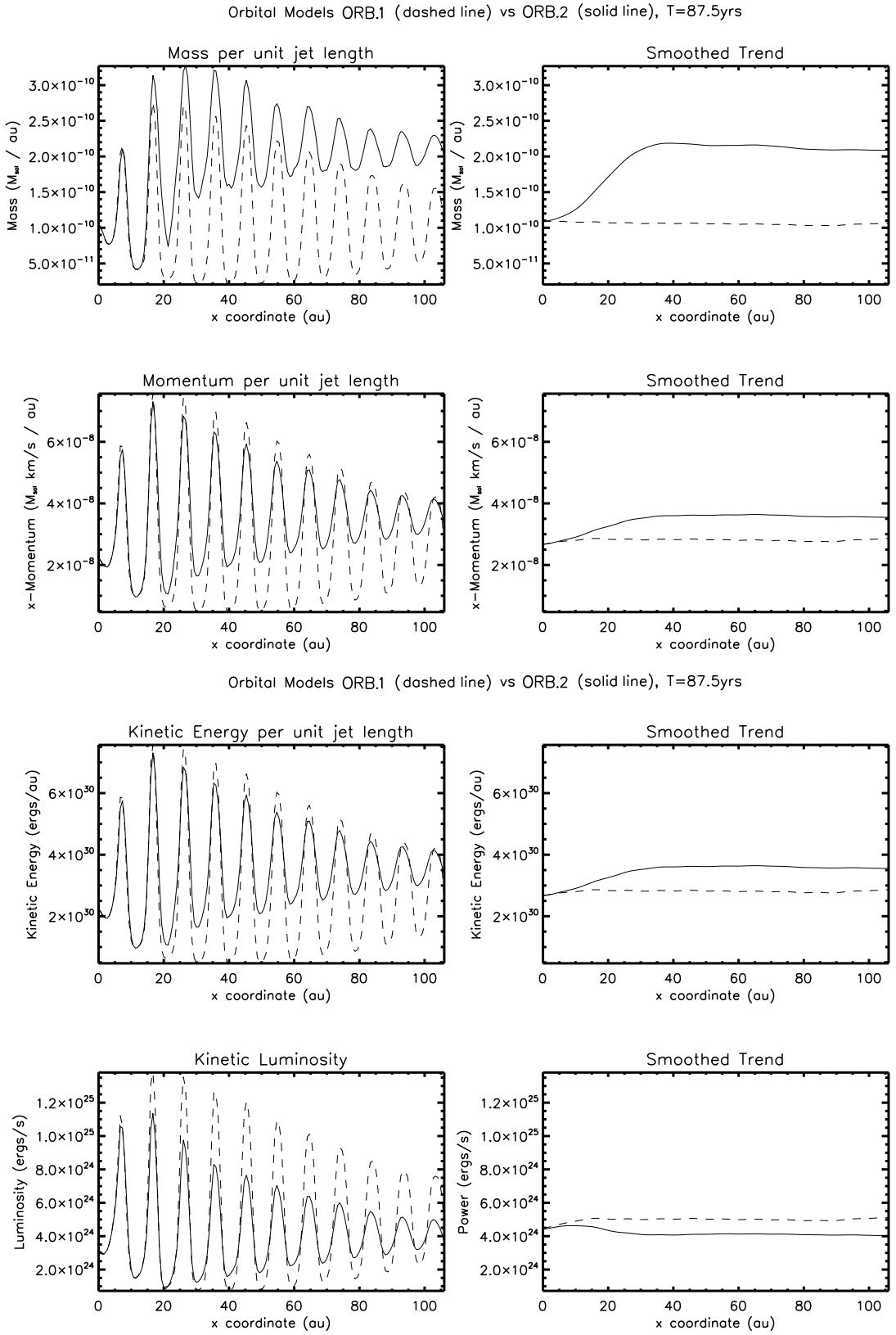

Figure F.3: Orbital models: atomic jet mass, momentum, kinetic energy and kinetic luminosity along propagation axis, T=87.5 years. Model numbers: ORB.2 (with molecular outflow) and ORB.1 (without).

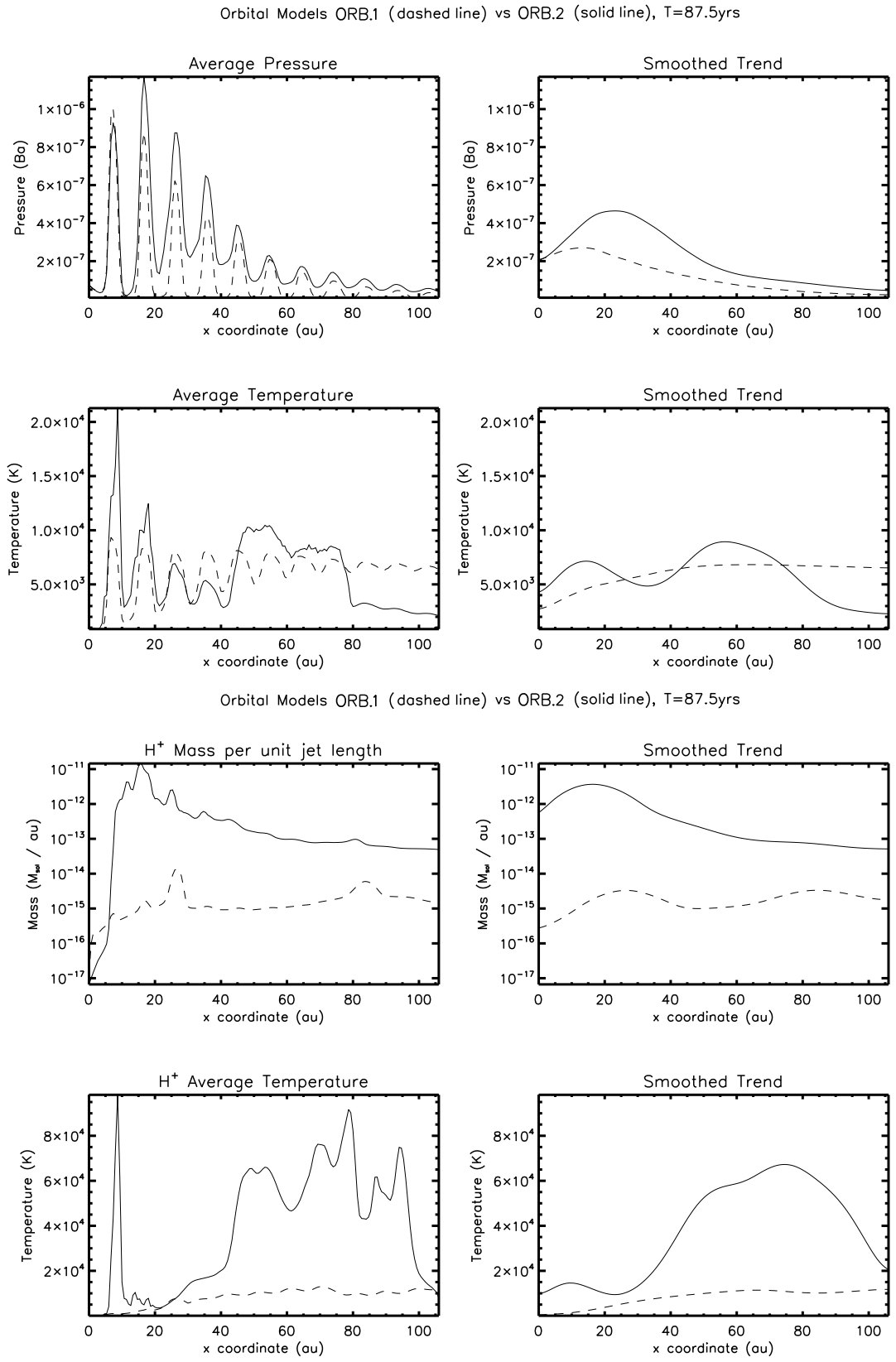

Figure F.4: Orbital models: atomic jet pressure, temperature, ionisation and ion temperature along propagation axis, T=87.5 years. Model numbers: ORB.2 (with molecular outflow) and ORB.1 (without).

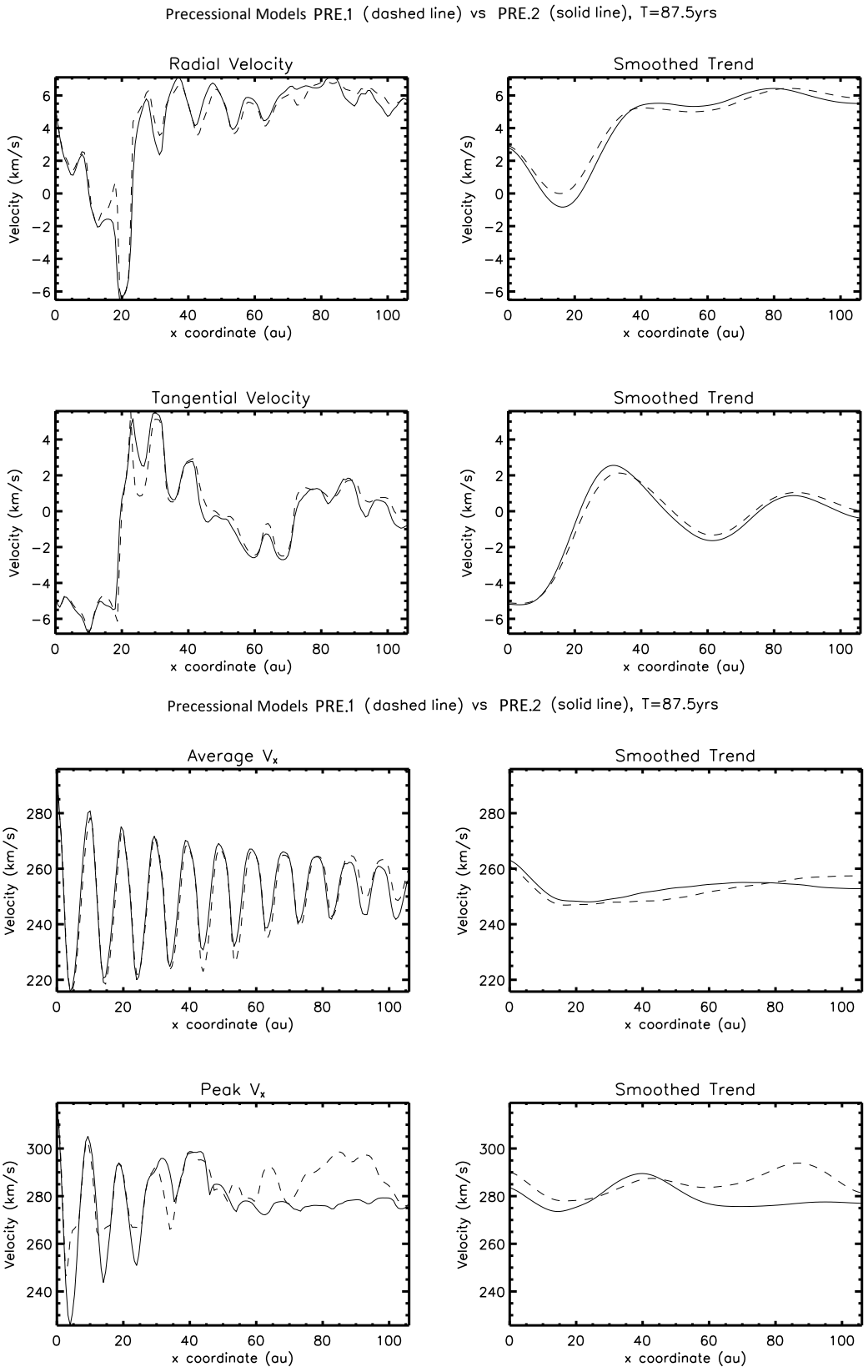

Figure F.5: Precessional models: atomic jet net radial, tangential, average and peak velocities along propagation axis, T=87.5 years. See explanatory notes on Fig.5.15. Model numbers: PRE.2 (with molecular outflow) and PRE.1 (without).

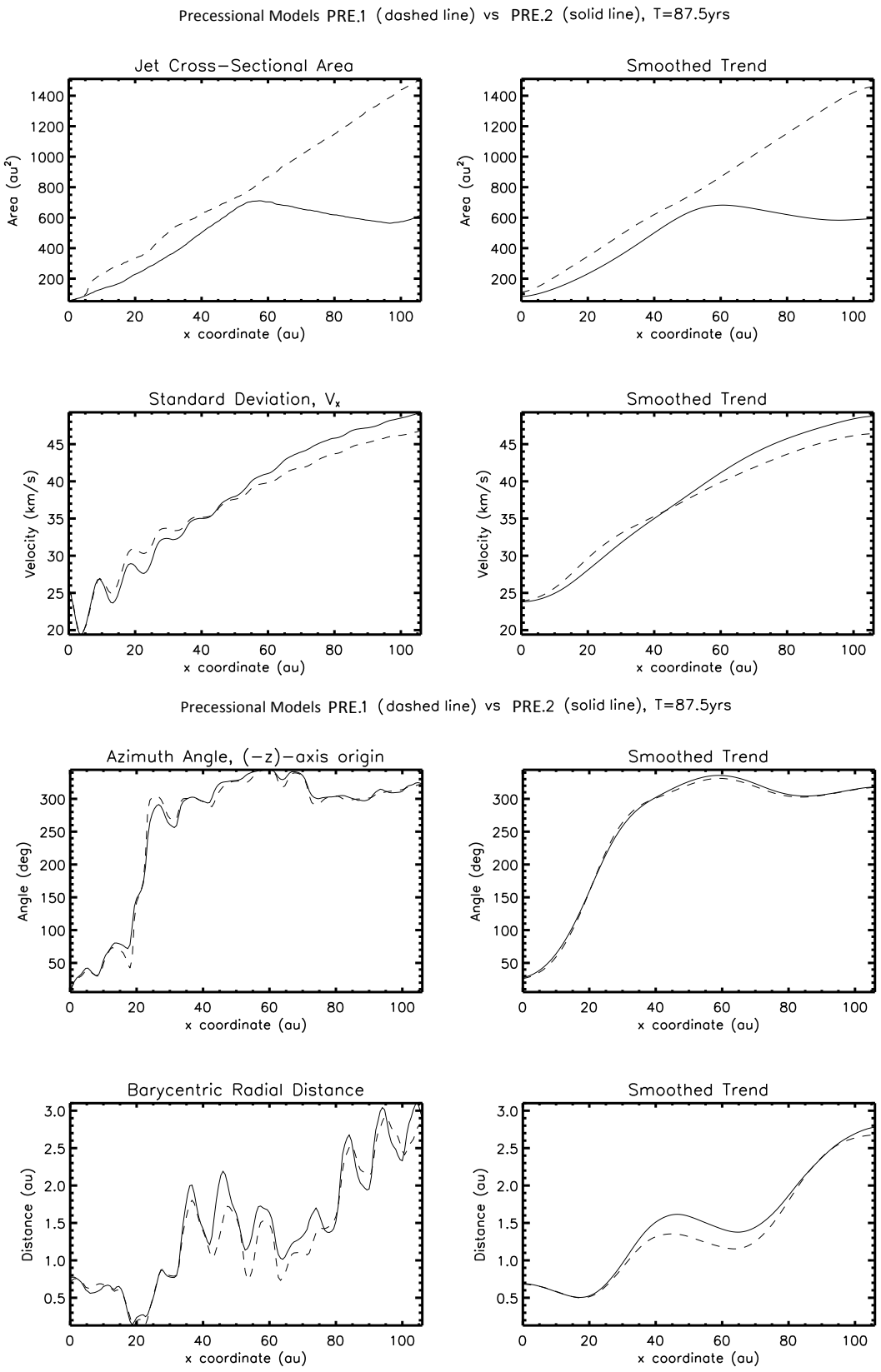

Figure F.6: Precessional models: atomic jet x-sectional area, velocity standard deviation, azimuth angle and radial distance along propagation axis, T=87.5 years. Model numbers: PRE.2 (with molecular outflow) and PRE.1 (without).

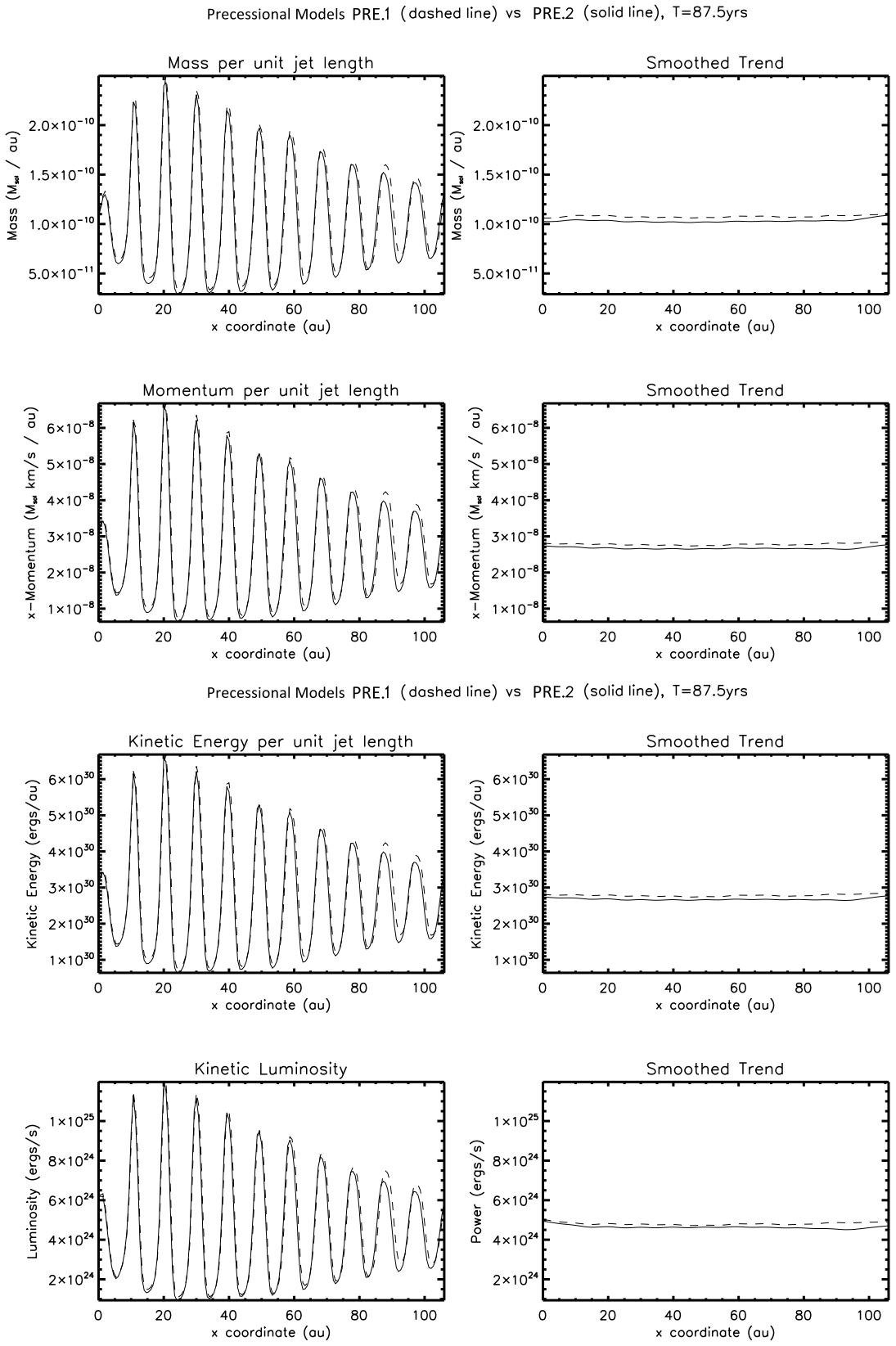

Figure F.7: Precessional models: atomic jet mass, momentum, kinetic energy and kinetic luminosity along propagation axis, T=87.5 years. Model numbers: PRE.2 (with molecular outflow) and PRE.1 (without).

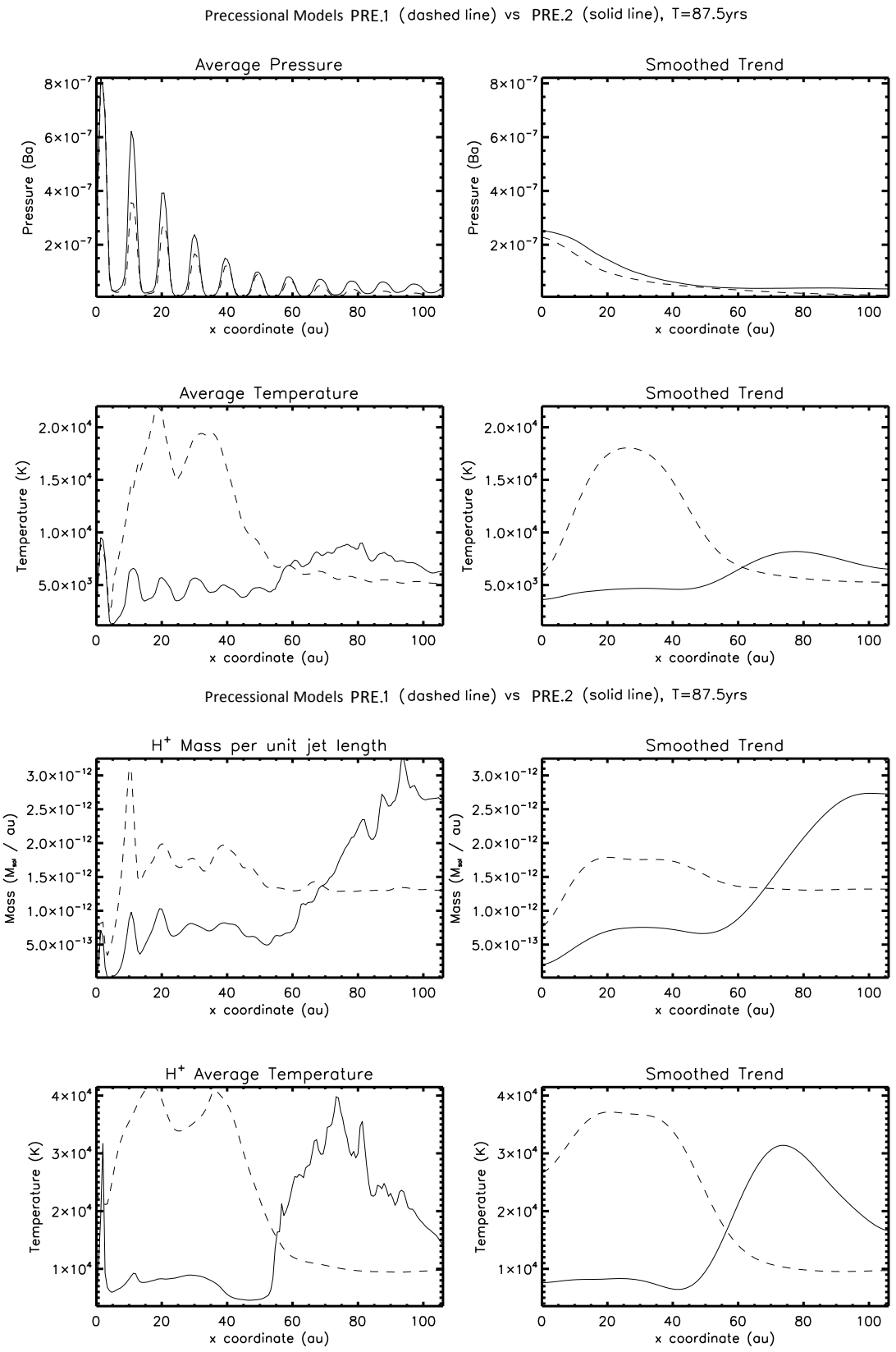

Figure F.8: Precessional models: atomic jet pressure, temperature, ionisation and ion temperature along propagation axis, T=87.5 years. Model numbers: PRE.2 (with molecular outflow) and PRE.1 (without).

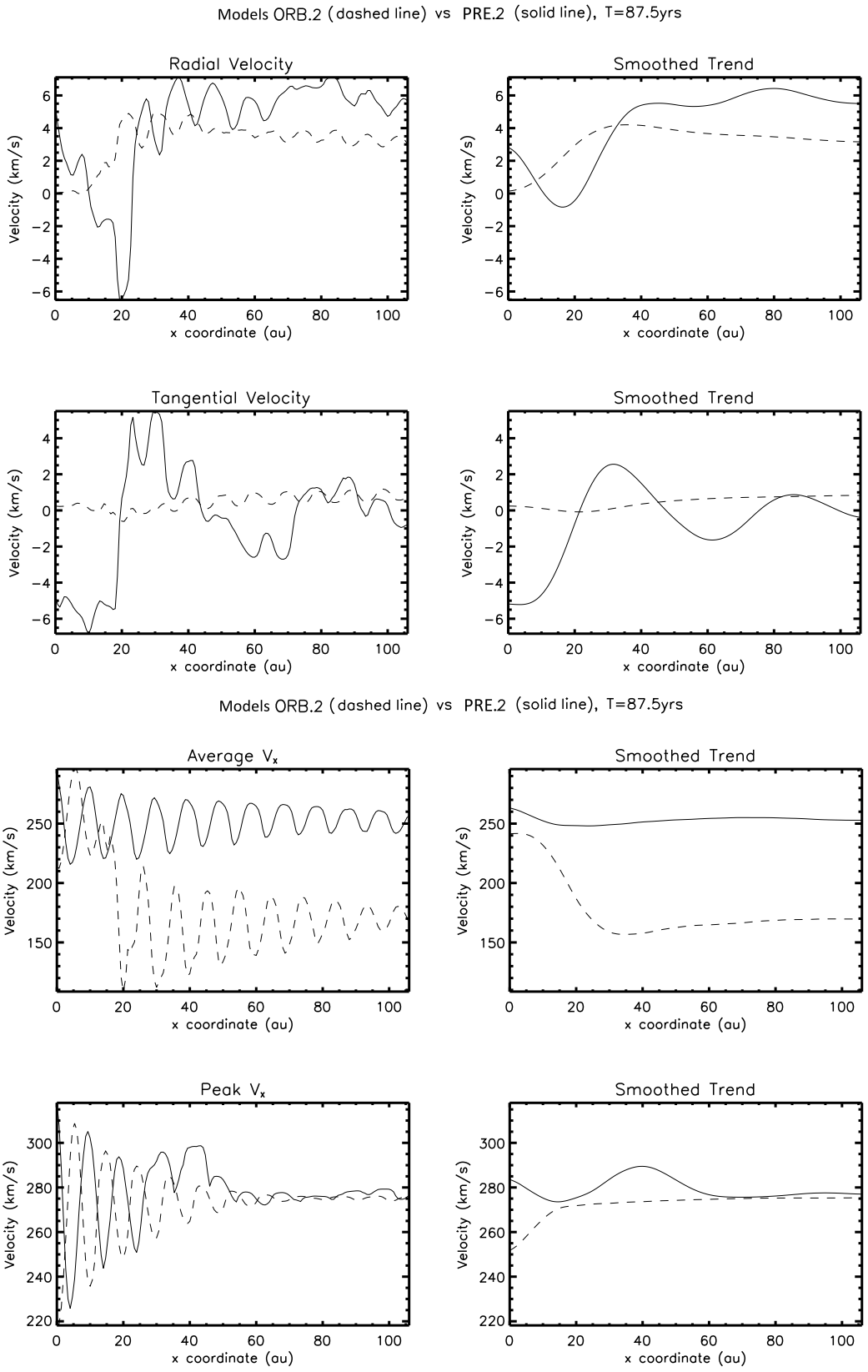

Figure F.9: Orbital vs. Precessional: atomic jet net radial, tangential, average and peak velocities along propagation axis, T=87.5 years. See explanatory notes on Fig.5.15. Model numbers: PRE.2 (Precessional) and ORB.2 (Orbital).

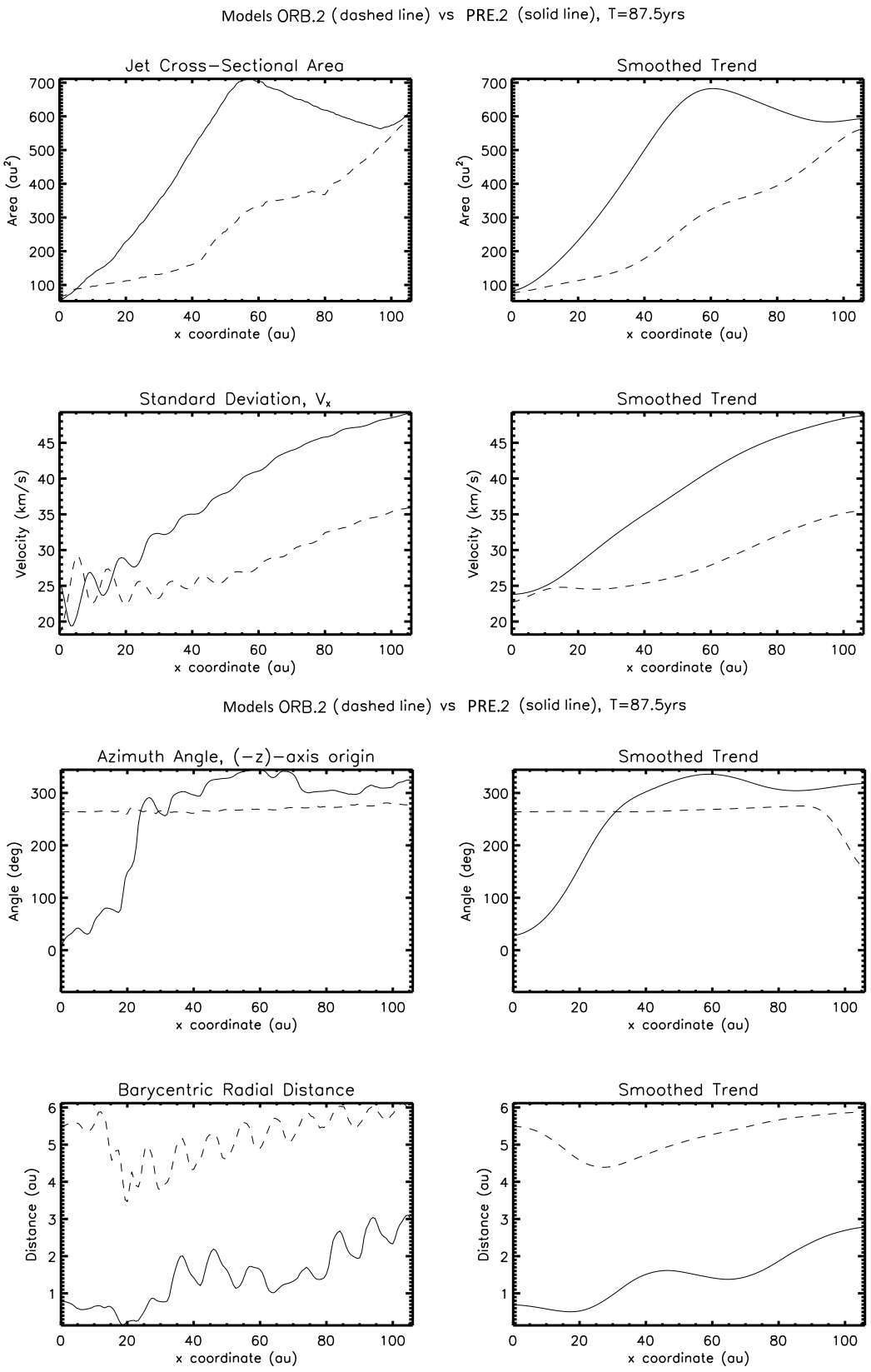

Figure F.10: Orbital vs. Precessional: atomic jet x-sectional area, velocity standard deviation, azimuth angle and radial distance along propagation axis, T=87.5 years. See explanatory notes on Fig.5.15. Model numbers: PRE.2 (Precessional) and ORB.2 (Orbital).

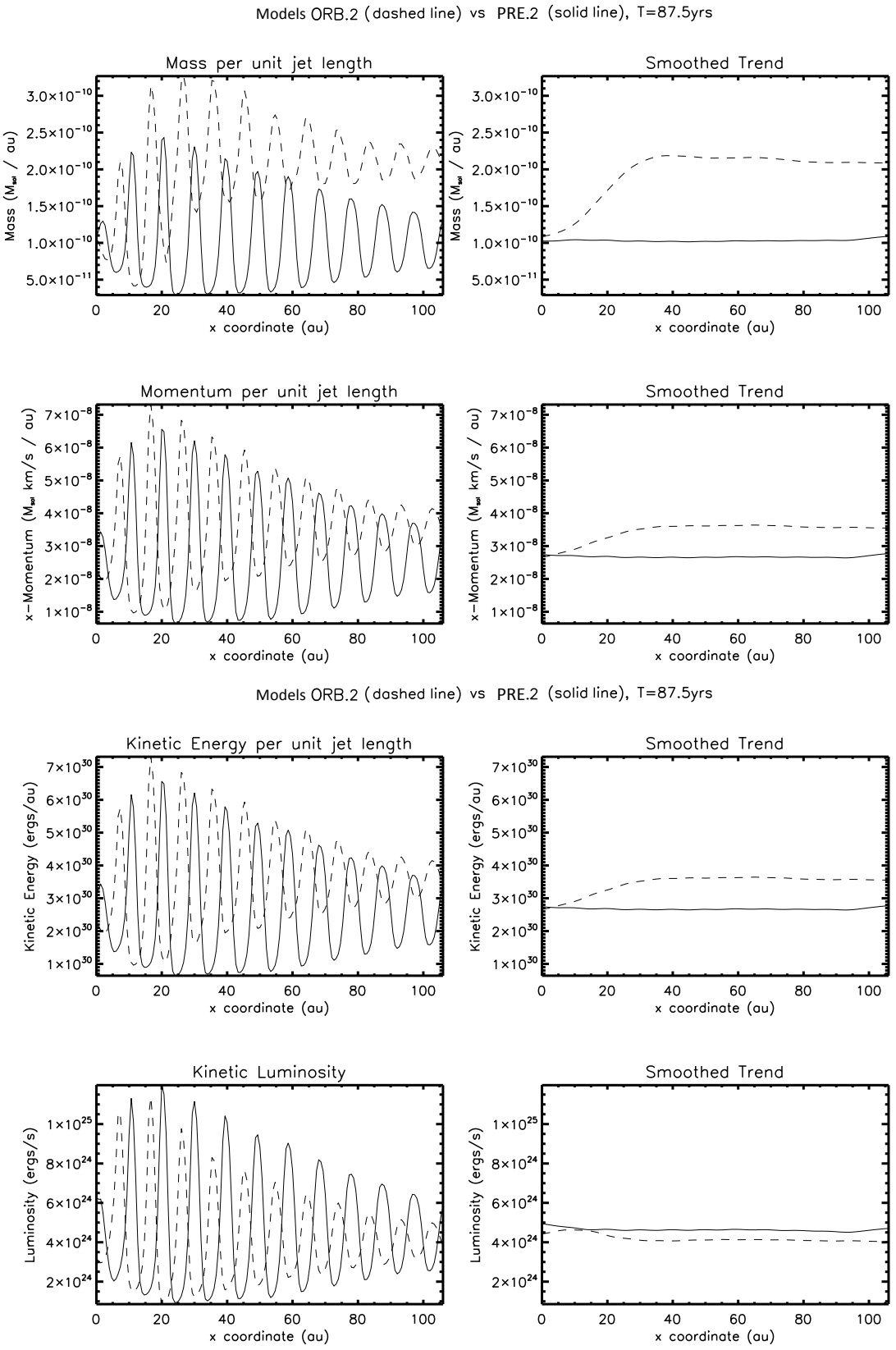

Figure F.11: Orbital vs. Precessional: atomic jet mass, momentum, kinetic energy and kinetic luminosity along propagation axis, T=87.5 years. Model numbers: PRE.2 (Precessional) and ORB.2 (Orbital).

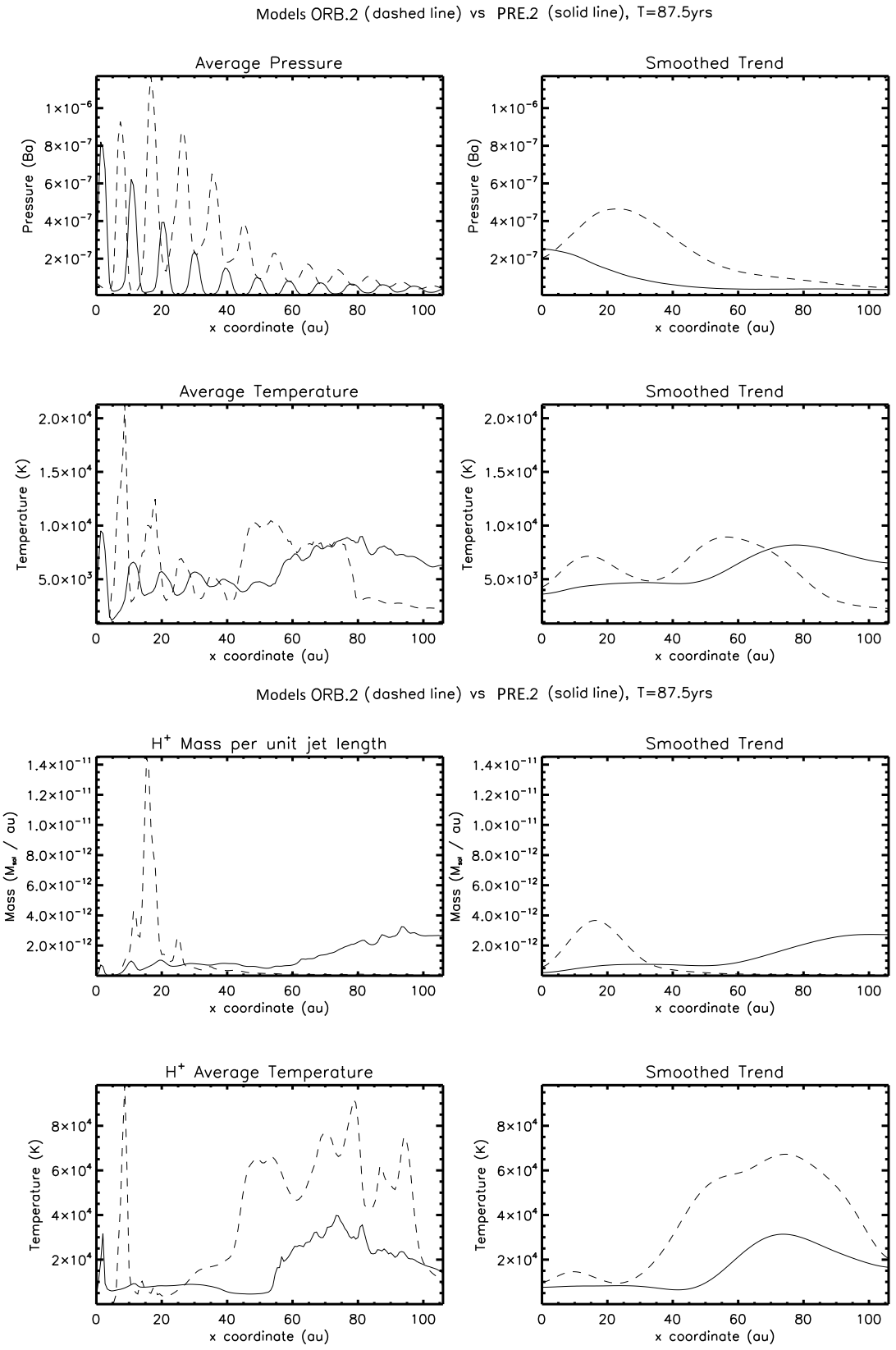

Figure F.12: Orbital vs. Precessional: atomic jet pressure, temperature, ionisation and ion temperature along propagation axis, T=87.5 years. Model numbers: PRE.2 (Precessional) and ORB.2 (Orbital).

Appendix G

MULTISYNTH

G.1 MULTISYNTH - An IDL® Synthetic Image Code

G.1.1 Structure and operation of MULTISYNTH

The MULTISYNTH program was written in IDL® 7.0 with the specific purpose of generating synthetic observations from our protostellar jet models, but efforts were made to make the code sufficiently flexible that it might be adapted for other astrophysical applications. The original basis of MULTISYNTH was an IDL® code (Moraghan A., Smith M.D.S.) for generating MPG movies from ZEUS output files, though much capability has been added since. As far as is sensible, characteristics of the jet models have been parameterised in the code so they can be changed easily, but it has been difficult to avoid hard coding for the specific topology of our models, particularly in the layout design of the outputs. Modifying this would not pose a difficult challenge to the user if it is desired to adapt the code to study other phenomena.

MULTISYNTH generates synthetic image flux files and accompanying position-velocity distribution files in HDF 4 format, which are then used as input to further IDL® scripts which produce particular final outputs. One flux file and one p-v distribution file is generated for each of four emission lines plus column density and p-v distribution files for the column densities binned by radial velocity w.r.t. the observer. A set of these files can be generated for up to six aspect angles θ, where θ is the angle the model's principal (x) axis makes to the sky plane.

A MULTISYNTH flux file consists of a series of frames, each of which is a depthwise-

integrated synthetic image of a particular transition such as the 656nm H-alpha line. MULTISYNTH operates on HDF 4 output files from ZEUS-MP, each of which is a grid model of the physical state of an astrophysical object such as a protostellar jet, captured at an instant during its evolution. The ZEUS-MP output files must hold information on the hydrogen species that comprise the material.

In addition to synthetic imaging of the total line emission, each frame in a MULTISYNTH flux file also stores the emission image binned into four channels based on the velocity of the emitting material in the sky plane, i.e. its proper motion.

The IDL® HDF 4 interface is subject to a maximum file size limit of 2GB. The p-v distribution files are $\sim 10\%$ larger than the flux files. By way of guidance, a model of spatial dimensions 1280 x 175 (x 175 though depth can be arbitrary), i.e. 2.24×10^5 'pixels' that is processed by MULTISYNTH will produce a p-v distribution file of a little under 2GB if the file contains 400 frames. The spatial depth of the integrated image is traded for a velocity 'depth' of 1000 bins.

In producing lengthy time-wise simulations, this limitation of file size can be overcome by dividing the operation of MULTISYNTH, on a given set of model output frames, between multiple instances of IDL® (which may also be desirable to produce results within a reasonable timescale); in which case, each IDL® instance will produce a separate flux file set. The IDL® program MSYNTHMOV can process and concatenate a specified grouping of MULTISYNTH flux file sets into a single movie (provided of course that the dimensions of the synthetic images in all the flux files are the same).

G.1.2 Further IDL® codes in the MULTISYNTH suite

A number of other IDL® programs were written to post-process the outputs from MULTISYNTH to generate final outputs in Postscript, JPEG and MPEG format.

- MSYNMOV, written to process up to 8 flux file sets of 4 emission lines into a single MPEG movie, also producing one JPEG snapshot per file set.
- MSYNVCHAN, which generates 4-channel velocity maps of 4 emission lines for a selected time frame. Postscript output.
- MSYNPOSVEL, which outputs position-velocity plots and line profiles for 4 emission lines, for a selected time frame. Postscript output.
- MSYNSTATS, which calculates statistics from up to 8 flux file sets of 4 emission lines, e.g. total emission of each line within a selected region per time frame, and outputs these figures to a text file.

Also, a modified version of MULTISYNTH was used to generate output data for Mass-Velocity spectra. This and other functions of MULTISYNTH were performed as post-processing operations, since integrating them into the ZEUS-MP code was difficult because of the parallel architecture. Though this was disadvantageous in terms of speed, there was an advantage of modularity in being able to re-generate synthetic image data with different parameters or coefficients from the ZEUS-MP HDF output without having to re-run ZEUS-MP.

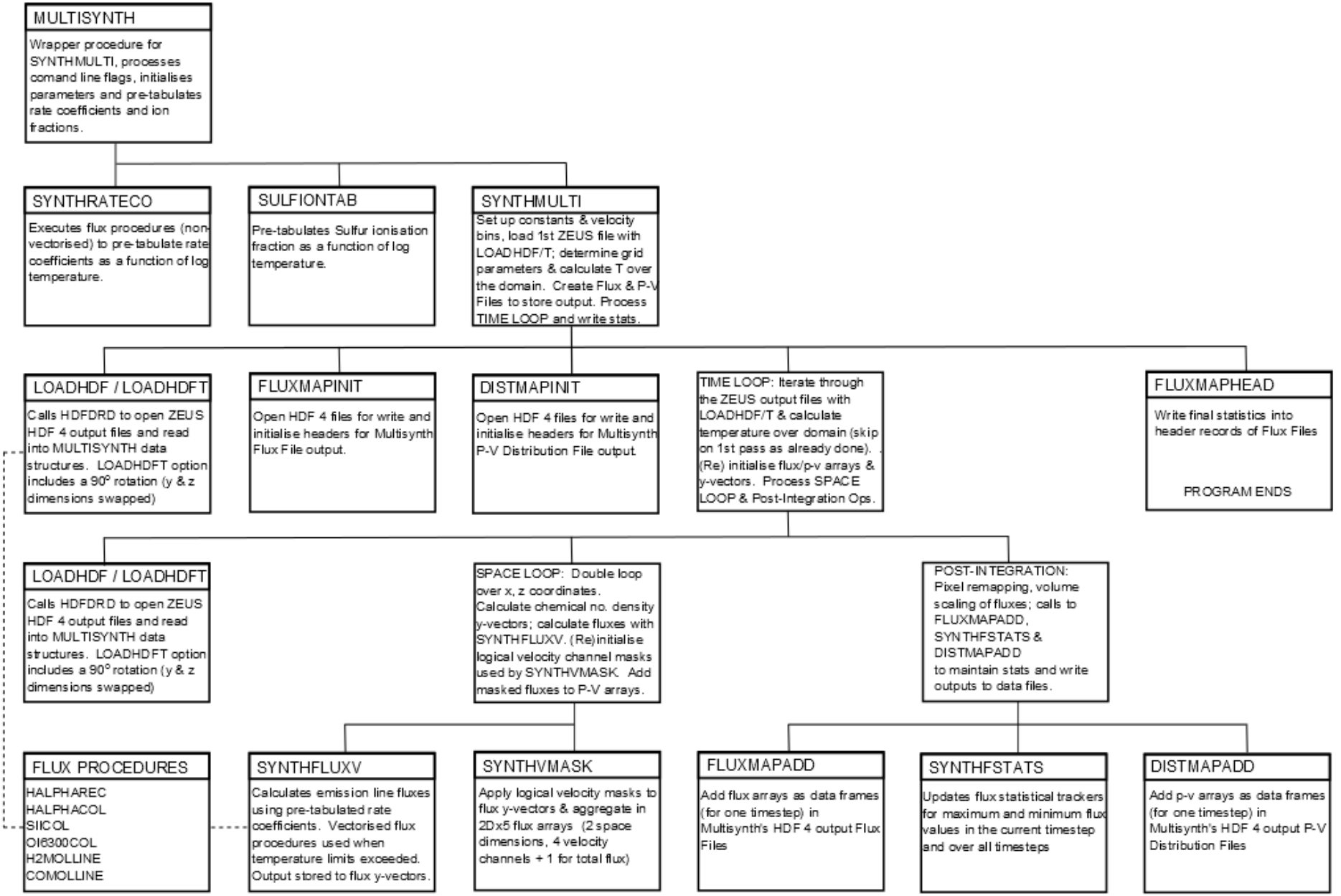

Figure G.1: MULTISYNTH Program Structure - Tree diagram is traversed via the solid lines Top-Bottom, Left-Right; at the bottom of a branch return to the previous level and continue.

G.1.3 Calculation of H-α Emission from a ZEUS Jet Model

The section that follows is based on material from Draine (2011)(25) and Krumholz (2014)(58), except where otherwise indicated.

The H-α line is a deep red visible spectral line in the Balmer series, with a wavelength of 656.28 nm. This emission is generated when an electron in an excited Hydrogen atom falls from the n=3 to n=2 energy state, where n is the principal quantum number.

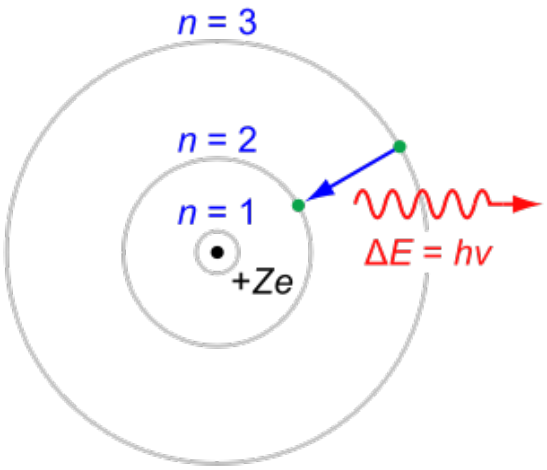

Figure G.2: H-α Production; ΔE = 1.89eV

To calculate this emission from our jet material and its surrounding environment we are interested in the rate at which transitions are occurring from the second excited state of Hydrogen, n=3, to the n=2 state. At any given instant, ZEUS records the populations of H, H_2, and H^+ species, but does not maintain any record of atoms in excited states. In fact Hydrogen atoms do not remain long in the n=3 state before de-exciting to lower energy states - the timescale is dramatically shorter than the dynamic timescale of the jet models - and so we may make the assumption that all H-α production occurs via instantaneous processes without needing to calculate or maintain the proportion of atoms that are in excited states from one timestep to another.

The main instantaneous processes of interest is H-α production by ionic recombination. The recombination produces a continuum radiation component due to the spread of energies of the recaptured electrons. Recombined Hydrogen atoms persist briefly in a variety of excited states, depending on the recombination rate coefficients for the interaction of H energy levels with the kinetic energy spectrum of the free electron population. The

excited atoms rapidly de-excite, cascading down through the energy levels according to branching ratios for the various allowed downward transitions that can occur from each state. A proportion of these cascades pass through the n: $3 \rightarrow 2$ Balmer series transition that produces the 656 nm H-α photon emission.

A secondary process of interest is that of Collisional Excitation/De-Excitation. Collisional excitation of atoms in a partially ionised medium occurs mainly through electron collisions. As with the recombination case, once an atom is in an excited state it rapidly cascades back down to the ground state with branching ratios identical to the case for recombination. The key difference then is simply the rate at which collisional excitation occurs.

G.1.4 H-α Production Rate Coefficients

Determining the rate at which ions and electrons recombine and then undergo the $n : 3 \rightarrow 2$ transition to produce H-α photons in a hot plasma is a complex calculation and the full detail is outside the scope of this thesis, but here we discuss the principles involved.

Consider a radiative recombination of some ion X^+ with a free electron:

$$X^+ + e^- \rightarrow X + h\nu$$

The rate at which these recombinations occur into a particular excited state X_{nl} is in proportion to the electron-ion radiative recombination cross-section for that state $\sigma_{rr,nl}(E)$, which is a resonance function that is dependent on the kinetic energy E of the incident electron. The Maxwellian velocity distribution for the electrons, expressed as a function of E is:

$$vf(E) = \left(\frac{8KT}{\pi m_e}\right)^{\frac{1}{2}} \frac{E}{KT} e^{-\frac{E}{KT}} \tag{G.1}$$

Let $\alpha_{rr,nl}(T)$ be the temperature-dependent rate coefficient for radiative recombination into state nl. We may obtain this by convolving $\sigma_{rr,nl}(E)$ with the velocity distribution for the electrons:

$$\alpha_{rr,nl}(T) = \left(\frac{8KT}{\pi m_e}\right)^{\frac{1}{2}} \int_0^\infty \sigma_{rr,nl}(E) x e^{-x} dx \tag{G.2}$$

Where $x = \frac{E}{KT}$. Since we are here multiplying a cross-sectional area by a velocity and

then integrating over a probability density function it follows that the dimensions of $\alpha_{rr,nl}(T)$ are $[L]^3[T]^{-1}$.

Having determined the rate coefficient $\alpha_{rr,nl}$, the rate at which neutral H atoms are created in state nl per unit volume may be obtained by multiplying by the volumetric number densities of the collision partners:

$$n_e n_{H^+} \alpha_{rr,nl} \tag{G.3}$$

These H_{nl} atoms then decay to lower states, with a probability per unit time given by the Einstein A coefficient. For the (n+1) → n decay process this coefficient is:

$$A_{n+1,n} \approx \frac{64\pi^6 m_e e^{10}}{3c^3 h^6 n^5} = 5.3 \times 10^9 s^{-1} n^{-5} \tag{G.4}$$

Note that for excited state n = 100, the decay timescale is of the order 1s; and so for n « 100 we may assume near-instantaneous decay to the ground state before other processes such as collisions or photoionisation are likely to change the state of an excited atom in our regime of interest.

If we are able to determine the Einstein A coefficients for all possible downward transitions from a given state nl, then we may determine the Branching Ratio Γ, i.e. the probability that an atom will follow a particular decay path.

$$\Gamma(nl \to n'l') = \frac{A(nl \to n'l')}{\sum_{n''l'',n''<n} A(nl \to n''l'')} \tag{G.5}$$

Combining this with G.3, the rate of photon emission per unit volume from the transition from state nl to the state $n'l'$ is:

$$n_e n_{H^+} \alpha_{rr,nl}(T) \Gamma(nl \to n'l') \tag{G.6}$$

But this only accounts for atoms that recombine directly into state nl. Yet atoms are also created in state nl from recombinations into higher excited states that then cascade down to state nl. If we include in our rate calculation the atoms that recombine into

all the possible l'' angular momentum states of the principal quantum number $(n+1)$, which then decay to state nl before decaying to state $n'l'$, we would write:

$$n_e n_{H^+} \Gamma(nl \rightarrow n'l') \left[\alpha_{rr,nl} + \sum_{l''} \alpha_{rr,(n+1)l} \Gamma((n+1)l'' \rightarrow nl) \right] \tag{G.7}$$

And more generally, if $P(n''l'' \rightarrow nl)$ is the probability that an atom created by recombination in state $n''l''$ will pass through state nl on its way to ground, which can be computed from a branching ratio calculation over all possible paths, then we may write:

$$n_e n_{H^+} \Gamma(nl \rightarrow n'l') \left[\alpha_{rr,nl} + \sum_{n''l'',n''>n} \alpha_{rr,n''l''} P(n''l'' \rightarrow nl) \right] \tag{G.8}$$

And thus the emissivity for H-α radiation in ergs per second per steradian is given by:

$$j_{H\alpha,rr} = \frac{h\nu_{H\alpha}}{4\pi} n_e n_{H^+} \Gamma(nl \rightarrow n'l') \left[\alpha_{rr,nl} + \sum_{n''l'',n''>n} \alpha_{rr,n''l''} P(n''l'' \rightarrow nl) \right] \tag{G.9}$$

In fact, for a complete calculation, the fine structure splitting of the H-α line should be considered, since coupling of the 2p orbital angular momentum state with the electron's spin provides two possible downward transition paths for an electron in the 3s orbital, with an energy difference of 4.5 x 10^{-5} eV or a difference in wavelength of 0.016 nm.

The total H-α emission in all directions, produced by recombination within a volume element dV will therefore simply be, in erg s^{-1}:

$$dL_{H\alpha,rr} = 4\pi j_{H\alpha,rr} dV \tag{G.10}$$

This has been calculated as follows (Dong & Draine, 2011)(22):

$$dL_{H\alpha,rr} = n_e n_{H^+} \times 4\pi \times 2.82 \times 10^{-26} T_4^{-0.942-0.031 ln T_4} dV \tag{G.11}$$

$$T_4 = T_e / 10^4$$

The contribution of Collisional Excitation / De-excitation is small compared with Recombination. The detailed calculation is omitted here, but has been found to be (Kim, Krumholz et al, 2013)(57):

$$dL_{H\alpha,col} = n_e n_H \times 1.30 \times 10^{-17} \frac{\Gamma_{13}(T_e)}{\sqrt{T_e}} e^{-12.1eV/k_B T_e} dV \tag{G.12}$$

$$\Gamma_{13}(T_e) = 0.350 - 2.62 \times 10^{-7} T_e - 8.15 \times 10^{-11} T_e^2 + 6.19 \times 10^{-15} T_e^3$$

Excluding the dependence on collision partner densities and spatial volume elements, the expressions on the R.H.S. of equations G.11, G.12 are the temperature dependent H-α production rate coefficients for recombination and collision, in erg cm^3 s^{-1}. Provided that we know the temperature of the medium and the number densities of H^+ and free electrons, we can use these expressions to calculate the H-α emission per unit volume per second from our material.

In fact, most of the free electrons in the medium are those liberated from the H^+ ions themselves; the next most abundant element is Helium, with a first ionisation potential of 24.6 eV. Helium ionisation does not become significant until temperatures rise well above 10^4 K, and the number density of Helium is roughly 10% that of Hydrogen (although at temperatures in excess of 4 x 10^4 K a fully ionised Helium atom provides 2 electrons). As an approximation, we may take the number of free electrons to be equal to the number of H^+ ions and this holds well over most of the temperature regime in our jets.

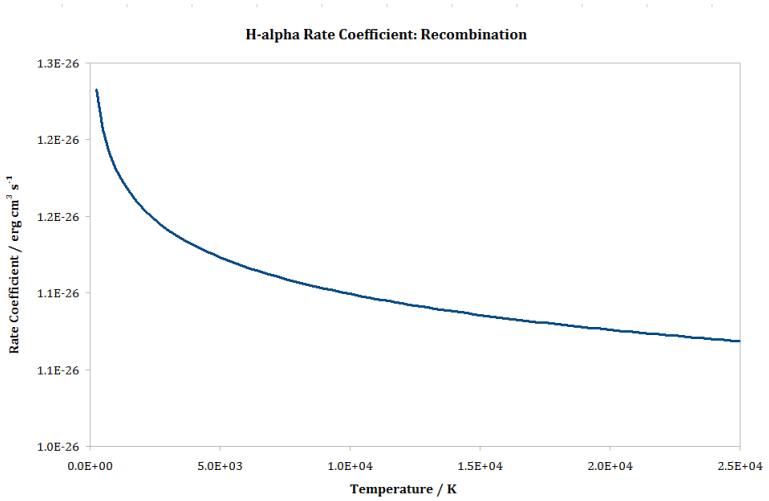

Figure G.3: H-α Recombination Rate Coefficient: Temperature Dependence

ZEUS output provides data on the three chemical species and the internal energy and

density of the medium, and this together with the H-α rate coefficients is enough for the MULTISYNTH code to calculate H-α emission from each zone in the jet model.

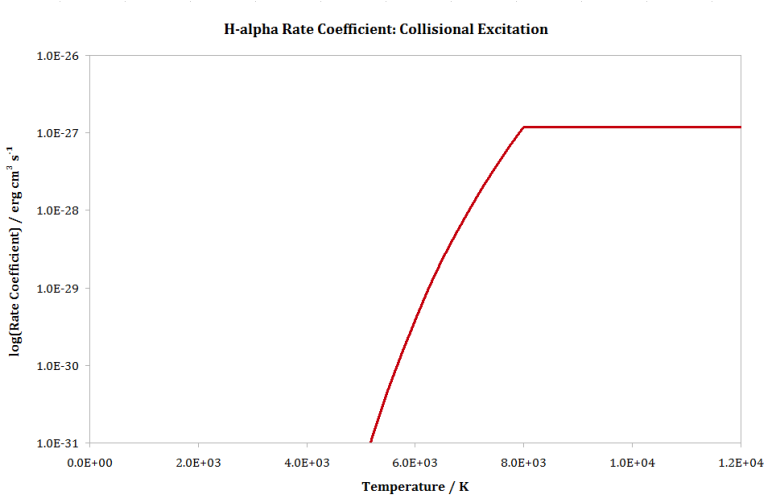

Figure G.4: H-α Collisional Rate Coefficient: Temperature Dependence

G.1.5 [SII] 671.7 nm Emission

This is a collisionally excited line of singly ionised Sulfur. The total emission from a volume of space in erg s^{-1} may be calculated as follows (Reynolds R J, 1989)(89):

$$dL_{[SII],col} = n_e n(S^+) \times h\nu_{[SII]} \times 7.30 \times 10^{-8} T_4^{-1/2} e^{-2.14/T_4} dV \tag{G.13}$$

where $h\nu_{[SII]} = 2.9578 \times 10^{-12}$ erg is the photon energy. The simple Hydrogen chemical network used by our ZEUS-MP jet models does not separately track the abundance of the S^+ ion and so this is calculated by MULTISYNTH based on an estimated relative abundance of S with respect to H of 1.58 $\times$ 10^{-5} (Reynolds R J, 1989)(89), and a tabulated S^+ ion fraction as a function of temperature (Arnaud M & Rothenflug R, 1985)(8).

G.1.6 H_2 1-0 S(1) 2.12 Micron Emission

This is a ro-vibrational state transition of molecular Hydrogen. The ro-vibrational energy levels of the H_2 molecule are chiefly excited by collisions with other molecules, atoms, ions and electrons (Wolfire & Königl, 1991)(123), and this mechanism will occur within the shocked regions of H_2 gas that protostellar jets can produce, though at temperatures much beyond 2000-3000K the available population of Hydrogen molecules grows increasingly sparse due to dissociation (Stanke T, 2000)(110). Another mechanism for this emission is electronic excitation by Ly-α photons, with these excited states decaying into ro-vibrational excited states which then cascade down producing the 1-0 S(1) emission line.

In the case of our T-Tauri jet models, the jets are atomic in nature and the temperatures reached within primary shocked regions are usually significantly higher than the expected regime for this transition. However we do explore a variety of initial ambient environments into which the jets are injected and there is interest in generating synthetic observations of the disturbance to a molecular environment, in which warm regions of weakly shocked molecular material may arise on the periphery of the outflow. This may be of even greater interest when applied to molecular jets from Class 0/1 protostars. Thus a procedure, H2MOLLINE is provided within MULTISYNTH to calculate this emission. Note that the Ly-α excitation mechanism is not included in this procedure as the jets we are studying are from pre-Main Sequence stars where Ly-α production is not occurring.

H2MOLLINE uses code adapted from a Fortran procedure VOLKER.F previously used by Smith, Volker et al., (1997)(106) to calculate the H_2 1-0 S(1) 2.12 μm synthetic emission.

G.1.7 ^{12}CO J=2-1 1.3mm Emission

This radio emission line arises from a rotational transition of the asymmetric ^{12}CO molecule. Emission lines from isotopologues of CO may be used as a tracer for cold H_2, because the rotational CO states are excited by collisions with H_2 molecules; hence the greater the H_2 density, the more CO emission is seen. (Smith, 2004)(100). The characteristic excitation temperature of the 1.3mm line is 11K. CO has a binding energy of 11.1eV and so appreciable dissociation does not occur until around 5000K (Fairbairn, 1969)(28).

The motivation for studying this emission line is to enable comparison between our jet models and the finding of (Pety et al., 2006)(81) and (Tambovtseva & Grinin, 2008)(118). A procedure, COMOLLINE, is provided with MULTISYNTH to calculate this emission. As with H2MOLLINE, this procedure was adapted from VOLKER.F (Smith, Volker et al., 1997)(106).

G.1.8 [FeII] 1.64 Micron Emission

This near-infrared electron transition line is collisionally excited, with a characteristic temperature of $\sim$ 10000K thus making it a useful shock tracer line. The procedure FEIICOL in MULTISYNTH synthesizes the emission for this line. This code is adapted from the procedure FELINES.F from release 1.1.1 of the CBOW shock simulation code by Michael Smith, 1999 (see also Smith, 1994)(99). In order to account for additional free iron atoms liberated by dust grain sputtering in shocks, the procedure contains a hard-coded assumption about the shock velocity differential which is based on the velocity pulse signal used in our fast atomic jet models of HH30. There is also a simplifying assumption made, that material in the problem domain with a speed $>$ 10 km/s and a temperature $>$ 1000K has been processed through one of these shocks and so possesses the higher abundance of [FeII] available for excitation. Post-processing of models based on simple Hydrogen chemistry necessitates the use of these simplifying assumptions. A more accurate approach that properly accounts for sputtering would be to use more complex chemistry within the jet models themselves, and this may be implemented in future work.

G.1.9 [OI] 630nm Emission

This is a collisionally excited line of atomic Oxygen. The total emission from a volume of space in erg s^{-1} may be calculated as follows (Reynolds R J, 1989)(89):

$$dL_{[OI],col} = n_e n(O) \times h\nu_{[OI]} \times 5.3 \times 10^{-8} \times 0.39 \times T_4^{0.95} \times T_4^{-1/2} e^{-2.28/T_4} dV \quad \text{(G.14)}$$

where $h\nu_{[OI]} = 3.1530 \times 10^{-12}$ erg is the photon energy. The simple Hydrogen chemical network used by our ZEUS-MP jet models does not separately track the abundance of atomic Oxygen and so this is calculated by MULTISYNTH based on an estimated relative abundance of O with respect to H of 4.85×10^{-4} (Reynolds R J, 1989)(89), multiplied by the neutral Oxygen fraction. The ionisation ratio of Oxygen is closely connected to that of Hydrogen, due to large charge exchange cross sections (Field & Steigman, 1971)(32). This permits us to calculate the neutral O fraction as:

$$\frac{n(O)}{n(O_{all})} = \frac{1}{1 + \frac{8}{9}\frac{n(H^+)}{n(H)}} \quad \text{(G.15)}$$

Appendix H

Velocity Channel Maps

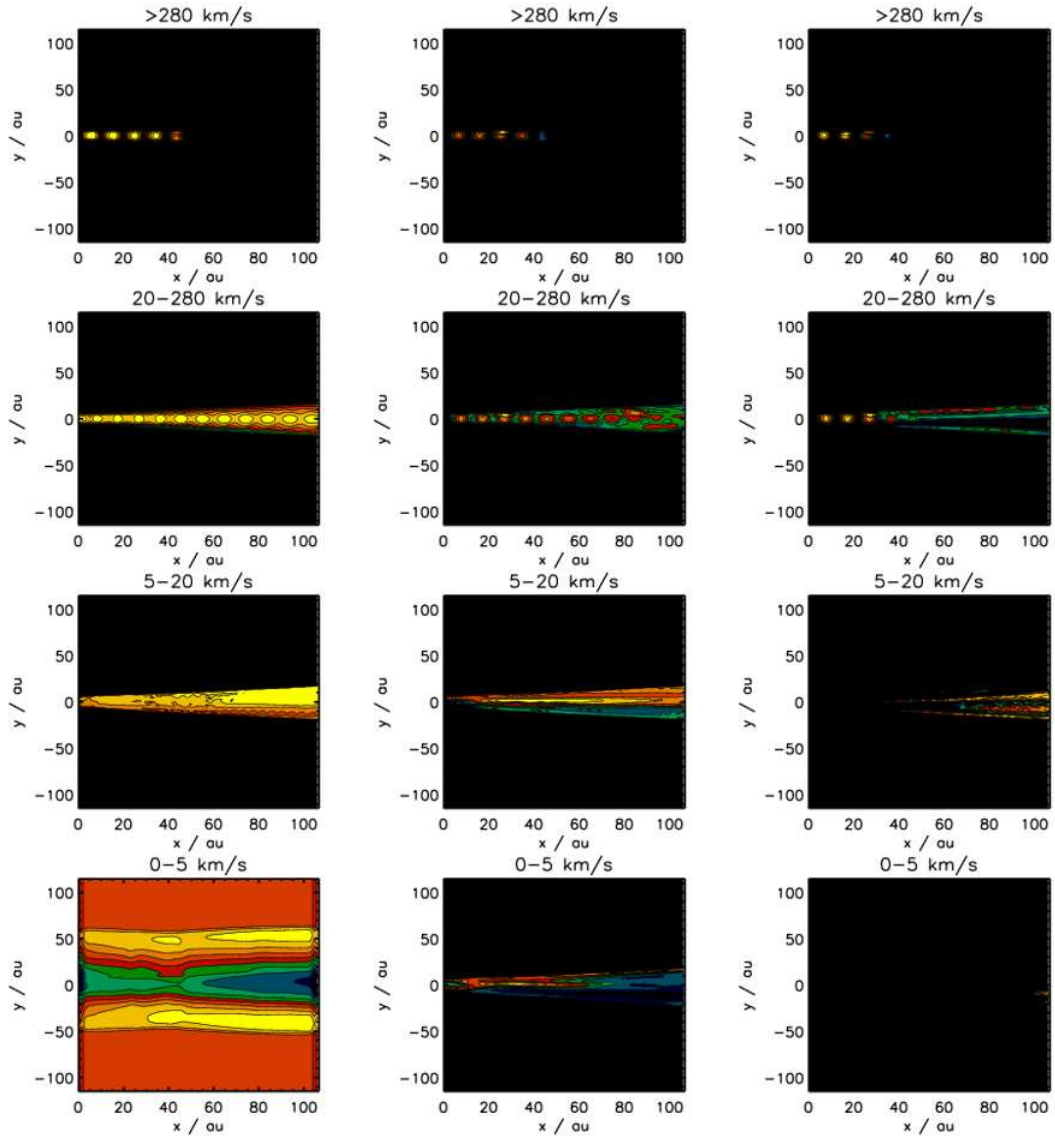

(a) column density (b) H-α, 656.28 nm (c) [SII], 671.6 nm

Figure H.1: Model ORB.1, V_x Channel Maps at simulation time T=87.5 Years. Axis scales are in Astronomical Units. Note x axis is 2 times y axis scale. Notional 30-contour colour scaling (yellow = highest, blue = lowest, black = zero) indicates column density of, or depth-integrated radiant flux produced by, material in motion within the indicated velocity bounds. Plots are scaled independently.

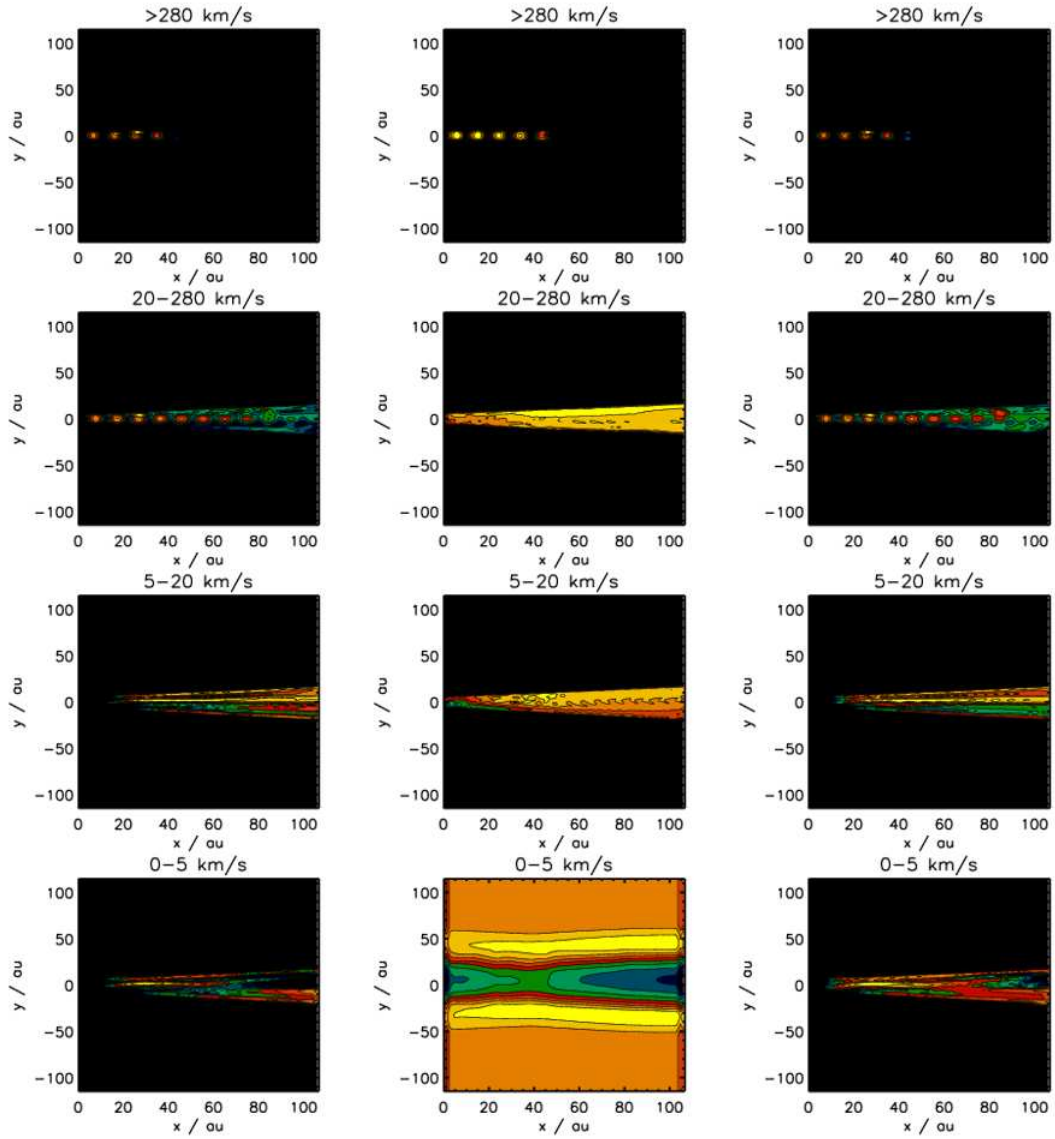

(a) [OI], 630.0 nm (b) CO 0-0 R(0), 1.3 mm (c) [FeII], 1.64 μm

Figure H.2: Model ORB.1, V_x Channel Maps at simulation time T=87.5 Years. Axis scales are in Astronomical Units. Note x axis is 2 times y axis scale. Notional 30-contour colour scaling (yellow = highest, blue = lowest, black = zero) indicates depth-integrated radiant flux produced by material in motion within the indicated velocity bounds. Plots are scaled independently.

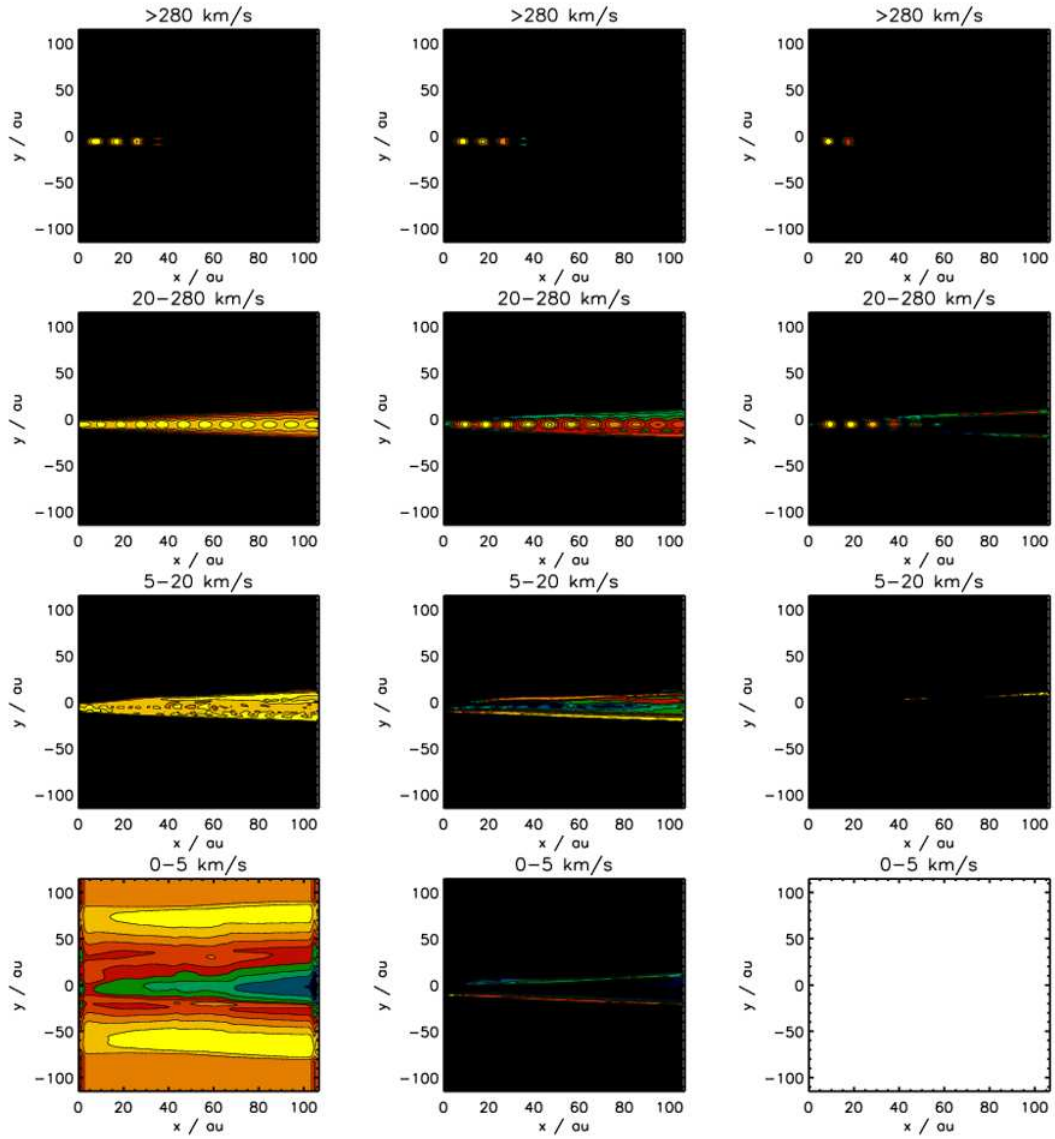

(a) column density (b) H-α, 656.28 nm (c) [SII], 671.6 nm

Figure H.3: Model ORB.1, V_x Channel Maps at simulation time T=175 Years. Axis scales are in Astronomical Units. Note x axis is 2 times y axis scale. Notional 30-contour colour scaling (yellow = highest, blue = lowest, black = zero) indicates column density of, or depth-integrated radiant flux produced by, material in motion within the indicated velocity bounds. Plots are scaled independently.

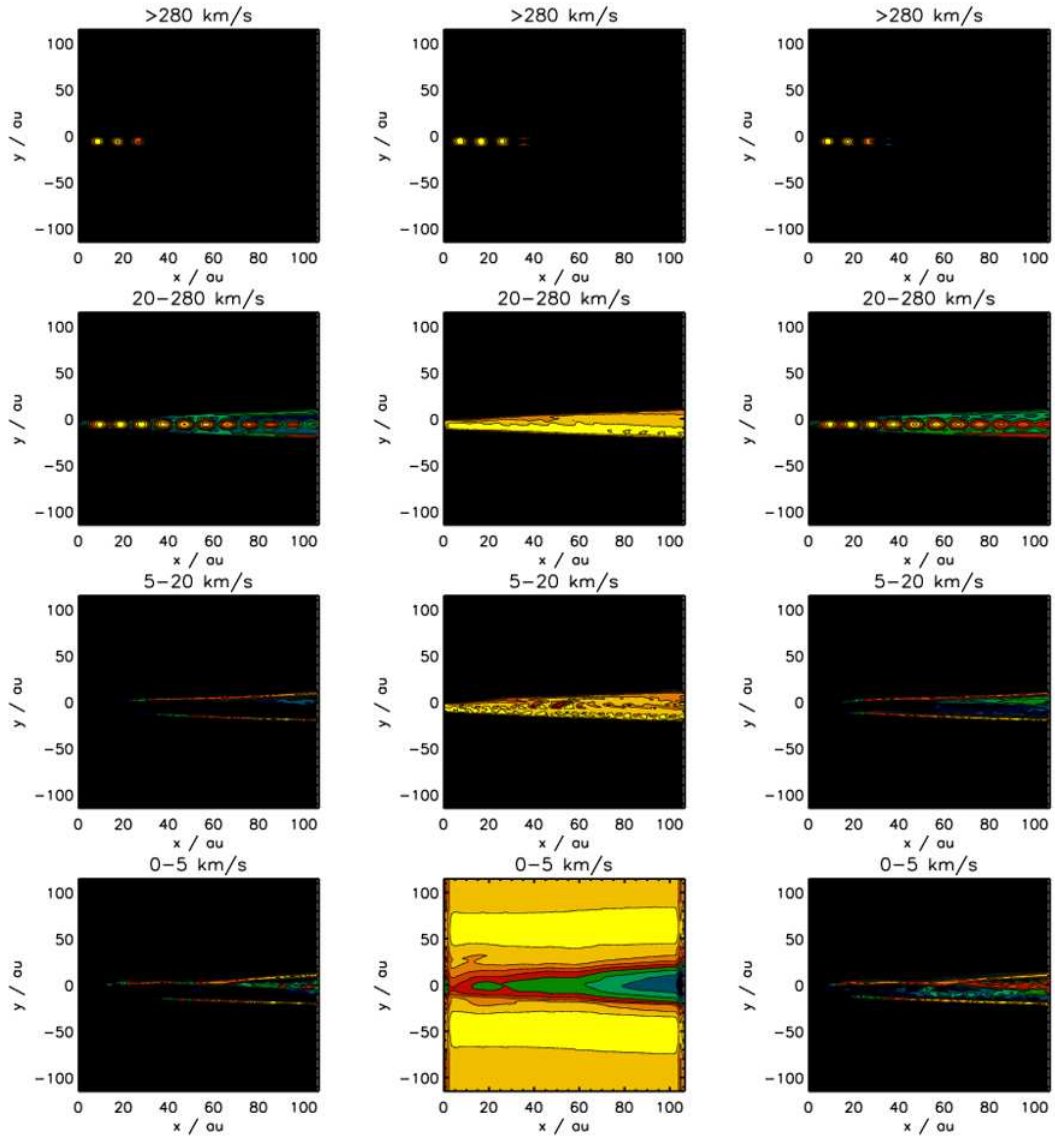

(a) [OI], 630.0 nm (b) CO 0-0 R(0), 1.3 mm (c) [FeII], 1.64 μm

Figure H.4: Model ORB.1, V_x Channel Maps at simulation time T=175 Years. Axis scales are in Astronomical Units. Note x axis is 2 times y axis scale. Notional 30-contour colour scaling (yellow = highest, blue = lowest, black = zero) indicates depth-integrated radiant flux produced by material in motion within the indicated velocity bounds. Plots are scaled independently.

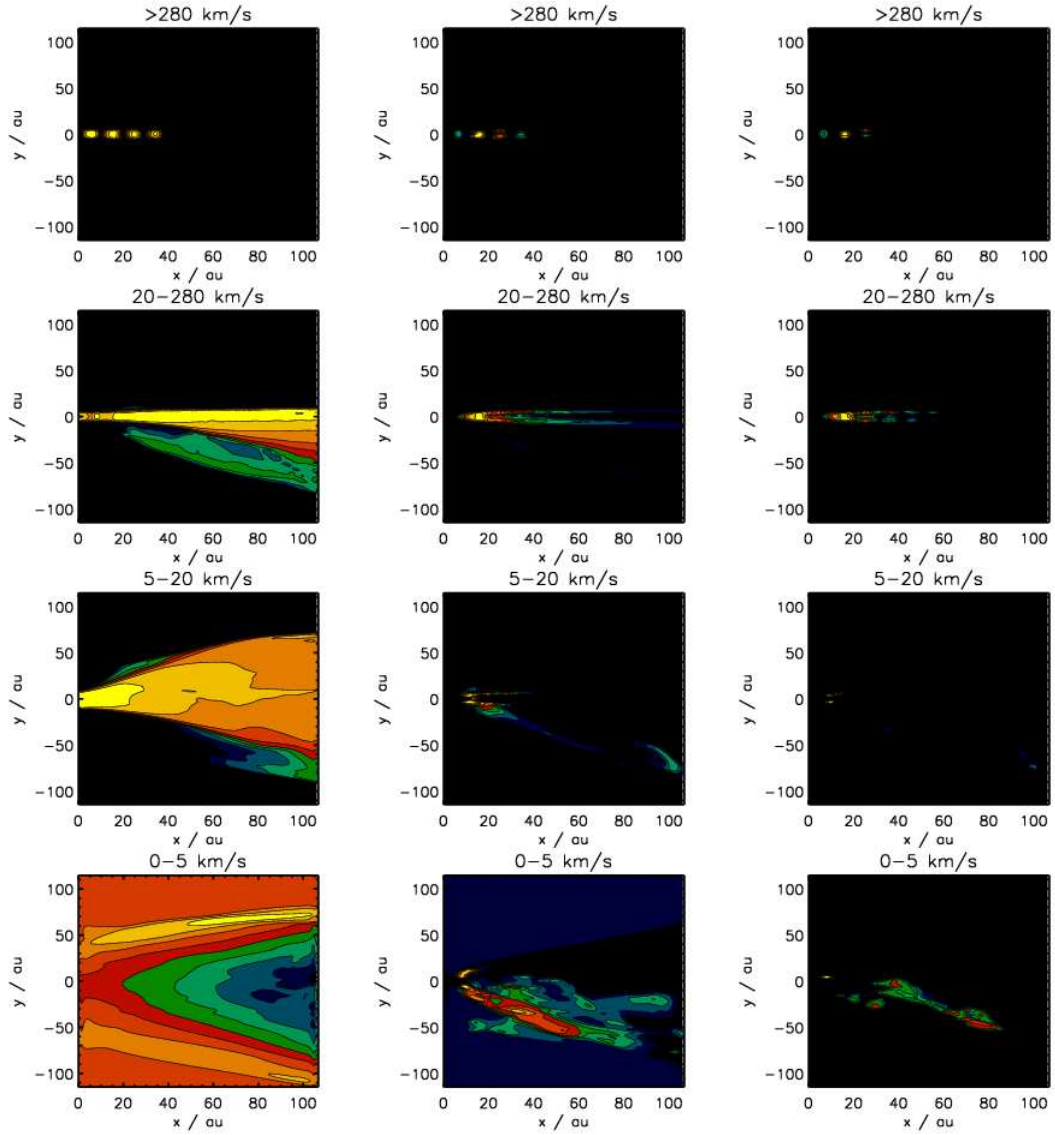

(a) column density (b) H-α, 656.28 nm (c) [SII], 671.6 nm

Figure H.5: Model ORB.2, V_x Channel Maps at simulation time T=87.5 Years. Axis scales are in Astronomical Units. Note x axis is 2 times y axis scale. Notional 30-contour colour scaling (yellow = highest, blue = lowest, black = zero) indicates column density of, or depth-integrated radiant flux produced by, material in motion within the indicated velocity bounds. Plots are scaled independently.

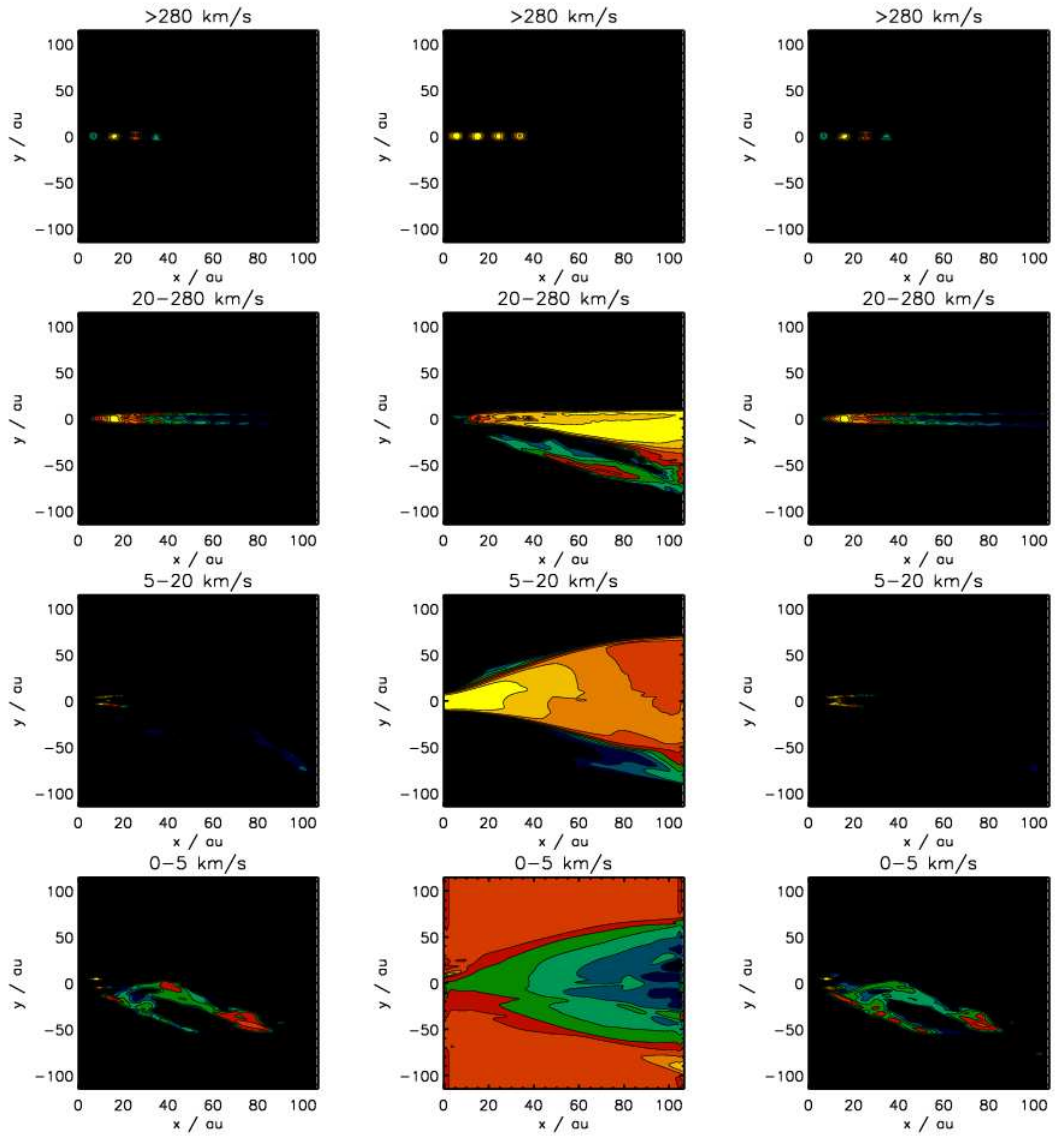

(a) [OI], 630.0 nm (b) CO 0-0 R(0), 1.3 mm (c) [FeII], 1.64 μm

Figure H.6: Model ORB.2, V_x Channel Maps at simulation time T=87.5 Years. Axis scales are in Astronomical Units. Note x axis is 2 times y axis scale. Notional 30-contour colour scaling (yellow = highest, blue = lowest, black = zero) indicates depth-integrated radiant flux produced by material in motion within the indicated velocity bounds. Plots are scaled independently.

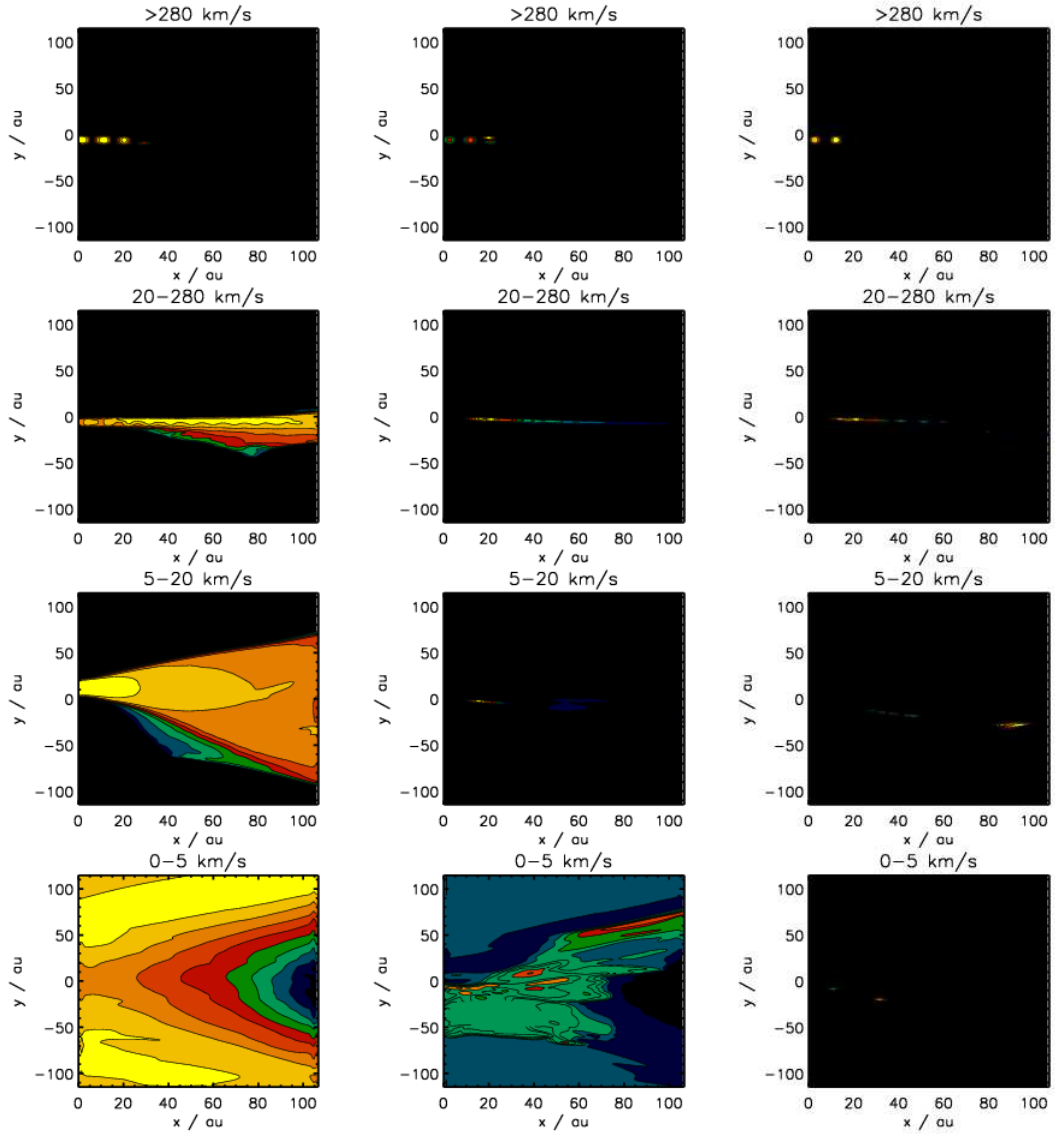

(a) column density (b) H-α, 656.28 nm (c) [SII], 671.6 nm

Figure H.7: Model ORB.2, V_x Channel Maps at simulation time T=175 Years. Axis scales are in Astronomical Units. Note x axis is 2 times y axis scale. Notional 30-contour colour scaling (yellow = highest, blue = lowest, black = zero) indicates column density of, or depth-integrated radiant flux produced by, material in motion within the indicated velocity bounds. Plots are scaled independently.

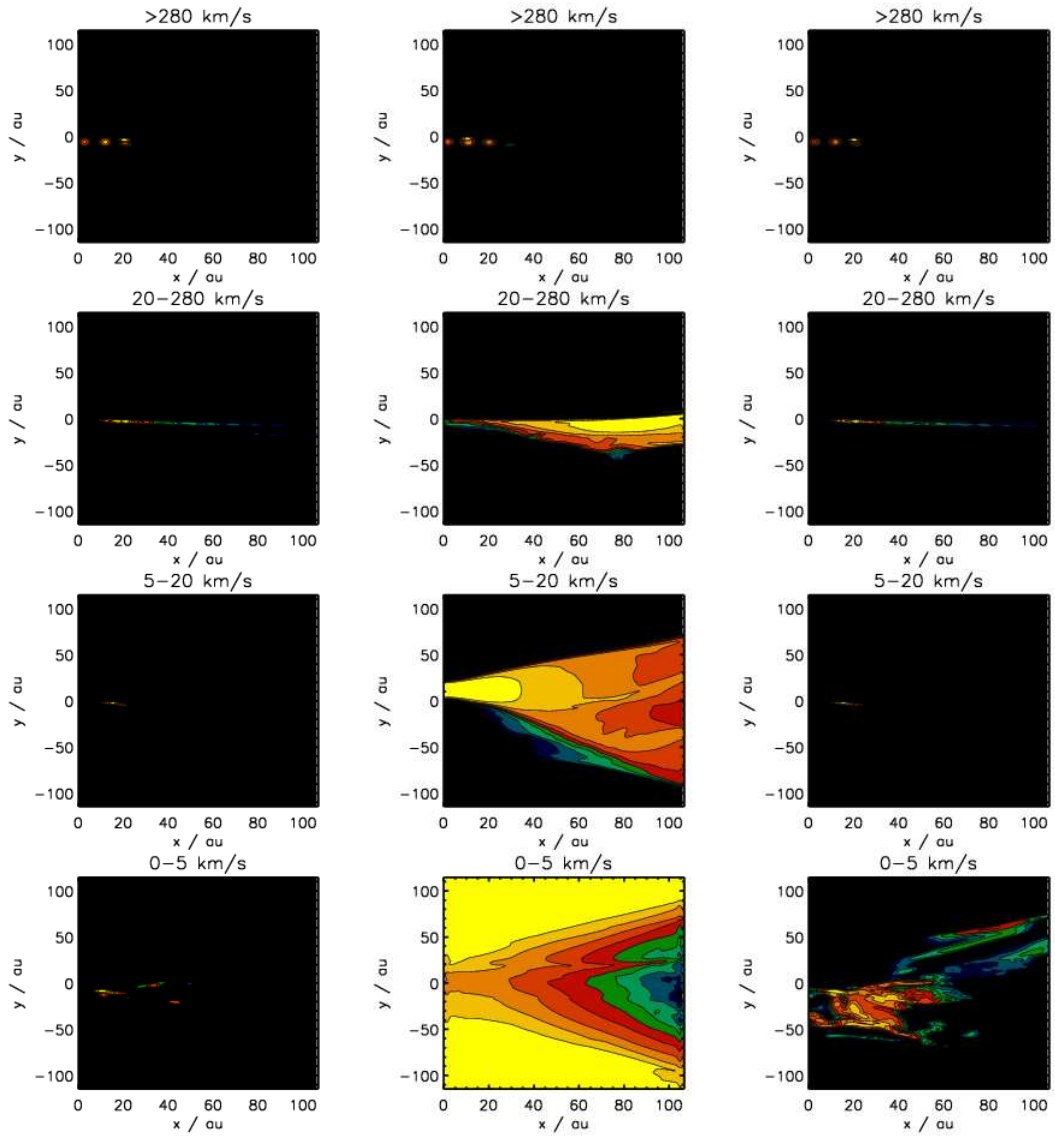

(a) [OI], 630.0 nm (b) CO 0-0 R(0), 1.3 mm (c) [FeII], 1.64 μm

Figure H.8: Model ORB.2, V_x Channel Maps at simulation time T=175 Years. Axis scales are in Astronomical Units. Note x axis is 2 times y axis scale. Notional 30-contour colour scaling (yellow = highest, blue = lowest, black = zero) indicates depth-integrated radiant flux produced by material in motion within the indicated velocity bounds. Plots are scaled independently.

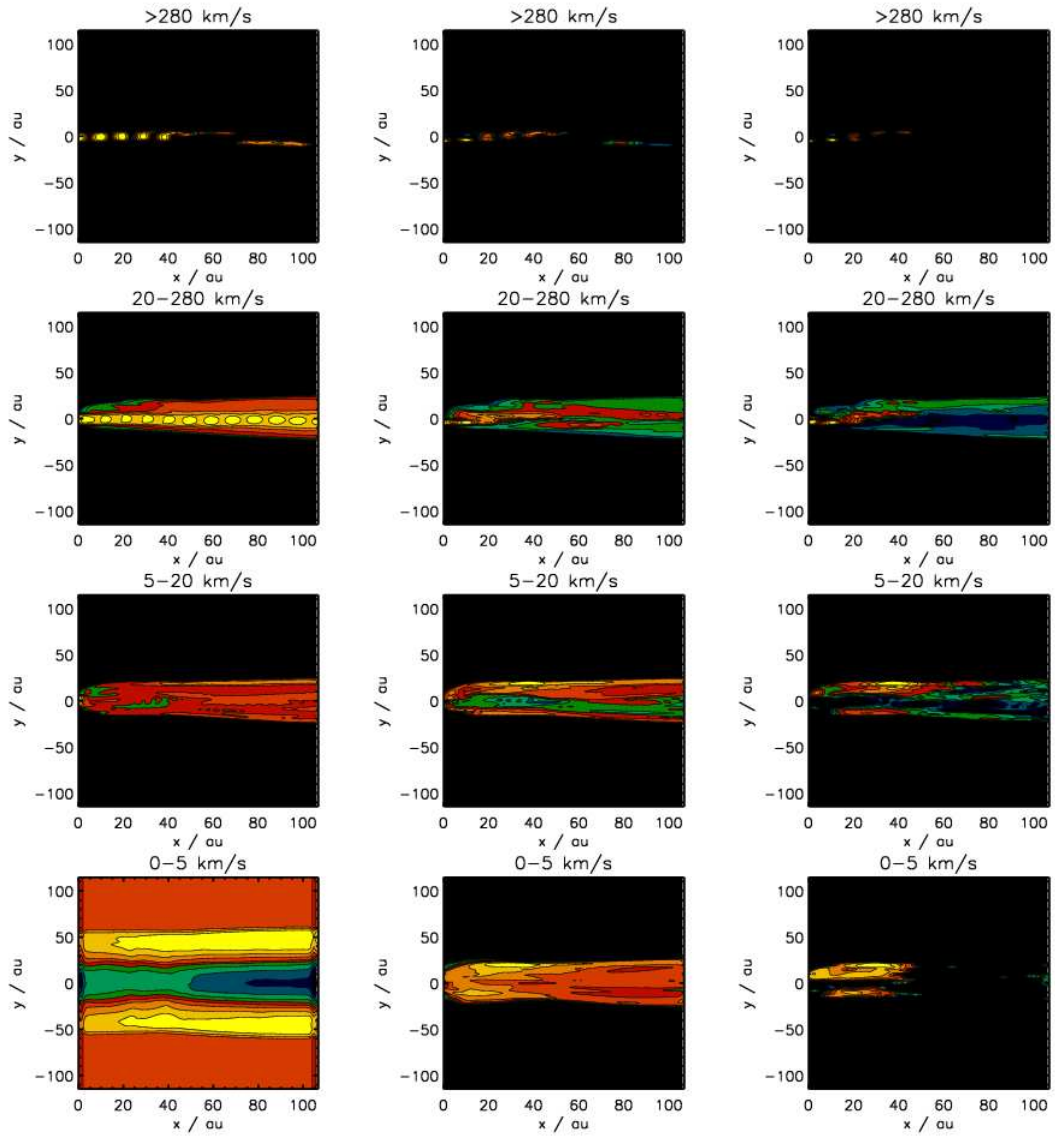

(a) column density (b) H-α, 656.28 nm (c) [SII], 671.6 nm

Figure H.9: Model PRE.1, V_x Channel Maps at simulation time T=87.5 Years. Axis scales are in Astronomical Units. Note x axis is 2 times y axis scale. Notional 30-contour colour scaling (yellow = highest, blue = lowest, black = zero) indicates column density of, or depth-integrated radiant flux produced by, material in motion within the indicated velocity bounds. Plots are scaled independently.

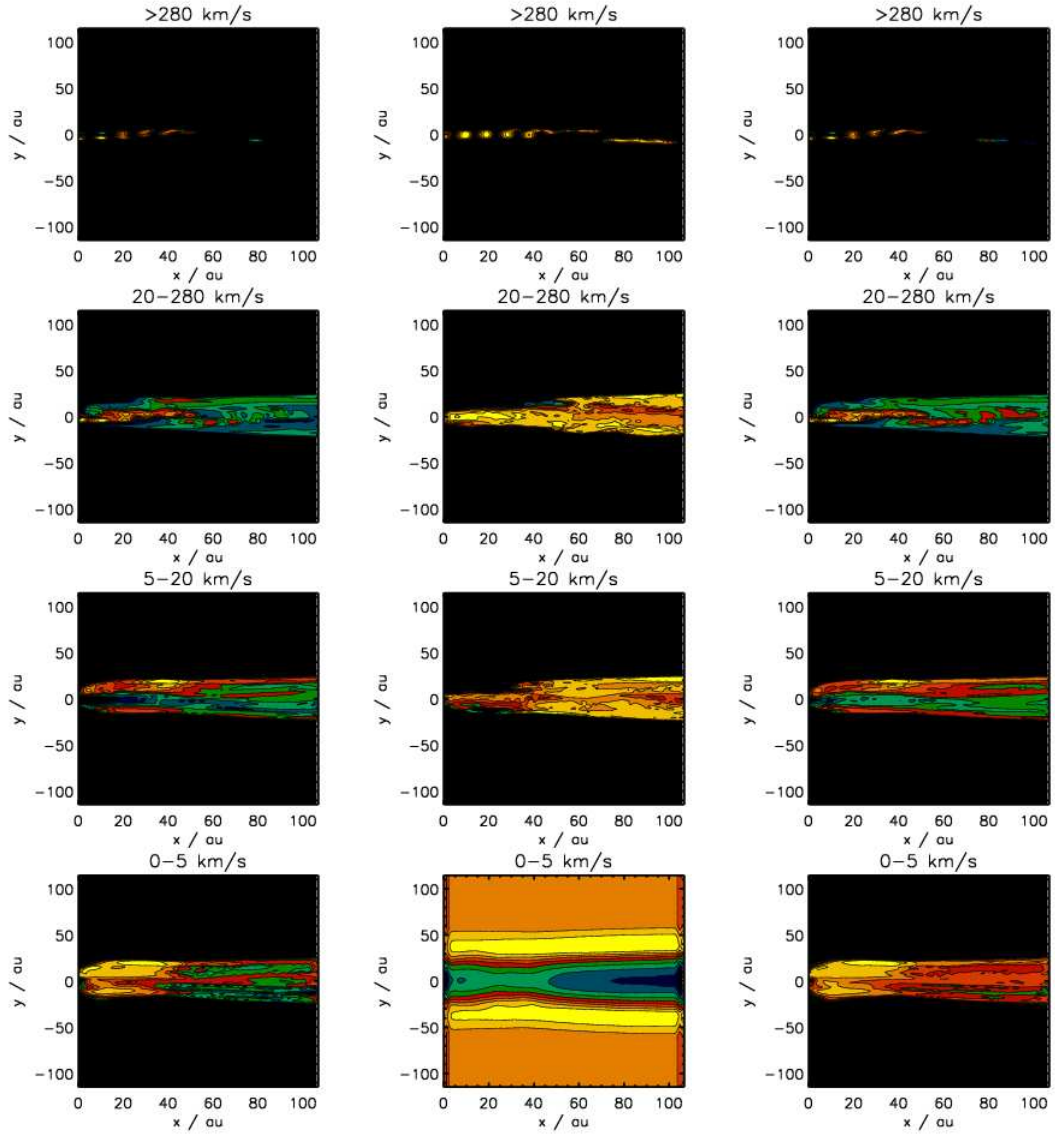

(a) [OI], 630.0 nm (b) CO 0-0 R(0), 1.3 mm (c) [FeII], 1.64 μm

Figure H.10: Model PRE.1, V_x Channel Maps at simulation time T=87.5 Years. Axis scales are in Astronomical Units. Note x axis is 2 times y axis scale. Notional 30-contour colour scaling (yellow = highest, blue = lowest, black = zero) indicates depth-integrated radiant flux produced by material in motion within the indicated velocity bounds. Plots are scaled independently.

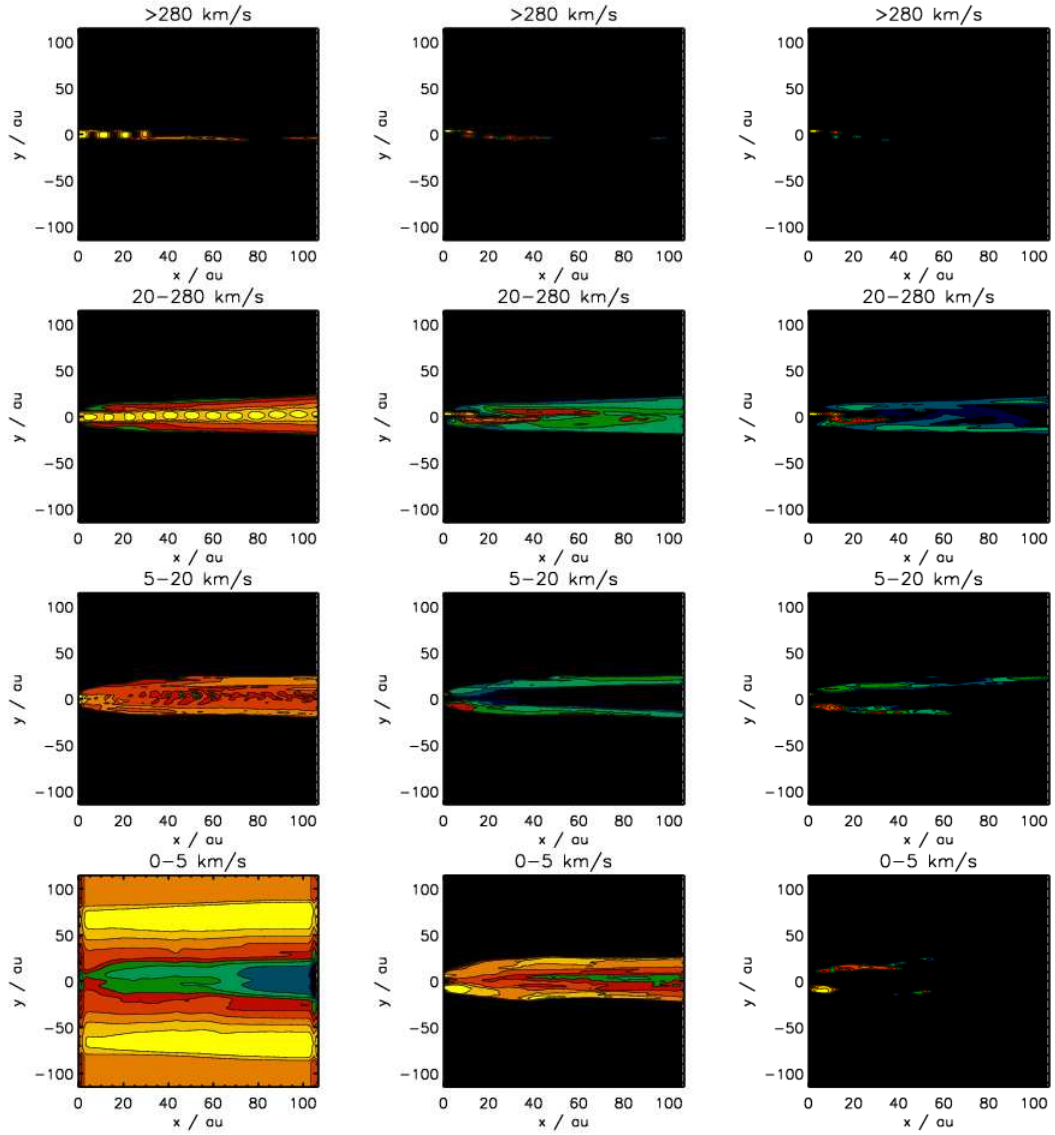

(a) column density (b) H-α, 656.28 nm (c) [SII], 671.6 nm

Figure H.11: Model PRE.1, V_x Channel Maps at simulation time T=175 Years. Axis scales are in Astronomical Units. Note x axis is 2 times y axis scale. Notional 30-contour colour scaling (yellow = highest, blue = lowest, black = zero) indicates column density of, or depth-integrated radiant flux produced by, material in motion within the indicated velocity bounds. Plots are scaled independently.

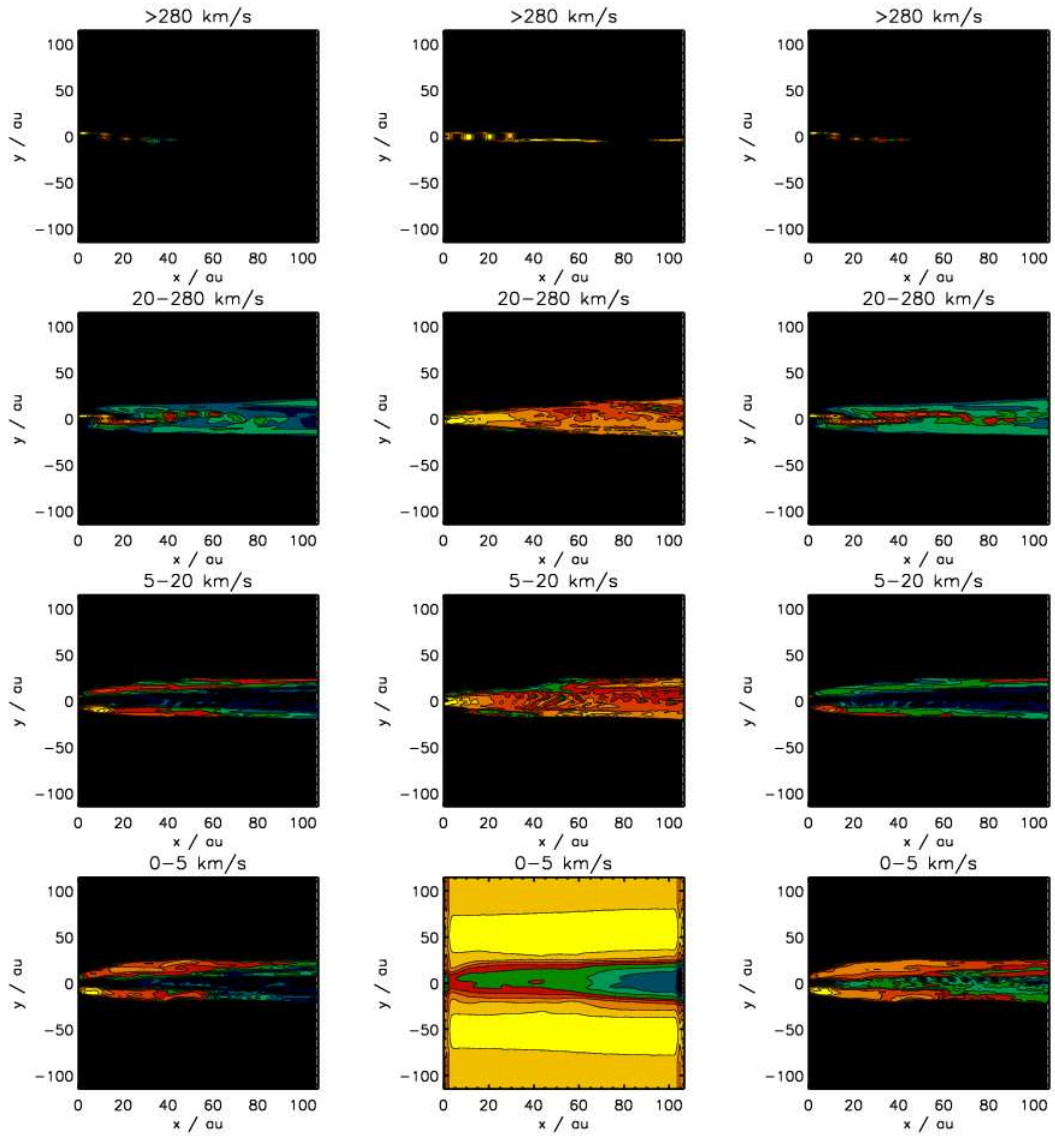

(a) [OI], 630.0 nm (b) CO 0-0 R(0), 1.3 mm (c) [FeII], 1.64 μm

Figure H.12: Model PRE.1, V_x Channel Maps at simulation time T=175 Years. Axis scales are in Astronomical Units. Note x axis is 2 times y axis scale. Notional 30-contour colour scaling (yellow = highest, blue = lowest, black = zero) indicates depth-integrated radiant flux produced by material in motion within the indicated velocity bounds. Plots are scaled independently.

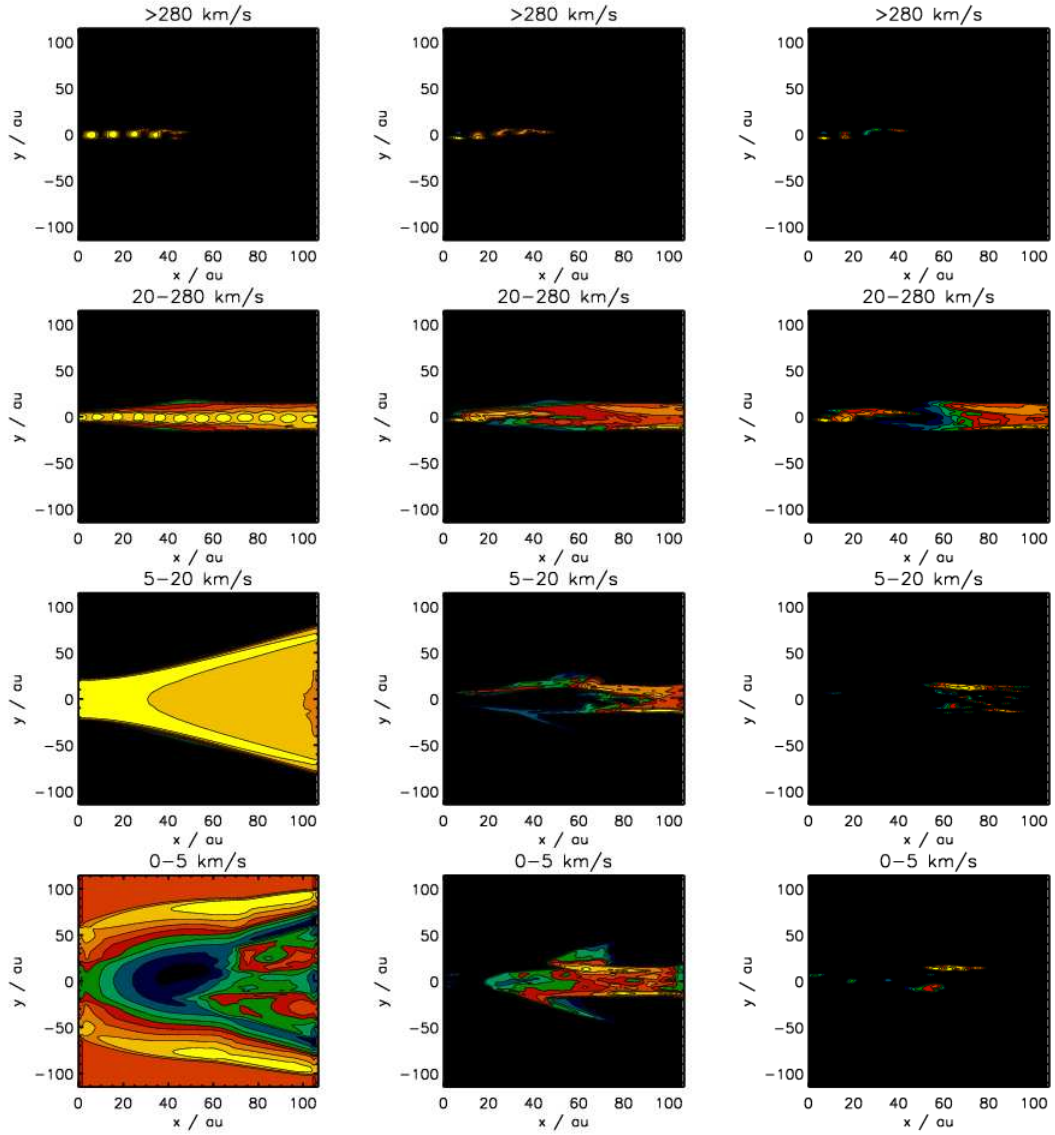

(a) column density (b) H-α, 656.28 nm (c) [SII], 671.6 nm

Figure H.13: Model PRE.2, V_x Channel Maps at simulation time T=87.5 Years. Axis scales are in Astronomical Units. Note x axis is 2 times y axis scale. Notional 30-contour colour scaling (yellow = highest, blue = lowest, black = zero) indicates column density of, or depth-integrated radiant flux produced by, material in motion within the indicated velocity bounds. Plots are scaled independently.

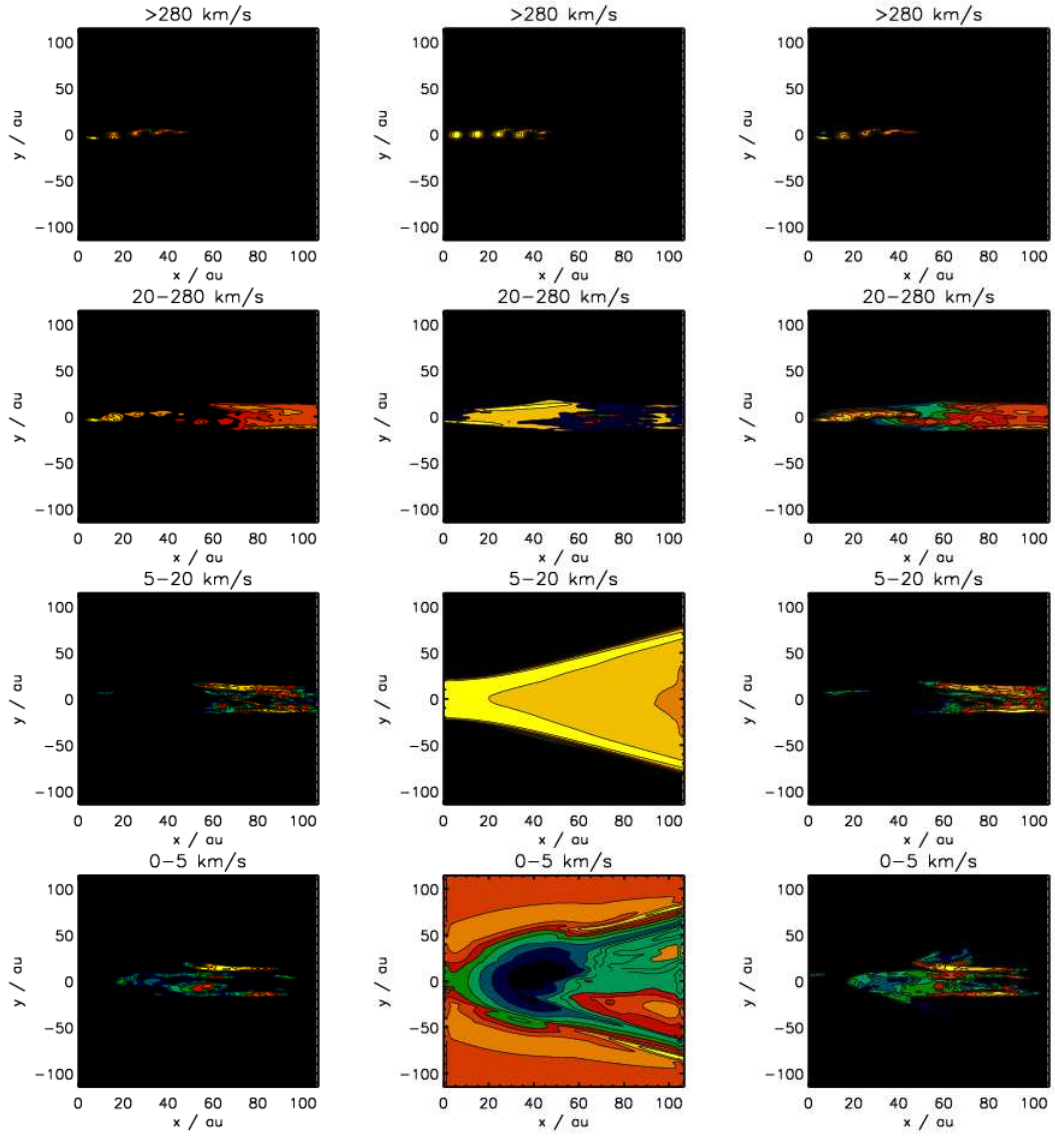

(a) [OI], 630.0 nm (b) CO 0-0 R(0), 1.3 mm (c) [FeII], 1.64 μm

Figure H.14: Model PRE.2, V_x Channel Maps at simulation time T=87.5 Years. Axis scales are in Astronomical Units. Note x axis is 2 times y axis scale. Notional 30-contour colour scaling (yellow = highest, blue = lowest, black = zero) indicates depth-integrated radiant flux produced by material in motion within the indicated velocity bounds. Plots are scaled independently.

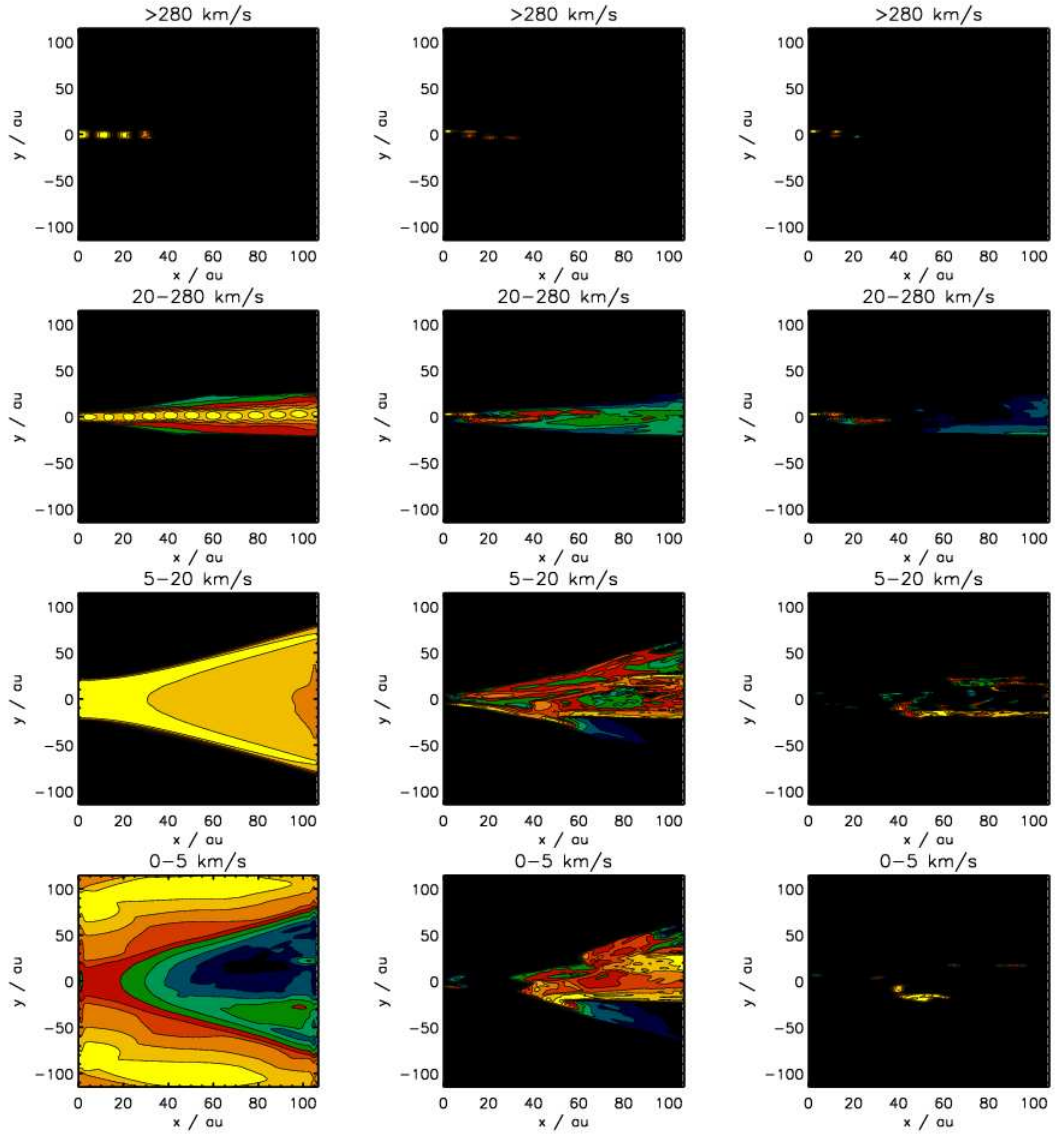

(a) column density (b) H-α, 656.28 nm (c) [SII], 671.6 nm

Figure H.15: Model PRE.2, V_x Channel Maps at simulation time T=175 Years. Axis scales are in Astronomical Units. Note x axis is 2 times y axis scale. Notional 30-contour colour scaling (yellow = highest, blue = lowest, black = zero) indicates column density of, or depth-integrated radiant flux produced by, material in motion within the indicated velocity bounds. Plots are scaled independently.

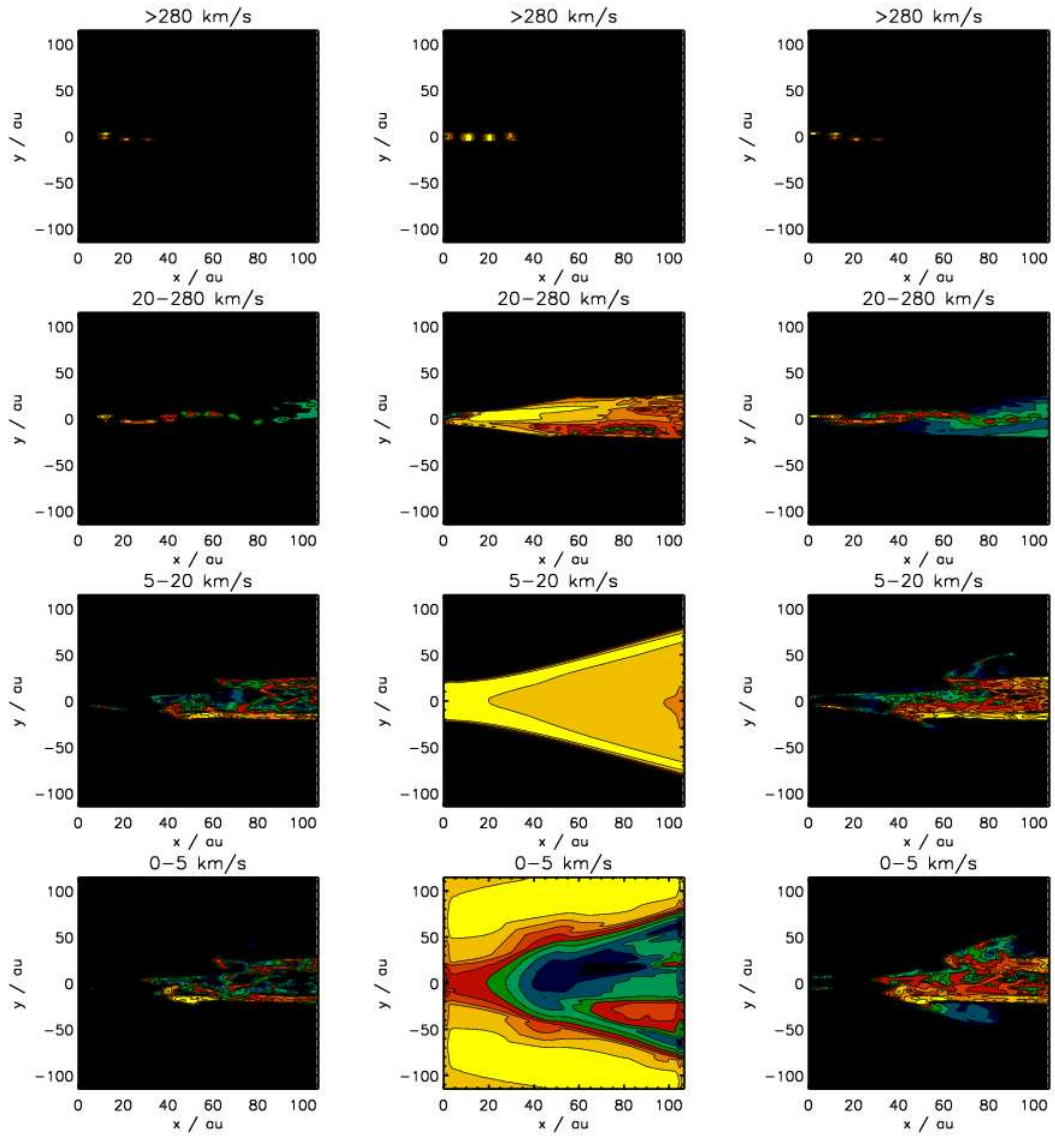

(a) [OI], 630.0 nm (b) CO 0-0 R(0), 1.3 mm (c) [FeII], 1.64 μm

Figure H.16: Model PRE.2, V_x Channel Maps at simulation time T=175 Years. Axis scales are in Astronomical Units. Note x axis is 2 times y axis scale. Notional 30-contour colour scaling (yellow = highest, blue = lowest, black = zero) indicates depth-integrated radiant flux produced by material in motion within the indicated velocity bounds. Plots are scaled independently.

Appendix I

Position-Velocity Diagrams

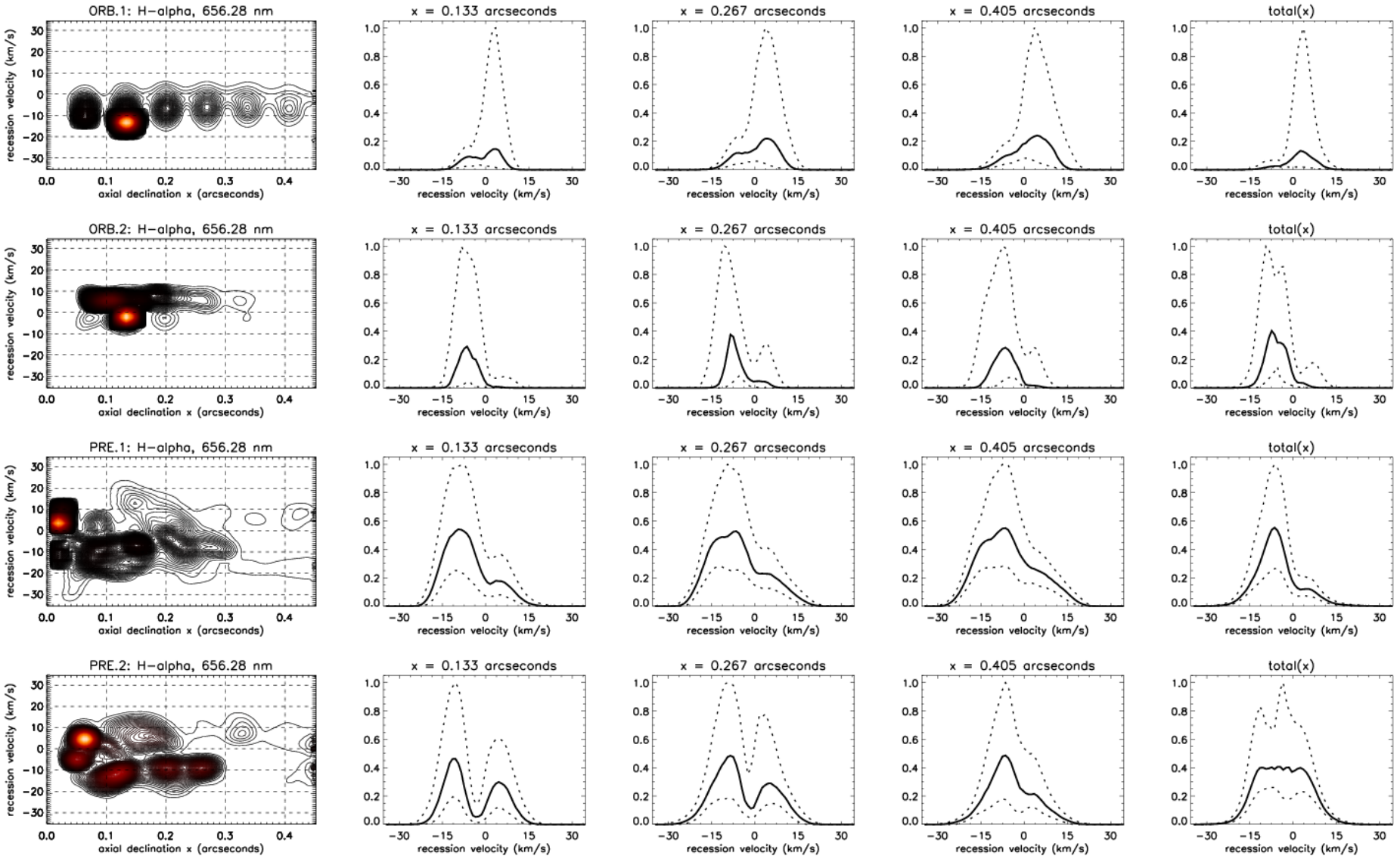

Figure I.1: Position-Velocity diagrams and line profiles for the H-α line, T=87.5 years, for the four simulated HH30 outflow scenarios in the early stage while the flows are still developing. Angular declination from the source object is in the direction of the outflow, along an axis parallel to the sky plane. λ dispersion arises from the recession velocity of emitting material in km/sec. The P-V plots are instantaneous examples at 87.5 yrs; contour scale is notional but linear. The line profiles indicate median emission over $0 < T < 87.5$ yrs; dashed lines are the upper and lower quartile boundaries for time variation. Total line profile is for whole-field emission; profiles with specified declination are given for comparison with a spatially resolved jet. Intensity is stated in dimensionless units of the upper quartile peak for each emission line.

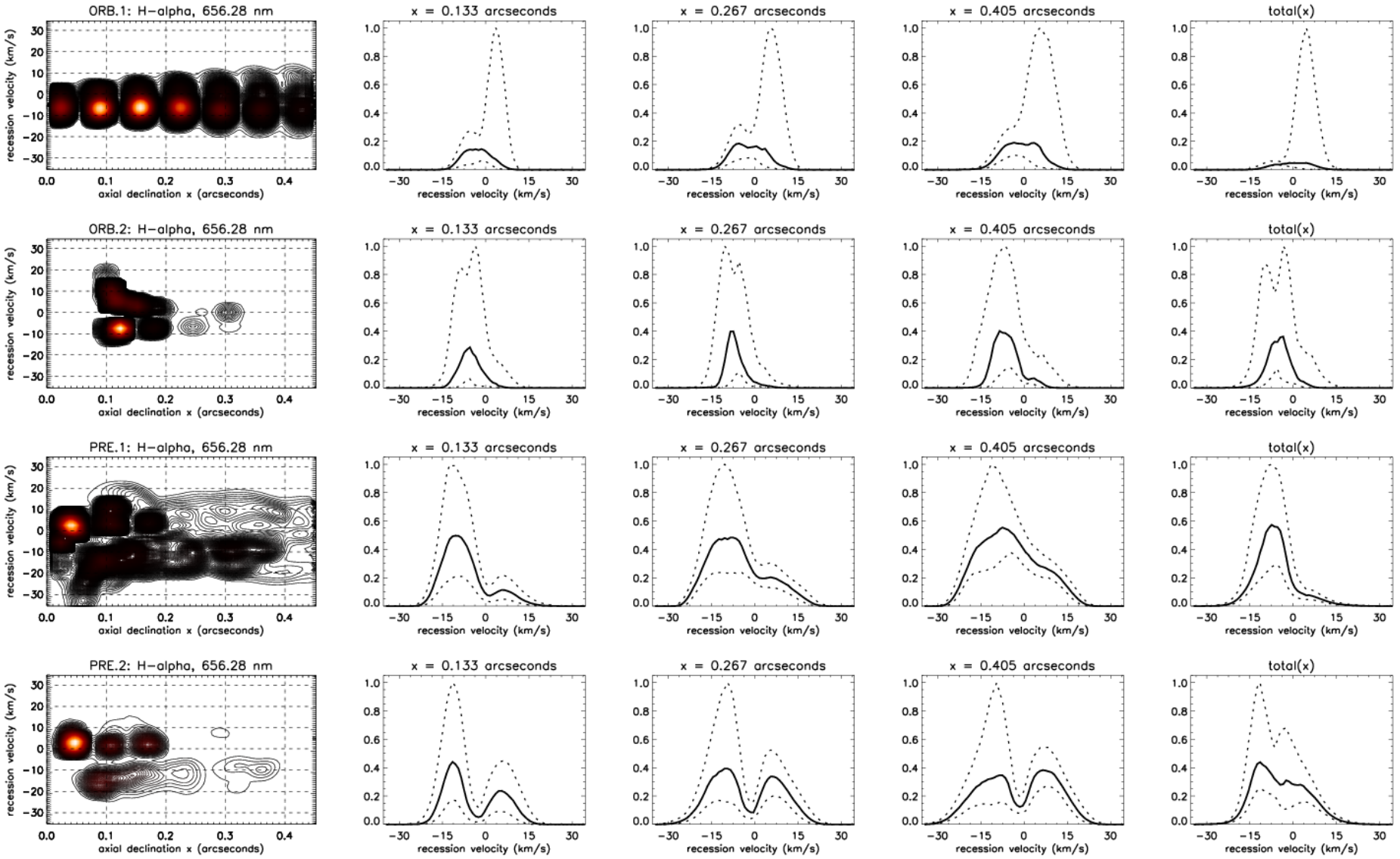

Figure I.2: Position-Velocity diagrams and line profiles for the H-α line, T=175 years, for the four simulated HH30 outflow scenarios when flows are well-developed. Angular declination from the source object is in the direction of the outflow, along an axis parallel to the sky plane. λ dispersion arises from the recession velocity of emitting material in km/sec. The P-V plots are instantaneous examples at 175 yrs; contour scale is notional but linear. The line profiles indicate median emission over $87.5 < T < 175$ yrs; dashed lines are the upper and lower quartile boundaries for time variation. Total line profile is for whole-field emission; profiles with specified declination are given for comparison with a spatially resolved jet. Intensity is stated in dimensionless units of the upper quartile peak for each emission line.

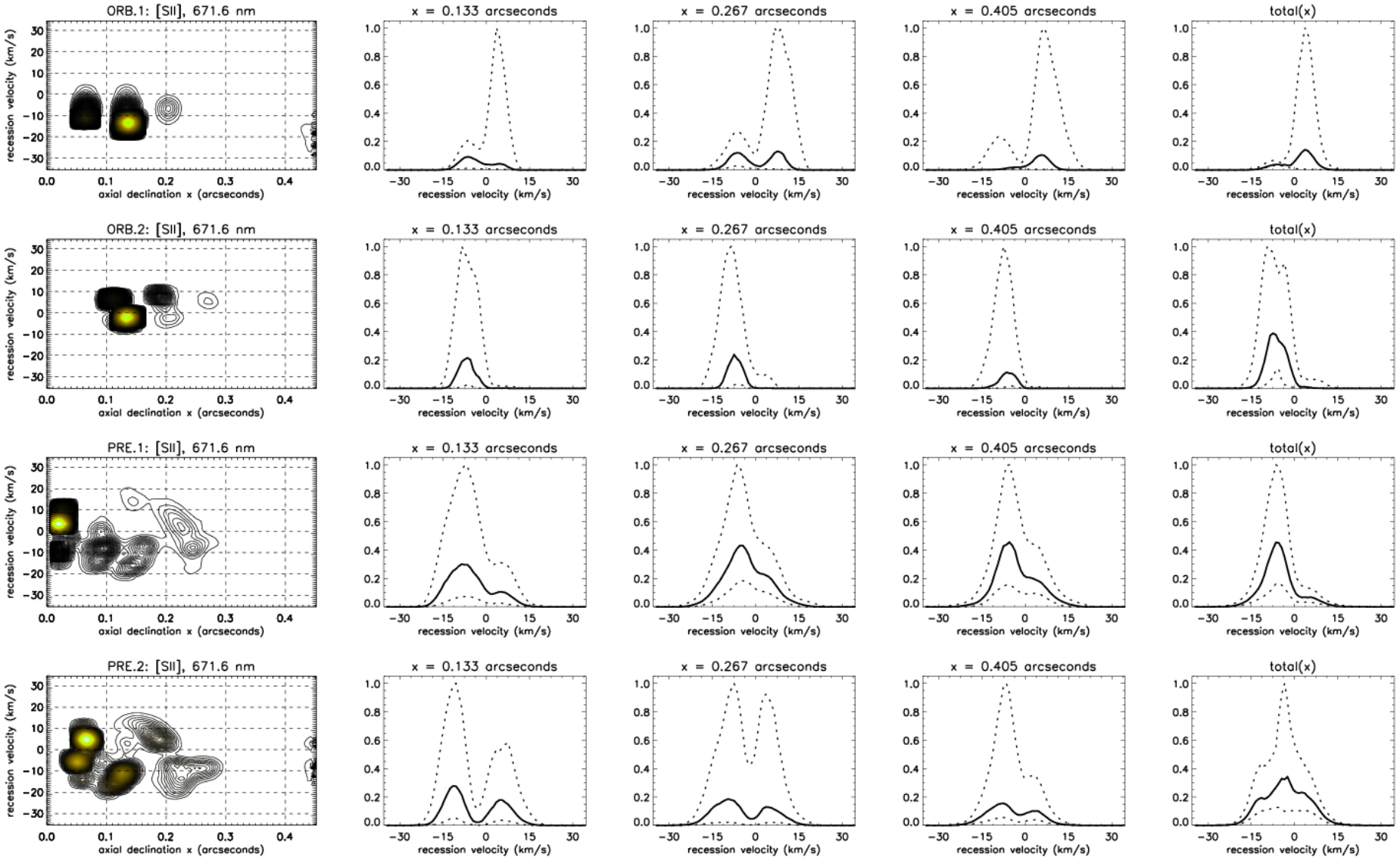

Figure I.3: Position-Velocity diagrams and line profiles for the [SII] line, T=87.5 years, for the four simulated HH30 outflow scenarios in the early stage while the flows are still developing. Angular declination from the source object is in the direction of the outflow, along an axis parallel to the sky plane. λ dispersion arises from the recession velocity of emitting material in km/sec. The P-V plots are instantaneous examples at 87.5 yrs; contour scale is notional but linear. The line profiles indicate median emission over $0 < T < 87.5$ yrs; dashed lines are the upper and lower quartile boundaries for time variation. Total line profile is for whole-field emission; profiles with specified declination are given for comparison with a spatially resolved jet. Intensity is stated in dimensionless units of the upper quartile peak for each emission line.

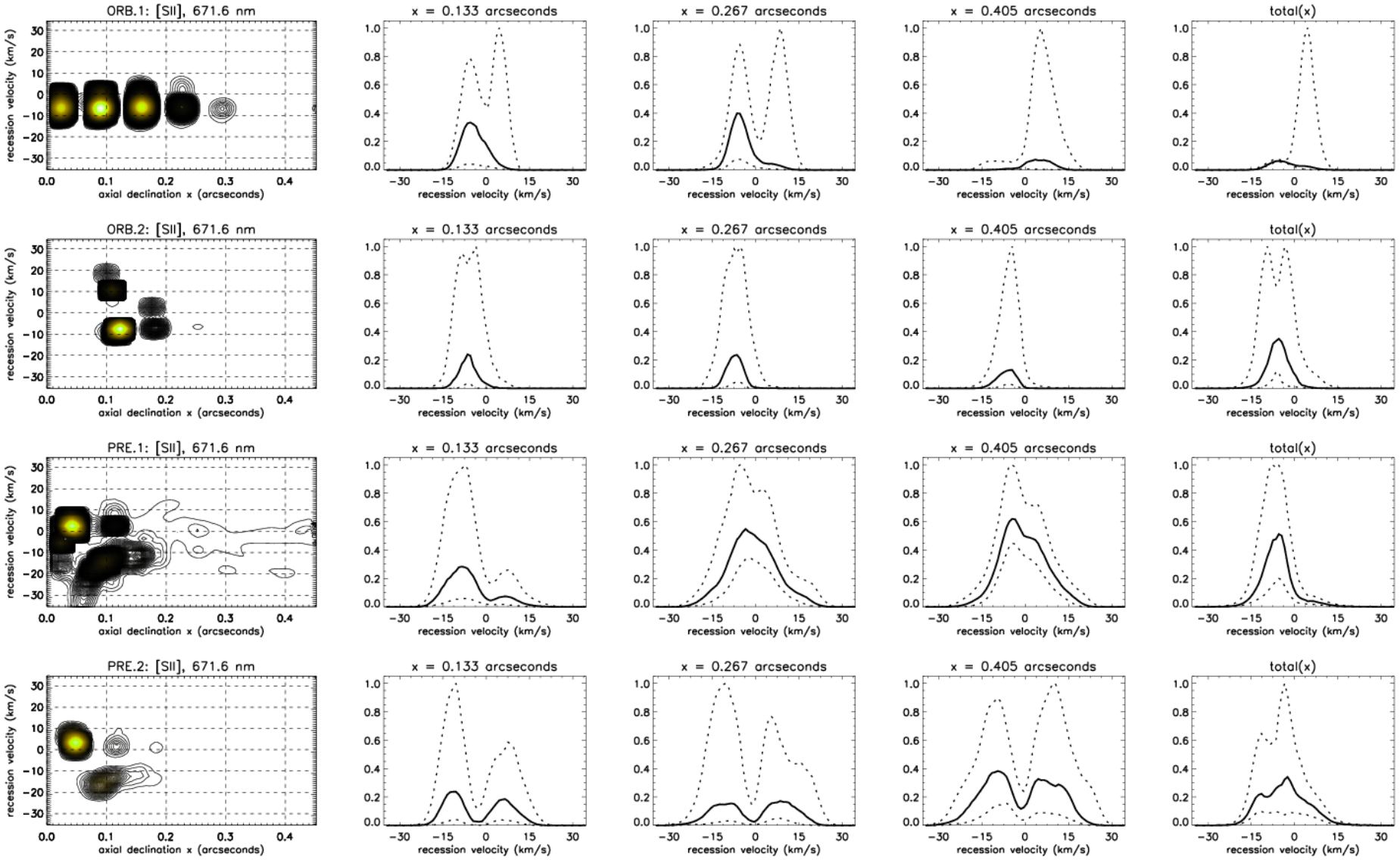

Figure I.4: Position-Velocity diagrams and line profiles for the [SII] line, T=175 years, for the four simulated HH30 outflow scenarios when flows are well-developed. Angular declination from the source object is in the direction of the outflow, along an axis parallel to the sky plane. λ dispersion arises from the recession velocity of emitting material in km/sec. The P-V plots are instantaneous examples at 175 yrs; contour scale is notional but linear. The line profiles indicate median emission over $87.5 < T < 175$ yrs; dashed lines are the upper and lower quartile boundaries for time variation. Total line profile is for whole-field emission; profiles with specified declination are given for comparison with a spatially resolved jet. Intensity is stated in dimensionless units of the upper quartile peak for each emission line.

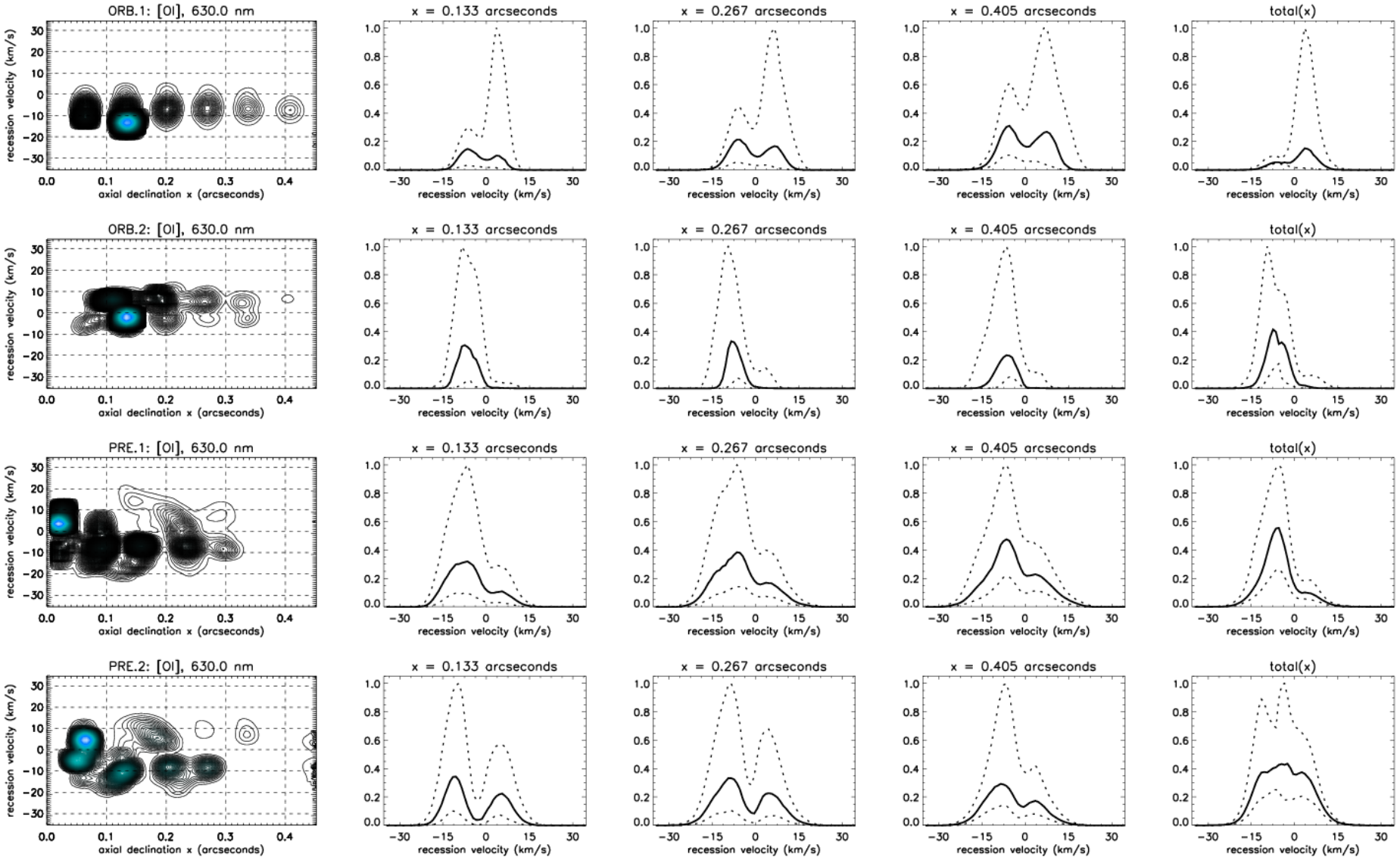

Figure I.5: Position-Velocity diagrams and line profiles for the [OI] line, T=87.5 years, for the four simulated HH30 outflow scenarios in the early stage while the flows are still developing. Angular declination from the source object is in the direction of the outflow, along an axis parallel to the sky plane. λ dispersion arises from the recession velocity of emitting material in km/sec. The P-V plots are instantaneous examples at 87.5 yrs; contour scale is notional but linear. The line profiles indicate median emission over $0 < T < 87.5$ yrs; dashed lines are the upper and lower quartile boundaries for time variation. Total line profile is for whole-field emission; profiles with specified declination are given for comparison with a spatially resolved jet. Intensity is stated in dimensionless units of the upper quartile peak for each emission line.

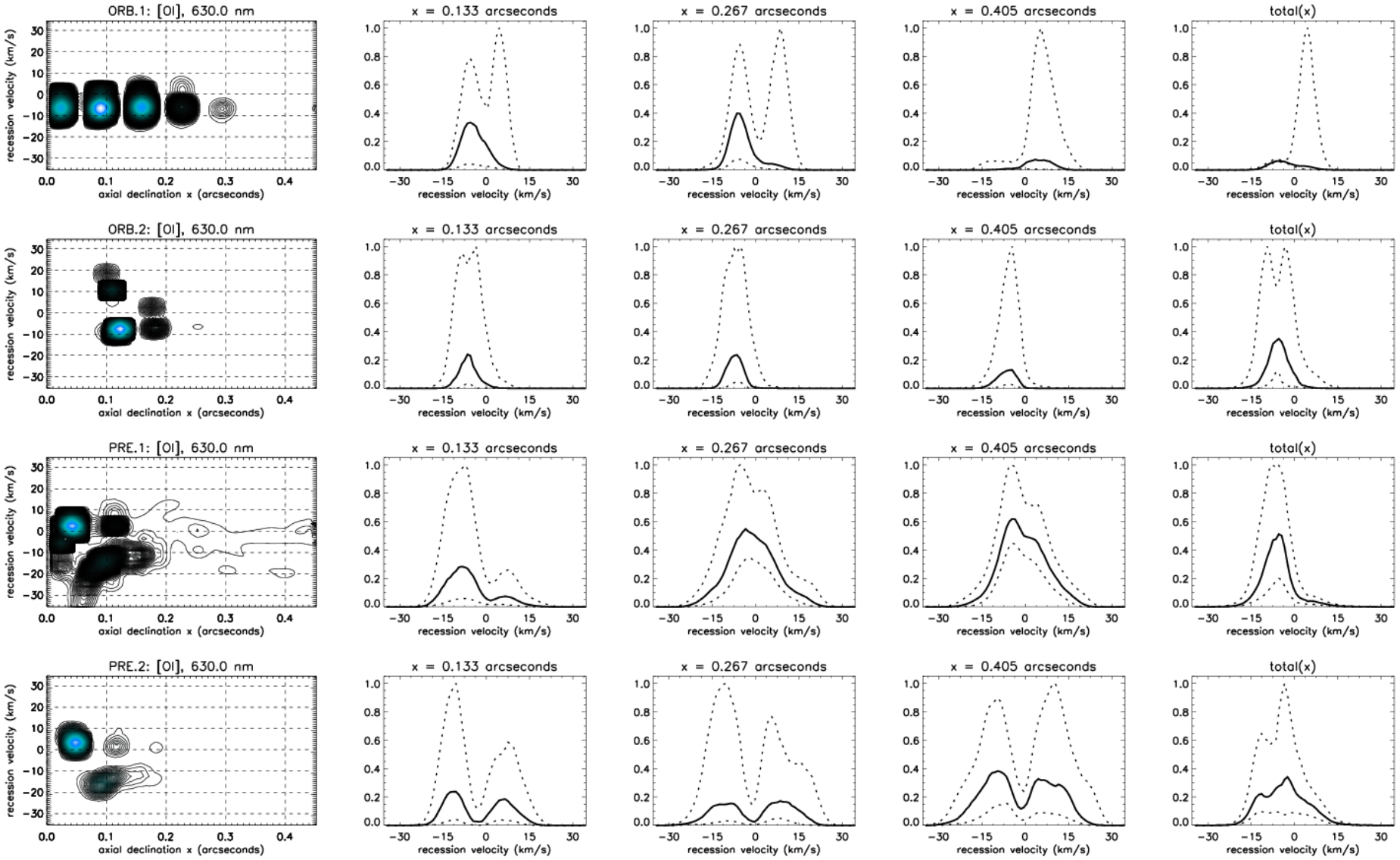

Figure I.6: Position-Velocity diagrams and line profiles for the [OI] line, T=175 years, for the four simulated HH30 outflow scenarios when flows are well-developed. Angular declination from the source object is in the direction of the outflow, along an axis parallel to the sky plane. λ dispersion arises from the recession velocity of emitting material in km/sec. The P-V plots are instantaneous examples at 175 yrs; contour scale is notional but linear. The line profiles indicate median emission over $87.5 < T < 175$ yrs; dashed lines are the upper and lower quartile boundaries for time variation. Total line profile is for whole-field emission; profiles with specified declination are given for comparison with a spatially resolved jet. Intensity is stated in dimensionless units of the upper quartile peak for each emission line.

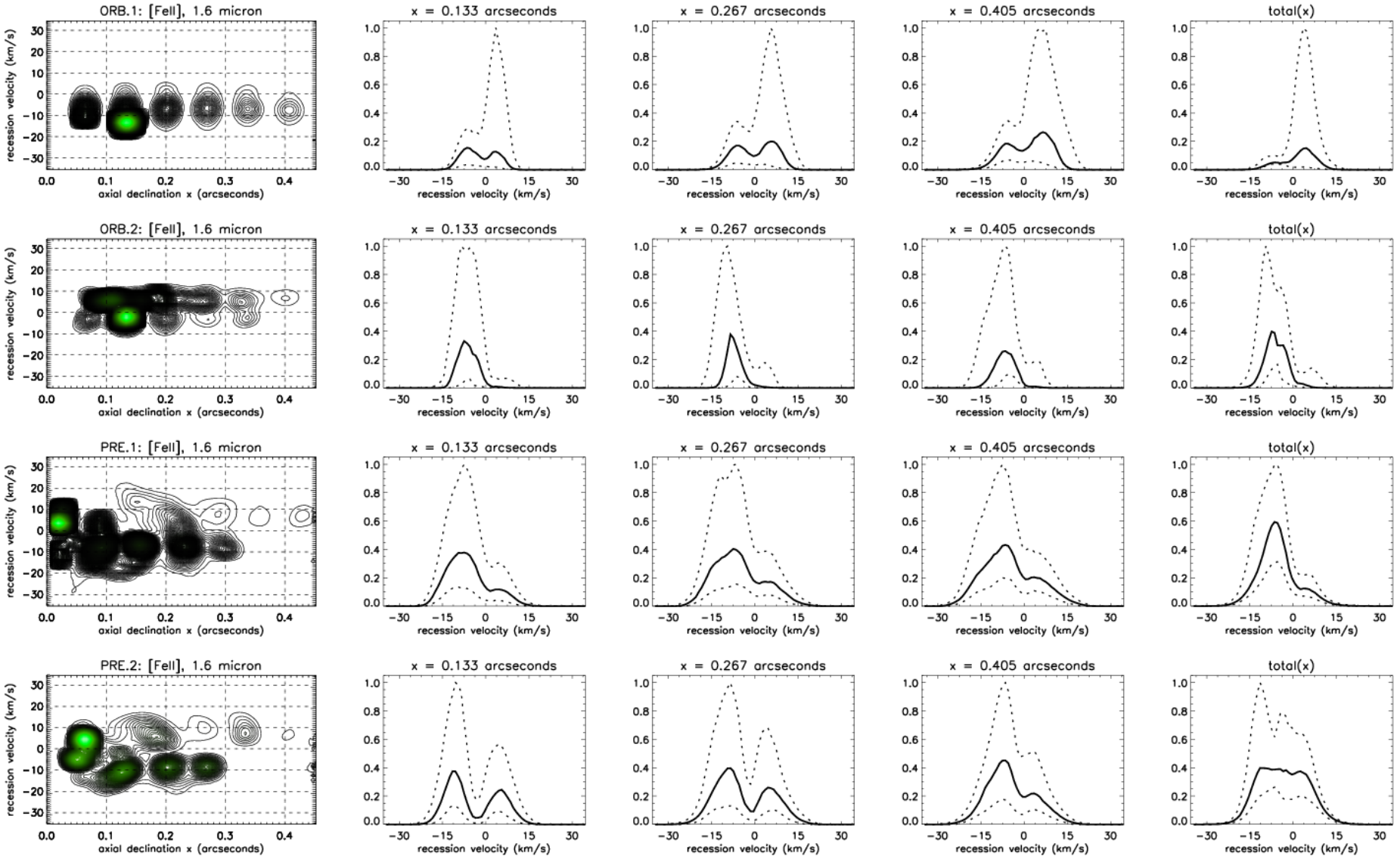

Figure I.7: Position-Velocity diagrams and line profiles for the [FeII] line, T=87.5 years, for the four simulated HH30 outflow scenarios in the early stage while the flows are still developing. Angular declination from the source object is in the direction of the outflow, along an axis parallel to the sky plane. λ dispersion arises from the recession velocity of emitting material in km/sec. The P-V plots are instantaneous examples at 87.5 yrs; contour scale is notional but linear. The line profiles indicate median emission over $0 < T < 87.5$ yrs; dashed lines are the upper and lower quartile boundaries for time variation. Total line profile is for whole-field emission; profiles with specified declination are given for comparison with a spatially resolved jet. Intensity is stated in dimensionless units of the upper quartile peak for each emission line.

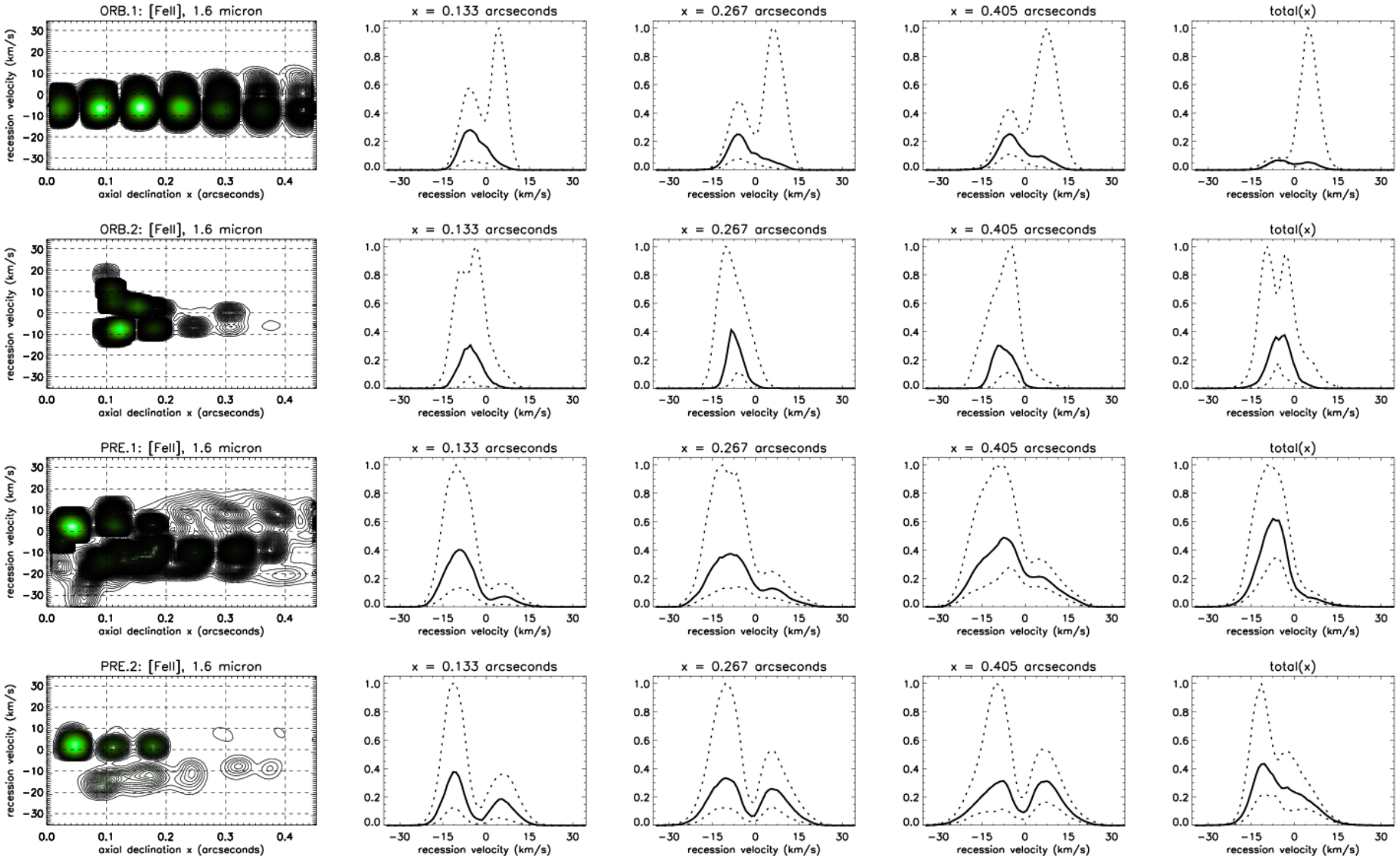

Figure I.8: Position-Velocity diagrams and line profiles for the [FeII] line, T=175 years, for the four simulated HH30 outflow scenarios when flows are well-developed. Angular declination from the source object is in the direction of the outflow, along an axis parallel to the sky plane. λ dispersion arises from the recession velocity of emitting material in km/sec. The P-V plots are instantaneous examples at 175 yrs; contour scale is notional but linear. The line profiles indicate median emission over $87.5 < T < 175$ yrs; dashed lines are the upper and lower quartile boundaries for time variation. Total line profile is for whole-field emission; profiles with specified declination are given for comparison with a spatially resolved jet. Intensity is stated in dimensionless units of the upper quartile peak for each emission line.

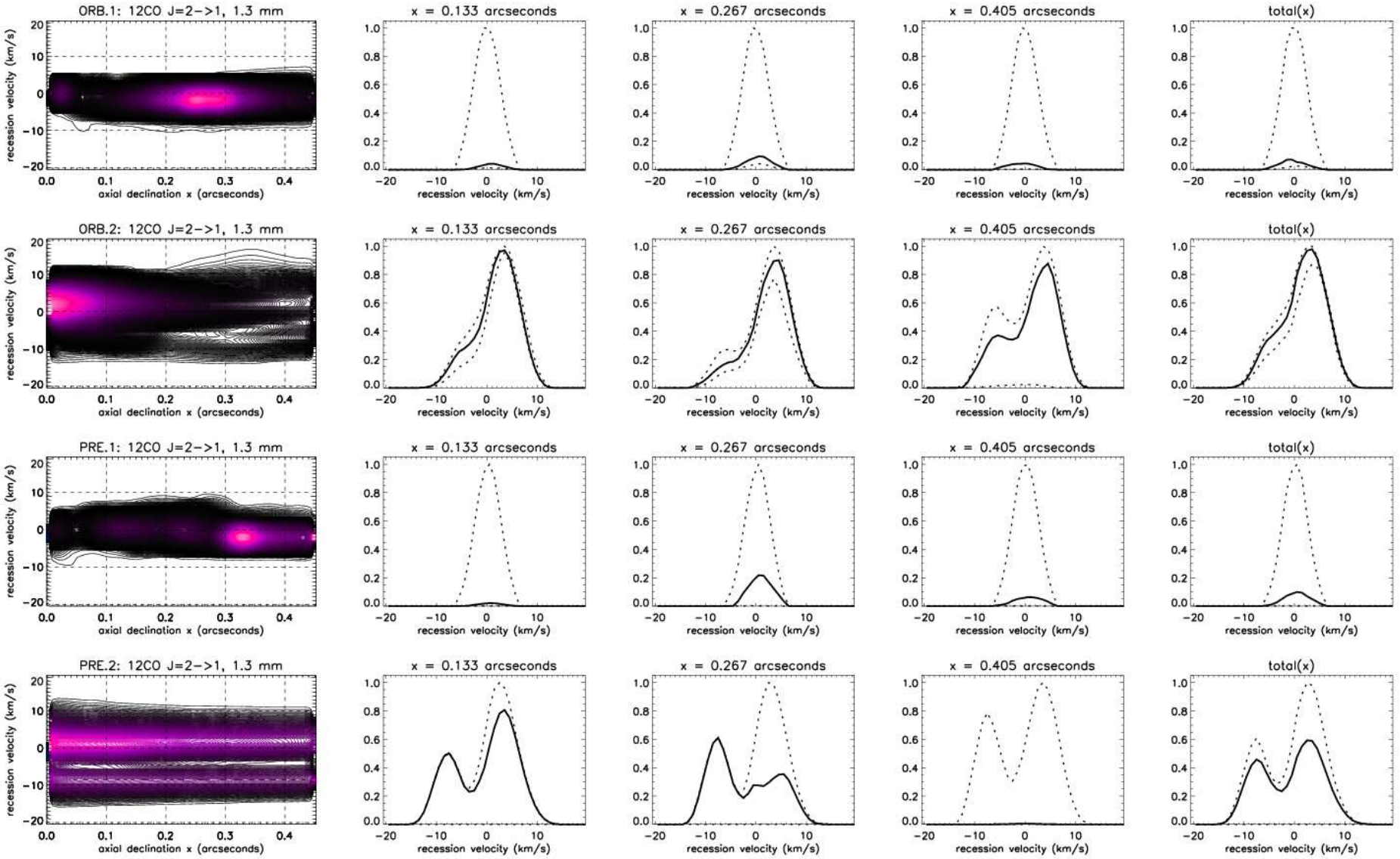

Figure I.9: Position-Velocity diagrams and line profiles for the ^{12}CO J=2-1 line, T=87.5 years, for the four simulated HH30 outflow scenarios in the early stage while the flows are still developing. Angular declination from the source object is in the direction of the outflow, along an axis parallel to the sky plane. λ dispersion arises from the recession velocity of emitting material in km/sec. The P-V plots are instantaneous examples at 87.5 yrs; contour scale is notional but linear. The line profiles indicate median emission over $0 < T < 87.5$ yrs; dashed lines are the upper and lower quartile boundaries for time variation. Total line profile is for whole-field emission; profiles with specified declination are given for comparison with a spatially resolved jet. Intensity is stated in dimensionless units of the upper quartile peak for each emission line.

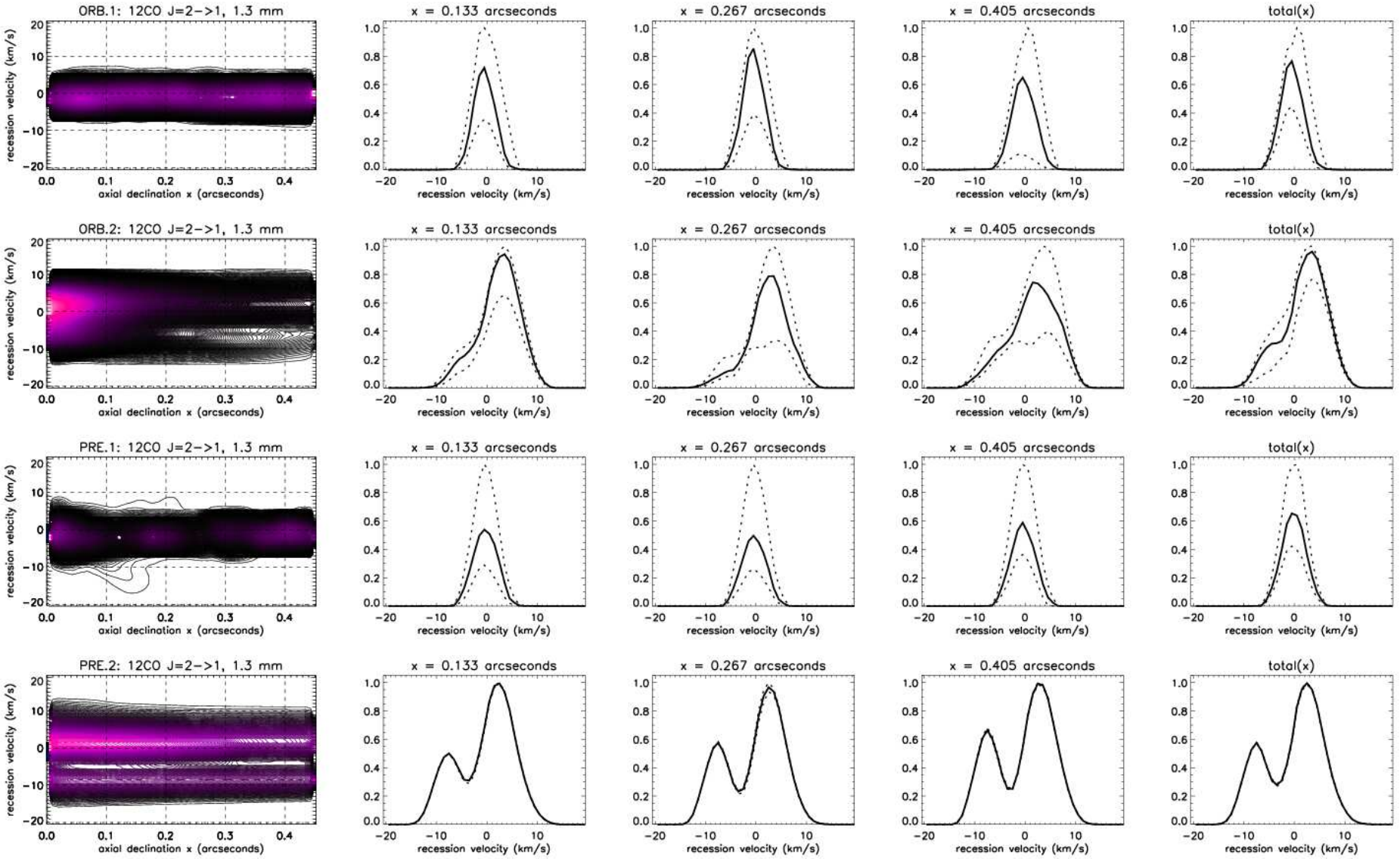

Figure I.10: Position-Velocity diagrams and line profiles for the ^{12}CO J=2-1 line, T=175 years, for the four simulated HH30 outflow scenarios when flows are well-developed. Angular declination from the source object is in the direction of the outflow, along an axis parallel to the sky plane. λ dispersion arises from the recession velocity of emitting material in km/sec. The P-V plots are instantaneous examples at 175 yrs; contour scale is notional but linear. The line profiles indicate median emission over $87.5 < T < 175$ yrs; dashed lines are the upper and lower quartile boundaries for time variation. Total line profile is for whole-field emission; profiles with specified declination are given for comparison with a spatially resolved jet. Intensity is stated in dimensionless units of the upper quartile peak for each emission line.

Appendix J

Mass-Velocity Spectra

J.1 Mass-Velocity Spectra

A first-order power law approximation to the M-V spectrum may be stated as:

$$\frac{dm(v_r)}{dv_r} \propto {v_r}^{-\gamma} \tag{J.1}$$

The exponent γ is the negative gradient of the spectrum when a log-log plot of ${dm(v_r)}/{dv_r}$ is plotted against v_r. We adopted a convention similar to that of Moraghan et al., (2006)(69), but specified different velocity ranges for the determination of our power laws, for $\theta \geq 15°$. The chosen velocity ranges were:

- 1-2 km/s
- 2-10 km/s
- 10-50 km/s
- 50-250km/s

For the shallow-angle spectra ($\theta = 1°$), due to the lower velocity regime, it was decided to use a scheme similar to that of Moraghan et al., (2006)(69):

- 2-4 km/s
- 4-8 km/s
- 8-16 km/s
- 16-32 km/s

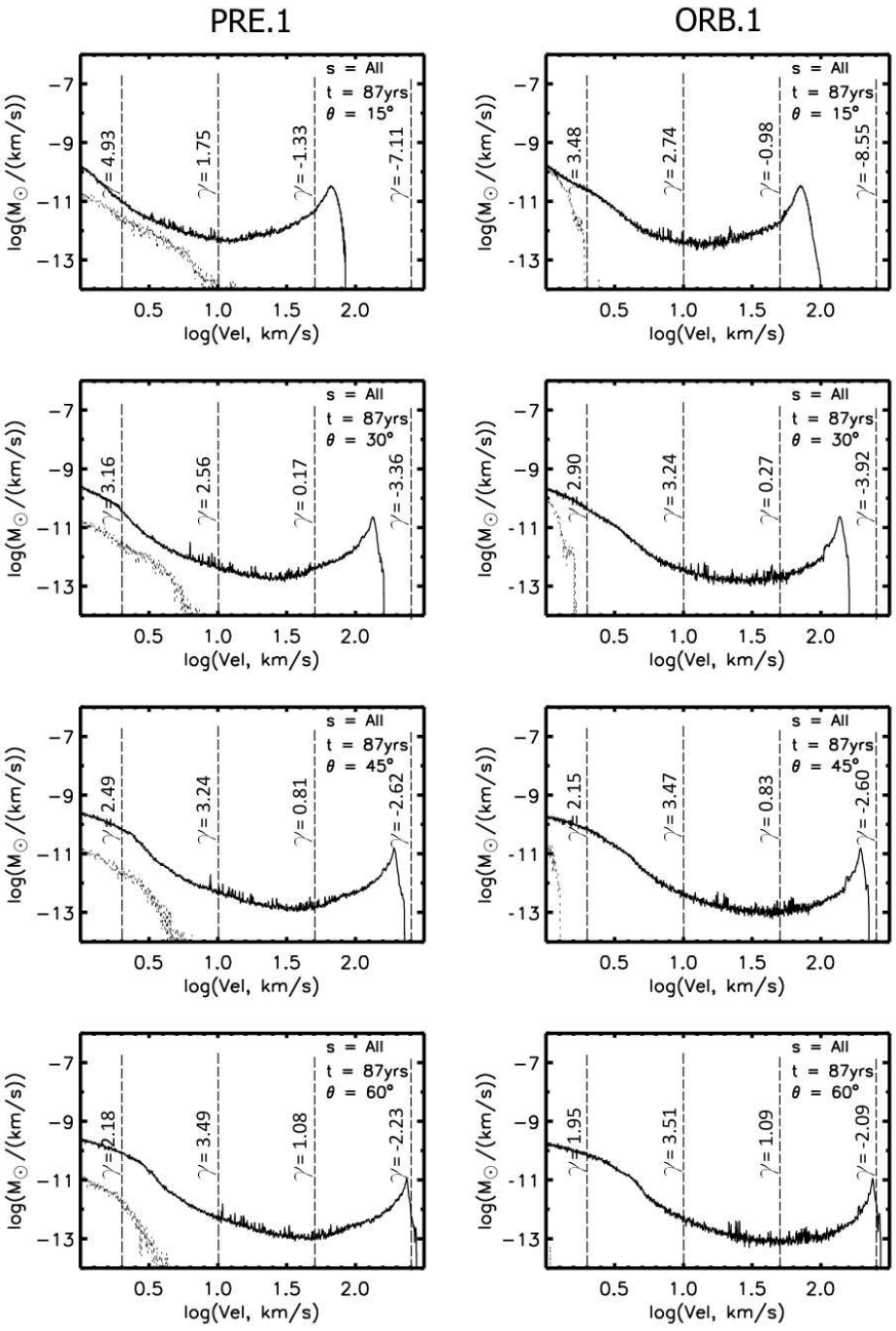

Figure J.1: All-Species Mass-Velocity Spectra: atomic-only outflow scenarios, 4 aspect angles, simulation time T=87.5 years.

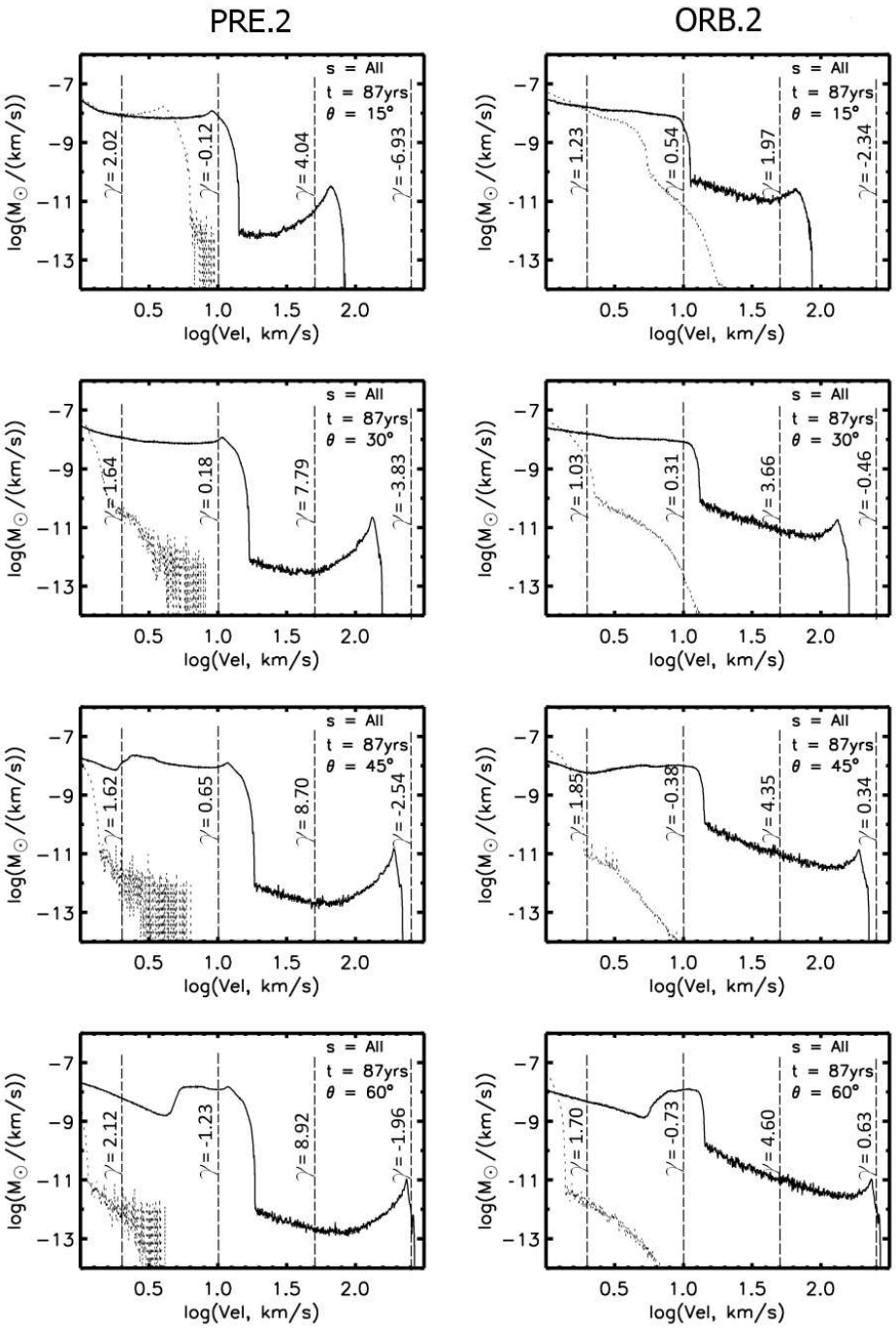

Figure J.2: All-Species Mass-Velocity Spectra: dual atomic-molecular outflow scenarios, 4 aspect angles, simulation time T=87.5 years.

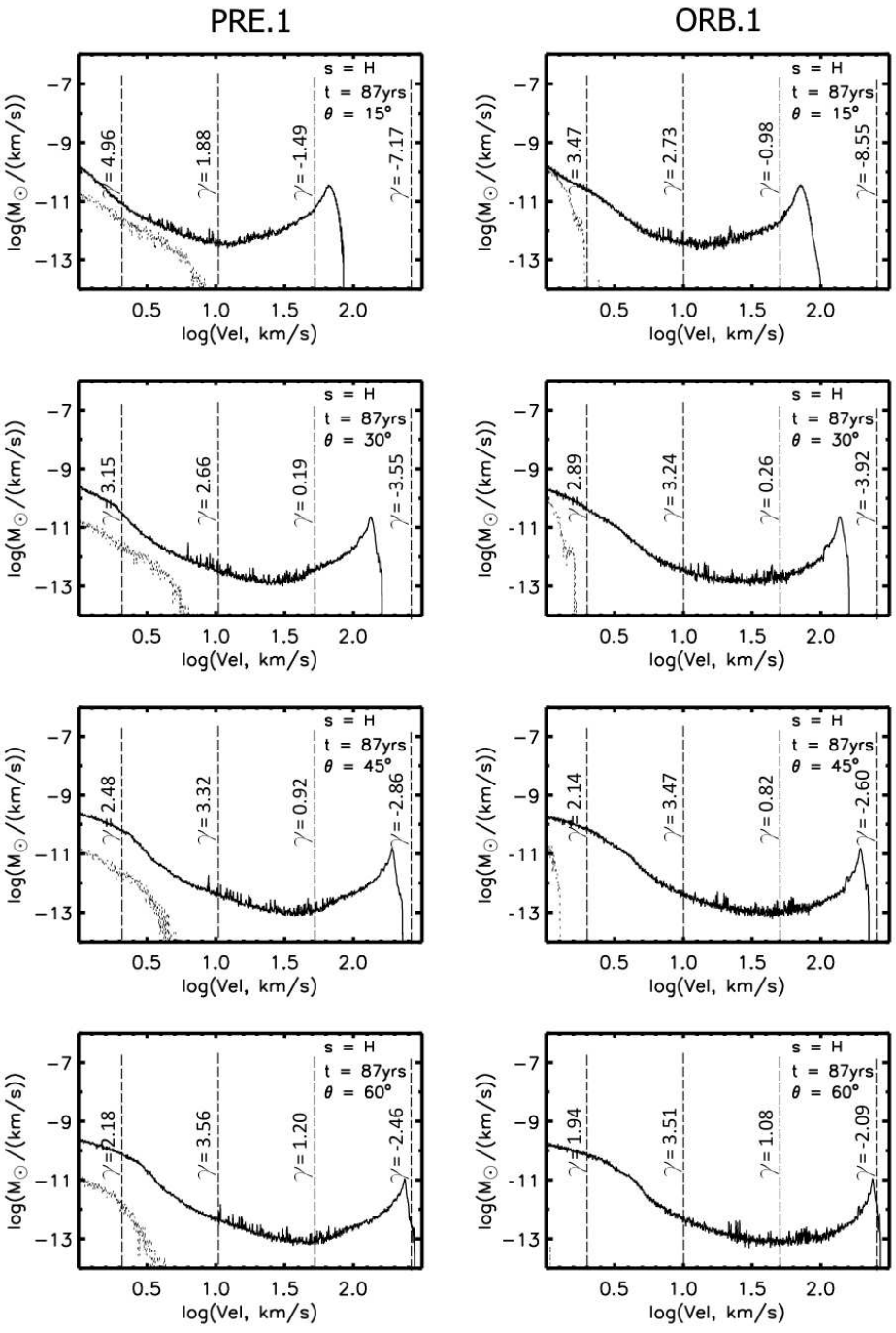

Figure J.3: Atomic Hydrogen Mass-Velocity Spectra: atomic-only outflow scenarios, 4 aspect angles, simulation time T=87.5 years.

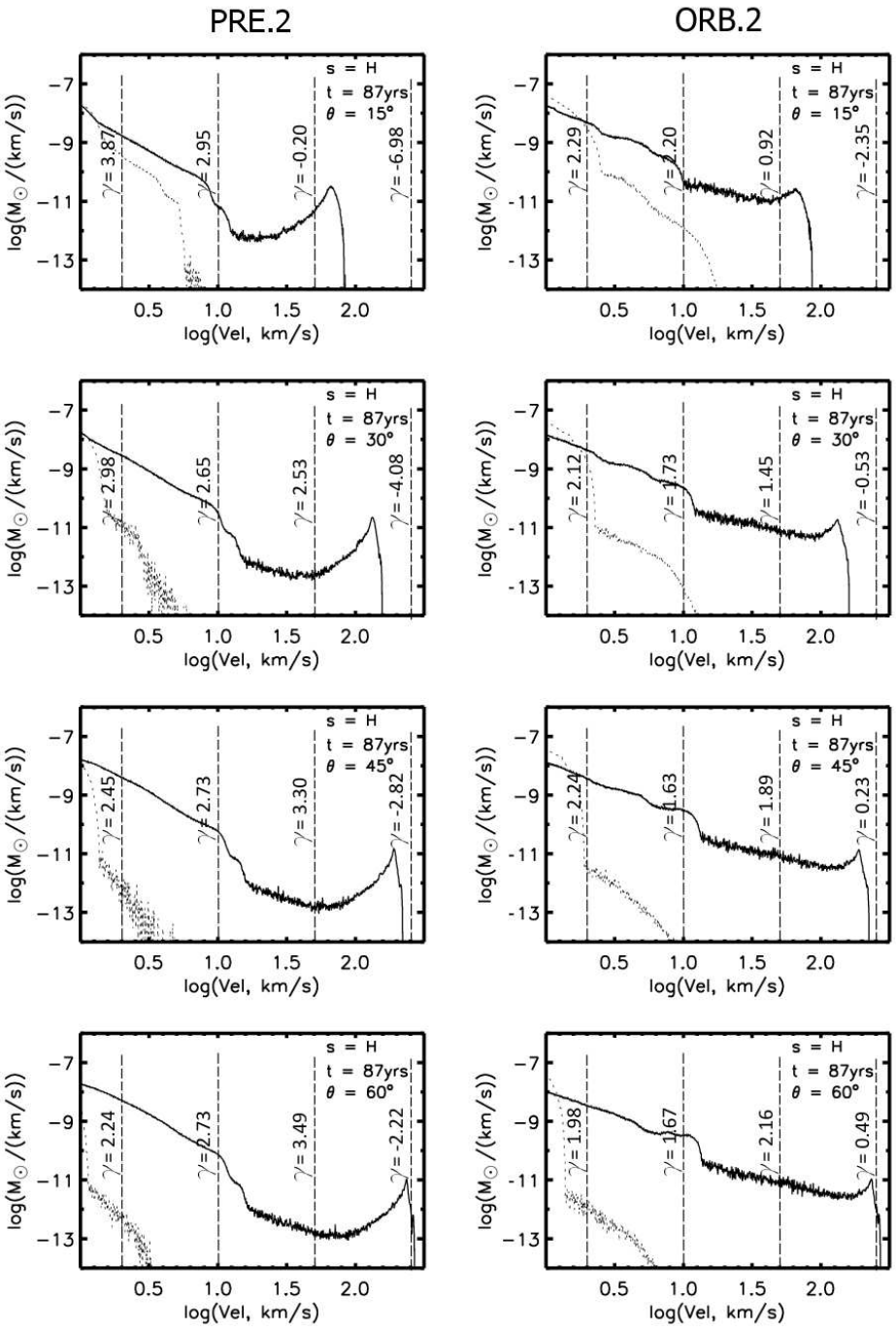

Figure J.4: Atomic Hydrogen Mass-Velocity Spectra: dual atomic-molecular outflow scenarios, all species, 4 aspect angles, simulation time T=87.5 years.

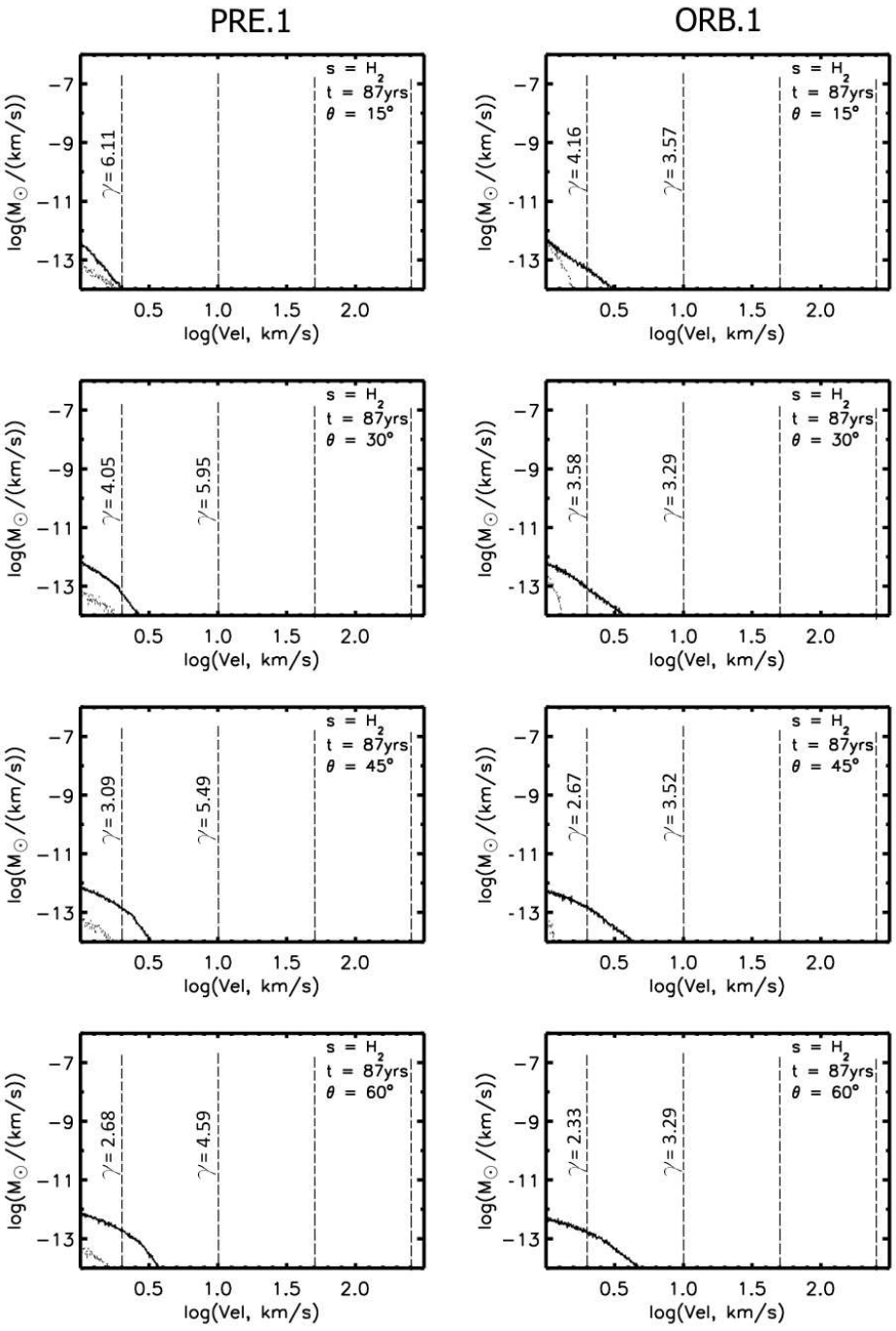

Figure J.5: Molecular Hydrogen Mass-Velocity Spectra: atomic-only outflow scenarios, 4 aspect angles, simulation time T=87.5 years.

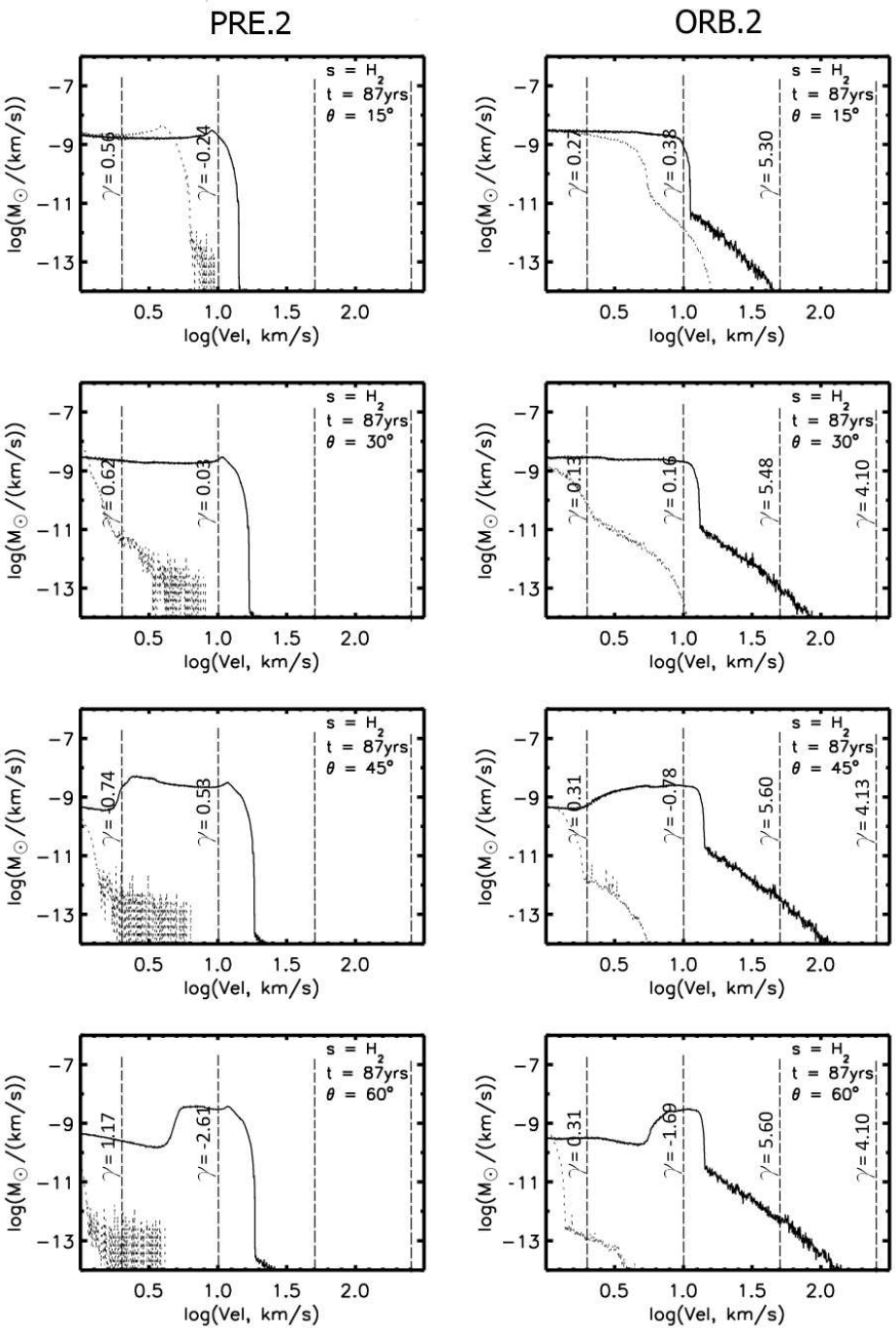

Figure J.6: Molecular Hydrogen Mass-Velocity Spectra: dual atomic-molecular outflow scenarios, all species, 4 aspect angles, simulation time T=87.5 years.

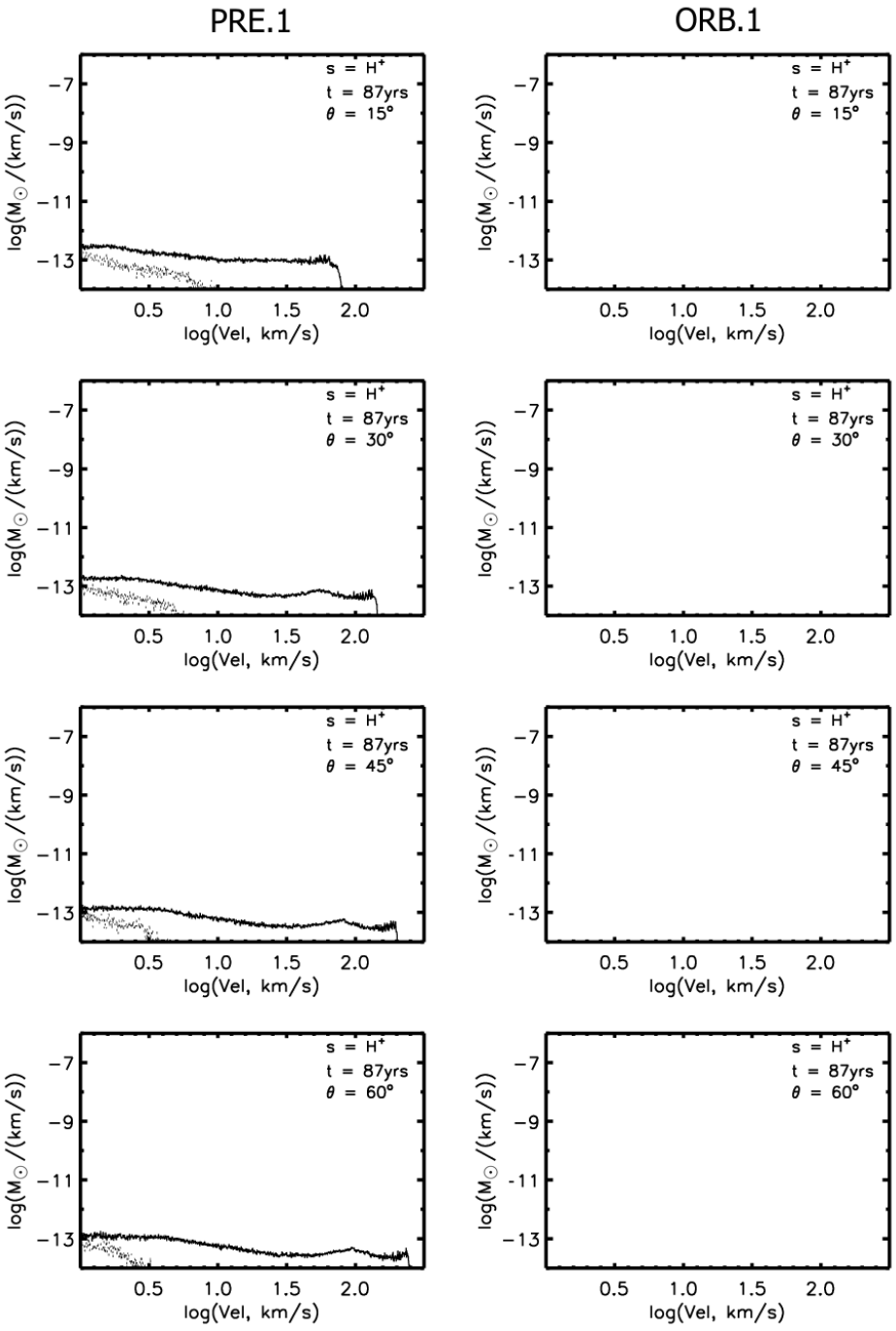

Figure J.7: Ionised Hydrogen Mass-Velocity Spectra: atomic-only outflow scenarios, 4 aspect angles, simulation time T=87.5 years.

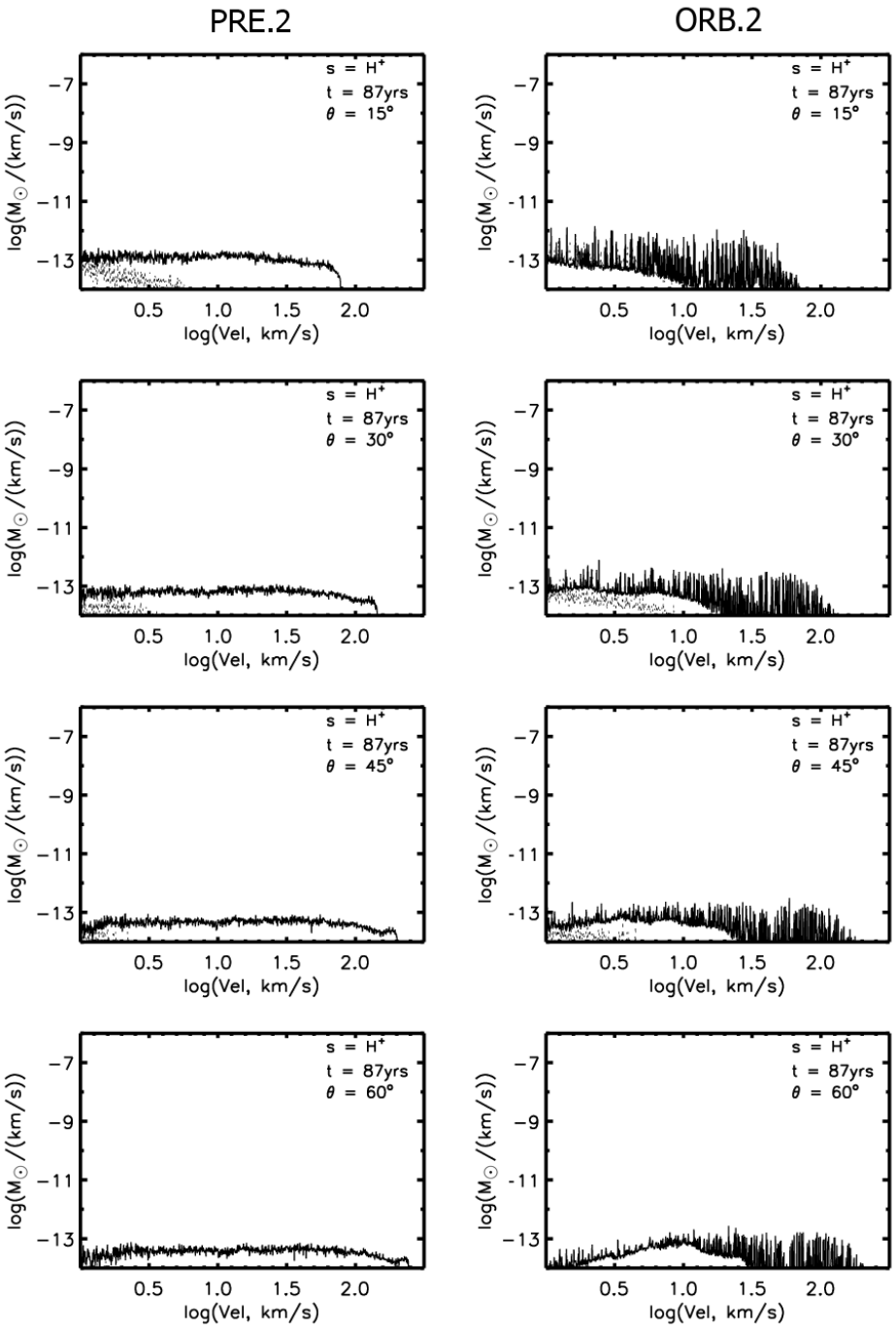

Figure J.8: Ionised Hydrogen Mass-Velocity Spectra: dual atomic-molecular outflow scenarios, all species, 4 aspect angles, simulation time T=87.5 years.

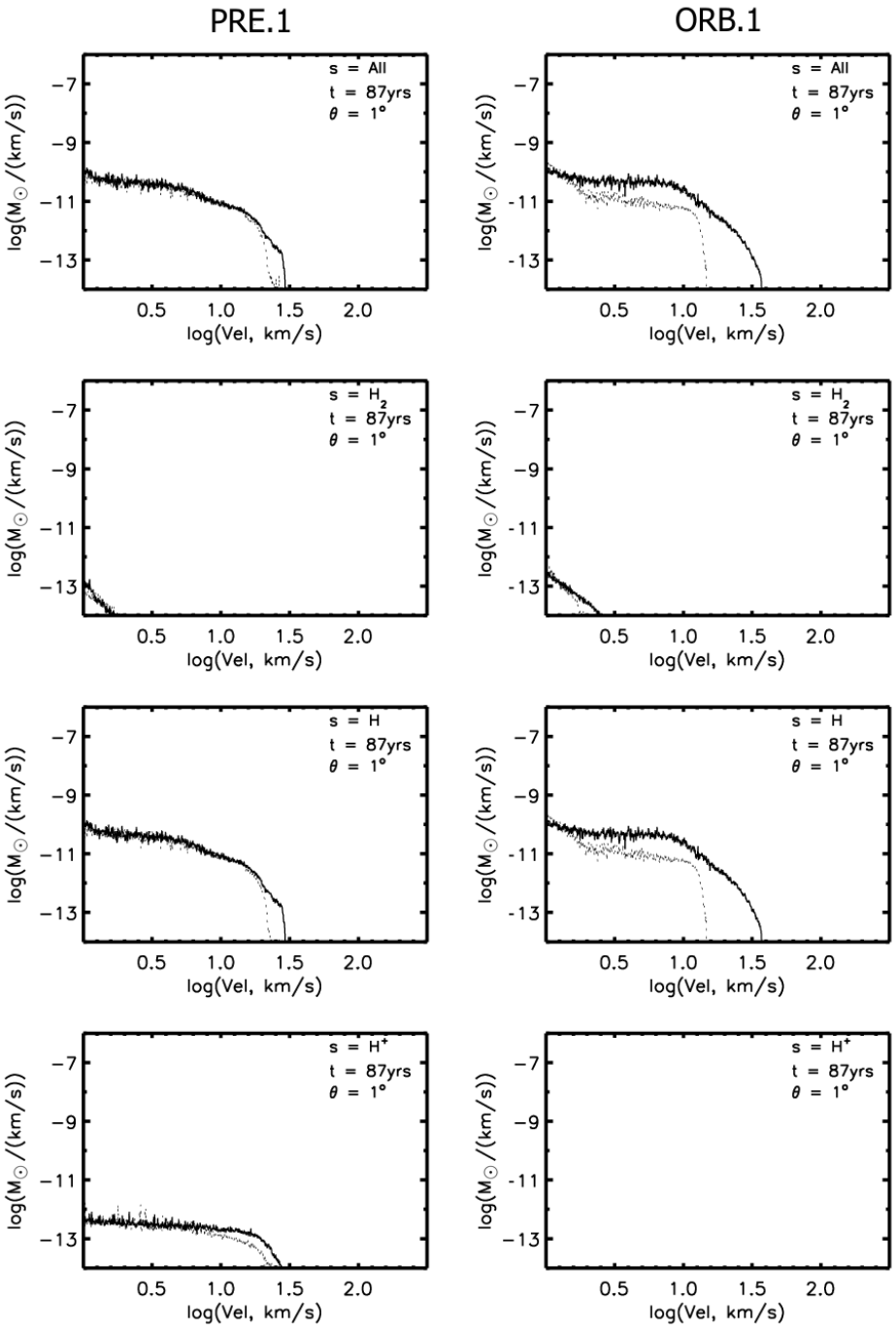

Figure J.9: Multispecies Mass-Velocity Spectra: atomic-only outflow scenarios, all Hydrogen species, aspect angle θ=1°, simulation time T=87.5 years.

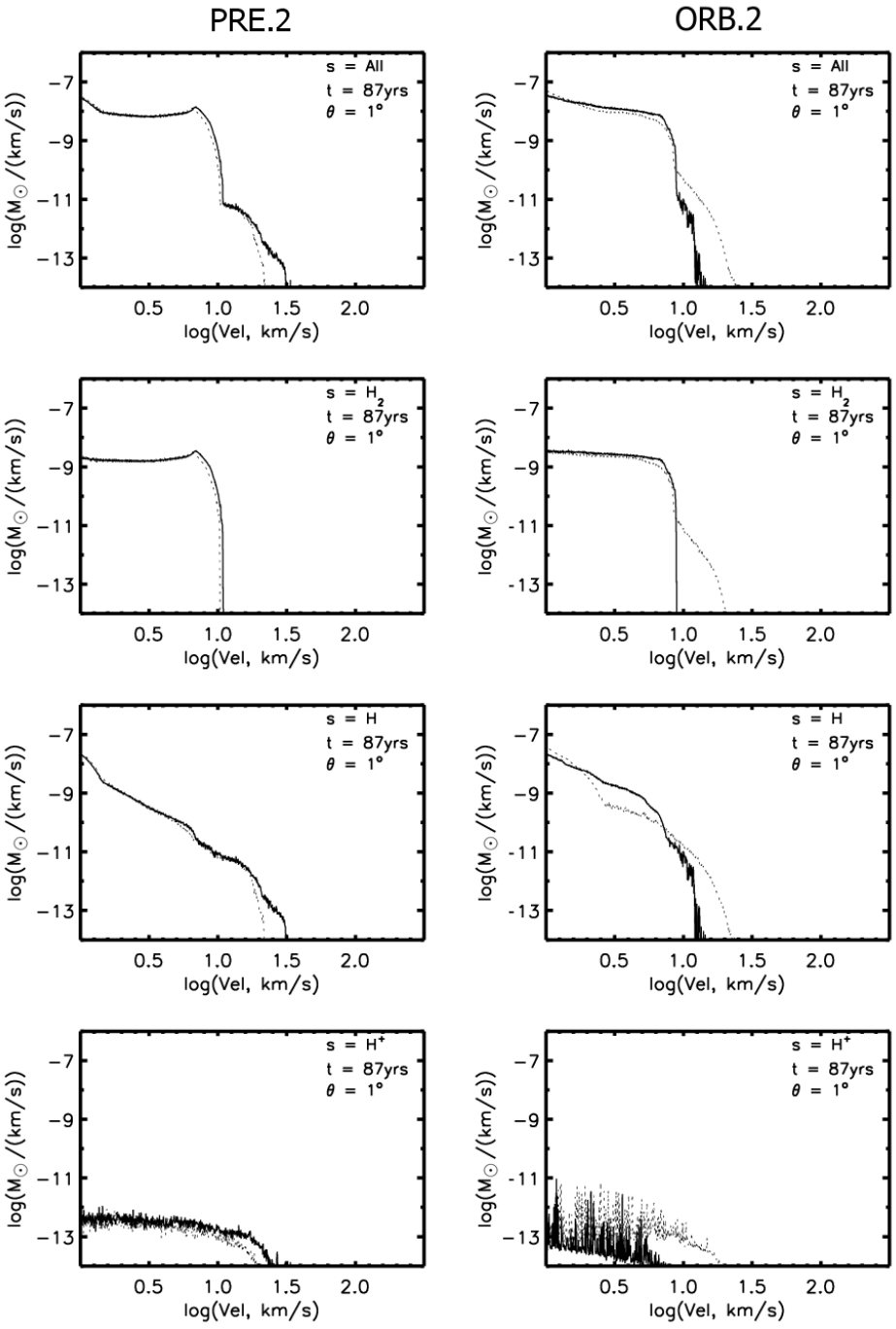

Figure J.10: Multispecies Mass-Velocity Spectra: atomic-molecular outflow scenarios, all Hydrogen species, aspect angle θ=1°, simulation time T=87.5 years.

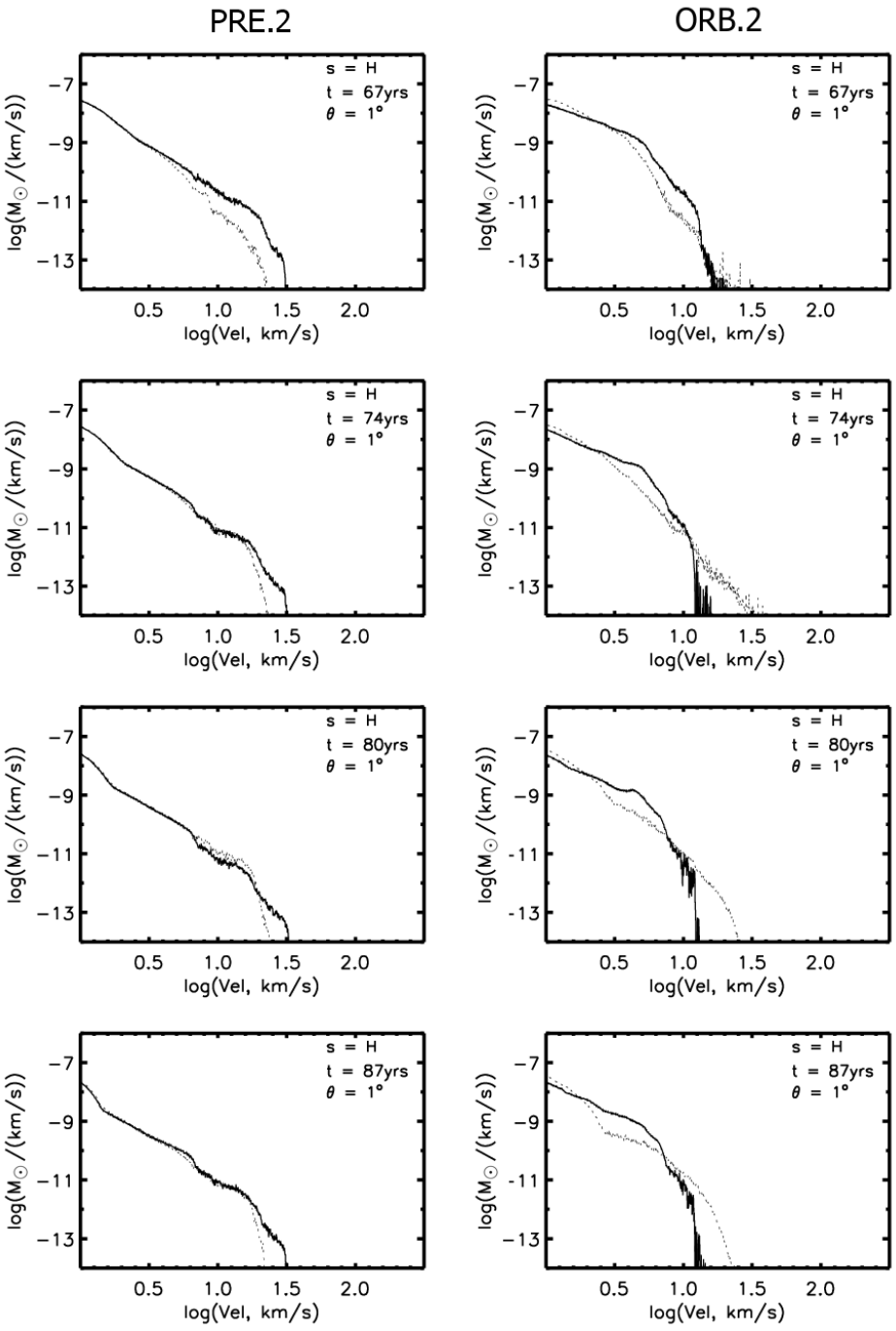

Figure J.11: Time-varying Mass-Velocity Spectra: atomic-molecular outflow scenarios, Atomic Hydrogen spectrum, aspect angle θ=1°, simulation times from 67 to 87 years.

Table J.1: **All-Species Mass-Velocity γ values**
Four velocity regimes, blue-shifted material at four aspect angles.

γ_{All}		1-2 (km/s)		2-10 (km/s)		10-50 (km/s)		50-250 (km/s)	
		PRE	ORB	PRE	ORB	PRE	ORB	PRE	ORB
15º	1. Atomic	4.93	3.48	1.75	2.74	-1.33	-0.98	-7.11	-8.55
	2. Dual A/M	2.02	1.23	-0.12	0.54	4.04	1.97	-6.93	-2.34
30º	1. Atomic	3.16	2.90	2.56	3.24	0.17	0.27	-3.36	-3.92
	2. Dual A/M	1.64	1.03	0.18	0.31	7.79	3.66	-3.83	-0.46
45º	1. Atomic	2.49	2.15	3.24	3.47	0.81	0.83	-2.62	-2.60
	2. Dual A/M	1.62	1.85	0.65	-0.38	8.70	4.35	-2.54	0.34
60º	1. Atomic	2.18	1.95	3.49	3.51	1.08	1.09	-2.23	-2.09
	2. Dual A/M	2.12	1.70	-1.23	-0.73	8.92	4.60	-1.96	0.63

Table J.2: **Atomic Hydrogen Mass-Velocity γ values**
Four velocity regimes, blue-shifted material at four aspect angles.

γ_H		1-2 (km/s)		2-10 (km/s)		10-50 (km/s)		50-250 (km/s)	
		PRE	ORB	PRE	ORB	PRE	ORB	PRE	ORB
15º	1. Atomic	4.96	3.47	1.88	2.73	-1.49	-0.98	-7.17	-8.55
	2. Dual A/M	3.87	2.29	2.95	2.20	-0.20	0.92	-6.98	-2.35
30º	1. Atomic	3.15	2.89	2.66	3.24	0.19	0.26	-3.55	-3.92
	2. Dual A/M	2.98	2.12	2.65	1.73	2.53	1.45	-4.08	-0.53
45º	1. Atomic	2.48	2.14	3.32	3.47	0.92	0.82	-2.86	-2.60
	2. Dual A/M	2.45	2.24	2.73	1.63	3.30	1.89	-2.82	0.23
60º	1. Atomic	2.18	1.94	3.56	3.51	1.20	1.08	-2.46	-2.09
	2. Dual A/M	2.24	1.98	2.73	1.67	3.49	2.16	-2.22	0.49

Table J.3: **Molecular Hydrogen Mass-Velocity γ values**
Four velocity regimes, blue-shifted at 4 aspect angles.

γ_{H_2}		1-2 (km/s)		2-10 (km/s)		10-50 (km/s)		50-250 (km/s)	
		PRE	ORB	PRE	ORB	PRE	ORB	PRE	ORB
15º	1. Atomic	6.11	4.16	0.00	3.57				
	2. Dual A/M	0.56	0.27	-0.24	0.38		5.30		
30º	1. Atomic	4.05	3.58	5.95	3.29				
	2. Dual A/M	0.62	0.13	0.03	0.16		5.48		4.10
45º	1. Atomic	3.09	2.67	5.49	3.52				
	2. Dual A/M	-0.74	0.31	0.53	-0.78		5.60		4.13
60º	1. Atomic	2.68	2.33	4.59	3.29				
	2. Dual A/M	1.17	0.31	-2.61	-1.69		5.60		4.10

Table J.4: **Blue-shifted Mass-Velocity 20-year average γ values**
Four velocity regimes viewed at a 1° aspect angle, for all Hydrogen species.

Blue Shifted		2-4 (km/s)		4-8 (km/s)		8-16 (km/s)		16-32 (km/s)	
		PRE	ORB	PRE	ORB	PRE	ORB	PRE	ORB
γ_{All}	1. Atomic	0.51		1.17	0.39	1.70	3.18	7.01	5.94
	2. Dual A/M	0.25	0.59	-0.65	1.69	13.09	17.38	6.94	
γ_H	1. Atomic	0.50		1.19	0.39	1.74	3.18	7.09	5.94
	2. Dual A/M	2.69	1.98	3.81	5.62	2.32	11.69	7.08	
γ_{H_2}	1. Atomic		2.60						
	2. Dual A/M	-0.02	0.23	-0.70	1.47	18.24	25.74		

Table J.5: **Red-shifted Mass-Velocity 20-year average γ values**
Four velocity regimes viewed at a 1° aspect angle, for all Hydrogen species.

Red Shifted		2-4 (km/s)		4-8 (km/s)		8-16 (km/s)		16-32 (km/s)	
		PRE	ORB	PRE	ORB	PRE	ORB	PRE	ORB
γ_{All}	1. Atomic	10.56		2.18	5.90	1.25	0.78	0.49	0.74
	2. Dual A/M	13.82	8.07	12.09	7.44	0.08	2.50	0.22	0.75
γ_H	1. Atomic	10.08		2.20	5.90	1.25	0.78	0.50	0.74
	2. Dual A/M	14.07	7.11	2.90	5.84	3.85	4.74	2.96	3.58
γ_{H_2}	1. Atomic								
	2. Dual A/M		7.55	17.84	7.79	0.04	2.45	-0.06	0.32

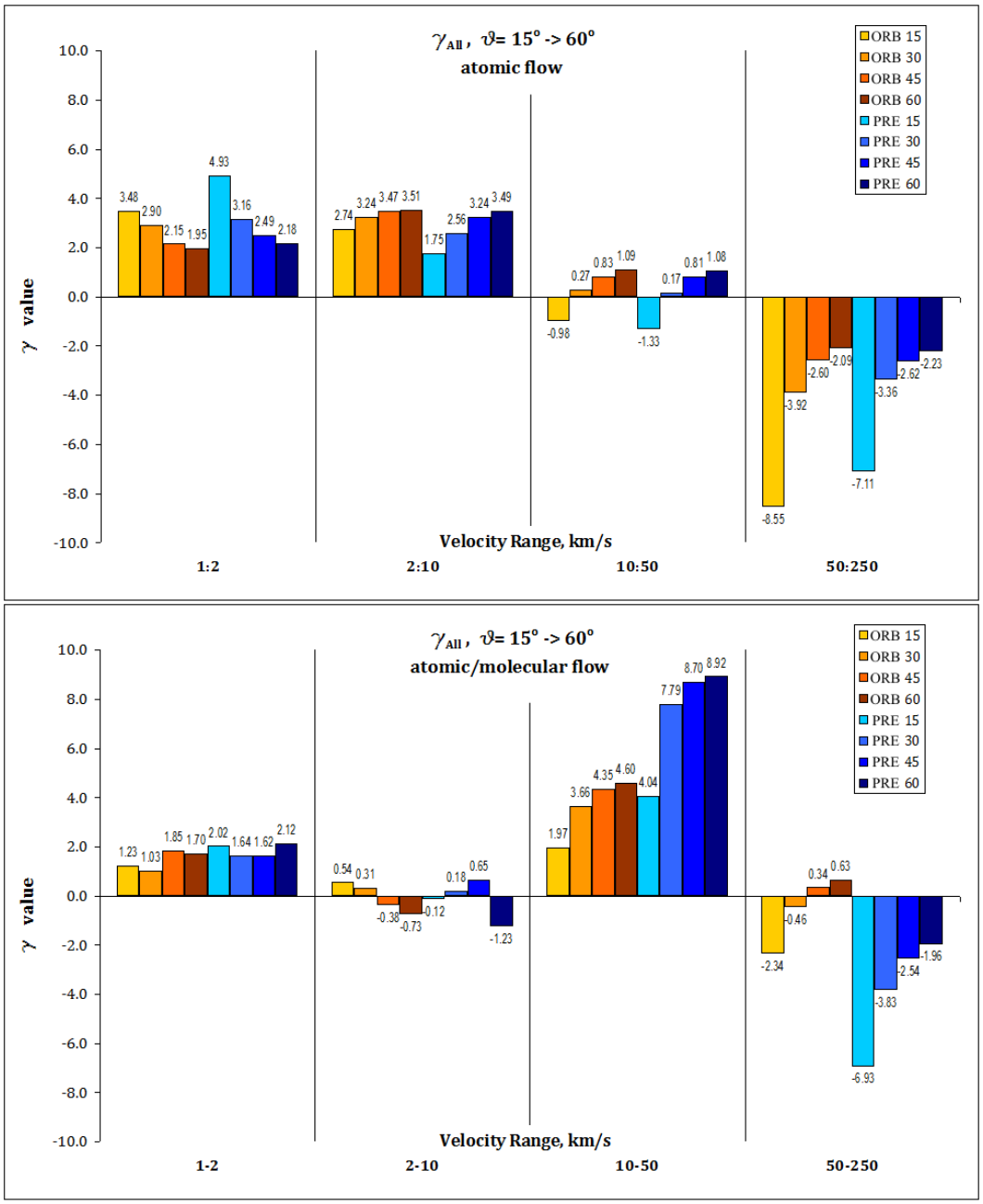

Figure J.12: Graphical comparison of Mass-Velocity spectrum values for blue-shifted material viewed at aspect angles of 15°, 30°, 45°, 60°, using total mass for all species. Bar heights represent γ values at T=87 years . Blue bars are Precessional model values, orange bars are Orbital. Upper plot shows models PRE.1 vs ORB.1; lower plot shows models PRE.2 vs ORB.2

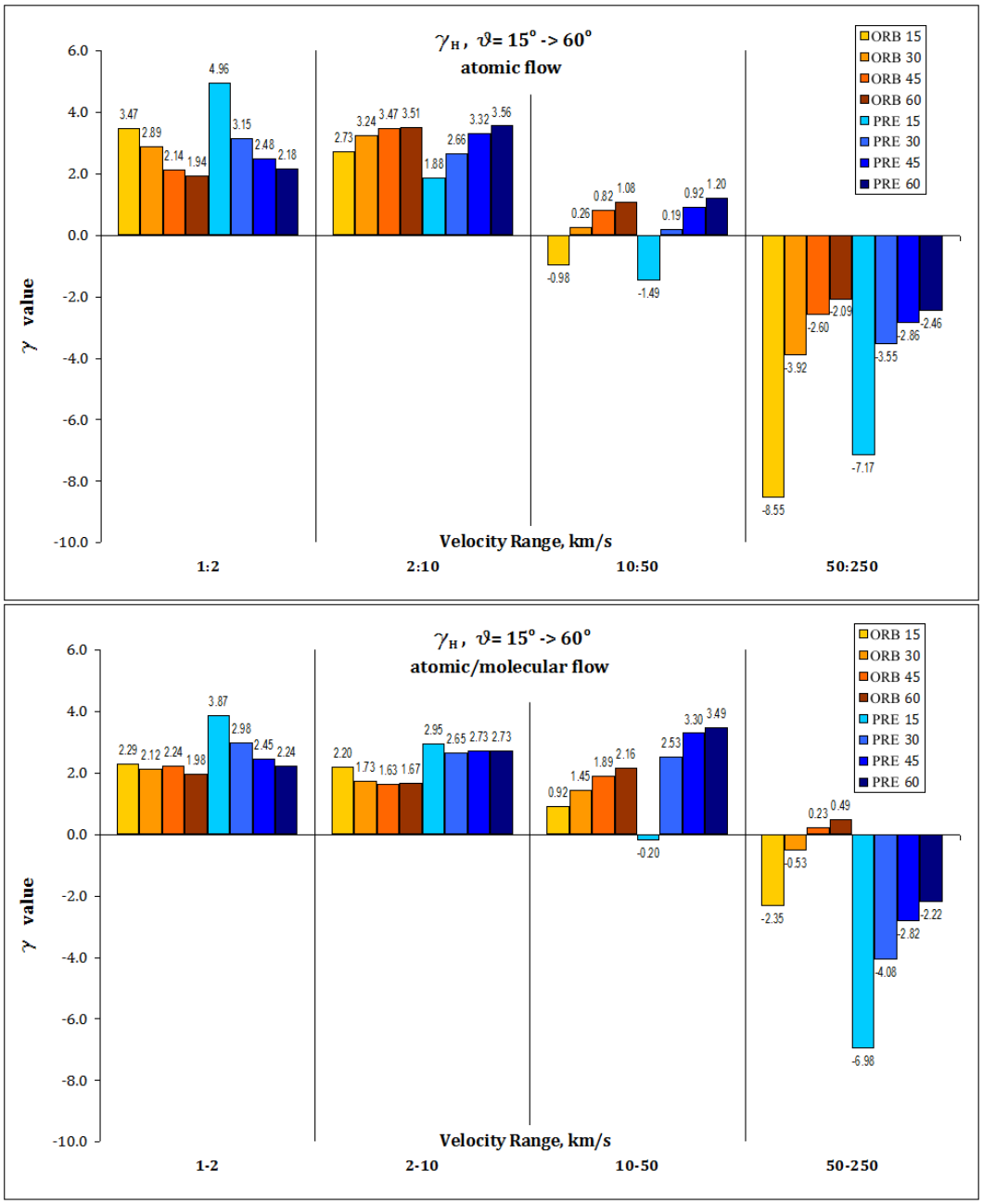

Figure J.13: Graphical comparison of Mass-Velocity spectrum values for blue-shifted atomic Hydrogen viewed at aspect angles of 15°, 30°, 45°, 60°, using total mass for all species. Bar heights represent γ values at T=87 years . Blue bars are Precessional model values, orange bars are Orbital. Upper plot shows models PRE.1 vs ORB.1; lower plot shows models PRE.2 vs ORB.2

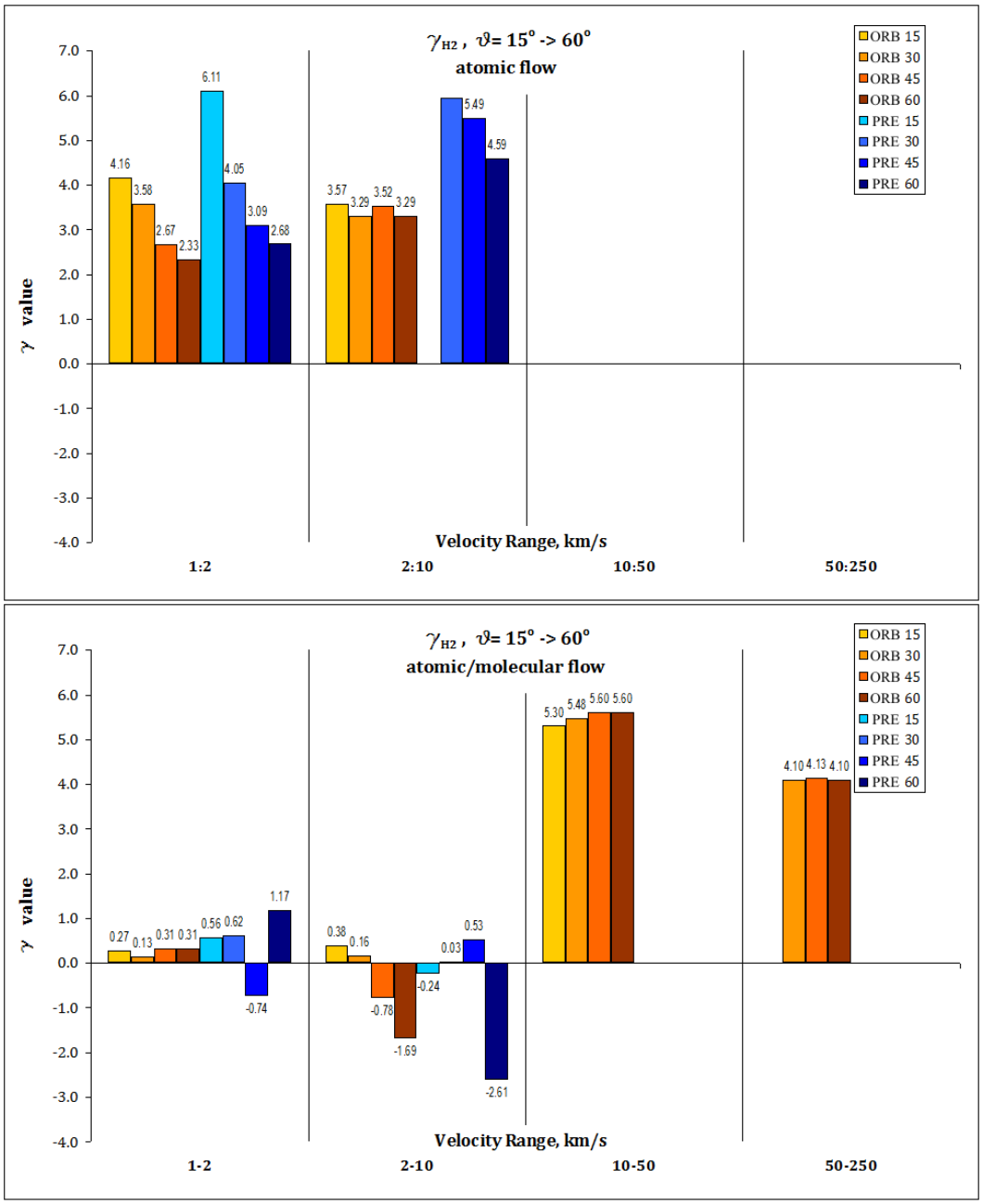

Figure J.14: Graphical comparison of Mass-Velocity spectrum values for blue-shifted molecular Hydrogen viewed at aspect angles of 15°, 30°, 45°, 60°, using total mass for all species. Bar heights represent γ values at T=87 years . Blue bars are Precessional model values, orange bars are Orbital. Upper plot shows models PRE.1 vs ORB.1; lower plot shows models PRE.2 vs ORB.2

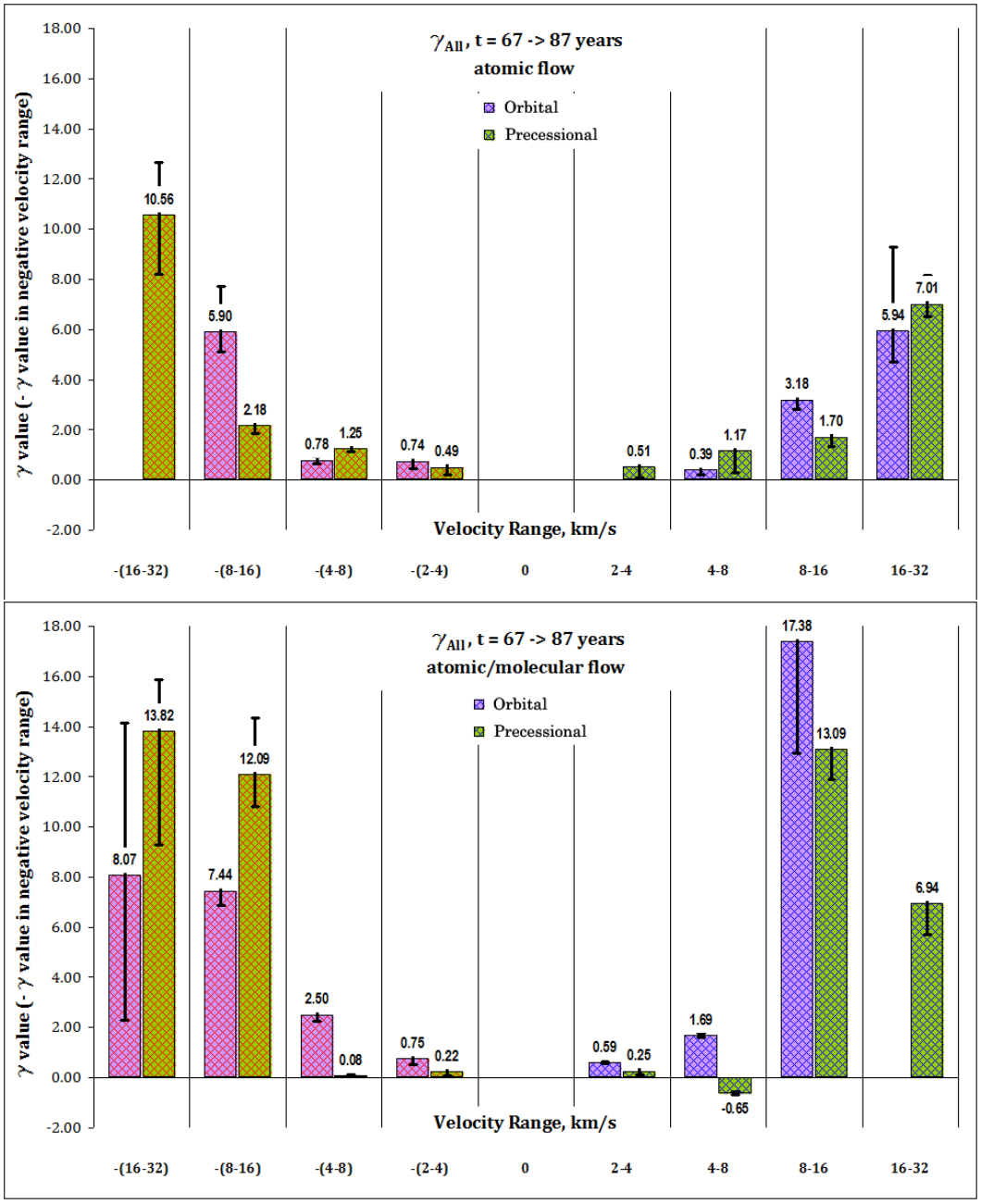

Figure J.15: Graphical comparison of Mass-Velocity spectrum γ values using total mass for all species viewed at aspect angle of 1°. Bar heights represent average γ over a 20-year period. Error bars show max and min values. Upper plot shows models PRE.1 vs ORB.1; lower plot shows models PRE.2 vs ORB.2

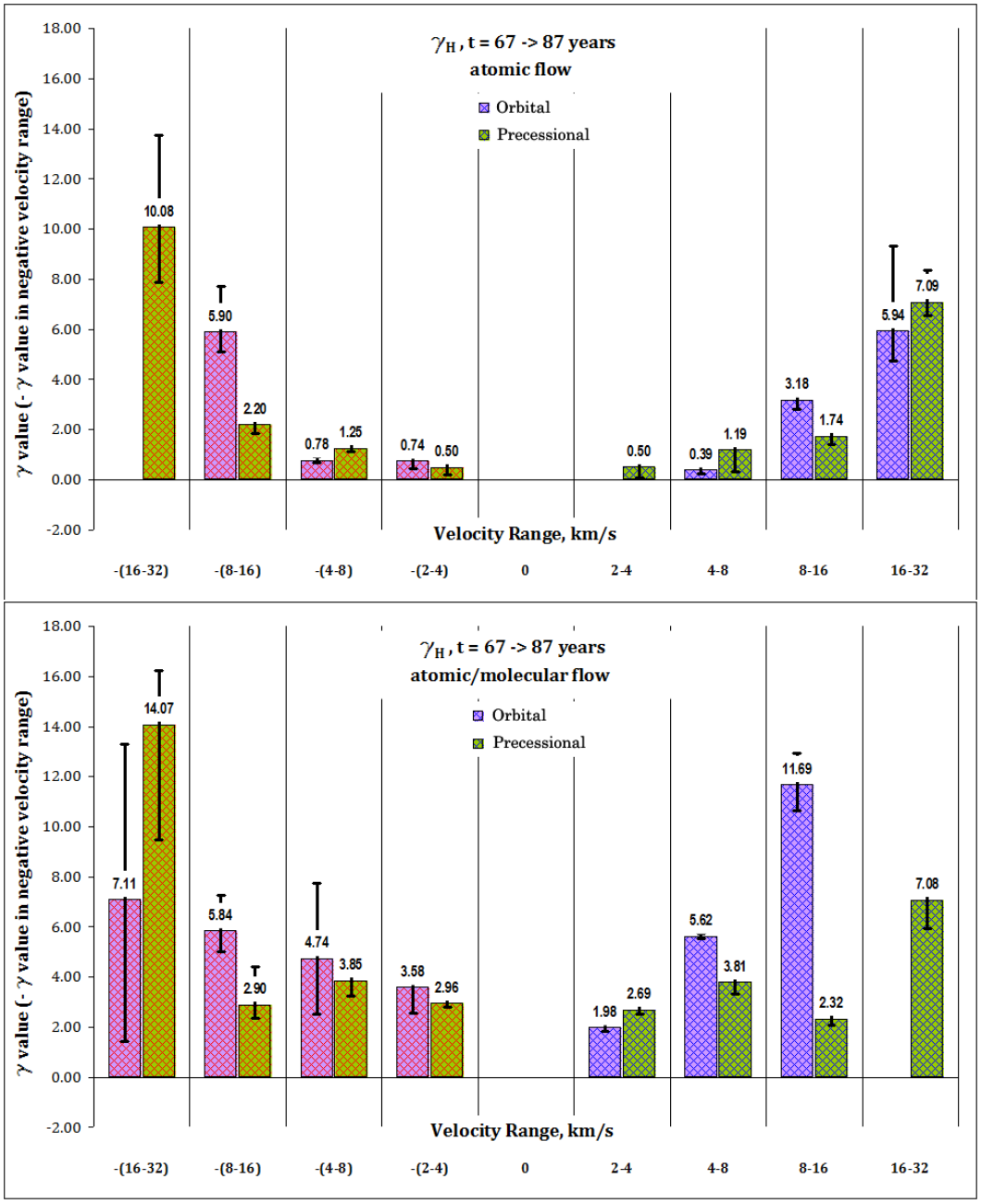

Figure J.16: Graphical comparison of Mass-Velocity spectrum γ values using atomic Hydrogen mass viewed at aspect angle of 1°. Bar heights represent average γ over a 20-year period. Error bars show max and min values. Upper plot shows models PRE.1 vs ORB.1; lower plot shows models PRE.2 vs ORB.2

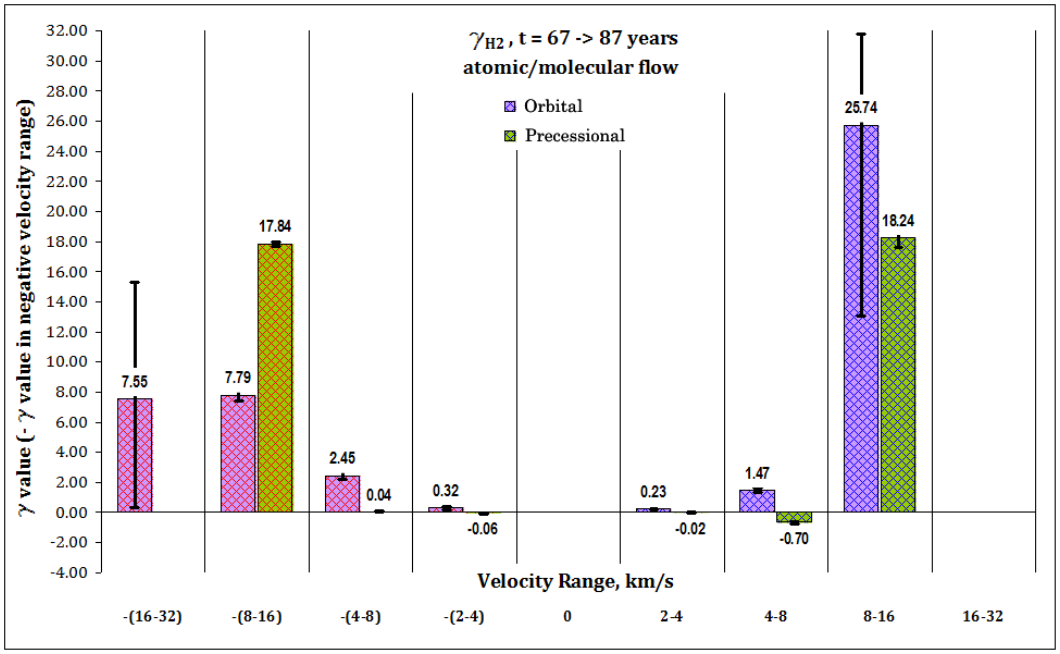

Figure J.17: Graphical comparison of Mass-Velocity spectrum values using molecular Hydrogen mass viewed at aspect angle of 1°. Bar heights represent average γ over a 20-year period. Error bars show max and min values. Single plot shows models PRE.2 vs ORB.2. Molecular Hydrogen, although present in trace amounts, is too sparse in the atomic-only flow models to produce meaningful M-V spectrum plots.